

PROCEEDINGS OF THE 1994 INTERNATIONAL SYMPOSIUM ON

NONLINEAR

SUPERCONDUCTING

DEVICES AND

HIGH-T<sub>c</sub> MATERIALS

Cortina, Italy 8-13 October 1994

Editors

R D Parmentier

N F Pedersen

DISTRIBUTION STATEMENT 1

Approved for public release;  
Distribution Unlimited

World Scientific

# REPORT DOCUMENTATION PAGE

Form Approved OMB No. 0704-0188

Public reporting burden for this collection of information is estimated to average 1 hour per response, including the time for reviewing instructions, searching existing data sources, gathering and maintaining the data needed, and completing and reviewing the collection of information. Send comments regarding this burden estimate or any other aspect of this collection of information, including suggestions for reducing this burden to Washington Headquarters Services, Directorate for Information Operations and Reports, 1215 Jefferson Davis Highway, Suite 1204, Arlington, VA 22202-4302, and to the Office of Management and Budget, Paperwork Reduction Project (0704-0188), Washington, DC 20503.

1. AGENCY USE ONLY (Leave blank)		2. REPORT DATE 17 November 1994		3. REPORT TYPE AND DATES COVERED Conference Proceedings	
4. TITLE AND SUBTITLE Nonlinear Superconducting Devices and High-T <sub>c</sub> Materials				5. FUNDING NUMBERS F6170894W0685	
6. AUTHOR(S) Conference Committee					
7. PERFORMING ORGANIZATION NAME(S) AND ADDRESS(ES) University of Salerno Baronissi I-84081 Italy				8. PERFORMING ORGANIZATION REPORT NUMBER N/A	
9. SPONSORING/MONITORING AGENCY NAME(S) AND ADDRESS(ES) EOARD PSC 802 BOX 14 FPO 09499-0200				10. SPONSORING/MONITORING AGENCY REPORT NUMBER CSP 94-1022	
11. SUPPLEMENTARY NOTES					
12a. DISTRIBUTION/AVAILABILITY STATEMENT Approved for public release; distribution is unlimited.				12b. DISTRIBUTION CODE A	
13. ABSTRACT (Maximum 200 words) The Final Proceedings for Nonlinear Superconducting Devices and High T <sub>c</sub> Materials, 8 October 1994 - 13 October 1994					
14. SUBJECT TERMS Nil				15. NUMBER OF PAGES 478	
				16. PRICE CODE N/A	
17. SECURITY CLASSIFICATION OF REPORT UNCLASSIFIED	18. SECURITY CLASSIFICATION OF THIS PAGE UNCLASSIFIED	19. SECURITY CLASSIFICATION OF ABSTRACT UNCLASSIFIED	20. LIMITATION OF ABSTRACT UL		

NSN 7540-01-280-5500

Standard Form 298 (Rev. 2-89)  
Prescribed by ANSI Std. Z39-18  
298-102

**NONLINEAR**  

---

**SUPERCONDUCTING**  

---

**DEVICES AND**  

---

**HIGH-T<sub>c</sub> MATERIALS**  

---

PROCEEDINGS OF THE INTERNATIONAL CONFERENCE

# NONLINEAR SUPERCONDUCTING DEVICES AND HIGH- $T_c$ MATERIALS

Capri, Italy      8-13 October 1994

Editors

**R D Parmentier**  
(University of Salerno, Italy)

**N F Pedersen**  
(Technical University of Denmark)

19980303 116

DMC QUALITY INSPECTED 3



**World Scientific**

Singapore • New Jersey • London • Hong Kong



---

*Published by*

World Scientific Publishing Co. Pte. Ltd.

P O Box 128, Farrer Road, Singapore 9128

*USA office:* Suite 1B, 1060 Main Street, River Edge, NJ 07661

*UK office:* 57 Shelton Street, Covent Garden, London WC2H 9HE

**NONLINEAR SUPERCONDUCTING DEVICES AND  
HIGH- $T_c$  MATERIALS**

Copyright © 1995 by World Scientific Publishing Co. Pte. Ltd.

*All rights reserved. This book, or parts thereof, may not be reproduced in any form or by any means, electronic or mechanical, including photocopying, recording or any information storage and retrieval system now known or to be invented, without written permission from the Publisher.*

For photocopying of material in this volume, please pay a copying fee through the Copyright Clearance Center, Inc., 27 Congress Street, Salem, MA 01970, USA.

ISBN 981-02-2091-X

Printed in Singapore.

## Preface

The International Conference "Nonlinear Superconducting Devices and High- $T_c$  Materials" took place 8–13 October 1994 in Capri, Italy. Our principal aim in organizing this meeting was to bring together a selected group of theoreticians and experimentalists, with the objective of trying to thrash out some of the outstanding (typically nonlinear) problems that have so far kept many device applications of superconductivity just a bit below the threshold of practical utility, and that have impeded a wider applicability of the new high- $T_c$  superconductors. This volume contains the Invited Papers plus a selection of the Contributed Papers that were presented during the meeting.

Chapter 1 contains two panoramic overviews of the field that were presented as Invited Talks during the meeting, the first by Arthur Davidson and the second by Paul Seidel. Both attempt to outline where we stand today and to indicate directions for future development.

Chapter 2 tackles various aspects of the materials problem. The first paper, presented as an Invited Talk during the meeting by Vladimir Kresin, sets the stage for a theoretical understanding of the various issues at hand. The theoretical context is further developed in the following paper by Golubov *et al.* Andreone *et al.* describe careful experimental measurements of penetration depth, designed to cast light on these fundamental questions. Brizhik presents calculations describing the bisoliton model of superconductivity, pioneered by the Kiev group. Finally, Attanasio *et al.* offer a detailed analysis of experimental data regarding flux motion in high- $T_c$  materials.

In Chapter 3 we move from materials to Josephson junctions. Lazarides and Sørensen extend the tunneling Hamiltonian formalism to the case of junctions made of anisotropic (high- $T_c$ ) materials. Romano *et al.* follow with a description of their experimental efforts to construct and characterize YBCO junctions. Thyssen *et al.* and Monaco *et al.* describe different aspects of the dynamics of 'window' junctions (in the context of the low- $T_c$  technology). Closing this chapter, Shagalov presents a computational model of the behavior of large junctions containing 'defects'.

Chapter 4 is dedicated to problems of nonlinear propagation in junctions that are 'large' in at least one spatial dimension. Yukon and Lin begin by illustrating some unexpected properties of mutually coupled long junctions. Ustinov *et al.* describe the dynamics of collective excitations in a long annular-geometry junction. Jaworski employs the Riemann theta-function formalism to describe the interaction of a long junction with an external microwave field. The papers by Zagrodziński and by Fernandez *et al.* treat two-dimensional junctions; Zagrodziński presents theoretical considerations needed for a consistent description of such structures, and Fernandez *et al.* describe computational and experimental results regarding the so-called Isoperimeter

### Pattern Dynamics.

In Chapter 5 we proceed from junctions to SQUIDs. Rotoli and Carelli describe the current status of an on-going study of Macroscopic Quantum Coherence via an analysis of tunneling in a double-well potential. Darula *et al.* and Chesca consider the analysis of two different SQUID structures containing multiple junctions. On the experimental side, Camerlingo *et al.* report recent progress on the fabrication and characterization of YBCO SQUIDs. Finally, Matarazzo *et al.* present computational and preliminary experimental results on the use of SQUID arrays as microwave generators.

Chapter 6 treats multilayer stacked Josephson junction structures. Hermann Kohlstedt, in his Invited Paper, gives a comprehensive review of recent results on the dynamics of stacked junctions constructed in the context of the low- $T_c$  technology. Barbara *et al.* and Petraglia *et al.* illustrate further aspects of this new and fascinating area. Kondratiev *et al.* develop a simple theoretical model to describe a hitherto unexplained experimental observation regarding the magnetic field diffraction pattern of a multilayer structure. Paul Müller, in a second Invited Paper dedicated to multilayer structures, provides a detailed review of intrinsic Josephson effects in the layered, anisotropic, high- $T_c$  materials. Schlenga *et al.* and Veith *et al.* follow with additional aspects of this exciting topic.

Chapter 7 focusses on arrays of discrete Josephson elements. Miguel Octavio, in his Invited Paper, gives an up-dated review of the dynamics of 'classical' two-dimensional Josephson arrays, *i.e.*, arrays having dimensions such that single-electron effects do not come into play. Further aspects of the dynamics of 2-D arrays are considered in the paper by Filatrella and Wiesenfeld and that by Ciria and Giovanella. The chapter closes with papers by Nuvoli *et al.* and Caputo *et al.* dedicated to an analysis of the static magnetic properties of junction arrays.

Chapter 8 illustrates briefly two experimental diagnostic techniques that are proving to be extremely powerful. Lachenmann *et al.* report on the use of Low Temperature Scanning Electron Microscopy (LTSEM) to study vortex dynamics in two-dimensional Josephson arrays. Holm and Mygind describe their first results on Cryogenic Scanning Laser Microscopy (CSLM), in which a laser beam takes the place of the electron beam used in LTSEM.

Chapter 9 gives a small sampling of the multi-faceted area of electronic applications. The first paper, presented during the meeting as an Invited Talk by Valery Koshelets, reviews the recent progress that has been obtained in the development of integrated flux-flow oscillators for sub-millimeter-wave receivers. The following paper by Shchukin *et al.* contains the very latest, up to the minute results in this area. The next paper, presented as an Invited Talk by Vsevolod Kaplunenko, reviews important aspects of Rapid Single Flux Quantum (RSFQ) logic. Pagano *et al.* illustrate a promising new approach for the detection of energetic particles using a tapered long Josephson junction. Another aspect of the particle detection problem, the use of NbN/Nb trapping bilayers to improve detection performance, is reported by Parlato

*et al.* Hebrank *et al.* describe the design and fabrication of a new type of hybrid integrated Josephson voltage standard. Finally, B. Davidson *et al.* present the latest results of the Madison group on high- $T_c$  Vortex Flow Transistors.

Acknowledgements:

The participation in this conference of a number of young European researchers was made possible by a grant from the European Union through its Human Capital and Mobility Program (contract number ERB-CHEC-CT93-0101). The active support and patronage of the University of Salerno, the SAT Project of the Consorzio INFM of Italy, the Istituto Italiano per gli Studi Filosofici (Napoli), and the Italian National Project "Superconductive and Cryogenic Technologies" of the CNR are deeply appreciated. We wish to thank the United States Air Force European Office of Aerospace Research and Development and the United States Army European Research Office for their contribution to the success of this conference. Finally, we are grateful to the International Science Foundation for a travel grant (number 4321) that has enabled also a limited participation by scientists from the former Soviet Union.

The high level of the scientific content of the meeting was guaranteed by the efforts of the Scientific Committee: Antonio Barone, Peter Leth Christiansen, Robert Dana Parmentier, Niels Falsig Pedersen, and Mads Peter Sørensen.

Finally, no scientific conference can succeed without the dedicated and tireless work of its Conference Secretariat, and in particular, this meeting in Capri would have been impossible without the substantial labors of Annamaria Mazzarella.

*Robert D. Parmentier*  
*Niels F. Pedersen*  
December 1994

## Contents

<b>Preface</b> .....	<b>v</b>
<b>Chapter 1 – Overview</b> .....	<b>1</b>
Progress in HTS Electronics .....	3
<i>A. Davidson, S. H. Talisa, M. G. Forrester, J. Talvacchio,</i> <i>J. Gaveler, M. A. Janocko</i>	
High- $T_c$ Josephson Junctions, dc-SQUIDs and Arrays .....	19
<i>P. Seidel</i>	
<b>Chapter 2 – Materials Issues</b> .....	<b>37</b>
Energy Spectrum in the High- $T_c$ Oxides .....	39
<i>V. Z. Kresin, S. A. Wolf, S. D. Adrian, M. E. Reeves</i>	
Strong Coupling Effects in <i>s</i> -Wave Two Band Superconductor .....	49
<i>A. A. Golubov, O. V. Dolgov, E. G. Maksimov, I. I. Mazin, S. V. Shulga</i>	
Measurement of the Electrodynamic Properties of High Temperature Superconducting Films .....	57
<i>A. Andreone, A. Cassinese, C. Cantoni, A. Di Chiara,</i> <i>F. Miletto Granozio, R. Vaglio</i>	
Doping and Pressure Influence on the Critical Temperature in the Frame of the Bisoliton Model of Superconductivity .....	67
<i>L. Brizhik</i>	
Flux Motion in HTSC: the Role of Washboard-Type Pinning Potential .....	75
<i>C. Attanasio, L. Maritato, C. Coccorese, S. L. Prischepa, M. Salvato</i>	
<b>Chapter 3 – Josephson Junctions</b> .....	<b>89</b>
Josephson Tunneling in SIS Junctions Made of Anisotropic Superconductors .....	91
<i>N. Lazarides, M. P. Sørensen</i>	
Planar Tunnel Junctions on $YBa_2Cu_4O_8$ .....	101
<i>P. Romano, A. M. Cucolo, R. Di Leo, A. Nigro, P. G. Radaelli</i>	
Fluxon Resonances in Window-Type Long Josephson Junctions: Experiment and Numerical Simulations .....	107
<i>N. Thyssen, A. V. Ustinov, H. Kohlstedt, J. G. Caputo,</i> <i>S. Pagano, N. Flytzanis</i>	

Fiske Resonances in Window Josephson Tunnel Junctions .....	115
<i>R. Monaco, G. Costabile, N. Martucciello</i>	
Critical Phenomena in Large Area Josephson Junctions with Defects .....	125
<i>A. G. Shagalov</i>	
<b>Chapter 4 – Nonlinear Propagation .....</b>	<b>135</b>
Fractional Fluxon Excitations in Coupled	
Long Josephson Junction Arrays .....	137
<i>S. P. Yukon, N. C. H. Lin</i>	
Simulation of Collective Excitations in a Modulated Josephson Ring .....	149
<i>A. V. Ustinov, A. Shnirman, Z. Hermon, E. Ben-Jacob, B. A. Malomed</i>	
Josephson Junction Irradiated with External rf Field – Some	
Nonlinear Effects .....	157
<i>M. Jaworski</i>	
Vortices in Continuous Josephson Medium .....	165
<i>J. Zagroźniński</i>	
Solitary Waves in 2-D Josephson Tunnel Junction .....	173
<i>J. C. Fernandez, T. Doderer, G. Filatrella,</i>	
<i>R. P. Huebener, S. G. Lachenmann</i>	
<b>Chapter 5 – SQUIDS .....</b>	<b>189</b>
Tunnelling in a Double-Well SQUID Potential .....	191
<i>G. Rotoli, P. Carelli</i>	
Phase Locking and Voltage - Flux Dependencies in Arrays	
of Josephson Junctions Closed in a Superconducting Loop .....	201
<i>M. Darula, A. Darulova, P. Seidel, Š. Beňacka, B. Mišanik</i>	
Double SQUID Behavior in Superimposed rf and dc Magnetic Fields .....	209
<i>B. Chesca</i>	
YBCO Bicrystal dc SQUIDS by Inverted Cylindrical Magnetron .....	217
<i>C. Camerlingo, H. Huang, B. Ruggiero, M. Russo,</i>	
<i>E. Sarnelli, G. Testa</i>	
High $T_c$ SQUID Arrays as Microwave Generators .....	227
<i>S. Matarazzo, S. Pagano, G. Filatrella, S. Barbanera, F. Murtas,</i>	
<i>C. Romeo, V. Boffa, F. Gatta, U. Gambardella</i>	

<b>Chapter 6 – Multilayer Structures .....</b>	<b>235</b>
Stacked Nb–Al/AlO <sub>x</sub> –Nb Josephson Tunnel Junctions .....	237
<i>H. Kohlstedt</i>	
Fluxon Dynamics in Stacked Long Josephson Junctions: Experiments and Numerical Simulations .....	257
<i>P. Barbara, J. Mygind, N. F. Pedersen, G. Costabile, A. D’Anna, R. D. Parmentier, B. A. Malomed</i>	
Dynamics in Stacked Josephson Structures .....	265
<i>A. Petraglia, N. F. Pedersen, A. V. Ustinov</i>	
Magnetic Field Diffraction Pattern in Multilayered Josephson Junctions ....	271
<i>V. L. Kondratiev, R. Vaglio, A. A. Varlamov</i>	
Intrinsic Josephson Effects in Layered Superconductors .....	277
<i>P. Müller</i>	
Intrinsic Josephson Junctions in Layered Superconductors as High Frequency Sources .....	297
<i>K. Schlenga, G. Hechtfisher, W. Walkenhorst, P. Müller, M. Veith, W. Brodkorb, E. Steinbeiss</i>	
Intrinsic Thin Film Tl–Ba–Ca–Cu–O Step Stack Josephson Junctions .....	305
<i>M. Veith, T. Eick, W. Morgenroth, W. Brodkorb, T. Köhler, L. Redlich, H.-G. Schmidt, E. Steinbeiss, H.-J. Fuchs, K. Schlenga, P. Müller</i>	
<b>Chapter 7 – Junction Arrays .....</b>	<b>313</b>
Dynamics of Classical Two-Dimensional Josephson Arrays .....	315
<i>M. Octavio</i>	
Two-Dimensional Josephson Junction Arrays in the Presence of a Magnetic Field .....	329
<i>G. Filatrella, K. Wiesenfeld</i>	
Dynamics in Complex RSJ Superconducting Systems: from Discretized Large Junctions to 2-D Arrays. A Microscopic View .....	337
<i>J. C. Ciria, C. Giovannella</i>	
Full Matrix Inductance and “Experimental” Protocols: Two Key Aspects in the Determination of the Static Magnetic Properties of 2D Arrays of Superconducting RSJ .....	347
<i>A. Nuvoli, A. Giannelli, J. C. Ciria, C. Giovannella</i>	
Positive Field Cooled D.C. Susceptibility in Josephson Junction Networks ..	355
<i>P. Caputo, G. Costabile, R. De Luca, S. Pace, A. Saggese</i>	

<b>Chapter 8 – Diagnostic Techniques .....</b>	<b>363</b>
Novel Vortex Dynamics in Two-Dimensional Josephson Arrays .....	365
<i>S. G. Lachenmann, T. Doderer, R. P. Huebener, P. A. A. Booij, S. P. Benz</i>	
In-Situ Spatially Resolved Investigations of Josephson Structures with a Scanning Laser Microscope .....	373
<i>J. Holm, J. Mygind</i>	
<b>Chapter 9 – Electronic Applications .....</b>	<b>381</b>
Integrated Flux Flow Oscillators for Sub-mm Wave Receivers .....	383
<i>V. P. Koshelets, S. V. Shitov, A. V. Shchukin, L. V. Filippenko, I. L. Lapitskaya</i>	
Submillimeter Wave Radiation Emission from Flux Flow Oscillators .....	403
<i>A. V. Shchukin, V. P. Koshelets, J. Mygind</i>	
Nonlinear Phenomena in RSFQ Logic Devices .....	411
<i>V. Kaplunenko, J. Mygind, N. F. Pedersen, V. Koshelets, T. Doderer</i>	
A Long Josephson Junction-Based Device for Particle Detection .....	437
<i>S. Pagano, C. Nappi, R. Cristiano, E. Esposito, L. Frunzio, L. Parlato, G. Peluso, G. Pepe, U. Scotti Di Uccio</i>	
NbN/Nb Bilayers for STJ Particle Detectors .....	451
<i>L. Parlato, G. Peluso, G. P. Pepe, U. Scotti Di Uccio, R. Cristiano, E. Esposito, L. Frunzio, S. Pagano, H. Akoh, H. Nakagawa, S. Takada</i>	
Development of a Hybrid Integrated Josephson Voltage Standard .....	461
<i>F. X. Hebrank, E. Vollmer, P. Gutmann, F. Müller, J. Niemeyer</i>	
Discrete Vortex Flow Transistors using Electron-Beam Scribed Josephson Junctions in YBCO .....	469
<i>B. A. Davidson, R. D. Redwing, T. Nguyen, J. E. Nordman</i>	



---

## Chapter 1

# Overview

## PROGRESS IN HTS ELECTRONICS

A. DAVIDSON, S.H. TALISA, M.G. FORRESTER, J. TALVACCHIO, J. GAVALER,  
and M.A. JANOCKO

*Westinghouse Science and Technology Center  
Pittsburgh, PA 15235  
USA*

### ABSTRACT

This paper will cover HTS applications becoming available in the near term, and the need for future development. Passive microwave filters and resonators constructed out of single layer HTS depositions are now becoming available. SQUID's and receiver components such as local oscillators and mixers are further away from commercial impact because they require the reliable formation of Josephson junctions. Finally, digital circuits are discussed, which will require junctions with tight tolerances, and a multi-level HTS technology. At the end there will be a brief discussion of the problems of matching superconductivity to the needs of the real world, using radar as an example.

### 1. Introduction

Electronic applications of HTS technology can be arranged in a hierarchy from simple passive devices to complex integrated circuits, as shown in Fig. 1. At the same time, the technology required for these applications can also be arranged according to increasing difficulty. Thus, microwave filters and delay lines that require only a single layer of HTS material, are already in an advanced state of development, while functional digital integrated circuits are just beginning

to get somewhere in the laboratory. Microwave filters that use a single level (or at most an HTS coating on front and back of a substrate) have been produced by several laboratories.<sup>1-3</sup> One small company in the US has traded public stock on a plan to sell such devices to cellular communications providers. Research has also shown that competitive SQUID's can be produced with a single layer of HTS, including the junctions and pick-up loop, and such SQUID's are on the market.<sup>4</sup> Much better

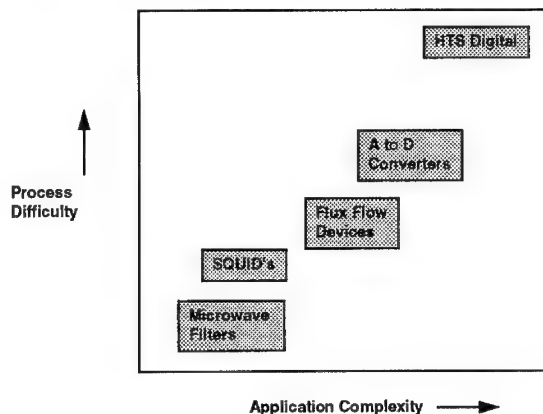


**Figure 1.** Schematic representation of the process difficulty and application complexity of different superconductive electronic devices. The Application complexity should be thought of as the minimum necessary for commercial success.

SQUID's will require multi-level processing to get the best coupling between SQUID and magnetic field.

Millimeter wave radio receivers are presently a challenge for HTS, since there is nothing yet available at high temperature that is comparable to SIS tunnel junctions. Some work on flux flow oscillators<sup>5</sup>, however, is promising for use in local oscillators. Analog-to-digital-converter circuit designs exist that can use the type of over damped junctions that have been demonstrated in HTS technology,<sup>6</sup> but the designs are ahead of the fabrication capability. These and more complex digital<sup>7</sup> circuits require the full development of an HTS multilayer technology. Junctions must be developed that can use isotropic fabrication methods. Tight control of critical currents is essential. Circuits and devices to shift levels to accommodate semiconductor components are necessary. These level shifting circuits are particularly important for the RSFQ type of digital circuit, since these operate with individual flux quanta, which make pulses too weak for direct detection with semiconductors.

The problem most in need of work is the development of an isotropic process for making Josephson junctions. In other words, we need a process that will make junctions facing in at least the four directions defined by the edges of a square, simultaneously and reproducibly. Many of the best junctions produced so far do not meet this condition, since they involve some amount of directionality. Fused substrate<sup>8</sup> grain boundary junctions all face the same way and must be produced along a straight line. Step edge SNS junctions<sup>9</sup> are usually produced with an angled deposition of the normal metal. The step edge junction is a candidate, as well as the step edge grain boundary type.<sup>10</sup>

At the end, the issue of coupling basic research to commercial application will be addressed. It is important to find a customer for the research early in the process. The Westinghouse CRYORADAR<sup>TM</sup> project will be used as an example.

## 2. Films

The presently preferred methods for depositing high quality thin films of YBCO are sputtering<sup>11</sup> and laser ablation.<sup>12</sup> These methods both involve transport of material from a stoichiometric target to a heated substrate. In ablation this transport is accomplished by focusing a nanosecond scale laser pulse of sufficient energy onto a stoichiometric target. The pulse heats the target immediately under the surface, vaporizing it, and causing an explosive discharge of material perpendicular to the target surface. Some of the ejected material is energetic enough to be in the form of a plasma; some is apparently in the form of particles and droplets. A heated substrate a few centimeters away collects the material to build up a film. Laser ablated films are typically of high quality, with excellent stoichiometry, and good superconductive parameters. Work is progressing to improve surface roughness, and to handle larger (>5 cm) wafers. The deposition rate for small wafers, however is fairly rapid, typically a few Å/s.

The sputtering method is slower than ablation, often in the range of 0.1 Å/s, but easier to scale up to large wafers, with 5 cm diameters common, and 10 cm under

development. The most common kind of sputtering is with RF magnetron systems, using an off-axis geometry. In the off-axis arrangement, the substrates are orthogonal to the target, and usually off to the side, to avoid direct bombardment by negative oxygen ions, which can come from either the sputter gas or the target itself, and which are energetically emitted from the target. Under conditions which minimize resputtering from hot surfaces in the vicinity of the substrate, sputtered YBCO films were the first to be grown without the presence of CuO precipitates. Smooth films resulting from the elimination of CuO particles have also been produced by laser ablation by employing an off-axis configuration.<sup>13</sup> The off-axis configuration reduces the high-deposition-rate advantage of laser ablation compared to sputtering. The ultimate importance of uniform deposition on large wafers should be emphasized. For this purpose other deposition techniques such as MOCVD<sup>14</sup> may prove to be the best technique.

Choice of substrate is extremely important to the successful completion of useful circuits. A  $\text{SrTiO}_3$  substrate<sup>15</sup> can be used to grow very high quality films, but with an extraordinarily high dielectric constant, which rules it out for any high speed applications.  $\text{LaAlO}_3$ <sup>16</sup> has a much lower dielectric constant, approximately 24, and has been used successfully for single layer applications, such as microstrip or co-planar microwave filters and delay lines. It has not worked so well for multi-layer circuits, however, because of motion of twin boundaries<sup>17</sup> when the wafer is heated for deposition of new HTS layers. The moving twins can shift the bottom film layers by several microns over the width of even a one centimeter chip, making alignment of subsequent layers impossible. At the moment,  $\text{NdGaO}_3$ <sup>18</sup> appears to be the substrate of choice for multilayer circuits. It has a low dielectric constant, similar to  $\text{LaAlO}_3$ , but without the shifting twins.

Consideration of multi-layer structures also determines the choice of HTS film material. The materials with the highest  $T_c$ 's are TBCCO, and, recently,  $\text{HgBCCO}$ ,<sup>19</sup> but their lack of stability means that for now there is no way to produce multiple levels. YBCO has

proven to have the best combination of transition temperature and superconductive properties, and with enough stability so that subsequent layers can be formed without degradation of prior layers.

In addition to superconducting films, epitaxial insulating films are required in multilayer superconducting circuits for isolation of ground planes, crossovers, lumped-element capacitors and inductors, and flux transformers. Epitaxial growth is not necessarily required to obtain

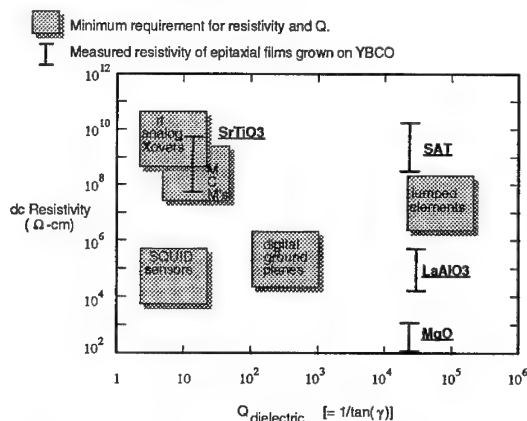


**Figure 2.** Comparison of different possible insulators for HTS multi-level film growth.

desired properties for the insulator but is necessary to support growth of subsequent high-quality superconducting film layers. Fig. 2 summarizes the dielectric loss properties of various thin-film dielectrics studied at Westinghouse in comparison with minimum requirements estimated for several applications. The loss tangent is based on data from bulk samples and the dc resistivity at 77K was measured on parallel-plate capacitor structures with YBCO on the bottom or on both sides. Both the  $\text{SrTiO}_3$  and  $\text{Sr}_2\text{AlTaO}_6$  (SAT)<sup>20</sup> grew as pinhole-free films but SAT appears to be the better choice for most applications based on lower values of both the real and imaginary parts of its dielectric constant.

### 3. Passive Microwave Devices

Passive microwave devices that use a single layer of HTS material (or at most a single layer on each side of a wafer) are very advanced in development, and will soon be tried in prototype applications. The basic system that stands to profit from passive superconductive microwave components is in sophisticated radio receivers, especially those used in cellular telephone base stations, and in radar.

A receiver with components at 77 K is shown in Fig. 3. The preselection filter, the local oscillator, and the detection and signal processing components can all profit from HTS technology. As an example of the benefits of cryogenic operation, consider the preselection filter.

Front end preselection is important in many microwave receiver applications, in order to partition the operational bandwidth into smaller bands. This has the advantage of rejecting unwanted signals that might interfere with the receiver's operation and prevent saturation of the low-noise-amplifier by those unwanted signals, resulting in degraded performance. Also, front-end filtering can simplify the receiver's architecture by reducing the filtering requirements after mixing, to eliminate unwanted mixing products. However, if the preselector filter has a high insertion loss, the receiver noise figure will be adversely affected, resulting in unacceptable system performance for some applications.

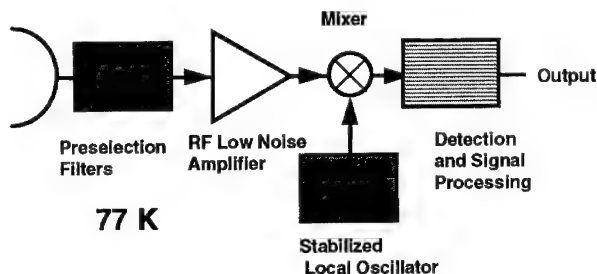
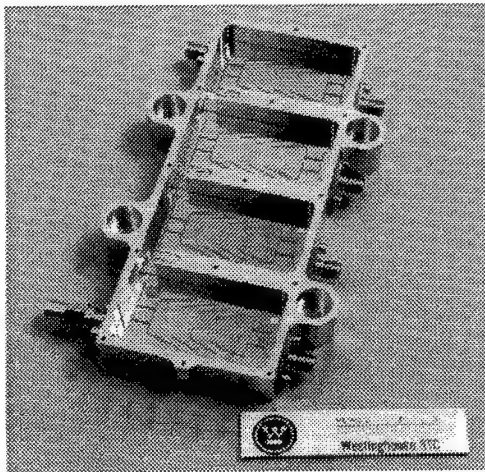


Figure 3. Typical receiver configuration. Note that the shaded boxes represent cryogenic components.



**Figure 4.** A view of the assembled thin film microstrip filter bank, with cover removed.

Filters constructed of HTS materials offer the advantage of very low loss in a relatively small volume over a wide range of frequencies. In addition, the noise figure for a cryogenic filter is lower than its insertion loss because of the low operating temperature (77 K or less for YBCO filters). This makes HTS filters ideal for front-end preselection applications.

A description of a Westinghouse HTS four-channel filterbank is described in ref. 1.

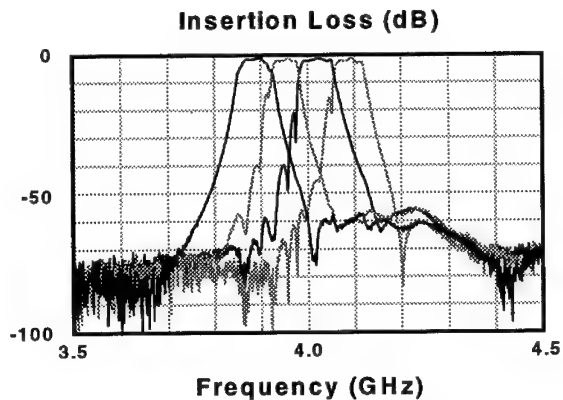


**Figure 5.** Composite showing the insertion loss of each channel of the device shown in Fig. 4.

A view of the packaged filters is shown in Fig. 4. These devices were formed on a 2 inch  $\text{LaAlO}_3$  wafer coated on one side with a  $\text{YBa}_2\text{Cu}_3\text{O}_8$  film, with a gold ground plane on the other. A measurement of the four passbands is shown in composite in Fig. 5. Insertion loss was less than 2 dB, for 50 MHz bands, with 16 MHz guard bands. There was less than 0.1 dB of ripple in the pass bands. Use of double sided superconducting wafers would reduce the insertion loss to less than 1 dB, and it is believed that improvements to the packaging method would cut insertion loss even more.

#### 4. Flux Flow Devices

Flux flow devices divide into two natural categories: those in which the vortices move down a long Josephson junction, and those in which they move across a thin film. The first type is often called a Josephson flux flow device, and the second an Abrikosov device. The Josephson type has the advantage of minimal pinning, but is limited to low voltages by its one dimensional nature. The Abrikosov device allows a two dimensional array of vortices to flow across the channel, and so is potentially higher voltage, but pinning is much more of a problem, and the interaction of the vortex core with the film will lengthen the vortex transit time. The original idea of flux flow amplifiers goes back to the work of Likharev<sup>21</sup>, Van Zeghbroeck<sup>22</sup>, and of McGinnis<sup>23</sup> et al. The Nordman-Beyer group has been leading in this area, having explored flux flow in LTS long Josephson junctions, using them for low noise wide band amplifiers, and also having studied fluxoid motion in HTS films. This and other work<sup>24</sup> has established these devices as high speed amplifiers with many desirable properties. Van Zeghbroeck's Josephson flux flow device is shown in Fig. 6. It originally achieved a current gain of nearly 10, and a transresistance of about 0.5 Ohm.

Josephson flux flow devices have operated as three terminal amplifiers with gain, isolation, saturation, and non-latching behavior. As such, they could function as the active device in logic and memory circuits. Their low output voltage, however, limits their applicability in interface and semiconductor driver circuits. Abrikosov devices are potentially very promising for these interface circuits, but gain and high transresistance in these devices has not yet been observed. On the other hand, Abrikosov flux flow is a mode of operation which is easier in HTS technology than in LTS. The higher temperature of operation and the natural granularity of the films, together with their very short coherence lengths makes flux pinning usually less strong than in most LTS superconducting films. The combination of the right geometry and film orientation and granularity is likely to lead to success.

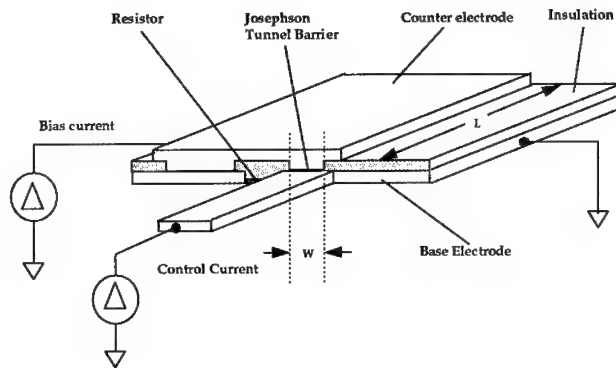


**Figure 6.** Van Zeghbroeck's flux flow transistor.  $L$  and  $W$  are the junction length and width, respectively. Typical dimensions were a few hundred  $\mu\text{m}$  and about  $3\ \mu\text{m}$ .

Long LTS junctions in the flux flow regime have been studied for use as submillimeter wave oscillators. There have already been demonstrations<sup>25</sup> of flux flow oscillators delivering the order of microwatts at frequencies as high as 600 GHz, with  $Q$ 's approaching  $10^6$ . By varying an applied magnetic field for frequency tuning, and varying the current bias for power adjustments, these devices can be tweaked for optimal SIS mixer performance.

An Abrikosov device, made with bulk YBCO ceramic, is shown in Fig. 7. This device was made by filing down a 1 cm long by 2 mm square cross section bar of ceramic. Leads were attached using pressed indium dots, and a copper coil was wound around it to supply

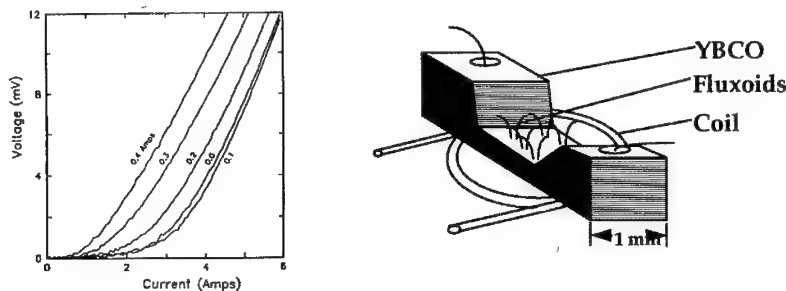


**Figure 7** Macroscopic Abrikosov Vortex Flux Flow Device, showing large current gain. The geometry produces a very low transresistance.



the magnetic flux. Current gain was again achieved, even with this very crude device, although the impedance was so low (due to the macroscopic dimensions of the device) that the transresistance was in the low  $10^{-3}$  Ohm regime. To date, no one has shown reproducible current gain in a thin film version of the Abrikosov flux flow transistor.

A geometry that would be favorable for increasing gain and transresistance is shown in Fig. 8. This is the tetrode configuration. The idea is to keep as much bias current as possible flowing through the edge of the film where fluxoids nucleate. In the tetrode this is accomplished by dividing the device bias current in two. One part, not directly connected to the load, is injected into the device near the nucleation region, and is kept constant. The other part is allowed to vary due to current sent to the load. Simulations of this structure<sup>26</sup> have shown promising improvements in current modulation depth, current gain, and transresistance. This work shows that the geometry of flux flow devices is very important to their operation, and needs further exploration.

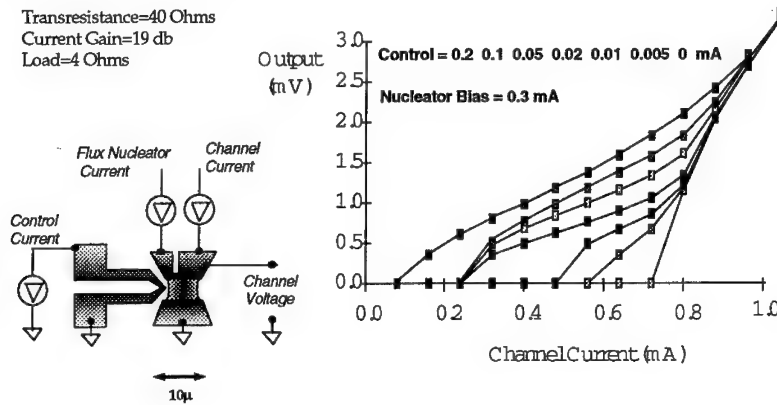


**Figure 8.** Geometric configuration and simulated characteristics for a tetrode structure device.

An important use for Abrikosov flux flow devices is in the interface circuits that will have to match RSFQ outputs to room temperature semiconductors. State of the art transistor comparators can make decisions at a 5 GHz rate based on a 15 mV signal<sup>27</sup>. 5 GHz is well within the capability of Josephson flux flow transistors, but possibly trouble some for Abrikosov devices. A simple two-fluid expression for vortex velocity is:

$$v = \frac{\rho J \lambda^2}{\phi_0} \quad \text{Eq. 1}$$

were  $v$  is the vortex velocity,  $\rho$  the YBCO resistivity,  $\lambda$  the London penetration depth, and  $\phi_0$  the fluxoid quantum,  $2.07 \times 10^{-15}$  Weber. For a current density of  $10^5$  A/cm<sup>2</sup>, a penetration depth of  $0.2 \mu\text{m}$ , and  $10^{-3}$  Ohm-cm<sup>2</sup> resistivity, this works out to a velocity of  $0.2 \mu\text{m/psec}$ , which would allow at least 20 GHz response for a  $10 \mu\text{m}$  long device. In a homogeneous single crystal film  $\rho$  may be a lot smaller, due to non-equilibrium effects that create excess quasiparticles in the moving vortex core. In real films, however, grains are only a few tenths of a micron in size, and vortex motion in a weak pinning film is likely to be confined to grain boundaries. This would limit the production of excess quasiparticles and tend to favor the high velocities. Reproducible experiments are needed to answer this question of speed.

## 5. SQUID's

HTS SQUID's are expected to have numerous applications in medical diagnostics and in Non Destructive Evaluation<sup>28</sup> (NDE). However, almost all HTS SQUIDS made presently rely on a single HTS deposition to form the SQUID loop. The coupling coil is either an HTS film deposited on a separate substrate, or a layer of gold or silver deposited over the insulated HTS SQUID. Optimal performance will require an HTS film deposited on an epitaxial insulator grown over the SQUID loop itself.

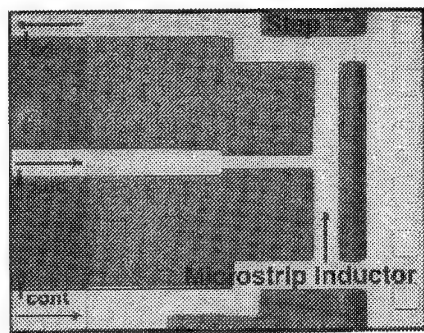


**Figure 9a.** Micrograph of Westinghouse multilevel SQUID. The microstrip inductor was  $10 \mu\text{m}$  wide and  $50 \mu\text{m}$  long, over  $2000 \text{ A}$  of insulated ground plane.

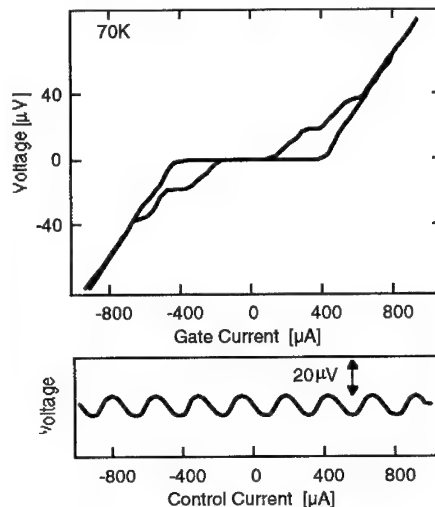


**Figure 9b.** top--Current-voltage characteristic of this device at 0 and  $\phi_0/2$  flux bias. bottom--Voltage vs  $\phi$  measurement. At  $77 \text{ K}$ , the inductance per square was about  $1.5 \text{ pH}$ .

This multilevel requirement has been explored recently. Forrester<sup>29</sup>, et al, constructed a SQUID over a ground plane, with the step-edge grain boundary junctions connected to ground, and one part of the SQUID loop in the form of a microstrip line over ground. By directly injecting and extracting current from this microstrip segment while simultaneously measuring the SQUID periodicity, the inductance of the microstrip could be measured as a function of temperature. Inductances A view of the device and inductance measurement is shown in Fig. 9a. This work clearly shows the feasibility of multilevel HTS structures, for SQUIDs and other applications, but it has not yet been translated into practical SQUID structures, nor have the junctions been perfected. Step-edge grain boundary junctions are adequate for producing small numbers of SQUID's, but not sufficient for the production of more complex digital circuitry.

## 6. Digital Circuits

Digital circuits are both the most demanding in terms of process requirements, and have the biggest potential payoffs in applications. If the multilevel HTS process can be extended to at least 7 layers of superconductor and insulator, and if a compatible and reproducible junction fabrication method can be devised, then production of working digital circuits will be feasible, and various applications will open up.

It may be impossible with HTS materials to make a classical Josephson junction, with low sub gap leakage and a strong current step at the gap. The trouble stems from a combination of extreme anisotropy due to the layered nature of HTS superconductors, and their very short coherence lengths (roughly 3 to 30 Angstroms). This means that superconductivity, and hence the Josephson effects, are suppressed at almost all interfaces of these materials. Usable junctions, however, have been made in some clever ways.

For electronics the most promising method is the edge junction<sup>30</sup>, where some property or configuration is altered where a superconductive film goes up over an edge of an underlying film. In some cases, a thin normal metal at the edge provides the coupling between films, in others a deposited oxide is used. The edge geometry does produce the distinctive features of a classical non-hysteretic Josephson junction. Where parasitic capacitance has been large, hysteresis has also been observed, but never with a true gap structure. Therefore these junctions are not suited for many of the classical superconductive circuit families that require hysteresis or a sharp gap.

There is one class of digital circuit which requires just what HTS edge Josephson junctions seem to deliver, and that is the Rapid Single Flux Quantum<sup>7</sup> (RSFQ) type of circuit. RSFQ circuits do not use voltage or current levels to represent ones and zeroes, as all transistor and most superconductive circuits do. Rather, bits are represented by the presence or absence of quantized fluxoids in different parts of the circuits. Quantization of magnetic flux is an integral part of superconductive circuits, where the magnetic flux enclosed by a superconductive path is forced to take on a value corresponding to an integral multiple of  $\phi_0$ . It is relatively simple, by selecting inductance and critical current

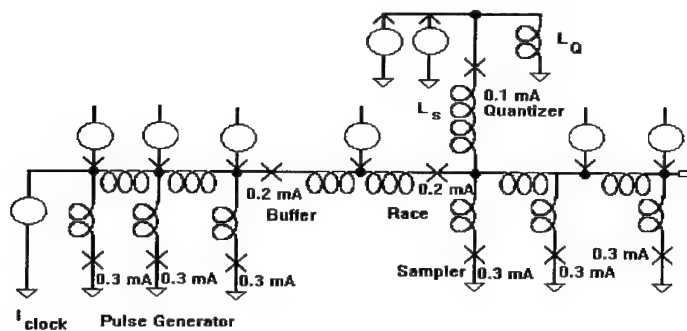


Figure 10. Schematic of RSFQ type flash analog-to-digital converter.

values, to control the motion of fluxons in these circuits. Any logic function can be generated by using some fluxons to control the motion of other fluxons through their interaction with the Josephson junctions. This can be illustrated with a simple circuit.

Fig. 10 is the schematic diagram of a comparator for a flash analog-to-digital converter, designed to use RSFQ principles with HTS junctions. Operation is as follows: Clock pulses create a series of flux quanta at the leftmost junctions. These fluxoids propagate to the right under the influence of bias current supplied at the junction nodes. At the same time, the analog signal is applied as a current source feeding the quantizer

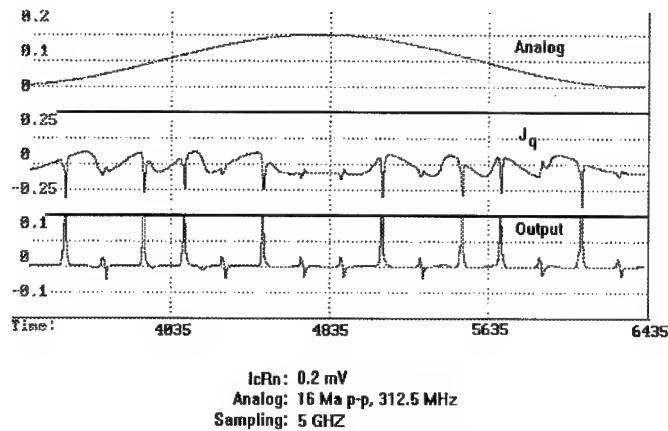
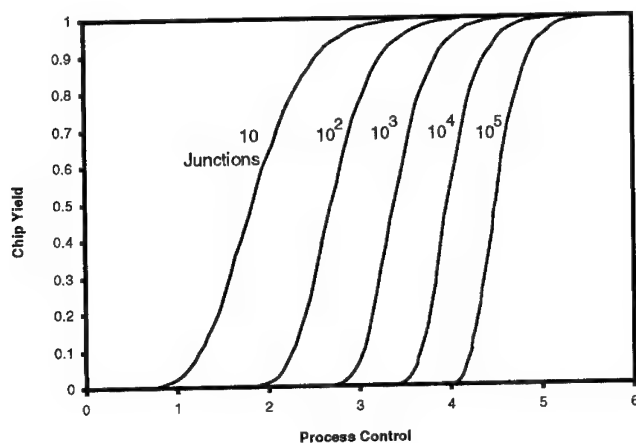


Figure 11. Simulation of RSFQ flash A-to D converter designed for HTS junctions. The top curve is the sinusoidal input, in this case with 16 mA peak to peak amplitude and 312.5 MHz frequency. The middle curve shows the current in the quantizer junction, and the bottom curve shows the pulses arriving at the output.

inductance  $L_Q$  shunting the 0.1 mA quantizer junction. This quantizer junction and  $L_Q$  form a quasi-one-junction SQUID<sup>31</sup>, and the current through the junction oscillates in sign as the analog current is increased. The period of oscillation is given by  $\phi_0/L_Q$ . If when the clock pulse arrives at the sampler junction the quantizer current is positive, the sampler junction will switch, and the clock pulse will propagate out to the right. If the quantizer current is negative when the clock pulse arrives, the race junction will switch instead and no pulse will appear at the output on the right. A simulation of exactly this behavior for the fourth bit of a flash a to d converter simulation is shown in Fig. 11.

The achievable scale of the HTS RSFQ application will be determined by the uniformity of the junction process. Fig. 12 is an estimate<sup>32</sup> of the chip yield for a given



**Figure 12.** Calculation of chip yield for a given level of process control and number of junctions per chip. Yield is given as a fraction. The Process Control is given as the ratio of circuit margin to the standard deviation of the process. For example, a 0.027 mA circuit margin, with a 0.01 mA process standard deviation will have a chip yield of about half for 100 junctions per chip.

number of junctions, for a given process capability, assuming statistical independence of the junctions. For example, a 50 per cent chip yield applies for a chip having the order 100 junctions with a 2.7 sigma process.

The focus of research on edge junctions is to find ways to minimize the spread in critical current values. At present it is common for junctions on the same chip to have a critical current spread of 30% or more, though some chips have been produced with spreads of only 10%. This magnitude of variation is sufficient for the small digital circuits, with the order of a hundred junctions. To fulfill the potential of RSFQ circuits with thousands of junctions, critical current spreads will have to shrink to significantly less than

10%. The allowed variation will shrink further when the assumption is removed of statistical independence of the junctions.

## 7. Finding the Customer

Figure 13 is a schematic representation<sup>33</sup> of the macro process whereby research ideas become useful products. This process is at least as nonlinear as the Josephson phenomena discussed in these pages, and the successful application of superconductivity to real problems will require us to understand it at least as well as we do nonlinear physics. What Fig. 13 shows is material and information coming into the process from the left, followed by well defined steps, one after the other, where the material and information is transformed into a product, and then the distribution of the product to customers at the right. The customers provide feedback, through management or other means, to guide each step. In principle, there should be customer feedback to those of us conducting research in superconducting devices, even those of us doing the most basic research.

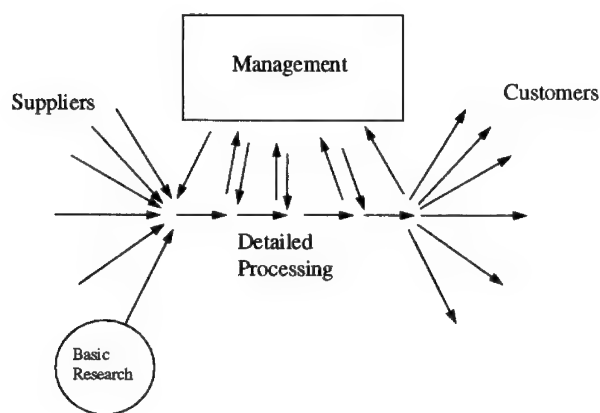


**Figure 13.** Schematic of nonlinear new product process.

The current effort at Westinghouse of inserting superconductivity into radar systems (CRYORADAR<sup>TM</sup>) provides an example of this process<sup>34</sup>. Critical HTS components for this application are low insertion loss, very compact RF switched filterbanks, extremely

high Q resonators for stable local oscillators (STALO), analog-to-digital converters (ADC) and digital signal processors. The switched filterbank will improve anti-jamming capability without sacrificing system sensitivity; the resonator will provide an ultra-low noise STALO for significant increase in radar sensitivity; the ADC will provide the required bandwidth and dynamic range to handle the clutter and signal without distortion. The demonstration of the capabilities of HTS in this system is currently underway.

As an example, let us follow customer feedback regarding the STALO. The customers know from long experience that the relevant stability of these oscillators is phase noise. Flux flow oscillators, mentioned earlier, are probably not good candidates for low phase noise. Measured line widths have been in the  $10^5$  to  $10^6$  Hz range. Moreover the vortex velocity depends on temperature, bias, and applied magnetic field, which would all have to be controlled to minimize phase noise. Resonant mode soliton oscillators are another candidate, and have demonstrated extremely high Q behavior. They can be projected to have excellent phase noise properties because of the quasi-relativistic behavior of the solitons. But further discussions with radar engineers reveals another requirement: The local oscillator phase must drive the phase of the high power outgoing pulse as well as drive the receiver mixer. The soliton oscillator may be able to drive the receiver mixer (especially if it is also a superconductive component), but to drive the output pulse would involve amplification from nanowatts to megawatts. Such amplification without degradation of phase noise would be extremely difficult to achieve. Therefore macroscopic superconductive resonators are being developed into CRYORADAR™ local oscillators, which can combine low phase noise with high energy. Knowing the requirements of radar customers helps us to find elegant solutions to real problems.

## 8. Summary

HTS electronics is poised for impact. In the short run, HTS microwave filters, delay lines, and resonators can do the job now in such a way that customers are willing to pay for them. The technology for producing these devices is good now, and still improving. Coupled with recent advances in cryocoolers for the HTS temperature range, these facts point to commercial success. The future for HTS SQUIDS is on the horizon, but needs more development to bring it in. Junction technology for SQUID's is adequate now, but for real customer interest, multilayer technology must be mastered. HTS digital circuits are over the horizon. Multilayer technology must expand to at least 7 epitaxial layers, and junction parameters need to be optimized, stabilized, and able to produce predictable devices in any direction. The immediate goal is to show progress in reducing critical current spreads to less than 10%. We need to develop interface devices, such as the flux flow transistor, so that HTS digital circuits can be operated and demonstrated at high speed. Finally, we must understand that we scientists and engineers must find customers now. We must understand their needs, so that what we spend our careers developing, will be put to use.

### Acknowledgements

We wish to express our gratitude for helpful consultation to John X. Przybysz, Hodge Worsham, and George Wagner. This work was supported in part by ONR/ARPA Contract No. N00014-91-C-0112, AFOSR Contract No. F49620-94-C-0021, and NRL Contract No. N00014-92-C-2043

### References

1. S.H. Talisa, M.A. Janocko, D.L. Meier, C. Moskowitz, R.L. Grassel, J. Talvacchio, P. LePage, G. Hira, D.C. Buck, S.J. Pieseski, J.C. Brown, and G.R. Wagner, To be published in *IEEE Trans. Appl. Supercond.*, (1995). (Proceedings of 1994 Applied Superconductivity Conference, Boston, Massachusetts)
2. R.R. Mansour, F. Rammo, and V. Dokas, *IEEE MTT-S Int. Microwave Symp. Digest*, 1281 (1993).
3. M. Nisenoff, J.C. Ritter, G. Price, and S.A. Wolf, *IEEE Trans. Appl. Supercond.* **Vol. 3**, 2885 (1993).
4. A.H. Miklich, D. Koelle, E. Dantsker, D.T. Nemeth, J.J. Kingston, R.F. Kromaun, and J. Clarke, *IEEE Trans. Appl. Supercond.* **VOL 3**, 2434 (1993).
5. Yu. Ya. Divan, J. Mygind, N.F. Pedersen, and P. Chaudhari, *IEEE Trans. Appl. Supercond.*, **VOL 3**, 2337 (1993).
6. John X. Przybysz, D.L. Miller, E.H. Naviasky, and J.H. Kang, *IEEE Trans. Appl. Supercond.* **Vol. 3**, 2732 (1993).
7. K.K. Likharev and V.K. Semenov, *IEEE Trans. Appl. Supercond.* **VOL 1**, 3 (1991).
8. R. Gross, P. Chaudhari, M. Kowasaki, M.B. Ketchen, and A. Gupta, *Appl. Phys. Lett.* **57**, 727 (1990).
9. N. Missert, T.E. Harvey, R.H. Ono, and C.D. Reintsma, *Appl. Phys. Lett.* **63**, 1690 (1993).
10. R.W. Simon, J.F. Burch, K.P. Daly, W.D. Dozier, R.Hu, A.E. Lee, J.A. Luine, H.M. Manasevit, C.E. Platt, S.M. Schwarzbek, D. St. John, M.S. Wire, and M.J. Zani, in *Science and Technology of Thin Film Superconductors 2*, Edited by R.D. McConnell, and R. Noufi, Plenum Press, New York 1(1990), p. 549.
11. J. R. Gavaler, J. Talvacchio, T. T. Braggins, M. G. Forrester, and J. Gregg, *J. Appl. Phys.* **70**, 4383 (1991).
12. T. Venkatesan, X. Wu, A. Inam C. C. Chang, M. S. Hegde, and B. Dutta, *IEEE J. Quantum Elec.* **25**, 2388 (1989).
13. Robin J. Kennedy, in *Adv. in Cryo. Eng. (Materials)* **Vol. 138**, 1005. Edited by F.R. Fickett and R.P. Reed, Plenum Press, New York (1992).
14. A. Erbil, K. Zhang, B. S. Kwak, and E. P. Boyd, in: *Processing of Films for HTS Electronics*, edited by T. Venkatesan, SPIE 1187, Bellingham, WA, pp. 104, (1990).



15. P. Chaudhari, R. H. Koch, R. B. Laibowitz, T. R. McGuire, and R. J. Gambino, *Phys. Rev. Lett.* **58**, 2684 (1987).
16. R.W. Simon, in: *Processing of Films for HTS Electronics*, edited by T. Venkatesan, SPIE 1187, Bellingham, WA, pp. 2. (1990).
17. Gong-Da-Yao, Shang-Yun Hou, M. Dudley, and J.M. Phillips, *J. Mater. Res.* **7**, 1847 (1992).
18. M. Sasaura, S. Miyazawa, and M. Mukaida, *J. Appl. Phys.* **68** (7), 3643 (1990).
19. A. Schilling, M. Cantoni, J.D. Guo, and H.R. Ott, *Nature* **30**, 56 (1993).
20. A.T. Findikoglu, C. doughty, S. Bhattacharya, Qi Li, X.X. Xi, T. Venkatesan, R.E. Fahey, A.J. Strauss, and Julia M. Phillips, *Appl. Phys. Lett.* **61**, 1718 (1993).
21. K.K. Likharev, V.K. Semenov, O.V. Snigerev, and B.N. Todorov, *IEEE Trans. on Mag.* **MAG-15**, 420, (1979).
22. B.J. Van Zeghbroeck, *Appl. Phys. Lett.*, **42**, 736 (1983).
23. D.P. McGinnis, J.E. Nordman, and J.B. Beyer, *IEEE Trans. Mag.* **MAG-23**, 699 (1987).
24. Y.M. Zhang, D. Winkler, P.A. Nilsson, and T. Claeson, *Appl. Phys. Lett.* **64**, 1153 (1994), and L. Alff, B. Meyer, S. Schuster, O. Frolich, R. Gerdemann, A. Beck, and R. Gross, *J. Appl. Phys.* **75**, 1843 (1994).
25. See Article by V.P. Koshelets, this volume.
26. A. Davidson and N.F. Pedersen, To be published in *IEEE Trans. Appl. Supercond.*, (1995). (Proceedings of 1994 Applied Superconductivity Conference, Boston, Massachusetts)
27. NTT Electronics, SST ECL Catalog, 1993, distributed by KBK, Inc., 330 Madison Ave, New York, NY 10017, USA.
28. J.P. Wikswo, Jr., Y.P. Ma, N.G. Sepulveda, S. Tan, I.M. Thomas, and A. Lauder, *IEEE Trans. Supercond.* **VOL 3**, 1995 (1993).
29. M.G. Forrester, A. Davidson, J. Talvacchio, J.R. Gavaler, and J.X. Przybysz, *Appl. Phys. Lett.* **65**, 1835 (1994).
30. R.P. Robertazzi, R.H. Koch, R.B. Laibowitz, and W.J. Gallagher, *Appl. Phys. Lett.* **61**, 711 (1992).
31. Paul Bradley, *IEEE Trans. Appl Supercond.* **VOL 3**, 2550 (1993).
32. D.L. Miller, J.X. Przybysz, and J.H. Kang, *IEEE Trans. Appl. Supercond.* **VOL 3**, 2728 (1993).
33. W.E. Deming, in *Quality, Productivity, and Competitive Position*, MIT Center for Adv. Eng. Study, 1982, p103.
34. Michael M. Fitelson, to be published in *IEEE Trans. Appl. Supercond.*, (1995). (Proceedings of 1994 Applied Superconductivity Conference, Boston, Massachusetts)

## HIGH- $T_c$ JOSEPHSON JUNCTIONS, DC-SQUIDS AND ARRAYS

PAUL SEIDEL

*Institut für Festkörperphysik, Friedrich-Schiller- Universität Jena  
Helmholtzweg 5, D-07743 Jena, Germany*

### ABSTRACT

An overview is given about experiments on some high- $T_c$  Josephson devices. The results are discussed using simulations based on the RCSJ model including white noise. The power dependence of Shapiro steps includes information about the existence of a junction network or a single junction only. Networks and other artificial many junction systems are discussed with respect to applications as radiation sources.

### 1. Introduction

There is great progress in thin film technology for the fabrication of different types of high- $T_c$  Josephson junctions for applications as single junctions, SQUIDS or many junction circuits necessary for cryoelectronic applications. Up to now there is no microscopic understanding of superconductivity in HTSC materials but it is possible to study the main properties of these devices using the well-known resistively shunted junction model including capacitance (RCSJ model) and noise. The possibilities and limitations of RCSJ based models will be discussed exemplarily on the parameter determination from experimental power dependence data of Shapiro steps. A more profound physical understanding of high- $T_c$  Josephson junctions will be useful for their application in cryoelectronic devices.

As another example, DC-SQUIDS will be discussed. In spite of all problems concerning junction properties and high- $T_c$  technology, these devices are today on a level to start applications in a wide range, e.g. geology, non-destructive evaluation and biomagnetism. Thus a detailed analysis of their properties, especially intrinsic noise behaviour, is necessary.

A third example are many junction arrays. Such arrays are of interest for basic research as well as radiation sources in the 100 GHz up to 1 THz range. Problems with synchronization resulting from parameter spread in junction technology are discussed.

### 2. Types of High- $T_c$ Josephson Junctions

There is a great variety of different types of high- $T_c$  Josephson junctions like grain boundary junctions, barrier junctions, modified bridges and intrinsic stack junctions, some of them given in Fig. 1.

The traditional concept of the superconductor-insulator-superconductor (SIS) junction is hard to realize because of the large anisotropy, short coherence length

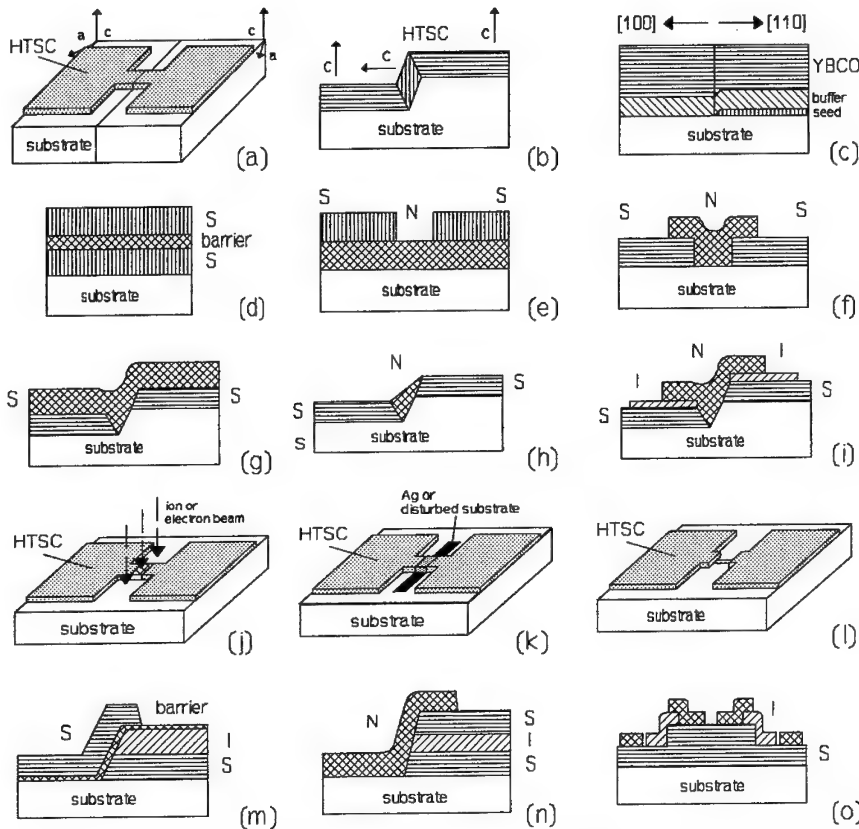


Fig. 1. Types of high- $T_C$  Josephson junctions (a) bicrystal junction, (b) step-edge junction, (c) biepitaxial junction, (d) planar barrier sandwich, (e) bilayer trench junction, (f) SNS trench junction (g) SNS step-edge junction, (h) etched SNS step-edge junction, (i) capacitively shunted SNS step-edge junctions, (j) focused beam modified bridge, (k) disturbed or poisoned bridge, (l) nanobridge junction, (m) barrier edge or ramp junction, (n) SNS side sandwich junction, and (o) intrinsic stack junction (mesa type).

and structural properties of multilayers involving high- $T_C$  superconductors. On the other side, there exist natural Josephson junctions inside high- $T_C$  superconductors caused or induced by microscopic defects of the crystal structure. For example, break junctions in polycrystalline films or bulk material show clear, pronounced Josephson effects<sup>1,2</sup>. Therefore, a whole group of high- $T_C$  junctions is based on artificially induced grain boundaries in thin film bridges (GBJ, grain boundary junction).

Fig. 1a shows the bicrystal junction where the grain boundary is induced by a bicrystalline substrate<sup>3</sup>. This technology is used for different high- $T_C$  superconduct-

tors (YBCO, Bi-2212) as well as a variety of substrates ( $\text{SrTiO}_3$ ,  $\text{NdGaO}_3$ ,  $\text{LaAlO}_3$ ,  $\text{MgO}$ ,  $\text{Si}$ )<sup>4,5,6,7,8</sup>. The advantages of that kind of junctions are the simple and reproducible preparation, the correlation between junction properties and grain boundary angle and that there is no use of additional barrier materials. Disadvantages are the fixed grain boundary angle and geometrical restrictions because junctions are induced in all crossing superconducting lines. This excludes large-scale integration and complex devices in multilayer technology. The conduction mechanism across the grain boundary is influenced by electronic states and resonant tunneling, both leading to a high level of intrinsic noise<sup>9</sup>.

Fig. 1b schematically shows another kind of a GBJ. A step in the substrate induces grain boundaries along the step by a mismatch in the film growth. The concept of such step-edge junctions (SEJ) was proposed some years ago<sup>10</sup>. Meanwhile the step angle, the ratio of step height to film thickness, the step processing and substrate as well as superconductor materials have been varied by many groups<sup>11,12,13,14,15,16,17</sup>. Even if there are differences depending on the materials used, this junction type offers some advantages. The geometrical restrictions can be reduced because it is possible to produce the steps in small dimensions and limited areas on the substrate or even in covering insulating layers<sup>14</sup> or buffer layers<sup>15</sup>. Their noise properties are better than those of most other types<sup>16,17</sup> but there are problems resulting from the network-like structure of the junctions<sup>12</sup>. Instead of a single well-defined weak link in the step region small networks result from the two different grain boundaries along the step and inhomogeneities within the junction.

Another kind of GBJ is the biepitaxial junction, Fig. 1c. A change of the crystal orientation of the YBCO film is induced by partially covering the substrate by some thin seed layer, e.g.  $\text{MgO}$  or  $\text{CeO}_2$ <sup>18</sup>, or by ion implantation of parts of a  $\text{MgO}$  substrate<sup>19</sup>. Disadvantages are the fixed grain boundary angle of  $45^\circ$  which enables only a low current density, some problems with the spatial formation of sharp structures and limitations of integration. The main problem are bad noise properties<sup>20</sup>.

The second group of junctions uses an artificial barrier layer. Because of the small transmission coefficient the thickness of an insulating material may be only of order of some nm and must be without pinholes. S-I-S structures were realized with a-oriented high- $T_C$  material and epitaxially grown insulating barrier layers, Fig. 1d. Even if there are some results with such kind of structures<sup>21,22</sup> SIS structures with the high gap values of a tunnel junction are only achieved for BKBO<sup>23</sup>. The transmission coefficient can be improved by using a semiconducting or normal conducting barrier like  $\text{PrBaCuO}$  or  $\text{NdCeCuO}$ . In this case the barrier thickness may be larger and the problems of thin barrier layer can be solved by a bilayer structure with a small trench in the superconductor<sup>24</sup>, Fig. 1e. The trench can be easily realized by e-beam lithography but a-orientation of the HTSC film is still required.

The restrictions of multilayer epitaxy can be solved if a noble metal is used as normal conducting barrier. Other metals generally cause a depression of superconducting properties<sup>25</sup>. There are different solutions for SNS junctions. The junction shown in Fig. 1f is a narrow trench in a HTSC bridge filled with silver or gold<sup>26,27,28</sup>. The main problems are the quality of the interfaces between the  $\text{CuO}_2$  planes and

the metal as well as the homogeneity of the barrier in the other direction.

If the preparation of trenches of a width smaller than 200 nm by electron or ion beam lithography is not possible, one may take advantage of steps in the substrate. The insulating intermediate or buffer layers also may carry the step, thus enabling a multilevel integration technology<sup>14</sup>. The first version of such SNS step-edge junctions (Fig. 1g) works with different angles of deposition of HTSC material and normal metals<sup>29</sup>. These structures show a very small  $I_C R_N$  product caused by normal shunts between large parts of the superconducting film and the normal metal. By etching away these shunts the properties can be improved and high  $I_C R_N$  products can be obtained<sup>30</sup>, Fig. 1h. A lot of applications of Josephson junctions are connected with a finite capacitance of the junction expressed by a nonzero McCumber parameter  $\beta_C$ , which leads to a hysteretic current-voltage characteristic. Such junction properties can be obtained by an additional insulating layer in the shunt regions, Fig. 1i. If a material with a high dielectric constant like  $\text{SrTiO}_3$  is used, finite McCumber parameters are possible even at 77 K<sup>31</sup>.

Other types of SNS junctions are edge or ramp junctions, Fig. 1m, where a barrier is formed at the etched edge of a superconductor-insulator bilayer. Various materials were used, from epitaxial systems, like  $\text{PrBaCuO}$ <sup>32</sup>, Co or Pr doped  $\text{YBCO}$ <sup>33,34,35</sup> to Nb doped  $\text{SrTiO}_3$ <sup>36</sup> or even insulator-like barriers<sup>37</sup>. While the crystallographically adjusted materials give good and reproducible results, the very thin and quite non-reproducible insulators show a microbridge and pinhole dominated behaviour. In general the barriers strongly influence the junction properties. Hopping conductivity<sup>38</sup> or resonant tunneling<sup>39</sup> can give additional contributions to conduction and noise<sup>40,41</sup>. If good SIS multilayers with thin but highly resistive insulators can be established it is possible to use the edge as a contact region for a normal metal, Fig. 1n. The thickness of the insulator gives the coupling length and the main problem are the interfaces at the edge, especially after preparation by ion beam etching.

A third group of junctions uses weakened bridges to produce a weak link behaviour. Small parts of the bridges are modified by ion or electron beams to obtain reduced superconducting or normal conducting behaviour in this region, which should be narrower than 200 nm to obtain good coupling. The direct writing with an electron beam produces good junction properties but there is no time stability of the devices at room temperature<sup>42,43</sup>. Focused ion beams<sup>44,45,46</sup> or ion implantation using masks<sup>47,48</sup> give similar results but these junctions are stable over a long time. Problems arise from the fact that these junctions often work near or in the flux flow regime and have a limited operating temperature range.

Small weakened parts of a bridge can also be obtained by a metal strip across the bridge poisoning the superconductivity<sup>49</sup>, Fig. 1k. This strip can be placed on the substrate prior to the deposition of the HTSC film or after preparation of the HTSC film combined with some treatment stimulating diffusion<sup>50</sup>. Similar junctions can be obtained by distortions in small substrate areas before establishing the HTSC bridge. Focused ion beams<sup>51</sup> as well as mechanically induced scratches<sup>52</sup> were used.

If the dimensions of the bridge can be reduced down to the order of the coherence length the traditional nanobridge concept of conventional superconductors

works. Even if the dimensions of such nanobridges, Fig. 11, with HTSC are too large compared to the short coherence length of these materials, realization of Josephson like junctions is reported<sup>53,54</sup>, while other groups obtained flux flow bridges<sup>55</sup>. It is possible that the preparation process of the nanobridges causes additional weakening by ion or electron interactions.

A new type of Josephson junctions, which is expected to become more importance in the near future, is based upon intrinsic Josephson effects in layered HTSC<sup>56,57</sup>. The stacked  $\text{CuO}_2$  planes coupled by insulating parts within the large unit cells of Bi- or Tl-based HTSC are natural series arrays of SIS Josephson junctions. If it is possible to prepare such a stack in a definite way it can be used for a cryoelectronic device. First results were obtained by etching such stacks, so-called mesas, into the surface of a single crystal<sup>58</sup> or by taking advantage of the plate-like growth of a Tl-2212 film across a deep step in the substrate<sup>59</sup>. They are quite similar to step-edge junctions which were described as a single SIS junction only<sup>60</sup>. Using thin film technology, such a stacked system can be etched out of a thin film followed by applying contacts to the upper and lower surface, Fig. 10. Additional insulating or even normal conducting shunt films around these mesas appear to be possible and could help to adjust their properties or improve coupling to radiation.

### 3. Single Junction Behaviour

Most types of high- $T_C$  Josephson junctions show weak link behaviour different from tunneling determined ideal Josephson junction properties. Thus, the description of their properties should be possible within the resistively shunted model (RSJ model)<sup>61,62</sup> using the critical current  $I_C$  and normal resistance  $R_N$  determining the characteristic frequency  $\omega_C = 2eI_C R_N / \hbar$ . Because of shunt capacitances resulting from high dielectric constants of substrates like  $\text{SrTiO}_3$  a finite capacitance  $C$  should be included. The corresponding McCumber parameters  $\beta_C = 2eI_C R_N^2 C / \hbar$  are near one at 77 K but increase up to 10 at 4,2 K. Higher values can be obtained utilizing additional capacitances in the junction region, e.g. by an insulating layer and a metal film across a step-edge junction<sup>63</sup>, or using capacitive shunting like in Fig. 11<sup>31</sup>.

The higher working temperature  $T$  of HTSC junctions is connected with a stronger influence of thermal noise. This can be taken into account by a white noise generator  $I_f(t)$  with  $\langle I_f(t) I_f(t') \rangle = 2\gamma \delta(t - t')$  and a characteristic parameter  $\gamma = 2ek_B T / \hbar I_C$ , where  $k_B$  is the Boltzmann constant<sup>64</sup>. A fit of the dc biased ( $i_0 = I_0 / I_C$ ) vs. averaged voltage  $v$  characteristics is possible by a variety of parameter combinations. It is hard to determine the influence of excess currents or even additional junctions contributing to the characteristic. Therefore, the irradiation of microwaves of an amplitude  $i_1 = I_1 / I_C$  and normalized frequency  $\Omega = \omega_{ex} / \omega_C$ , can be used as a tool to determine relevant junction parameters. A detailed analysis of the induced Shapiro steps in the I-V characteristics is of great interest.

The experiments should be compared to results of RCSJ simulations of the phase difference  $\varphi$  across the junction including noise and microwave irradiation according to the equation

$$\beta_C \frac{d^2\varphi}{d\tau^2} + \frac{d\varphi}{d\tau} + \sin\varphi = i_0 + i_1 \sin(\Omega\tau) + i_f(\tau), \quad (1)$$

where normalized time  $\tau = \omega_C t$  is introduced. The averaged voltage is obtained by averaging the time-dependent phase difference.

Some results for different types of junctions will be given as an example. In general, the knowledge of the  $I_C R_N$  product determining the characteristic frequency  $\omega_C$  of the junction and thus the relative frequency  $\Omega$  is of great interest. The simple method of taking  $I_C$  from I-V characteristic by assuming some approximation because of noise rounding of  $R_N$  from the higher voltage part of the characteristic gives parameters influenced by the method of determination<sup>65</sup> as well as by additional conduction processes reflected in the characteristics. Some improvement may be achieved if special determination methods based on the RSJ model are used to obtain  $I_C$ <sup>66</sup> and if the normal resistance  $R_N$  is taken from linearized parts around  $V=0$  at high microwave levels.

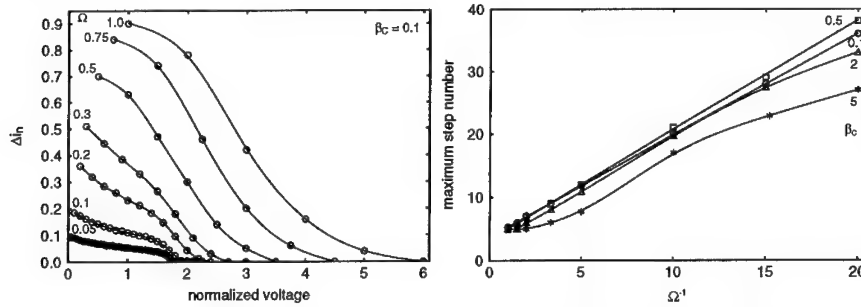


Fig. 2. a) Step heights vs. normalized voltage position, b) Maximum number of Shapiro steps as function of relative frequency

A new method<sup>67</sup> has been developed to determine  $\Omega$  from a single experimental I-V curve for a microwave amplitude  $I_1$  corresponding to the first minimum of the zeroth step in the function  $I_C(I_1)$ . From this curve the heights  $\Delta I_n$  of all Shapiro steps and the corresponding step voltages  $V_n$  are taken. The points given by  $\Delta I_n(V_n)$  are approximated by a smooth function that crosses the zero axis at a voltage where the Shapiro steps vanish (Fig. 2a). Normalizing this voltage by the step distance corresponding to the Josephson relation determined by the external frequency one obtains the maximum step number. This maximum step number has a typical dependence on  $\Omega^{-1}$ , Fig. 2b, and can be used to estimate  $\Omega$  and hence the  $I_C R_N$  product. The advantages of this method are the weak dependence on  $\beta_C$ , see Fig. 2b, and that it is almost independent on noise rounding of Shapiro steps. The obtained value of the  $I_C R_N$  product gives a better description of the junction behaviour compared to the RSJ model than the values obtained from I-V curves in the usual way because effective parameters of the junction are evaluated. The McCumber and the noise

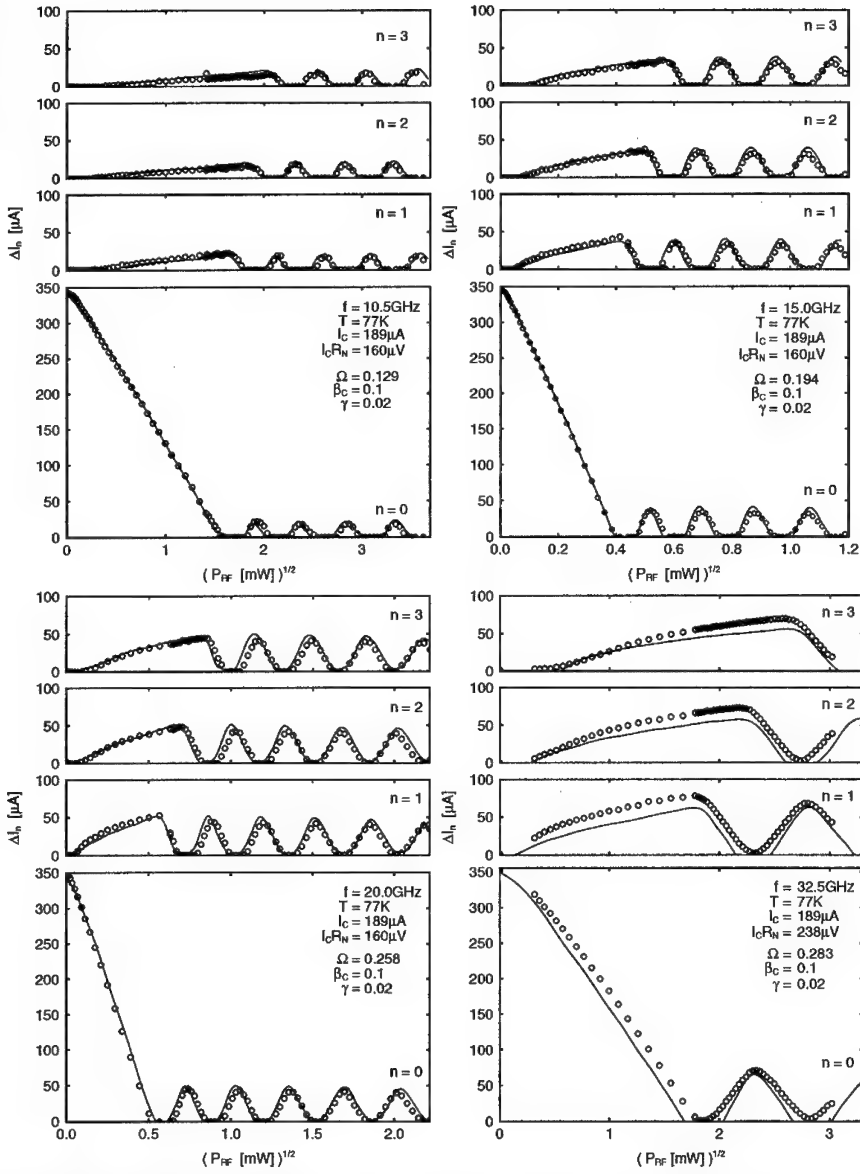


Fig. 3. Heights of Shapiro steps vs. RF amplitude for an YBCO bicrystal junction at  $T = 77K$  for different microwave frequencies



parameter can be determined from detailed measurements of the power dependence of the Shapiro steps and comparison to simulations according to eq. (1). In the ideal case the junction can be described by the RCSJ model with the same parameter set  $I_C$ ,  $R_N$ ,  $\beta_C$  and  $\gamma$  for different external frequencies. An example is given in Fig. 3.

The experimental I-V characteristics of a bicrystal junction (YBCO on SrTiO<sub>3</sub> with a misfit angle of 36,8°) at 77 K can be fitted by  $I_C = 189 \mu A$ ,  $\beta_C = 0.1$  and  $\gamma = 0.02$  but different  $R_N$  values. While the Shapiro step behaviour at 10, 15 and 20 GHz yields  $R_N$  of 0.85  $\Omega$  the fit of the behaviour at 32 GHz as well as the fit of the I-V curve without radiation provides 1.26  $\Omega$ . The reason of this difference is not clear up to now but we assume that it may be due to frequency dependent RF properties of the SrTiO<sub>3</sub> substrate and the junction environment, e.g. changes of additional capacitances and inductances.

#### 4. Networks of Two Josephson Junctions

In some cases a multi-junction instead of the expected single junction behaviour is found from the I-V curve or the power dependence of Shapiro steps. This is caused by the microscopic structure of the junctions as well as by current density inhomogeneities. For example, in the case of a step-edge junction two different grain boundaries are formed at the upper and the lower edge of the step. For non-ideal growth even additional grain boundaries in the step area arise. Perpendicular to the step the interface is perturbed by small outgrowths as well as different transmission coefficients leading to a strong inhomogeneity of the current distribution as observed by means of Low Temperature Scanning Electron Microscopy<sup>68</sup>. Thus, a step-edge junction is rather a small junction network than a single junction.

As a simple example, we have investigated a series connection or a parallel connection of two junctions forming a well-known DC-SQUID. Both cases show interesting possibilities to determine the junction parameters characterizing the nonlinear behaviour from the power dependence of Shapiro steps.

The dependence of Shapiro step height on microwave amplitude for an asymmetric

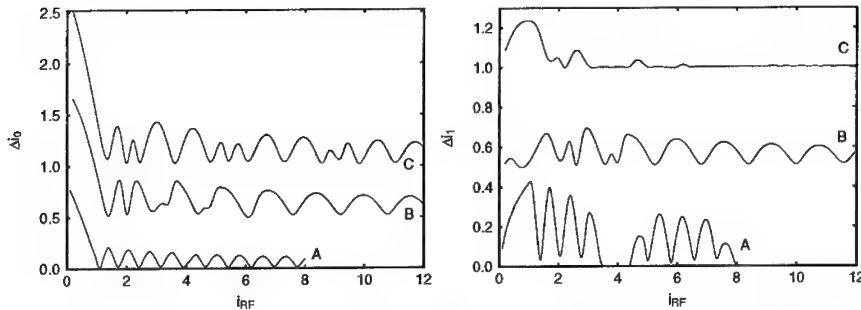


Fig. 4. Heights of Shapiro steps for a two junction serial array at different RF power. A:  $R_{N1}=4R_{N2}$ ,  $I_{C1}=1.5I_{C2}$ ; B:  $R_{N1}=R_{N2}$ ,  $I_{C1}=2.33I_{C2}$ ; C:  $R_{N2}=1.5R_{N1}$ ,  $I_{C1}=1.5I_{C2}$

two junction series network is very complicated in general. The most important parameter is the resistance ratio of both junctions  $R_{N1}/R_{N2}$ , Fig. 4. Only in the case  $R_{N1} \approx R_{N2}$  or if  $I_{C1} \approx I_{C2}$  the series connection behaves like a single junction with doubled step distance for higher RF amplitude. In the case of different resistances the step width oscillation is strongly disturbed and deviates significantly from the single junction behaviour. For large differences the behaviour is dominated by the junction with the largest resistance reflecting only this junction in the Shapiro step behaviour at lower microwave power and step order. Thus, the oscillation of the steps can give hints about the asymmetry in the two junction series array.

Similar results can be obtained from Shapiro steps measured on a DC-SQUID. As additional parameters the inductance parameter  $\beta_L = 2\pi I_C L / \Phi_0$  and the external flux  $\Phi_{ex}$  must be taken into account. At  $\Phi_{ex} = 0$  and  $\beta_L \ll 1$  the SQUID does not differ from a single junction with  $I_C = I_{C1} + I_{C2}$ . With increasing  $\beta_L$  there are deviations up to chaotic behaviour for  $\beta_L \gg 1$ . Additional oscillations and regions where the steps disappear can be seen, Fig. 5.

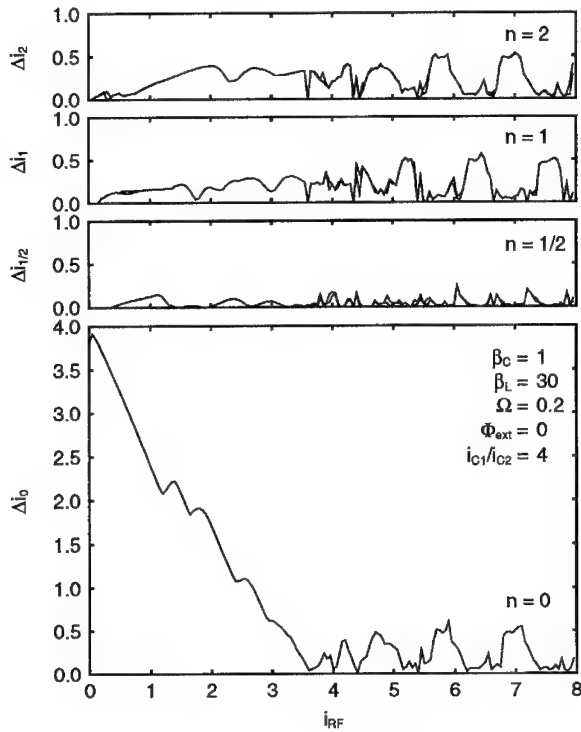


Fig. 5. Calculated height of Shapiro steps for a DC SQUID with high loop inductance

For finite external flux well pronounced half integer subharmonic steps are present in the I-V curve<sup>69</sup>. They show maximum height for  $\Phi_{ex} = \Phi_0/2$  and  $I_{C1} = I_{C2}$ . Their height depends sensitively on the critical current asymmetry and on the relative frequency  $\Omega$ , while there is only small influence of  $\beta_L$ ,  $\beta_C$ , or  $\gamma$ . Since  $\Omega$  can be determined by the method described above, this effect may provide a useful method to determine the asymmetry of DC-SQUIDS experimentally<sup>67</sup>.

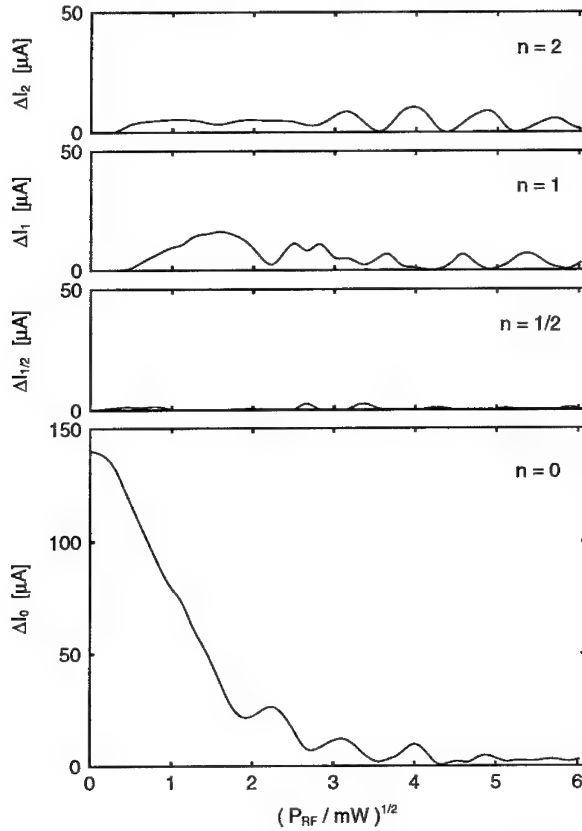


Fig. 6. Height of Shapiro steps for a YBCO step-edge DC-SQUID

Fig. 6 shows experimental results similar to the predicted behaviour measured on a YBCO step-edge junction DC-SQUID. I would like to point out that substeps can be explained even within the framework of a simple RCSJ model especially for  $\Omega \geq 1$ <sup>70</sup>. The main differences should be in the dependence of the step height on microwave amplitude. In the RCSJ case the height is given by

$$\Delta I_{\frac{1}{2}} \approx I_C |J_0(A)J_1(A)|, \quad A = \frac{i_1}{\Omega} (1 + \beta_C^2 \Omega^2)^{-\frac{1}{2}}. \quad (2)$$

This dependence of the substep  $n=1/2$  for a single junction is clearly different from the dependence of such a substep in the case of a SQUID. From this differences, especially the periodicity compared to the integer steps, one obtains hints concerning the existence of a network rather than of a single junction. In the case of strong inhomogeneities the single junction may be considered as a complicated network<sup>71</sup>.

## 5. DC-SQUIDS with more than Two Junctions

It was shown that the dynamic properties of a DC-SQUID drastically change if the number of junctions in each branch is larger than one, e.g. a four-junction SQUID in the simplest case<sup>72,73</sup>. If there is a small spread in junction parameters, phase locking between all junctions can exist and the SQUID operates in a mode with a different flux quantum state compared to the two-junction SQUID. As a consequence, a hysteresis in the I-V characteristic as well as an unusual voltage-flux dependence appear. Only for very large spread or if the bias current leaves only one junction in each branch in the voltage state, such a SQUID behaves like a two-junction SQUID.

This should be taken into account if the HTSC Josephson junction is not a single weak link. For example in the case of a step-edge junction DC-SQUID this was discussed assuming for each junction a small network with two parallel branches each with more than one junction in series<sup>74</sup>. The main effect observable on such a system is an additional low-frequency noise depending on the external magnetic field. Such a two-level fluctuator or telegraph-like noise behaviour was experimentally observed<sup>74,75,76</sup>, but may have other origins, too.

The influence of microwave irradiation on such a SQUID should be studied in detail to obtain informations about parameter spread and asymmetry in such systems. This work is still in progress. A first result is shown in Fig. 7 as an illustration of the complicated behaviour of hysteretic and disturbed steps.

On the other hand, this new phase-locking state can be used to establish coherent oscillator arrays where the allowed junction parameter spread is higher than for traditional concepts like the linear array<sup>77</sup>. The proposal of such a circuit, called ACISL (two linear arrays closed into a superconducting loop) was studied<sup>78</sup> and experimentally realized for the case of four HTSC junctions<sup>73</sup>. The allowed large spread of parameters up to 15%, the tunability of the radiated frequency, the small influence of thermal noise and external flux were discussed<sup>78</sup>. Some new aspects will be given in another contribution of these proceedings<sup>79</sup>.

Similar effects can be observed in coupled DC-SQUIDS. When we built up a planar single-layer gradiometer SQUID<sup>80</sup> we first used two SQUIDS on both sides of a small line through which the resulting current of the gradiometer flows. This gives us the possibility to select the best of these SQUIDS to obtain highest resolution. The second SQUID must be destroyed because it is directly coupled to the detector SQUID, Fig. 8a. In other case, this leads to a multi-junction circuit where in the case

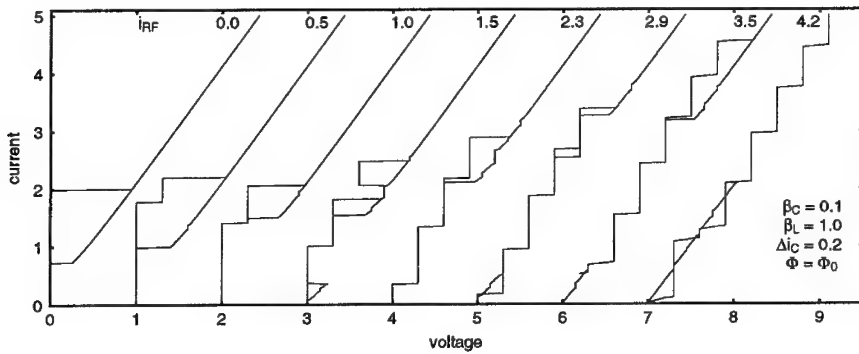


Fig. 7. Current-voltage characteristics of a 4-junction SQUID with RF bias

of finite parameter spread additional new modes are possible. The result is switching between these modes which can be seen in a complicated voltage-flux dependence different from ideal sinusoidal behaviour of a normal SQUID (Fig. 8b)<sup>81</sup>.

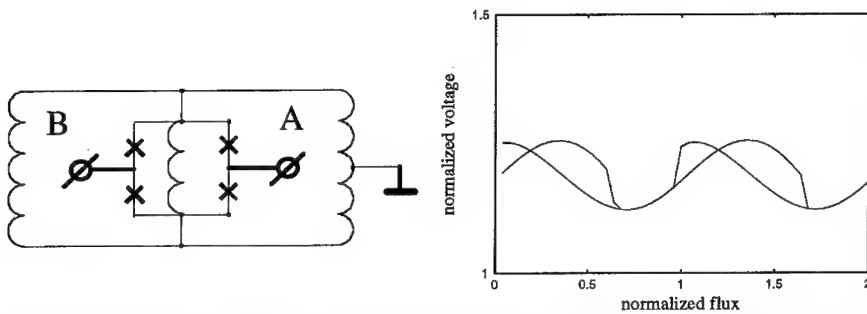


Fig. 8. a) Circuit of a DC-SQUID gradiometer containing two SQUIDs in the middle of the structure, b) Calculated flux-voltage dependence in the case that second SQUID is not cut off ( $I_{C1} = 0.1 I_{C2}$ )

There is great interest in SQUID-like circuits with a low number of junctions and additional inductances, capacitances and even resistances because such models can describe real HTSC "single" junctions and their complicated behaviour. By this way one obtains more information about the structure of special junctions and can improve them by changes in technology, materials and layouts.

## 6. Many-Junction Arrays

Networks containing a large number of Josephson junctions are studied in many groups<sup>82,83,84,85</sup>. The theoretical investigations are concentrated to basic aspects of phase transitions, vortex configurations and flux dynamics or synchronization. Phase-locking in these arrays plays an important role if one thinks about application of

arrays as sources of coherent radiation at very high frequencies. Their tunability is based upon the Josephson relation between voltage and frequency. Because the radiation output of a single junction is very small, large numbers of junctions are required. Another effect which is highly welcome is the reduction of the linewidth with the number of junctions. But all these improvements are strongly connected to the parameter spread which up to now is a serious technological problem especially for HTSC junctions.

We have studied the maximum parameter spread possible without destruction of the phase locking<sup>86</sup>. As mentioned above, it was shown that two linear arrays of junctions connected to a superconducting loop similar to a many-junction SQUID allow a parameter spread twice as large as for the simple linear array<sup>78</sup>. In general, similar values of allowed spread were obtained for the common type of a 2-D array, where meshes containing four junctions build up large arrays. These results did not take into account external flux or the influence of the network inductances<sup>86</sup>. External flux coupled into the meshes and movement of vortices have a strong influence on the properties of these arrays. Even without external flux these effects must be considered

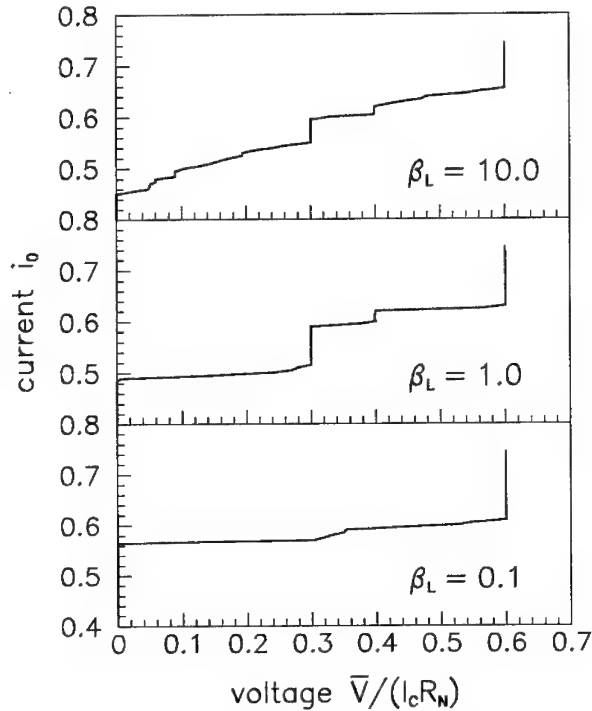


Fig. 9. Influence of inductance parameter  $\beta_L$  on height of Shapiro step at  $n=1/2$

because the inhomogeneity within the network causes a current distribution which produces locally different fluxes changing in time.

To illustrate the effects of inductance, we have calculated the current-voltage characteristics of 2-D networks taking into account not only the mutual inductance of one mesh but interactions between all meshes similar to<sup>87</sup> but assuming a simple metallic bare geometry<sup>88</sup>.

Fig. 9 shows the first half integer Shapiro substep ( $n=1/2$ ) for different inductive coupling expressed by the SQUID parameter  $\beta_L$  of a mesh defined like above. The step height clearly depends on  $\beta_L$ . Pronounced substeps can be seen even if the external flux is zero. Thus, from the appearance of half integer substeps without external flux some inductively coupled junction network with quite large inductances can be used to simulate even single HTSC junctions. This supports a model proposed for SNS step-edge junctions<sup>71</sup> and so-called transmission line models<sup>89</sup>.

## 7. Conclusions

There are many different types of HTSC Josephson junctions showing properties depending on their internal structure and on the junction materials. The RCSJ model of a single junction with white noise describes the main behaviour well but junction-dependent properties often must be described by equivalent circuits with more than one junction and additional elements. The nonlinear dynamics of such junctions and of cryoelectronic devices built up by them becomes complicated but very interesting for further investigations.

## Acknowledgements

Many thanks to Erik Heinz, Marian Darula, Falko Busse, Jürgen von Zameck Glyscinski and Thomas Flegel for their contributions to this work.

This work was partially supported by the German BMFT under contract numbers 13 N 6132 and 13 N 5924 A and the Alexander von Humboldt Foundation.

## References

1. R. H. Koch, C. P. Umbach, G. J. Clark, P. Chaudhari, R. B. Laibowitz *Appl. Phys. Lett.* **51** (1987) 200.
2. B. A. Aminov, A. A. Kaul, L. L. Leonyuk, T. E. Oskina, M. V. Sudakova, M. V. Pedyash D. K. Petrov, Ya. G. Ponomarev, H. T. Rakhimov, K. Sethupathi *Superconducting Devices and Their Appl.* (Springer-Verlag, Berlin, 1992), 45.
3. D. Dimos, P. Chaudhari, J. Mannhart, F. K. LeGoues *Phys. Rev. Lett.* **61** (1988), 219.
4. R. Gross, P. Chaudhari, M. Kawasaki, A. Gupta *Phys. Rev.* **B42** (1990), 10735.
5. T. Amrein, M. Seitz, D. Uhl, L. Schultz, K. Urban *Appl. Phys. Lett.* **63** (1993), 1978.

6. Z. G. Ivanov, P. A. Nilsson, D. Winkler, J. A. Alarco, T. Claeson, E. A. Stepantsov, A. Ya. Tzalenchuk *Appl. Phys. Lett.* **59** (1991), 3030.
7. H. B. Lu, T. W. Huang, J. J. Wang, J. Lin, S. L. Tu, S. J. Yang, S. E. Hsu *IEEE Trans. Appl. Supercond.* **3** (1993), 2325.
8. H. Suzuki, H. Kurosawa, J. Chen, Y. Hirotsu, N. Nakajima, T. Yamashita, H. Myorlu, Y. Osaka *Supercond. Sci. Technol.* **4** (1991), 479.
9. R. Gross, B. Mayer *Physica C* **180** (1991), 235.
10. K. P. Daly, W. D. Dozier, J. F. Burch, S. B. Coons, C. E. Platt, R. Hu, R. W. Simon, *Appl. Phys. Lett.* **58** (1991), 543.
11. A. I. Braginski *Proc. HTSED Workshop* (Whistler, May 1994), p. 39
12. P. Seidel *Weak Superconductivity*, Eds. S. Benacka, P. Seidel, V. Strbik, SAS Press, Bratislava, 1994, p. 13.
13. S. Tanaka, H. Kado, T. Matsuura, H. Itozaki *IEEE Trans. Appl. Supercond.* **3** (1993), 2461.
14. M. S. DiIorio, S. Yoshizumi, K. Y. Yang, M. Maung, J. Zhang, B. Power *IEEE Trans. Appl. Supercond.* **3** (1993), 2011.
15. R. Adam, S. Benacka, S. Chromik, V. Strbik, S. Gazi, I. Kostic, E. Pincik *Weak Superconductivity*, Eds. S. Benacka, P. Seidel, V. Strbik, SAS Press, Bratislava, 1994, p. 72.
16. V. N. Glyantsev, M. Siegel, J. Schubert, W. Zander, U. Poppe, H. Soltner, A. I. Braginski, C. Heiden, *IEEE Trans. Appl. Supercond.* **3** (1993) 2472.
17. L. Hao, J. C. Macfarlane, C. M. Pegrum *Physica C* **232** (1994), 111.
18. K. Char, M. S. Colclough, L. P. Lee, G. Zaharchuk *Physica* **185-189** (1991), 2561.
19. N. G. Chew, S. W. Goodyear, R. G. Humphreys, J. S. Satchell, J. A. Edwards, M. N. Keene *Appl. Phys. Lett.* **60** (1992), 1516.
20. S. G. Hammond, Y. He, C. M. Muirhead, P. Wu, M. S. Colclough, K. Char, *IEEE Trans. Appl. Supercond.* **3** (1993), 2319.
21. J. B. Barner, C. T. Rogers, A. Inam, R. Ramesh, S. Bersey *Appl. Phys. Lett.* **59** (1991), 742.
22. G. F. Virshup, M. E. Klausmeier-Brown, I. Bozovic, J. N. Eckstein *Appl. Phys. Lett.* **60** (1992), 2288.
23. R. L. Fink, M. Thompson, C. Hilbert, H. Kroger *IEEE Trans. Appl. Supercond.* **3** (1993), 2219.
24. Y. Tarutani, T. Fukuzawa, A. Tsukamoto, M. Hiratani, K. Takagi *Appl. Phys. Lett.* **58** (1991), 2707.
25. K. K. Likharev *Rev. Mod. Phys.* **51** (1979), 101.
26. B. Schwartz, P. M. Mankiewich, R. E. Howard, L. D. Jackel, B. L. Straughn, E. G. Burkhardt, A. H. Dayem *IEEE Trans. Mag.* **MAG-25** (1989), 1298.
27. D. Cohen, E. Polturak *Physica B* **165&166** (1990), 71.
28. M. S. Wire, R. W. Simon, J. A. Luine, K. P. Daly, S. B. Coons, A. E. Lee, R. Hu, J. F. Burch, C. E. Platt *IEEE Trans. Mag.* **MAG-27** (1991), 3106.
29. R. H. Ono, J. A. Beall, M. W. Cromar, T. E. Harvey, M. E. Johansson, C. D. Reintsema, D. A. Rudman *Appl. Phys. Lett.* **59** (1991), 1126.



30. P. A. Rosenthal, E. N. Grossman, R. H. Ono, L. R. Vale *Appl. Phys. Lett.* **63** (1993), 1984.
31. Z. W. Dong, P. Hadley, R. Besseling, J. E. Mooij *Proc. Workshop HTS Josephson junctions*, p. 72.
32. J. Gao, W. A. M. Aarnink, G. J. Gerritsma, H. Rogalla *Physics C* **171** (1990), 126.
33. G. Koren, E. Polturak, G. M. Reisner, B. Fischer, L. Patlagon *Physica C* **225** (1994), 21.
34. K. Char, L. Antognazza, T. H. Geballe *Appl. Phys. Lett.* **63** (1993), 2420.
35. C. Stötzl, M. Siegel, G. Adrian, C. Krimmer, J. Söllner, W. Wilkens, G. Schulz, H. Adrian *Appl. Phys. Lett.* **63** (1993), 2970.
36. D. K. Chin, T. Van Duzer *Appl. Phys. Lett.* **58** (1991), 753.
37. G. Koren, E. Aharoni, E. Polturak, D. Cohen *Appl. Phys. Lett.* **58** (1991), 634.
38. M. A. J. Verhoeven, Yu. M. Boguslavskij, E. M. C. M. Reuvekamp, G. J. Gerritsma, H. Rogalla *Physica B* **194-196** (1994), 1345.
39. M. Yu. Kupriyanov, J. S. Tsai *Weak Superconductivity*, Eds. S. Benacka, P. Seidel, V. Strbik, SAS Press, Bratislava, 1994, pp. 1-12.
40. V. N. Glyantsev, M. Siegel, J. Schubert, W. Zander, A. I. Braginski *Applied Superconductivity*, Ed. H. C. Freyhardt, (DGM Oberursel, 1993), p. 1227.
41. J. Halbritter *Phys. Rev. B* **46** (1992), 14861.
42. A. J. Pauza, A. M. Campbell, D. F. Moore, R. E. Somekh, A. N. Broers *IEEE Trans. Appl. Supercond.* **3** (1993), 2405.
43. S. Tolpygo, S. Shokhor, B. Nadgorny, A. Bourdillon, J. Y. Lin, S. Y. Hou, J. M. Phillips, M. Gurvitch *Appl. Phys. Lett.* **63** (1993), 1696.
44. M. J. Zani, J. A. Luine, R. W. Simon, R. A. Davidheiser *Appl. Phys. Lett.* **59** (1991), 234.
45. Y. G. Gheem, Y. Okabe *Ext. Abstr. ISEC'93*, (Boulder, Aug. 11-14, 1993), p. 229.
46. P. Seidel, F. Schmidl, H. Schneidewind, F. Machalet, A. Matthes, L. Dörrer, K. Zach, S. Linzen, T. Schmauder, V. Zakosarenko, P. D. Prewett, P. McConville *Applied Superconductivity*, Ed. H. C. Freyhardt, (DGM Oberursel, 1993), p. 1167.
47. S. S. Tinchev *Supercond. Sci. Technol.* **3** (1990), 500.
48. F. Machalet, P. Seidel, E. Heinz, Yijie Li, E. Steinbeiß, T. Eick, K. Steenbeck, W. Brodkorb, U. Hübner *Abstr. Tagung Kryoelektronische Bauelemente*, (Schmiedefeld, Sept. 26-27, 1994).
49. R. W. Simon, J. B. Bulman, J. F. Burch, S. B. Coons, K. P. Daly, W. D. Dozier, R. Hu, A. E. Lee, J. A. Luine, C. E. Platt, S. M. Schwarzbek, M. S. Wire, M. J. Zani, *IEEE Trans. Magn.* **MAG-27** (1991), 3209.
50. Z. G. Ivanov, G. Brosson, T. Claeson *IEEE Trans. Magn.* **MAG-27** (1991), 3324.
51. M. Fujimoto, K. Suzuki, I. Terasaki, S. Yoshikawa, K. Yamaguchi, K. Hayashi, Y. Enomoto *Adv. Supercond. VI*, Eds. T. Fujita, Y. Shiohara, (Springer, Tokyo

- 1994), p. 1045.
52. M. Schmitt, S. Eckert, Th. Beckerer, H. Adrian, *Proc. M<sup>2</sup>S-HTSC IV*, (Grenoble, July 5-9, 1994), to appear in *Physica C*.
53. S. E. Romaine, P. M. Mankiewicz, W. J. Skocpol, E. Westerwick *Appl. Phys. Lett.* **59** (1991), 2603.
54. J. R. Wendt, J. S. Martens, C. I. H. Ashby, T. A. Plut, V. M. Hietala, C. P. Tigges, D. S. Ginley, M. P. Siegal, J. M. Phillips, G. K. G. Hohenwarter *Appl. Phys. Lett.* **61** (1992), 1597.
55. J. Schneider, H. Kohlstedt, R. Wördenweber *Applied Superconductivity*, Ed. H.C. Freyhardt, (DGM Oberursel, 1993), p. 1151.
56. R. Kleiner, F. Steinmeyer, G. Kunkel, P. Müller *Phys. Rev. Lett.* **68** (1992), 2394.
57. R. Kleiner, P. Müller *Phys. Rev. B* **49** (1994), 1327.
58. F. X. Regi, J. Schneck, J. F. Palmier, H. Savary (Proc. M<sup>2</sup>S-HTSC IV, Grenoble, 5-9 July, 1994) to appear in *Physica C*.
59. M. Veith et al. *these proceedings*
60. J. S. Martens, T. E. Zipperian, G. A. Vawter, D. S. Ginley, V. M. Hietala, C. P. Tigges *Appl. Phys. Lett.* **60** (1992), 1141.
61. W. C. Stewart *Appl. Phys. Lett.* **12** (1968), 277.
62. D. E. McCumber *J. Appl. Phys.* **39** (1968), 3113.
63. K. P. Daly, J. F. Burch, R. Hu, A. E. Lee, J. Luine, C. Pettiette-Hall *IEEE Trans. Appl. Supercond.* **3** (1993), 2345.
64. V. Ambegaokar, B. I. Halperin *Phys. Rev. Lett.* **22** (1969), 1364.
65. F. Busse, R. Nebel, P. Herzog, M. Darula, P. Seidel *Appl. Phys. Lett.* **63** (1993), 1687.
66. P. Seidel, E. Heinz, F. Schmidl, K. Zach, H.-J. Köhler, H. Schneidewind, J. Borck, L. Dörrer, S. Linzen, T. Köhler, W. Michalke, M. Manzel, E. Steinbeiß, H. Bruchlos, E.-B.- Kley, H.-J. Fuchs *IEEE Trans. Appl. Supercond.* **3** (1993), 2353.
67. E. Heinz, P. Seidel, F. Busse, H. Schneidewind *Weak Superconductivity*, Eds. S. Benacka, P. Seidel, V. Strbik, SAS Press, Bratislava, 1994, p. 78.
68. F. Schmidl, L. Alff, R. Gross, K.-D. Husemann, H. Schneidewind, P. Seidel *IEEE Trans. Appl. Supercond.* **3** (1993), 2349.
69. C. Vanneste, C. C. Chi, W. J. Gallagher, A. W. Kleinsasser, S. I. Raider, R. L. Sandstrom *J. Appl. Phys.* **64** (1988), 242.
70. P. Seidel, M. Siegel, E. Heinz *Physica C* **180** (1991), 284.
71. R. L. Kautz, S. P. Benz, C. D. Reintsema *Appl. Phys. Lett.* **65** (1994), 1445.
72. M. Darula, P. Seidel, F. Busse, S. Benacka, *J. Appl. Phys.* **74** (1993) 2674.
73. M. Darula, A. Darulova, P. Seidel, B. Misanik, F. Busse, M. Siegel, S. Beuven, S. Benacka *Weak Superconductivity*, Eds. S. Benacka, P. Seidel, V. Strbik, SAS Press, Bratislava, 1994, p. 160
74. P. Seidel, F. Schmidl, H. Schneidewind, L. Dörrer, M. Darula, *Advances in Superconductivity VI*, Eds. T. Fujita, Y. Shiohara, (Springer, Tokyo, 1994), p. 1111.

75. V. N. Glyantsev, M. Siegel, J. Schubert, W. Zander, U. Poppe, H. Soltner, A. I. Braginski, C. Heiden *Supercond. Sci. Technol.* **7** (1994), 253.
76. G. Jung, B. Savo, A. Vecchione *Europhys. Lett.* **21** (1993), 947.
77. M. Darula, P. Seidel, B. Misanik, F. Busse, E. Heinz, S. Benacka *Physica B* **194-196** (1994), 1749.
78. M. Darula, P. Seidel, F. Busse, S. Benacka *Supercond. Sci. Technol.* **7** (1994), 317.
79. M. Darula, A. Darulova, P. Seidel, S. Benacka, B. Misanik *these proceedings*.
80. V. Zakosarenko, F. Schmidl, H. Schneidewind, L. Dörrer, P. Seidel *Appl. Phys. Lett.* **65** (1994), 779.
81. P. Seidel, V. Zakosarenko, F. Schmidl, L. Dörrer, H. Schneidewind, S. Linzen, E.V. Il'ichev, M. Darula *Proc. ASC'94*, to appear in *IEEE Trans. Appl. Supercond.*.
82. Workshop report *Physica B* **152** (1988), pp. 1-302.
83. L. L. Sohn, M. S. Rzchowski, J. U. Free, M. Tinkham, C. J. Lobb *Phys. Rev. B* **45** (1992), 3003.
84. S. P. Benz, C. J. Burroughs *Appl. Phys. Lett.* **58** (1991), 2162.
85. S. Han, B.W. Zhang, J.E. Lukens *Appl. Phys. Lett.* **64** (1994), 1424.
86. M. Darula, P. Seidel, J. von Zameck Glyscinski, A. Darulova, F. Busse, S. Benacka *Applied Superconductivity*, Ed. H. C. Freyhardt, (DGM Oberursel, 1993), p. 1245.
87. J. R. Phillips, H. S. J. van der Zant, J. White, T.P. Orlando *Physica B* **194-196**, (1994), 1777.
88. F. Busse, M. Darula, P. Seidel *Weak Superconductivity*, Eds. S. Benacka, P. Seidel, V. Strbik, SAS Press, Bratislava, 1994, p. 146.
89. T. A. Fulton, R. C. Dynes, P. W. Anderson *Proc. IEEE* **61**, (1973), 28.

---

Chapter 2

**Materials Issues**

dimensional chain structure in addition to the CuO planes. For the compound that is fully oxygenated ( $\delta = 0$ ) the chain structure is particularly well developed. The chains provide doping for the CuO planes, but in addition, and this is particularly important for our model, they form an independent conducting subsystem. As a result, the superconducting state of the material displays a two-gap structure. Namely, each of the subsystems is characterized by its own energy gap. Let us denote by  $\alpha$  and  $\beta$  the plane and chain subsystems, so that  $\epsilon_\alpha$  and  $\epsilon_\beta$  are the corresponding energy gaps.

First of all, one should give an explicit definition of the two-gap spectrum. Each subsystem has its own order parameter. This means that the density of states has two peaks which can be determined spectroscopically. In the following, we will use the two-gap picture to refer to the two peaks in the density of states.

The effects of anisotropy and the two-gap structure are similar. Both of them correspond to deviations from the simple isotropic one-gap picture. Anisotropy of the energy gap means that the value of the energy gap is different for different directions in momentum space, whereas two-gap superconductivity implies that for a fixed direction, there are different gap values. The effects of anisotropy have been discussed in detail in review articles.<sup>2</sup> The inequality  $l \ll \xi$  ( $l$  is a mean free path,  $\xi$  is the coherence length) leads to isotropization of the gap in the conventional materials.

The plane ( $\alpha$ ) and chain ( $\beta$ ) subsystems are coupled by charge transfer. Because of the charge transfer, the system is characterized by a single value of  $T_c$  (in the absence of charge transfer there would be two different transition temperatures:  $T_c^\alpha$  and  $T_c^\beta$ ).

The superconducting state in the CuO plane is caused by the same intrinsic mechanism in all the cuprates. We think that this mechanism is phonon exchange, but at the moment this is not essential. As for the chain subsystem, the pairing is induced by two channels. The first is an intrinsic proximity effect; the word "intrinsic" stresses the fact that, unlike the usual proximity effect observed in thin-film sandwich structure, we are dealing with a phenomenon occurring on the scale of unit cell. Nevertheless, the physics of the phenomenon is similar and represents the tunneling of the Cooper pair  $\alpha \leftrightarrow \beta$ . The process can be described by the McMillan tunneling model of the proximity effect.<sup>3</sup> The second pairing channel is an inelastic channel.<sup>1</sup>

The major parameters of YBCO are the values of  $T_c$  and the energy gaps  $\epsilon_\alpha(0)$  and  $\epsilon_\beta(0)$ . Note that, unlike the BCS model, in the two-gap analysis there is not any universal relation between the values of the energy gaps and  $T_c$ .<sup>4</sup>

For the planes,  $2\epsilon_\alpha(0)$  is equal to approximately  $5T_c$ . The smaller gap, on the other hand, is very sensitive to the oxygen content and for  $\delta = 0$  is approximately equal to  $1.25T_c$ . This latter number has been obtained from careful measurements of the temperature dependence of the penetration depth at low temperature. This value of  $1.25T_c$  is also consistent with measurements of the temperature dependence of the surface resistance, which is smaller than the BCS value of  $1.25T_c$ . Since the material is characterized by two order parameters  $\Delta_\alpha$  and  $\Delta_\beta$ , there are two sets of Cooper pairs and correspondingly, two different coherence lengths  $\xi_\alpha$  and  $\xi_\beta$ . The coherence lengths are  $\xi_\alpha = 15\text{\AA}$  (planes) and  $\xi_\beta = 25\text{\AA}$  (chains).<sup>1</sup>

dimensional chain structure in addition to the CuO planes. For the compound that is fully oxygenated ( $\delta = 0$ ) the chain structure is particularly well developed. The chains provide doping for the CuO planes, but in addition, and this is particularly important for our model, they form an independent conducting subsystem. As a result, the superconducting state of the material displays a two-gap structure. Namely, each of the subsystems is characterized by its own energy gap. Let us denote by  $\alpha$  and  $\beta$  the plane and chain subsystems, so that  $\epsilon_\alpha$  and  $\epsilon_\beta$  are the corresponding energy gaps.

First of all, one should give an explicit definition of the two-gap spectrum. Each subsystem has its own order parameter. This means that the density of states has two peaks which can be determined spectroscopically. In the following, we will use the two-gap picture to refer to the two peaks in the density of states.

The effects of anisotropy and the two-gap structure are similar. Both of them correspond to deviations from the simple isotropic one-gap picture. Anisotropy of the energy gap means that the value of the energy gap is different for different directions in momentum space, whereas two-gap superconductivity implies that for a fixed direction, there are different gap values. The effects of anisotropy have been discussed in detail in review articles.<sup>2</sup> The inequality  $l \ll \xi$  ( $l$  is a mean free path,  $\xi$  is the coherence length) leads to isotropization of the gap in the conventional materials.

The plane ( $\alpha$ ) and chain ( $\beta$ ) subsystems are coupled by charge transfer. Because of the charge transfer, the system is characterized by a single value of  $T_c$  (in the absence of charge transfer there would be two different transition temperatures:  $T_c^\alpha$  and  $T_c^\beta$ ).

The superconducting state in the CuO plane is caused by the same intrinsic mechanism in all the cuprates. We think that this mechanism is phonon exchange, but at the moment this is not essential. As for the chain subsystem, the pairing is induced by two channels. The first is an intrinsic proximity effect; the word "intrinsic" stresses the fact that, unlike the usual proximity effect observed in thin-film sandwich structure, we are dealing with a phenomenon occurring on the scale of unit cell. Nevertheless, the physics of the phenomenon is similar and represents the tunneling of the Cooper pair  $\alpha \leftrightarrow \beta$ . The process can be described by the McMillan tunneling model of the proximity effect.<sup>3</sup> The second pairing channel is an inelastic channel.<sup>1</sup>

The major parameters of YBCO are the values of  $T_c$  and the energy gaps  $\epsilon_\alpha(0)$  and  $\epsilon_\beta(0)$ . Note that, unlike the BCS model, in the two-gap analysis there is not any universal relation between the values of the energy gaps and  $T_c$ .<sup>4</sup>

For the planes,  $2\epsilon_\alpha(0)$  is equal to approximately  $5T_c$ . The smaller gap, on the other hand, is very sensitive to the oxygen content and for  $\delta = 0$  is approximately equal to  $1.25T_c$ . This latter number has been obtained from careful measurements of the temperature dependence of the penetration depth at low temperature. This value of  $1.25T_c$  is also consistent with measurements of the temperature dependence of the surface resistance, which is smaller than the BCS value of  $1.25T_c$ . Since the material is characterized by two order parameters  $\Delta_\alpha$  and  $\Delta_\beta$ , there are two sets of Cooper pairs and correspondingly, two different coherence lengths  $\xi_\alpha$  and  $\xi_\beta$ . The coherence lengths are  $\xi_\alpha = 15\text{\AA}$  (planes) and  $\xi_\beta = 25\text{\AA}$  (chains).<sup>1</sup>

### 3. Gapless State

The concept of gapless superconductivity was introduced in Ref. 5. The gapless superconducting state may arise through several channels. One should note that the gapless state, despite the absence of the energy gap, is still a superconducting state.<sup>5,6</sup> The absence of the gap leads to a power law, rather than exponential dependences of the electronic heat capacity, surface impedance, penetration depth, etc., but nevertheless, the material still exhibits the Meissner effect and zero resistance. A very interesting case of gapless superconductivity occurs if the material contains magnetic impurities.

Consider the two-gap case when the chains in YBCO are in the induced superconducting state. If the  $\beta$ -system (chains) contains magnetic impurities, then we are dealing with an unusual case of gapless superconductivity, namely at some value of the impurity concentration the energy gap becomes equal to zero, whereas the shift in  $T_c$ , unlike the usual case, is relatively small. Such a case occurs when oxygen is removed. Indeed, the removal of oxygen greatly affects the chain's states. Instead of a well-developed chain structure, we have a set of broken chains with Cu atoms at the end. These Cu atoms form local magnetic states, similar to surface states. These magnetic moments act as strong pairbreakers in the chain band. As a result, the chains rapidly develop a gapless state.

The critical concentration  $n$ , which corresponds to the appearance of the gapless state can be calculated by use of the method developed for the usual proximity system. For  $\delta = 0.1$ , that is for  $YBa_2Cu_3O_{6.9}$  compound, we are dealing with the gapless state. It corresponds to the criterion  $l^c = \xi_\beta$  where  $l^c = v_f \tau_c^m$  is the mean free path for magnetic scattering.

It is essential that, although the magnetic moments are introduced in the chain sites only, the energy gaps become equal to zero in both subsystems, chains and planes. Namely, as a consequence of the charge transfer, both densities of states  $N_\alpha(w)$  and  $N_\beta(w)$  are not equal to zero up to  $\omega = 0$ . Note also, that even when the gaps are equal to zero, the density of states  $N_\alpha(w)$  displays a peak at  $\omega = \epsilon_\alpha$ , and this peak can be observed experimentally, e.g., by tunneling measurements. The gapless regime is very narrow in the conventional isotropic case,<sup>5</sup> namely  $n_{cr} = 0.91n'$ ,  $n'$  corresponds to  $T_c = 0$ , that is, to the total disappearance of superconductivity. The presence of different subsystems, such as planes and chains, leads to a different picture (see above), and the gapless region becomes much wider.<sup>7</sup> The presence of magnetic impurities drastically affects the value of the induced energy gap without any noticeable impact on the critical temperature.<sup>5</sup>

### 4. Penetration Depth

This section is concerned with the temperature dependence of the penetration depth in layered superconductors, such as the high  $T_c$  oxides. At present, this problem has attracted much interest. The experimental data look contradictory. Indeed, some

authors<sup>8,9</sup> have observed exponential dependences for Nd-based cuprates and for fully oxygenated YBCO films. According to others<sup>10,11</sup>  $\Delta\lambda \propto T$ , whereas a quadratic dependence has also been reported<sup>9,12,13</sup>. It will be shown that the approach developed by us<sup>1</sup> can explain all data<sup>8-13</sup> in a unified way, and that the dependence  $\Delta\lambda(T)$  indeed can vary and is very sensitive to oxygen content. This paper also contains some predictions related to conventional S-N-S multilayers.

The evaluation of the penetration depth is based on a model that has been presented previously,<sup>1</sup> and will briefly be described here. The YBCO compound contains two conducting (and, consequently at  $T < T_c$ , two superconducting) subsystems,<sup>1</sup> namely, CuO planes ( $\alpha$ ) and chains ( $\beta$ ), bound by charge transfer. Each of the subsystems is characterized by its own order parameter  $\Delta_i(\omega_n)$ ,  $i = (\alpha, \beta)$  with  $\omega_n = (2n + 1)\pi T$  (we are using the thermodynamic Green's function formalism). The presence of the two order parameters corresponds to a two gap picture, meaning the superconducting density of states contains two peaks.<sup>1</sup> In YBCO,  $\epsilon_\alpha \simeq 25$  meV and  $\epsilon_\beta \simeq 6$  meV. The planes are intrinsically superconducting, whereas the superconducting state in the chains is due to charge transfer. The superconducting state in the chains is induced by the intrinsic proximity effect and, in addition, through an inelastic channel.

Oxygen depletion leads to a transition into the gapless regime. This regime is caused by the pair breaking effect in the chains which is due to the appearance of uncompensated  $\text{Cu}^{++}$  ions, the presence of which has been established experimentally.<sup>14</sup> One can show that such a transition, contrary to the conventional case<sup>5,6</sup> does not lead to a noticeable change in  $T_c$ , but does make a great impact on the transport tunneling, microwave properties, etc. which are sensitive to the structure of the energy spectrum.<sup>1</sup>

The screening is provided by both subsystems, and the temperature dependence of the penetration depth in the London case  $\xi \ll \lambda$  is described by the equation:<sup>15</sup>

$$\frac{\lambda(T)}{\lambda(0)} = \frac{[Q_\alpha(T) + Q_\beta(T)]^{-\frac{1}{2}}}{[Q_\alpha(0) + Q_\beta(0)]^{-\frac{1}{2}}} \quad (1)$$

The kernels  $Q_\alpha$  and  $Q_\beta$  are equal to:

$$Q_\alpha(T) = \rho\pi T \sum_{\omega_n=0}^{\infty} \frac{1}{Z_\alpha(i\omega_n)} \frac{\Delta_\alpha^2(i\omega_n)}{[\omega_n^2 + \Delta_\alpha^2(i\omega_n)]^{\frac{3}{2}}}$$

$$Q_\beta(T) = \pi T \sum_{\omega_n=0}^{\infty} \frac{1}{Z_\beta(i\omega_n)} \frac{\Delta_\beta^2(i\omega_n)}{[\omega_n^2 + \Delta_\beta^2(i\omega_n)]^{\frac{3}{2}}}$$

The quantities  $Z_\alpha(i\omega_n)$  and  $Z_\beta(i\omega_n)$  are the renormalization functions, and  $\rho = \nu_\alpha m_\beta / \nu_\beta m_\alpha$  ( $\nu$  is the density of states). The order parameters and the renormalization functions are satisfied by the equations<sup>1</sup>:



$$\begin{aligned} \Delta_\alpha(i\omega_n)Z_\alpha(i\omega_n) &= \lambda_\alpha\pi T \sum_{n'=-\infty}^{\infty} D_{nn'} \frac{\Delta_\alpha(i\omega_{n'})}{K_{n'}^\alpha} + \\ &+ \lambda_{\alpha\beta}\pi T \sum_{n'=-\infty}^{\infty} D_{nn'} \frac{\Delta_\beta(i\omega_{n'})}{K_{n'}^\beta} + \Gamma_{\alpha\beta} \frac{\Delta_\beta(i\omega_n)}{K_n^\beta} \end{aligned} \quad (2)$$

$$\Delta_\beta(i\omega_n)Z_\beta(i\omega_n) = \lambda_{\beta\alpha}\pi T \sum_{n'=-\infty}^{\infty} D_{nn'} \frac{\Delta_\alpha(i\omega_{n'})}{K_{n'}^\alpha} + \Gamma_{\beta\alpha} \frac{\Delta_\alpha(i\omega_n)}{K_n^\alpha} \quad (3)$$

$$Z_\alpha(i\omega_n) = \left[ 1 + \frac{\lambda_\alpha\pi T}{\omega_n} \sum_{n'=-\infty}^{\infty} D_{nn'} \frac{\omega_{n'}}{K_{n'}^\alpha} + \frac{\lambda_{\alpha\beta}\pi T}{\omega_n} \sum_{n'=-\infty}^{\infty} D_{nn'} \frac{\omega_{n'}}{K_{n'}^\beta} + \Gamma_{\alpha\beta} \frac{1}{K_{n'}^\beta} \right] \quad (4)$$

$$Z_\beta(i\omega_n) = \left[ 1 + \frac{\lambda_{\beta\alpha}\pi T}{\omega_n} \sum_{n'=-\infty}^{\infty} D_{nn'} \frac{\omega_{n'}}{K_{n'}^\alpha} + \Gamma_{\beta\alpha} \frac{1}{K_{n'}^\alpha} + \Gamma_M \frac{1}{K_{n'}^\beta} \right] \quad (5)$$

Here  $K_n^i = [\omega_n^2 + \Delta_i^2(i\omega_n)]^{\frac{1}{2}}$  ( $i = \alpha, \beta$ ),  $\Gamma_{\alpha\beta}$  and  $\Gamma_{\beta\alpha}$  describe the intrinsic proximity effect,  $\lambda_\alpha$  is the in-plane coupling constant describing the pairing in the CuO plane,  $\lambda_{\alpha\beta}$  and  $\lambda_{\beta\alpha}$  are the off diagonal coupling constants,  $D_{nn'} = \tilde{\Omega}^2 / [\tilde{\Omega}^2 + (\omega_n - \omega_{n'})^2]$  is the phonon Green's function, and  $\tilde{\Omega}$  is the characteristic phonon frequency. In accordance with Ref. 1, we are considering the electron-phonon interaction as the pairing mechanism. Note that the model can easily be generalized for another type of interaction. The absence of the term containing  $\lambda_\beta$  corresponds to the induced nature of the pairing in the chains. The presence of the last term on the rhs of Eqn. (5) is very important for our present purpose. The term describes the presence of the magnetic moments in the chains. Oxygen depletion leads to an increase in  $\Gamma_M$ . Eqns. (2)-(5) were solved using a Newton-Raphson method and inverting the resulting matrices using band diagonal techniques.

First of all, we would like to formulate a qualitative result, namely, that the temperature dependence is different for various concentrations of the impurities. Therefore, for YBCO the dependence  $\Delta\lambda(T)$  is different for various oxygen contents. If  $\Gamma_M=0$ , then an exponential dependence is obtained for  $\Delta\lambda(T)$  as  $T \rightarrow 0$ . An increase in  $\Gamma_M$ , that is, an increase in magnetic impurities, leads to a modification of this dependence. A weaker exponential dependence is observed for small values of  $\Gamma_M$  corresponding to a smaller energy gap. For  $\Gamma_M = 90K$  ( $\delta \approx .1$ ) a linear dependence is obtained. For even larger values of  $\Gamma_M$ , the calculated dependence becomes quadratic.

In the calculation, the following set of intrinsic parameters were specifically used:  $\lambda_\alpha=3.0$ ,  $\lambda_{\alpha\beta}=.24$ ,  $\lambda_{\beta\alpha}=.17$ ,  $\Gamma_{\alpha\beta}=90$ ,  $\Gamma_{\beta\alpha}=64$ , and  $\tilde{\Omega}=385$ . These values were obtained in<sup>1,16</sup> and by analysis of various experimental data.

According to the approach developed in Ref. 1, the value of the parameter  $\Gamma_M$  is directly related to the oxygen content, which allows one to compare our calculations with the experimental data.<sup>8-13</sup> The value ( $\Gamma_M = 0$ ) corresponds to the stoichiometric composition, and the dependence of  $\Delta\lambda(T)$  is exponential as  $T \rightarrow 0$ . The energy spectrum has a two-gap structure, and  $\Delta\lambda(T)$  is dominated by the smaller gap, so

that  $\Delta\lambda(T) \propto \exp(-\epsilon_\beta/T)$ . Such exponential dependence, indeed, has been observed<sup>9</sup> for a fully oxygenated YBCO thin film. The oxygen depletion leads initially to a decrease in the energy gap and, correspondingly, to the weaker exponential law. We think such an effect has been observed in<sup>2</sup> for a small deviation from the stoichiometry. The value ( $\Gamma_M = 90K$ ) corresponds to the transition to the gapless state.<sup>1</sup> Then the dependence  $\Delta\lambda(T)$  is not exponential, but is described by a power law. According to our calculations, the dependence becomes linear. For greater oxygen depletion, the calculated curves exhibit a quadratic tendency. Such quadratic dependence has also been seen,<sup>12</sup> with the data more closely matching calculated curves with  $\Gamma_M > 90K$ . This is consistent with the depressed critical temperatures of the samples used in<sup>12</sup>.

According to our analysis, the linear dependence in<sup>10</sup> is characteristic of an oxygen depleted sample, which seems at odds with the high  $T_c$  of the crystals. This can be understood in light of recent work by Skelton *et al.*<sup>17</sup> who found that some single crystals of YBCO become highly oxygen deficient at the surface while maintaining the stoichiometry in the bulk.

Our approach allows us to describe, in a unified way, the experimental data on the penetration depth in YBCO displaying different temperature dependences. According to our theory, these differences are sample dependent and correlate with the oxygen content. The stoichiometric compound is gapped and is characterized by an exponential dependence. Note that such a dependence has been observed also in the Nd-based cuprate and is related to the corresponding energy gap. Oxygen depletion leads initially to a decrease in the energy gap and then to the transition to the gapless state. Then the dependence is described by a power law, initially linear, and then quadratic.

The approach developed in this paper can be applied not only to the layered compounds such as YBCO which are characterized by the intrinsic proximity effect and the off-diagonal inelastic coupling constants, but also to the usual proximity systems, including conventional S-N-S multilayers. Eqns. (2)-(5) can be used to study the screening properties; the usual proximity system is obtained by setting  $\lambda_{\alpha\beta}$  and  $\lambda_{\beta\alpha}$  equal to 0. The magnetic impurities should be placed in the N-layer, and this should not drastically effect  $T_c$  but will strongly modify the energy spectrum. Because of the appearance of a gapless state, the penetration depth data should display a transition from an exponential behavior to a power law. In addition one can observe the linear law for relatively small  $\Gamma_M$ , and a quadratic dependence for larger values. It would be interesting to carry out the measurements of the penetration depth to experimentally verify our conclusion about the change in  $\Delta\lambda(T)$  due to an increase in the concentration of magnetic impurities.

The temperature dependence of the penetration depth  $\Delta\lambda(T)$  for YBCO is characterized by peculiar features. Based on our approach, one can demonstrate that the nature of this dependence strongly depends on the oxygen content. Our analysis provides a unified description of recent experimental data. The oxygen depletion leads to the transformation:  $\Delta\lambda_1(T) \rightarrow \Delta\lambda_2(T) \rightarrow \Delta\lambda_3(T) \rightarrow \Delta\lambda_4(T)$  where  $\Delta\lambda_1(T) \propto \exp(-\epsilon_\beta/T)$ ,  $\Delta\lambda_2(T) \propto \exp(-\epsilon'_\beta/T)$  ( $\epsilon'_\beta < \epsilon_\beta$ ),  $\Delta\lambda_3(T) \propto T$ , and  $\Delta\lambda_4(T) \propto T^2$ . A similar change should also be observed in the conventional S-N-

S-N multilayers with a change in concentration of magnetic impurities placed in the N-layer.

### 5. Intrinsic Asymmetry, SQUIDS

The presence of the two conducting subsystems (planes and chains) makes a great impact on various properties of the materials. This factor is important also for the analysis of Josephson junctions, particularly, if we are dealing with untwinned crystals. Indeed, the conductance of the junction depends strongly on the relative orientation of the chains. Let us illustrate this point by analyzing the corner SQUID which contains an untwinned YBCO crystal.

In the SQUID experiment, described in Ref. 18, a d-wave pairing function would lead to a phase shift  $\delta = \pi$  between the "a" and "b" directions in the CuO plane, whereas s-wave symmetry would not display such a shift. The idea to use such a difference<sup>19</sup> in order to determine the symmetry of the pairing is very attractive and formed the basis for the experiment. According to Ref. 18, the data are not totally conclusive (for example, it is difficult to avoid an additional shift caused by trapped vortices, or some extrinsic properties of the junctions), and there is a spread in values of the  $\delta_{AB}$ .

Consider corner YBCO-Sc SQUID (Sc is a conventional superconductor, e.g. Pb, or Nb<sup>18</sup>). The magnetic field modulates the current, and for a symmetric SQUID:

$$I = I_{\text{mod}} \sin q \quad (6)$$

where  $I_{\text{mod}} = 2I_0 \cos(\pi\Phi/\Phi_0 + \delta_{AB})$ . Note that for a symmetric SQUID one can separate the factor containing  $\Phi$ ; as a result, for the d-wave case  $I=0$  for  $\Phi = 0$ , and  $I=2I_0$  even if  $I < I_{\text{max}}$ .

An important point is that the SQUID contains a large intrinsic asymmetry, caused by the presence of the superconducting chains. The presence of the second subsystem is a key ingredient of our approach (see above). As a result, the total current is

$$I = I_1 \sin q_1 + I_2 \sin q_2 \quad (7)$$

where  $I_1 = I_{\text{pl}} + I_{\text{ch}}$ ,  $I_2 = I_{\text{pl}}$ . In the presence of a magnetic field it is impossible to reduce (7) to the form (6), that is, to factorize the field. In the presence of the field, the expression for  $I$ , after some manipulations can be written in the form:

$$I = I_1 [\sin(q + \gamma) \cos(\pi\Phi/\Phi_0 - \gamma) + \sin(q - \gamma) \cos(\pi\Phi/\Phi_0 + \gamma)] \quad (8)$$

where  $q = q_1 + q_2$ , and  $\cos 2\gamma = I_2/I_1$ . If  $I_1 = I_2$ , then  $\gamma = 0$ , and we obtain Eqn. (6). One can directly deduce from Eqn. (8) that the parameter  $\gamma$  enters as a phase factor, and the value of the current  $I$  at  $\Phi = 0$  depends strongly on  $\gamma$ . For example, if  $I_2 \ll I_1$  (then  $\gamma = \pi/4$ ), and  $I$  is small (we consider the case when the bias current  $I < I_{\text{max}}$ ), we obtain  $I=0$  at  $\Phi = 0$ , and  $I=I_1$  at  $\Phi = \Phi_0/2$ .

Therefore  $I_{\Phi=\Phi_0/2} \gg I_{\Phi=0}$ , that is, the picture is similar to that for d-wave pairing (cf. Eqn. (6)), but the effect is caused by the intrinsic asymmetry ( $I_1 \gg I_2$ ) of the

corner SQUID with s-wave pairing. Note, that the small value of  $I$  at  $\Phi = 0$  does not require such a strong inequality  $I_1 \gg I_2$ , in particular, if we take into account the spread of the data.<sup>18</sup> Even for realistic values of  $I_1$  and  $I_2$  one can obtain such a picture, observed in<sup>18</sup>.

The remark made in<sup>18</sup> about there being no difference between untwinned and twinned crystals is strange, because, in the general case, the twinning should lead to the situation when the "a" and "b" directions are equivalent, and the effect claimed is absent. Probably, one can deal with some special type of twinning, where the twin spacing is large compared to the junction size and the intrinsic asymmetry will be kept.

Note that the model described above considers the chains as intrinsically normal. The superconducting state is induced by an intrinsic proximity effect and an inelastic charge transfer channel. As a result, the phase shift between the chain structure and Pb is the same as for the planes and Pb. If we include an additional intrinsic pairing for the chains even with a small coupling constant  $\lambda_{pl}$ , it would lead to an additional shift and even more complicated structure.<sup>20</sup>

We think that the method of phase coherence<sup>18,19</sup> is very interesting, but it probably requires the use of the superconductors without intrinsic asymmetry, such as, for example, LaSrCuO.

From these considerations, it can be seen that the chain alignment plays a very important role. The parameters of the Josephson junction can be greatly affected by the mutual orientation of the contact and the b-axis. We discuss this problem in more detail elsewhere.

## 6. Conclusion

The main results of the paper can be summarized as follows:

1. The presence of various structural low-dimensional units (planes, chains), along with short coherence length lead to a unique opportunity to observe a two-gap spectrum. The spectroscopy of the stoichiometric YBCO compound (microwave properties, tunneling, etc.) is determined by the smaller energy gap.
2. The chains are characterized by the induced superconductivity which is due to the charge transfer, e.g. to the intrinsic proximity effect.
3. Oxygen depletion leads to a gapless state. This state is manifested in the change in the temperature dependence of the penetration depth which is then described by a power law.
4. The chains can make a noticeable contribution to the Josephson current, and this contribution is determined by the orientation of the chains.

## Acknowledgements

The research of VZK is supported by the US Office of Naval Research under Con-

tract No. N00014-94-F0006, and the research of MER is supported under Contract No. N00014-94-1-G027.

## References

1. V.Kresin and S.Wolf, a) *Phys.Rev.* **B41** (1990) 4278; b) *Physica C* **169** (1990) 476; c) *Phys. Rev.* **B46** (1992) 6458.
2. J.Clem, *Am. Phys.* **40** (1966) 268; A.Shepelev, *Sov. Phys.-Usp.* **96** (1968) 217.
3. W. McMillan, *Phys. Rev.* **175** (1968) 537.
4. H.Suhl et al., *Phys. Rev. Lett.* **3** (1959) 552; B.Geilikman et al., *Sov. Phys.-Solid State* **9** (1967) 642; V.Kresin, *J. Low Temp. Phys.* **11** (1973) 519.
5. A.Abrikosov and L.Gor'kov, *Sov. Phys.-JETP* **12** (1961) 1243.
6. K.Maki, in *Superconductivity*, ed. R. Parks, (Marcel Dekker, NY 1969) p.1035; P.De Gennes, *Superconductivity of Metals and Alloys*, (W. Benjamin, NY 1966), Ch. VIII.
7. A.Kaizer and M.Zuckermann, *Phys. Rev.* **B1** (1970) 229.
8. S.Anlage et al., *Phys. Rev.* **B44** (1991) 9764.
9. N.Klein et al., *Phys. Rev. Lett.* **71** (1993) 3355.
10. W. Hardy et al., *Phys. Rev. Lett.* **70** (1993) 3999.
11. S.Anlage et al. (preprint).
12. M.Beasley, *Physica C* **209** (1993) 43.
13. Zhengxiang Ma et al., *Phys. Rev. Lett.* **71** (1993) 781.
14. V.Kresin and S.Wolf, *Phys. Rev. B* (to be published).
15. A.Abrikosov and I.Khalatnikov, *Adv. Phys.* **8** (1959) 45.
16. M.Reeves et al., *Phys. Rev.* **B47** (1993) 6065.
17. E.Skelton et al., *Science* **263** (1994) 1416.
18. D.Wollman et al., *Phys. Rev. Lett.* **71** (1993) 2134; D.Brawer and H.Ott (preprint).
19. V.Gershkenbein, A.Larkin, and A. Barone, *Phys. Rev.* **B36** (1987) 235.
20. A.Golubov and I.Mazin (preprint).

# STRONG COUPLING EFFECTS IN S-WAVE TWO BAND SUPERCONDUCTOR

A.A.GOLUBOV

*Institute of Solid State Physics  
Chernogolovka, Moscow district, 142 432 Russia*

and

O.V.DOLGOV, E.G.MAKSIMOV

*P.N.Lebedev Physical Institute, 117924 Moscow, Russia*

and

I.I.MAZIN

*Geophysical Laboratory, Carnegie Institution of Washington, NW, Washington DC 20015, USA*

and

S.V.SHULGA

*Institute of Spectroscopy, 117924 Moscow district, Russia*

## ABSTRACT

We have studied theoretically a two-band superconductor in which superconductivity is induced by a strong retarded pairing interaction in one of the bands and has s-wave symmetry. This picture results in strongly anisotropic order parameter. The Eliashberg equations are solved for two bands with account taken of intraband and interband impurity scattering (usual and magnetic). Magnetic field penetration depth and electronic densities of states in each band are calculated numerically. Gapless superconductivity is discussed. Conditions are considered when the solution with different signs of the order parameters in different bands exists. This interband gap sign reversal can manifest itself in Josephson experiments.

## 1. Introduction

As follows from many tunneling, optical and microwave studies of high  $T_c$  superconductors (see eg.<sup>1-4</sup>), the low-frequency response of these materials is consistent with either absence of an energy gap or with a small gap  $2\Delta_g/T_c < 3.5$ . This suggests d-wave or strongly anisotropic s-wave pairing state. Our purpose is to study the latter case, but with interband anisotropy instead of the more conventional angular one.

The extension of the BCS theory for two or more superconducting bands was worked out by Suhl, Matthias, and Walker<sup>5</sup> and independently by Moscalenko<sup>6</sup>, and later elaborated on by many. Later, it was realized<sup>7</sup> that the fact that several bands cross Fermi level is not sufficient to have considerable many-band effects in superconductivity. Only when the bands in question have really different physical origin, a substantial effect may appear.

This is the case in many high- $T_c$  cuprates. In particular,  $YBa_2Cu_3O_7$  is known

to have four sheets of the Fermi surface, all four having different physical origin<sup>8,9</sup>: one is formed by the chain  $pd\sigma$  (seen by positron annihilation), another is an apical oxygen band (seen in de Haas-van Alphen experiments), and the last two are bonding and antibonding combinations of the two  $pd\sigma$  plane bands (seen by angular-resolved photoemission). Basing on the richness of the band structure of  $YBa_2Cu_3O_7$ , several groups pointed out that at least two-band<sup>10</sup>, or probably the whole four-band<sup>11,12</sup>, picture should be used to describe superconductivity in this system. Various experiments have been interpreted as indicating two or more different superconducting gaps.

A simplest solvable model containing all essential physics is a two-band model. We shall consider two bands for  $YBa_2Cu_3O_7$ : a chain band and a plane band. It is generally believed that superconductivity appears because of the plains and in the chains is induced. Consequently, we shall assume the coupling constant in the planes,  $\lambda_s$ , to be much larger than that for the chains,  $\lambda_n$ . We shall also include a finite interband coupling,  $\lambda_{ns}$ , and a finite scattering rate ('interband tunneling') between the bands,  $\Gamma_{ns}$ . This model has been considered in<sup>10</sup>, where  $T_c$  and energy gaps in both bands were calculated. In order to make comparison with experimental data electromagnetic response and energy spectrum should be investigated in more detail. We present the results of a general treatment of this two-band model in a strong coupling regime. Magnetic penetration depth and densities of states in each band are calculated. Josephson effect between two-band superconductors as well as between two-band superconductor and conventional one is studied.

## 2. The model

We shall now remind the basic equations of the multiband BCS theory<sup>5-7</sup>. The Hamiltonian has the following form:

$$H = \sum_{i,k\alpha} \epsilon_{i,k} c_{i,k\alpha}^* c_{i,k\alpha} + \sum_{ij,kk'\alpha\beta} (t_{ij}^{\alpha\beta} c_{i,k\alpha}^* c_{j,k'\beta} - \frac{g_{ij}}{2} c_{i,k\alpha}^* c_{j,k'\alpha} c_{i,-k\beta}^* c_{j,-k'\beta}) \quad (1)$$

where  $i, j$  are  $\alpha, \beta$  are band and spin indices, respectively,  $\epsilon_{i,k}$  is kinetic energy in  $i$ -th band,  $c_{i,k\alpha}^*$  and  $c_{i,k\alpha}$  are corresponding creation and annihilation operators.  $g_{ij}$  are the averaged pairing interaction energies resulting from intraband and interband phonon emission and absorption, minus the corresponding screened Coulomb interaction terms, and  $t_{ij}^{\alpha\beta}$  are matrix elements describing elastic intraband scattering as well as interband one (interband tunneling).

In the simplest case  $t_{ij}^{\alpha\beta} = 0$  the order parameter  $\Delta_i$  on the  $i$ -th sheet of the Fermi surface is given by the equation

$$\Delta_i = \sum_j \lambda_{ij} \Delta_j \int_0^{\omega_D} dE \frac{\tanh(\sqrt{E^2 + \Delta_j^2}/2k_B T)}{\sqrt{E^2 + \Delta_j^2}}, \quad (2)$$

where the cut-off frequency  $\omega_D$  is assumed the same for all sheets.  $T_c$  is defined in the usual way by the effective coupling constant,  $\lambda_{eff}$ , as  $\ln(2\gamma^*\omega_D/\pi T_c) = 1/\lambda_{eff}$ ,

$\gamma^* \simeq 1.78$ . The coupling constant  $\lambda_{eff}$  is the maximal eigenvalue of the matrix  $\Lambda_{ij} = g_{ij}\nu_j$ , where  $\nu_j$  is the density of states at the Fermi level (per spin) in the  $j$ -th band.

In a case of strong coupling ( $\lambda_{ij} > 1$ ) the BCS approximation is not applicable. The Eliashberg strong-coupling theory takes into account effects of retardation due to finite ratio  $T_c/\omega_D$ , as well as decay of quasiparticle excitations. The equations of this theory for a many-band case have the form:

$$\Delta'_{i,n} \equiv \Delta_{i,n} Z_{i,n} = \pi T \sum_j \sum_{n'} \left\{ (\lambda_{i,j} D_{n,n'} - \mu^*) + (\gamma_{ij} - \gamma_{ij}^s) \right\} \frac{\Delta'_{j,m}}{\sqrt{(\Delta'_{j,m})^2 + (\omega'_{j,m})^2}} \quad (3)$$

$$\omega'_{i,n} \equiv \omega_n Z_{i,n} = \omega_n + \pi T \sum_j \sum_{n'} \left\{ \lambda_{i,j} D_{n,n'} + (\gamma_{ij} + \gamma_{ij}^s) \right\} \frac{\omega'_{j,m}}{\sqrt{(\Delta'_{j,m})^2 + (\omega'_{j,m})^2}} \quad (4)$$

where  $D_{n,n'}$  is a phonon Green's function,  $Z_{i,n}$  is a renormalization function,  $\gamma_{ij} = \sum_{\alpha} |t_{ij}^{\alpha\alpha}|^2 \nu_j$  is the scattering rate from band  $i$  into band  $j$  due to nonmagnetic impurities, and  $\gamma_{ij}^s = \sum_{\alpha \neq \beta} |t_{ij}^{\alpha\beta}|^2 \nu_j$  is the same for magnetic impurities. For a weak coupling case  $\lambda_{ij} \ll 1$  Eqs.(3,4) reduce to the equations of the BCS model.

Let us consider now specific case of a two-band superconductor. We assume that electrons in one of the bands (s-band) interact strongly with phonons, the corresponding coupling constant  $\lambda_s = 3$ , and electrons in another band (n-band) are weakly coupled. In the notations of Kresin and Wolf<sup>10</sup> the corresponding coupling constants are  $\lambda_{11} \equiv \lambda_s = 3$ ,  $\lambda_{22} \equiv \lambda_n \ll \lambda_s$ . To choose interband coupling constants,  $\lambda_{12} \equiv \lambda_{sn}$  and  $\lambda_{21} \equiv \lambda_{ns}$ , one can use the relation  $\lambda_{sn}/\lambda_{ns} = \nu_n/\nu_s$ . According to the band structure calculations<sup>8</sup>  $\nu_n/\nu_s \ll 1$  for YBCO chain and plain bands, therefore we used in our calculations  $\lambda_{sn} = 0$ , while  $\lambda_{ns}$  is a free parameter. Similarly, we have chosen scattering rates  $\gamma_{ij}, \gamma_{ij}^s$  in Eqs.(3,4) as:  $\gamma_{12} \ll \gamma_{21}$ ,  $\gamma_{12}^s \ll \gamma_{21}^s$ ,  $\gamma_{11}^s = 0$ . Intraband elastic scattering rates are  $\gamma_{11} = \gamma_{22} = 0.1\pi T_c$  (clean limit, where results do not depend on specific choice of these parameters). Interband elastic scattering,  $\gamma_{21} = \Gamma_{ns}$ , interband magnetic scattering,  $\gamma_{21}^s$ , and magnetic scattering in the n-band,  $\gamma_{22}^s = \Gamma_n$ , are the parameters of the model. Introduction of nonzero magnetic scattering in the s-band,  $\gamma_{11}^s$ , does not lead to qualitatively different results (it simply shifts  $T_c$  of the whole system), whereas finite interband magnetic scattering,  $\gamma_{21}^s$ , can lead to sign reversal of the gap in different bands and therefore can manifest itself in Josephson experiments, as discussed below. With the parameters specified above, the Eliashberg equations (3,4) were solved numerically for two bands.

### 3. Electromagnetic response and energy spectrum

Electromagnetic response of a two-band superconductor can be calculated by generalization of standard approach developed for strongly-coupled superconductors<sup>14</sup>. The static response is determined by effective superfluid density,  $\delta^{-2}(T)$ , where  $\delta(T)$  is the magnetic field penetration depth. Details of calculations as well as the results for high-frequency response will be given elsewhere.



The results of the calculations of a normalized superfluid density are shown in fig.1 for the coupling constants  $\lambda_n/\lambda_s = 0.2$ ,  $\Gamma_{ns} = 0.1T_c$  and various  $\lambda_{ns}/\lambda_s$ . Large deviations are seen from isotropic BCS as well as from isotropic strong-coupling (SC) curves at low  $T$ , where the model predicts  $\delta^{-2}(T)/\delta^{-2}(0) \propto 1 - \exp(-\Delta_{\min}/T)$  with  $2\Delta_{\min}/T_c \sim 0.5 \div 1$  and  $2\Delta_{\max}/T_c \approx 5$  in the considered parameter range.

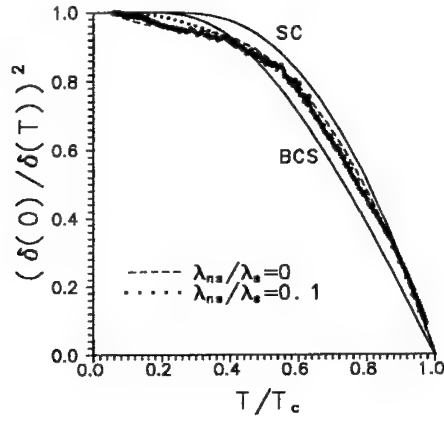


Fig. 1. Normalized superfluid density for  $\lambda_n/\lambda_s = 0.2$  and various  $\lambda_{ns}/\lambda_s$  ratios

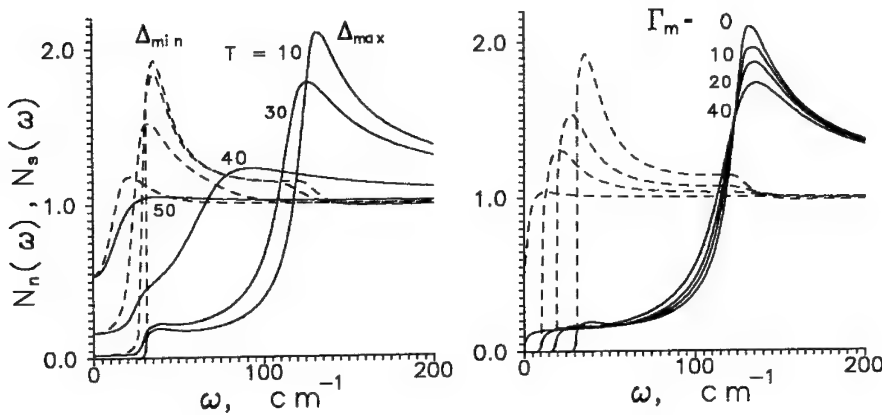


Fig. 2. Left: DOS in s-band (solid lines) and in n-band (dashed lines) at various temperatures  $T$  (in  $\text{cm}^{-1}$ ). Right: the same for various  $\Gamma_m$  (in  $\text{cm}^{-1}$ ) at  $T = 10$

Nonexponential behavior at low temperatures,  $T^\alpha$  (with  $\alpha > 2$ ), can take place due to scattering of carriers by low-frequency excitations (phonons, soft plasmons or two-level centers), independently on a pairing mechanism<sup>15,16</sup>. Experimental data

for epitaxial  $YB_2Cu_3O_7$  films from <sup>17</sup> are also shown for illustration. Qualitative similarity is seen at low temperatures. Quantitative comparison of the theory with penetration depth measurements for different high  $T_c$  materials is in progress.

DOS in each band were calculated numerically from the solution of Eqs.(3,4), analitically continued to the real energy axis  $\epsilon = -i\omega_n$ . The results for  $\lambda_{ns} = 0$  and  $\Gamma_{ns} = T_c$  are shown in fig.2. DOS in the s-band is peaked at  $\omega = \Delta_{\max}$  whereas DOS in the n-band is peaked at  $\omega = \Delta_{\min}$  with  $2\Delta_{\max}/T_c = 5.3$  and  $2\Delta_{\min}/T_c = 1.5$ . As seen from fig.2, there exists a finite gap at low  $T$ , but at higher temperatures a gapless state develops, which is due to pair-breaking effect of thermal phonons.

The influence of magnetic scattering in the n-band is shown in fig.2. Here  $\Gamma_m$  is the scattering rate on magnetic impurities in the n-band. It is seen that with increase of  $\Gamma_m$  the small gap  $\Delta_{\min}$  decreases rapidly, whereas the larger gap  $\Delta_{\max}$  is almost not changed (as well as  $T_c$ ). As a result, for sufficiently large  $\Gamma_m \approx T_c$  a gapless state develops. This effect was first predicted in <sup>10</sup>. On the other hand, our numerical solutions do not depend on nonmagnetic intraband impurity scattering (Anderson theorem). The sensitivity of a small gap to the magnetic scattering can be a reason for complicated gap structure observed in  $YB_2Cu_3O_7$  in tunneling measurements <sup>1,2</sup>.

#### 4. Interband sign reversal of the gap and Josephson effect

In the given model the small gap,  $\Delta_{\min}$ , is determined by the value of  $\Delta_{\max}$  and by interband interactions. As a result, under certain conditions  $\Delta_{\min}$  can become negative. To analyze these conditions, let us note that near  $T_c$  the solution of Eq.(2) is  $\Delta_2/\Delta_1 = (\lambda_{eff} - \lambda_{11})/\lambda_{12}$ . Due to  $\lambda_{eff} > \lambda_{11}$ , one can see directly that the interband sign reversal of the gap (ISRG),  $sign(\Delta_2/\Delta_1) = -1$ , takes place when *nondiagonal matrix elements  $\lambda_{12}$  and  $\lambda_{21}$  are negative*.

Below we shall demonstrate that even a fully attractive interaction  $g_{ij} \geq 0$  can lead to the sign reversal when at least one of two conditions is satisfied: (a) interband pairing interaction is weaker than Coulomb pseudopotential, (b) there is sufficiently strong interband scattering on magnetic impurities.

(a) If  $g$ 's are electron-phonon pairing potentials, then Eq.(2) should be corrected for a Coulomb repulsion, which can be readily done<sup>7</sup> by substituting  $g_{ij}$  by  $g_{ij} - U_{ij}^* \approx g_{ij} - U^*$ , where effective Coulomb repulsion  $U^*$  is logarithmically renormalized in the same way as in one-band superconductivity theory ( $U^*$  is assumed to be independent on  $i, j$ ). A direct consequence of that is that if the interband electron-phonon coupling is weak, the situation with a negative gap,  $g_{ij} - U^* < 0$ , can easily realize because of the interband repulsion.

(b) In the weak coupling limit and near  $T_c$  Eqs.(3,4) can be solved analytically. For two bands, in the linear in  $\gamma, \gamma^s$  approximation, Eq.(2) is recovered, with the effective coupling matrix  $\Lambda$ :

$$\Lambda_{eff} = \Lambda - \frac{\pi}{8T_{co}} \Lambda \cdot \begin{pmatrix} 2\gamma_{11}^s + \gamma_{12}^s + \gamma_{12} & \gamma_{12}^s - \gamma_{12} \\ \gamma_{21}^s - \gamma_{21} & 2\gamma_{22}^s + \gamma + \gamma_{21} \end{pmatrix} \cdot \Lambda. \quad (5)$$

When all  $\lambda$ 's are equal (isotropic case), the standard Abrikosov-Gorkov result <sup>18</sup> is recovered:  $\delta\lambda \approx -\pi\lambda^2(\gamma_{11}^s + \gamma_{12}^s + \gamma_{21}^s + \gamma_{22}^s)/8T_{co}$ .

An interesting special case is  $\lambda_{12}, \lambda_{21} \ll \lambda_{11}, \lambda_{22}$ . Then in the effective  $\Lambda$  matrix nondiagonal elements can become negative,  $\lambda_{ij}^{eff} (i \neq j) = \lambda_{ij} + \pi\lambda_{ii}\lambda_{jj}(\gamma_{ij} - \gamma_{ij}^s)/8T_{co}$ ,

if  $\gamma_{ij}^s$  is sufficiently large. As discussed above, this situation will lead to ISRG. In order to demonstrate this effect quantitatively, we solved the Eqs.(3,4) numerically, using the following parameters:  $\lambda_{11} = 1, \lambda_{22} = 0.5, \lambda_{12} = 0.025, \lambda_{21} = 0.1, \gamma_{21} = 4\gamma_{12}, \gamma_{21}^s = 4\gamma_{12}^s$ . The results for low-temperature regime,  $T \ll T_c$ , are shown in fig.3. In accord with the condition derived above, when the difference  $\gamma_{12}^s - \gamma_{12}$  becomes larger than some critical value (in this case,  $0.042\pi T_c$ ), the second gap changes sign. In other words, when attractive interband coupling is relatively weak and the magnetic interband scattering is strong, the system will choose to have two gaps of the opposite signs, losing in pairing energy, but avoiding the pair-breaking due to interband scattering.

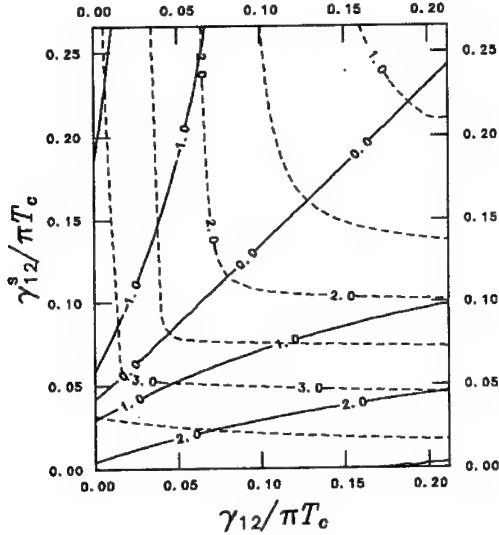


Fig. 3. Superconducting gaps at  $T \ll T_c$  in a two-band system with interband scattering on magnetic and non-magnetic impurities. Solid lines show  $2\Delta_2/T_c$  (negative values are in the upper left corner), dashed lines show  $2\Delta_1/T_c$ . Note the straight line corresponding to  $\Delta_2 = 0$

Let us discuss the consequences for the Josephson effect. A lot of unusual experimental results have been reported so far for  $YB_2Cu_3O_7$ <sup>19,20,21,22,23</sup>. Below we shall indicate qualitative predictions of our model and relation to these measurements.

The Josephson current density between many-band superconductors can be written as  $J_s = \sum_{ij} J_c^{ij} \sin \phi^{ij}$ , where  $J_c^{ij}$  is the critical current density for tunneling between the bands  $i$  and  $j$ , and  $\phi^{ij}$  is the gauge-invariant phase difference of  $\Delta_i, \Delta_j$ . In the simplest case of the Ginzburg-Landau regime<sup>24</sup>

$$J_c^{ij} = \pi \Delta_i \Delta_j / 4e R_{ij} k_B T \quad (6)$$

where  $R_{ij} = (\hbar/e^2)(p_F/2\pi\hbar)^2 / < D >$  is the resistance per unit area,  $< D >$  is angle averaged transparency of the boundary and  $p_F = \min(p_{Fi}, p_{Fj})$ . Following

Geshkenbein and Larkin<sup>25</sup>, we obtain that if  $\text{sign}(\Delta_i) = -\text{sign}(\Delta_j)$ , then in the stationary case ( $J_s = 0$ ) the finite phase difference appears,  $\phi_{ij} = \pi$ . This, ISRG can lead to existence of a “ $\pi$ -contact” considered first by Bulaevskii et al.<sup>26</sup>

Generally, the total critical current,  $J_c^{\text{tot}}$ , depends on orientation of the boundary relative to crystallographic axes because of angular dependence of  $R_{ij}$ . It can become negative for certain directions, when the contribution due to interband tunneling prevails. The condition is  $J_c^{12} + J_c^{21} > J_c^{11} + J_c^{22}$  when both electrodes are two-band superconductors (TB/TB), and  $J_c^{12} > J_c^{11}$  if one of them is a conventional one-band superconductor (TB/OB). This effect is similar to that considered by Sigrist and Rice<sup>27</sup> for the  $d$ -pairing, resulting from spin-fluctuation mediated interaction<sup>28</sup>. However, some of our predictions differ qualitatively, as discussed below.

For a TB/OB junction the tunnel resistance  $R_{12}(\theta)$  depends strongly on the angle  $\theta$  relative to the  $b$  axis, namely  $R_{12}(\theta)$  has a sharp minimum at  $\theta = 0$  due to strong  $D(\theta)$  dependence for a tunneling process. Moreover, according to the band structure calculations<sup>8</sup>, kinetic energy of carriers along the chains is larger than that in the plains, thus leading to larger  $\langle D \rangle$  ( $\theta = 0$ ) values along the chains. As a result, for small  $\theta$  we have  $J_c^{\text{tot}}(\theta) < 0$ , whereas for all other angles  $J_c^{\text{tot}}(\theta) > 0$ . Therefore an intrinsic  $\pi$ -phase shift will occur in this case between tunneling along  $a$ - and along  $b$ -directions. Then a dc SQUID with junctions on  $a$  and  $b$  faces of a crystal, will show  $\Phi_0/2$  shift of a field dependence  $I_c(H)$ . This effect was first observed in ref.<sup>19</sup> and attributed to the  $d_{x^2-y^2}$  pairing state. Another consequence is a local minimum of a Fraunhofer pattern at  $H = 0$  for a single junction formed on the corner of a crystal, because  $J_c$  changes sign along the junction. Moreover, the existence of nonzero Josephson current observed for  $c$ -axis tunneling in  $Pb/\text{insulator}/Y_{1-x}Pr_xBa_2Cu_3O_7$  tunnel junctions in ref.<sup>21</sup> contradicts to the  $d_{x^2-y^2}$  symmetry, but is consistent with the suggested scenario (*chains-plains*). The reason is that, contrary to the case of  $d_{x^2-y^2}$  symmetry, an average order parameter in  $ab$  plane is nonzero.

Interesting consequences appear for TB/TB junctions (in a case of  $YBa_2Cu_3O_7$  these are grain-boundary junctions). As follows from the above arguments, if  $\theta = 0$  in *only one* of the grains, then the grain boundary is a  $\pi$ -contact, otherwise it is a conventional one. Consider a closed contour crossing  $N$  grain boundaries. Flux quantization condition in zero external field reads  $n\Phi_0 = LI_s^{ij} + \sum_{m=1,N}(\Phi_0/2\pi)\phi_{ij}^{(m)}$ , where  $L$  is a self-inductance of a ring and  $\phi_{ij}^{(m)}$  is a phase difference across  $m$ -th junction. Then if a contour crosses an *odd number of*  $\theta = 0$  junctions, a spontaneous magnetisation of a ring with half-integer flux quantum will occur, whereas for even number of  $\theta = 0$  junctions - with integer flux quantum.

Spontaneous magnetization with half-integer flux quantum in a three-junction ring and with integer flux quantum in a two-junction ring was demonstrated recently for  $YBa_2Cu_3O_7$  in ref.<sup>22</sup>. In this experiment all grain boundaries were of  $\theta = 0$  type ( $\pi$ -junctions). Thus, the results<sup>22</sup> are in agreement with our proposal. To distinguish it from the  $d$ -wave scenario, measurements for different grain orientations are necessary, because the criteria for a  $\pi$ -junction, and therefore angle dependences, are quite different. On the other hand, the absence of angular dependence of  $J_c$  for some different grain-boundary orientations was observed in ref.<sup>20</sup> in  $YBa_2Cu_3O_7$ . It does not contradict to our scheme. Indeed, in<sup>20</sup> all six grain boundaries have had  $\theta \neq 0$  which results in  $J_c^{\text{tot}}(\theta) \simeq J_c^{11}(\theta) \simeq \text{const.}$

Another interesting phenomenon observed first in Bi-based HTS<sup>23</sup> and more recently in  $YBa_2Cu_3O_7$  (ref.<sup>29</sup>) is the paramagnetic Meissner effect ("Wohleben effect"). The explanation was proposed in refs.<sup>23,27</sup> in terms of intrinsic  $\pi$ -junctions between weakly coupled regions. An external magnetic field will align spontaneous current loops and can produce a net positive magnetization (paramagnetic). As discussed above, such intrinsic  $\pi$ -junctions are naturally predicted by the two-band model, thus making this effect possible.

#### Acknowledgements

We are grateful to G.M.Eliashberg, V.Z.Kresin, B.Aminov, N.Klein, G.Mueller, S.Orbach-Werbig, M.R.Trunin and S.I.Vedenev for many useful discussions. The work was supported in part by RFFI under Grant N 94-02-03236 and by INTAS under Grant N 94-2452.

#### References

1. B.Aminov *et al*, J.Supercond. **7** (1994) 361.
2. S.I.Vedenev *et al*, Phys. Rev. **B49** (1994) 9823.
3. W.Hardy *et al*, Phys.Rev.Lett. **70** (1993) 3999.
4. N.Klein *et al*, Phys.Rev.Lett. **71** (1993) 3355.
5. H.Suhl, B.T.Matthias, and L.R.Walker, Phys.Rev.Lett. **3** (1959) 552.
6. V.A.Moscalenko, Fiz.Met.Met. **4** (1959) 503.
7. W.H. Butler and P.B. Allen, in *Superconductivity in d- and f-Band Metals*, ed. D.H.Douglass (AIP, New York, 1976).
8. O.K.Andersen *et al*, Physica C **185-189** (1991) 147.
9. W.E.Pickett *et al*, Science **255** (1992) 46.
10. V.Z.Kresin and S.A.Wolf, Phys.Rev. **B41** (1990) 4278; **B46** (1992) 6458.
11. I.I. Mazin *et al*, Physica C **209** (1993) 125.
12. L.Genzel *et al*, Z. Phys. **B90** (1993) 3.
13. O.K.Andersen *et al*, Physica C (1991).
14. S.B.Nam, Phys.Rev. **156** (1967) 487.
15. O.V.Dolgov, A.A.Golubov and A.E.Koshelev, Sol.St.Comm. **72** (1989) 81.
16. G.V.Klimovich, A.V.Rylyakov and G.M.Eliashberg, JETP Lett **53** (1991) 381
17. S.Orbach-Werbig *et al*, Physica C, to be published.
18. A.A. Abrikosov and L.P. Gor'kov, JETP **12** (1961) 1243.
19. D.A. Wollman *et al*, Phys. Rev. Lett. **71** (1993) 2134.
20. P. Chaudhari and S.-Y. Lin, Phys. Rev. Lett. **72** (1994) 1084.
21. A.G.Sun *et al*, Phys. Rev. Lett. **72** (1994) 2267.
22. C.C.Tsuei *et al*, Phys.Rev.Lett. **73** (1994) 593.
23. W.Braunisch *et al*, Phys.Rev.Lett. **72** (1992) 1908.
24. V.Ambegaokar and A.Baratoff, Phys.Rev.Lett. **10** (1963) 486.
25. V.B. Geshkenbein and A.I. Larkin, JETP Lett. **43** (1986) 395.
26. L.N.Bulaevskii, V.V.Kuzii, and A.A.Sobyanin, JETP Lett. **25** (1977) 290.
27. M. Sigrist and T.M. Rice, J. Phys. Soc. Jpn. **61** (1992) 4283.
28. P. Monthoux and D. Pines, Phys. Rev. **B49** (1994) 4261.
29. S.Riedling *et al*, Phys. Rev. **B49** (1994) 13283.

## MEASUREMENT OF THE ELECTRODYNAMIC PROPERTIES OF HIGH TEMPERATURE SUPERCONDUCTING FILMS

A.ANDREONE, A.CASSINESE, C.CANTONI, A.DI CHIARA, F.MILETTO GRANOZIO  
and R.VAGLIO

*Dipartimento di Scienze Fisiche, Universita' degli Studi di Napoli "Federico II", Piazzale V.  
Tecchio 80, I-80125, Napoli, ITALY*

### ABSTRACT

A technique to accurately measure the magnetic field penetration depth  $\lambda$  of superconducting thin films using a microstrip resonator is described. Measurements of the temperature dependence  $\lambda(T)$  performed on the high temperature superconductors  $\text{Nd}_{1.85}\text{Ce}_{0.15}\text{CuO}_{4-\delta}$  and  $\text{YBa}_2\text{Cu}_3\text{O}_{7-\delta}$  are reported and compared, particularly in the low temperature region. Their features are discussed in the light of recent theoretical models predicting for the high  $T_c$  superconductors a pairing state with a  $d_{x^2-y^2}$  symmetry instead of the usual  $s$  symmetry.

### 1. Introduction

In spite of the tremendous efforts made by both the theoretical and experimental researchers, the key issues for High Temperature Superconductors (HTS), namely the physical origin of the anomalous normal state properties, the mechanism for superconductivity at high temperatures, and the superconducting pairing state, are still unclear.

The scientific community is presently divided between two different approaches: conventional, based on the attempt to extend the classical BCS theory into the new area of ceramic oxides, and unconventional, in which exotic new mechanisms are proposed. One of the currently most popular unconventional theories is based on the spin-fluctuation mechanism for the high temperature superconductivity. This magnetic scenario can explain the anomalous spin and charge response in the normal state and account for the value of  $T_c$  observed in the cuprates. Moreover, it predicts that the antiferromagnetic correlations between the quasi-particles must lead to a superconducting transition into a pairing state with a  $d_{x^2-y^2}$  symmetry instead of the usual  $s$  symmetry<sup>1</sup>.

In the last two years many experiments are claimed to provide strong evidence in favor of  $d$ -wave pairing state, mainly in the field of nuclear magnetic resonance, photoemission, penetration depth, microwave surface resistance, and tunneling measurements. However,

most of these experiments has received an alternative explanations in terms of an isotropic or possible anisotropic s-wave theory.

Among them, the low temperature behavior of the magnetic penetration depth  $\lambda(T)$  is an important clue as to the symmetry of the superconducting order parameter  $\Delta(k)$ . In a conventional superconductor  $\Delta(k)$  has the full rotational symmetry of the lattice, corresponding to a finite energy gap over the entire Fermi surface. In an unconventional superconductor  $\Delta(k)$  has a reduced rotational symmetry, that in the special case of a  $d_{x^2-y^2}$  pairing state results in a energy gap showing line nodes on the Fermi surface. While an even anisotropic s-wave pairing state manifests its presence in a  $\lambda(T)$  dependence with an exponentially activated behavior at temperatures well below  $T_c$ , in a pure  $d_{x^2-y^2}$  superconductor the penetration depth at low temperatures has been predicted to show a linear dependence because of the availability of low-lying excitations of arbitrarily small energy<sup>2</sup>. It has been also pointed out that for a d-wave superconductor impurity scattering could induce a crossover from linear to quadratic behavior in the penetration depth temperature dependence<sup>3</sup>. In the framework of the BCS theory, however, the  $T^2$  law can be interpreted as evidence for gapless behavior<sup>4</sup> or as a manifestation of weak links between grains<sup>5</sup>. In any event, the occurrence of an exponential temperature dependence of  $\lambda$  for  $T < T_c/2$  should rule out d-wave theories.

Experimentally, however, it can be extremely hard to distinguish an activated behavior from a power dependence in the low temperature region, where the penetration depth variations are extremely small. In order to get reliable data, a high-sensitivity technique is needed.

Here accurate microwave measurements of  $\lambda(T)$  of  $Nd_{1.85}Ce_{0.15}CuO_{4-\delta}$  (NCCO) and  $YBa_2Cu_3O_{7-\delta}$  (YBCO) thin films are reported. In the low temperature region the method employed allows to achieve a resolution of a few angstroms in the penetration depth variations.

The behavior observed on fully c-axis oriented NCCO thin films shows without any ambiguity that the electrodynamics of this superconductor can be well described by the BCS theory. On the contrary, the results obtained on YBCO thin films grown with different orientations are quite controversial. In c-axis oriented samples a  $T^2$  dependence is observed, whereas a film with an high degree of a-axis orientation shows an activated-like behavior with a very small value of the energy gap ( $2\Delta/K_B T_c \approx 1.2$ ) for  $T$  less than 10 K.

## 2. Technique Description

The measurements are carried out by employing an inverted microstrip ring resonator, first designed to determine the surface impedance of low  $T_C$  superconducting thin films<sup>6</sup>. The configuration chosen for HTS consists of an annular microstrip (width  $W \approx 500 \mu\text{m}$ , diameter  $D = 8 \text{ mm}$ ) and a ground plane, both made of thin films with nominally equal properties, deposited at the same conditions on (100)  $\text{LaAlO}_3$   $1 \times 1 \text{ cm}^2$  substrates. The dielectric layer is a thin ( $h \approx 130 \mu\text{m}$ ), low loss, single-crystal sapphire. The ratio  $W/D$  is small enough to ensure that in the frequency range of investigation (1-20 GHz) only the  $\text{TM}_{n10}$  modes can propagate in the resonator. This corresponds to a r.f. magnetic field approximately parallel to the plane of the substrates<sup>7</sup>. The microwave measurements are performed at the first harmonic, between 3 and 4 GHz, using a vector network analyzer. Unlike the configuration used for low  $T_C$  materials, in this geometry the high values of radiation and dielectric losses don't allow to determine the surface resistance  $R_s$  for  $T < T_C/2$ . The estimated sensitivity of the technique for  $R_s$  measurements is around  $1 \text{ m}\Omega$ . This method is nevertheless adequate to measure penetration depth variations with a high sensitivity. It is worthwhile to observe that even in conventional low  $T_C$  superconductors, like Nb or A15 compounds, the temperature dependence of the penetration depth is less susceptible to extrinsic loss mechanisms than is  $R_s$ <sup>6,8</sup>.

In an isolated resonator the temperature dependence of the penetration depth of the HTS thin films is related to the temperature changes of the resonant frequency  $\nu_o(T)$  through the relation<sup>9</sup>:

$$\nu_o(T) = \frac{c / \pi D}{\sqrt{\epsilon_{\text{eff}}(T)}} \times \left[ 1 + \frac{\lambda_1(T)}{h} \coth \frac{t_1}{\lambda_1(T)} + \frac{\lambda_2(T)}{h} \coth \frac{t_2}{\lambda_2(T)} \right]^{-1/2} \quad (1)$$

where  $c$  is the speed of light,  $\epsilon_{\text{eff}}$  is the effective permittivity of the device, and  $t_1$  and  $t_2$  are the thickness of the ring microstrip and the ground plane respectively. The  $\nu_o$  values are measured observing the power transmitted by the resonator as a function of frequency. The input and output signal launchers are capacitively coupled to the device and are adjusted so that the resonator can be considered in the unloaded regime (insertion losses IL greater than 20 dB). The microwave power is usually set between -20 and -10 dBm; this condition, together with the IL high values, ensures that the measurements are performed at low excitation levels, avoiding the possible dependence of the data from the r.f. power applied to



the resonator. In the low temperature region ( $T < T_C/2$ ) the typical quality factor measured are around  $10^3$ , giving a 3 dB bandwidth of the resonator of few MHz. The determination of the resonant frequency is usually done sweeping the signal source through a frequency window equal or less than the bandwidth and recording the maximum in the transmitted power as a function of temperature. The measurements, using a data acquisition system and a temperature controller, can be fully automatized and run overnight. The sweep rate is set to be much less than the bandwidth of the resonance, to avoid distortion of the line shape and to allow a large number (1601) of frequency data points be taken near the peak. Thus, the minimum resolvable fractional frequency variation will be:

$$\frac{\delta\nu}{\nu} = \frac{\Delta\nu_{3dB}}{1601 \cdot \nu} \approx \frac{1}{1601 \cdot Q} \leq 10^{-6} \quad (2)$$

where  $\Delta\nu_{3dB}$  is the 3 dB bandwidth of the resonant frequency  $\nu_0$  and  $Q = \nu_0/\Delta\nu_{3dB}$ .

Using Eq. (1), it is easy to show that the minimum resolvable penetration depth change  $\delta\lambda$  corresponding to  $\delta\nu$  is

$$\Delta\lambda = \frac{\delta\nu}{\nu_0} h \quad (3)$$

For  $T$  less than  $T_C/2$ , this relation ensures a measurement resolution of approximately 1 Å.

Particular attention, of course, has to be paid to avoid that systematic errors can arise in the penetration depth measurements. These errors are mainly due to the thermal variations of the microstrip parameters and may invalidate the  $\lambda(T)$  data, especially in the low temperature region.

The effects related to the thermal expansion coefficients of both the dielectric layer and the HTS thin films can be considered negligible and ignored<sup>9</sup>. However, the temperature dependence of the effective permittivity of the device,  $\epsilon_{eff}(T)$ , must be taken into account.  $\epsilon_{eff}$ , due to the fringing fields ( $W/h \approx 4$ ) and to the open structure of the resonator, will include not only the dielectric constant of the sapphire layer, but also contributions related to the propagation of the e.m. radiation inside the film substrates and into the medium surrounding the package. From the measurements it is found that the temperature changes of  $\epsilon_{eff}$  are essentially due to the temperature dependence of the dielectric permeability of the

helium vapor filling the dewar, as the microwave probe with the sample approaches the liquid helium surface.

For an ideal, nonpolar gas, the dielectric constant  $\epsilon_r$  as a function of temperature  $T$  and pressure  $P$  is given by

$$\epsilon_r = 1 + \frac{\alpha P}{k_B T} \quad (4)$$

where  $k_B$  is the Boltzmann constant and  $\alpha$  is the electronic polarizability ( $\alpha_{\text{He}} \approx 2.5 \cdot 10^{-24} \text{ cm}^3$ ).

To avoid that these effect can mask, in the low temperature region, the variations of the resonant frequency related to the penetration depth, the measurements are performed at low pressure conditions ( $P = 1 \div 10 \text{ Pa}$ ) inserting the resonator inside a vacuum copper can. The thermal linkage between the samples and the LHe bath is provided flowing a small but constant amount of helium exchange gas inside the probe chamber during the experiment.

### 3. Experimental Results

The NCCO samples were obtained at the IBM laboratories by laser ablation from a target of the desired stoichiometry in  $\text{N}_2\text{O}$  ambient on  $\text{LaAlO}_3$  (100) substrates<sup>10</sup>. The nominal thickness of the films is 3000 Å. The critical temperature values are in the 16-20 K range, and the X-ray diffraction (XRD) data show c-axis orientation.

In fig. 1 the penetration depth shift  $\Delta\lambda(T) = \lambda(T) - \lambda(0)$  for one of the samples is reported on a logarithmic scale as a function of the inverse of the reduced temperature  $T/T_c$  in the low temperature region ( $T < T_c/2$ ). The zero temperature value  $\lambda(0)$  is obtained from a standard best-fit of the full-range experimental  $v_o(T)$  curve using the complete theoretical BCS expression in the local limit ( $\lambda \gg \xi_o$ ). A clear exponential dependence is displayed by  $\Delta\lambda(T)$ , in accordance with the s-wave behavior (continuous curve in fig. 1), which predicts at low temperatures<sup>11</sup>

$$\Delta\lambda(T) = \lambda(0) \sqrt{\frac{\pi\Delta_o}{2K_B T}} \exp\left(-\frac{\Delta_o}{K_B T}\right) \quad (5)$$

yielding<sup>12</sup> an energy gap ratio  $2\Delta_o/K_B T_c \approx 3.1$ .

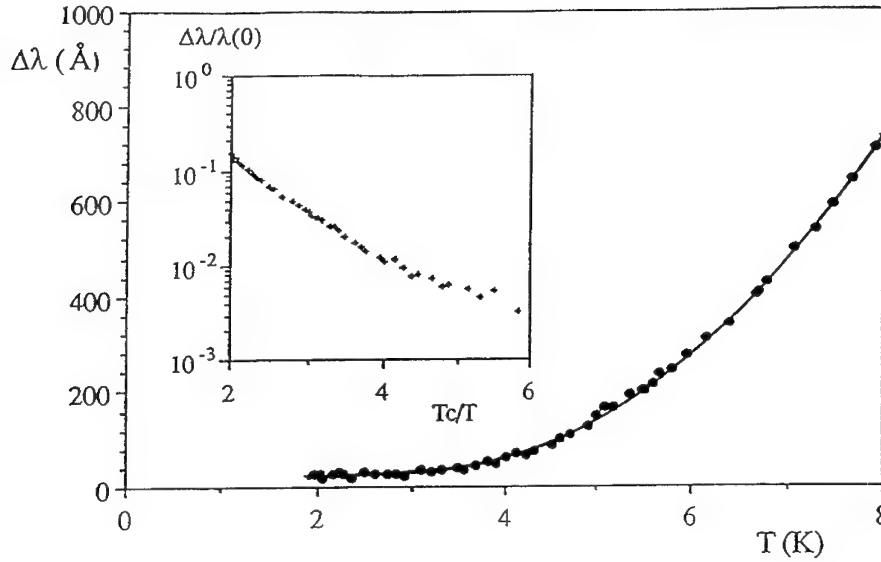


Fig. 1: low temperature dependence of  $\Delta\lambda(T)$  for a c-axis oriented NCCO thin film. The solid curve is the best-fit of the data using the BCS expression in the local limit (Eq. 5). In the inset the same quantity, normalized to the zero temperature penetration depth  $\lambda(0)$ , is shown on a logarithmic scale as a function of  $T_c/T$ .

For all the measured films both the exponential behavior for  $T < T_c/3$  and a value of  $2\Delta_0/K_B T_c$  in the BCS weak-coupling regime were clearly verified and any attempt to fit the low temperature data with a power law was unsuccessful. These results are in perfect agreement with previous measurements of surface impedance on both NCCO thin films and single crystals, obtained using a different technique<sup>13</sup>.

The YBCO thin films were prepared on  $\text{LaAlO}_3$  (100) substrates by an inverted cylindrical magnetron sputtering technique<sup>14</sup>. They show excellent d.c. transport properties:  $T_c$  values over 90 K and critical current densities in excess of  $10^7 \text{ A/cm}^2$  at 77 K are observed for c-axis oriented samples. The film thickness ranges between 2000 and 3000 Å and the room temperature resistivity is around  $120 \mu\Omega\text{-cm}$ . The deposition temperature can be varied to give c-axis or a-axis orientation of the samples, as evidenced by XRD patterns.

In fig. 2, the quantity  $\Delta\lambda(T)$  for one of the c-axis oriented samples is shown in the low temperature region. With no specific model for superconductivity in YBCO in mind, a

reasonable way to obtain the zero temperature penetration depth is to apply to the complete  $\lambda(T)$  experimental curve a simple two-fluid model, where  $\lambda(T) = \lambda(0) \{1 - (T/T_C)^4\}^{-1/2}$ .

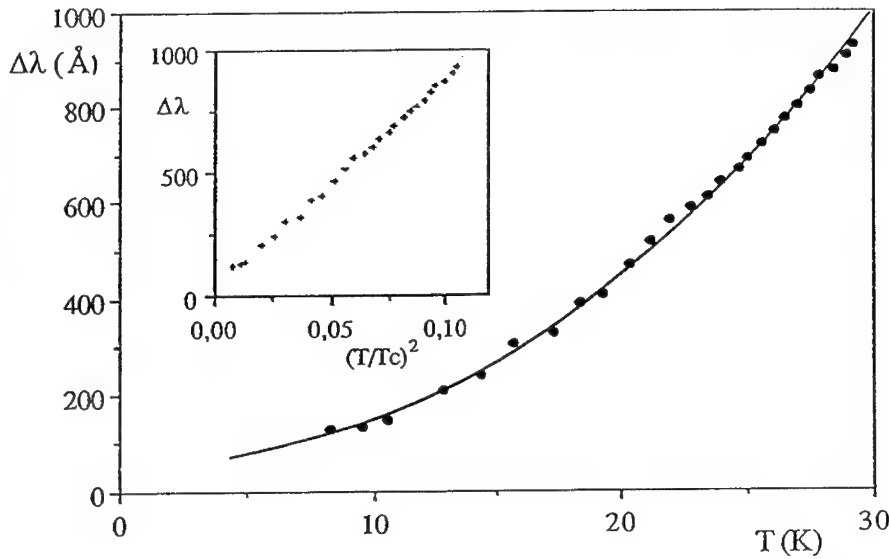


Fig. 2:  $\Delta\lambda$  vs.  $T$  for a c-axis oriented YBCO thin film in the low temperature region. The solid line represents the best-fit of the data using the expression  $\lambda(T) = \lambda(0) (1 + AT^2)$ . The value of  $\lambda(0)$  is obtained by the fit of the full-range  $\lambda(T)$  experimental curve using a simple two-fluid model (see text). In the inset the same quantity, normalized to the zero temperature penetration depth  $\lambda(0)$ , is shown as a function of  $(T/T_C)^2$ .

As a matter of fact,  $\lambda(T)$  measurements of YBCO films cannot be self-consistently fitted to a BCS temperature dependence derived from a single energy gap over the entire range below  $T_C$ . With the two-fluid choice, a value of  $\lambda(0) \approx 2200$  Å is found, higher than single-crystals data, but in good agreement with similar thin film samples. In any case, the quadratic temperature dependence of  $\Delta\lambda(T)$ , clearly demonstrated in fig. 2, is not much affected by the  $\lambda(0)$  value used.

In fig. 3, the low temperature behavior of the penetration depth is shown for a film exhibiting a high degree of a-axis orientation.

For this sample an activated-like behavior with a very small value of the energy gap ( $2\Delta/K_B T_C \approx 1.2$ ) is observed for  $T$  less than 10 K.

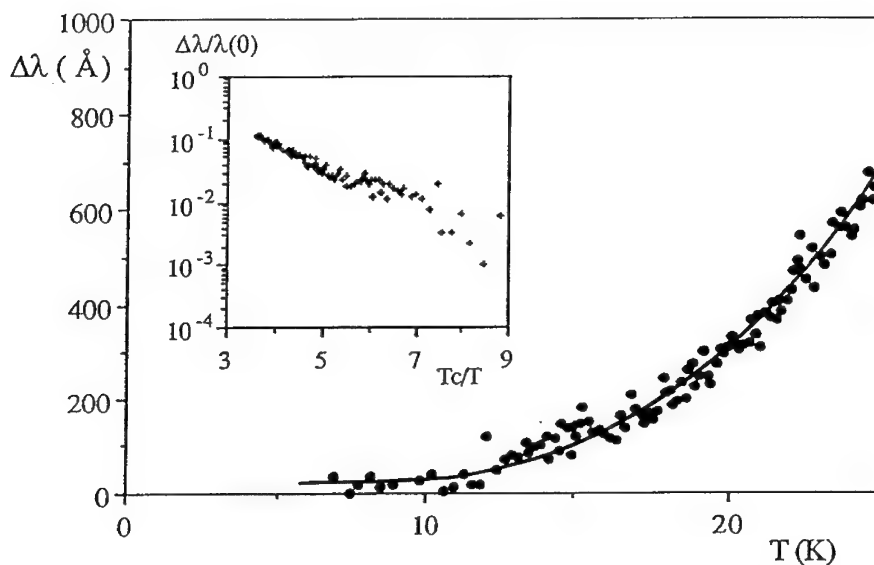


Fig. 3:  $\Delta\lambda$  vs.  $T$  for an highly a-axis oriented YBCO thin film in the low temperature region. The solid line represents the best-fit of the data using Eq. 5. The value of  $\lambda(0)$  is obtained by the fit of the full-range  $v_o(T)$  experimental curve using a simple two-fluid model (see text). In the inset the same quantity, normalized to the zero temperature penetration depth  $\lambda(0)$ , is shown on a logarithmic scale as a function of  $T_C/T$ .

In conclusion, the behavior observed in NCCO thin films shows without any ambiguity that the electrodynamics of this superconductor can be well described by the BCS theory. On the contrary, the results obtained on YBCO thin films are quite controversial. The  $\lambda(T)$  behavior seems to be dependent on the orientation of the samples respect to the applied magnetic field. Further measurements are needed in order to clarify the questions about the pairing mechanism in HTS and also to enlight possible anisotropic mechanisms in the penetration depth temperature dependence observed.

A detailed study on a possible dependence of the penetration depth behavior on the direction of the screening currents in the YBCO films is in progress.

### Acknowledgements

The contribution of Dr. A. Del Vecchio to this research is gratefully acknowledged. The authors would like also to thank Profs. A. Barone, V. Z. Kresin, and V. G. Vaccaro, for useful comments and suggestions.

The work has been supported by the National Research Council (C.N.R.) under the P.F. "Su.Cry.Tec." and by the National Institute of Physics of Matter (I.N.F.M.) of Italy.

### References

1. P.Monthoux, A.V.Balatsky, and D.Pines, *Phys. Rev. Lett.* **67** (1991) 3448
2. M.Prohammer and J.P.Carbotte, *Phys. Rev.* **B43** (1991) 5370
3. P.J.Hirschfeld and N.Goldenfeld, *Phys. Rev.* **B48** (1993) 4219
4. A.A.Abrikosoov and L.P.Gor'kov, *Sov. Phys. JETP* **12** (1960) 1243
5. J.Halbritter, *J. Appl. Phys.* **71** (1992) 339
6. A.Andreone, C.Attanasio, A.Di Chiara, L.Maritato, M.Santoro, and R.Vaglio, *J. Appl. Phys.* **73** (1993) 4500
7. Y.S.Wu and F.J.Rosenbaum, *IEEE Trans. Microwave Theory Techn.* **MTT-21** (1973) 487
8. A.Andreone, C.Attanasio, A.Cassinese, A.Di Chiara, L.Maritato, M.Salluzzo, and R.Vaglio, submitted to *J. Appl. Phys.*
9. B.W.Langley, S.M.Anlage, R.F.W.Pease, and M.R.Beasley, *Rev. Sci. Instrum.* **62** (1991) 1801
10. A.Kusmaul, J.S.Moodera, P.M.Tedrow, and A.Gupta, *Appl. Phys. Lett.* **61** (1992) 2715
11. M.Tinkham, *Introduction to Superconductivity* (McGraw-Hill, New York, 1975)
12. A.Andreone, A.Cassinese, A.Di Chiara, R.Vaglio, A.Gupta, and E.Sarnelli, *Phys. Rev.* **B49** (1994) 6392
13. D.H.Wu, J.Mao, S.N.Mao, J.L.Peng, X.X.Xi, T.Venkatesan, R.L.Greene, and S.M.Anlage, *Phys. Rev. Lett.* **70** (1993) 85
14. A.Andreone, A.Di Chiara, F.Fontana, F.Miletto, G.Peluso, U.Scotti di Uccio, and M.Valentino, *Sov. J. Low Temp. Phys.* **18** (1992) 1113

**DOPING AND PRESSURE INFLUENCE  
ON THE CRITICAL TEMPERATURE  
IN FRAME OF THE BISOLITON MODEL OF SUPERCONDUCTIVITY**

L. BRIZHIK

*Bogolyubov Institute for Theoretical Physics  
252143 Kiev, Ukraine*

**ABSTRACT**

It is shown that in the zero adiabatic approximation the ground state of electrons interacting with acoustical phonons in a 1D chain is described by a self-consistent cnoidal wave in the deformation potential. This cnoidal wave at sufficiently small doping level corresponds to the condensate of autolocalized bisolitons. The dependence of the condensate gap width on concentration of charge carriers is shown to have a nonmonotonic character close to that observed in experiments. The analysis of the pressure dependence of the condensate critical temperature is done and shown to reproduce well the results of experimental investigation of HTSC under pressure.

## 1. Introduction

Experimental studies of high-temperature superconductors revealed their remarkable properties that to some extent go beyond the framework of the conventional BCS theory. Soon after the discovery of HTSC it was shown that the critical temperature  $T_c$  strongly depends on the hole concentration and pressure<sup>1-4</sup>. Since then, many experimental and theoretical works have been devoted to the study of doping and pressure influences on  $T_c$ . Here we investigate these properties in frame of the bisoliton model of superconductivity<sup>5</sup>. In Section 2 the general description of the model is given and the dependence of the energy gap width on quasiparticles concentration is analyzed, and in Section 3 the dependence of the critical temperature on pressure is studied.

## 2. Bisoliton Energy Gap

In view of the distinctly established strong anisotropy of physical properties, the superconducting oxides are referred to the class of low-dimensional systems in which, as is well known, the electron-phonon interaction plays an especially significant role. The bisoliton model of superconductivity is based on the assumption that the superconductivity of high-temperature compounds is generated by the interaction of charge carriers (electrons or holes, for instance, of copper-oxygen complexes, called in what follows 'quasi-particles') with acoustical phonons. Here, for the sake of simplicity, we use a one-dimensional model. The extension of the model for higher dimensionalities

is given elsewhere (e.g., <sup>6,7</sup>).

In the zero adiabatic approximation two quasiparticles with opposite spins under their interaction with the local deformation of a chain are shown to bind into the autolocalized singlet spin state, called bisoliton<sup>8</sup>. Because of the spin interaction two bisolitons repel one another<sup>9</sup>, and at some concentration of quasi-particles,  $\delta$ , the periodic cnoidal wave is formed in a self-consistent deformation potential of the chain. The wave function  $\Psi$  of this cnoidal wave at some approximations can be described by the nonlinear Schrödinger equation

$$\left\{ i\hbar \frac{\partial}{\partial t} + J \frac{\partial^2}{\partial x^2} + 4Jg|\Psi(x,t)|^2 \right\} \Psi(x,t) = 0, \quad (1)$$

where the dimensionless electron-phonon coupling coefficient is introduced

$$g = \frac{\chi^2}{2J\kappa(1-s^2)}. \quad (2)$$

Here  $J$  and  $\chi$  are the constants of exchange and electron-phonon interactions, respectively,  $\kappa$  is the elasticity coefficient, and  $s$  is the ratio of the cnoidal wave velocity  $V$  to the velocity of sound in the chain. Two extra conditions are imposed on the wave function, the periodicity and normalization conditions, namely,

$$\Psi(x,t) = \Psi(x+l,t), \quad \int_0^l |\Psi(x,t)|^2 dx = 1, \quad (3)$$

in which  $l = 1/\delta$  is the period of the cnoidal wave measured in units of lattice constant  $a$ .

Equation (1) admits delocalized and localized solutions, which are separated by the energy gap. The delocalized solution is described by the function with constant envelope, and corresponds to the energy

$$|\Psi_{del}(x,t)|^2 = \frac{1}{l}, \quad E_{del}(V) = -\frac{4Jg}{l} + mV^2, \quad (4)$$

respectively. Here  $m$  is effective mass of a quasiparticle,  $m = \hbar^2/2Ja^2$ . The second type solution is described by the modulated Jacobi elliptic function

$$\Psi_{loc}(x,t) = \phi(\xi) \exp \left\{ \frac{i}{\hbar} \left[ mVax - \left( E + \frac{mV^2}{2} \right) t \right] \right\}, \quad \xi = x - x_0 - Vt/a, \quad (5)$$

where  $E$  is the energy per period and

$$\phi(\xi) = \sqrt{\frac{g}{2}} E^{-1}(k) dn \left[ \frac{g\xi}{E(k)}, k \right]. \quad (6)$$

The modulus the density of quasi-particles from the condition

$$g = 2\delta E(k)K(k). \quad (7)$$



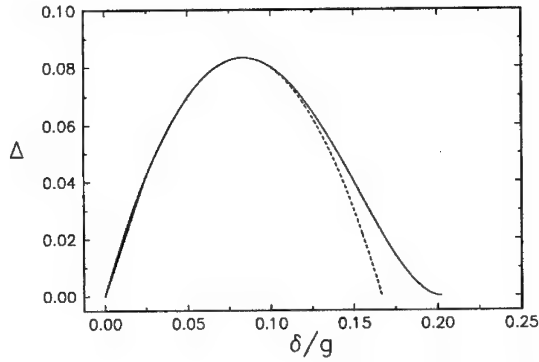


Fig. 1. The bisoliton energy gap width (in units of  $Jg^3/3$ ) as a function of charge carrier density (in units of  $g$ ). The solid and dashed lines correspond to the exact (10) and approximate (12) expressions, respectively.

in which  $K(k)$  and  $E(k)$  are complete elliptic integrals of the first and second kinds, respectively.

This solution corresponds to the condensate of a periodically distributed lattice of 'bisolitons' moving coherently in the deformation potential along the chain. The corresponding energy per period, including deformation energy, reads as

$$E_{loc}(V) = mV^2 + 2J \int_0^l \left[ \left( \frac{d\phi}{d\xi} \right)^2 - 2g \frac{1-3s^2}{1-s^2} \phi^4 \right] d\xi$$

$$= -\frac{2}{3}Jg^2 [E(k)(2-k^2) + K(k)(1-k^2)] E^{-3}(k). \quad (8)$$

The energetic gap width of the bisoliton condensate is determined by the difference of the densities of energies corresponding to the solutions (1) and (5) at zero velocities, and, hence, is the function of quasiparticle density,

$$\Delta = \delta [E_{del}(0) - E_{loc}(0)] = \frac{1}{3}Jg^3 F(\delta), \quad (9)$$

$$F(\delta) = \frac{E(k)(2-k^2) + K(k)(1-k^2)}{E^4(k)K(k)} - \frac{3}{E^2(k)K^2(k)}. \quad (10)$$

Fig. 1 shows the dependence of the energy gap width on the density of charge carriers.

The numerical analysis of expression (10) shows that there exists the critical value of quasiparticle density

$$\delta_{cr} = 2g/\pi^2, \quad (11)$$

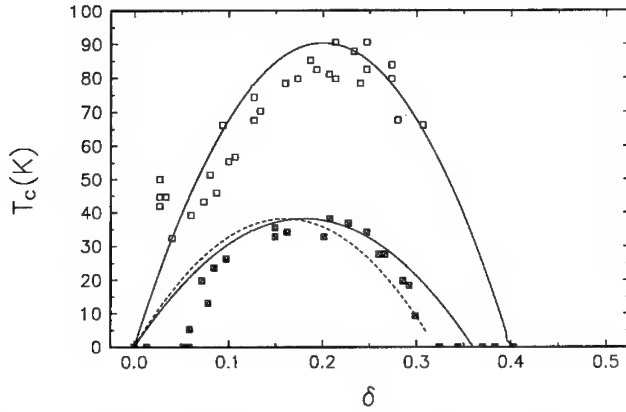


Fig. 2. The critical temperature (in Kelvin) as a function of hole concentration. The upper and lower curves correspond to yttrium and lanthanum compounds, respectively. Solid lines are obtained by fitting Eq. (12) to the experimental value of  $\delta_0$ , dashed line by fitting to the value  $\delta_{cr}$ . Empty and full squares are experimental data<sup>1,2</sup>

above which the energy gap width vanishes. It follows from Eq. (10), that the gap attains the maximum value at small values of density, when, according to Eq. (7), the modulus of elliptic function takes values close to unit. Using the expansions of complete elliptic integrals at  $k_1^2 = 1 - k^2 \ll 1$ , we get the following expression

$$\Delta \approx \frac{2}{3} Jg\delta(g - 6\delta), \quad \delta \approx \frac{g}{2 \ln(4/k_1)}, \quad (12)$$

which corresponds to the dashed curve on Fig. 1.

From Eq. (12) the optimal density value and corresponding gap width follow

$$\delta_o = \frac{g}{12}, \quad \Delta_{max} = \frac{Jg^3}{36}. \quad (13)$$

Notice that in frame of the bisoliton model of superconductivity the critical temperature  $T_c$  is proportional to the energy gap width at zero temperature<sup>5</sup>  $\Delta = \alpha T_c$ , where  $\alpha$  is a numerical constant. By fitting the maximum value of critical temperature obtained in our model to the experimental value ( $T_c = 38K$  for lanthanum compound and  $T_c = 90K$  for yttrium compound), we get<sup>10</sup>  $C=460$  and  $C=1090$ , respectively, where  $C = Jg^3/(3\alpha)$ . This results in good agreement with the experimental data on the dependence of  $T_c$  on  $\delta$  (see Fig. 2).

More sharp decrease of  $T_c$  at densities close to the critical value, as compared with the analytical result can be explained by taking into account the Coulomb repulsion between electrons, whose role increases with increasing electron density.

### 3. Pressure Dependence of Critical Temperature

To analyze the pressure dependence of critical temperature the following relation is useful

$$\frac{\partial T_c}{\partial P} = - \frac{T_c}{B} \frac{\partial \ln T_c}{\partial \ln V} \approx - \frac{T_c}{3B} \frac{\partial \ln T_c}{\partial \ln a}, \quad (14)$$

where  $P$ ,  $V$ ,  $a$ ,  $B$  are pressure, volume, lattice constant and bulk modulus, respectively.

As mentioned above, the critical temperature is connected with the energy gap width at zero temperature by the relation  $\Delta = \alpha T_c$ , in which  $\alpha$  is a numerical constant<sup>5</sup>. The logarithmic derivative of the energy gap can be obtained from Eq. (13),

$$\frac{\partial \ln \Delta}{\partial \ln a} = \tilde{J}' + \left(1 + \frac{g}{g - 6\delta}\right) \tilde{g}' + \left(1 - \frac{6\delta}{g - 6\delta}\right) \tilde{\delta}', \quad \delta < \delta_{cr}, \quad (15)$$

where  $\tilde{p}'$  denotes the logarithmic derivative of parameter  $p$ ,

$$\tilde{p}' = \frac{\partial \ln p}{\partial \ln a}, \quad p = g, \delta, \chi, \kappa, J. \quad (16)$$

In its turn, according to Eq. (2), the following equality is valid

$$\tilde{g}' = 2\tilde{\chi}' - \tilde{J}' - \tilde{\kappa}'. \quad (17)$$

Substituting relation (14) into (13) and taking into account Eq. (9), we find

$$\frac{\partial T_c}{\partial P} = - \frac{C}{3B} \left\{ F(\tilde{J}' + \tilde{g}' + \tilde{\delta}') + \frac{2\delta}{g} \tilde{g}' - \frac{12\delta^2}{g^2} \tilde{\delta}' \right\}, \quad (18)$$

where  $F$  is the function defined in (11), and  $C = Jg^3/(3\alpha)$ .

The parameters (16) appearing in Eq. (18), can be estimated as follows. The elasticity coefficient can be obtained from the potential energy of the copper-oxygen ion interaction, which can be described by the Buckingham potential  $U = -A_1 r^{-6} + A_2 \exp(-cr)$ ,

$$\kappa = \left[ \frac{d^2 U}{dr^2} \right]_{r=a} = \frac{6A_1}{a^8} (ca - 7), \quad (19)$$

from which the logarithmic derivative follows

$$\tilde{\kappa}' = - \frac{7(ca - 8)}{ca - 7} \approx -7. \quad (20)$$

The electron-phonon coupling constant can be estimated as the coefficient of the term  $(u_{2n+2} - u_{2n})$  in the expansion of the energy of extra electron at an oxygen ion in the chain

$$E = - \frac{ze^2}{|R_{2n+1} - R_{2n}|} - \frac{ze^2}{|R_{2n+1} - R_{2n+2}|}. \quad (21)$$

Here  $ze$  is the charge of the copper ion,  $R_m = R_m^0 + u_m$  is the coordinate of the  $m$ -th ion,  $u_m$  is the displacement of copper ( $m = 2n$ ) or oxygen ( $u = 2n + 1$ ) ion from its equilibrium position. Performing the expansion of expression (21), we get

$$\chi = \frac{4ze^2}{a^2}, \quad \tilde{\chi}' = -2. \quad (22)$$

Finally, the copper-oxygen exchange integral in the tight-binding approximation can be written as

$$J = - \int \Psi_O^*(\vec{r}) [W(\vec{r}) - w(\vec{r})] \Psi_{Cu}(\vec{r}) d\vec{r}, \quad (23)$$

where  $W(\vec{r}) - w(\vec{r})$  is the potential energy of electron interactions with all ions except the one it occupies,  $\Psi_O(\vec{r})$  and  $\Psi_{Cu}(\vec{r})$  are the wave functions of oxygen and copper ions in states  $2p^5$ ,  $3d^{10}$ , respectively. Substituting the explicit form of radial parts of functions into Eq. (23) and carrying out the integration, we get

$$J \approx A \left( \frac{12}{\rho} \sinh \frac{\rho}{12} - \cosh \frac{\rho}{12} \right) e^{-5\rho/12} \approx ca^2 \exp(-\beta a), \quad (24)$$

where  $\rho = a/2a_B \approx 3.7$  with  $a_B$  being the Bohr radius,  $\beta = 5/(24a_B)$ ,  $A$  and  $c$  are constants independent of lattice constant. Differentiating expression (24), we find

$$\tilde{J}' = 2 - \beta a \approx 0.45, \quad (25)$$

which, together with Eqs. (20), (21) and (17), results in  $\tilde{g}' \approx 2.4$ .

The only parameter whose pressure dependence cannot be estimated analytically in our model is the charge carrier density  $\delta$ . Instead we can use the values obtained experimentally from Hall effect measurements<sup>11</sup>. For instance, for yttrium compound this value was estimated in<sup>4</sup> as  $\tilde{\delta}' = -90$ , less value of  $\tilde{\delta}'$  is found for lanthanum compound (see<sup>12</sup>).

Provided the charge density is less than the critical value determined in Eq. (11), the approximate equality follows from Eq. (18)

$$\frac{\partial T_c}{\partial P} \approx - \frac{2C\delta}{3Bg} \left\{ \tilde{J}' + 2\tilde{g}' + \tilde{\delta}' - 6 \frac{\delta}{g} (\tilde{J}' + \tilde{g}' + 2\tilde{\delta}') \right\}. \quad (26)$$

Substituting into the last equation the values  $\tilde{J}'$ ,  $\tilde{g}'$  obtained above, and the experimental value of  $\tilde{\delta}'$ , we can conclude that in frame of our model the critical temperature

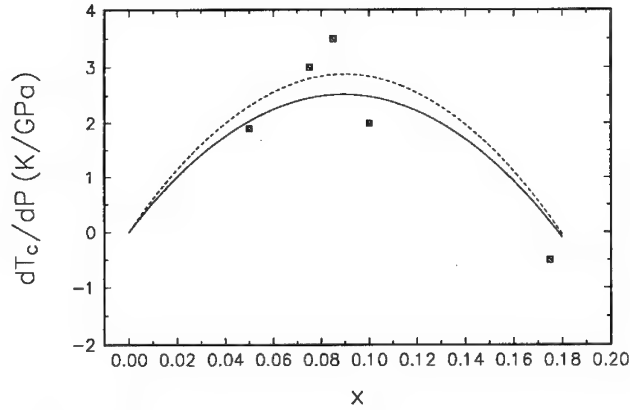


Fig. 3. The pressure derivative of critical temperature as a function of composition  $x$  in  $\text{La}_{2-x}\text{M}_x\text{CuO}_4$  compound. Solid line corresponds to  $\delta' = -80$ , dashed line to  $\delta' = -90$ ; bulk modulus is  $B = 180$  GPa. The experimental data are taken from Ref. 12.

can increase or decrease with increasing pressure depending on the charge carrier density. This explains the wide scattering of (or even the "contradictions" among) the experimental data on the pressure dependence of critical temperature.

In conclusion, we represent in Fig. 3  $\partial T_c / \partial P$  as a function of  $x$  for the compound  $\text{La}_{2-x}\text{M}_x\text{CuO}_4$  given by Eq. (27). The experimental data are taken from Fig. 12 in Ref. 12. Note that the bisoliton model reproduces well the general trend of the experimental data. Strictly speaking, our model should be compared with the experimental data on uniaxial compression of superconducting samples instead of hydrostatic pressure. But, first, at present they are very few, and second, the comparison we have done indicates that the bisoliton model even in a one-dimensional formulation without attraction of any extra mechanism or assumption describes very well the behavior of superconducting oxides under pressure.

#### Acknowledgements

This work was stimulated by discussions with Prof. R. Pucci and part of it was done in collaboration with A. La Magna, R. Pucci, and F. Siringo. The author is indebted to R. D. Parmentier and to A. D'Anna for remarks and assistance in drawing up the paper. The author expresses her sincere gratitude to the International Science Foundation for the financial support (travel grant No. 4321).

## References

1. Y. Tokura, J.B. Torrance, T.C. Huang and A.I. Nazzal, *Phys. Rev.* **B38** (1988) 7156.
2. J.B. Torrance, Y. Tokura, A.I. Nazzal, A. Bezing, T.C. Huang and S.S.P. Parkin, *Phys. Rev. Lett* **61** (1988) 1127.
3. R. Griessen, *Phys. Rev.* **B36** (1987) 5284.
4. R.J. Wijngaarden, E.N. van Enig, J.J. Scholtz, H.K. Hemmes and R. Griessen, in *Molecular Systems under High Pressure*, ed. R. Pucci and G. Piccito (North-Holland, Amsterdam, 1991).
5. A.S. Davydov, *Phys. Rep.* **190** (1990) 192.
6. L.S. Brizhik and A.S. Davydov, *Phys. Stat. Sol. (b)* **143** (1987) 689.
7. L.S. Brizhik, *Phys. Stat. Sol. (b)* **157** (1990) 649.
8. A. La Magna, R. Pucci and F. Siringo, in press.
9. L.S. Brizhik and A.A. Eremko, *Physica D*, in press.
10. L. Brizhik, A. La Magna, R. Pucci and F. Siringo *High Press. Res.* **11** (1994) 375.
11. I.D. Parker and R.H. Friend, *J. Phys. C: Solid State Phys.* **21** (1988) L345.
12. R.J. Wijngaarden and R. Griessen in *Studies of High Temperature Superconductors*, ed. A.V. Narlikar (Nova Science Publishers Inc., New York, 1993), p. 160.

# FLUX MOTION IN HTSC: THE ROLE OF WASHBOARD-TYPE PINNING POTENTIAL

C. ATTANASIO, L. MARITATO, C. COCCORESE

*Department of Physics, University of Salerno  
Baronissi (Sa), I-84081, Italy*

S.L. PRISCHEPA

*State University of Informatics and RadioElectronics  
Minsk, 220600, Belarus*

and

M. SALVATO

*Ansaldo-CRIS, Napoli, I-80147, Italy*

## ABSTRACT

Transport measurements of the pinning potential for *c*-axis oriented films of  $\text{Bi}_2\text{Sr}_2\text{CaCu}_2\text{O}_x$  (BSCCO) in the absence of an external magnetic field (only self-field due to the bias current) have been realized. The experimental data are elaborated within the flux creep theory. The obtained current and temperature dependences of the pinning potential are discussed in terms of sinusoidal shape of the pinning potential well. The results of numerical simulations strongly prove the important role of a washboard-type pinning potential in HTSC in the case of approximation of an isolated vortex.

## 1. Introduction

An enormous amount of experimental work has been performed in order to investigate the pinning properties of high temperature superconductors (HTSC). These investigations reveal the importance of the classical Anderson-Kim model<sup>1</sup> for the description of activated phenomena and give rise to further theory developments taking into account HTSC's peculiarities<sup>2,3</sup>. The special interest to the flux creep phenomena in HTSC is caused by the fact that both magnetic relaxation velocity measurements and transport measurements are extremely fruitful experimental probes of the strength of the pinning interaction between vortices and pinning centers clearing up the nature of the pinning centers, dimensionality and other effects.

The important moment of Anderson-Kim model is the suggestion about linear dependence of the net pinning barrier height  $U$  on the bias current  $I$ :  $U/U_0 \sim (1 - I/I_{c0})$ , where  $I_{c0}$  is the critical current in the absence of flux creep and  $U_0$  is the pinning barrier height in the limit of zero current<sup>4</sup>. Using a linear correlation between activation energy and external driving force an unusual temperature dependence of the apparent pinning energy  $U_{app}$  was obtained by measuring the magnetic relaxation process both in bulk materials<sup>5-7</sup> and in thin films<sup>8</sup>: as the temperature

reduces down to zero the  $U_{app}$  also goes to zero, in contrast with the conventional theories of type II superconductors where  $U(T)$  is supposed to be a constant at low temperatures. Two main explanations have been advanced in order to explain such anomalous behavior of  $U_{app}$  at  $T$  close to zero. The first one is connected with the collective phenomena in superconductors. The power law dependence of the vortex bundle activation barrier  $U$  on current  $I$  ( $U(I) \sim I^{-\alpha}$ ) was obtained<sup>2</sup> in the presence of vortex lattice, when the magnetic induction  $B$  is  $B_{c1} < B < B_{c2}$ , where  $B_{c1}$  and  $B_{c2}$  are the first and the second critical magnetic fields of superconductor. The value of  $\alpha$  depends upon dimensionality of the system. The second one is based on the existence of a pinning energy distribution which can give rise to the analogous temperature dependence of  $U_{app}$ <sup>9</sup>. Also Beasley *et al.*<sup>4</sup> first mentioned that the nonlinearity of  $U(I)$  dependence may be due to a spatial variation of the pinning potential wells. In the case of complex shapes of pinning potential wells one obtain different types of  $U(I)$  dependence<sup>10</sup>. Zeldov *et al.*<sup>11</sup> proposed logarithmically type dependence of  $U(I)$ ,  $U/U_0 \sim \ln(I/I_{c0})$ . In spite of observed good agreement with experimental data both for  $\text{YBa}_2\text{Cu}_3\text{O}_x$  and  $\text{Bi}_2\text{Sr}_2\text{CaCu}_2\text{O}_x$  epitaxial thin films<sup>11,12</sup> such dependence suppose that activation energy diverges as  $I$  approaches zero. On the other hand Matsushita and Otabe<sup>13</sup> considered the simple case of sinusoidal washboard potential

$$F(x) = \left( \frac{U_0}{2} \right) \sin \frac{2\pi x}{a_f} - f_L x \quad (1)$$

where  $f_L$  is the Lorentz force,  $a_f$  is the period. In this case the energy barrier is

$$\frac{U(j)}{U_0} = [1 - j^2]^{0.5} - j \cos^{-1} j \quad (2)$$

where  $j = I/I_{c0}$ . Evidently the linear dependence of pinning energy  $U$  on bias current  $I$  is no longer valid for sinusoidal washboard potential. As usual, hopping motion of the vortices due to the thermal activation leads to the induced electric field  $E \sim \exp(-U/k_B T)$ , where  $k_B$  is the Boltzmann constant. On the other hand the Maxwell equation gives  $E \simeq -\partial < \phi > / \partial \tau \sim -\partial I / \partial \tau$ , where  $< \phi >$  is the mean value of the magnetic flux density and  $\tau$  is the time. Combining these equations for the electric field we have

$$\partial j / \partial \tau^* = -\exp(-aU(j)/U_0). \quad (3)$$

where  $a = U_0/k_B T$ ,  $\tau^* = (2B\nu_0 a_f / \mu_0 d^2 J_{c0}) \tau \equiv c\tau$ ,  $\nu_0$  is the attempt frequency of the vortex vibration,  $d$  is the sample thickness and  $J_{c0}$  is the critical current density related to  $I_{c0}$ . Matsushita and Otabe<sup>13</sup> detected that the relaxation of  $I$  in this case deviates from the logarithmic type resulting from the original model of Anderson and Kim. The mean creep rate  $< dI/d\ln \tau >$  defined in a certain time interval gives the apparent pinning potential  $U_{app}$ . According to the result of ref.13,  $U_{app}$  has the anomalous temperature dependence far from the critical temperature  $T_c$ ,  $U_{app} \rightarrow 0$  when  $T \rightarrow 0$ .



Another result of the "giant" flux creep in HTSC is the unusual broadening of the resistance versus temperature in magnetic field<sup>14</sup> and at different values of bias current<sup>11,12</sup>. Small values of  $U$  lead to the emergence of a long tail on the resistive transition down to small temperatures. In this case the flux creep resistance can be described, in the limit of small applied currents ( $I < I_{c0}$ ), by<sup>15</sup>

$$R = R_0 \exp(-U/k_B T) \quad (4)$$

where  $R_0$  is some coefficient related to the vortex volume, average hopping distance of vortices, magnetic inductance and characteristic frequency with which vortices try to escape from the well. Taking into consideration that  $U$  is a function both of  $T$  and  $I$  (at fixed value of  $B$ ), from Eq.4 follows that analyzing experimental curves  $R(T)$  at different values of bias current  $I$  one can extract information about  $U$  and its current dependence.

The  $I - V$  characteristics give important informations about the flux creep<sup>16-18</sup> too. In the Anderson-Kim model the  $I - V$  characteristic can be written<sup>16</sup>

$$V = I r_0 \exp\{-(U_0/k_B T)(1 - I/I_{c0})\} \quad (5)$$

where  $r_0$  is a coefficient. In this case the magnetic field is created by the transport current and it is rather weak. That is why the behavior of the system can be well approximated by that of an isolated vortex<sup>29</sup>. From Eq.(5) follows that voltage across the sample is not equal zero even for currents below  $I_{c0}$  when thermally activated flux creep is taken into account. The range of  $I$  where this occurs depends upon the ratio  $U/k_B T$ . The barrier height can be found by analyzing the form of the  $I - V$  characteristics at low voltages. It follows from Eq.(5) that  $\ln(V/I) \sim (1 - I/I_{c0})$ . If  $U$  depends upon  $I$  in more complicated way (see, for example, Eq.(2)), the slope of  $\ln(V/I)$  versus  $I$  dependence gives the apparent value of pinning potential, i.e.  $U_{app}$ .

The goal of our work is the experimental determination of  $U$  versus  $I$  and  $U$  versus  $T$  dependences in BSCCO films by means of transport measurements without external magnetic field. In this case the properties of the superconductor are determined by the interaction of the single vortex with the pinning centers and the shape of pinning potential becomes very important.

## 2. Experimental Procedures

The results of this paper have been obtained on high textured  $\text{Bi}_2\text{Sr}_2\text{CaCu}_2\text{O}_x$  films with the  $c$ -axis perpendicular to the  $\text{MgO}(100)$  substrate surface. Films have been prepared both by vacuum electron beam evaporation of stoichiometrical (2212) BSCCO pellets<sup>20</sup> and by molecular beam epitaxy technique<sup>21</sup>. In the last case the four elements (Bi, Sr, Ca, Cu) were evaporated by four different shutter controlled sources: bismuth and calcium were evaporated by two Knudsen cells while strontium and copper were evaporated by two electron guns. After the deposition and the annealing in air at temperature  $870-880^\circ\text{C}$  the films showed  $T_c \geq 80\text{K}$ . The

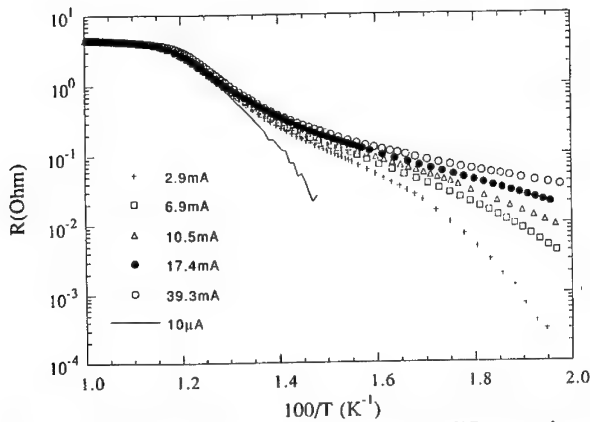


Fig. 1. Arrhenius plot of the  $R(T)$  of a BSCCO film for different values of the bias current.

constriction has been fabricated by usual photolithographic method. Transport properties have been measured with the help of a *dc* current source generator. The whole measurement procedure have been computer managed and controlled. The level of temperature stabilization, measured by a platinum thermometer, was of the order of  $10^{-2} K$  during the whole procedure of data acquisition. The sample was attached to a copper rod inside a cryocooler by low temperature silver glue. The heater of maximum power  $4W$  was put into the clearance inside the rod close to the sample. The acquisition time of one  $I - V$  characteristic varied from 10s up to 1 min. During the  $R$  versus  $T$  curve registration the cooling rate was of  $25K/h$ .

### 3. Results and Discussion

#### 3.1. $R(T)$ dependences

First we analyze our resistive data. Special attention is given to the low temperature part of the  $R(T)$  curves. Fig.1 shows the  $R$  versus  $T$  data of a BSCCO film having  $100 \mu m$  width and  $50 \mu m$  length plotted in the Arrhenius fashion. We assume the slope of the  $\ln R$  versus  $T^{-1}$  curves at low temperature to be the value of the effective pinning potential,  $U^*$ . For example, from Fig.1 follows that for large values of the driving force (curve for  $I = 39.3mA$ ), the slope decreases when the temperature decreases. But this does not mean that the value of  $U$  decreases as we lower the temperature. It is well known that the slope of the Arrhenius curves does not correspond to the actual pinning energy,  $U(T)$ , but rather to  $U^* = -k_B d(\ln R)/d(T^{-1}) = U(T) - TdU(T)/dT$ . So, analyzing data of Fig.1, it is necessary to take into account the temperature dependence of the pinning potential which at temperatures close to  $T_c$  is very pronounced.

Up till now there is no explicit form for the temperature dependence of the

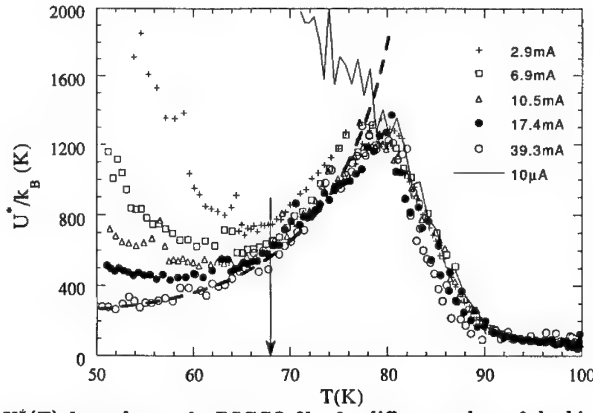


Fig. 2. The  $U^*(T)$  dependence of a BSCCO film for different values of the bias current. The dashed line corresponds to the Eq.(6) related to the experimental points for  $I=39.3\text{mA}$

pinning potential. The reasonable approach is to write the expression for  $U(T)$  in the form  $U(T) = (1/2\mu_0)B_c^2(T)\xi^n(T)L^{3-n}$ , where  $B_c$  is the induction of the thermodynamical critical magnetic field,  $\xi$  is the coherence length,  $L$  is the temperature independent pinning length and the exponent  $n$  identifies the temperature scaling behavior of the pinning energy<sup>22</sup>. Assuming  $B_c(t) \sim (1-t^2)$  and  $\xi(t) \sim (1-t^4)^{0.5}(1-t^2)^{-1}$ , we get  $U(t) = U(0)(1-t^2)^{2-n}(1-t^4)^{n/2}$ , where  $t = T/T_c$ . Since the choice  $n = 1$  is usually assumed<sup>22</sup> when  $B > 0.2B_{c2}$  we consider only the cases  $n = 2$  and  $n = 3$ . For  $n = 2$  we get  $U(t) = U(0)(1-t^4)$  and  $U^* = U(0)(1+3t^4)$ . This means that the slope of the Arrhenius plot gives the value of  $U^*$  enhanced by  $(1+3t^4)/(1-t^4)$  with respect to the value of  $U$ . In the case of  $n = 3$  the expression for  $U(t)$  is :  $U(t) = U(0)(1-t^4)^{1.5}/(1-t^2)$ , which gives  $U^*$

$$U^*(t) = U(t) - t dU/dt = U(t) \left( 1 + \frac{6t^4}{1-t^4} - \frac{2t^2}{1-t^2} \right) \quad (6)$$

Eq.(6) means that the value of  $U^*$  is enhanced by  $(1 + 6t^4/(1-t^4) - 2t^2/(1-t^2))$  with respect to the actual value of  $U(t)$ .

In Fig.2 we show the dependence of  $U^*$  versus  $T$  for different values of the bias currents. The arrow shows the temperature at which we calculate the  $U$  values for different bias currents at  $t = 0.8$ . It is seen that as we cool down the temperature to 80K, the experimental points related to different values of the bias current ( $10\mu\text{A}, \dots, 39.3\text{mA}$ ) practically are not shifted with respect to each other. In this range of temperature, slightly below  $T_c^{\text{onset}}$ , the pinning potential is still small if we compare it with the energy of the thermal fluctuations and that is why the regime of flux flow is accomplished (the resistivity of the sample is independent from the current at the fixed temperature value). The further fall of temperature gives rise to the increasing of the pinning potential and the relation  $U/k_B T$  increases becoming

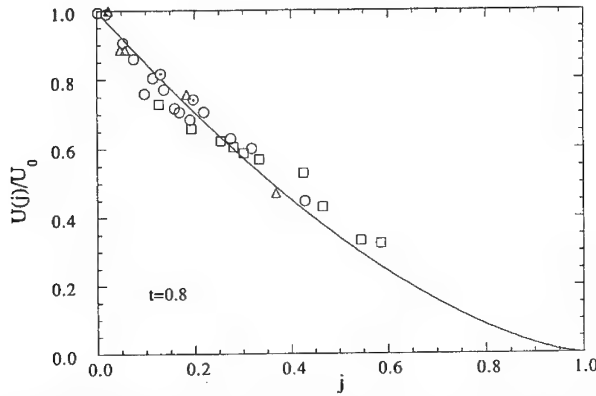


Fig. 3. The  $U(I)$  dependence in normalized coordinates for four BSCCO samples at  $t=0.8$ . The solid line corresponds to the Eq.(2).

of the order of one. As a result the weak pinning and the pronounced flux creep start to take place. This affects the horizontal part of the  $U^*$  versus  $T$  curves. As temperature decreases the pinning potential grows up much faster and the relation  $U/k_B T$  becomes greater than one, promoting large pinning and increasing of  $U^*$ . At this point the "true" superconducting state comes up; this is confirmed by the fact that the increase of  $U^*$  coincides with the temperature at which the resistance of the sample, measured with an accuracy of  $10^{-3}\Omega$ , becomes zero. The increase of the bias current leads to the lowering of the pinning potential and the all picture is naturally shifted toward the region of low temperatures. In Fig.2 by dashed line we show the best fit obtained using Eq.(6) for the scaling factor  $n = 3$  related to the experimental points for  $I = 39.3mA$ . The agreement is evident. So for our anisotropic system we can rewrite  $\xi^3$  as  $\xi_{ab}^2 \xi_c$ . This fact assumes the existence of pancake vortices at  $T < 0.8T_c$  which are localized in the  $CuO_2$  planes. This result confirms the two dimensional nature of vortices in BSCCO and is in agreement with our previous work<sup>23</sup> in which the evidence of the 2D nature of the vortices has been obtained from  $I_c$  versus  $B$  measurements for the same quality BSCCO films.

The above mentioned procedure has been performed for other three samples. The obtained  $U(I)$  dependence in normalized coordinates for the four samples and  $t = 0.8$  is presented in Fig.3. The solid curve corresponds to the Eq.(2). Here  $I_{c0}$  and  $U_0$  are fit parameters. For all the samples the values of pinning potential  $U_0$  are in the range between 62 and 70 meV and  $I_{c0}$ , the "critical current" at which  $U$  goes to zero, corresponds to densities of the order of  $10^5 A/cm^2$ . The value of  $U(t = 0.8, I = 0) \sim 65meV$  is slightly higher than the one obtained from the suggestion of linear  $U$  versus  $I$  dependence<sup>23</sup>. However, it is possible to obtain  $U_0 \sim 30meV$  from the slope of the  $U(j)$  curve at large currents. Thus the value of  $U_0$  calculated from the Anderson-Kim model is usually lower than the real one.

### 3.2. Investigation of the $U(j)$ dependence for a periodic $U(x)$

Eq.(2) is well approximated by  $U(j) \sim (1-j)^{1.5}$ . Let us show that  $U(j)$  is not sensitive to the precise form of  $U(x)$  and that above approximation is valid for any washboard-type pinning potential. It is worth to mention that during measurements we extract some medium value and shape of  $U$  which, in principle, could be different from the real form of the pinning potential in the physical object.

We consider the single vortex in a generic periodic potential:  $U(x) = U(x + a_f)$ ,  $a_f$  is the medium vortex hopping distance (the vortex mean free path). In the absence of externally applied bias current the vortex is at the bottom of the potential well with depth  $U = U(x_{max}) - U(x_{min})$ , where  $x_{max}$  and  $x_{min}$  correspond, respectively, to the nonequilibrium and equilibrium positions of the vortex and are determined from conditions

$$\frac{dU}{dx}(x_{min}) = \frac{dU}{dx}(x_{max}) = 0; \quad \frac{d^2U}{dx^2}(x_{min}) > 0, \quad \frac{d^2U}{dx^2}(x_{max}) < 0 \quad (7)$$

(Here we suppose that the second derivative of  $U$  exists and is continuous). Applying a bias current we suppress the potential barrier so that  $U = W(\bar{x}_{max}) - W(\bar{x}_{min})$ , where  $W(x) = U(x) - f_L x$ .  $\bar{x}_{max}$  and  $\bar{x}_{min}$  are, respectively, the new nonequilibrium and equilibrium positions of the vortex:

$$\frac{dU}{dx}(\bar{x}_{min}) - f_L = \frac{dU}{dx}(\bar{x}_{max}) - f_L = 0 \quad (8)$$

When the bias current reaches the value of  $I_{c0}$ , where  $I_{c0} \sim \max(\frac{dU}{dx}) = \frac{dU}{dx}(x_0)$ , the potential well vanishes and superconductivity is destroyed. Because  $j = I/I_{c0}$  the height of the pinning barrier can be written as

$$U = U(\bar{x}_{max}) - U(\bar{x}_{min}) - j \frac{dU}{dx}(x_0) \cdot [\bar{x}_{max} - \bar{x}_{min}] \quad (9)$$

In the limit of  $j \rightarrow 1$  (in practice, as we will see later, this case corresponds to the low temperature limit), we may assume  $\bar{x}_{min} = x_0 - \delta$ ,  $\bar{x}_{max} = x_0 + \delta$ , where  $\delta/x_0 \ll 1$ . The eq.(8) for  $\bar{x}_{min}$  can be rewritten as

$$\frac{dU}{dx}(\bar{x}_{min}) - f_L = \frac{dU}{dx}(x_0 - \delta) - j \frac{dU}{dx}(x_0) = 0 \quad (10)$$

Expanding Eq.(10) in Taylor series we can obtain the expression for  $\delta$ :

$$\delta \simeq (1-j)^{0.5} \left[ -2 \frac{\frac{dU}{dx}(x_0)}{\frac{d^3U}{dx^3}(x_0)} \right]^{0.5} \quad (11)$$

Combining Eq.(9) and Eq.(11) we finally get

$$U \simeq \frac{4}{3} (1-j)^{1.5} \frac{dU}{dx}(x_0) \left[ -2 \frac{\frac{dU}{dx}(x_0)}{\frac{d^3U}{dx^3}(x_0)} \right]^{0.5} \quad (12)$$

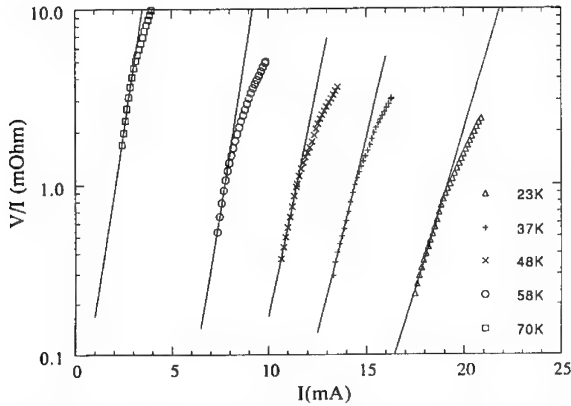


Fig. 4.  $V/I$  versus  $I$  dependences of BSCCO film for different temperatures.

From Eq.(12) follows that for a washboard type potential the dependence  $U(j) \sim (1-j)^{1.5}$  is always valid. But only from the  $U$  versus  $j$  dependence it is not possible to extract the precise spatial form of the pinning potential.

### 3.3. $I-V$ characteristics

The analysis of  $I-V$  characteristics gives us a more precise information about flux motion and pinning potential shape in BSCCO. Fig.4 shows typical examples of the function  $V/I$  versus  $I$  for the sample in the temperature range  $20K-70K$ . The values of  $V/I$  are plotted in a logarithmic scale. It is seen that  $V/I$  versus  $I$  dependence deviates from a logarithmic type but nevertheless these curves can be approximated by exponential function up to  $V \sim 20\mu V$ . It is possible to find the apparent depth of potential well for each value of the temperature from the slopes of the straight lines according to Eq.(5). The  $U_{app}$  temperature dependence for the BSCCO film is given in Fig.5. We can see that at low temperatures the  $U_{app}$  versus  $T$  behavior is anomalous, i.e. as temperature decreases the effective potential well value aspires to zero. As we have already mentioned the same  $U_{app}(T)$  behavior is usually obtained from magnetic measurements in the time windows up to  $1000 s^{5-7}$ . In our case on the edge of the film the maximum of self-induced magnetic field due to transport current does not exceed  $50G^{18}$ . The minimum vortex distance is approximately equal to  $1\mu m$ . This value exceeds the magnetic penetration depth  $\lambda \sim 0.2\mu m$ . That is why we take into account only the single vortex interaction instead of collective pinning.

As starting point we analyze our data from the point of view of uncorrelated interaction of isolated vortices with a sinusoidal washboard potential. The task is to solve numerically the Eq.(3). During this procedure we take  $B = 0.004T$ ,  $J_{c0} = 2 \times 10^9 A/m^2$ , and  $d = 10^{-6}m$ . We assume the attempt frequency value

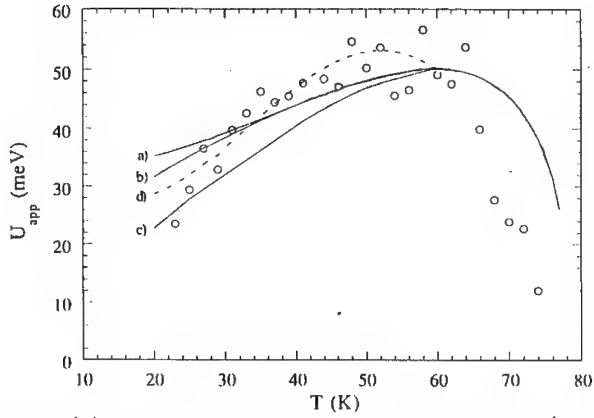


Fig. 5. The  $U_{app}(T)$  dependence as obtained from I-V characteristics (circles). The lines a), b), and c) correspond to the results of the numerical simulations for a time interval  $10^{-7}$ ,  $\dots$ ,  $10^{-6}$  seconds using a log-normal distribution of the critical current densities with  $\sigma=0$ , 0.1, and 0.2 respectively. Curve d) has been calculated for a time interval  $10^{-6}$ ,  $\dots$ ,  $10^{-3}$  seconds and  $\sigma=0$ .

of  $10^9 s^{-1}$  and the medium distance between pinning centers to be of the order of  $\xi_{ab}$ . The only fit parameter which we use in order to obtain agreement with the experimental data is the integration time interval. Because in experiment we analyze the  $I - V$  curves in the range  $1-10 \mu V$ , first we check time intervals of one order of magnitude. The best result is obtained when Eq.(3) is integrated over the time interval ranging from  $10^{-7}$  to  $10^{-6}$  seconds. These are typical time values for vortices entering in the sample in the case of small amount of vortex chains in the microvolt region. The absolutely small values of time indicate the large degree of potential well deformation during the transport measurements. In this case it is worth to speak about thermally activated flux motion than creep of vortices. As can be seen from Fig.5 (curve a), the quantitative agreement between the theory and our experimental data is not very good. The above procedure has also been applied in the case  $n = 2$ , leading to a even poor accordance with the experimental points. In the above procedure it is implicitly assumed that the pinning potential is a perfectly sinusoidal function. It is clear that this assumption is not verified in a real physical object. In this case it is necessary to take into account the critical current density and pinning potential height distribution. So it is quite obvious to write the pinning potential dependence on the current as

$$\frac{U(I)}{\bar{U}_0} = \int_I^\infty \left\{ \sqrt{1 - (I/I_{c0})} - (I/I_{c0}) \cos^{-1}(I/I_{c0}) \right\} P(I_{c0}) dI_{c0} \equiv \int_I^\infty U(I, I_{c0}) P(I_{c0}) dI_{c0} \quad (13)$$

where  $P(I_{c0})$  is a distribution function of the critical current, and  $\bar{U}_0$  is some medium parameter of normalization. Because  $I_{c0}$  is mostly governed by the gradient  $\partial U / \partial x$ , but not by the pinning potential  $U$ , the statistical distribution of the critical currents

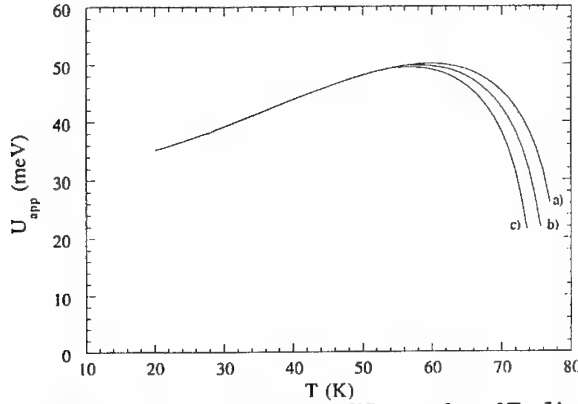


Fig. 6. The calculated  $U_{app}(T)$  dependences for different values of  $T_c$ . Lines a), b), and c) correspond to  $T_c=78\text{K}$ ,  $76\text{K}$ , and  $74\text{K}$ , respectively.  $\sigma=0$  and the time interval is  $10^{-7}, \dots, 10^{-6}$  seconds.

is closely related to a dishomogeneity of the depth and shape in the pinning potential wells. In this case the electrical field due to the thermally activated hopping motion of the flux lines is given by<sup>16</sup>

$$E = B\nu_0 a_f \int \exp\left(-\bar{U}/k_B T\right) P(U - \bar{U}) d\bar{U} \quad (14)$$

and Eq.(3) is then modified to become

$$\frac{\partial I}{\partial \tau} = -c \int_I^\infty \exp\left\{-a \frac{U(I, I_{c0})}{\bar{U}_0}\right\} P(I_{c0}) dI_{c0} \quad (15)$$

if the critical currents related to each potential well are thought to be independent. We assume a log-normal distribution for the critical currents

$$P(I_{c0}) = \frac{1}{I_{c0} \sigma \sqrt{2\pi}} \exp\left(-(\log I_{c0})^2 / 2\sigma^2\right) \quad (16)$$

and we solve Eq.(15) for  $n = 3$  in the time window from  $10^{-7}$  to  $10^{-6}$  seconds for various values of the width  $\sigma$  of the distribution. The results of these numerical calculations are reported in Fig.5. From this we can see that the effect of the statistics becomes less important at high temperatures. At the same time the dependence of the pinning potential upon  $I$ , given by Eq.(13) with  $\sigma = 0.1$ , again well describes our experimental data reported in Fig.3. Such  $U_{app}(T)$  dependence and the influence on it due to the statistics is in good agreement with the model of the ideal critical state. In fact, at temperatures close to  $T_c$  the thermal energy in HTSC is rather high and values of  $U$  are even small. That is why small values of current ( $I \ll I_{c0}$ ) can create the activated flux motion. At low temperatures the



$k_B T$  energies are quite small and it is necessary to apply large values of current ( $I \leq I_{c0}$ ) to observe the same degree of vortex activated motion. It means that  $U_{app}$  becomes smaller and more sensitive to the distributions in  $I_{c0}$  as the temperature goes down. Also the fact that we nevertheless did not obtain good agreement with our experimental data for the time interval of one order of magnitude is related to the distribution in shape and amplitude of pinning potential. The characteristic frequency,  $\nu = \nu_0 \exp(-U/k_B T)$ , of such a sample can be highly nonuniform even in the case of weak inhomogeneities in  $U(x)$ . This suggestion is confirmed by the results of numerical simulations for the integration period of  $10^{-6}, \dots, 10^{-3}$  seconds and the agreement with the experimental data is much better in this case (curve *d* in Fig.5). At high temperatures the magnetization of the sample becomes zero at  $\tau \leq 10^{-3}$  s. The large discrepancies in time causes the zero critical current and then at temperatures close to  $T_c$  it is necessary to take into account another time interval with smaller values of  $\tau$ . Moreover, at high temperatures the results of simulations are very sensitive to the  $T_c$  value, which also could give the uncertainty in the final result (Fig.6).

#### 4. Conclusions

The results of transport measurements of BSCCO thin film microbridges as well as the results of numerical simulations are well described in the framework of the classical flux creep and ideal critical state models in the presence of a washboard-type pinning potential. The 2D nature of vortices is proved from the experimental data. The obtained frequencies of the vortices entering in the sample being in the range 1KHz–1MHz confirm the presence of critical current densities and pinning potential shape distributions. Assuming a log-normal distribution of the critical current densities we were able to explain quantitatively the  $U_{app}(T)$  dependence extracted from the  $I - V$  characteristics.

#### Acknowledgements

We acknowledge the technical assistance of L. Falco during the measurements. This work is partially supported under the Belarus Basic Research Foundation, Grant F258.

#### References

1. P.W.Anderson and Y.B.Kim, *Theory of Motion of Abrikosov Flux Lines*, Rev. Mod. Phys. **36** (1964) 39–43.
2. M.V.Feigelman, V.B.Geshkenbein, A.I.Larkin, and V.M.Vinokur, *Theory of Collective Flux Creep*, Phys. Rev. Lett. **63** (1989) 2303–2305.
3. B.I.Ivlev and N.B.Kopnin, *Flux Creep and Flux Pinning in Layered High-Temperature Superconductors*, Phys. Rev. Lett. **64** (1990) 1828–1830.

4. M.R.Beasley, R.Labush, and W.W.Webb, *Flux Creep in Type-II Superconductors*, Phys. Rev. **181** (1969) 682-700.
5. M.Tuominen, A.M.Goldman, and M.L.Mcartney, *Time Dependent Magnetization of a Superconducting Glass*, Phys. Rev.B **37** (1988) 548-551.
6. Y.Xu, M.Suenaga, A.R.Moodenbangh, and D.O.Welch, *Magnetic Field and Temperature Dependence of Magnetic Flux Creep in c-Axis Oriented YBa<sub>2</sub>Cu<sub>3</sub>O<sub>7- $\delta$</sub>  Powder*, Phys. Rev.B **40** (1989) 10882-10890.
7. I.A.Campbell, L.Fruchter, and R.Cabanel, *Flux Creep in the Critical State of a High-Temperature Superconductor*, Phys. Rev. Lett. **64** (1990) 1561-1564.
8. J.Z.Sun, C.B.Eom, B.Lairson, J.C.Bravman, T.H.Geballe, and A.Kapitulnik, *Vortex Motion and Time Dependent Magnetic Responses in High Temperature Superconductors*, Physica C **162-164** (1989) 687-688.
9. C.W.Hagen and R.Griessen, *Distribution of Activation Energies for Thermally Activated Flux Motion in High-T<sub>c</sub> Superconductors: An Inversion Scheme*, Phys. Rev. Lett. **62** (1989) 2857-2860.
10. D.O.Welch, *A Theoretical Comparison of the Effects of the Shape of the Pinning Potential and a Distribution of Pinning Energies on the Apparent Pinning Energy as Measured by Magnetic Flux Creep*, IEEE Trans. Magnetics **27** (1991) 1133-1138.
11. E.Zeldov, N.M.Amer, G.Koren, A.Gupta, M.W.McElfresh, and R.J.Gambino, *Flux Creep Characteristics in High-Temperature Superconductors*, Appl. Phys. Lett. **56** (1990) 680-682.
12. E.Zeldov, N.M.Amer, G.Koren, and A.Gupta, *Flux Creep in Bi<sub>2</sub>Sr<sub>2</sub>CaCu<sub>2</sub>O<sub>8</sub> Epitaxial Films*, Appl. Phys. Lett. **56** (1990) 1700-1702.
13. T.Matsushita and E.S.Otabe, *Flux Creep in Sinusoidal Washboard Potential in Superconductors*, Jpn. J. Appl. Phys. **31** (1992) L33-L35.
14. T.T.M.Palstra, B.Batlogg, L.F.Schneemeyer, and J.V.Waszcak, *Thermally Activated Dissipation in Bi<sub>2.2</sub>Sr<sub>2</sub>Ca<sub>0.8</sub>Cu<sub>2</sub>O<sub>8+ $\delta$</sub>* , Phys. Rev. Lett. **61** (1988) 1662-1665.
15. D.Dew-Hughes, *Model for Flux Creep in High T<sub>c</sub> Superconductors*, Cryogenics **28** (1988) 674-677.
16. A.N.Lykov and S.L.Prischepa, *Thermally Activated Flux Creep in A15 Lattice Superconductor Microbridges*, Sov. Phys. Solid State **26** (1984) 587-591.

17. R.M.Schalk, G.S.Hosseinali, H.W.Weber, S.Proyer, P.Schwab, D.Bauerle, and S.Grundorfer, *Temperature Dependence of the Pinning Potential in  $\text{YBa}_2\text{Cu}_3\text{O}_{7-x}$  Superconductors*, Phys. Rev. **B49** (1994) 3511-3519.
18. A.N.Lykov, L.Maritato, S.L.Prischepa, and S.V.Zhdanovitch, *Pinning Potential Transport Measurements of Bi-Sr-Ca-Cu-O Thin Films*, J. Superconductivity **7** (1994) 849-851.
19. A.N.Lykov, *The Superconducting Mixed State of Artificial Microstructures*, Adv. Phys. **42** (1993) 263-342.
20. C.Attanasio, L.Maritato, A.Nigro, S.L.Prischepa, and R.Scafuro, *Realization and Characterization of e-Beam Completely Evaporated BSCCO Thin Films*, Mod. Phys. Lett. **5** (1991) 1203-1211.
21. M.Salvato, C.Coccorese, C.Attanasio, L.Maritato, and S.L.Prischepa, *Superconducting and Structural Properties of BSCCO Thin Films by Molecular Beam Epitaxy*, Cryogenics (1994) in press.
22. M.Tinkham, *Resistive Transition of High Temperature Superconductors*, Phys. Rev. Lett. **61** (1988) 1658-1661.
23. C.Attanasio, L.Maritato, S.L.Prischepa, and R.Scafuro, *Flux Creep Effects in the Transport Properties of c-Axis Oriented BSCCO Thin Films*, J. Superconductivity **5** (1992) 107-114.

---

## Chapter 3

# **Josephson Junctions**

## JOSEPHSON TUNNELING IN SIS JUNCTIONS MADE OF ANISOTROPIC SUPERCONDUCTORS

N. LAZARIDES and M. P. SØRENSEN

*Institute of Mathematical Modelling, The Technical University of Denmark  
DK-2800, Lyngby, Denmark*

### ABSTRACT

We employ the tunneling Hamiltonian formalism to calculate the quasiparticle and the two Josephson currents through a superconductor-insulator-superconductor (SIS) tunnel junction made of anisotropic superconductors. The formalism is generalised for the case of non-constant tunneling matrix elements and superconductors with different pairing states. The numerical calculation reveals a dramatic change of the three currents compared to the standard BCS theory. Several apparently contradictory experimental results can be explained by assuming anisotropic pairing which leads to an anisotropic gap function.

### 1. Introduction

The tunneling studies of superconducting junctions that have been performed in the past focus on superconductors which possess an isotropic  $s$ -wave gap<sup>1,2,3,4</sup>. This is apparently well justified for the conventional, low- $T_c$  materials. But for the heavy fermion and the high- $T_c$  superconductors this does not seem to be true. The heavy fermion materials are characterised as unconventional superconductors, in the sense that their gap function has a different symmetry than that of the low- $T_c$  superconductors. On the other hand, the high- $T_c$  superconductors exhibit crystal anisotropy and short coherence lengths, and thus one expects to see a strong influence of anisotropy on the tunneling current. The crystal anisotropy leads to an anisotropic gap function, whose symmetry is presently a matter of intense discussions. Experiments performed to resolve that question converge toward either an anisotropic  $s$ -wave or a  $d$ -wave symmetry. In practice, it is very difficult to realise superconductor-insulator-superconductor Josephson junctions made of high- $T_c$  materials. Despite of that, some junctions were already fabricated, and their  $I - V$  characteristics showed good agreement with calculations using the  $RSJ$  model<sup>5,6,7</sup>.

We shall study the influence of the anisotropy on the quasiparticle and the two Josephson currents, considering an  $s + d$ -wave pairing state. An isotropic  $s$ -wave component is included as well, due to the expecting mixing of pairing states with different  $l$ . In order to account for rough interfaces and impurities in the junction barrier, we consider the general case of diffuse tunneling, which makes the tunneling matrix elements  $k$ -dependent. The BCS spectral functions shall be used in the calculation of the tunneling currents. In the next section we describe briefly the theory, and quote the formulae used to calculate the tunneling currents. In section 3 we present and discuss the numerical results and in the last section we give the

conclusion.

## 2. The Extended Tunneling Hamiltonian Formalism.

The total Hamiltonian is written as a sum of the Hamiltonians for the right hand side ( $H_R$ ) and the left hand side ( $H_L$ ), respectively, plus the tunneling term  $H_T$  of the junction i.e.:

$$H = H_R + H_L + H_T . \quad (1)$$

Here

$$H_T = \sum_{kp} (T_{kp} c_k^\dagger c_p + h.c.) . \quad (2)$$

where  $c_k^\dagger, c_k$  are the creation and destruction operators for electrons.  $T_{kp}$  is the tunneling matrix element which transfers particles through the junction. In the case of diffuse tunneling, the tunneling matrix elements are of the form <sup>8</sup>

$$|T_{kq}|^2 = c_1 |T_k| |T_q| = c_1 \left| \frac{\partial \epsilon(k)}{\partial k_l} \right| \left| \frac{\partial \epsilon(q)}{\partial q_l} \right| , \quad (3)$$

where  $c_1$  is a constant describing the properties of the barrier and  $\epsilon(k)$  is the quasi-particle energy assumed to have the tight binding form

$$\epsilon_k = A[-2(\cos(k_x \alpha_x) + \cos(k_y \alpha_y)) + 4B \cos(k_x \alpha_x) \cos(k_y \alpha_y) - 2C \cos(k_z \alpha_z) - \mu] . \quad (4)$$

The  $A, B, C$  are constants determined from the band structure.  $\alpha_x, \alpha_y, \alpha_z$  are the lattice constants in the  $x, y, z$  direction respectively, and  $\mu$  is the chemical potential. In Eq.(3)  $k_l$  denotes the component of the wavevector along the tunneling direction.

For this purpose we start from the BCS pairing Hamiltonian, with the following pairing potential

$$V(k, k') = g_0 + 2g_x \cos((k_x - k'_x) \alpha_x) + 2g_y \cos((k_y - k'_y) \alpha_y) , \quad (5)$$

In the above formula  $g_x$  and  $g_y$  are the strength of the hole-hole interaction in the  $x$  and  $y$  directions, and  $g_0$  is the on-site interaction strength. Introducing  $V(k, k')$  into the well known gap equation we get

$$\Delta_k = \frac{1}{N} \sum_{k'} V(k, k') F_{k'} \quad (6)$$

where

$$F_k = \frac{\Delta_k}{2E_k} \tanh\left(\frac{1}{2}\beta E_k\right) , \quad E_k = \sqrt{\Delta_k^2 + \epsilon_k^2} \quad (7)$$

and  $\beta = 1/k_B T$ ,  $k_B$  is Boltzmann's constant. Furthermore, because of the form of the potential  $V(k, k')$ ,  $\Delta_k$  is guaranteed to be of the form <sup>9,10,11</sup>

$$\Delta_k = \Delta_0 + 2\Delta_x \cos(k_x \alpha_x) + 2\Delta_y \cos(k_y \alpha_y) . \quad (8)$$

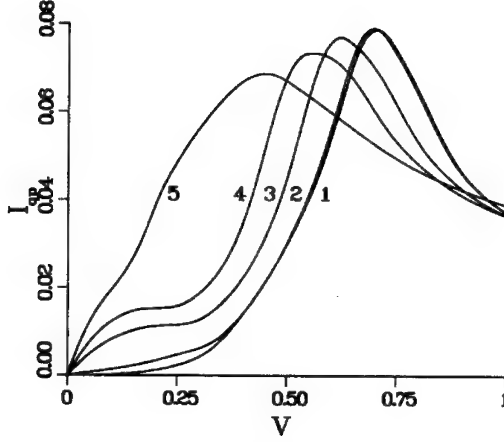


Figure 1: The quasiparticle current at various temperatures. 1:  $T=0.0$ , 2:  $T=0.05$ , 3:  $T=0.10$ , 4:  $T=0.12$ , 5:  $T=0.15$ .

the time does not appear explicitly on the right hand side of the equations. It can be shown, that for low, or slowly varying voltages, the tunneling current can be written in the form <sup>15</sup>

$$I(t) = I_{qp}(V, T) + I_{J1}(V, T)\sin(\phi(t)) + I_{J2}(V, T)\cos(\phi(t)) , \quad (16)$$

where  $\phi$  is the superconducting phase difference between the two electrodes.

### 3. Numerical Results.

We calculate numerically the tunneling currents as a function of the applied voltage from equations (10)-(12) for a junction made of two identical superconductors in a mixed  $s + d$ -pairing state. Guided from earlier works <sup>12,18</sup>, we choose the phenomenological parameters in Eqs.(5) and (9) as follows

$$A = 0.05 \text{ eV} , \quad B = 0.45 , \quad C = 0.1 , \quad \mu = -2.0 , \quad (17)$$

$$g_0 = 0.3 , \quad g_x = g_y = 1.2 . \quad (18)$$

Setting  $A = 1.0$  in Eq.(4) correspond to measuring the energy in units of  $A$  temperatures in units of  $k_B/A = 580 \text{ K}$ . For such a superconductor, our model gives a critical temperature  $T_c = 0.155$ . In physical units, the critical temperature is around 90 K, which is a high  $T_c$  superconductor. Due to the large crystal anisotropy for

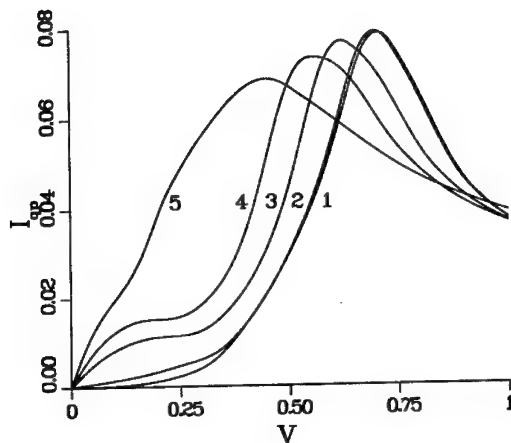


Figure 1: The quasiparticle current at various temperatures. 1:  $T=0.0$ , 2:  $T=0.05$ , 3:  $T=0.10$ , 4:  $T=0.12$ , 5:  $T=0.15$ .

the time does not appear explicitly on the right hand side of the equations. It can be shown, that for low, or slowly varying voltages, the tunneling current can be written in the form<sup>15</sup>

$$I(t) = I_{qp}(V, T) + I_{J1}(V, T)\sin(\phi(t)) + I_{J2}(V, T)\cos(\phi(t)), \quad (16)$$

where  $\phi$  is the superconducting phase difference between the two electrodes.

### 3. Numerical Results.

We calculate numerically the tunneling currents as a function of the applied voltage from equations (10)-(12) for a junction made of two identical superconductors in a mixed  $s + d$ -pairing state. Guided from earlier works<sup>12,18</sup>, we choose the phenomenological parameters in Eqs.(5) and (9) as follows

$$A = 0.05 \text{ eV}, \quad B = 0.45, \quad C = 0.1, \quad \mu = -2.0, \quad (17)$$

$$g_0 = 0.3, \quad g_x = g_y = 1.2. \quad (18)$$

Setting  $A = 1.0$  in Eq.(4) correspond to measuring the energy in units of  $A$  temperatures in units of  $k_B/A = 580 \text{ K}$ . For such a superconductor, our model gives a critical temperature  $T_c = 0.155$ . In physical units, the critical temperature is around 90 K, which is a high  $T_c$  superconductor. Due to the large crystal anisotropy for



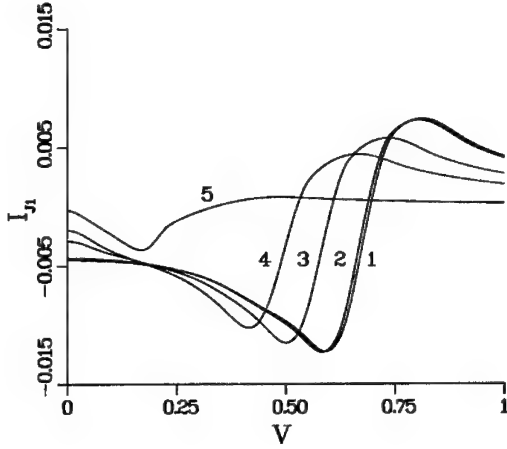


Figure 2: The supercurrent  $I_{J1}$  at various temperatures. 1:  $T=0.0$ , 2:  $T=0.05$ , 3:  $T=0.10$ , 4:  $T=0.12$ , 5:  $T=0.15$ .

these materials, the tunneling current changes considerably when the orientation of the material with respect to the barrier changes. In this work, we consider tunneling along the  $c$  crystallographic direction for both the electrodes. Here by tunneling direction is meant the crystal direction normal to the barrier.

In that case, the tunneling matrix element  $T_{kp} \propto \sin(k_z \alpha_z) \sin(p_z \alpha_z)$ . The results of this calculation are shown in Figs.(1)-(3). The different curves labeled 1-5 correspond to different values of temperature. In normalised units, these are 1:  $T = 0.0$ , 2:  $T = 0.05$ , 3:  $T = 0.10$ , 4:  $T = 0.12$ , 5:  $T = 0.15$ . Voltages are normalised to  $50mV$ . In these figures we observe some important features in comparison with the standard BCS theory<sup>1,2</sup>. A calculation based on the standard BCS theory for the coefficient of the  $\sin \phi$  term  $I_{J1}$  gives a logarithmic singularity (the Riedel peak) at the gap voltage  $V_g$ . This is an artifact due to the fact that the BCS quasiparticle and pair densities of states go to infinity when the voltage approaches the gap voltage. In our case the effective densities of states calculated numerically from Eq.(13) are finite and have non-zero values only in a certain energy interval determined by  $A, B, C$  and  $\mu$ . As it is apparent from Fig.(1) the logarithmic singularity has been eliminated. Furthermore, the curves have been rounded off significantly as a result of the anisotropic gap.

Let us now turn our attention to the other two currents, the quasiparticle current  $I_{qp}$  and the quasiparticle-pair interference current  $I_{J2}$ . These are discontinuous at the gap voltage according to the standard BCS theory. When anisotropy is taken into

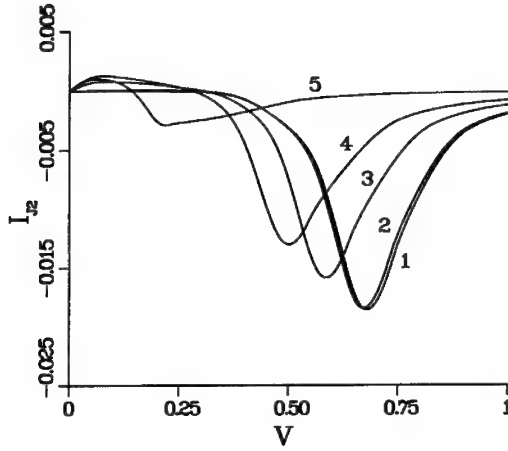


Figure 3: The supercurrent  $I_{J2}$  at various temperatures 1:  $T=0.0$ , 2:  $T=0.05$ , 3:  $T=0.10$ , 4:  $T=0.12$ , 5:  $T=0.15$ .

account, both  $I_{qp}$  and  $I_{J2}$  are changing in a rather smooth way, and they exist for very low voltages even at zero temperature (Figs.(2) and (3)). Because the gap changes on the Fermi surface from a minimum value  $\Delta_{min}$  to a maximum  $\Delta_{max}$  it does not make sense to define a gap voltage.

The Josephson current  $I_{J1}$  was calculated as a function of temperature at  $V = 0$  for three different junctions. The results are presented in Fig.(4), where the  $I_{J1}(T)$  is normalised to  $I_{J1}(T = 0, V = 0)$  and  $T$  is normalised to  $T_c$ . The curve labeled 1 corresponds to a junction made of two  $s + d$ -wave superconductors, the curve labeled 2 corresponds to a junction made of two isotropic  $s$ -wave superconductors, and the curve labeled 3 corresponds to a junction made of an  $s + d$ -wave and an isotropic  $s$ -wave superconductors. The parameters for the  $s$ -wave superconductor are

$$A = 1.0, \quad B = 0.0, \quad C = 1.0, \quad \mu = -2.0, \quad (19)$$

$$g_0 = 1.345, \quad g_x = g_y = 0.0. \quad (20)$$

The critical temperature for this material is (in physical units)  $T_c = 7.2 \text{ K}$ , it thus corresponds to a low- $T_c$  material.

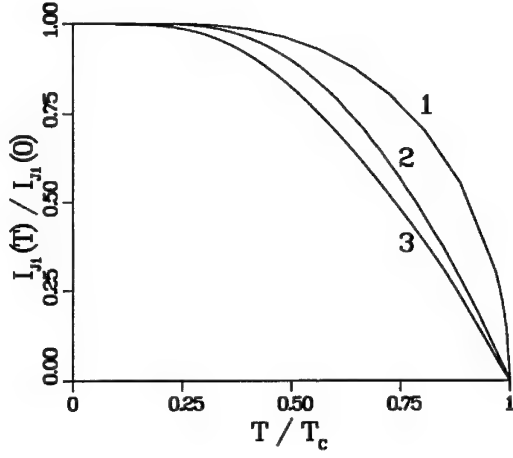


Figure 4: The supercurrent  $I_{J1}(V = 0)$  for three different junctions. The description of the junctions is given in the text.

#### 4. Discussion and Conclusions.

The gap anisotropy plays a very important role in the tunneling currents through a superconducting junction. Experiments on high- $T_c$  superconductors show a large gap anisotropy in these materials, with ratios of the maximum gap value to the minimum  $\Delta_{max}/\Delta_{min}$  which even go up to 6<sup>19</sup>. These materials are also characterised by large measured values of the ratio  $r = 2\Delta/k_B T_c$  which is usually attributed to strong coupling effects and failure of the BCS approach which gives  $r = 3.53$ . This belief is based on the isotropic model, and is likely to be wrong in the anisotropic case<sup>20</sup>. When the gap is determined by tunneling conductance measurements, what it is actually measured is the ratio  $r' = \Delta_{max}/k_B T_c$ . Using a simple model Abrikosov<sup>20</sup> showed that in the case of anisotropy  $\Delta_{max} > \Delta_{BCS}$  and  $\Delta_{min} < \Delta_{BCS}$ . These results are general, since his model does not depend on the details of the Fermi surface or the form of the anisotropy. Thus, obviously  $r' > r$ .

Although there is a significant difference in the tunneling currents, for a real junction which is operated at rather low voltages, up to about 1 mV the change is not so dramatic. As we can see from figures 1-3, at low voltages, the quasiparticle current increases linearly with voltage and  $I_{J1}$  is practically constant. The second supercurrent  $I_{J2}$  is very small and can be neglected in a first approximation. Thus, the resistively shunted junction model is expected to work well for junctions made of anisotropic superconductors.

Because of the short coherence length one expects to see manifestations of the anisotropy in many situations. Tunneling has offered a lot of information on the properties of superconductors. Thus, it might be possible to extract some information from tunneling about the fundamental question of the gap symmetry. Experiments up to now have given controversial results, not being able to provide the pairing state of the high- $T_c$  superconductors. For the high- $T_c$  superconductors a rather low critical voltage  $V_c = I_{J1}R_N$  has been repeatedly measured, compared to what is expected from the conventional Ambegaokar-Baratoff theory.  $R_N$  is the normal state resistance, which is assumed to be temperature independent. Since the manufacturing of SIS junctions is not a very easy task, the reduction of the critical voltage could be merely a result of a defective barrier. On the other hand, it has been speculated that this reduction could be due to a  $d$  pairing superconducting state. Model calculations showed<sup>21,22</sup> that a  $d$ -wave state gives considerably (about a factor of two) lower critical voltage than an  $s$ -wave state.

In conclusion, we have calculated the tunneling currents through an SIS Josephson junction, using the BCS spectral functions with an anisotropic gap function. The results suggest that the RSJ model works well in the case of junctions made of anisotropic superconductors. Furthermore, the Riedel peak in the quasiparticle current is rounded off, and the supercurrents change continuously as a function of the applied voltage. Finally, the reduction of the critical voltage for high- $T_c$  superconductors might result from a dominant  $d$ -wave component in the gap function.

### Acknowledgements

The authors gratefully acknowledge financial support from the EU Human Capital and Mobility programme (NL) and from the United States Army European Research Office (MPS) (contract No. N68171-94-M-5885). NL acknowledges support from the Greek Secretariat for Research and Technology (IIENE $\Delta$  programmes). This work is supported by the Danish Research Council through contract No. 5210551-1 (supercomputing projects). The authors would like to thank M. H. Pedersen and T. Schneider for helpful discussions.

### References

1. R. E. Harris, *Phys. Rev.* **B10**, 84 (1974).
2. R. E. Harris, *Phys. Rev.* **B11**, 3329 (1975).
3. U. K. Poulsen, *Phys. Lett.* **41A**, 195 (1972).
4. W. Schlup, *Solid State Comm.* **12**, 631 (1973).
5. P. Seidel and E. Heinz, *Acta Physica Polonica*, February 15, 1, (1993).
6. P. Seidel, E. Heinz, F. Schmidl, K. Zach, H.-J. Köhler, H. Schneiderwind, J. Borck, Dörner, S. Linzen, T. Köhler, W. Michalke, M. Manzel, E. Steinbeiss and H. Bruchlos, 1992 Superconductivity Conference, Chicago, Illinois, USA, August 1992.
7. M. Siegel, E. Heinz, P. Seidel and V. Hilarius, *Z. Phys.* **B83**, 323 (1991).

8. M. Frick and T. Schneider, *Z. Phys.* **B78**, 159 (1990) .
9. T. Pavlopoulos, P. L. Christiansen, M. P. Sørensen, N. Lazarides and P. N. Spathis, Proc. of the NATO ASI on "Chaotic Dynamics: Theory and Practice". ed. T. Bountis, July 11-20, 1991, Patras, Greece.
10. T. Pavlopoulos, N. Lazarides, P. L. Christiansen, M. P. Sørensen and P. N. Spathis, Proc. of the NATO-MIDIT ASI on "Future Directions of Nonlinear Dynamics in Physical and Biological Systems". Eds. P.L. Christiansen, J.C. Eilbeck and R.D. Parmentier. July 23 - August 1, 1992, Lyngby, Denmark.
11. T. Pavlopoulos, P. L. Christiansen, M.P. Sørensen, *Z. Phys.* **B91**, 43 (1993).
12. P. N. Spathis, M. P. Sørensen and N. Lazarides, *Phys. Rev.* **B45**, 7360 (1992).
13. N. R. Werthamer, *Phys. Rev.* **147**, 255 (1966).
14. V. Ambegaokar and A. Baratoff, *Phys. Rev. Lett.* **10**, 486 (1963).
15. A. Barone and G. Paternó, *Physics and Applications of the Josephson Effect*, John Wiley & Sons, New York, 1982.
16. G. D. Mahan, *Many-Particle Physics*, Plenum Press, New York, 1990.
17. V.Nam, *Phys. Rev.* **156**, 486 (1963).
18. T. Schneider and M. P. Sørensen, *Z. Phys.* **B80**, 331 (1990) .
19. K. Langfeld and E. Frey, *Phys. Rev.* **B48**, 4176 (1993).
20. A. A. Abrikosov, *Physica* **C214**, 107 (1993).
21. M. P. Sørensen and N. Lazarides, Proc. of the 7<sup>th</sup> Inter. Symposium on Superconductivity (Invited paper), Eds. Š. Beňačka, P. Seidel and V. Štbrík. Smolenice Castle/Bratislava, June 6-10, 1994, Slovak Republic.
22. N. Lazarides and M. P. Sørensen, Proc. of the 3<sup>rd</sup> IMACS Int. Conf. on "Nonlinear Dynamical Phenomena in Physical, Chemical and Biological Systems", Eds. P. L. Christiansen and E. Mosekilde. August 1-4, 1994, Lyngby, Denmark.

# PLANAR TUNNEL JUNCTIONS ON $YBa_2Cu_4O_8$

P. ROMANO, A.M. CUCOLO, R. DI LEO, A. NIGRO

*Dipartimento di Fisica, Università di Salerno  
I-84081 Baronissi (Sa), Italy*

and

P.G. RADAELLI

*Materials Science Division, Argonne National Laboratory  
Argonne, IL 60439, USA*

## ABSTRACT

We have fabricated planar tunnel junctions on  $YBa_2Cu_4O_8$  single crystals and compared the tunneling spectra to those previously obtained on  $YBa_2Cu_3O_{7-\delta}$ . In the superconducting state, the 1:2:4 phase shows a smeared structure around 18mV, similar to that observed in the 1:2:3 phase, while the main difference in the tunneling spectra is the absence in the 1:2:4 phase of the 5mV gap-like feature. These results can be interpreted in terms of a decreased interlayer coupling in the 1:2:4 phase.

## 1. Experimental Results

High-pressure  $YBa_2Cu_4O_8$  (Y124) crystal growth was performed from mixtures of polycrystalline  $YBa_2Cu_3O_{7-\delta}$  (Y123),  $BaCuO_2$  and CuO, as described in Ref.1, using  $ZrO_2$  crucibles at 1100°C with 600 bar of  $O_2$  at 3 Kbar total pressure.

Susceptibility measurements were performed on all crystals using a Lake Shore Cryotronics AC susceptometer, in a 1 Oe ac field at 100 Hz. The onset critical temperatures  $T_c$  were found to be of about 80 K. As an example, the susceptibility vs temperature curve for a Y124 crystal is reported in Fig.1. From the numerically computed first derivative, shown in the inset, it can be seen that the width of the transition is less than 2 K. This result is representative of all the samples used in this work. Moreover, the crystals are orthorhombic and untwinned as shown by single-crystal X-ray diffraction. This fact, combined with a stable oxygen content, makes Y124 an ideal material for determining the superconducting and normal state properties.

One of the major structural features of Y124 which is different from that of Y123 is an additional Cu-O layer which leads to double chains of CuO stacked up along  $c$  between the Ba-O planes. These chains are shifted relative to each other by  $b/2$  along the  $b$  axis. It is thus possible to characterize the  $Y_2Ba_4Cu_{6+n}O_{14+n}$  family (with  $n=0,1,2,4$ ), consisting of Ba-Y-Ba perovskite blocks separated by single and/or double or triple CuO chains. We will focus on the first member with  $n=0$ , the well-known 1:2:3 phase, Y123, with  $T_c = 90K$ , and the  $n=2$  member, the 1:2:4

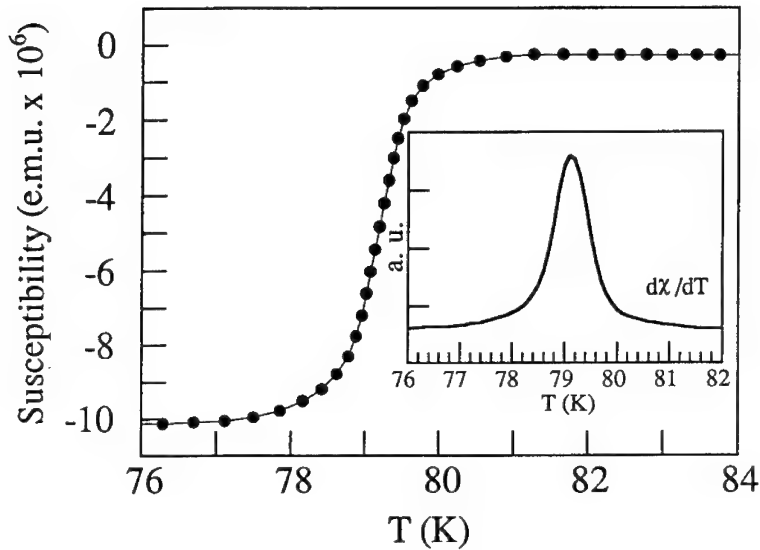


Fig. 1. Susceptibility vs temperature curve for a Y124 crystal. In the inset the numerically computed first derivative is shown.

phase, Y124, with  $T_c = 80K$ .<sup>2</sup> The existence of this series allows us to investigate systematically the significance of the chains on the normal and superconducting features. In contrast, the Bi-Sr-Ca-Cu-O and Tl-Sr-Ca-Cu-O families provide insight in the importance of the number of  $CuO_2$  layers.

In this work, Y123 and Y124 single crystals have been used as base electrodes in planar tunnel junctions. Chemical etching of the crystals in a 1% Br solution in methanol ensured the cleaning and the passivation of the crystals' surface.<sup>3</sup> Furthermore, the appearance of many etch pits exposed to the tunneling process also the  $a$  and  $b$  directions on nominally  $c$ -axis oriented crystals. After the etching, the crystals were exposed to the atmosphere for about 30 min, forming a natural barrier, and finally placed in a vacuum system where a Pb thin film counterelectrode was evaporated through a metallic mask. Junction dimensions were about  $0.1 \times 1.0 mm^2$  and resistances ranged between 500 and 5000 Ohm. Four terminal measurements of the differential resistance  $dV/dI$  were performed using the standard low-frequency lock-in technique.

We have performed a number of quality controls on our junctions, both at low

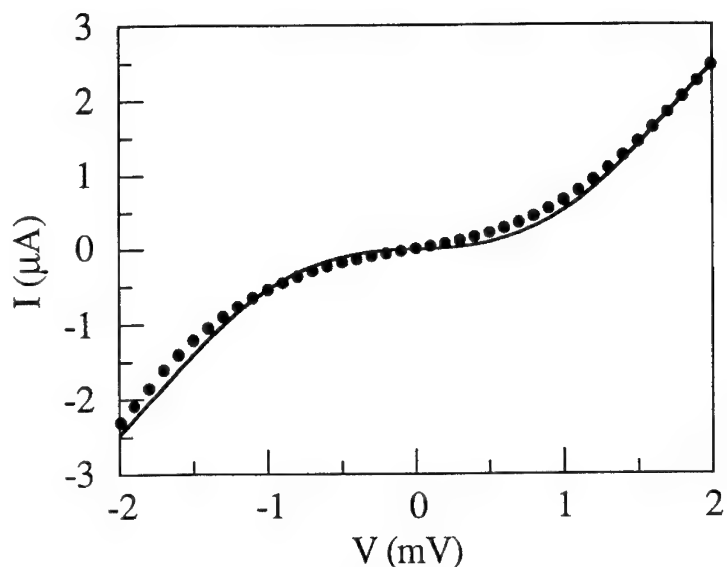


Fig. 2. I-V characteristic at low bias for a Pb/Y124 junction at  $T=4.2$  K

and high biases.<sup>4</sup> We have measured the I-V characteristic at low biases and at low temperature, and compared it to the theoretical expression for the current flowing through an S-N junction at the same temperature. The good agreement obtained on a typical Pb/Y124 junction is shown in Fig.2. Checking that, at low bias, the Pb gap and phonon structures were at the correct energies and had the right amplitudes implied that the conductance was mainly due to a single-step tunneling process through the barrier. Under these conditions, we can attribute the structures observed in the  $dV/dI$  to structures in the density of states of the Y-Ba-Cu-O material.

In Fig.3 we show the dynamic resistance vs voltage for a Pb/Y124 junction at different temperatures. It is possible to observe a finite zero-bias resistance and a gap-like features at about  $\pm 18$  mV, that appear in the resistance curve below  $T_c$ . This behavior is similar to that observed for Y123, the principal difference consisting in the absence, in the Y124, of the low bias  $\pm 5$  mV gap-like feature present in the tunneling spectra of Y123 together with the 18 mV structure.<sup>3,5</sup>

Further information can be obtained by studying the behavior of the zero-bias resistance as a function of temperature. Tunneling spectroscopy is in fact a surface



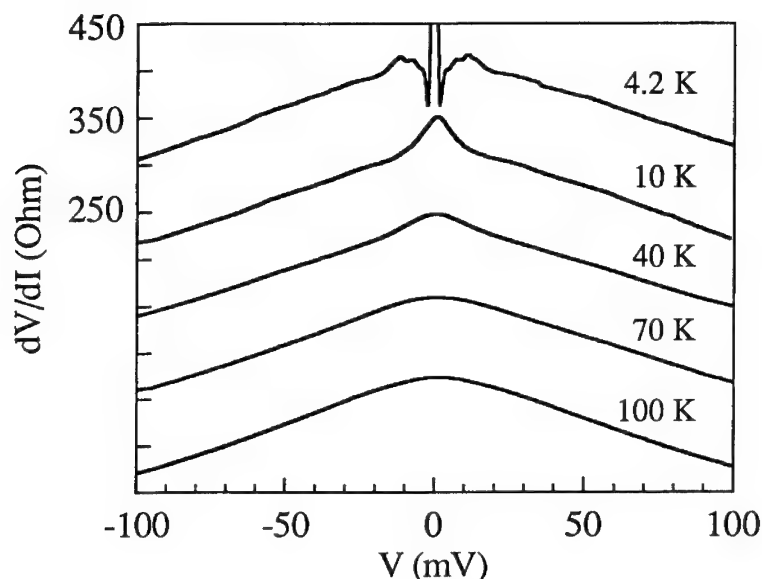


Fig. 3. Dynamic resistance vs voltage for a Pb/Y124 junction at different temperatures. The vertical axis has been shifted for clarity.

technique that, on a scale of the coherence length, measures the  $T_c$  of the material layer close to the barrier. For a typical Pb/Y124 junction, the temperature dependence of the normalized zero-bias resistance (Fig.4) shows a discontinuity at  $T_c$ , similar to the opening of an energy gap in tunnel junctions made with BCS superconductors.

## 2. Discussion

The double structures observed in the Y123 system by tunneling spectroscopy and other experimental techniques,<sup>6</sup> have been attributed to a double gap-like feature, coming from the layered structure of this system. The 18 mV feature can be related to the strongly superconducting  $\text{CuO}_2$  layers. These layers are alternated by CuO chains, thus the low bias feature at 5 mV has been related to a superconducting energy gap in the planes of the chain structures.<sup>7,8</sup> On the other hand, if the chain superconductivity were intrinsic, an enhancement of the low-energy

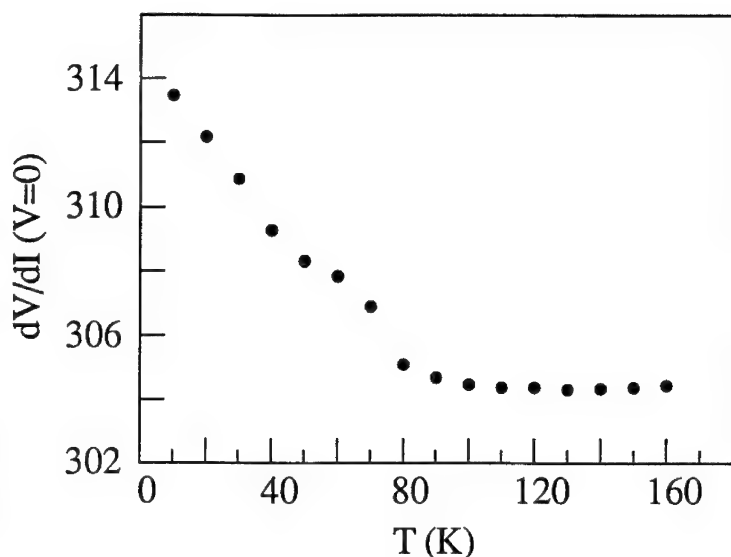


Fig. 4. Normalized zero-bias resistance vs temperature for a Pb/Y124 junction.

structure should be expected in the Y124 material. Disappearance of this feature is thus consistent with a normal metal (or weakly superconductive) behavior of the chains, already proved by means of different experimental techniques.<sup>9,10</sup> In the Y123 with a single CuO layer, chain superconductivity is induced from the  $\text{CuO}_2$  adjacent planes by a kind of internal proximity effect. Both the absence of the 5 mV structure and the smearing of the main feature at 18 mV can be interpreted in terms of an increased normal contribution of the double CuO chain layers in the Y124 system.

The present study suggests that the in-plane superconducting properties remain unaltered in the Y124 and Y123, while a lower strength of the interlayer coupling is inferred in the Y124, due to the different role of the CuO chains in this material.<sup>11</sup>

#### Acknowledgement

P.R. wishes to thank the Human Capital and Mobility Program (EU) for Euro-conference financial support.

## References

1. B. Dabrowski, K. Zhang, J.J. Pluth, J.L. Wagner, D.G. Hinks, "Single-crystal growth and characterization of  $YBa_2Cu_4O_8$  with  $T_c \sim 80$  K", *Physica C* **202**, 271, (1992).
2. B. Bucher, J. Karpinski, E. Kaldis, P. Wachter, "Optical studies of untwinned  $Y_2Ba_4Cu_{6+n}O_{14+n}$  ( $n=1,2$ ): Interpretation of superconducting gaps", *Phys. Rev. B* **45**, 3026, (1992).
3. M. Gurvitch, J.M. Valles Jr., A.M. Cucolo, R.C. Dynes, J.P. Garno, L.F. Schneemeyer, J.V. Waszczak, "Reproducible tunneling data on chemically etched single crystals of  $YBa_2Cu_3O_{7-\delta}$ ", *Phys. Rev. Lett.* **63**, 1008, (1989).
4. A.M. Cucolo, "Quality controls on high- $T_c$  based tunnel junctions", *Int. J. Mod. Phys.* **7**, 2549, (1993).
5. A.M. Cucolo, R. Di Leo, P. Romano, L.F. Schneemeyer, J.V. Waszczak, "Influence of the oxygen content on the tunneling characteristics of  $YBa_2Cu_3O_{7-\delta}$ ", *Phys. Rev. B* **44**, 2857, (1991).
6. K.F. McCarty, J.Z. Liu, R.N. Shelton, H.B. Radousky, "Electronic Raman scattering of  $YBa_2Cu_3O_7$  using  $c$ -axis polarization: Evidence for two characteristic energies", *Phys. Rev. B* **42**, 9973, (1990).
7. A.M. Cucolo, C. Noce, A. Romano, "Model for tunneling experiments on the 90- and 60-K  $YBa_2Cu_3O_{7-\delta}$  phases", *Phys. Rev. B* **46**, 5864, (1992).
8. S. Takahashi and M. Tachiki, "Optical conductivity in superconducting layered cuprate oxides", *Physica C* **170**, 505, (1990).
9. Z. Sclesinger, R.T. Collins, F. Holtzberg, C. Feild, S.H. Blanton, U. Welp, G.W. Crabtree, Y. Fang, J.Z. Liu, "Superconducting energy gap and normal-state conductivity of a single-domain  $YBa_2Cu_3O_7$  crystal", *Phys. Rev. Lett.* **65**, 801, (1990).
10. T.A. Friedmann, M. W. Rabin, J. Giapintzakis, J.P. Rice, D.M. Ginsberg, "Direct measurements of the anisotropy of the resistivity in the  $a$ - $b$  plane of twin-free, single-crystal, superconducting  $YBa_2Cu_3O_{7-\delta}$ ", *Phys. Rev. B* **42**, 6217, (1990).
11. A.M. Cucolo, R. Di Leo, P. Romano, B. Dabrowski, D.G. Hinks, P.G. Radaelli, "Tunneling spectroscopy into  $YBa_2Cu_4O_8$ : Intralayer and interlayer analysis", *Phys. Rev. B* **50**, 10397, (1994).

# FLUXON RESONANCES IN WINDOW-TYPE LONG JOSEPHSON JUNCTIONS: EXPERIMENT AND NUMERICAL SIMULATIONS

N. THYSSEN, A. V. USTINOV, H. KOHLSTEDT

*Institute of Thin Films and Ion Technology, Research Center Jülich (KFA)  
D-52425 Jülich, Germany*

and

J. G. CAPUTO

*Institut National de Sciences Appliquées, BP8, F-76131 Mont-Saint-Aignan, France*

and

S. PAGANO

*Istituto di Cibernetica del CNR, I-80072 Arco Felice, Italy*

and

N. FLYTZANIS

*Department of Physics, University of Crete, GR-71409 Iraklion, Greece*

## ABSTRACT

We investigate the influence of the electromagnetic surrounding on fluxon dynamic regimes in long Josephson junctions. Experimental data were compared with numerical simulations using the modified two-dimensional perturbed sine-Gordon equation. Measurements have been done with long Nb/AlO<sub>x</sub>/Nb Josephson tunnel junctions made in a "window" in the thick insulating layer between two overlapping superconducting electrodes. We compare the data obtained for junctions of the same dimensions but with different ratio of the junction width  $W$  to the width of the idle ("window") part  $W'$  of the electrodes surrounding them. Zero-field steps were found to be stable only in structures with  $W'/W < 3$ . In addition to conventional zero-field steps at low voltages, we also find very high frequency cavity-like zero field resonances. With increasing the ratio  $W'/W$ , the effective fluxon propagation velocity is found to increase and fine structure resonances appear on the  $I-V$  characteristics. Qualitative agreement between experiment and numerical simulations is found.

## 1. Introduction

The ideal quasi-one-dimensional Josephson junction of length  $L \gg \lambda_J$  and width  $W < \lambda_J$ , where  $\lambda_J$  is the Josephson penetration depth, is a model system for the demonstration of the complex behavior of nonlinear systems. The nonlinearity of the Josephson term, due to the tunneling of supercurrent, causes localisation of the magnetic flux that penetrates the oxide and the superconducting (within the London penetration depth) layers. For a long junction the fluxons are described successfully by

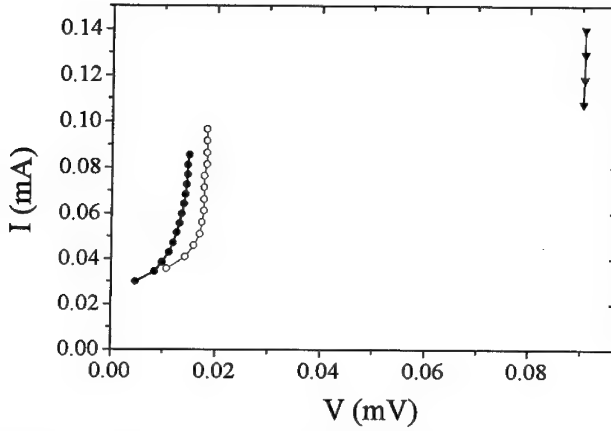


Fig. 2. Numerically calculated  $I - V$  characteristic for three different values of  $W'/W$ : 0.2 (solid circles), 0.8 (open circles) and 1.8 (solid triangles).

distributed RSJ model which consists of a resistor  $R_i$  (the normal electronic current) in parallel with a capacitor  $C_i$  (capacity between superconducting layers) and the non-linear Josephson element connecting the two superconductors. This model is equivalent to Maxwell's equations together with Josephson's constitutive equations. The normalized equation for the current at node  $i$  reads in a dimensionless form as

$$\tilde{C}_i \ddot{\phi}_i + \sum_j \frac{\phi_i - \phi_j}{\tilde{L}_{ij}} + \frac{1}{\tilde{\lambda}_J^2 \tilde{L}_J} \sin(\phi_i) + \frac{\dot{\phi}_i}{\tilde{R}} = \frac{I_{dc} L_I}{\Phi_0} \quad (1)$$

with the last two terms being absent in the idle region as there is no tunneling of supercurrent or normal current there. Since the width of the dielectric (idle region) is much larger than the oxide layer in the window the characteristic times are much shorter in the idle region; the capacitance  $C_i$  and inductance  $L_i$  have therefore been normalized by  $C_I$  and  $L_I$  their values at the nodes of the idle region. We have introduced here the mesh normalized Josephson length  $\tilde{\lambda}_J = \sqrt{\Phi_0 / (L_J I_0)}$  and normalized  $R_i$  by  $\sqrt{L_I / C_I}$ , where  $\Phi_0$  is the magnetic flux quantum and the current is normalised in units of  $\Phi_0 / L_I$ . The numerical values used for the computations were chosen to be close to that in experiments described in the next section. We used  $\tilde{C}_J = 100$ ,  $\tilde{L}_J = 0.5$ , and  $\tilde{R} = 50$  for the junction; all other normalized parameters were equal to unity. We have applied the external current homogeneously across the longer sides of the rectangular domain, like in the overlap geometry. In the case of a large idle region the detailed bias current distribution at the outside boundary is not very important. The initial condition is obtained by solving numerically the static problem<sup>3</sup> with zero external current. The fluxon is then accelerated by a slow increase of the external current and damping. For each point of the  $I - V$  characteristic we have

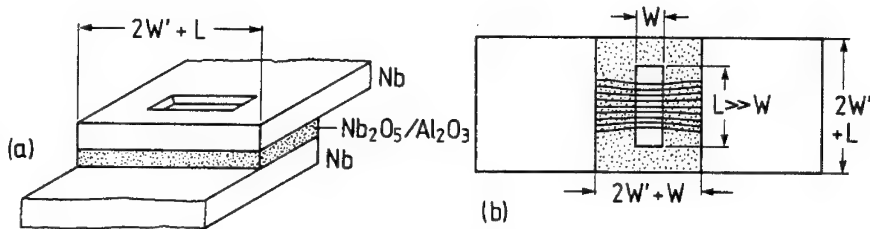


Fig. 1. (a) Schematic view of a window-type Josephson tunnel junction. The tunnel barrier area is surrounded by the idle part which consists of superconducting electrodes (Nb) separated by a thick insulating layer ( $\text{Nb}_2\text{O}_5$ ). Sketch (b) shows the top view of the window junction with a fluxon inside.

the sine-Gordon (or its perturbed form) system even in the presence of perturbations or various boundary conditions due to the bias current or an external magnetic field. So far the influence of the external electromagnetic environment due to the idle (no tunneling) parts of the superconducting electrodes has been neglected. However, one may expect that the properties of both linear and nonlinear electromagnetic waves, which propagate into the junction, can be considerably influenced by the idle part around it. The reason is that the free energy of the device has a large contribution from the magnetic energy due to the surface currents especially in the large idle region where no tunneling occurs, preferring to delocalise the fluxons. The inhomogeneity of the energy distribution leads to a curvature of the constant phase lines.

In practical Josephson devices, due to the preparation procedure in the Nb/Al technology, the Josephson junction perimeter is often surrounded by an overhanging superconducting electrode which forms a sort of a 'window', also called 'idle part' (see Fig. 1) above. The idle part results from oversized dimensions of the wiring Nb layer which covers the ground Nb electrode. Lee<sup>1</sup> suggested a simple model to calculate the dispersion relation for linear waves modified by the presence of the idle window around the junction. Later, Lee and Barfknecht<sup>2</sup> showed a good agreement of this model with the experimental data on *linear* Fiske resonances in Nb/Al- $\text{AlO}_x$ /Nb junctions. So far, there has been no study of the effects of the idle window around the junction on the *nonlinear* resonances which occur due to the resonant motion of solitons (fluxons, or Josephson vortices) in long quasi-one-dimensional junctions.

## 2. Model and numerical simulations

The electromagnetic properties of the device can be described with the phase difference of the superconducting order parameter across the two layers  $\phi(x, y)$ . The model used to describe the window junctions is a two-dimensional sine-Gordon equation for the junction region, coupled to a two-dimensional wave equation for the idle part<sup>3</sup> due to the absence of tunneling there. In the numerical calculations we discretise the junction area. Thus we consider each superconductor to be represented by a two dimensional array of inductances. For each element of area  $a^2$  we use the

studied about eighty fluxon oscillations leading to long computations (about 12 hours on a Sun Sparc 10) for a grid of about seventy by seventy. We have also varied the space discretisation to make sure the results were stable. For speed we have used the fixed step Runge-Kutta method of the 4-th order, but in many cases the results were checked by using a variable step procedure based on the Stoer-Burlisch algorithm<sup>4</sup>.

Figure 2 shows the numerically calculated  $I - V$  characteristics with the well-known resonances, the zero-field steps (ZFSs), for the window junction with different width of the surrounding idle region  $W'$  and the same length  $L = 6\lambda_J$ . For smaller idle regions ( $W' = 0.2\lambda_J$  and  $W' = 0.8\lambda_J$ ) the first ZFS is seen in Fig. 2. One may notice also the fine scale structure for  $W' = 0.8\lambda_J$ . For  $W' = 0.2\lambda_J$  the instantaneous charge evolution shows a well formed fluxon as can be seen in Fig. 3.

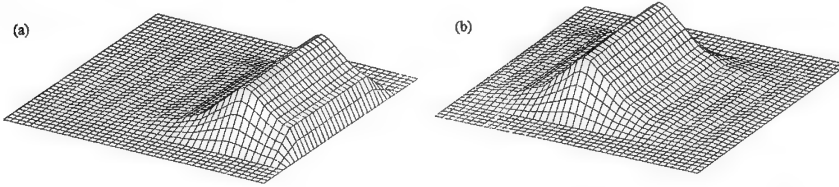


Fig. 3. Instantaneous charge evolution for  $L = 6\lambda_J$  and  $W'/\lambda_J = 0.2$ , applied current  $I = 0.07 I_0$ . (a)  $t = 96.0 \times 10^3$ , (b)  $t = 96.5 \times 10^3$ .

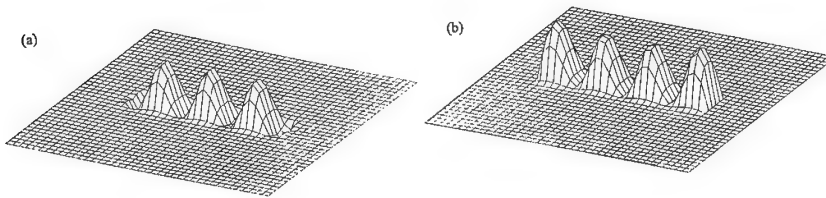


Fig. 4. The same as Fig.3 except  $W'/\lambda_J = 1.8$ . (a)  $t = 98.3 \times 10^3$ , (b)  $t = 99.0 \times 10^3$ .

Fig. 4 shows the instantaneous charge for  $W' = 1.8$ . In contrast to Fig. 3 the voltage oscillations have invaded the whole junction leading to a cavity-like oscillation of the phase. This gives a very sharp resonance in the  $I - V$  curve, so that the obtained dc voltage is practically independent of the bias current. We have repeated these experiments with a junction of length  $L = 10.5\lambda_J$  and found no such resonances, furthermore we have not been able to produce a stable ZFS for  $W' > 3\lambda_J$ .

### 3. Experimental results

In experiments we used Nb/Al-AlO<sub>x</sub>/Nb Josephson junctions of overlap geometry. The junction geometry is schematically shown in Fig. 1. On each wafer we prepared chips of several junction dimensions, typically,  $L \times W = 350 \times 20 \mu\text{m}^2$ . Each

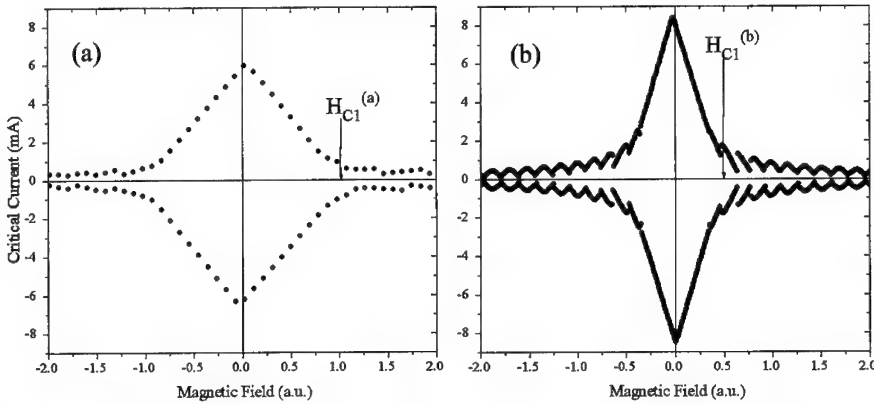


Fig. 5. Experimentally measured  $I_c(H)$  dependence for two junctions of the same dimensions but with different values of  $W'/W = 1$  (a) and  $W'/W = 10$  (b).

chip contained 5 junctions of the same tunnel barrier size ( $L, W$ ) but with different width  $W'$  of the idle area surrounding them. The spread in the Josephson critical current density  $j_c$  was less than 5% across the wafer. A typical value of  $j_c$  was about  $360 \text{ A/cm}^2$ , which corresponds to the Josephson penetration depth of  $\lambda_J \approx 20 \text{ }\mu\text{m}$ . Measurements were performed at 4.2 K in an rf-shielded room.

### 3.1. $I_c(H)$ dependence

Measurements of the critical current  $I_c$  versus external field  $H$  showed a remarkable dependence on  $W'/W$ , as seen in Fig. 5. As the idle region is enlarged three effects are observed: (i)  $I_c(0)$  increases; (ii) the critical field  $H_{c1}$ , corresponding to the threshold for magnetic field penetration in the junction, decreases; (iii) the secondary lobes in the magnetic pattern become more pronounced and show a smooth transition from overlapping to separated shapes. The first effect should occur due to the current redistribution occurring in the idle region. Increasing of  $W'/W$  leads to a more homogeneous distribution of the bias current along the junction. The second phenomenon is due to a magnetic field focusing effect, as can be deduced from the geometrical configuration of window-type junctions (Fig. 1). The third effect we discuss in the next section.

### 3.2. $I - V$ characteristics

Several features affecting the experimental  $I - V$  characteristics were found to depend on the dimensions of the idle part  $W'$  around the junctions. In zero magnetic field, the  $I - V$  characteristics of all junctions with the smallest width of the idle part  $W' = 2.5 \text{ }\mu\text{m}$  showed a series of ZFSs. An example of the  $I - V$  characteristics



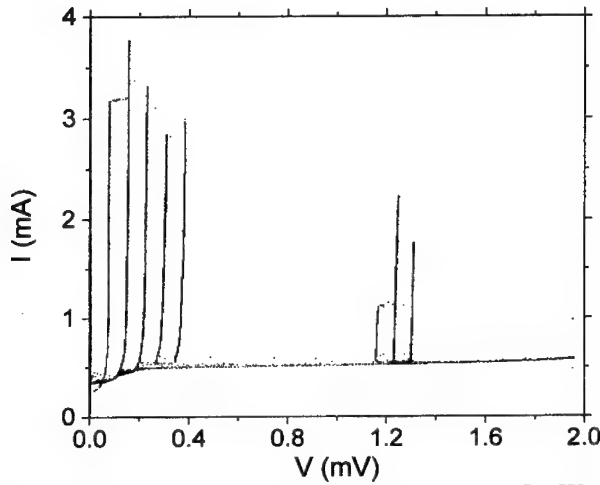


Fig. 6. Experimental  $I-V$  characteristic for the junction with dimensions  $L \times W = 200 \times 10 \mu\text{m}^2$  and  $W' = 2.5 \mu\text{m}^2$ .

is given in Fig. 6. In addition to conventional zero-field steps at low voltages, we also observed sharp cavity-like resonances at high voltages. With increasing  $W'$ , the number of observable ZFSs was decreasing. In our measurements we never found any ZFS for  $W'/W < 3$ .

In all sample series we found a systematic increase of the asymptotic voltages of the zero field steps with increasing  $W'/W$ . The asymptotic voltage is  $V_{\text{ZFS1}} = \Phi_0 \bar{c}/L$ , where  $\bar{c}$  is the Swihart velocity. Thus, the voltage  $V_{\text{ZFS1}}$  allows one to directly measure the velocity  $\bar{c}$  in the junction. We find that with increasing of  $W'$  the effective fluxon propagation velocity is also increasing. Qualitatively, the increase of the fluxon velocity can be explained by the increase of the effective inductance per unit length of a Josephson transmission line along the  $L$  dimension. The idle part impedance per unit length appears to be connected in parallel with the junction impedance. The comparison of the experimental data with estimation according to Lee's formula<sup>1</sup> showed a reasonable agreement.

A distinct feature which has been experimentally observed in window junctions is the fine structure resonances on ZFSs. Fig. 7 shows ZFS1 in the junctions with  $W' = 2.5 \mu\text{m}$  (a) and  $W' = 30 \mu\text{m}$  (b). Fine structure in the  $I-V$  curve can be easily recognized for the case (b) and is even better seen on the corresponding  $dV/dI$  vs  $V$  plot. Additional small steps occur on the ZFS1 for larger idle parts. This fine structure appears only for larger idle parts while almost no fine structure has been observed for the smallest  $W'$  [see Fig. 7(a)]. One possible reason for the fine structure is the interaction between the Josephson plasma waves and the moving fluxon<sup>5</sup>. Another explanation refers to the stable cavity modes in the junction and the idle region<sup>6</sup>. Since the observed resonances are rather irregular, at present it

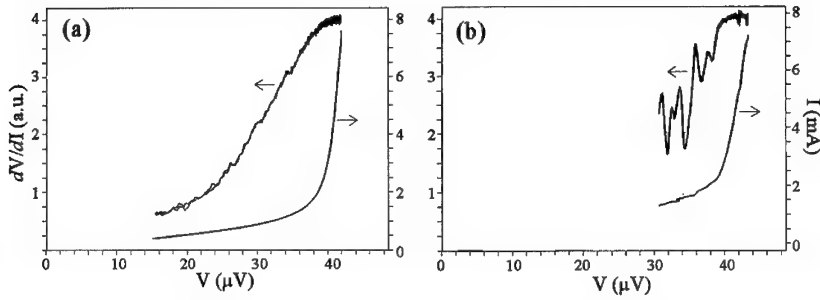


Fig. 7.  $dV/dI - V$  and  $I - V$  curves for ZFSJs in junctions with  $W' = 2.5 \mu\text{m}$  (a) and  $W' = 30 \mu\text{m}$ .

seems to be hardly possible to explain this fine structure by a single model.

#### 4. Discussion

Numerical calculations of static phase distributions, assuming various boundary conditions for the current bias, show most of the effects observed experimentally in  $I_c(H)$  dependence. In the small  $W'$  limit the behavior is similar to the inline geometry leading to large  $H_{c1}$  and small  $I_c(0)$ . In this case the magnetic field lines remain concentrated around the ends of the junction. When  $W'$  is large the geometry is closer to the overlap case, the current is distributed more homogeneously around all sides of the junction, this leads to a smaller  $H_{c1}$  and a larger  $I_c(0)$ . The transition from overlapping to separated  $I_c(H)$  lobes at  $H > H_{c1}$  can be understood by noting that a long junction in a large idle region leads to fluxons of effective width<sup>3</sup>  $\lambda_J^2/W$ . Thus, the junction behaves almost like a short junction with more Fraunhofer-like pattern of  $I_c(H)$ .

The reason for the loss of stability in zero-field fluxon oscillations can be inferred from numerical simulations of the junction dynamics. In zero magnetic field, the fluxon is expected to reflect from the boundaries which work as open ends of the transmission line. With the large idle part surrounding the junction, the flux lines of a fluxon approaching the boundary close around the junction edge, thereby producing a local self-induced magnetic field of the opposite polarity<sup>3</sup>. This effect prevents fluxon reflections from the junction boundaries, and no zero-field resonances occur. The same reason accounts for the fine structure observed in experimental [Fig. 7(b)] and numerically calculated (open circles in Fig. 2) zero field steps. Even for the case of small idle size shown in Fig. 3, fluxon motion is accompanied by visible small-amplitude oscillation which may lead to fine structure resonances.

Experimentally found behavior showing the increase of the fluxon propagation velocity with  $W'$  is in agreement with numerical simulations: Fig. 2 shows the increase of the critical velocity with increasing  $W'$  from 0.2 to 0.8. Similar effect has been observed for the phase velocity of the linear waves<sup>2,7</sup>. Moreover, numerically,

calculated ZFS with the highest voltage (shown by triangles in Fig. 2) very much resembles sharp high-voltage resonances in experimental Fig. 6. These resonances have been observed numerically and experimentally only for intermediate length junctions for which the fluxon "invades" the whole junction when the idle region is enlarged. We note, that, in contrast to cavity-induced resonances in structures with small junction imbedded in the idle window<sup>8</sup>, the spatially-dependent voltage oscillations in our case are present in the long junction itself (see Fig. 4). When the idle region becomes larger, most part of the system is linear and the linear cavity modes are expected to dominate.

Since the fluxon is "dressed" with the magnetic energy of the idle region, its effective width changes from  $\lambda_J$  to  $\lambda_J^2/W$ . Thus, even for  $L \gg \lambda_J$  the fluxon width may become comparable to the junction length  $L$  if  $W$  is small and  $W'$  is large enough. In this case the junction should behave as a short junction and no ZFSs should be observed. In numerical simulations we have considered two junctions of equal width  $W = 0.5\lambda_J$  and lengths  $L = 6\lambda_J$  and  $L = 10.5\lambda_J$ . No ZFSs were found numerically for the smaller  $L$ .

In conclusion, we investigated the influence of the electromagnetic surrounding of long Josephson junctions on its fluxon properties. We show that the electromagnetic surrounding is substantially modified by the presence of the idle window around the junction. We found that the idle part influences both the static and the dynamic properties of long junctions.

### Acknowledgments

We acknowledge useful discussions with G. Costabile, V. P. Koshelets, and R. Monaco and thank V. Palmieri for assistance in measurements.

### References

1. G. S. Lee, *IEEE Trans. Appl. Supercond.* **1** (1991) 121
2. G. S. Lee and A. T. Barfknecht, *IEEE Trans. Appl. Supercond.* **2** (1992) 67
3. J. G. Caputo, N. Flytzanis, and M. Devoret, *Phys. Rev. B* **50** (1994) 6471
4. W. Press, B. Flannery, S. Teukolsky and W. Vetterling, *Numerical Recipes*, Cambridge University Press, 1986
5. N. F. Pedersen and D. Welner, *Phys. Rev. B* **29** (1984) 2551
6. R. Monaco, P. Barbara, and J. Mygind, *Phys. Rev. B* **47** (1993) 12292
7. R. Monaco, G. Costabile, and N. Martucciello, "The influence of the idle region on the dynamic properties of window Josephson tunnel junctions", preprint (1994)
8. A. Larsen, H. Dalsgaard Jensen, and J. Mygind, *Phys. Rev. B* **43** (1991) 10179

# **FISKE RESONANCES IN WINDOW JOSEPHSON TUNNEL JUNCTIONS**

R. MONACO

*Istituto di Cibernetica del C.N.R., I-80072, Arco Felice, Italy  
Dipartimento di Fisica, Università di Salerno, I-84081, Baronissi, Italy*

and

G. COSTABILE, N. MARTUCCIello

*Dipartimento di Fisica, Università di Salerno, I-84081, Baronissi, Italy*

## **ABSTRACT**

We report experimental data about the Fiske step voltages in window Josephson junctions showing that the phase velocity of electromagnetic waves is strongly affected by the insulating region surrounding the junction. We have investigated separately in unidimensional junctions the effect either of an idle region along the long dimension or at the extremities of the junction, finding that the former increases the phase velocity and causes dispersion, the latter only decreases the velocity. We propose two simple models to account for these phenomena.

## **1. Introduction**

In its simplest version a Josephson junction can be fabricated simply depositing two superconducting films onto a substrate through stencil masks; in this case (but not the only one) the area of the junction is defined by the extent to which the films overlap. The analysis of the propagation of electromagnetic waves in such a structure is based on the theory of superconducting striplines, made by Swihart<sup>1</sup>. A prediction of the theory is that the phase velocity of waves in a superconducting transmission line can be quite lower than in the vacuum, as it depends on the ratio  $t/d$  between the electric and the magnetic field penetration, and this effect is expected to be enhanced in the case of the Josephson transmission lines, since the thickness of the dielectric barrier is much smaller than the London penetration depth  $\lambda_L$ . In fact, the linear analysis applies well to lossless Josephson transmission lines, in spite of their non-linear nature, with a strong experimental evidence that the phase velocity of traveling waves in Josephson junctions (*Swihart velocity*) is determined by parameters intrinsic to the junction itself, as far as the junctions are of the kind described above, *i.e.*, at the junction edge the dielectric barrier is terminated abruptly into vacuum. However, this kind of junctions (*naked junctions*) has become a rarity nowadays, as the improvements in the junction fabrication techniques have made window junctions<sup>2</sup> (sketched in Fig.1) widespread. In these junctions, the area is defined by a relatively thick insulating layer, and both the electrodes are larger than the junction area, so that the junction edges are terminated into an *idle region* consisting of a passive SIS

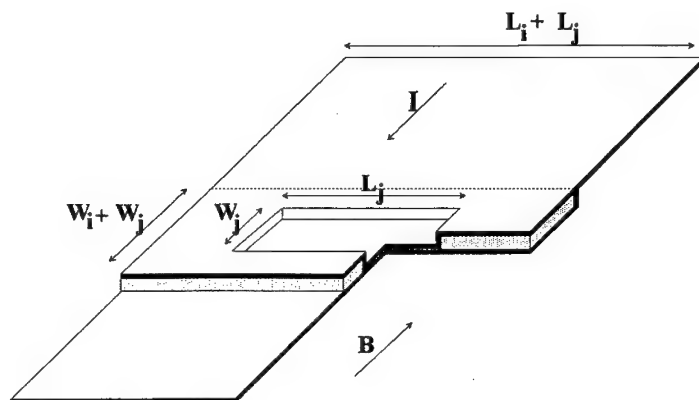


Fig. 1. Cut-away view of a *window* Josephson tunnel junction of width  $W_j$  and length  $L_j$  surrounded by an *idle* region of width  $W_i + W_j$  and length  $L_i + L_j$ . For a *naked* junction  $W_i = 0$  and  $L_i = 0$ . The dimensions are not to scale.

structure surrounding the junction. In this paper we show, from the measurement of the Fiske step voltages in *naked* and *window* junctions, that the phase velocity of traveling waves is modified by the presence of an idle region, that acts either as a parasitic, highly dispersive, transmission line running along the junction edges, or as a capacitive energy tank at the junction extremities.

## 2. Experiment

### 2.1. Sample fabrication

Most of the measurements that we report were obtained from junctions prepared in a planar trilayer Nb/Al/Nb technology. The trilayers were fabricated through a standard procedure, but for the addition of a thin (2nm) Al layer on top of the AlOx that had been thermally grown. The reason for this is to get a current density much lower than what is normally expected from a Nb/Al trilayer, as the junction area cannot be made too small; in fact, at least one of the dimensions shall be large, since it is preferable to keep as low as possible the frequency of the Fiske resonances in order to separate the effect of the idle region from the effects arising at higher frequencies from dispersion and losses in the junction. In fact, the Al layer is oxidized by the oxygen adsorbed in the Al oxide, making the tunnel barrier thicker; moreover, it prevents the unbound oxygen from diffusing into the top Nb electrode, contributing to an improvement of the junction quality. Then the films were patterned by standard photo lithographic procedures and the junction area was defined by selective anodization of the Nb top electrode<sup>3</sup> followed by the deposition of a wiring

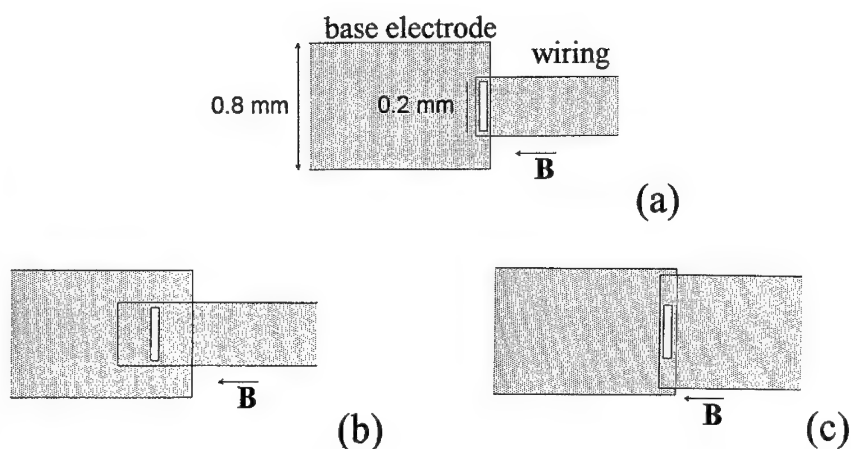


Fig. 2. The three different configurations investigated in this work: *a)* *naked* junction; *b)* *sided* junction; *c)* *ended* junction. The alignment tolerance was  $3\mu\text{m}$ . The dimensions are not to scale.

Nb film patterned by lift-off. The sandwich made by the Nb base electrode, the anodic Nb oxide and the wiring all around the junction constitutes the idle region. Using this fabrication process, we obtained, in samples that had also been heated above the room temperature during the thermal growth of the barrier, current densities as low as  $10\text{A}/\text{cm}^2$  and junction quality factor (defined as the product of the critical current times the subgap resistance at  $2\text{mV}$ ) always better than  $40\text{mV}$  (up to  $98\text{mV}$ ) and independent of the junction size

## 2.2. Sample geometry

A sample consisted of four junctions with overlap geometry having length  $L_j = 200\mu\text{m}$  and width  $W_j$  ranging from 10 to  $20\mu\text{m}$ \*. The geometries of the junctions and of the idle regions are shown in Fig.2 ; they were intentionally mixed in each sample to emphasize the differences. After the first run of measurements some samples underwent a reduction of the idle region by photolithography and were remeasured. We used three configurations: *i)* *naked* (Fig.2a), for which  $L_i = W_i = 0$ ; *ii)* *sided* (Fig.2b), that is  $W_i > 0$ ,  $L_i = 0$ , and *iii)* *ended* (Fig.2c), where  $W_i = 0$ ,  $L_i > 0$ . We chose geometries *ii)* and *iii)* instead of the most general ( $W_i > 0$ ,  $L_i > 0$ ) to evidence the different effects of a lateral or a terminal idle region, since, as we shall see, they are such that they can balance each other to some extent.

We remark that the words *lateral* and *terminal* should not be referred to the geometrical configuration, but rather to the direction of traveling waves in the junc-

\*In the followings the indices *i* and *j* will always refer to the idle region and to the junction, respectively.

tion; since we chose, for the sake of simplicity, a unidimensional geometry, the two coincide.

### 2.3. Measurements

We measured the asymptotic voltage of the Fiske steps obtained applying a magnetic field in the plane of the junction, perpendicular to the long dimension. All measurements were performed at 4.2K.

#### 2.3.1. Naked junctions.

In naked junctions the Fiske steps (FS) appear to be evenly spaced by the voltage:

$$\Delta V = \Phi_0 \frac{\bar{c}}{2L_j}, \quad (1)$$

where  $\bar{c}$  is the Swihart velocity and  $\Phi_0$  the flux quantum. From this formula, we obtained  $\bar{c} = 0.035c_0 \pm 5\%$ , the same, within the error for all the *naked* junctions that we tested ( $c_0$  here is the speed of light in vacuum). From the magnetic field pattern of electrically small junctions, we obtained the value of the critical field and hence an estimate of the total magnetic penetration depth as  $d_j \cong 140nm$ . Given the above values, we may calculate, using the formula:

$$\bar{c} = c_0 \sqrt{\frac{t_{j,eff}}{d_j}}, \quad (2)$$

the effective (or reduced) barrier thickness  $t_{j,eff} \equiv t_j/\epsilon_j$ , where  $t_j$  is the barrier thickness and  $\epsilon_j$  is its relative dielectric constant. We get  $t_{j,eff} = 0.23nm$ .

#### 2.3.2. Sided junctions.

The Fiske steps in *sided* junctions do not exhibit the simple behavior found in *naked* junctions. There are two relevant differences:

1. The voltage of the 1st FS grows with the ratio  $W_i/W_j$  (Fig.3) (we found up to twice the value seen in *naked* junctions), *i.e.*, the phase velocity  $v_p$  of the 1st FS is a growing function of that ratio.
2. The steps are no longer evenly spaced, as  $\Delta V$  appears to be a decreasing function of the step order  $n$ , or, in other words, dispersion occurs, as  $v_p$  appears to be a decreasing function of the frequency. In Fig.4 we compare the voltages of the Fiske steps *in the same junction* with two different widths of the lateral idle region, obtained by partially trimming the wiring Nb film after the first test; it is seen clearly that dispersion is stronger when the ratio  $W_i/W_j$  is larger, as we repeatedly found in other similar cases.

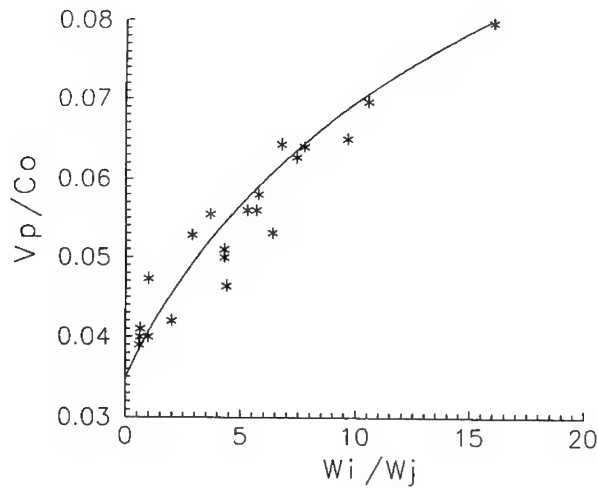


Fig. 3. Phase velocity at the fundamental frequency of the Fiske resonance in *sided* junctions as a function of the ratio  $W_i/W_j$ . The stars represent the experimental data, the solid curve is the theoretical prediction according to the simple model of Sec. 3.1.

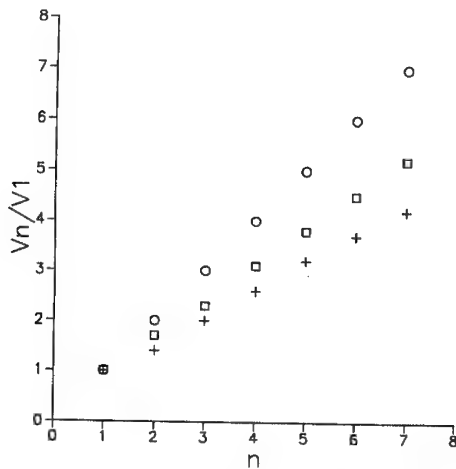


Fig. 4. Fiske step voltages in a *sided* junction before (crosses) and after (squares) trimming the *idle* region, showing that the frequency dependence of the phase velocity becomes stronger when the ratio  $W_i/W_j$  is larger. The upper points (circles) represent the normal behavior in a *naked* junction.



### 2.3.3. Ended junctions.

Dispersion in this case was negligible, the major effect being opposite to that in sided junctions. In fact the voltage of the 1st FS can be quite lower than in the *naked* junctions (Fig.5), and is a decreasing function of the idle region area. The choice to represent the 1st FS voltage as a function of the capacitance  $C$  of the idle region takes into account the model that will be described in the next section. The value of  $C$  was estimated from the parameters of the Nb anodization, while the junction capacitance  $C_0$  was evaluated from the *naked* junctions.

A final remark concerning both kinds of window junctions is that we checked that the trimming of the idle region always shifts the FS voltages towards the values expected for the *naked* junctions.

## 3. Theoretical models

A global theoretical approach to the dynamical problem in window junctions would imply the solution of two  $2 + 1$  partial differential equations. Resorting to long junctions and separating the effects of lateral and longitudinal idle junctions allow to interpret the main features by simple models which help to understand the essential physics of the phenomena.

### 3.1. Sided junctions

In this case the device can be modeled as a complex stripline structure made by a Josephson transmission line in parallel with two passive superconducting transmission lines. If we disregard the losses, according to Swihart<sup>1</sup> the distributed inductance and capacitance for each line are:

$$\mathcal{L}_{i,j} = \frac{\mu_0 d_{i,j}}{W_{i,j}}, \quad \mathcal{C}_{i,j} = \frac{\epsilon_0 \epsilon_{i,j} W_{i,j}}{t_{i,j}}. \quad (3)$$

A look at the two phase velocities

$$v_{pj} = \bar{c}, \quad v_{pi} = \bar{c} \sqrt{\frac{t_i \epsilon_j d_j}{t_j \epsilon_i d_i}} \quad (4)$$

says that the latter is always the larger. In the TEM approximation, one can calculate the phase velocity  $v_p$  in the whole structure from the total distributed inductance and capacitance. Carrying on the calculations with elementary algebra, and introducing  $w = W_i/W_j$ , we get

$$v_p/c_0 = D \sqrt{\frac{1 + Aw}{1 + Bw}} \approx D \left( 1 + \frac{A - B}{2} w \right), \quad (5)$$

where the last equality holds for small  $w$ . In this equation  $A = d_j/d_i$ ,  $B = t_{j,eff}/t_{i,eff}$  and  $D = \bar{c}/c_0$ , which we estimated from the fabrication parameters and from experimental data to be 0.4, 0.035 and 0.04, respectively. With these figures we calculated the solid curve in Fig.3. The scattering of the experimental data with respect to the theoretical prediction may depend on the scattering of the fabrication parameters and on the practical difficulty to define the pure geometrical configurations of Fig.2. With this model in mind, the dispersive behavior can be accounted for by quasi-TEM propagation in thick striplines due to the discontinuity of the dielectric constant<sup>4</sup>; it has been shown<sup>5</sup> that dispersion cannot be neglected especially in the case of low impedance striplines.

### 3.2. Ended junctions

The fundamental Fiske resonance in our samples is close to 30 GHz, corresponding to a wavelength of about 2 mm in Nb oxide, much larger than the dimensions of the terminal idle region, that therefore may be approximated as a lumped capacitive load  $C_1$ . Tentatively, we guess that  $\bar{c}$  is modified by the load at the junction boundaries over a region of length  $\lambda_j$ , as this is roughly the width of the zone involved in reflection phenomena, and take the average value of the velocity in this region as the modified value  $v'_{pi}$ . To be specific, we shall suppose that the effective capacity of such a region is the sum of its intrinsic capacitance and of the loading capacitance. Indicating with  $\Delta T$  the variation of the Fiske oscillation period with respect to the naked junction, we get:

$$\Delta T = 4\lambda_j \left( \frac{1}{v'_{pi}} - \frac{1}{\bar{c}} \right), \quad (6)$$

where the factor 4 takes into account the occurrence of the idle region at both the extremities of the junction and the fact that both incident and reflected waves are affected. From the above formula, with some elementary algebra, we obtain:

$$V = \frac{V_0}{1 + \frac{4}{l} \left( \frac{\bar{c}}{v'_{pi}} - 1 \right)}, \quad (7)$$

where  $V$  and  $V_0$  are the 1st FS step voltages in the *ended* and the *naked* junctions respectively, and  $l = L_j/\lambda_j$  is the electrical length. Considering that the local phase velocity is inversely proportional to the square root of the specific capacitance, we end with:

$$V = \frac{V_0}{1 + \frac{4}{l} \left( \sqrt{\frac{C_1 l}{C_0}} + 1 - 1 \right)}. \quad (8)$$

In Fig.5 we compare this formula with the experimental data, emphasizing that we did not use free parameters to fit the formula to the data. However, the choice

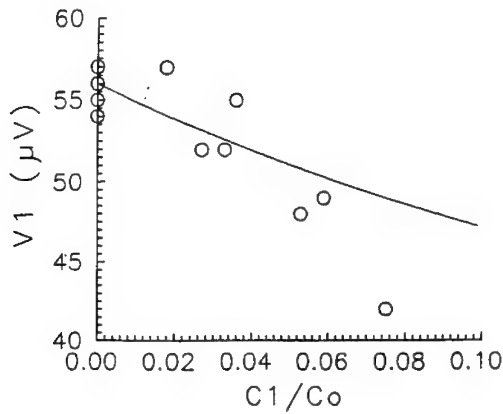


Fig. 5. Voltage of the first Fiske step in *ended* junctions as a function of the ratio of the capacitance of the *idle* region to the capacitance of the junction. The circles represent the experimental data, the solid line is the theoretical prediction of the model in *Sec. 3.2*. Here  $l = 6$ .

of  $\lambda_j$  as the width of the affected zone is not crucial since  $V$  is a slow function of  $l$ ; the physical meaning is that a different (not too much) choice would increase (or decrease) the length over which the phase velocity is influenced but, at same time, would decrease (or increase) the velocity itself producing some compensation.

Finally, we report that, in accordance with this picture, samples with smaller electrical length exhibit a comparatively smaller reduction of the FS voltages.

#### 4. Conclusions

The idle region, in spite of its name, plays a prominent role in determining the phase velocity in window junctions, and it is possibly the major cause of the large spread of data reported in the literature relative to the Swihart velocity in Josephson junctions and to their specific capacitance. We have investigated separately the effect of a lateral and a terminal idle region, which allowed to formulate simple models to interpret quantitatively some of the experimental data, but further work is required to account quantitatively for the effects due to dispersion and for the behavior of window junctions with a generic geometry.

#### Acknowledgements

The authors wish to thank Prof. R.D. Parmentier for stimulating discussions. This work was partially supported by the Consiglio Nazionale delle Ricerche under the Progetto Finalizzato Superconducting and Cryogenic Technologies, by the European

Union under the Science program and by the MURST (Italy).

### References

1. J.C. Swihart, *J. Appl. Phys.* **21** (1961) 461.
2. W. Schroen and J.P. Pritchard, *J. Appl. Phys.* **40** (1980) 2118.
3. H. Kroger, L.N. Smith, and D.W. Jillie, *Appl. Phys. Lett.* **40** (1981) 280.
4. H.A. Wheeler, *IEEE Trans. on Microwave Theory and Techniques* **13** (1965) 172.
5. T.C. Edwards and R.P. Owens, *IEEE Trans. on Microwave Theory and Techniques* **24** (1976) 506.

# CRITICAL PHENOMENA IN LARGE AREA JOSEPHSON JUNCTIONS WITH DEFECTS

A. G. SHAGALOV

*Institute of Metal Physics, S. Kovalevskaya 18, GSP-170  
Ekaterinburg 620219, Russia  
svt@thphys.urgu.e-burg.su*

## ABSTRACT

A model of large area Josephson junctions with highly inhomogeneous distributions of bias currents or magnetic field penetrations has been proposed. The model is based on approximation of the inhomogeneities by point-like singularities (or "defects"). The features of the critical phenomena associated with driven instability of mixed states are investigated within the scope of a singular boundary problem for the 2D sine-Gordon equation.

## 1. Introduction

The strong spatial localization of boundary injected currents or magnetic field permeations are the typical phenomena for large two-dimensional Josephson junctions with sizes much greater than the Josephson penetration depth  $\lambda_J$ . It is known that the boundary currents are concentrated near the corners for junctions with wide current-feeding superconductive strips<sup>1</sup> (see Fig. 1a,b where the typical diagrams of junctions under investigation are shown). The similar localization occurs in an applied parallel<sup>1</sup> or perpendicular<sup>2</sup> magnetic field. Moreover it was supposed<sup>1,3</sup> that such inhomogeneities may be approximated as point-like ones situated in corners of the junction by the following ratios:

- junction with bias current applied and zero magnetic field

$$\text{crossed} : I_1 : I_2 : I_3 : I_4 = 3/4 : 1/4 : -1/4 : 1/4 \quad (1)$$

$$\text{overlap} : I_1 : I_2 : I_3 : I_4 = 1/2 : 1/2 : 1/2 : 1/2 \quad (2)$$

- junction with zero bias current and parallel magnetic field

$$\text{crossed} : I_1 : I_2 : I_3 : I_4 = 1/2 : -1/2 : -1/2 : 1/2 \quad (3)$$

$$\text{overlap} : I_1 : I_2 : I_3 : I_4 = 1/2 : -1/2 : -1/2 : 1/2 \quad (4)$$

- junction with zero current and perpendicular magnetic field

$$\text{crossed} : I_1 : I_2 : I_3 : I_4 = 1/2 : -1/2 : 1/2 : -1/2 \quad (5)$$

$$\text{overlap} : I_1 : I_2 : I_3 : I_4 = 1/2 : -1/2 : 1/2 : -1/2 \quad (6)$$

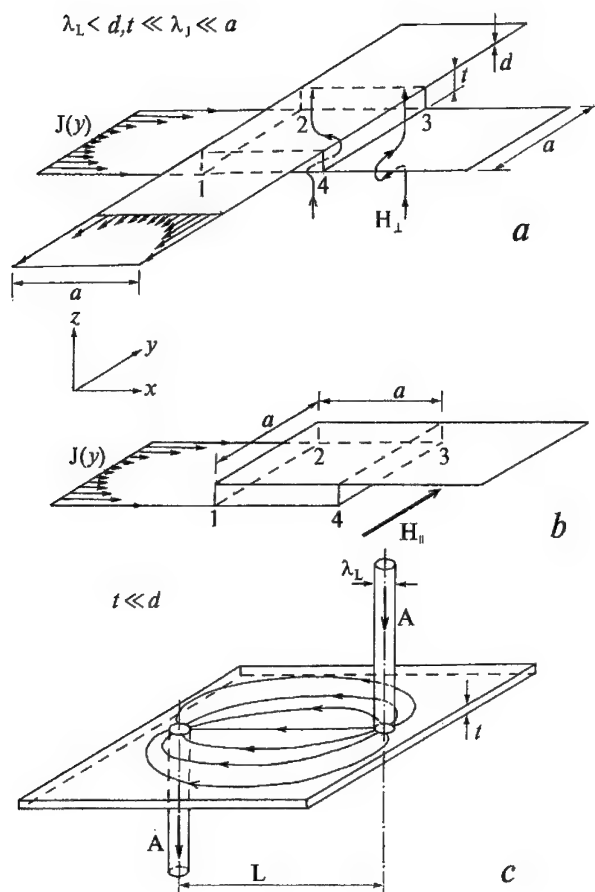


Fig. 1. (a) - crossed junction with wide current-feeding superconductive strips and inhomogeneous dc currents; (b) - overlap junction; (c) - distribution of magnetic field lines for the dipole defect in a junction with thick strips ( $A$  - Abrikosov vortices).

Another case is the penetration of Abrikosov vortices from thick superconductive strips into the junction<sup>2,4</sup>, which corresponds to appearance of local magnetic impurities with sizes  $\sim \lambda_L \ll \lambda_J$  ( $\lambda_L$  - London penetration depth) inside the junction. They may be interpreted as point-like inhomogeneities too (see Fig. 1c).

We shall call these point-like current or field inhomogeneities together with induced phase-difference distributions around them as "defects". The full classification of the defect structures has been given in Ref. 5. *It seems reasonable that the critical properties and dynamics of large area Josephson junctions are predominantly defined by a distribution of the defects.* This paper gives a review of our computer investigations of critical phenomena for this case in the framework of the (2+1)-dimensional sine-Gordon (SG) model

$$-\phi_{tt} + \phi_{xx} + \phi_{yy} = \sin(\phi) + f(t) + \gamma\phi_t \quad (7)$$

where  $\phi(x, y, t)$  is the phase-difference distribution in the two-dimensional junction. Eq. (7) is written in dimensionless form where coordinates are normalized by  $\lambda_J$  and time by  $\omega_p^{-1}$  ( $\omega_p$  being the "plasma" frequency for the junction).

## 2. Classification Problem for the Defects

In a stationary case (and with  $f = 0$ ) the SG Eq. (7) admits a full solution of the classification problem<sup>5</sup>, which is based on the fundamental theorem for the structure of solutions for equations with a sublinear nonlinearity. The defect-like solutions may be of two basic types - "sources" and "vortices". All more complex defect configurations consist of these two basic types.

The source defect corresponds to the point-like injection of bias current to a junction. It was discussed in Ref. 3 as a current injection to corners of the cross-type junction. The defect is a system of snugly packing ring fluxons with common center in a source-type singularity \*

$$\phi \sim \alpha \log(1/r), \quad r \rightarrow 0 \quad (8)$$

("core" of defect)<sup>5</sup>. The radius of the defect grows linearly with  $\alpha$  as

$$R \approx (3/4)\alpha - 2 \quad (9)$$

for  $\alpha > 5$ , and  $R \rightarrow 0$  for  $\alpha \rightarrow 0$ . For  $r > R$  the phase disappears exponentially:  $\phi \sim \exp(-r)$ .

In terms of the Dirac  $\delta$ -function the source defect is a solution of the elliptic equation

$$\phi_{xx} + \phi_{yy} = \sin(\phi) - 2\pi\alpha\delta(r),$$

which exhibits its physical meaning as a point-like injection of bias currents.

\*Detailed computations have shown that the source defects obtained in Ref. 5 are metastable solutions. They are contracted to more compact stable states with sizes defined by Eq. (9).

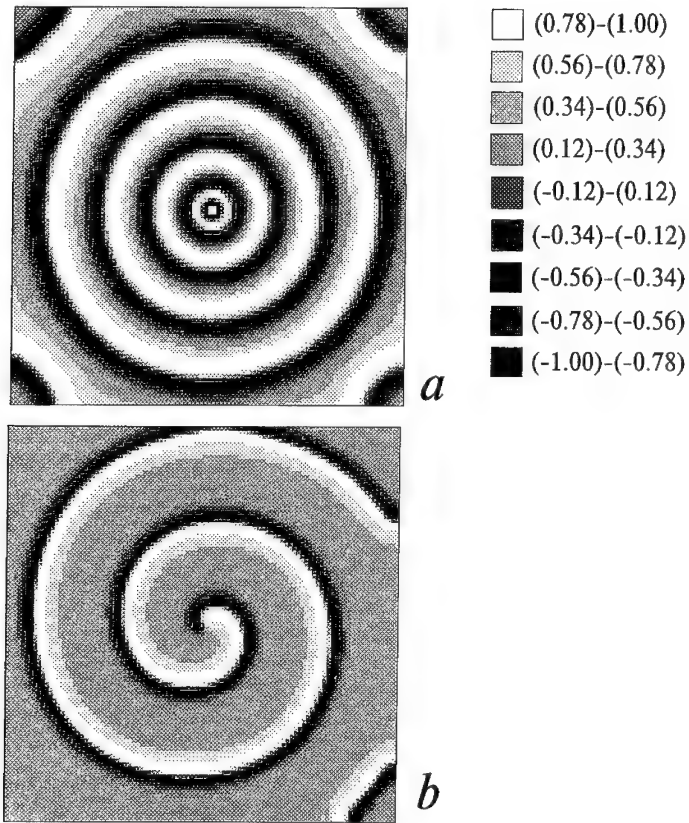


Fig. 2. Dynamical structures formed by isolated unstable source (a) and vortex (b) defects in a square junction. The distribution of the Josephson current  $J = \sin(\phi)$  is shown by the grey-level scale at the right hand side of the picture. (a) The ring fluxon moves outside the core with constant velocity;  $f = 0.9 > f_c$ ,  $\alpha = 4.0$ ,  $a = 30$ . (b) The spiral rotates with constant frequency around the core,  $f = 0.9$ ,  $a = 60$ .



The topological vortex solution corresponds to the entrance of the unit Abrikosov vortex into a junction and consists of a semi-infinite fluxon line starting from the core

$$\phi \sim k \tan^{-1}(x/y) \quad (10)$$

( $k = \pm 1$  - topological charge). Multivortex solutions also exist. The simplest one is a dipole configuration which consists of a fluxon segment linking two singular points with opposite topological charges and corresponds to the entrance of an Abrikosov vortex in one point and its exit in another point of a junction. The distribution of magnetic field lines for the dipole is schematically shown in Fig. 1c. It is an experimentally observed situation<sup>4</sup>.

In the model of large area junctions under discussion we suppose that the current or field injections into the junction are carried through the defect cores only. From the mathematical point of view we have a *singular boundary problem* for SG (7), where one imposes current free boundary conditions  $\partial\phi/\partial\mathbf{n}|_C = 0$ ,  $\partial/\partial\mathbf{n}$  - normal derivative to area border  $C$ , and the phase distribution inside the junction area is defined solely by positions of the defect cores.

An implicit unconditionally stable numerical scheme was used to compute SG Eq. (7) on a rectangular grid  $100 \times 100$ . The method of definition of the defect cores has been discussed in Ref. 8.

One notes that Eq. (7) in the stationary case is a completely integrable model and some defect-like solutions may be obtained in analytic form or their asymptotic investigations may be performed by the Inverse Scattering Transform method<sup>6,7</sup>.

### 3. Stability of the Isolated Defects

Stability properties of the defects and their distributions are the key problem for critical phenomena in large area junctions because the transfer from the stable region to unstable one usually results in the motion of the defects, and a junction goes from the superconductive state to the dynamic resistive one. Parameters when this transition occurs we shall call as *critical parameters*. We start to discuss the problem for a particular case of isolated defects when their interactions with the boundaries are negligible.

Usually the defect cores are fixed inside the junction area by peculiarities of area border (for boundary localized source defects) or by pinning of Abrikosov vortices (for vortex defects). In this case the isolated defects were found to be stable with respect to a wide class of small perturbations<sup>5</sup>. But there are two special types of perturbations that can destroy the isolated defects under the effect of bias currents  $f(x, y, t)$  spread in a junction area (see Eq. (7)):

- stationary uniform current  $f = \text{const}$  when its value is greater than some critical level  $f > f_c$ ,
- small periodic  $f(t)$  for the special set of frequencies.

The second type of perturbations will be investigated in the following section. Now we restrict ourselves to the first type, and we consider an overdamped case only

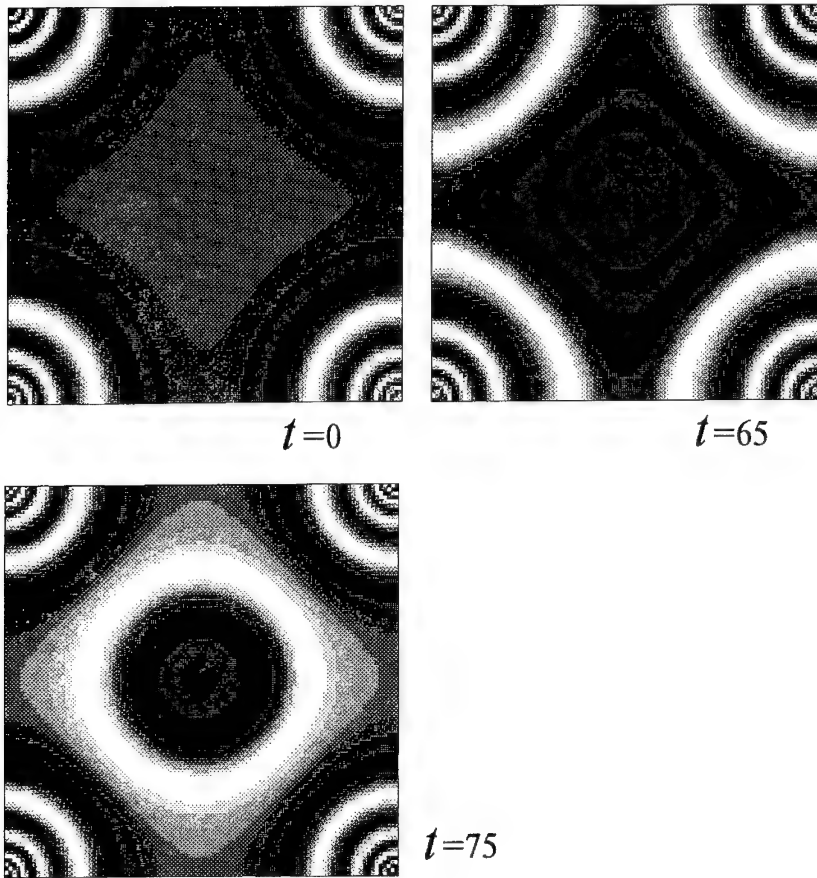


Fig. 3. The dynamics of the overlap junction in the unstable region ( $\alpha > \alpha_{cr}$ ). The boundary injected currents are approximated as source-like defects in the corners with ratio (2) and  $\alpha = 10$ . The size of the junction is  $a = 15$ . The Josephson current distribution is pictured. The meanings of the painting masks are the same as in Fig. 2.

(i.e. we drop the term  $\phi_{tt}$  and set  $\gamma = 1$  in Eq. (7)). This allows one to emphasize the characteristic properties of the structures appeared which can be ruined by turbulent fluctuations in the opposite case of low dissipation. Moreover an overdamped model is a typical one for SNS junctions.

The source type defect is stable under the influence of driving force  $f < f_c(\alpha)$ , where the critical value decreases with growing  $\alpha$  as  $\sim 1/\alpha$ . If  $f > f_c(\alpha)$  the defect loses stability<sup>9</sup>, and ring fluxons begin to move outside with constant velocity forming the steady structure like *target pattern* (Fig. 2a).

The stationary driving force has the most destructive effect on the isolated vortex solution. In this case  $f_c = 0$  and even small current rolls up the fluxon to a *spiral pattern* with center in the defect core<sup>9</sup>. It rotates with a constant frequency around the core and has a constant radial step (Fig. 2b).

The physical mechanism of pattern formation as a result of driven instability of source or vortex solutions is simple enough. Really, it is well known that driving force  $f$  in SG Eq. (7) causes moving of a quasi-one-dimensional fluxon in the direction associated with its topological charge (see e.g. Ref. 10). The asymptotic velocity of the moving fluxon is established as a balance between driving ( $f$ ) and dissipation ( $\gamma$ ). The same effect of driving force to fluxons remains valid in the 2D case, but now the core of the vortex is fixed and the fluxon line will be reeling around the core. Because the normal velocity of the moving fluxon is bounded, the steady spiral pattern shown in Fig. 2b is formed. This supposition for physics of spiral formation is confirmed by simulation. The target patterns are formed for  $f\alpha > 0$  when driving force acts on ring fluxons outside the centre and seeks for its divergence. If the force exceeds some critical value the ring fluxons leave the core and a divergent pattern forms (Fig. 2a).

#### 4. Critical Currents

If  $f = 0$  then isolated defects are stable and only their interactions with boundaries or one with another can initiate instability. Now the value of injected currents becomes a critical parameter. For small currents the stationary defect-like phase distribution is adjusted and a mixed superconductive state with Josephson current  $J = \sin(\phi)$  is formed. Here  $\phi(x, y)$  is a stationary solution of Eq. (7). With increasing of the current a stationary distribution may lose its stability and a resistive dynamic state is formed. The current for creation of the resistive state is called as "critical current" for a junction.

The first example of such critical phenomenon was given in Ref. 3 for a crossed junction with corner defects. We discuss here the similar process for an overlap square junction with currents injected to the corners in ratio (2). The overdamped approximation will be used again.

For small currents (parameter  $\alpha$ ) the stable ring-like phase distribution is formed near each corner of the junction. Then the defect radius increases with  $\alpha$  and defects begin to interact one with another. After this, the stationary state becomes impossible, and collapsing ring fluxons are formed periodically in the centre of the junction which then transfer into the dynamic resistive state. Some stages of this dynamics

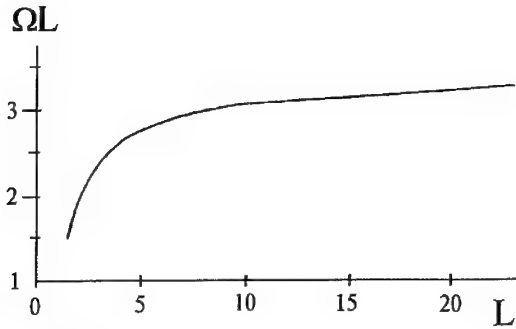


Fig. 4. The dependence of the main resonant frequency  $\Omega$  on the dipole size  $L$ . For large  $L$  the curve tends to a constant, which confirms the string-like dependence  $\Omega \sim L^{-1}$ .

are shown in Fig. 3. The critical value of  $\alpha$  is subject to the simple empirical rule  $\alpha_{cr} \approx 0.6a$  for  $a > 5$ . In contrast to the above case, one notes that the distributions of currents with ratios (3)-(6) are stable for any intensity of magnetic field.

## 5. Critical Temperature and KT-type Phase Transitions

The Kosterlitz-Thouless (KT) phase transition<sup>11</sup> is a possible mechanism for destruction of the Josephson junction superconductive state by thermal fluctuations. This problem is actively discussed to explain some properties of high- $T_c$  ceramics near the critical temperature, where the intrinsic twin-boundary weak links in grains are thought to be a candidate for application of the large area Josephson junction theory<sup>12</sup>.

Vortex-type defects are the main active objects in the KT phase transitions. Strictly speaking, the KT theory<sup>11</sup> is the correct one in linear region of Eq. (7), that is for area sizes much less than  $\lambda_J$ . In this case the linear vortices  $\phi \approx \pm \tan^{-1}(x/y)$  have a logarithmic interaction energy, and the KT phase transition is associated with the breakup of thermally created vortex dipoles at some critical temperature  $T_{KT}$ . For  $T > T_{KT}$  the vortices become free, and they are disseminated inside the junction area destroying the superconducting state.

Another situation takes place for large area junctions. If the distance between vortex cores becomes greater than  $\lambda_J$  the fluxon line linking the cores is formed and the interaction energy acquires a linear growth with distance, which must prevent the dipole dissociation<sup>8</sup>. Starting from this stage another process comes into effect. The phase transitions may be caused now only by thermal break-down of fluxons.

It turns out that the main destructive factor is associated with internal resonant properties of fluxon lines as "strings". We found that fluctuations of the dipoles have a discrete spectrum with the main frequency  $\Omega$  and its harmonics  $n\Omega$ . For a large distance  $L$  between cores the dependence  $\Omega \sim L^{-1}$  was obtained, which confirms the

string-like character of the resonances (see Fig. 4). For small dissipation  $\gamma$  in Eq. (7) the computer experiments indicate a high Q-factor of the resonator. External periodic perturbations with resonant frequencies effectively destroy the dipole even for small amplitude of perturbations.

In spite of this very effective mechanism of resonant destruction the thermal fluctuations have a weak effect on the dipoles because of difference in the frequency ranges. Really, the frequency range of the dipoles, which display the good quality resonance properties, is  $\Omega < 1$  (see Fig. 4). On the other hand it seems reasonable that the temperature fluctuations are concentrated in the region  $\Omega > 1$ , i.e. in the range of small "plasma" oscillations with dispersion law  $\omega = \sqrt{1 + k^2} > 1$  that follows from Eq. (7) in linear approximation. Thus the dipoles with  $L > 1.5 \div 2.0$  are stable with respect to thermal fluctuations and the KT phase transitions in large area Josephson junctions are *forbidden* in the nonlinear SG model (7).

## References

1. A. Barone, F. Esposito, K. K. Likharev, V. K. Semenov, B. N. Todorov and R. Vaglio, *J. Appl. Phys.* **53** (1982) 5802.
2. S. L. Miller, K. R. Biagi, J. R. Clem and D. K. Finnemore, *Phys. Rev.* **B31** (1985) 2684.
3. S. A. Vasenko, K. K. Likharev and V. K. Semenov, *IEEE Trans. Magn.* **19** (1983) 1027; *ZhETF* **86** (1984) 1032.
4. J. Mannhart, J. Bosch, R. Gross and R. P. Huebener, *J. Low Temp. Phys.* **70** (1988) 459.
5. A. G. Shagalov, *Phys. Lett.* **A165** (1992) 412.
6. A. B. Borisov, S. N. Ionov and A. G. Shagalov, New types of vortices and the solutions of the boundary value problems for sine-Gordon equation by the Inverse Scattering Transform, in "Nonlinear world": IV International Workshop on Nonlinear and Turbulent Processes in Physics, World Scientific Publishing Co., 1990, v.1, p.65-72.
7. A. B. Borisov, *Phys. Lett.* **A143** (1990) 52.
8. A. B. Borisov, A. P. Tankeyev and A. G. Shagalov, *Fizika Tverdogo Tela* **31** (1989) 140 [*Sov. Phys. Solid. State*].
9. A. G. Shagalov, *JETP Lett.* (to be published).
10. D. W. McLaughlin and A. C. Scott, *Phys. Rev.* **18A** (1978) 1652.
11. J. M. Kosterlitz and D. J. Thouless, *J. Phys* **C6** (1973) 1181.
12. D. Browne and B. Horovitz, *Phys. Rev. Lett.* **61** (1988) 1259.

---

Chapter 4

**Nonlinear Propagation**

# FRACTIONAL FLUXON EXCITATIONS IN COUPLED LONG JOSEPHSON JUNCTION ARRAYS

STANFORD P. YUKON

*Electromagnetics Directorate, Rome Laboratory  
Hanscom AFB, MA 01731-3010, USA*

and

NATHANIEL CHU H. LIN

*ARCON Corporation, 260 Bear Hill Road, Waltham, MA 02154, USA*

## ABSTRACT

We have investigated the dynamics and symmetries of fractional fluxon excitations that appear in systems of coupled long Josephson junctions(JJ's). The system of 3 coupled JJ's enclosing a half flux quantum supports three distinct permanently bound topological  $1/3$  fluxon subkinks. Exact solutions are found for this system operating in the flux flow mode. A novel feature of this system is that parallel forcing currents across two JJ's of the system results in their developing a non zero DC voltage, while the third JJ acts as a driven rf oscillator with zero DC voltage. An array using these systems as elements is modeled numerically and found to be stable with respect to large ( $\sim \pm 80\%$ ) variations in JJ critical currents, to be capable of a large series output voltage and impedance, to have negligible power emitted into higher harmonics, and to have rf output power and polarization varying as a function of external axial flux at constant frequency. The same array composed of short JJ's is shown to have similar properties plus a capability for varying the frequency of the rf output with small changes in rf power.

## 1. Introduction

Due to the low impedance and rf output power available from a single small JJ oscillator( $\sim 3.0$  nW) or a single long JJ in the flux flow mode( $\sim .5$   $\mu$ W), it is desirable to couple each into an array capable of providing coherent large amplitude rf output voltages. We shall consider two basic coupling schemes for long JJ's and some of the possible kink and flux flow solutions for them. In the simplest system ( $N=3$ ) three superconductors separated by tunneling oxide layers are arranged in a 3 conductor bundle to form 3 long JJ's as shown in Fig. 1. In the second system ( $N=4$ ) four superconductors are bundled to form 6 long JJ's. Both of these configurations allow each superconductor to interact with all of the other superconductors in an equivalent way, leading to triangular and tetrahedral symmetries of the Lagrangian and its kink solutions. We then consider forming an array using  $N=3$  systems as array elements. The results obtained for long JJ's will also apply to short JJ's if appropriate consideration is given to the absence of the spatial degree of freedom.

The Lagrangian density can be written in terms of the energy densities of the

electric and magnetic fields  $\phi_t$  and  $\phi_x$  and the junction potential energies  $U[\phi_i(x)] = J_c(1 - \cos[\phi_i])$  as

$$\begin{aligned} \mathcal{L} = & \frac{1}{2} \sum_{i=1}^{N_J} (\phi_{i,t}^2 - \phi_{i,x}^2) + \frac{1}{2} \sum_{i=1}^M (\eta_i \psi_{i,t}^2 - \bar{\eta}_i \psi_{i,x}^2) \\ & - \sum_{i=1}^{N_J} J_i U[\phi_i] - \sum_{i=1}^M j_i U[\psi_i] + \sum_{i=1}^M \lambda_i (\psi_i - \phi_i + \phi_{i+1} - 2\pi\Phi/\Phi_0 + n \cdot 2\pi) \end{aligned} \quad (1)$$

where we have normalized space and time variables to the Josephson penetration depth  $\lambda_J = \sqrt{\Phi_0/(2\pi J_{c0}L)}$  and plasma frequency  $\omega_p = 1/\sqrt{LC\lambda_J^2}$ . We have assumed that all superconductors are thicker than the London penetration depth  $\lambda_L$ , which imposes a phase constraint on the junction gauge invariant phases  $\phi_i$  around each axial cavity

$$(-)\phi_i(x) + \phi_{i+1}(x) + \psi_{i-1}(x) + 2\pi\Phi/\Phi_0 = n \cdot 2\pi \quad (2)$$

where  $\Phi$  is an externally imposed magnetic flux threading each axial cavity and  $\Phi_0$  is the flux quantum ( $=h/2e$ ). These constraints have been included in the Lagrangian by means of Lagrange multipliers  $\lambda_i$ . We have also assumed that the self inductance around each cavity is small and can be neglected. We have labeled  $\{J_i, j_i\}$  as the critical current densities of the  $\{\phi_i, \psi_i\}$  JJ's and have defined  $M$  to be the number of axial cavities, and  $N_J$  to be the number of independent JJ's. The capacitance per unit length  $C$  and the inductance per unit length  $L$  for the  $\psi_i$  junctions have been allowed to differ from those of the  $\phi_i$  junctions by including multiplicative factors  $\eta_i$  and  $\bar{\eta}_i$ . For this section of the paper we shall assume that  $\eta_i/\bar{\eta}_i = 1$  so that the velocity of light in all junctions will be the same and equal to  $\bar{c} = 1/\sqrt{LC}$ .

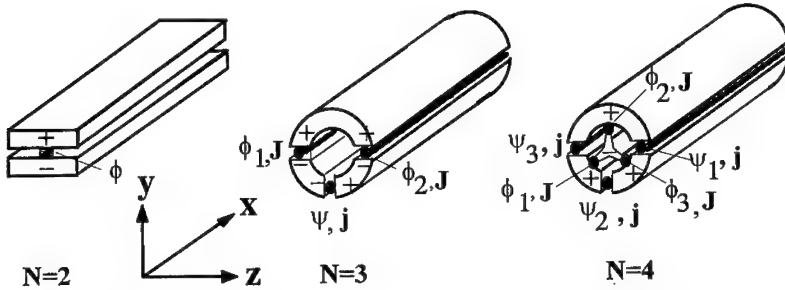


Fig. 1. Schematic drawing of  $N=2, 3$ , and  $4$  coupled long Josephson junction systems.

## 2. Kink Solutions and Symmetries for $N=3,4$ Systems

Variation of the Lagrangian with respect to  $\phi_i(x, t)$  and  $\psi_i(x, t)$  for the  $N=3$  case leads to the equations of motion

$$\phi_{1,tt} - \phi_{1,xx} = \{-(1+\eta)J \sin \phi_1 - \eta J \sin \phi_2 - j \sin(\phi_1 - \phi_2 + 2\pi\Phi/\Phi_0)\}$$



$$+(\eta - \bar{\eta})(\phi_{2,xx} - \phi_{1,xx})/(1 + 2\eta) \quad (3)$$

with the equation of motion for  $\phi_2$  being given by Eq. (3) with subscripts 1 and 2 interchanged. To obtain the static kink solutions, one can consider  $x$  to be a fictitious time variable for the system with an effective potential given by<sup>1</sup>  $V_{eff} = -\sum U_i$ . Due to the presence of cross terms like  $\phi_{1,x} \times \phi_{2,x}$  in the Lagrangian, it is first necessary to diagonalize the derivative terms in the Lagrangian, which yields the orthonormal coordinates

$$\begin{aligned} \rho_1 &= (\phi_1 + \phi_2)/\sqrt{2} \\ \rho_2 &= \sqrt{1 + 2\eta}(\phi_1 - \phi_2)/\sqrt{2}. \end{aligned} \quad (4)$$

### 2.1. Coordinates and Symmetries for $J_i = j_i = \eta_i = 1$

Writing Eq. (3) in terms of  $\{\rho_1, \rho_2\}$  and considering only static solutions, the  $x$  derivative terms can then be considered to be Newton's equations of motion for the coordinates  $\rho_1$  and  $\rho_2$  of a unit mass in the potential  $V_{eff}[\rho_1, \rho_2]$  shown in Fig. 2 for the case  $J=j=\eta=1$ . The kink solutions, found by simple quadrature will then trace out in  $x$ , the motion of a unit mass traveling from one peak of the two dimensional potential  $V_{eff}[\rho_1, \rho_2]$  to another. In terms of  $\phi_1, \phi_2$  coordinates, the three basic kinks are given by<sup>2</sup>

$$\begin{aligned} \text{AB} : \quad & \phi_1(x) = 2\Pi(-x), \quad \phi_2(x) = 0, \\ \text{DA} : \quad & \phi_1(x) = 0, \quad \phi_2(x) = 2\Pi(-x), \\ \text{DB} : \quad & \phi_1(x) = 2\Pi(-x), \quad \phi_2(x) = 2\Pi(-x), \end{aligned} \quad (5)$$

where  $\Pi(x)$  is the Lobachevsky function  $\Pi(x) = 2 \cdot \arctan[e^{-x}]$ .

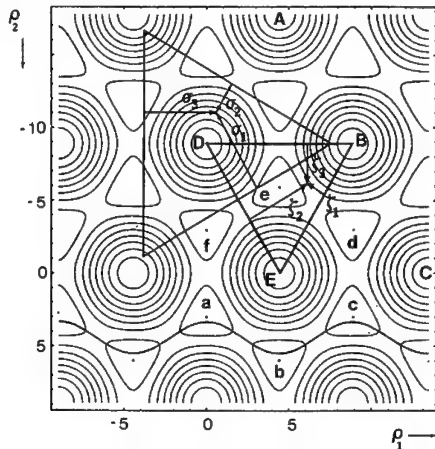


Fig. 2. Contour plot of the potential energy  $U(\rho_1, \rho_2)$  for an  $N=3$  system (with  $\Phi = \Phi_0/2$ ) with superimposed parametric plot of  $\psi (= \rho_1/2\sqrt{2})$  vs.  $\theta (= \rho_2/\sqrt{2})$  centered around  $\psi = +\pi/2$ .

Since the rest energy of each of these kinks is 16,  $V_{eff}[\rho_1, \rho_2]$  should be invariant under rotations of  $2\pi/3$  and reflections about any of the 6 symmetry axes separated by  $\pi/6$ , transformations that constitute the triangular group  $C_{3v}$ . To show this in the simplest way we can employ triangular coordinates. These can be defined in terms of the perpendicular distances  $\zeta_i$  from a point to each of the sides of an equilateral triangle as indicated in Fig. 2 ( $\zeta_i$ 's pointing away from the interior are taken as negative). Since the area of the triangle is simply the sum of half the perpendicular distances from a given point times the base length, the phase constraint Eq. (2) can be interpreted as a geometric constraint inherent in the use of triangular coordinates. If we take the base length  $a = DB = (4\pi/\sqrt{3})\Phi/\Phi_0$ , this leads to the relation  $\zeta_1 + \zeta_2 + \zeta_3 = 2\pi\Phi/\Phi_0$  for triangle **DEB**. We may now define the coordinates  $\sigma_i$  as the triangular coordinates of the triangle perpendicular to **DEB** that are orthogonal to the  $\phi_i$ . The relation between these coordinates and the  $\zeta_i$  coordinates can be obtained from the geometry of the two triangles as

$$\begin{aligned} \sigma_1 &= (\zeta_1 - \zeta_3)/\sqrt{3} + \sqrt{3}a/4 - a/2; \quad \sigma_2 = (\zeta_3 - \zeta_2)/\sqrt{3} + \sqrt{3}a/4; \\ \text{and } \sigma_3 &= (\zeta_2 - \zeta_1)/\sqrt{3} + a/2 + \sqrt{3}a/4. \end{aligned} \quad (6)$$

Defining  $\tilde{\phi}_i = \sigma_i/\sqrt{3}$ ,  $\phi_i = (-1)^{\delta_{i1}} \zeta_i$ , then leads to  
 $(-\phi_1) = \tilde{\phi}_1 - \tilde{\phi}_3 + 2\pi\Phi/\Phi_0$ ,  $\phi_2 = \tilde{\phi}_3 - \tilde{\phi}_2$ ,  $\phi_3 = \tilde{\phi}_2 - \tilde{\phi}_1$ .

In  $\tilde{\phi}_i$  coordinates, the Lagrangian density for  $\Phi = n\Phi_0$  can be written as

$$\mathcal{L} = N \sum_{i=1}^N (\tilde{\phi}_{i,t}^2 - \tilde{\phi}_{i,x}^2) / 2 + \sum_{i \neq j=1}^N J (1 - \cos(\tilde{\phi}_i - \tilde{\phi}_j)) \quad (7)$$

Cyclic  $\zeta_i \rightarrow \zeta_{i+1}$ ,  $\tilde{\phi}_i \rightarrow \tilde{\phi}_{i+1}$  and pair  $\zeta_i \leftrightarrow \zeta_j$ ,  $\phi_i \leftrightarrow \phi_j$  replacement of coordinates in the Lagrangian density of Eq. (1) and (7) will then describe all of these symmetry operations, demonstrating that the Lagrangian and kink solutions are invariant under  $C_{3v}$ . A similar exercise can be carried out for  $\Phi \neq \Phi_0$  and for the  $N=4$  system using tetrahedral coordinates showing that the  $N=4$  system is invariant under the tetrahedral group  $\tau_d$ .

By transforming the descriptions of the  $N=3$  and  $N=4$  systems in this manner, it is now possible to take advantage of the connection established by Ha<sup>3</sup> who showed that a bosonized version of the Lagrangian density for quantized  $SU(N)$  Gross Neveu theory can be written in the form of Eq. (7) for arbitrary  $N$ . In the quantized theory, the commutators of the currents and charges form an  $SU(N)$  algebra while the eigenvalues of the charges commute, their weight diagrams forming the groups  $C_{3v}$  and  $\tau_d$  for  $N=3$  and 4 respectively. The  $C_{3v}$  and  $\tau_d$  symmetries of the fluxons (that are the 'charges' of the coupled long JJ model) in the  $N=3$  and  $N=4$  systems, can thus be considered as the classical limit of the  $SU(N)$  symmetry of the quantized theory. This connection with  $SU(N)$  Gross Neveu theory also suggests that results concerning dynamical subkinks in the following section may also be useful in describing other systems modeled by Gross Neveu, or similarly coupled sine-Gordon systems such as DNA<sup>4</sup> and charge density wave conducting polymers like TTF-TCNQ<sup>5</sup>.

## 2.2. Broken Symmetry and Formation of Dynamical Subkinks

When the parameters of the JJ's in the N=3 (or 4) system are not equal, the triangular(tetrahedral) symmetry is broken and triangular(tetrahedral) coordinates offer no advantage. The system is now best described in terms of the orthonormal coordinates  $\rho_i$ . For the N=3 system we shall use the orthogonal set

$$\theta = \frac{\phi_1 + \phi_2}{2}, \quad \psi = \frac{\phi_1 - \phi_2}{2} \quad (8)$$

The equations of motion in these coordinates may be written exactly as

$$\theta_{,tt} - \theta_{,xx} = -J \sin \theta \cos \psi \quad (9)$$

$$(1 + 2\eta)\psi_{,tt} - (1 + 2\eta)\psi_{,xx} = -J \sin \psi \cos \theta + j \sin(2\psi + 2\pi\Phi/\Phi_0) \quad (10)$$

which can be looked upon as describing a single sine Gordon(SSG) system ( $\theta$ ) coupled to a double sine Gordon(DSG) system ( $\psi$ ). For  $J=j=\eta=1$  the DSG kink **AE** has a rest mass = 37 and is unstable against breaking up into the two kinks<sup>2</sup> **AB** and **BE**. If  $j > 1/2$  and  $\eta \lesssim 0.22j$ , this kink is stable and we shall restrict values of  $j$  and  $\eta$  considered here to be in this range. It has been pointed out by Bullough et al.<sup>6</sup> that the DSG kink can be considered as a bound state of two SSG subkinks separated by  $2\Delta$  (where  $\Delta = \ln[\sqrt{1+2j} + \sqrt{2j}]$ ). For the N=3 case both the  $\theta$  and the  $\psi$  fields form distinct subkinks that are conserved and have a fractional fluxon content of  $\Phi_0/2$ . As an example, the **AB** kink (which is an exact SSG  $\Delta\phi_1 = 2\pi$  kink for  $j=1$ ) develops a non zero component in  $\phi_2$  if  $j$  is increased from  $j=1$  to  $j > 1$ . In terms of the Lorentz boosted subkinks

$$\theta = \Pi(-\beta_\theta(x - vt)/\sqrt{1 - v^2}), \quad \psi = \Pi(-\beta_\psi(x - vt)/\sqrt{1 - v^2}) \quad (11)$$

the **AB** kink can now be approximated as **AB**  $\simeq \theta(x, t) + \psi(x, t)$ , where the propagation constants  $\beta_\theta$  and  $\beta_\psi$  can be found by using the Hirota technique. To the lowest order these are determined to be<sup>7</sup>

$$\beta_\theta = 1, \quad \beta_\psi = \sqrt{(1 + 2j)/(1 + 2\eta)} \quad (12)$$

Introducing first order corrections<sup>8</sup> these agree with numerical results to within 0.3%.

Since the **AE** kink is now stable, the set of basic  $2\pi$  kinks has increased to four, and they can be approximated in terms of the  $\theta$  and  $\psi$   $1\pi$  subkinks as

$$\begin{aligned} \mathbf{AB} &\simeq \theta(x, t) + \psi(x, t) & \mathbf{BE} &\simeq \bar{\theta}(x, t) + \psi(x, t) \\ \mathbf{DB} &\simeq \theta(x, t) + \theta(x, t) & \mathbf{AE} &\simeq \psi(x + \Delta/\beta_\psi, t) + \psi(x - \Delta/\beta_\psi, t) \end{aligned} \quad (13)$$

We have termed the subkinks that arise from symmetry breaking 'dynamical' subkinks to distinguish them from the 'topological' subkinks that arise when  $\Phi = \Phi_0/2$ . The utility of the subkink description becomes manifest if two or more kinks are allowed to interact. As an example in Fig. 3 we have plotted the position of the

subkink EM field energy density ( $\theta_x^2 + \theta_t^2$  and  $\psi_x^2 + \psi_t^2$ ) peaks for the duration of a collision between an incoming  $\text{AB}(\theta + \psi)$  kink and a stationary  $\text{AE}(\psi + \psi)$  kink at the origin (the  $\theta$  trajectories have been plotted with a  $.5\lambda_J$  shift to the left for clarity). The incoming  $\psi$  subkink belonging to  $\text{AB}$  can be seen displacing the right  $\psi$  subkink of  $\text{AE}$  with a small exchange of energy (slightly exciting the outgoing  $\text{AB}$  and  $\text{AE}$ ) and momentum (slightly slowing  $\text{AB}$  and speeding up  $\text{AE}$ ). The incoming  $\theta$  subkink knocks off the  $\theta$  subkink of a  $\theta + \bar{\theta}$  pair, that was induced when the systems began to interact at  $t \approx 10$ , and also shares in the energy momentum exchange. We have termed the final  $\text{AE}$  excited state a hybrid breather since it consists of a  $\theta + \bar{\theta}$  breather that could not exist on its own without an accompanying excited DSG  $\psi + \psi$ . Breaking the symmetry still further to  $j > J_2 > J_1$  leads to  $\theta$  and  $\psi$  subkinks splitting into higher and lower energy pairs  $\theta \rightarrow \{\theta_1, \theta_2\}, \psi \rightarrow \{\psi_1, \psi_2\}$  that have also been computed using the Hirota technique<sup>8</sup>. Thus a  $\phi_1$   $2\pi$  kink will now be composed of  $(\theta_1 + \psi_1)$  while  $\phi_2 = (\theta_2 + \psi_2)$ . Each variety of  $\theta$  and  $\psi$  subkink will now be conserved separately during interactions.

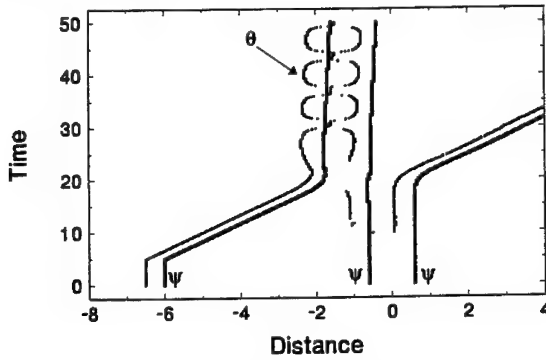


Fig. 3. Plot of the  $\{x, t\}$  position of  $\theta$  and  $\psi$  field energy density peaks during a  $\theta\psi \rightarrow \psi\psi$  collision. The  $\theta$  track is offset to the left by  $0.5 \lambda_J$  for clarity.

For the  $N=4$  system with six JJ's there are numerous possibilities for breaking the symmetry of the system. The appropriate coordinates for the simplest case, where  $j_1 = j_2 = j_3 > J_1 = J_2 = J_3$ , are the tetrahedral coordinate  $\theta = (\phi_1 + \phi_2 + \phi_3)/3$  and three  $\eta_i$ . The  $\eta_i$  are the projections of the three remaining tetrahedral coordinates that form triangular coordinates in the  $\theta = 0$  plane. All of the subkinks for this system will then have a flux content of  $\Phi_0/3$ .

### 2.3. Formation of Topological Subkinks when $\Phi = \Phi_0/2$ , $J=j=\eta=1$

We now turn to the  $N=3$  symmetric case when there is a non zero enclosed axial magnetic flux  $\Phi = \Phi_0/2$ . From the expression for  $V_{eff} = -\sum U_i$  it can be seen that taking  $2\pi\Phi/\Phi_0 = \pi$  has the effect of shifting the origin to  $\{\phi_1 = \pi, \phi_2 = \pi\}$  and inverting the potential. The possible kink solutions for this situation will connect the peaks labeled a, b, c, d, e, and f. By employing triangular coordinates  $\tilde{\phi}_i$ , the kinks

$ab, bc$ , etc., can be described in terms of  $\Phi_0/3$  flux loop quarks around each of the superconductors. Labeling the  $\Phi_0/3$  flux loops around conductors 1, 2, and 3 as  $d, s$ , and  $u$  yields the description of the kinks  $ab, bc$ , etc., in terms of fluxon quarks. They are thus a classical fluxon version of six of the meson octet ( $\pi^+, \pi^-, K^+, K^-, K_0, \bar{K}_0$ ). The two remaining neutral members  $\pi_0$  and  $\eta_0$  may be considered as being formed from pairs of  $u\bar{u}, s\bar{s}$  and  $d\bar{d}$  breathers (we note that these three breathers are not stable and decay radiatively). The coupled  $N=3$  system also offers a classical analog to quark confinement. If the potential between two fluxon quarks is calculated as a function of separation distance  $z$  between them using a simple collective coordinate model<sup>2</sup>, it is found that asymptotically the potential energy  $V_{cd}$  is proportional to  $z$ . The two fluxon quarks are thus permanently confined in a linear potential well. An attempt to separate the  $d$  and  $\bar{s}$  fluxons composing the  $cd$  kink by a large impulsive force will yield a  $cd$  kink in an excited state plus a train of kink antikink pairs.

### 3. Oscillator Arrays with $N=3$ Systems as Elements

If operated as a resonant fluxon oscillator, an  $N=3$  system with  $\Phi = \Phi_0/2$  containing a  $cd$  kink for example would have the desirable property that subkinks on adjacent JJ's are permanently bound. If an array is formed with  $N=3$  systems as elements as drawn on Fig. 4, and filled with  $cd$  kinks across the array (one kink deep in the  $x$  direction), this property persists and subkinks on all adjacent JJ's remain permanently bound. If this array is operated as a coupled array of flux flow oscillators by filling each long JJ with a lattice of merged fluxon kinks, it should be possible to produce even more rf power. For this purpose, a flux flow lattice (in the  $x$  direction) composed of a chain of merged  $ab + bc$ ... kinks is more suitable than a chain of merged  $cd + cd'$ ... kinks since the voltage wave form for the latter case will lead to substantial power going into higher harmonics.

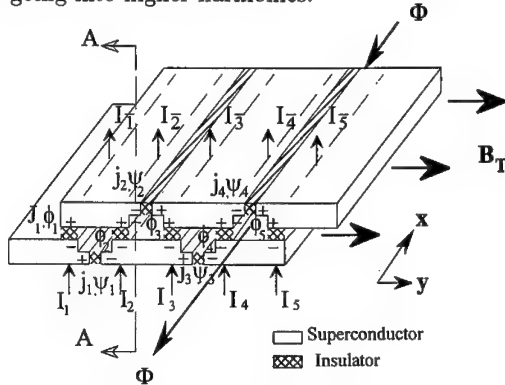


Fig. 4. Schematic drawing of a series array of  $i=\{1, N_J\}\{\phi_i, J_i\}$  JJ's and  $(N_J - 1)\{\psi_i, j_i\}$  JJ's, for the case  $N_J=5$ .

We consider first a single  $N=3$  system with  $\Phi = \Phi_0/2$  where an appropriate flux lattice can be induced by an external transverse magnetic field through the

$\phi_1$  and  $\phi_2$  junctions. It is possible to generate an analytic solution (based on a solution given by Costabile and Parmentier for a single long JJ<sup>9</sup>) for a single N=3 coupled JJ system operating as a flux flow oscillator if periodic boundary conditions and quadratic damping are assumed. Thus with quadratic damping and forcing  $(-\Gamma | \theta_t | \theta_t + j_\theta)$  added to the right hand side of Eq. (9) and  $-\Gamma(1+2\eta) | \theta_t | \psi_t$  added to Eq.(10), we may write a solution to these coupled equations as

$$\begin{aligned}\theta &= \sin^{-1} \left\{ cn \left[ \frac{\gamma(x-ut)}{\sqrt{\kappa}}, \kappa^2 \right] \right\} + \delta_0 \text{ and} \\ \psi &= -\pi/2 + \sin^{-1} \left\{ \kappa sn \left[ \frac{\gamma(x-ut)}{\sqrt{\kappa}}, \kappa^2 \right] \right\},\end{aligned}\quad (14)$$

where  $cn[u, \kappa^2]$  and  $sn[u, \kappa^2]$  are Jacobi elliptic functions with elliptic modulus  $\kappa$  and where

$$\begin{aligned}\gamma^2 &= [(1-u^2)^2 + \Gamma^2 u^4]^{-1/2}, \quad \cos \delta_0 = \gamma^2(1-u^2), \quad \sin \delta_0 = \Gamma u^2 \gamma^2, \\ \text{and } \kappa &= \Gamma u^2 \gamma^2 / j_\theta = \gamma^2(1-u^2)\eta/j.\end{aligned}\quad (15)$$

Flux flow is imposed by demanding that there be  $n$  fluxons within a length  $L$  i.e.

$$\theta_{,x} = n \cdot \Phi_0 / L. \quad (16)$$

which then determines the velocity  $u$  for a given  $j_\theta$  and  $\Gamma$ .

In Fig. 2 we have drawn a parametric plot of  $\psi$  vs.  $\theta$ , centered about  $\psi = \pi$  and shifted by  $\delta_0$  in  $\theta$  so that its maxima and minima line up with the peaks **a, b, c** ... indicating that a lattice of merged **ab + bc + ...** kinks has been produced. Alternatively one could plot  $\phi_{1,x}$  and  $\phi_{2,x}$  vs.  $x$  which would show  $\phi_{1,x}$  flux lattice peaks interleaved with  $\phi_{2,x}$  flux lattice peaks. The voltages  $\theta_t$  and  $\psi_t$  can be expanded in a Fourier series in terms of the complete elliptic integrals  $K$  and  $K'$ :

$$\begin{aligned}\theta_t &= \frac{u\gamma}{\sqrt{\kappa}} dn[\rho, \kappa^2] = \left( \frac{u\gamma\pi}{\sqrt{\kappa}2K} \right) \left\{ 1 + 4 \sum_{n=1}^{\infty} \frac{q^n}{1+q^{2n}} \cos \left[ \frac{n\pi\rho}{K} \right] \right\} \\ \psi_t &= -\sqrt{\kappa}u\gamma cn[\rho, \kappa^2] = -4 \left( \frac{u\gamma\pi}{\sqrt{\kappa}2K} \right) \sum_{n=0}^{\infty} \frac{q^{n+1/2}}{1+q^{2n+1}} \cos \left[ \frac{(2n+1)\pi\rho}{2K} \right]\end{aligned}\quad (17)$$

where  $\rho = \gamma(x-ut)/\sqrt{\kappa}$  and where  $q = e^{-\pi K'/K}$ .

From this one can see that the fundamental frequency in the  $\psi$  channel is given by  $\Omega = (\pi/2K)\gamma u/\sqrt{\kappa}$ , and that the next harmonic at  $3\Omega$  will be very small due to the factor  $q$ , where  $q$  ranges from 0 to .043 as  $\kappa \rightarrow \{0, .7\}$ . In the  $\theta$  channel there will be mainly a DC component and an rf voltage at  $2\Omega$ . The analytic results have been compared with a numerical model of flux flow with periodic boundary conditions and linear damping. For ranges of  $\theta_t$  where the excursion of  $\theta_t$  about its mean is small the results of both calculations agree when the linear damping coefficient  $\alpha$  is set to

$\Gamma |\langle \theta_t \rangle|$ . The periodic boundary model in turn provides a good approximation to the full numerical model of flux flow if restricted to the region around  $x = L/2$  where effects from the boundaries at  $x = \{0, L\}$  have diminished. The expressions for  $\theta_t$  and  $\psi_t$  in Eq. (17) are found to be a good approximation to the voltages at  $x=L$  in the full model if their magnitudes are doubled. This relation,  $\phi_t(x=L) = 2\phi_t(x=L/2)$ , is also found in a model for flux flow by Nagatsuma et al.<sup>10</sup> by applying standing wave theory. If the axial flux is not exactly  $\Phi = \Phi_0/2$ , the frequency in the  $\theta$  channel will drop from  $2\Omega$  to  $\Omega$ . We have not yet obtained an exact solution for this case, but the reason for this behavior can be understood by examining a potential energy plot like Fig. 2 for the case  $\Phi < \Phi_0/2$ . For this situation, the small peaks like a and c above the line  $\psi = \pi/2$  will be lower than those below the line, so that a particle rolling down the  $\psi = \pi/2$  ridge will have to go twice as far in  $\theta$  to get back to its original energy state as it would have when  $\Phi = \Phi_0/2$ . This doubling of the period then translates into a  $\theta$  frequency half that for the case  $\Phi = \Phi_0/2$  where the symmetry of states above and below  $\psi = \pi/2$  is not broken.

Operating an array of  $N=3$  systems in this manner as shown in Fig. 4, requires an external transverse magnetic field threading the  $\phi_1 \rightarrow \phi_N$  JJ's and parallel forcing currents  $I_1 = I_2 = \dots I_N$  applied across the array bottom to top. If the magnitude of the axial flux threading the array is increased or decreased away from  $\Phi = \Phi_0/2$ , the total rf voltage across the  $\psi_i$  array will diminish (with a concurrent increase in the rf voltage across the  $\theta_i$ ) while the stability of the flux flow state and the rf output frequency are not affected.

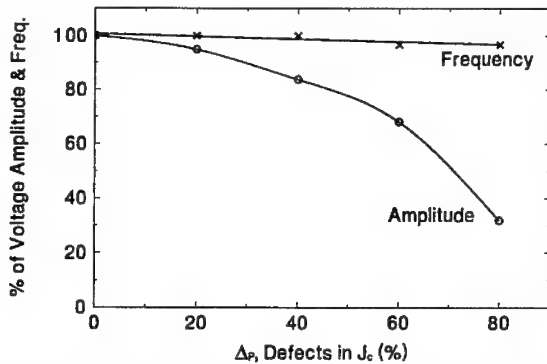


Fig. 5. Plot of the fundamental frequency  $\Omega$  and the amplitude of the Fourier transform of  $\Sigma\psi_{i,t}$  at  $\omega = \Omega$  vs.  $\Delta_p$ , the  $J_c$  defect magnitude.

We have also investigated the effect that a random distribution of JJ critical current defects will have on the stability of the array. Fig. 5 shows the rf power at the fundamental frequency resulting from a random distribution of defects  $\{r_i\}$  (where  $-1 \leq r_i \leq 1$ ) in the critical currents  $J_i$  and  $j_i$  of the array. The critical current  $J_i$  or  $j_i$  for each JJ is changed as  $J_i = J_{c0} \rightarrow J_{c0}(1 + r_i\Delta_p)$ , where  $\Delta_p$  is the defect magnitude. Thus  $\Delta_p=80\%$  implies that defects up to  $\pm 0.8J_{c0}$  are allowed. It can be seen that as the rf voltage drops to a minimum of 30% of zero defect voltage with up

to  $\pm 80\%$   $J_{c0}$  defects, the array is still able to find a stable operating equilibrium with minimal ( $-3\%$ ) change in rf frequency.

In Fig. 6 we have plotted the  $\psi_i$  junction voltages at  $x=L$  for an array with  $N_J = 6$  (11 JJ's) and  $\pm 60\%$  discrepancies in JJ critical currents. Although the voltage waveforms on each junction are distorted elliptic sinusoids, the sum of the lower (or upper)  $\psi_i$  junctions voltages  $V_L = \sum_{i \text{ odd}} [\psi_{i,t}]$  is practically sinusoidal as can be seen from the inset plot of  $V_L$  vs. frequency. Both the upper and lower total DC voltages  $\langle V_{U,L} \rangle$  are zero since there is no transverse forcing current. The rf voltages on the  $\psi_i$  junctions add in series and are found to increase as  $V_{U,L} \sim 1.7 \cdot (N_J - 1)/2$  as a function of array size. The impedance of the array is also expected to increase as  $(N_J - 1)$ , allowing the array to be matched to a load impedance.

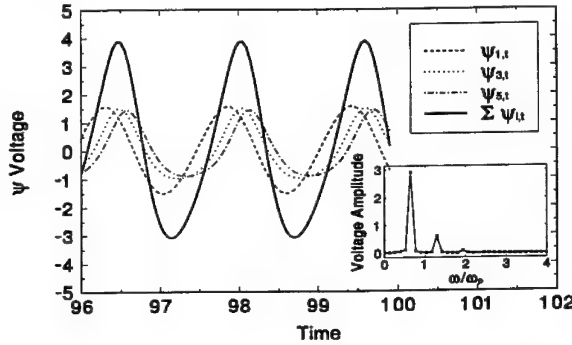


Fig. 6. Plot of  $\psi_i(x=L, t)$  voltage amplitudes and frequencies with random  $J_{c0}$  defects of  $\pm 60\%$  for  $N_J=6$ ,  $B_T=4$ ,  $L=20$ ,  $I_{bc}=1.1$ ,  $\eta=1$  and  $\alpha = .25$ . Inset: Amplitude of Fourier transform of  $\sum \psi_{i,t}$  vs. frequency.

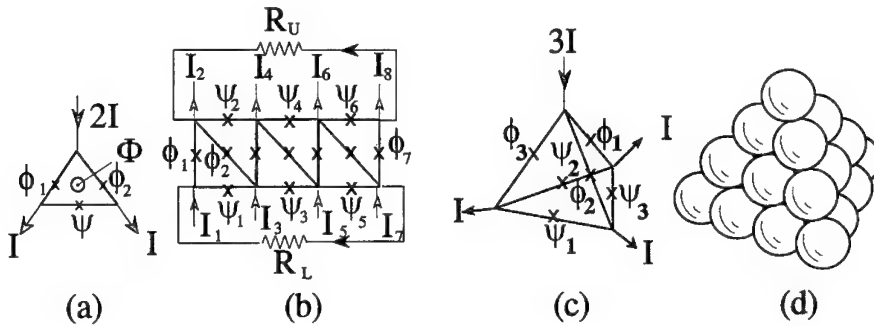


Fig. 7. Schematic drawing of (a) small JJ  $N=3$  triangular system, (b)  $1 \times (N_J - 1)$  triangular row array, (c) small JJ  $N=4$  tetrahedral system and (d) close packed spherical array.

A  $\delta x$  transverse slice of the array in Fig. 4 will form an array of short JJ's equivalent to one row of a 2D triangular array as shown in Fig. 7b. We have shown in



Ref. 11 that a stable triangular row array will result if the array can be considered as being built in a modular fashion with an  $N=3$  small JJ system (Fig. 7a) as the module. An exact solution for the  $N=3$  module can be obtained from the solution for the  $N=3$  long JJ system (Eq. 14) by taking  $x=0$ ,  $\Omega = (\gamma u / \sqrt{\kappa}) \pi / 2K$  and using a time average of the  $\theta$  equation of motion to determine the allowed frequencies<sup>11</sup>. Qualitatively the results for the 1 row array of  $N=3$  modules subjected to parallel forcing are the same as for the long JJ array. Both develop rf voltages and impedances across the transverse  $\psi$  JJ's that add in series. Both are able to reach a stable equilibrium with discrepancies in the  $J_c$ 's of all JJ's up to  $\pm 60\%$  while developing at least 65% of their zero defect power. If  $\Phi$  is changed away from  $\Phi = \Phi_0/2$ , the transverse rf voltages in both arrays will decrease, vanishing at  $\Phi=0$ . One difference is that for the small JJ array it is possible to change  $\Omega$  by changing the forcing current in a linear fashion along with a small  $\sim 10\%$  change in output voltage, while changing the forcing current in the long JJ array leads to larger changes in output voltage.

The short JJ version of the  $N=4$  long JJ system is a tetrahedral system of small JJ's with a forcing current applied as shown in Fig. 7c. Oscillations in the transverse JJ's are possible if the axial flux  $\Phi$  through each triangular face  $\psi_i \phi_{i+1} \phi_{i+2}$  does not differ from  $\Phi = \Phi_0/2$  by more than  $\Phi_0/4$ , i.e.  $|\Phi - \Phi_0/2| \leq \Phi_0/4$ . The transverse oscillations in the  $\psi_i$  JJ's will be centered around  $\psi_i = 2\pi/3$  for two of the three  $\psi_i$ 's and  $4\pi/3$  for the third  $\psi_i$  while the rf voltage amplitude for the third  $\psi_i$  will be the negative sum of the first two. There is also a phase shift of  $2\pi/3$  between adjacent  $\psi_i$ 's.

A three dimensional array of tetrahedral systems is possible based on the JJ array formed between adjacent spheres of a close packed spherical array of niobium balls. A planar triangular array, using niobium balls has already been successfully fabricated<sup>12</sup>. The simplest two layer tetrahedral array would thus represent a straightforward extension of this technique.

#### 4. Conclusions

We have outlined the symmetries and some of the possible interactions among the kink excitations that can exist for  $N=3$  and  $N=4$  long JJ systems with and without an axial magnetic flux of  $\Phi_0/2$ . When the symmetry of these systems is broken by non equal JJ critical currents, the kink excitations can be described in terms of  $1/2$  ( $N=3$ ) and  $1/3$  ( $N=4$ ) fluxon subkinks that persist (unless annihilated by a matching anti-subkink) throughout all interactions. These interactions are in general inelastic in contrast to the elastic interaction of solitons that can result only in a phase shift and no exchange of energy and momentum.

We have investigated using arrays of  $N=3$  systems, biased about an axial flux of  $\Phi_0/2$ , in the flux flow mode. This allows rf power to be developed in the transverse  $\psi$  JJ's with no DC voltage present. For a single  $N=3$  system, it is possible to obtain an exact solution in terms of Jacobi elliptic functions. For an array, the rf voltages and impedances of the  $\psi_i$  JJ's add in series, allowing the transverse oscillator array to be matched to an external load impedance. The flux flow arrays have been shown

to be stable with respect to large( $\pm 20\% \rightarrow \pm 80\%$ ) variations in JJ critical currents. The presence of the axial magnetic field allows the rf power to be switched from the  $\psi_i$  JJ's to the  $\theta_i$  JJ's with no change in output frequency. The 2D triangular and 3D tetrahedral analogs of these systems using small JJ's, can also be biased about an axial magnetic flux of  $\Phi_0/2$  to generate rf output from the transverse  $\psi_i$  JJ's. The one row triangular array has properties as a transverse oscillator, similar to those of the  $N=3$  flux flow array.

The effects of transverse circuit inductance on the stability of short junction arrays and the calculation of radiation linewidth will be addressed in future work.

#### Acknowledgements

This work was carried out with support from Air Force Office of Scientific Research (AFOSR).

#### References

1. R. Rajaraman, *Solitons and Instantons* (North-Holland, Amsterdam, 1982), p. 17.
2. S. Yukon and N. C. H. Lin, *IEEE Trans. Mag.* **27** (1991) 2736.
3. Y. K. Ha, *Phys. Rev.* **D29** (1983) 1744.
4. S. Homma and S. Takeno, *Prog. Theor. Phys.* **72**, (1984) 679.
5. A. M. Dikande and T. C. Kofane, *Phys. Scr.* **49** (1994) 110.
6. R. K. Bullough, P. K. Caudry and H. M. Gibbs, *Solitons* (Springer-Verlag, Berlin, 1980) p. 107.
7. S. Yukon and N. C. H. Lin, *IEEE Trans. Appl. Sup.*, Vol.3, no.1(1993).
8. S. Yukon and N. C. H. Lin, (to be published)
9. R. D. Parmentier, G. Costabile, *Rocky Mountain J. of Math.*, Vol.8, no.1,2 (1978) 117.
10. T. Nagatsuma, K. Enpuku, K. Yoshida and F. Irie, *J. Appl. Phys.* **56** (1984) 3284.
11. S. Yukon and N. C. H. Lin, submitted to *IEEE Trans. Appl. Sup.*, (6/1995).
12. F. Busse, P. Seidel, M. Darula, R. Nebel and P. Herzog *Int. Conf. Mat. & Mech. of Supercond. High-Temp. Superconductors*, M<sup>2</sup>S-HTSC IV, Grenoble, France(7/1994).

# SIMULATION OF COLLECTIVE EXCITATIONS IN A MODULATED JOSEPHSON RING

A. V. USTINOV

*Institute of Thin Films and Ion Technology, Research Center Jülich (KFA)  
D-52425 Jülich, Germany*

and

A. SHNIRMAN, Z. HERMON, E. BEN-JACOB

*School of Physics and Astronomy, Raymond and Beverly Sackler Faculty of Exact Sciences  
Tel Aviv University, Ramat Aviv 69978, Israel*

and

B. A. MALOMED

*Department of Applied Mathematics, School of Mathematical Sciences  
Raymond and Beverly Sackler Faculty of Exact Sciences  
Tel Aviv University, Ramat Aviv 69978, Israel*

## ABSTRACT

Dynamics of a soliton chain placed in a periodically modulated Josephson junction is investigated. In order to eliminate soliton collisions with boundaries, we consider a Josephson ring (annular Josephson junction). Due to the interaction of the solitons with periodically placed obstacles, collective excitations such as linear deformation modes of the soliton chain lead to new resonances which can be observed experimentally. Numerical results are found to be in good agreement with linear theory in an appropriate parameter range. In the relativistic limit, the simulations reveal a new dynamical mode which is characterized by a strongly nonlinear interaction between the moving solitons in the chain. On average, we find that in this regime one half of the elementary topological charge (equal  $\pi$  in the sine-Gordon system) is effectively moving along the junction. We suggest a qualitative explanation to this regime by an extrapolation of the linear behavior.

## 1. Introduction

Solitons in a long Josephson junction are superconducting Josephson vortices (magnetic flux quanta, or fluxons) described by the perturbed sine-Gordon equation. Since the first theoretical work by Lebowitz and Stephen<sup>1</sup>, collective excitations in a multi-fluxon chain have received very limited study. The reason probably is that in a typical experiment with homogeneous Josephson junctions it appears to be difficult to excite any collective mode except the progressive motion of a the fluxon chain as a whole, known as a flux-flow regime. The situation changes if some spatial modulations are present in the system. For the periodic fluxon chain it is natural to consider a periodically modulated medium (e.g., a long Josephson junction with a

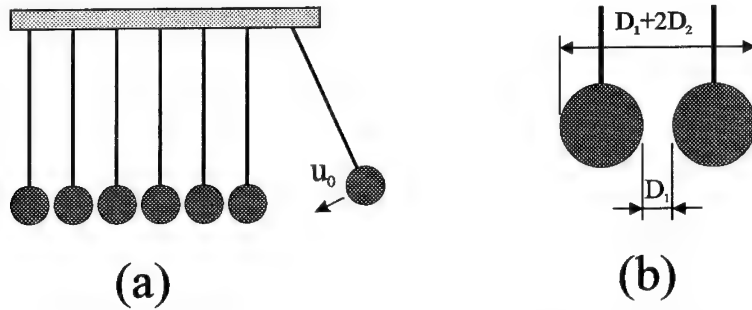


Fig. 1. (a) Mechanical analog: a chain of rigid balls as a simplest model for a chain of interacting solitons. (b) A fragment of the ball chain with its geometrical dimensions.

periodic lattice of obstacles). Linear effects, like coherent emission of linear waves by a chain of equidistant fluxons, produce additional resonance structure on the current-voltage characteristics of the Josephson junction<sup>2</sup>. Nonlinear collective excitations, called supersolitons (i.e. solitary excitations propagating in a pinned fluxon lattice), were found numerically<sup>3</sup> and investigated experimentally<sup>4</sup> and analytically<sup>5</sup>. Such excitations can be viewed as waves of the fluxon density.

Let us consider fluxons in one-dimensional long Josephson junction as rigid balls with the diameter  $D_2$  and the spacing between their surfaces  $D_1$  (Fig.1). Let also assume that the balls interact only if they touch each other. Since the long-range interaction between sine-Gordon solitons is exponential, this model can be viewed as a limiting case of Toda lattice with exponential interaction between the atoms, where fluxons play role of atoms in the lattice. A well-known example of a nonlinear collective excitation in this system is a localized shock wave excited when the last ball with the velocity  $u_0$  hits its neighbor, as shown in Fig.1(a). The speed of the propagating wave can be calculated as  $u_1 = u_0(D_1 + 2D_2)/D_1$ . If  $D_1 \rightarrow 0$ , the velocity  $u_1$  is limited only by the sound velocity inside the balls. This picture gives a rough idea for a similar sort of nonlinear density excitations which were recently found to exist in the fluxon lattice moving in the homogeneous junction with a strong external stimulation at its boundary. Fluxon density waves were first indicated by experiments<sup>6</sup> and later simulated numerically<sup>7</sup>.

In this paper, we focus on collective excitations in a fluxon chain (using the simplest version of it, consisting of two fluxons) trapped in a periodically modulated Josephson junction. In order to eliminate collisions with boundaries, we consider a Josephson ring (annular Josephson junction) with a periodic lattice of obstacles (inhomogeneities). This structure has recently been fabricated and studied in experiments<sup>8</sup>. Linear deformation modes ("phonons") in the fluxon chain excited by its interaction with the lattice of obstacles should bring about new resonances that can be observed experimentally. We compare the linear analysis with numerical simulations, and find good agreement in the appropriate parameter range. In the "relativistic" limit, the

numerical simulations reveal a new dynamic mode which is characterized by a strongly nonlinear interaction between moving fluxons in the chain. On average, we find in this regime one half of the elementary topological charge (equal  $\pi$  in the sine-Gordon system) effectively moving around the junction. We suggest a qualitative explanation to this regime by an extrapolation of the linear behavior. The analytical calculations in the linear approximation are presented elsewhere<sup>9</sup>, here, due to space limitations, we concentrate mainly on numerical results and discussion.

## 2. Model and numerical simulations

A long Josephson junction is governed by the following equation, known as the perturbed sine-Gordon equation, for the gauge-invariant phase difference across the barrier,  $\varphi$ :

$$\varphi_{tt} - \varphi_{xx} + \sin \varphi = \gamma - \alpha \varphi_t + \varepsilon_0 \sum_{m=1}^N \delta(x - Lm/N) \sin \varphi, \quad (1)$$

where  $\gamma$  is the bias current density,  $\alpha$  is the damping coefficient,  $\varepsilon_0$  is the amplitude of the obstacles,  $N$  is the number of obstacles, and  $L$  is the length of the junction. Lengths are measured in units of  $\lambda_J$ , the Josephson penetration depth, and time is measured in units of  $\lambda_J/\bar{c}$ , where  $\bar{c}$  is the Swihart velocity. We assume the periodic boundary condition:

$$\varphi(x + L) = \varphi(x) + 2n\pi, \quad (2)$$

which means that there are  $n$  trapped fluxons in the annular junction.

In numerical simulations we focused on the simplest case of  $n = 2$  trapped fluxons in a ring with  $N = 3$  obstacles, as illustrated by an inset in Fig. 2. The current-voltage characteristics for various values of the Josephson-junction length  $L$  were obtained by direct numerical simulations of the model (1) with the periodic boundary conditions (2). The current-voltage characteristic is given by the dependence of the average fluxon velocity  $v$  on the applied bias current density  $\gamma$ . In order to realize different fluxon densities, in simulations we varied the ring circumference  $L$  in the range from 3 to 12. The coefficient  $\varepsilon(x) \equiv \varepsilon_0 \sum_{m=1}^N \delta(x - Lm/N)$  was approximated by a more smooth hyperbolic function<sup>10</sup>. The details of numerical simulations are presented elsewhere<sup>9</sup>. In the characteristics shown below instead of the averaged total voltage  $V$  we plot the average velocity  $v = VL/(2\pi n)$  per fluxon, normalized to  $\bar{c}$ .

The calculated  $\gamma - v$  characteristic is shown in Fig. 2. The parameters are  $L = 5$ ,  $\alpha = 0.02$ ,  $\varepsilon_0 = 0.2$ , i.e., weak damping and rather strong modulation. This characteristic displays three very pronounced resonances at  $v$  just below 1.0, 0.5, and at about 0.25. The dynamic states corresponding to these three regimes are illustrated by Fig. 3, showing the evolution of the spatial derivative of the phase difference  $\varphi_x(x, t)$ . Physically,  $\varphi_x$  corresponds to a local magnetic field which has a maximum in the center of each fluxon. In Fig. 3 the field  $\varphi_x$  is shown as a function of  $x$  and  $t$  in a grey scale, with white parts corresponding to the highest values of the

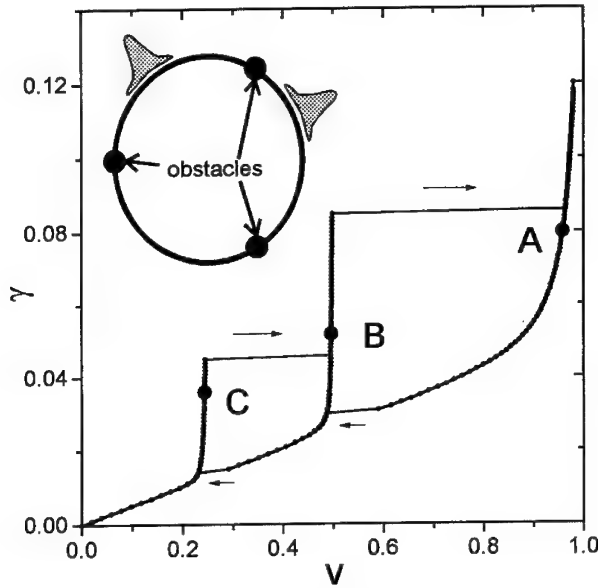


Fig. 2. The numerically calculated current-voltage curve for the Josephson ring, switches are indicated by the arrows. The inset shows a sketch of the simulated geometry: a Josephson ring containing 2 trapped fluxons and 3 equidistantly placed obstacles (inhomogeneities).

field. Thus, two white domains in Fig. 3(a) moving from right to left with increasing  $t$ , correspond to two fluxons moving with velocity close to the Swihart velocity ( $v = 1$ ). In contrast, the state shown in Fig. 3(b) indicates a solitary excitation moving in the opposite direction. This regime coincides with the so-called supersoliton mode<sup>3,5</sup>. In this mode, one may regard the two-fluxon state as a superposition of three static fluxons pinned by the three obstacles and a single anti-fluxon associated with the darkest area in Fig. 3(b) moving to the right.

The most interesting regime essential for the present work is the third one shown in Fig. 3(c). It looks somewhat surprising by its clear indication of a well-localized single light domain moving with almost the Swihart velocity to the left. If one assumes that this domain is the only localized kink which contributes to the dc voltage, this must be a  $\pi$ -like kink, and not the usual  $2\pi$ -kink of the sine-Gordon system. The dc voltage corresponding to  $v$  of about 0.25 is exactly one half of the voltage expected for a  $2\pi$ -kink moving with the Swihart velocity.

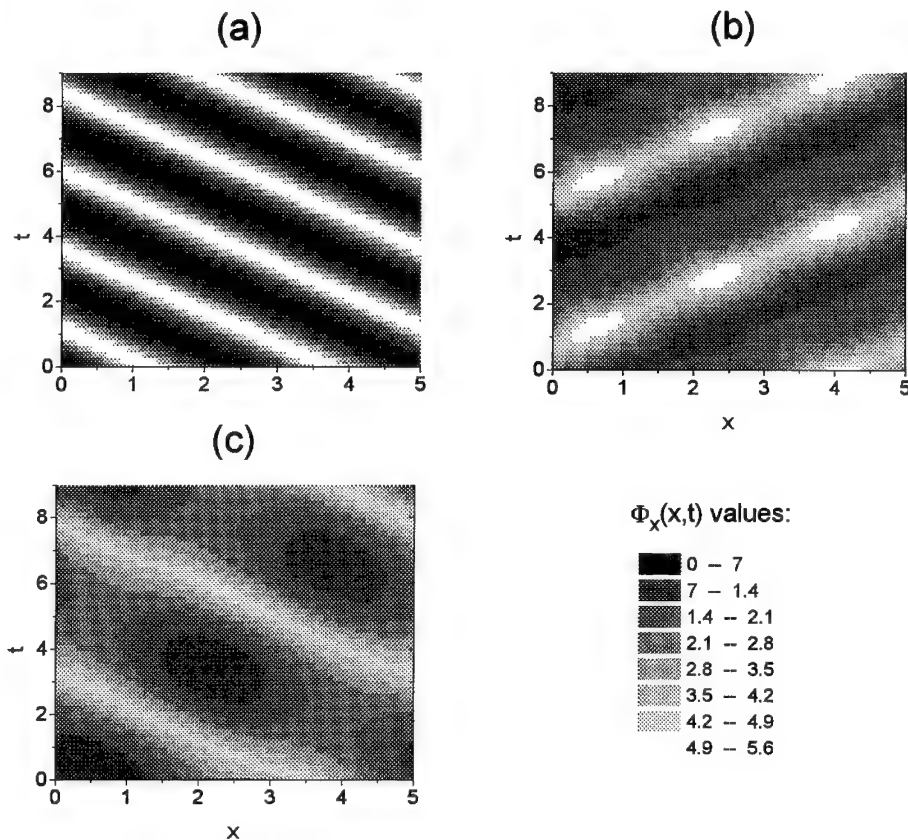


Fig. 3. The spatio-temporal evolution of  $\varphi_x(x, t)$  corresponding to different points of the current-voltage characteristic shown in Fig. 2 : (a) point A; (b) point B; (c) point C. The values for  $\varphi_x$  are given in grey scale.

### 3. Comparison with linear theory and discussion

In the linear case, one may expect a resonance due to a phonon-like excitation in the system of two interacting solitons. In this mode, the spacing between the solitons rotating in the ring does not remain constant but oscillates with time. The resonance is excited due to soliton collisions with obstacles.

Figure 4 shows a comparison of theoretical prediction of the linear theory<sup>9</sup> with the numerical data for the resonance step positions for rather strongly damped case ( $\alpha = 0.1$ ), using different lengths  $L$  of the ring with  $\varepsilon_0 = 0.1$ . Comparing the theoretical and numerical values, we see a good accord for  $L > 5$ , i.e., for the region where the analytical method produces  $v$  to be a decreasing function of  $L$ . For  $L < 5$ ,

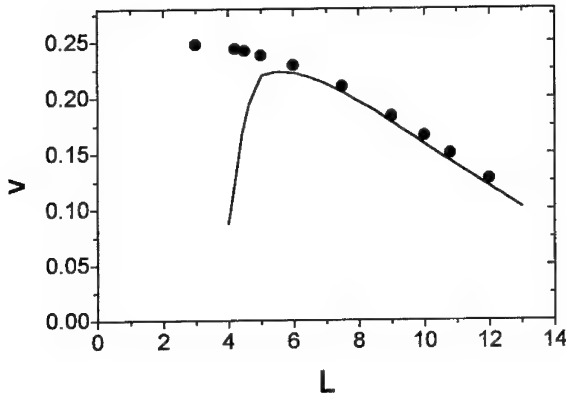


Fig. 4. Comparison of the numerical data (points) with the analytical result of the linear theory (continuous line) derived in Ref. [9].

numerical simulations show that  $v$  tends to saturate to the value 0.25 as  $L$  goes to zero. The failure of the analytical method in this region is expected<sup>9</sup>, since the linear approximation is valid for sufficiently long junctions only.

Similar saturation of the step position at  $v \approx 0.25$  has been also found for longer rings with as low damping as  $\alpha = 0.02$ . Furthermore, for  $L > 7.5$  the resonance is found to split in two. The lower resonance is very close to the prediction of the linear analysis (see Fig. 4), and the higher resonance remains close to the “golden value” of 0.25. In this regime we found a strongly relativistic dynamics with hard collisions of the well-localized fluxons.

Qualitatively, we can explain the nonlinear regime by an extrapolation of the linear behavior. In general, there is a phase shift of  $\pi/2$  between the vibration of the fluxons and the driving force produced by the obstacles. This is the well-known property of an oscillator driven by an external force. It means that when the driving force is minimal, the displacement of the oscillator is maximal, and vice versa. In our system, the force is maximal when one of the fluxons is exactly at the position of the obstacle. So, when the perturbation of the phase is maximal, one of the obstacles is exactly in the middle between two fluxons. Thus, when the two fluxons are closest to each other, one obstacle is located just between them. In the non-linear regime, where the amplitude of the vibration becomes large, the fluxons will eventually collide, and the collision will take place exactly at the location of one of the obstacles. The next collision should also occur at an obstacle. Since we have two fluxons and three obstacles, and 8.33), this can only happen if one of the fluxons reaches the nearest obstacle at the distance  $L/3$  away, exactly when the other fluxon reaches the same obstacle moving in the opposite direction, thus covering a distance twice as large,  $2L/3$ . Since the velocity of any fluxon is limited by the Swihart velocity, we conclude that the fast fluxon moves with almost the Swihart velocity, while the slower one has



to have, in average, half of this velocity in the opposite direction. The velocities are exchanged after each collision, just as with two identical massive particles. Thus, we obtain the time average velocity per fluxon to be about  $1/2$ . In Fig. 3(c) we find the localized moving light domain which indicates the fast fluxon only (due to the relativistic effect its  $\varphi_x$  amplitude is expected to be large), and fluxons exchange their velocities after each mutual collision.

Instead of this picture of two fluxons going back and forth between the collisions, one may think of two fluxons moving through each other without changing their velocities (this qualitative picture is somewhat less physical, as two fluxons repel each other). Since the ideal fluxons are solitonic solutions of the completely integrable sine-Gordon equation, the collisions are totally elastic, their sole effect being spatial shifts, which can be positive or negative. In our case the velocities of the colliding fluxons are opposite, therefore both spatial shifts are positive. These spatial shifts produce a contribution to the mean velocities, which renders them larger than the real velocities (between collisions). We have seen this effect in the two-dimensional plots. Recall, that the mean velocity of the fast fluxon seems to be the Swihart velocity. Still, we are not sure if this velocity is simply close to its limit value, or there is some general mechanism enforcing it to be exactly equal to the Swihart velocity.

### Acknowledgments

A.V.U. gratefully acknowledges the EEC grant ERB-CHEC-CT93-0101 which supported his participation at this conference. This work was partially supported by a Grant from the Israeli Ministry of Energy and a Grant from the Wolfson Foundation via the Israeli Academy of Sciences. One of us (Z.H.) thanks the Ministry of Sciences for a Ben-Gurion Ph.D. fellowship.

### References

1. P. Lebwohl and M. J. Stephen, *Phys. Rev.* **163** (1967) 376
2. B. A. Malomed and A. V. Ustinov, *Phys. Rev. B* **41** (1990) 254
3. A. V. Ustinov, *Phys. Lett. A* **136**(1989) 155
4. V. A. Oboznov and A. V. Ustinov, *Phys. Lett. A* **139** (1989) 481
5. B. A. Malomed, *Phys. Rev. B* **41** (1990) 2616
6. A. V. Ustinov, J. Mygind, N. F. Pedersen, and V. A. Oboznov, *Phys. Rev. B* **46** (1992) 578
7. O. H. Olsen, A. V. Ustinov, and N. F. Pedersen, *Phys. Rev. B* **48** (1993) 13133
8. I. V. Vernik, V. A. Oboznov, and A. V. Ustinov, *Phys. Lett. A*, **168** (1992) 319
9. A. Shnirman, Z. Hermon, A. V. Ustinov, B. A. Malomed, and F. Ben-Jacob, *Phys. Rev. B* **50** (1994) 12793
10. A. A. Golubov and A. V. Ustinov, *IEEE Trans. Magn.* **23** (1987) 781

## JOSEPHSON JUNCTION IRRADIATED WITH EXTERNAL rf FIELD — SOME NONLINEAR EFFECTS

MAREK JAWORSKI

*Institute of Physics, Polish Academy of Sciences, Al. Lotników 32/46  
02-668 Warszawa, Poland*

### ABSTRACT

The influence of external rf radiation on some nonlinear effects in a long Josephson junction is investigated. The model consists of the perturbed sine-Gordon (SG) equation with the driving rf field taken into account as the oscillatory boundary condition. The rf radiation is not treated perturbatively but enters the formalism directly as an exact multiperiodic solution of the unperturbed SG equation. In the next step, the dissipative term is included by using a simple perturbation scheme. As an example, the fluxon dynamics in the presence of external rf radiation is briefly discussed. The results are compared with those available from the literature as well as with direct numerical simulations.

### 1. Introduction

A long Josephson junction irradiated with an external rf field exhibits a variety of interesting nonlinear phenomena, such as excitation of breathers and/or plasma waves, hysteresis loop, flux-flow steps etc.<sup>1-4</sup> In particular, in Ref. 1 the fluxon dynamics under the influence of external radiation was investigated, with the rf driving field applied as an oscillatory boundary condition.

The aim of the present paper is twofold. First, we present a new version of the perturbation method, which can be applied to a general solution being a combination of nonlinear localized objects (fluxons, breathers etc.) and small-amplitude quasi-linear (plasma) waves. Second, we consider a problem similar to that discussed in Ref. 1, using however a more rigorous approach based on the exact solution of the unperturbed Sine-Gordon (SG) equation. As a result, we are able to derive approximate analytical expressions, describing the fluxon dynamics in the presence of an external rf field.

### 2. Model

We consider the perturbed SG equation<sup>5</sup> in the dimensionless form:

$$\phi_{xx} - \phi_{tt} = \sin \phi + \alpha \phi_t, \quad (1)$$

where  $\phi$  is the phase difference of the wavefunctions in both superconducting electrodes,  $\alpha$  is the loss parameter corresponding to dissipative currents.

The driving rf field enters the formalism as the oscillatory boundary condition at the right edge of the junction ( $x = 0$ ):

$$\phi_x|_{x=0} = a \cos \omega t, \quad (2)$$

where  $a$  denotes the amplitude of the rf field.

For simplicity we consider a very long junction ( $L \gg 1$ ) such that the reflection of the damped plasma wave from the left edge can be neglected.

Let us consider first the unperturbed (lossless) case ( $\alpha = 0$ ). It is well known that the general (exact) solution of the unperturbed SG equation can be expressed as follows<sup>6,7</sup>:

$$u = 2i \ln \frac{\Theta(\mathbf{z} + \mathbf{e}/2|B)}{\Theta(\mathbf{z}|B)}, \quad (3)$$

where  $B$  is a  $g \times g$  Riemann matrix,  $\mathbf{e}$  denotes the  $g$ -dimensional unit vector,  $\mathbf{z} \in C^g$  is a linear function of space and time coordinates  $z_j = k_j x + \omega_j t + z_j^0$  and  $\Theta(\mathbf{z}|B)$  denotes the  $g$ -dimensional Riemann theta function

$$\Theta(\mathbf{z}|B) = \sum_{\mathbf{n} \in Z^g} \exp(i2\pi \mathbf{n} \mathbf{z} + i\pi \mathbf{n} B \mathbf{n}). \quad (4)$$

Usually, the general solution consists of highly nonlinear localized objects (fluxons, breathers etc.) accompanied by small-amplitude contributions (plasma waves). Using the method presented in Ref. 8, one can linearize Eq. (3) in the presence of arbitrary nonlinear solution  $\phi_0$

$$\phi = \phi_0 + \sum_{i=1}^{\infty} q_i \psi_i, \quad (5)$$

where  $\phi_0$  denotes a highly nonlinear component of the solution while  $\psi_i$ 's are small-amplitude quasi-linear contributions.

In particular, at the boundary we have:

$$\left[ \phi_{0,x} + \sum_{i=1}^{\infty} q_i \psi_{i,x} \right]_{x=0} = a \cos \omega t, \quad (6)$$

and the coefficients  $q_i$  can be determined from (6) using standard methods.

When the dissipation term is small, we can treat it perturbatively and still use the Eq. (3) as an approximate solution, but allowing some of the parameters to be slowly varying functions of space and/or time coordinates.

In particular, the frequency of the plasma wave is fixed by the external rf source, while its amplitude becomes a "slow" (exponential) function of  $x$ . On the other hand,

a nonlinear localized object will change its dynamics as a result of perturbation, i.e. some dispersion parameters and consequently the velocity may be a "slow" function of time  $t$ .

Let us substitute the linearized solution into Eq. (1) and compare independently fast and slowly-oscillating terms. For the rapidly oscillating term we obtain modified dispersion relations:

$$\alpha\omega_i = 2k_i\mu_i \quad (7a)$$

and

$$\omega_i^2 = k_i^2 + 1 - \mu_i^2, \quad (7b)$$

where the propagation constant  $k$  has been replaced by  $k - i\mu$ .

The slowly-varying term yields a modified perturbed SG equation:

$$\phi_{0,xx} - \phi_{0,tt} - \sin \phi_0 = \frac{1}{2}(\sum q_i^2 \psi_i^2) \sin \phi_0 + \alpha \phi_{0,t}, \quad (8)$$

where  $\langle \cdot \rangle$  denotes the time average.

It should be noted that the term  $\sim \psi^2$ , although quadratic in the small parameter  $q$  has important consequences for the dynamics of the nonlinear part of the solution<sup>1</sup>.

Eq. (8) can be solved using one of the well known perturbation methods, e.g. based on the IST formalism<sup>9,10</sup> or using modified conservation laws<sup>10,11</sup>. In this way, we can investigate the influence of the external rf radiation on the dynamics of nonlinear components of the solution via the excitation of small-amplitude plasma waves.

### 3. Example

As an example, let us consider the fluxon interaction with a sinusoidal plasma wave excited by the external rf field.

It can be shown<sup>12</sup> that the general form of  $\psi$  for one fluxon interacting with a single plasma wave reduces to:

$$\psi = 8 [\cos \eta \cos(\pi\delta) - \sin \eta \sin(\pi\delta) \tanh \eta_0], \quad (9)$$

where  $\eta = kx + \omega t$ ,  $\eta_0 = (x - ut)/\sqrt{1 - u^2}$ ,  $u$  denotes the fluxon velocity,  $\delta$  is the fluxon-plasma interaction parameter, and for  $\alpha \neq 0$  the small parameter  $q$  should be replaced by  $q_0 \exp(\mu x)$ ,  $q_0 = a/(8\sqrt{k^2 + \mu^2})$ .

Fig. 1 shows the example of a fluxon interacting with a plasma wave in a very long junction for time  $t$  fixed.

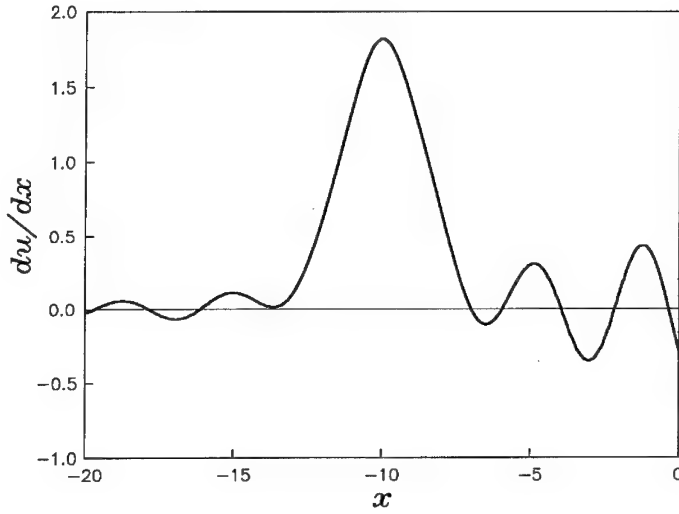


Fig. 1. A static fluxon interacting with a plasma wave in a long junction.  $\alpha = 0.2, a = 0.5, \omega = 2$ .

Evolution equation for the momentum  $P$  in the presence of perturbations can be written as:

$$\frac{dP}{dt} = -\frac{1}{2} \int_{-\infty}^{\infty} \langle \psi^2 \rangle \phi_{0,x} \sin \phi_0 dx - \alpha P, \quad (10)$$

where

$$P = - \int_{-\infty}^{\infty} \phi_{0,x} \phi_{0,t} dx, \quad (11)$$

$$\langle \psi^2 \rangle = \frac{a^2}{4(k^2 + \mu^2)} e^{2\mu x} \left( 1 - \frac{\sin^2(\pi \delta)}{\cosh^2 \eta_0} \right), \quad (12)$$

and we have extended the upper limit of integration to  $+\infty$ , since the integrands in Eqs. (10) and (11) are negligibly small at the junction edge.

Substituting the expression for the unperturbed kink into Eqs. (10) and (11) we can find the differential equation for the fluxon velocity  $u(t)$ :

$$\frac{du}{dt} = C_0(1 - u^2)^2 e^{2\mu u t} - \alpha u(1 - u^2), \quad (13)$$

where  $C_0$  can be evaluated precisely due to the analytical expression (9) for the plasma wave  $\psi$ .

Numerical results show that the fluxon velocity  $u$  is very small and nearly constant over the large time interval, thus the solution of Eq. (13) can be approximated by the solution of a transcendental equation with respect to  $u$ :

$$u = C_0 \left[ \frac{e^{2\mu u t}}{2\mu u + \alpha} - \frac{e^{-\alpha t}}{\alpha} \right]. \quad (14)$$

Fig. 2 shows a comparison of the fluxon trajectory resulting from numerical solution of Eq. (13), analytical estimate (14), and full numerical simulation of the perturbed SG equation<sup>1</sup> taken as a reference.

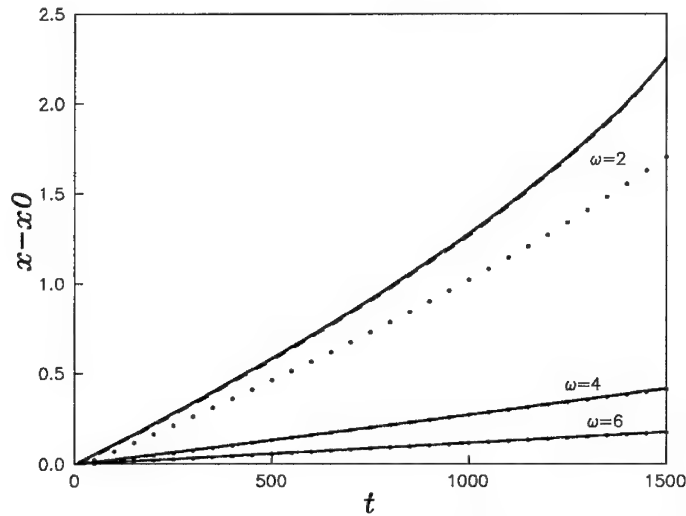


Fig. 2. Comparison of the fluxon trajectory resulting from numerical solution of Eq. (13) (solid line), analytical expression (14) (dashed line), and direct numerical simulation<sup>1</sup> (dotted line) for  $\alpha = 0.2, a = 0.5$ . The initial fluxon position is  $x_0 = -10$ .

One can see that  $u$  resulting from the approximate expression (14) reproduces perfectly the numerical solution of Eq. (13). On the other hand, the agreement with the full numerical results is good for lower frequencies ( $\omega = 2$ ) and excellent for higher.

In Fig. 3 we show similar results obtained for the higher rf field amplitude at the boundary ( $a = 1$ ). It is clear that the influence of the radiation of higher amplitude is much stronger. The fluxon driven by a rf radiation of lower frequency ( $\omega = 2$  and 3) accelerates and eventually hits the boundary.

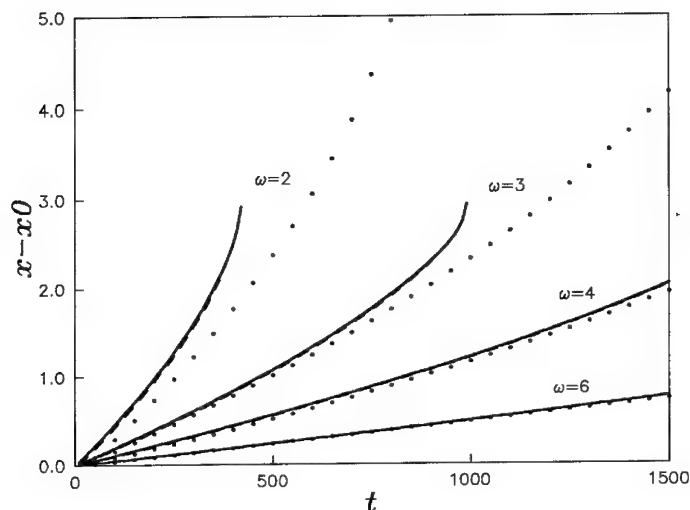


Fig. 3. The same as Fig.2 but for  $a = 1$ .

Again, for lower frequencies we can see rather good agreement with the numerical results, although for rapidly accelerating fluxon the perturbation approach fails at higher velocities. For higher frequencies, the agreement is again excellent.

#### 4. Conclusions

The results of this paper can be summarized as follows.

- (i) We present here a new version of the perturbation method which can handle effectively various problems arising from the influence of the external rf radiation on the junction dynamics.
- (ii) The method is more general and simultaneously more rigorous than various perturbative procedures reported recently, since it is based on exact analytical solutions of the SG equation, describing the interaction of nonlinear localized structures with small-amplitude plasma waves.
- (iii) An example of a fluxon interacting with a single plasma wave shows that the fluxon moves towards the boundary as a result of the driving rf field. Our analytical predictions agree well both with the perturbation results of Ref. 1 and direct numerical simulation of the perturbed SG equation.

#### Acknowledgements

This work was supported by the KBN grants No. PB2.0480.91.01 and 2.P302.179.06.

## References

1. Y. S. Kivshar, O. H. Olsen, M. R. Samuelsen, and A.V. Ustinov, *Phys. Rev.* **B47** (1993) 5212.
2. O. H. Olsen and M. R. Samuelsen, *Phys. Rev.* **B33** (1986) 595.
3. T. Nagatsuma, K. Enpuku, F. Irie, and K. Yoshida, *J. Appl. Phys.* **54** (1983) 3302.
4. A. V. Ustinov, J. Mygind, N. F. Pedersen, and V. A. Oboznov, *Phys. Rev.* **B46** (1992) 578.
5. A. Barone and G. Paterno, *Physics and Application of the Josephson Effect* (Wiley, New York, 1982).
6. V. O. Kozel and V. P. Kotlarov, *Dop. AN UkrSSR* **A10** (1976) 878, (in Ukrainian).
7. M. G. Forest and D. W. McLaughlin, *J. Math. Phys.* **23** (1982) 1248.
8. M. Jaworski, in *Future Directions of Nonlinear Dynamics*, eds. P. L. Christiansen, J. C. Eilbeck, and R. D. Parmentier (Plenum, New York, 1993).
9. D. W. McLaughlin and A. C. Scott, *Phys. Rev.* **A18** (1978) 1652.
10. Y. S. Kivshar and B. A. Malomed, *Rev. Mod. Phys.* **61** (1989) 763.
11. P. L. Christiansen and O. H. Olsen, *Wave Motion* **4** (1982) 163.
12. M. Jaworski, *Phys. Lett.* **A125** (1987) 115.



# VORTICES IN CONTINUOUS JOSEPHSON MEDIUM

J. ZAGRODZIŃSKI

*Institute of Physics, Polish Academy of Sciences  
al. Lotników 32/46, 02-668 Warszawa, Poland, email: zagro@ifpan.edu.pl*

## ABSTRACT

Dynamic processes in a continuous plane Josephson medium are discussed. An approach starting from the Hamiltonian coincides on the static level with those starting from the discrete Josephson array. Some elementary excitations are reported. A modified density of 2D Hamiltonian is proposed which coincides with known results in 1D case, but it is also invariant with respect to the rotation of a coordinate system. For the axially symmetric problem relevant equations reduce to ode, whose solutions can have a vortex character with the same asymptotics as it follows from the spin-glass models. In a time dependent case, the vortex solution of the solitary wave type was found.

There are two reasons for considering the continuous limit of the discrete Josephson structures, such as 2D regular or hexagonal arrays of Josephson junctions. The first reason is that the plane arrays are fabricated containing more than 20000 junctions and then the collective effects can have an essential significance. The second one is related to the models of HTcS materials, where a lot of properties are ascribed to the tunneling effects between the neighbor grains. For the man-made artificial structures one can accept the dependence of a concrete geometry in contrast to the case of the granular medium, where a model should be invariant with respect to the rotation of a coordinate system in the plane of the film. The consideration of the continuous limit has also another positive feature: it allows one to clarify some details of the commonly discussed models less legible as the discrete ones and to compare the different models among themselves.

The model should be self-consistent in the sense that starting from either Lagrange or Hamilton formalism one obtains the same system of field equations and the discrete model pendant to the continuous one should exist.

There is a numerous literature of the problem. Here, we mention the papers<sup>1-7</sup>.

In the first paper the field equations are derived starting from a discrete or loop model<sup>1</sup>. In the second one, authors were trying to determine the energy of a structure, proposing certain form of the Hamiltonian<sup>2,3</sup>.

The next requirement concerns the invariance with respect to a rotation of the coordinate system. If the stochasticity is not involved, the model pretending to be useful for HTcS granular materials must be invariant with respect to the rotation of coordinate systems, (SO2-group). In order to elucidate the problem, we intend to consider and to compare the continuous limits of the two most popular models.

The first model is the commonly known XY-model used recently in the spin-glass theory<sup>2,3</sup>. The second one was originally starting from regular array of Josephson

junctions, but can be also derived from a Hamiltonian<sup>4,5</sup>. The continuous limit of the first model automatically is invariant with respect to SO(2)-group in contrast to the second one, where we propose some modification. Its consequences leading to a new equation describing the vortices will be discussed in the sequel.

As the first one, let us consider the continuous limit of the XY-model formed by a regular array of superconductive islands, e.g.<sup>2,3</sup>. To each island the order parameter  $\Theta_i$  is ascribed and the Josephson junctions are formed between adjacent islands. Since the whole structure can be embedded in the external magnetic field, whose potential  $\mathbf{A}$  is given, for each pair of neighbor islands the following integrals are defined:

$$A_{ij} = \int_i^j \mathbf{A} d\mathbf{l}. \quad (1)$$

Sometimes the quantity  $f$ , known as a frustration, is introduced too

$$\sum_{\text{plaquette}} A_{ij} = f\Phi_o, \quad (2)$$

where  $\Phi_o$  is the flux quantum and the sum is taken over all sites of plaquette.

One considers Hamiltonian

$$\mathcal{H} = J \sum_{\langle i,j \rangle} (1 - \cos(\Theta_i - \Theta_j + A_{ij})), \quad (3)$$

where  $J$  is the coupling constant and the minimization of Hamiltonian (3) leads to

$$\sum_i \sin(\Theta_i - \Theta_j + A_{ij}) = 0, \quad (4)$$

which obviously represents the Kirchhoff equations for  $j$ -th node that the sum of all currents at each node vanishes, if the currents between  $i$ -th and  $j$ -th nodes are given by

$$I_{ij} = \sin(\Theta_i - \Theta_j + A_{ij}). \quad (5)$$

It is worthwhile to point out that in this model the magnetic field is fixed and considered as a parameter of a model.

A certain purely mathematical statement can be helpful. For any regular function  $g(x, y)$ , one can prove that

$$\lim_{\Delta x \rightarrow 0} \sum_{k=1}^N \sum_{m=1}^N \{1 - \cos[g(x_k, y_m)\Delta x]\} = \frac{1}{2} \int_0^L \int_0^L g^2(x, y) dx dy, \quad (6)$$

where  $N = L/\Delta x$ ,  $x_k = (k + 1/2)\Delta x$ ,  $y_m = (m + 1/2)\Delta x$ . Equation (6) was used already in the past, but as an approximative one<sup>4</sup>.

Applying the reported theorem (6) to (3) we obtain the continuous limit of Hamiltonian density

$$\mathcal{H} = \frac{1}{2} \int_0^L \int_0^L (\nabla\Theta + \mathbf{A})^2 dx dy, \quad (7)$$

with a condition of minimalization

$$\text{div}(\nabla\Theta + \mathbf{A}) = 0, \quad \text{or} \quad \Delta\Theta = -\text{div}\mathbf{A}, \quad (8)$$

which can be derived also as a limit of the Kirchhoff relation. This means that in the limit, the density of the current is given by

$$\mathbf{j} = \nabla\Theta + \mathbf{A}. \quad (9)$$

Equation (8) is essential for the determination of the vortices. Let us observe that it is linear in  $\Theta$  and the nonhomogeneous term is equal to  $-\text{div}\mathbf{A}$ . It means that the solution of (8) is determined up to the solution of homogeneous equation

$$\Delta\Theta = 0. \quad (10)$$

A particular solution of (10) is known as a single vortex in the XY-model (see e.g.<sup>2)</sup> and when centered at point  $r = \sqrt{x^2 + y^2} = 0$ , it is given by

$$\Theta_1 = \arctan(y/x) = \varphi, \quad (11)$$

where  $\varphi$  represents an angular coordinate in the cylindrical coordinate system  $(r, \varphi)$ . Here we obtained this formula as an exact solution of the limiting equation (8). Since  $\nabla\Theta = \mathbf{e}_\varphi/r$ , where  $\mathbf{e}_\varphi$  is an "angular" versor in the cylindrical coordinate system, the integral over a closed contour surrounding the vortex is

$$\oint \nabla\Theta dl = 2\pi. \quad (12)$$

Note, however, that this quantity is not quantized since the equation is linear and hence the flux (12) is determined up to a constant. Thus the vortex is always represented by a singular solution of (10), even when  $\text{div}\mathbf{A}$  vanishes.

In the sequel we would like to show that in a model starting from the loop representation the situation is slightly different, i.e. the vortex is given by the equation for a vector quantity.

In the paper<sup>1</sup>, the field equation was derived starting from the regular array containing horizontal and vertical short Josephson junctions. The "milestones" were here:

1. the Kirchhoff equations for the currents at each node,
2. the fluxoid equations for each closed loop,
3. the first Maxwell equation, which in discretized version reduces to the relation between the jump of the magnetic field when the line with the current is crossed.

The same equations can be derived starting either from the Lagrangian or from the Hamiltonian with densities<sup>4,5</sup>

$$\mathcal{L} = \frac{1}{2}(\mathbf{Q}_i^2 - \text{rot}^2 \mathbf{Q}) - \sum_{i=1}^2 (1 - \cos Q_i), \quad (13)$$

$$\mathcal{H} = \frac{1}{2}(\mathbf{Q}_i^2 + \text{rot}^2 \mathbf{Q}) + \sum_{i=1}^2 (1 - \cos Q_i), \quad (14)$$

respectively, where  $\mathbf{Q} = (\varphi_h, \varphi_v)$  and in the discretized version  $\varphi_h, \varphi_v$  represent the phase differences of horizontal and vertical junctions, respectively. In the continuum version they represent simply the two independent quantities. Using a standard technique and considering  $\varphi_h, \varphi_v$  as independent ones, we obtain the system of equations

$$\varphi_{h,yy} - \varphi_{v,xy} = \sin \varphi_h - \varphi_{h,tt}, \quad \varphi_{v,xx} - \varphi_{h,xy} = \sin \varphi_v - \varphi_{v,tt}, \quad (15)$$

where terms on the right hand sides represent the full currents, (a dissipation is neglected).

Similar relations, but in a form of a system of three equations for three independent quantities can be derived in case of hexagonal array<sup>6</sup>.

As it was mentioned, manipulating with solutions of sine Gordon equation (sGe) one can find particular solutions of the above system<sup>7</sup>. Firstly, let us observe that when  $\varphi$ -functions depend on one space coordinate only, the system is splitted into two independent sGe's.

Another recipe follows from the statement: if  $\Phi(\zeta, \tau)$  satisfies sGe:  $\Phi_{,\zeta\zeta} - \Phi_{,\tau\tau} = \sin \Phi$ , then the functions  $\varphi_v = \Phi(\delta x + t, -\epsilon \delta y + t)$  and  $\varphi_h = \epsilon \varphi_v + \pi$  (with  $\epsilon = \pm 1$  and  $\delta = \pm \sqrt{2}$  independently) satisfy the system (15). As it is seen, solutions of this type have a dynamic character, but as a starting point the soliton, quasi-periodic, positon or another solution of sGe can be chosen.

One can look for the traveling wave solutions in the form  $\varphi_h = \varphi_h(z)$ ,  $\varphi_v = \varphi_v(z)$  with the argument  $z = \kappa x + \nu y + \omega t$ . Then the system (15) reduces to the system of ode's with dynamic and static branches. Reader is referred to the paper<sup>7</sup>, where the problem was discussed in the past.

Comparing (3) with (15), one can suppose that when the vector and scalar potentials are considered as independent generalized coordinates, the suitable density of Lagrangian would have a form identical as (14), where in place of  $\mathbf{Q}$  the quantity  $\nabla \Theta + \mathbf{A}$  is substituted

$$\mathcal{L} = \frac{1}{2} [(\nabla \Theta + \mathbf{A})_{,i}^2 - \text{rot}^2 \mathbf{A}] - \sum_{i=1}^2 [1 - \cos(\nabla_i \Theta + A_i)] \quad (16)$$

We assume that the appearing quantities are regular, such that  $\text{rot}(\nabla \Theta) = 0$ . But now there is a question about the choice of independent quantities. Previously, in the 2+1 problem we had two quantities:  $\varphi_v$  and  $\varphi_h$ . Now, according to any textbook, it seems we have three of them:  $A_1, A_2$  and  $\Theta$ , i.e. a vector potential and a scalar potential (or its integral vs. time  $\Theta$ , which does not change the problem). A clarification of this problem leads to a correct construction of Hamiltonian and next to the compatibility of the equations which follow either from Lagrangian or Hamiltonian. We

intend to discuss these apparent discrepancies, being aware, however, of an important attempt of a choice of a suitable form of Hamiltonian made in<sup>2</sup>.

The standard procedure requires a calculation of functional derivatives

$$\frac{\delta \mathbf{L}}{\delta \mathbf{A}} = 0, \quad \text{and} \quad \frac{\delta \mathbf{L}}{\delta \Theta} = 0, \quad (17)$$

where by  $\mathbf{L}$  we understand a full Lagrangian and the first equation represents in fact two equations with derivatives with respect to  $A_1, A_2$  (in the 2+1 problem). An elementary calculation gives the equations

$$\text{rot} \mathbf{A} + (\mathbf{A} + \nabla \Theta)_{,tt} + \sin(\mathbf{A} + \nabla \Theta) = 0, \quad (18)$$

$$\text{and} \quad \text{div}[(\mathbf{A} + \nabla \Theta)_{,tt} + \sin(\mathbf{A} + \nabla \Theta)] = 0, \quad (19)$$

respectively. Note that the first equation is isomorphic with the system (15) and, if the functions are regular, the second equation follows from the first one. A standard definition of canonical momenta leads to relations

$$\mathbf{p} := \frac{\delta \mathbf{L}}{\delta \mathbf{A}_{,t}} = (\mathbf{A} + \nabla \Theta)_{,t} \quad \text{and} \quad p_0 = \frac{\delta \mathbf{L}}{\delta \Theta_{,t}} = -\text{div} \mathbf{p}. \quad (20)$$

Now the Hamiltonian can be defined and for its density we have

$$\mathcal{H} = \frac{1}{2} [(\nabla \theta + \mathbf{A})^2 + \text{rot}^2 \mathbf{A}] + \sum_{i=1}^2 [1 - \cos(\nabla_i \theta + A_i)]. \quad (21)$$

The field equations calculated from the Hamiltonian should coincide with those calculated from Lagrangian. Indeed, the "first" Hamilton equations lead to

$$\mathbf{p}_{,t} := -\frac{\delta \mathbf{H}}{\delta \mathbf{A}} \quad \text{and} \quad p_{0,t} = -\frac{\delta \mathbf{H}}{\delta \Theta} \Rightarrow (18) \quad \text{and} \quad (19), \quad (22)$$

respectively, as should be, but the "second" ones, to

$$\mathbf{A}_{,t} := \frac{\delta \mathbf{H}}{\delta \mathbf{p}} \quad \text{and} \quad \Theta_{,t} = \frac{\delta \mathbf{H}}{\delta p_0} \Rightarrow \nabla \Theta_{,t} = 0 \quad \text{and} \quad \Theta_{,t} = 0, \quad (23)$$

respectively. The last result is of course unacceptable confining the processes to those for which  $\Theta_{,t} = 0$ .

The reason of a discrepancy between the Lagrangian and Hamiltonian formalism is the presence of the term  $\nabla \Theta_{,t}$ , which can be considered as a gradient of a generalized velocity, and its presence in Lagrangian usually is not permitted. One can show, that if this term appears in Lagrangian, "second" Hamilton equations (22) cease to be valid<sup>4,5</sup>.

Since the consideration of  $\Theta$  as an independent quantity leads to the dependent equation (19) or quantities as  $p_0$  in (20), the simplest remedy lies in a choice of generalized coordinates. Instead of  $\mathbf{A}$  and  $\Theta$ , as the generalized coordinates one can choose components of the vector  $\nabla \Theta + \mathbf{A}$ , which leads to the previously considered

situation if  $\mathbf{Q}$  in (13) and (14) will be interpreted as  $\mathbf{Q} = \nabla\Theta + \mathbf{A}$ . Then  $\Theta$  will be only a gauge parameter.

Thus we have a new interpretation of  $\mathbf{Q}$ : either  $\mathbf{Q} = (\varphi_h, \varphi_v)$ , or  $\mathbf{Q} = \nabla\Theta + \mathbf{A}$ , which means that the functions  $-\varphi_h$  and  $-\varphi_v$  in a continuous model can be interpreted as components of a vector potential in case of trivial gauge  $\Theta = 0$ . The Hamiltonian has of course the form (14) and the field equation - the form (18). Instead of (22), we get the identity  $\mathbf{Q}_{,t} = -\delta\mathbf{H}/\delta\mathbf{p} = -\delta\mathbf{H}/\delta\mathbf{Q}_{,t} = \mathbf{Q}_{,t}$ .

The following question arises: if in the XY approach a vortex is related to the singular solution  $\Theta$ , according to (10), where now, in case of a zero gauge are the vortices hidden? The answer is straightforward: the vortices are determined by a singular solution  $\mathbf{A}$  of (18). Indeed, looking for the axially symmetric solution in the form of  $\mathbf{A} = f(r) \mathbf{e}_\psi$ , (in the cylindrical coordinate system  $r, \psi$ , where  $\mathbf{e}_\psi$  represent a versor in  $\psi$  direction) and adopting a simplification  $\sin(\mathbf{A}) \simeq \sin[f(r)]\mathbf{e}_\psi$ , the function  $f(r)$  should satisfy the equation which has singular solutions

$$f''(r) + f'(r)/r - [f(r)/r^2 + \sin f(r)] = 0. \quad (24)$$

Note, that equation (24) appears as a result of a simplified approach here, where the simplification is rather hard to justify, since we deal with singular solutions. We shall show below that there exists a model from which equation (24) follows as a natural and exact consequence.

Equations (18) are of course not invariant with respect to a rotation of the coordinate system in the plane  $x, y$ , as well a starting model in form of a regular array. If the continuous Josephson medium has to pretend to be a model of a granular film structure (2D) with small grains and junctions formed between them, the equations should be invariant with respect to rotations in the plane of structure. It can be done either introducing an average procedure over all possible oriented realizations or by a suitable modification of starting quantities, first of all - the Lagrangian. We shall discuss just this last eventuality. Our idea is to modify the Lagrangian in such a way that it will be invariant with respect to the SO2 group and it would be reduced to (13) when 1D structure is considered. Observe that in expression (13) the term which violates invariance is related to the sum with cosine functions and the Lagrangian will be invariant if the invariant quantity is chosen as an argument of cosine function. The simplest operation on a vector giving the invariant quantity is the calculation of its length. This is the reason that we devote the last part of this paper to the consequences of the rotationally invariant Lagrangian in the form

$$\mathcal{L} = \frac{1}{2} [(\mathbf{Q}_{,t})^2 - \text{rot}^2 \mathbf{Q}] - [1 - \cos |\mathbf{Q}|], \quad \text{where } \mathbf{Q} = \nabla\Theta + \mathbf{A}, \quad (25)$$

with components of the vector  $\mathbf{Q}$  being a generalized coordinate. Then the Hamiltonian takes a form

$$\mathcal{H} = \frac{1}{2} [(\mathbf{Q}_{,t})^2 + \text{rot}^2 \mathbf{Q}] + [1 - \cos |\mathbf{Q}|], \quad (26)$$

and field equations following either from the Lagrangian or Hamiltonian<sup>4,5</sup>

$$\text{rot} \text{rot} \mathbf{Q} + \mathbf{Q}_{,tt} = \mathbf{Q} \sin |\mathbf{Q}| / |\mathbf{Q}|, \quad (27)$$

and it also has a rotationally invariant form. It is clear that when  $\mathbf{Q}$  is considered as one dimensional vector then (27) reduces to sGe. Let us consider the static and axially symmetric solution of the above equation. Substituting, as previously  $\mathbf{Q} = f(r) \mathbf{e}_\psi$ , in the static case, equation (27) reduces to (24), but now it does exactly. Neglecting the sinus operation in (24), we have the Bessel equation  $f'' + f'/r - (f/r^2 + f) = 0$ , whose singular solution is given by the Mac Donald function  $K_1(r)$ . Close to the point  $r = 0$ , the function  $K_1(r)$  has an asymptotic evaluation  $\sim 1/r$ . Hence one obtains a known relation of the flux "quantum" as  $\lim_{R \rightarrow 0} \oint K_1(r) dl = 2\pi$ , where the integration is over a circle of radius  $R$ , surrounding the point  $r = 0$ . Because of a relation with the Bessel equation, it is natural to name equation (24) - the sinus-Bessel equation (sBe), in analogy to sGe.

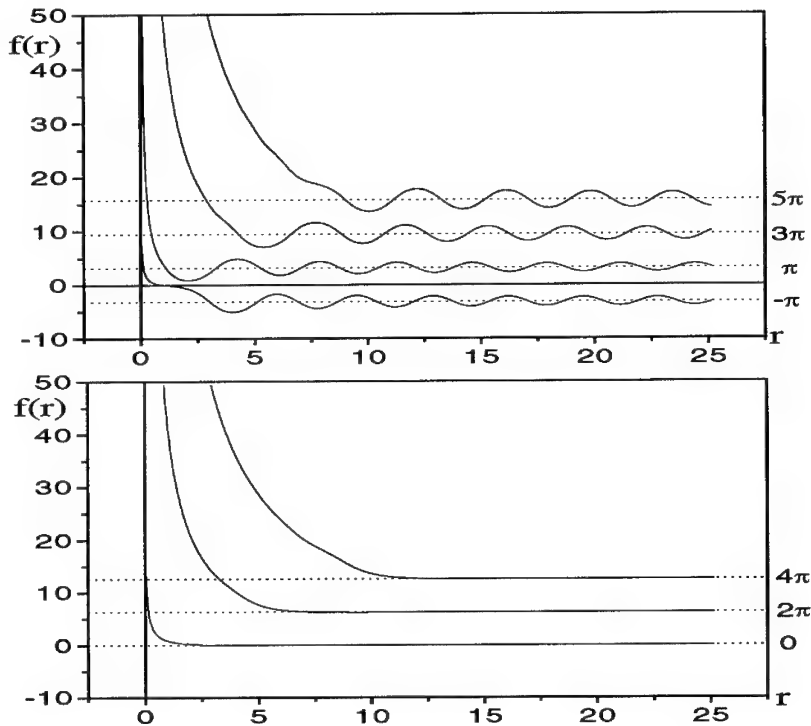


Fig.1. Sine-Bessel equation singular solutions with the different asymptotic behaviour at infinity.

It is easy to deduce that the solutions of sBe bounded at infinity asymptotically tend to  $n\pi$ , where  $n$  - integer. There are two classes of solutions: the regular ones at  $r = 0$ ,  $(f(r) \sim C_1 r + C_2 r^2 + \dots, C_i - \text{const})$  and the singular ones  $(f(r) \sim G_{-1}/r +$

$G_0 + G_1 r + \dots, G_i - \text{const}$ ). For singular solutions, as for the Mac Donald function mentioned before, we have a similar evaluation

$$\lim_{R \rightarrow 0} \oint_{C_R} f(r) dl = 2\pi G_{-1}, \quad (28)$$

and  $G_{-1}$  can be considered as a flux associated with the axially symmetric vortex determined by the singular solution  $f(x)$  of sBe. Some singular solutions of sBe with asymptotics at infinity  $n\pi$ , with  $n$  odd and even are presented in Fig. 1.

Thus, the vortex, which in the XY approach is described by a singular  $\Theta$ -solution, now, in a case of a trivial gauge, is described by a singular solution of **A**, which has quite the same asymptotic behavior. We would like to stress that as in case of the XY approach and also now, there is no single solution having close to zero  $1/r$  asymptotics, but there is a family of them. In the XY approach it is a consequence of the fact that equation (10) is linear and thus its solution is determined up to an arbitrary constant and hence the flux, too. In the frame of the approach presented here, there is another reason since the equation we deal with is nonlinear. The details are explained in the paper<sup>4</sup>, where it is shown that for fixed point  $r_0$  there exist the curves  $f'(r_0) + f(r_0)/r_0$  vs.  $r_0 f(r_0)$  that solutions exist. This means that the flux related to a vortex is also here not quantized.

One can also construct here a single vortex traveling solution (which in the soliton theory would be a solitary wave). If  $f(r)$  is the solution of sBe (24), then

$$\mathbf{q}(x, y) = [-y\mathbf{e}_x + \beta(x - vt)\mathbf{e}_y]f(\rho)/\rho \quad (29)$$

where  $\rho = [\beta^2(x - vt)^2 + y^2]^{1/2}$ ,  $\beta = (1 - v^2)^{1/2}$ , and  $\mathbf{e}_x, \mathbf{e}_y$ —versors, represents the solution of (27) i.e. the vortex traveling in  $x$ -direction with a velocity  $v$ . Note that the circular cross section of static vortex becomes elliptic one when it moves.

### Acknowledgements

The author is grateful to M. Jaworski, S. Lewandowski and R. Pawlikowski for stimulating discussions. The paper was supported by KBN Grants No. 2-0480-91-01 and 2-P302-179-06.

### References

1. K. F. Nakajima and Y. Sawada, *J. Appl. Phys.* **52** (1981) 5732.
2. T. P. Orlando *et al.*, *Phys. Rev.* **B43** (1991) 10218.
3. E. K. F. Dang and B. L. Gourff, *Phys. Rev.* **B47** (1993) 3290.
4. J. Zagrodziński, *Phys. Rev B* (to be published 1994).
5. J. Zagrodziński, *1993 Interdiscip. Workshop on Nonlin. Coher. Struct. in Physics and Biology*, Bayreuth, Germany, (Plenum Press 1994).
6. J. Zagrodziński, *Future Directions of Nonlin. Dynamics in Phys. and Biol. Systems*, (Plenum Press, NATO ser.ASI 1993) 367
7. J. Zagrodziński, *Physica* **C180** (1991) 216.



# SOLITARY-WAVES IN 2-D JOSEPHSON TUNNEL JUNCTION

J.C. FERNANDEZ\*

CNRS - C4I, Centre de Recherche Universitaire  
Archamps, F-74166 France

and

T. DODERER, G. FILATRELLA, R.P. HUEBENER, S.G. LACHENMANN

*Lehrstuhl Experimentalphysik II,  
Universität Tübingen, Auf der Morgenstelle 14,  
D-72076 Tübingen, Germany*

## ABSTRACT

We observed a Zero Field current Step (ZFS) in several square Josephson tunnel junctions of intermediate size (i.e. size  $\simeq \lambda_j$ ). Using simple physical arguments we explain this step as the signature of a particular dynamical pattern in a two-dimensional sine-Gordon system. This pattern looks like a solitary wave moving along the two diagonals of the junction. A reasonable idea of the stability of such modes is numerically showed. The invariance of the total length of the  $\pm 2\pi$ -wavefronts constituting the pattern plays an important role to ensure this stability. For that reason we call that Isoperimeter Pattern Dynamics (IPD). This invariance is consistent with energy conservation considerations. The dynamical behavior is also investigated using Low Temperature Scanning Electron Microscopy (LTSEM). Finally numerical simulations are performed to simulate the effect of the LTSEM "hot spot" on the IPD. The comparison between experimental LTSEM data and numerical simulations, pleads for the validity of the IPD model in order to explain the observed ZFS.

## 1. Introduction

Long Josephson tunnel junctions are good candidates for studying the dynamics of perturbed sine-Gordon solitons <sup>1,2</sup>. In these Josephson junctions the vortex (also called fluxons) are "bounded" by a current loop connecting surface currents in the superconductors and Josephson current (due to electrons pair tunneling) crossing the insulator, through which flows a magnetic flux quanta oriented parallel to the barrier surface.

Up to now, most of the experimental, theoretical, and numerical studies deal with one-dimensional junctions. A question arise to know if we can recover a kind of such vortex <sup>3,4</sup> or solitary wave in two dimensions (2-D) square junctions of cross type geometry <sup>1</sup>. Following the mathematics developpments, the answer to the question — does exist a 2-D soliton solution for the 2-D sine-Gordon equation ? — , is

\*Permanent Adress: CNRS - URA 1279, Rue A. Einstein, Sophia Antipolis, F-06560 Valbonne Cedex, France.

definitely no. Nevertheless the stability of soliton type solutions is so strong, mainly due to topological properties, that one may expect, most of the cases in very special configurations (i.e. a given set of the involved parameters), to get such type of rather stable solitary wave oscillating in a finite 2-D "box".

## 2. The Mathematical Description

A first approximation description of the dynamics of the phase  $\Phi$  for a 2-D square Josephson junction of length  $l$  is given by the following perturbed sine-Gordon equation (PSGE) where  $\Phi$  describes the phase difference between the two electrodes of the tunnel junction.

$$\Delta\Phi - \Phi_{tt} - \alpha\Phi_t + \beta(\Phi_{xxt} + \Phi_{yyt}) = \sin\Phi \quad . \quad (1)$$

In the following numerical simulations, for simplicity, and without significantly perturbing the quantitative results we obtain, we will qualitatively neglect the surface loss  $\beta$ -term, but take it into account quantitatively, by a renormalisation of the quasi-particle tunneling losses term  $\alpha$ . Such a choice also speed-up the time consumed by the code.

Depending on the experimental conditions, additional terms must be included in this PSGE, such as a dc or rf bias current. For a dc bias feeding corresponding to a cross type geometry the boundary conditions are <sup>1</sup> (see Fig.1):

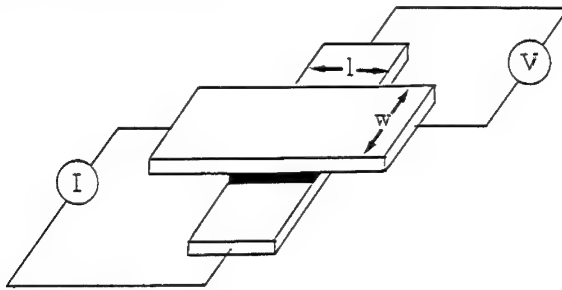


Fig. 1. Sketch of a 2-D Josephson tunnel junction of cross type geometry showing the dc bias current. In this paper we always consider square junctions ( $w = l$ ).

$$\Phi_x(x=0) = \eta(y) \quad , \quad (2)$$

$$\Phi_y(y=0) = \eta(x) \quad , \quad (3)$$

$$\Phi_x(x=l) = \Phi_y(y=l) = 0 \quad . \quad (4)$$

In Eqs. (1-4) the spatial coordinates  $x$  and  $y$  are normalized to the Josephson penetration depth  $\lambda_j = (h/4\pi ed\mu_0 j_1)^{1/2}$  (where  $h$  is Planck's constant,  $e$  the electron charge and  $d = \lambda_{L1} + \lambda_{L2} + t'$ , where  $\lambda_{L1,2}$  denotes the London penetration depth of the

two superconducting electrodes and  $t'$  the thickness of the dielectric barrier;  $\mu_0$  and  $j_1$  are respectively the permeability and the critical current density of the junction). The time  $t$  is normalized to the inverse of the plasma frequency  $\omega_p = (4\pi e j_1 / \hbar C_s)^{1/2}$  with  $C_s$  denoting the specific capacitance of the junction. As usually, the subscripts of  $\Phi$  denote partial derivatives. As often, boundary conditions are of major importance. The energy input which balances the damping  $\alpha$  is obtained through the boundary conditions (2-4). These boundary conditions account for the effect of the induced magnetic field generated by the bias current feeding the square Josephson junction through the  $x = -l/2$  boundary and leaving it through the  $y = -l/2$  boundary. These boundary conditions are one of the conditions influencing deeply the results obtained. The symmetry axis lying along one diagonal might not lead to any known quasi one-dimensional fluxon dynamics, as it is expected when the axis of symmetry is parallel to the  $x$  or  $y$  axis<sup>6</sup>. We insert a more realistic spatial dependent shape of the dc bias, as is expected from experiments<sup>1</sup>, namely:

$$\eta(x) = \frac{\eta}{4} \left[ \frac{\cosh\left(\frac{x}{2}\right) + \cosh\left(\frac{x-l}{2}\right)}{\sinh\left(\frac{l}{2}\right)} \right] , \quad (5)$$

$$\eta(y) = \frac{\eta}{4} \left[ \frac{\cosh\left(\frac{y}{2}\right) + \cosh\left(\frac{y-l}{2}\right)}{\sinh\left(\frac{l}{2}\right)} \right] . \quad (6)$$

### 3. The Numerical Approach

The problem is of Cauchy type. We assume the following initial condition, taken at  $t = 0$ :

$$\begin{aligned} \Phi(x, y, t) = & 4 \tan^{-1} \left\{ \frac{1}{v} \sinh \left[ \frac{l/2\sqrt{2}-vt}{\sqrt{1-v^2}} \right] \operatorname{sech} \left[ \frac{x+y}{\sqrt{2(1-v^2)}} \right] \right\} \\ & - 4 \tan^{-1} \left\{ \frac{1}{v} \sinh \left[ \frac{l/2\sqrt{2}+vt}{\sqrt{1-v^2}} \right] \operatorname{sech} \left[ \frac{x-y}{\sqrt{2(1-v^2)}} \right] \right\} . \end{aligned} \quad (7)$$

This means that we take two bions located along the two diagonals of the square junction, with an initial velocity  $v$  very close to the limit velocity equal to 1, in dimensionless units. Typical values taken for the numerical simulations are:

$$l \simeq 4 \quad ; \quad v = 0.99 \quad . \quad (8)$$

Fig.(2) shows the dynamics of the closed wave-front pattern. Note the surprising  $(-8\pi)$  jump of the field amplitude, which occurs at the corners when the two diagonal fronts collide in figure (2c) and (2g). Looking at figures (2a) and (2h), it becomes clear that the 2-D cycle has a periodic uniform decrease of the field amplitude  $\Phi$  equal to  $(-8\pi)$ .

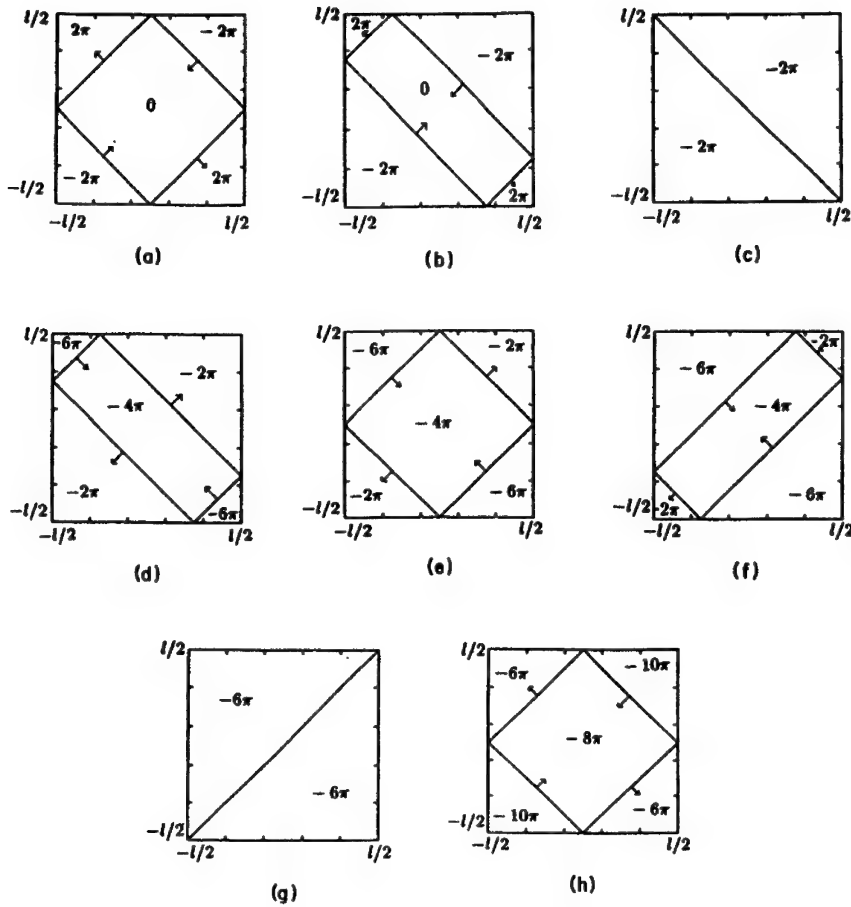


Fig. 2. Sketch of the Isoperimeter Pattern Dynamics displayed over one period in the  $(x,y)$  plane; each figure of the series displays the kink like wave front lines  $(2\pi \pm 2n\pi)$ .

For such a cycle, there is obviously an equivalent  $+8\pi$  field jump time series obtained by reversing the direction of the velocity of each diagonal wave front.

In this simulation the numerical scheme is a modification of the one used by Eilbeck et. al.<sup>6</sup>. It is a Lax stabilized leapfrog method discretized at second order both in space and time.

Using the discretization

$$\Phi(ih, jh, n\Delta t) = \Phi_{i,j}^n, \quad 1 \leq i, j \leq N \quad , \quad (9)$$

where  $h$  represents the square mesh and  $\Delta t$  the time step, the numerical scheme reads

$$\begin{aligned} \left(\frac{\alpha\Delta t}{2} + 1\right)\Phi_{i,j}^{n+1} &= \left(\frac{\alpha\Delta t}{2} - 1\right)\Phi_{i,j}^{n-1} + \left[2 - 4\left(\frac{\Delta t}{h}\right)^2\right]\Phi_{i,j}^n \\ &+ \left(\frac{\Delta t}{h}\right)^2 \left[\Phi_{i+1,j}^n + \Phi_{i-1,j}^n + \Phi_{i,j+1}^n + \Phi_{i,j-1}^n\right] \\ &- (\Delta t)^2 \sin\left[\frac{1}{4}(\Phi_{i+1,j}^n + \Phi_{i-1,j}^n + \Phi_{i,j+1}^n + \Phi_{i,j-1}^n)\right]. \end{aligned} \quad (10)$$

The boundary conditions are introduced by using an extra set of points outside the mesh

$$\begin{aligned} \Phi_{0,j}^n &= \Phi_{2,j}^n - 2\eta h & \Phi_{N+1,j}^n &= \Phi_{N-1,j}^n \\ \Phi_{i,0}^n &= \Phi_{i,2}^n + 2\eta h & \Phi_{i,N+1}^n &= \Phi_{i,N-1}^n. \end{aligned} \quad (11)$$

The linear stability analysis gives the so called Courant-Friedrichs-Lewy (CFL) condition:  $c = \sqrt{2}\Delta t/h \leq 1$ . Due to the fact that this is a linear condition, for stability we use a constant  $c$  lower than 1. The highest the  $c$  value, the lowest the numerical viscosity. Fig.(3) displays, as a sample, the 2-D result at a given time taken during the stationary regime. This result comes from the numerical simulation of the 2-D problem defined by the system of Eqs. (7-11). Actually, and to be more precise, a small structural perturbation simulating the electron beam heating (see section 6) is added to Eq. (10). An illustrating sequence representing the 2-D behaviour over a full period is shown by Fig. (2) of Ref. (12). During such a period, in a well-established asymptotic dynamical regime, the field amplitude  $\Phi$  decreases uniformly over  $-8\pi$ .

The period of the cycle is :

$$T = l\sqrt{2} = 4\sqrt{2}, \quad (12)$$

with an accuracy of 1%, and with the choice of the parameters given by formulae (8) for this numerical experiment.

As one can see through Figs.(2,3) the pattern, consisting mainly of kink like  $(\pm 2\pi)$  wave front lines connected in order to build up a rectangular wave front, evolves, preserving a constant length of the wave front perimeter (so called IPD) due to both energy conservation and symmetry considerations.

It is not too much surprising, that, despite the presence of damping and energy input, a non linear solitary wave looks like stationary, if we remind the behaviour of one-dimensional (1-D) sine-Gordon systems under the influence of both perturbing term (with respect to an integrable equation) damping and driving ones. But we must emphasize, that in our case it was never demonstrated that the 2-D sine-Gordon equation (without perturbation terms) is an integrable one. Consequently, and from a mathematical point of view, one can say, that the analogy with the 1-D situation could be wrong. But still remains possibilities of resonances giving quasi stationary patterns like the one showed in Fig.3. Moreover, the time until which the integration of the 2-D equation was performed (around 15000 in reduced unit time) is by far lower than the characteristic time involved in the physical situation in order to get a measurement (either I-V type or LTSEM one).

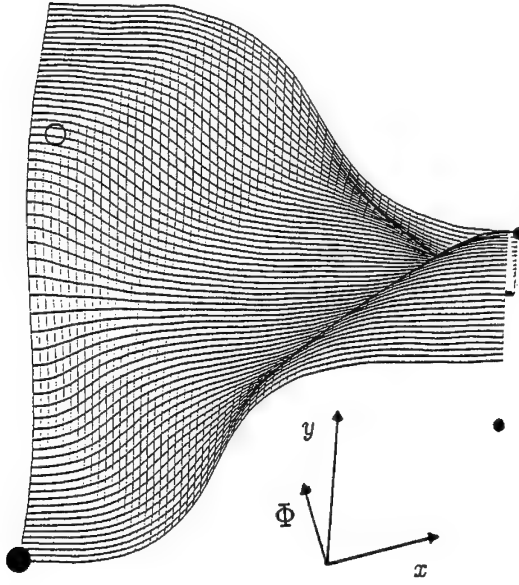


Fig. 3. The simulated IPD pattern displayed as  $\Phi(x, y)$ , plotted over the whole junction area. The central projection has its focal point on the right hand side of the figure. The dots mark the four corners of the junction on the  $x-y$  plane. Parameters of the simulations are:  $\alpha_1 = 0.6$ ,  $\delta = 0.17$  (see section 6),  $\alpha_0 = 0.01$ ,  $l = 4$ ,  $\eta = 0.2$ . The beam spot is placed in the center of the junction area.

#### 4. Phenomenology and Macroscopic Quantities

The two macroscopic quantities which determine the dynamics of a Josephson junction and which can easily be measured, are the bias current, basically determined by the value of  $\eta$ , and the voltage across the junction, which is given, in units of the flux quantum  $\hbar/2e$ , by <sup>1</sup>:

$$V = \Phi_t = \frac{\Delta\Phi}{\Delta t} \quad . \quad (13)$$

In the steady-state regime sketched by Figs. 2 and 3, the voltage  $V$  can be estimated as the ratio of the  $\Delta\Phi = 8\pi$  uniform jump of the junction phase over the period  $\Delta t = T$  given by Eq. (12),

$$V_{2D} = \frac{8\pi v}{(l\sqrt{2})} = \sqrt{2}\pi \quad . \quad (14)$$

This voltage has to be compared to the Zero-Field-Step (ZFS) voltage of the trivial

$y$ -degenerated shuttling kink front, which is:

$$V_{1D} = \frac{4\pi v}{2l} = \frac{\pi}{2} \quad , \quad (15)$$

since the shuttling period of a relativistic kink is close to  $2l = 8$  (see Eq. (8)), while the net phase change over this period is  $4\pi$ . Therefore :

$$\frac{V_{2D}}{V_{1D}} = 2\sqrt{2} \quad . \quad (16)$$

This quasi 1-D soliton motion might be observed with a different current feeding geometry, namely from a symmetrical configuration described by <sup>6</sup>:

$$\Phi_x(x = \pm \frac{l}{2}) = 0 \quad ; \quad \Phi_y(y = \pm \frac{l}{2}) = \pm \eta \quad , \quad (17)$$

## 5. Experimental Results

We studied five  $Nb/AlO_x/Nb$ -tunnel junctions of square cross-type geometry (see Fig.1). Details on the junction geometry can be found in Hebrank et al. <sup>7</sup>. Sizes and main experimental results are listed in Table 1. We studied the current-voltage characteristic (IVC) of the samples with and without an externally applied magnetic field. In addition, with the technique of LTSEM we obtained detailed information on the dynamics inside the junctions giving rise to the current steps in the IVC <sup>8,9</sup>. Basically, with the LTSEM technique the sample surface is scanned by an electron beam. A junction response signal is recorded as a function of the coordinate point  $(x_0, y_0)$  of the electron beam focus. The dominant physical effect with this imaging technique is the beam-induced local heating of the sample. With the beam parameters used for the present studies (27.5 kV, 100 pA) we estimate the local temperature increase to be less than 1K. During the scanning process, the superconducting tunnel junction was kept near 4K, i.e., well below the transition temperature of the  $Nb$  electrodes of the junction. The main influence of the irradiation is a local enhancement of the quasi-particle tunneling and the surface losses near the beam focus point. The spatial extension of the heated area is given by the thermal healing length  $\delta$  <sup>10,11</sup> of the sample configuration, and is typically in the order of a few  $\mu m$ .

For an IPD mode, the local increase of the losses results in a local breaking down of the wavefront speed when crossing the electron beam focus.

Since the scanning time for one line across the sample is about one second, and since the frequency of the IPD motion is in the 100 GHz-range, we can consider the perturbation induced by the electron beam as a quasi static one. Due to the electron beam induced reduction of the average IPD mode velocity and because of the Josephson frequency-voltage relation, a decrease  $\Delta V$  of the corresponding step voltage  $V_{2D}$  is expected <sup>9</sup>, leading to a shift of the IVC.

#	in units of $\lambda_j$	in units of $\mu m$	remarks to ZFS at $V_{2D}$
1	2.0	50	not found
2	3.2	124	single-mode cavity excitation
3	4.0	100	IPD
4	4.3	50	IPD
5	8.6	100	not found

Table 1. Length (width) of the square cross type junctions and main experimental results.

We expect <sup>12,13</sup>, that the IPD only exists in junctions of intermediate size. For small junctions, there is not enough space for the nonlinear pattern and for large area junctions, there is an unfavorable balance between driving and damping. Furthermore it was found <sup>12,13</sup>, that the IPD mode is only stable for high wave front velocities which means in the language of the IVC, that the corresponding ZFS should have a very low differential resistance. The last property is also interesting for applications, because the linewidth of the rf-radiation emitted from the junction is expected to be small if the junction is biased on a low-resistance step <sup>14</sup>. The existence of a ZFS at  $V_{2D}$  with junctions of intermediate size as well as the low differential resistance of that step was found experimentally. The typical sample on which we will focus is the sample #4 of Table I. We observed a ZFS at  $V_{2D}$  within an accuracy of 2% <sup>15</sup>. This was confirmed by calculating  $2\sqrt{2}$  of the second 1-D Fiske step voltage which was measured by applying a magnetic field oriented parallel to one junction edge. The lowest voltage ZFS of these junctions is at  $V_{2D}$ .

Furthermore, two additional ZFS's were observed, the larger one (X step) at a voltage  $V_x = V_{2D} + V_{1D}$ . The origins of this X step and of the tiny one between  $V_{2D}$  and  $V_x$  still remain unexplained. We found  $V_x = 1.445mV$  (Fig.4), with a corresponding Josephson frequency of 700 GHz. Applying an external dc magnetic field in the plane of the junction parallel to one of the diagonals, both ZFS at  $V_{2D}$  and at  $V_x$  disappear and one- and two-dimensional Fiske steps appear instead. In particular, with a field of 1.1mT the two dimensional  $\{4,4\}$ -Fiske resonance appears at a voltage  $V_{4,4}$  close to  $V_{2D}$ . The voltage  $V_{4,4}$  of the  $\{4,4\}$  Fiske step is  $30\mu V$  smaller than the voltage of the IPD step. This difference can be explained with the frequency dependence of the Swihart velocity <sup>16</sup>. The observed  $\{4,4\}$ -Fiske step is not as steep as the ZFS at  $V_{2D}$  shown in Fig.4.

Both, the difference of the step voltage as well as the different resistance of the  $\{4,4\}$ -Fiske steps and the ZFS at  $V_{2D}$  indicate, that the two steps are most probably



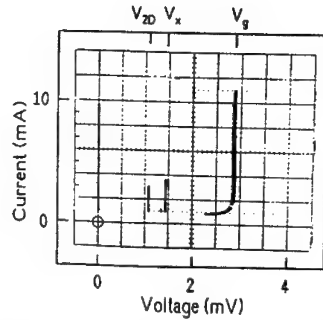


Fig. 4. Current-voltage characteristic of sample #4 without external magnetic field and without electron beam irradiation at  $T \simeq 4K$ .  $V_{2D}$ ,  $V_x$ , and  $V_g$  denote the voltage corresponding to the ZFS of IPD, the ZFS of unknown origin, and the energy gap, respectively.

due to different dynamical states of the junction.

To obtain further information on the dynamical states of the steps we performed LTSEM measurements. The voltage imaging by LTSEM of the  $\{4, 4\}$ -Fiske resonance clearly showed 2-D single-mode standing-wave excitation<sup>8,9</sup>. On the other hand, the voltage image of the ZFS at  $V_{2D}$  looked very different (Fig.4). The maximum electron beam induced decrease of the step voltage is about  $100nV$ , whereas the step voltage  $V_{2D}$  is  $1.080mV$ . Therefore, the LTSEM technique is a measurement tool only slightly perturbing the IPD mode and not destroying the dynamical behavior. Whether the signature of this image is related to the IPD in the junction is not clear from the LTSEM studies alone. Therefore, we performed extensive numerical simulations of the LTSEM imaging procedure. The results will be shown in the following section.

Qualitatively, it is expected, that the e-beam is more effective in slowing down the soliton motion (i.e., it gives rise to larger signal response) when its position coincides with a point of collision of two parallel soliton-like wave fronts<sup>9</sup>, i.e.,  $-\Delta V(x_0, y_0)$  peaks are expected along the two diagonals. At the center, within each period two collisions occur. At each of the four junction corners, there is an additional collision with a virtual antisoliton due to the boundary conditions. In these five points one might expect an enhancement of the signal peaks since double collisions take place during one period. Actually such peaks have been detected as shown in Fig.5. It displays the voltage-image  $-\Delta V(x_0, y_0)$  of the ZFS at  $V_{2D}$  of sample #4 with the length and width of  $4.3\lambda_j$ , supposed to result from the IPD mode propagating along the two diagonals. In addition to these five signal peaks, we observed four peaks to the middle of the junction edges (Fig.5(a)). Note that along the boundaries a kind of collision between two perpendicular wave-fronts occurs. Since only collisions between parallel wave-fronts have been investigated<sup>9</sup>, nothing can be said *a priori* about the e-beam induced voltage signal in this case. We conclude that these four peaks have no qualitative explanation but they are well reproduced by the numerical simulations

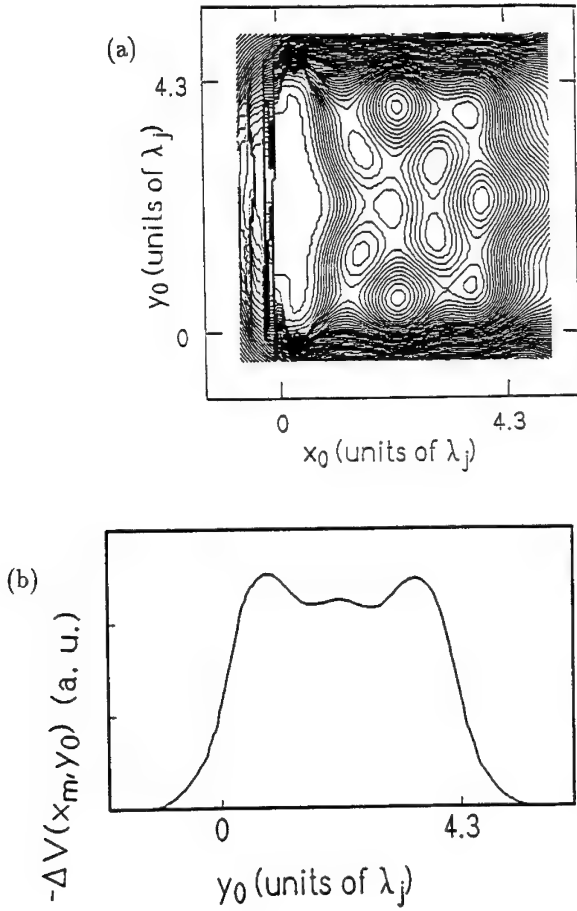


Fig. 5. (a) Contour plot representation of the voltage-image  $-\Delta V(x_0, y_0)$  of the ZFS at  $V_{2D}$  (sample #4) at  $T \simeq 4K$ . The dc bias current enters the junction at the left side and emerges at the bottom one. The large signal at the left of the image is due to the larger total film thickness in that region, where a wiring layer is on top of the counterelectrode (see. Ref. 7). The junction boundaries lie between 0 and 4.3 in both directions. The darker the image, the larger the  $-\Delta V$  value.

(b) Voltage signal profile  $-\Delta V(x_m, y_0)$  (in arbitrary units) along a linear vertical scan across the middle of the junction ( $x_0 = x_m = l/2$ ) shown in (a).

as shown hereafter.

## 6. Numerical Results Including Electron Beam Heating

We performed numerical simulations of the system described by Eqs. (1-4). In order to simulate the effect of the e-beam we assume a local increase of the temperature. For a small change of temperature ( $\Delta T < 1K$ ) the dominant effect will result in an increase of the dissipation term  $\alpha$ . For that Eq. (1) has to be modified by introducing a spatial dependence for the quasi-particle loss term  $\alpha$  (here  $\alpha_0$  denotes the uniform value of the unperturbed junction)

$$\alpha(x, y; x_0, y_0) = \alpha_0 + \alpha_1 \exp \left[ \frac{(x_0 - x)^2}{\delta^2} \right] \exp \left[ \frac{(y_0 - y)^2}{\delta^2} \right], \quad (18)$$

where the coordinates  $(x_0, y_0)$  identify the position of the beam center,  $\alpha_1$  is related to the intensity of the beam,  $\delta$  to the radius of the area perturbed by the beam. For each couple of values  $(x_0, y_0)$  we get a new partial differential equation. The asymptotic regime for the IPD mode in such an equation will differ from the asymptotic regime of another one. Each regime will show an average velocity, proportional to the average voltage (through the Josephson relation), that is exactly the signal available from the LTSEM technique. By comparing the spatial distribution of  $\Delta V(x_0, y_0)$  in the asymptotic regimes we will try to recover the experimental signature of the IPD pattern. Consequently, it is therefore necessary to reach the asymptotic regime avoiding transients (we recall that in the experiments the typical times are much longer than the characteristic times of the fluxons). This has been done in several steps:

- 1) Determine the typical times to reach a stationary state for the beam perturbed system. It was found that the system stabilizes in less than 500 normalized units with the chosen initial conditions <sup>12,13</sup>;
- 2) Find the minimal time step to stabilize the average voltage in order to get numerical fluctuations smaller than the expected change  $\Delta V$  (see also next section for a discussion on this point). We have found a value  $\Delta t = 0.02$  in normalized units;
- 3) Find the minimal step size of the spatial grid for a given radius  $\delta$  of the hot spot, avoiding numerical instabilities due to high gradients. It was found that the hot spot has to contain 3 – 4 grid points to fulfill this condition.

All the conditions were verified for several sample cases with the method of doubling (halving) the above quantities. In any case the CFL coefficient should be high enough to avoid numerical instabilities <sup>12,13</sup>. In our case we have found that a value 0.44 of this parameter is high enough for our purpose. Fig.3 shows the 2-D sine-Gordon field  $\Phi(x, t)$  for a typical set of parameters, including the electron beam perturbation. Note that the presence of the hot spot does not induce any significant field deformation.

## 7. The Physical Parameters

In addition to the numerical parameters, that were fixed with the procedure described here above, in Eqs. (7-11,18) some other physical parameters appear, namely,  $\alpha_0$ ,  $\alpha_1$ ,  $\delta$ ,  $\eta$ , and  $l$ . In principle we can get these parameters from the experimental tests except  $\alpha_1$ , that could be calibrated for instance from the maximum electron beam induced voltage change. In practice the accuracy of an estimate of some of the parameters is rather poor; in particular the dissipation terms ( $\alpha_0$  and  $\alpha_1$ ) and the radius of the hot spot ( $\delta$ ) can be determined only with an accuracy that is of the same order of magnitude than the measured signal, while the current and the normalized length can be measured within an accuracy of about 5%. Therefore, to be sure that the results of the numerical simulations have a physical meaning one should explore the parameter range widely enough to cover the experimental values. This was done in different steps:

- 1) The homogeneous dissipation  $\alpha_0$ . For real junctions the determination of the dissipation is very difficult; the expected value lies between  $\alpha_0 \simeq 0.001$  and  $\alpha_0 \simeq 0.01$ . Since small values of dissipation increase the CPU time we choose the highest estimates :  $\alpha_0 = 0.01$  and  $\alpha_0 = 0.02$ . For several sample runs we have not found any significant difference in the results for these two  $\alpha_0$  values.
- 2) The localized dissipation  $\alpha_1$ . This value is not directly accessible, but it can be roughly estimated in the following way: Measuring the maximum signal of the LTSEM and then increasing  $\alpha_1$  until the same signal is recovered through the numerical simulations. For instance, in our case, where the LTSEM signal gives rise to a change of  $0.1 \div 0.01\%$  of the voltage, one should increase  $\alpha_1$  until the asymptotic voltage in the most "sensitive point" is decreased by the same amount in the simulations. In practice, to recover such a small relative voltage change ( $10^{-3} \div 10^{-4}$ ), we need to measure the voltage numerically with a higher precision (i.e.,  $10^{-5} \div 10^{-6}$ ). However, with increasing precision the simulation takes longer. Then by increasing  $\alpha_1$  we have increased the maximum signal up to 1% of the maximum voltage, i.e. to a value that is still small enough to assume that we are in the limit of small perturbations (note that in Fig.3 the perturbation due to the beam is not visible). This allows us to work with a smaller precision and to keep the computational time within a reasonable range. Again for some cases the value has been halved to check that no significant changes occur.
- 3) The actual value of the radius of the area perturbed by the beam  $\delta$ . It was found by changing  $\delta$  in the range that is expected from the experiments ( $\lambda_j/6 \leq \delta \leq \lambda_j/2$ ), namely that the characteristic length scales of the LTSEM-like pattern are larger or comparable to  $\delta$ . We extract from those measurements an average value of  $\delta$  of about  $0.15\lambda_j$ . The qualitative features of the LTSEM-like pattern are conserved in the above  $\delta$  range.

- 4) The bias current  $\eta$ . We have checked that the IPD is stable and that the simulated LTSEM signal does not change significantly in the current range of  $0.15 \leq \eta \leq 0.6$ . Below the minimal threshold the simulated beam destroys the fluxons and a switch to the zero voltage state occurs, as it has been also observed in the experiments. Above this range the switch occurs towards higher voltage (McCumber-like solutions).
- 5) The normalized length. We keep  $l$  around  $4\lambda_j$  in order to be consistent with the previous numerical observations<sup>12</sup> and the experiments showing that the IPD mode disappears for longer junctions.

The IPD mode signature extracted from numerical simulations is the presence of a large signal at the junction center, at the four corners, and in the middle of the boundaries (see Fig.6). All such peaks are clearly observed in the experiment but the relative height of the peaks differs between experiment and simulation (see Figs.5(b) and 6(b)). As already mentioned, the absolute voltage change cannot be compared. The qualitative similarity between the simulated signal and the experimental one is systematically found in a large range of parameters.

## 8. Conclusion

The IPD mode seems to be stable only for suitable values of the junction parameters  $(l, \alpha, \eta)$ <sup>12,13</sup>. In addition, an instability can also occur due to the e-beam which induces a transition to another state. As already mentioned in the introduction, the existence of a 2-D solitary wave type solution for such a system seems less realistic than the signature of a resonance phenomenon. This is mainly deduced from the mathematical state of the art<sup>17,18,19</sup> and is still an open problem. Experimentally we also recall that the junction length should lie in the intermediate range rather than in the extreme case  $l \gg 1$ . If one interprets the *IVC* branch at a voltage  $V = 2\sqrt{2}V_{1D}$  as an IPD mode branch, the experiments give also the bias range of stability of such a mode. A comparison with numerical data is less reliable because close to the switch point the dissipation terms, in particular the  $\beta$ -term, become important<sup>20</sup>. In our simulations for sake of simplicity we have renormalized the  $\alpha$ -term to take into account the  $\beta$ -term. Moreover the fact that we neglect noise effects leads us to conclude that only a qualitative agreement might be expected. In fact simulations show the instability at the top of the step to occur at a value  $\eta \simeq 0.7$ , which is much higher than the experimentally observed value ( $\eta \simeq 0.32$ ). But under the light of our previous discussion, such discrepancy is expected.

A different case is the instability due to the presence of the e-beam. There exists a maximum threshold for both the intensity of the beam spot and its size, above which the IPD mode is destroyed. When the IPD mode is destroyed, new dynamical states occur. We have numerically observed a quasi 1-D mode, the  $V = 0$  state (fluxons annihilation), or the McCumber state. The 1-D dynamics can be induced by the spot probably because the spot, except for very special points, destroys the specific symmetry of the square cross type biased junctions and the propagation along only

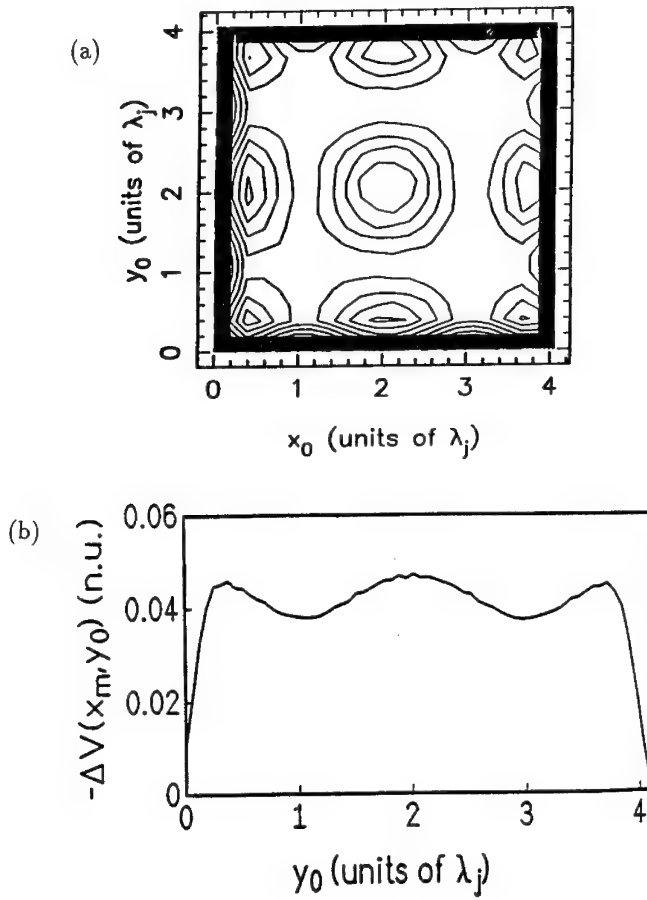


Fig. 6. (a) The numerically simulated two-dimensional LTSEM signal. Parameters of the simulations are:  $\alpha_1 = 0.4$ ,  $\delta = 0.17$ ,  $\alpha_0 = 0.02$ ,  $l = 4$ ,  $\eta = 0.2$ . The bias current orientation is the same as in Fig.(5)

(b) The simulated LTSEM signal  $-\Delta V(x_m, y_0)$  in normalized units (n.u.) across the  $x_m = l/2 = 2$  section of the junction. Parameters of the simulations are:  $\alpha_1 = 0.4$ ,  $\delta = 0.17$ ,  $\alpha_0 = 0.02$ ,  $l = 4$ ,  $\eta = 0.2$ ,  $x_m = 2$ .

one direction seems to be favored. In fact the IPD mode is possible only if a diagonal is an axis of symmetry for the junction. However, this is in general not any more the case when the beam spot is present. For a given set of parameters, the energy of the beam will determine the threshold value for the disappearance of the IPD mode. The efficiency of the beam  $E_b$  can be estimated from Eq. (18) to be

$$E_b \propto \alpha_1 \delta^2 \quad (19)$$

In Table 2 the threshold value for two different values of  $\alpha_0$  are reported, indicating that Eq. (19) gives a good preliminary estimation for the transition region between the IPD and other types of dynamics. The other parameters of the simulations are  $l = 4$  and  $\eta = 0.2$ .

$\alpha_0$	$\delta$	$\alpha_1$	$\alpha_1 \delta^2$
0.01	0.32	$0.7 \pm 0.1$	$0.072 \pm 0.010$
0.01	0.40	$0.42 \pm 0.06$	$0.067 \pm 0.010$
0.01	0.48	$0.42 \pm 0.06$	$0.097 \pm 0.014$
0.02	0.32	$0.36 \pm 0.04$	$0.037 \pm 0.004$
0.02	0.40	$0.22 \pm 0.02$	$0.035 \pm 0.003$
0.02	0.48	$0.15 \pm 0.05$	$0.035 \pm 0.012$

Table 2.

### Acknowledgements

We thank G. Reinisch for comments and suggestions in the early stage of this work, P. Lacroix and D. Quenter for their assistance and for interesting discussions. The manufacturing of the samples at the ETL, Ibaraki, Japan by M. Koyanagi and R. Gross is gratefully acknowledged. G.F. wishes to thank the C4I Center (Archamps) for its hospitality during part of this work and the financial support from the EC under the program 'Human capital and Mobility' (Contract No. ERBCHBGCT920215). The work was also supported by the EEC Science contract N<sup>o</sup> SC1-CT91-0760.

## References

1. A. Barone and G. Paternò, *Physics and applications of the Josephson effect* (Wiley, New York, 1982).
2. N.F. Pedersen in: *SQUID '91 – Superconducting Devices and their Applications*, Springer Proceedings in Physics, H. Koch and H. Lübbig eds. (Springer, Berlin), p. 369 (1992).
3. A.B. Borisov and A.G. Shagalov, *Nonlinear World*, Proceedings of the IV International Workshop on Nonlinear and Turbulent Processes in Physics, (Kiev, october 9-22, 1989), bf 2, 213, (1989)
4. S.G. Lachenmann, G. Filatrella, T. Doderer, J.C. Fernandez and R.P. Huebener, Phys. Rev. **B 48**, 16623, (1993).
5. R. Monaco, S. Pagano, and G. Costabile, Phys. Lett. **A 131**, 122 (1988).
6. C. Eilbeck, P.S. Lomdahl, O.H. Olsen, and M.R. Samuelsen, J. Appl. Phys. **57**, 861 (1985).
7. F. Hebrank, S. Lemke, R.P. Huebener, R. Gross, Nucl. Instr. and Meth. **A 288**, 541 (1990).
8. B. Mayer, T. Doderer, R.P. Huebener, and A.V. Ustinov, Phys. Rev. **B 44**, 12463 (1991).
9. S.G. Lachenmann, T. Doderer, D. Quenter, R.P. Huebener, J. Niemeyer, and R. Pöpel, Phys. Rev **B 48**, 3295, (1993).
10. R.P. Huebener, Rep. Prog. Phys. **47**, 175 (1984).
11. T. Doderer, R.P. Huebener, C.A. Krulle, B. Mayer, J. Niemeyer, R. Pöpel, D. Quenter in: *SQUID '91 – Superconducting Devices and their Applications*, Springer Proceedings in Physics, H. Koch and H. Lübbig eds. (Springer, Berlin), p. 419 (1992).
12. E. Turlot, D. Esteve, C. Urbina, M. Devoret, R. Grauer, J.C. Fernandez, H. Politano, and G. Reinisch, Phys. Rev. **B 42**, 8418 (1990).
13. E. Turlot, D. Esteve, C. Urbina, M. Devoret, J.C. Fernandez, R. Grauer, H. Politano, and G. Reinisch, in: *Nonlinear Coherent Structures*, Lectures Notes in Physics, Vol. **353**, eds. M. Barthes and G. Leon, (Springer, Berlin, 1990). p. 181.
14. E. Joergensen, V.P. Koshelets, R. Monaco, J. Mygind, M.R. Samuelsen, and M. Salerno, Phys. Rev. Lett. **49**, 1093 (1982).
15. Susanne G. Lachenmann, Diploma-thesis, University of Tübingen, 1992.
16. R.F. Broom and P. Wolf, Phys. Rev. **B 16**, 3100 (1977).
17. M. Boiti, J.J.P. Leon, L. Martina and F. Pimpinelli, Phys. Lett. **A 132**, 432, (1988).
18. A.S. Fokas and P.M. Santini, Phys. Rev. Lett. **63**, 1329, (1989).
19. M. Boiti, J. Leon and F. Pimpinelli, Inverse Problems **7**, 175, (1991).
20. S. Pagano, M.P. Soerensen, R.D. Parmentier, and P.L. Christiansen, Phys. Rev. **B 38**, 4677 (1988).



---

Chapter 5

**SQUIDS**

## TUNNELLING IN A DOUBLE-WELL SQUID POTENTIAL

G. ROTOLI and P. CARELLI

*MQC Collaboration, INFN sezione di Roma1.*

and

*Dipartimento di Energetica, Università dell'Aquila*

*Località Monteluco, Roio Poggio I-67040, Italy.*

### ABSTRACT

The rising interest in the test of quantum physics at the macroscopic level has focused attention toward Josephson devices as the natural candidates for crucial experiments, mainly for their property of having some macroscopic degree of freedom, *e.g.*, the flux in a SQUID, whose behavior is directly subject to the laws of quantum mechanics. The new proposed experiments include a test of the so-called Macroscopic Quantum Coherency (MQC) which would exist in a two-state (macroscopic) system if the laws of quantum mechanics have to be obeyed. The essential parameter in any MQC experiment is the tunnel frequency between the two states that fixes the timescale of the coherent quantum oscillations. Typically the tunnel frequency depends critically on the barrier height between the two states in the form of an exponential times a (less critical) term known as the 'pre-factor' (Arrhenius law). The tunnel frequency for a SQUID with double-well potential is evaluated numerically and compared with the standard perturbative approach (WKB), for a quadratic-plus-quartic and a SQUID potential, in order to predict the dependence in the quantum limit of both the pre-factor and the exponential on the barrier height. The relation between these and the SQUID parameters is an important result to predict the feasibility of the whole procedure, so an investigation of a real-life MQC experiment is carried out for both a simple rf-SQUID and a configuration developed by Lukens *et al.* to study the thermal branch of the Arrhenius law. We conclude with some hints to the problem of controlling dissipation and/or coupling of the system with the external world, which typically destroy the quantum coherency properties.

### 1. MQC Experiment with an RF-SQUID

It is a well known result of elementary Quantum Mechanics that a system with two equivalent states may undergo coherent oscillations between these. The two-state systems are typically characterized by an observable, for example, the position in a double well potential. The coherent oscillation signals nothing more than the tunnelling through the barrier. An MQC experiment is mainly devoted to demonstrate the existence of quantum coherent oscillations for a variable describing a macroscopic number of particles ( $\sim 10^{10}$ ). From this experiment it is possible to extract interesting consequences for both the Macro Realistic theories equivalent to QM and the so-called Non-Invasive Measurement property (NIM)<sup>2,3</sup>.

The RF-SQUID appears as a natural device for an MQC experiment<sup>1</sup>. The RF-

SQUID potential is:

$$V(\phi) = \frac{1}{2L}(\phi - \phi_{ext})^2 - \frac{I_0\phi_0}{2\pi} \cos\left(\frac{2\pi}{\phi_0}\phi\right) \quad (1)$$

where  $\phi_{ext}$  is an external magnetic flux,  $\phi_0$  is the flux quantum,  $L$  is the self-inductance of the ring. If we take  $\phi_{ext} = \phi_0/2$  the potential is of double well type with two equal minima (symmetric potential). The variable that is involved in the tunnelling in the double well is just the magnetic flux in the ring; this variable can be considered 'macroscopic' because the associated current involves a very large number of particles (see ref.<sup>2</sup> for a critical comment about this).

An MQC experiment with an RF-SQUID can be outlined as follows: suppose we start the RF-SQUID at time zero in the left well; then the system oscillates between the two wells, and according to QM the difference  $P(t)$  between the probabilities  $P_L$  and  $P_R$ , to find the system in the left or in the right well, will be given by  $P(t) = \cos\omega_T t$  where  $\omega_T$  is the tunnelling frequency. Therefore, performing a measurement<sup>4</sup> at  $t = \pi/2\omega_T$ , one has to find  $P(t) = 0$ , so  $P_R = 0$  and  $P_L = P_R = 50\%$ . By repeating the measurement many times, exactly with the same procedure, these values can be checked. By performing a set of measuring at  $t = \pi/\omega_T$ , one gets:  $P(t) = -1$ , and so  $P_L = 0\%$  and  $P_R = 100\%$ , i.e., the flux will be found always in the right state. Of course, with no quantum interference, but with a mixture of states, we always should found  $P_L = 50\%$ ,  $P_R = 50\%$ <sup>5</sup>.

One of the main problems in this experiment arises from the tunnelling frequency, whose values, *at least* in order of magnitude, will be known in advance. Unfortunately, the nature of the tunnelling phenomena is such that the tunnelling frequency depends exponentially on the barrier height, so a small difference in the parameters which determine the barrier height can reflect *fatally* on the tunnelling frequency, shifting it by many orders of magnitude. Another limitation which influences the tunnelling frequency comes from the effects of the dissipation<sup>1,6</sup> in the system, which produces a decrease of the tunnelling frequency and a damping of the quantum coherent oscillations. For this reason the experiment must be performed at very low temperature, typically  $T \sim 10$  mK.

## 2. Schrödinger Equation for the SQUID Quantum Behavior

The conjugate variable to the flux is the charge  $Q$ , so we can introduce the momentum operator as  $\hat{Q} = \frac{\hbar}{i} \frac{\partial}{\partial \phi}$ . On the other hand the Hamiltonian of the RF-SQUID is written as the sum of the potential plus the kinetic term due to the charge:

$$\mathcal{H} = \frac{Q^2}{2C} + V(\phi) \quad (2)$$

where  $C$  is the capacitance of the SQUID. Both the momentum and the potential can be written in terms of a scaled angular variable  $\alpha = \frac{2\pi}{\phi_0}\phi$  in order to scale the energy

levels to the SQUID typical energies. So we obtain:

$$\hat{Q} = \frac{\hbar 2\pi}{i \phi_0} \frac{\partial}{\partial \alpha} \quad (3)$$

$$V(\phi) = \frac{\phi_0 I_0}{2\pi} f(\alpha) \quad (4)$$

with

$$f(\alpha) = \frac{1}{2\beta_L} \alpha^2 + \cos \alpha \quad (5)$$

where  $\beta_L = 2\pi L I_0 / \phi_0$ . We note that in writing the potential we assume that the SQUID is biased by  $\phi_0/2$ , *i.e.*,  $\alpha \rightarrow \alpha - \pi$ , so the potential is in the form of a double well with two symmetric minima.

A Schrödinger equation can be written following the standard procedure of substituting momentum with the momentum operator in the Hamiltonian and then writing the eigenvalue problem for the Hamilton operator:

$$-\frac{\hbar^2}{2C} \left( \frac{2\pi}{\phi_0} \right)^2 \frac{\partial^2}{\partial \alpha^2} \Psi + \frac{\phi_0 I_0}{2\pi} f(\alpha) \Psi = E \Psi \quad (6)$$

Now set:

$$E_c = \frac{4e^2}{2C} \quad \text{charging energy} \quad (7)$$

$$E_j = \frac{\phi_0 I_0}{2\pi} \quad \text{Josephson energy} \quad (8)$$

$$E_p = \hbar \omega_p \quad \text{plasma energy} \quad (9)$$

where  $\omega_p$  is the Josephson plasma frequency. Then introduce  $E_{jp} = E_j/E_p$  and  $E_{pc} = E_p/E_c$ ; moreover, it can be shown that  $E_{pc} = 2E_{jp}$ . Finally the Schrödinger equation can be written as:

$$\frac{\partial^2}{\partial \alpha^2} \Psi = 2E_{jp} [E_{jp} f(\alpha) - E'] \quad (10)$$

where  $E' = E/E_p$ , *i.e.*, energies are scaled with respect to the plasma energy.

### 3. Solutions of Schrödinger Equation

The above Schrödinger equation was solved numerically in order to find the first two energy levels corresponding to a symmetric or antisymmetric wavefunction. These can be obtained with repeated integrations of the first order system of differential equations equivalent to the Schrödinger equation from the origin with two different initial data on the wavefunction and its derivative. The value of the energy is adapted until the correct behavior of the wavefunction at the infinity is found. Though very simple the method is very precise as we see below at least to a difference in the energy

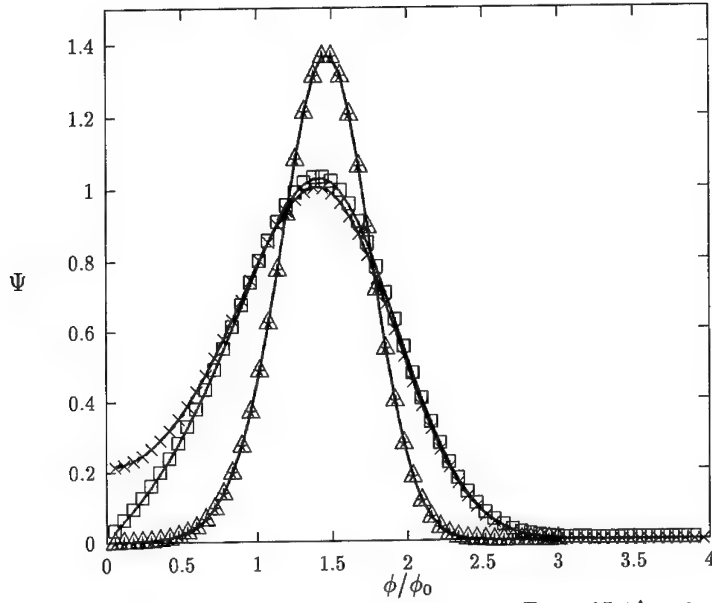


Fig. 1. Normalized wavefunctions for  $E_{jp} = 5$  ( $\square$  and  $\times$ ), and  $E_{jp} = 15$  ( $\triangle$  and  $\star$ ). The plot shows only the wavefunctions on the left well of the potential.

levels of about  $10^{-10}$ . Results for the wavefunction are shown in Fig. 1, where we can see the symmetric and the antisymmetric wavefunctions for two values of  $E_{jp}$ .

#### 4. The WKB Regime: Quantum Arrhenius Law

The tunnelling frequency is defined as the difference of two energy levels divided by  $\hbar$ . In our units this difference gives directly the order of magnitude of the tunnel frequency with respect to the plasma frequency of the two junctions making the SQUID. The dependence of the tunnelling frequency on barrier height, which is a function of  $\beta_L$  and  $E_{jp}$ , is reported in the log-lin plot of Fig. 2 for different values of the parameters.

We note that, except for very small values of the barrier, the dependences shown in Fig. 2 are, as a function of  $E_{jp}$  alone, essentially linear when on the ordinate is plotted the log of the tunnelling frequency. This means that tunnelling obeys a (Quantum)-Arrhenius law of the type:

$$\omega_T = A e^{-B\Delta U} \quad (11)$$

where  $\Delta U$  is the normalized barrier height (note that  $\Delta U$  is given by  $E_{jp}$  times a  $\beta_L$  dependent function).  $A$  and  $B$ , known as the 'prefactor' and the 'exponential' can be fitted directly from our data. The results are collected in Fig. 3 as a function of

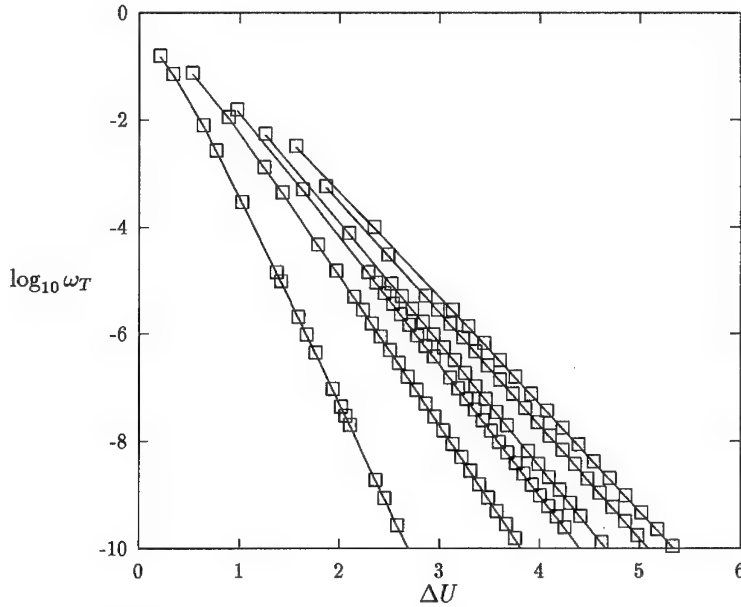


Fig. 2. Arrhenius plots for the following values of  $\beta_L$  starting from the left 1.2, 1.5, 1.8, 2.0, 2.5 and 3.0. For a fixed  $\beta_L$  the plots are obtained varying the parameter  $E_{jp}$ .

the parameter  $\beta_L$ . We note that the prefactor variation is small, as can be predicted by the WKB approach, and it does not influence the order of magnitude of  $\omega_T$ . On the other hand the exponential is very sensitive to the variation in  $\beta_L$  for  $\beta_L \rightarrow 1$ ; moreover, its variation can change drastically the tunnel frequency.

Another prediction about the tunnelling frequencies can be made by the WKB method if the height of the barrier is sufficiently large. For example, for a quartic plus quadratic potential<sup>7</sup> the exponential is also shown in Fig. 3; we see that for large values of  $\beta_L$  the values tend toward the same limit. On the same plot is shown also a WKB result for small values of  $\beta_L$  obtained with the SQUID potential<sup>8</sup>; the result appears to be between the numerical and the quartic plus quadratic WKB result, but somewhat nearer the perturbative one.

We note that in order to make an MQC experiment feasible the tunnel frequencies have to be of the order  $10^5 - 10^6$  Hz<sup>5</sup>. This means that the SQUID must be fabricated with a precision less than 1% in view of the critical exponential dependence of the tunnelling frequency on the barrier height. Alternatively, a different configuration can be studied.

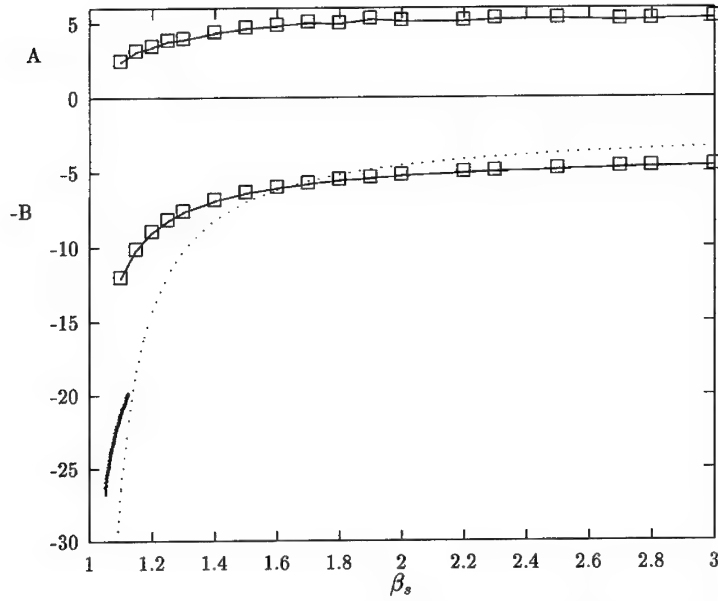


Fig. 3. Prefactor  $A$  and exponential  $B$  as function of  $\beta_L$ . The dotted line present the WKB results for the quadratic plus quartic potential with a SQUID-like barrier height of the type  $\sim I_0\phi_0(1 - f(\beta_{min}))$ . The bold line are the WKB results obtained for the SQUID potential.

### 5. Tunability of Tunnel Frequencies: Double RF-SQUID Configuration

A valid alternative to the simple RF-SQUID is the double RF-SQUID shown in Fig. 4.

This configuration was introduced by Han et al.<sup>9</sup> to study the thermal branch of the (Classical) Arrhenius law, *i.e.*, the thermal hopping of the flux above the double well barrier. The analysis of the double DC-SQUID leads to the following Schrödinger equation for its quantum behavior (refer to Fig. 4 for the various parameters):

$$-E_{cg}\frac{\partial^2}{\partial\alpha^2}\Psi - E_{cp}\frac{\partial^2}{\partial\beta^2}\Psi + E_j f(\alpha, \beta)\Psi = E\Psi \quad (12)$$

with:

$$f(\alpha, \beta) = \frac{1}{2\beta_G}\alpha^2 + \frac{1}{2\beta_P}\beta^2 + \cos\left(\frac{\beta_0 + \beta}{2}\right)\cos\alpha \quad (13)$$

where  $\alpha$  and  $\beta$  are, respectively, the scaled fluxes in the large and small rings;  $\beta_0$  is the static flux in the small ring. We note that the main difference is that now we have two degrees of freedom.

For  $\beta_P \ll 1 < \beta_G$  the potential is again a double well, but two-dimensional. In this limit the Schrödinger equation can be separated and the perturbation introduced

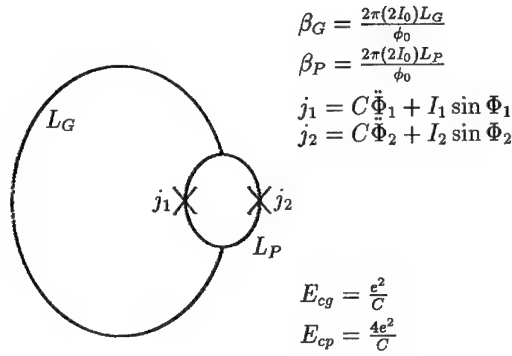


Fig. 4. Double RF-SQUID configuration. Junctions are assumed have the same Josephson current  $I_0$  and capacitance  $C$ ;  $\Phi_i$  represent the phase across the junction.

by the other degree of freedom can be treated perturbatively. To the first order in  $\beta_P$  the potential reads:

$$f(\alpha, \beta) \simeq \frac{1}{2\beta_G} \alpha^2 + \cos \frac{\beta_0}{2} \cos \alpha - \frac{\beta}{2} \sin \frac{\beta_0}{2} \cos \alpha \quad (14)$$

We note that the coefficient of the cosine term, *i.e.*, the effective Josephson current, is now controlled by the static flux  $\beta_0$  biased in the small ring. So the main difference with respect to the previous case is that the barrier can be lowered by putting magnetic flux into the small ring. The above potential can be considered as a first step toward an 'effective' potential for the large ring flux variable by setting the values of the small flux ring to its 'most probable' value using an 'effective' action calculation<sup>10</sup> similar to that performed by Chen<sup>11</sup>. However, here we limit ourselves to study only the effect on the tunnelling of the flux controlled barrier, *i.e.*, we study only the first two terms of the potential, which are independent of  $\beta$ . The results are reported in Fig. 5 for some values of  $\beta_G$ . We see that the tunnelling frequency is tunable over many orders of magnitude just by putting a small fraction of a flux quantum into the small ring.

## 6. Real Life Parameters and the Problem of Dissipation Effects

From the above data we note that the values of  $E_{jp}$  have to be the smallest possible. However, this is severely limited by the fabrication standards of the junctions in the SQUID, in fact:

$$E_{jp} \simeq 56.73 \cdot \left[ \frac{I_0}{10 \mu A} \right]^{\frac{1}{2}} \left[ \frac{C}{100 fF} \right]^{\frac{1}{2}} \quad (15)$$



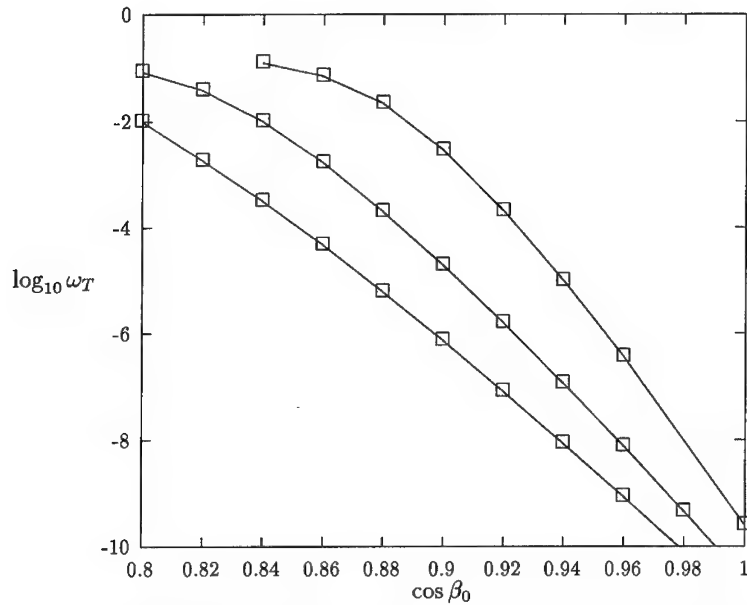


Fig. 5. Arrhenius plots by tuning procedure, from the top  $\beta_G = 1.2, 1.3, 1.4$ . Values of  $E_{jp}$  are respectively 50, 40 and 30.

The data reported in the square parentheses are typical for  $1\ \mu\text{m} \times 1\ \mu\text{m}$  junctions, so a further improvement can be obtained only with *submicron* junctions or with very small critical currents that are not simple to obtain. On the other hand, the alternative is use small values of  $\beta_L$  ( $\beta_G$ ), typically less than 1.5.

Until now we have ignored the effect of the dissipation that in general reduce the tunnelling effects<sup>1</sup>. More precisely it can be shown that the (Quantum) branch of the Arrhenius law can be written as<sup>6</sup> (to the first order of the perturbation theory in  $Q$ , where  $Q$  is the quality factor of the system):

$$\omega_T = A' \exp^{-B\Delta U - C/Q} \quad (16)$$

where  $A'$  is a prefactor different from  $A$  and slightly dependent on  $Q$ . Both  $A'$  and  $C$  can be predicted for any two-level (double well) system using the theory of Caldeira and Leggett. The same predictions can be obtained also by adding a dissipative term in the standard quantum mechanics<sup>12</sup>.

From a theoretical point of view the knowledge of the  $Q = \omega_j RC$ , in which  $R$  is the equivalent noise resistor of the Josephson junction in the SQUID, would seem to solve completely the problem of knowing the damping effects. However, the main difficulties in the treatment of the damping mechanism can be stated as follows: i) Is the damping mechanism in the SQUID ohmic? ii) If the damping mechanism can

be assumed ohmic, *what* is the relevant resistance that models the damping in the SQUID?

Regarding point i) we note that a Josephson junction can hardly be considered as an ohmic component due to the complex structure below the gap in its I-V characteristic. We note that for some data reported by Han *et al.*<sup>9</sup> in the thermal hopping regime, in which the order of magnitude of resistance used to fit the experimental data is just that of  $R_N$ , the values found can be explained as follows: if we think of the oscillation as a classical trajectory above the barrier, as is surely verified for the thermal hopping, the nonlinearity in the I-V characteristic involves an infinite number of frequencies. So, since the frequencies above the gap are the dominating ones in the variance of the process, the results will be that the dissipation occurs with the normal resistance  $R_N$ . However, the large indetermination in the values of the resistance found by Han *et al.* cannot permit drawing definite conclusions. We note that: 1) especially in the so-called intermediate damping regime the deduction of the values of the resistance from the escape rate can be affected by a relatively large error due to the poor dependence of the prefactor on the loss; 2) it will be reasonable that at very low temperature the gap structure will play a role in the sense that the losses decrease due to the shortage of the quasiparticle carriers below the gap; anyway the resistance will not attain the values of the subgap resistance if we assume that the data for the single junction<sup>13</sup> are comparable with those for the SQUID. The combination of these two facts probably explains both the large indetermination and the resistance values found by Han *et al.* in their work.

### Acknowledgements

We fully acknowledge all the other members of Rome MQC Collaboration for their useful comments and discussion about the MQC experiment that is presently being carried out in Rome. Particular thanks go to G. Diambri-Palazzi, M. G. Castellano, C. Cosmelli, C. Bravi and L. Chiatti. The MQC Collaboration and the MQC experiment in Rome are supported by INFN.

### References

1. A.J.Leggett and A.Garg, *Phys.Rev.Lett.***54**, 857, 1985; A.J.Leggett *et al.*, *Rev.Mod.Phys.***59**, 1, 1987.
2. L.Chiatti, M.Cini and M.Serva, *Phys.Lett.A.* *in press*.
3. G.Ghirardi *et al.*, *Phys.Rev.***D34**, 470, 1986.
4. We do not specify the characteristic of the readout system, whose study is programmed for the next years. Essentially the readout system is another SQUID maintained in a subcritical state (see the next ref.5 for the details).
5. Rome MQC Collaboration proposal, INFN, Addendum 29-11-1993.
6. A.O.Caldeira and A.J.Leggett, *Ann.Phys.(N.Y.)* **149**, 374, 1983; **153** 445(E), 1984.
7. D.Olive, S.Sciuto and R.J.Crewther, *Riv.Nuovo Cim.***2**, 2, 1979.

- 
8. C.Bravi, physics graduate thesis, University of Rome "La Sapienza", October 1994, unpublished.
  9. Siyuan Han, J.Lapointe and J.E.Lukens, *Phys.Rev.***B46**, 6338, 1992.
  10. G.Rotoli, unpublished 1994.
  11. Y.C.Chen, *J.Low Temp.Phys* **65**, 133, 1986.
  12. L.Chiatti, internal note MQC Collaboration 1994.
  13. R.Cristiano et al., *Phys.Rev.Lett.***60**, 844, 1988.

**PHASE LOCKING AND VOLTAGE - FLUX DEPENDENCIES  
IN ARRAYS OF JOSEPHSON JUNCTIONS  
CLOSED IN A SUPERCONDUCTING LOOP**

M. DARULA<sup>\*,+</sup>, A. DARULOVA, P. SEIDEL

*Institut für Festkörperphysik, Friedrich Schiller Universität D-07743 Jena, Germany*

and

Š. BEŇAČKA

*Institute of Electrical Engineering, Slovak Academy of Sciences, 842 39 Bratislava, Slovak Republic*

B. MIŠANIK

*Computer Centre, Slovak Academy of Sciences, 842 35 Bratislava, Slovak Republic*

**ABSTRACT**

The existence and stability of phase locking in arrays of Josephson junctions closed in a superconducting loop (ACISL) is analyzed. The existence of multiple dynamical states is shown using a transformation of the dynamical equations of ACISL to the dynamical equations of dc SQUID. The voltage - flux dependencies of ACISL for different numbers of junctions is calculated and the stability is determined using the method of Floquet exponents. It is shown that disorder influences significantly the stability.

## 1. Introduction

The circuit consisting of two series arrays of Josephson junctions closed in a superconducting loop (ACISL) can be considered as an extension of a dc SQUID. Because of the presence of arrays of Josephson junctions instead of single junctions in the SQUID loop, coherence effects (mutual phase locking between junctions) play important role and influence the total dynamical behaviour of the ACISL. Unlike for the dc SQUID, where the static and dynamic properties are rather well understood, the properties of ACISL still have to be investigated.

Some static properties of this kind of circuit have been studied<sup>1,2</sup>, and it has been shown that, in the loop, multiple quantum states can exist even for a negligible loop inductance providing that the total number of junctions is larger than four<sup>3,4</sup>. ACISL have also been studied in the context of some particular applications. The response to external radiation and its possible application as voltage standard has been discussed by Kobayashi *et al.*<sup>5</sup>. A modified circuit used as an amplifier has been described by McDonald<sup>6</sup> and the possible application as a magnetic field sensor has

<sup>\*</sup>Present address: Institut für Schicht-und Ionentechnik, Forschungszentrum Jülich GmbH, D-52425 Jülich, Germany

<sup>+</sup>Permanent address: Institute of Electrical Engineering, Slovak Academy of Sciences, Bratislava, Slovak Republic

also been analysed<sup>7</sup>. However, a systematical study of synchronisation of junctions (phase locking) which plays a crucial role in the dynamical behaviour of ACISL has not been done yet (some preliminary studies based on computer simulation were reported by Darula *et al.*<sup>8</sup>). Moreover, understanding of phase locking in this circuit will give the possibility of application of ACISL as microwave oscillators, mixers and parametric amplifiers<sup>9</sup>.

Recently, ACISL consisting of four high  $T_C$  superconductor bicrystal Josephson junctions have been fabricated<sup>10</sup>. In spite of a relatively large spread in junction parameters the phase locking of all junction has been observed. Experiments supported by computer simulations showed the enhancement of stability of phase locking due to an internal circuit resonance<sup>11</sup>.

In the present paper we concentrate on the description of basic dynamical properties of ACISL. Using a transformation of the equations of ACISL to the equations of a dc SQUID we dramatically simplify the analysis. We calculate voltage - flux dependencies of ACISL and show the existence of multiple dynamical states depending on the number of junctions in the arrays. Applying the Floquet exponent method, the stability of these state is analysed. The influence of disorder in the form of spread in critical current is taken into account.

## 2. Model Description

The circuit under consideration (Fig.1) consists of two series arrays of Josephson junctions where each of them contains  $M$  junctions.

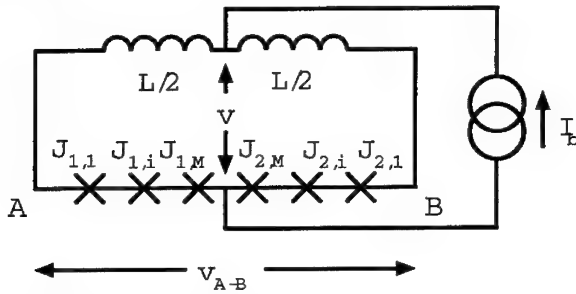


Fig. 1. Equivalent circuit of two arrays of Josephson junctions closed in a superconducting loop.

The  $j$ -th junction in the  $k$ -th array have critical current  $I_{Ck,j}$ . This can be expressed using spread parameters  $\delta_{k,j}^{I_c}$  as  $I_{Ck,j} = (1 + \delta_{k,j}^{I_c})I_C$ , where  $I_C$  is the average value of all critical currents. We define the maximum spread as  $\sigma^{I_c} = \max |\delta_{k,j}^{I_c}|$ . We will assume that the junctions have identical McCumber parameter  $\beta_C$ . Recently, it was shown that the spread in McCumber parameters has a weaker influence on the phase locking in arrays than the spread in critical currents<sup>12</sup>. Considering the current conservation and flux quantization condition in the superconducting loop and expressing currents through each junction by applying the RCSJ model we obtain the dynamic equations of the circuit as

$$(1 + \delta_{k,j}^{I_c})[\beta_C \ddot{\varphi}_{k,j} + \dot{\varphi}_{k,j} + \sin(\varphi_{k,j})] = -\frac{(-1)^k}{\beta_L} \phi_S + \frac{i_b}{2}, \quad k = 1, 2; j = 1, \dots, M, \quad (1)$$

where  $\phi_S = \sum_{l=1}^2 \sum_{i=1}^M (-1)^i \varphi_{k,i} + 2\pi \phi_{ext}$ ,  $\varphi_{k,j}$  are the junction phases,  $\phi_{ext} = \Phi_{ext}/\Phi_0$ ,  $\Phi_{ext}$  is the external magnetic flux penetrating the loop,  $\beta_L = 2\pi L I_C / \Phi_0$  and  $i_b = I_b / I_C$ . The normalized voltage across the ACISL can be expressed as  $v = (\sum_{k=1}^2 \sum_{j=1}^M \dot{\varphi}_{k,j})/2$ . Its time averaged value is denoted as  $\hat{v}$ , where averaging over a time interval much larger than all time constants of the circuit is assumed. In the same way we define the voltage between points A and B in Fig.1 by  $v_{A-B} = \sum_{k=1}^2 (-1)^k \sum_{j=1}^M \dot{\varphi}_{k,j}$  and its average value by  $\hat{v}_{A-B}$ .

### 3. Voltage - Flux Dependencies in the Case of $\sigma^{I_c} = 0$

#### 3.1. Possible Dynamical States

We start to discuss the dynamical states of the ACISL for the case of identical junctions:  $\sigma^{I_c} = 0$ . The ACISL circuit is similar to the dc SQUID (which is in fact the ACISL with  $M = 1$ ) but instead of one junction there is an array of junctions in each branch. To examine the possibility of existence of phase locking in this circuit we suppose that the phases of the junctions in each branch are locked, i.e.  $\varphi_{k,j} - \varphi_{k,l} = c_{j,l}^k$ , where  $c_{j,l}^k$  are constants. In Eqs.(1) we extract from each equation with  $k = 1$  (equations of left branch) the equation with  $k = 1, j = 1$  and from each equation with  $k = 2$  (right branch) the equation with  $k = 2, j = 1$ . Then, because time derivatives of phase differences are zero due to phase locking, we obtain

$$\cos\left(\frac{\varphi_{k,j} + \varphi_{k,1}}{2}\right) \sin\left(\frac{\varphi_{k,j} - \varphi_{k,1}}{2}\right) = 0, \quad k = 1, 2; j = 1, \dots, M. \quad (2)$$

From (2) we see immediately that, in the case of phase locking of junctions, the phases of all junctions can be expressed through phases  $\varphi_{1,1}$  and  $\varphi_{2,1}$  as

$$\varphi_{k,j} = \varphi_{k,1} + 2n_{k,j}\pi, \quad k = 1, 2; j = 1, \dots, M, \quad (3)$$

where  $n_{k,j} = 0, \pm 1, \pm 2, \dots$  ( $n_{k,1} = 0$ ). Expression (3) means that the junctions in each array oscillate in-phase and the voltage across each array has an amplitude of oscillation which is  $M$  times the amplitude of oscillation of an individual junction. Substituting (3) into eqs.(1), we obtain two differential equations:

$$\beta_C \ddot{\varphi}_{k,j} + \dot{\varphi}_{k,j} + \sin(\varphi_{k,j}) = -\frac{(-1)^k}{\beta_L^{ef}} (\varphi_{2,1} - \varphi_{1,1} + 2\pi \phi^{ef}) + \frac{i_b}{2}, \quad k = 1, 2 \quad (4)$$

where

$$\phi^{ef} = n + \phi^{ext}/M, \quad n = \sum_{j=1}^M (n_{2,j} - n_{1,j})/M \quad \text{and} \quad \beta_L^{ef} = \beta_L/M. \quad (5)$$

The eqs.(4) are formally identical to the differential equations describing the dynamical behavior of a dc SQUID with external flux  $\phi^{ef}$  and inductance parameter  $\beta_L^{ef}$ . Therefore, the dynamical properties of an ACISL (in-phase locking) can be derived from the well known dynamics of a dc SQUID and discussion of effective terms (5). To analyse the possible dynamical states, we first assume no external magnetic flux in the ACISL, i.e.,  $\phi^{ext} = 0$ . As known from the theory of the dc SQUID, a shift of external flux in the dc SQUID by one flux quantum leads to the same dynamical state (the state with the same  $v$ ), therefore the shift  $\phi^{ef} = 0 \rightarrow \phi^{ef} = 1$  results also in the same dynamical state. Moreover, because of symmetry, a change of direction of the magnetic field in a dc SQUID also does not create a different state. Therefore, we can confine ourselves to a study of possible values of  $\phi^{ef}$  from the interval  $\phi^{ef} \in [0, 1)$  and as possible values of  $n$  we have  $n = 0, 1/M, \dots, (M-1)/M$ . There are  $M$  different states with different voltages.

### 3.2. Dynamical States of ACISL in a Magnetic Field

It is well known that the voltage across a dc SQUID depends on magnetic field. The voltage flux dependence in a dc SQUID is a periodical function of external flux with period 1 (in units of  $\Phi_0$ ), the modulation depth (difference between maximal and minimal voltage) being determined by  $\beta_L$ . The typical voltage - flux dependence of a dc SQUID is shown in Fig.2 in the curve  $M = 1$ .

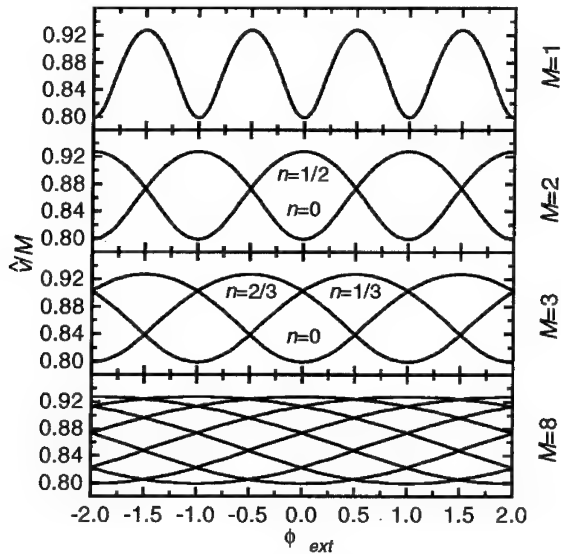


Fig. 2. The voltage - flux dependence of ACISL containing identical junctions ( $\sigma^{Ic} = 0$ ) calculated for different number of junctions in the arrays. In all cases  $\beta_C = 1$ ,  $\beta_L = M$  and  $i_b = 2.2$ .

As we have seen in the previous section, the electrical characteristics of ACISL with  $M > 1$  and among these also voltage - flux dependencies can be calculated from the corresponding characteristics of the dc SQUID with effective values (5). Based on (5), some general conclusions can be drawn. Because for a fixed external flux  $\phi_{ext}$   $\phi_{ef}$  can have  $M$  different values determined by possible values of  $n$  the voltage - flux dependence will be a multivaluated function of external flux and will consist of  $M$  different curves. The period of each curve is  $M$ , and, for fixed  $\beta_L$ , the modulation depth scales with the number of junctions  $M$ . At  $\phi_{ext} = 0$ , the minimal value of voltage occurs for  $n = 0$ , the maximum occurs for  $n = 1/2$ . However, such state is possible only for odd  $M$ . The voltage - flux dependencies for different number of junctions in the arrays are shown in Fig.2. The curves for  $M > 1$  have been obtained from the curve for  $M = 1$  taking into account (5).

We note that the state  $n = 0$  at  $\phi_{ext} = 0$  has  $v_{A-B} = 0$  and  $v$  has an amplitude of oscillation  $M$  times that of the individual junction. In the state with  $n = 1/2$ , the voltage  $v$  is constant in time and  $v_{A-B}$  has an amplitude of oscillation  $2M$  times that of the individual junction. This is an important difference to a dc SQUID, where, without external magnetic field, it is not possible to generate oscillations between terminals A-B (Fig.1).

### 3.3. The Stability of Dynamical States

All results presented above have been obtained under the assumption of existence of phase locked states. To justify these results, it is necessary to analyse the dynamical stability of these states. This can be carried out by numerical calculations of the Floquet exponents  $\lambda_i^F$  for periodical solutions of (1). This approach is similar to the analysis of resistively shunted series arrays (RSSA) of Josephson junctions by Hadley *et al.*<sup>13</sup> and Darula *et al.*<sup>12</sup>. The number of equations to be solved can be dramatically reduced using the analogy between ACISL and dc SQUID discussed above. The sign of the real part of  $\lambda_i^F$  determines the stability. When defining  $\lambda^F = \max \text{Re} \lambda_i^F$ , the stable phase locked state exists only if  $\lambda^F < 0$ . The dependence of  $\lambda^F$  on magnetic flux in the case of  $M = 2$  for both  $n = 0$  and  $n = 1/2$  states and two values of  $\beta_L$  is shown in Fig.3.

It is rather surprising that, even in the case of identical junctions, there are intervals of magnetic flux where one state is unstable. As we see, the length of this interval depends on circuit parameters (compare Fig.3 (a) and (b)). The voltage - flux dependencies where only the stable part of characteristics is shown are given in Fig.4. At the boundary of stability, switching into a different dynamical state occurs as indicated by arrows in Fig.4.



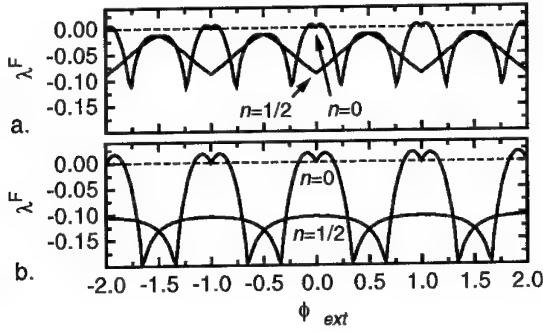


Fig. 3. Dependence of the Floquet exponent  $\lambda^F$  on magnetic flux in the case of an ACISL with  $M = 2$  for both  $n = 0$  and  $n = 1/2$  dynamical states. Dashed line represents the boundary of stability. Calculated for (a)  $\beta_L = 2$ ,  $\beta_C = 1$ ,  $i_b = 2.2$  and (b)  $\beta_L = 1$ ,  $\beta_C = 1$ ,  $i_b = 2.2$

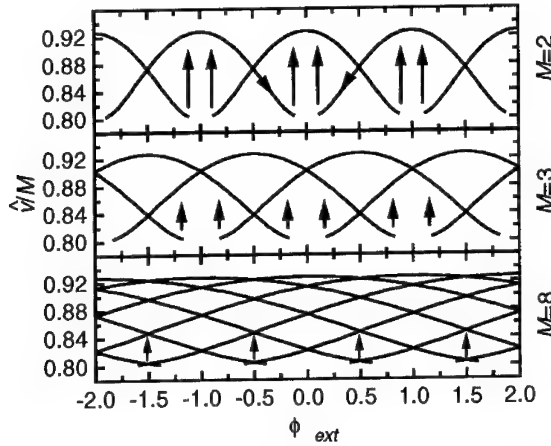


Fig. 4. The stable parts of voltage - flux dependencies of ACISL containing identical junctions ( $\sigma^{Ic} = 0$ ) calculated for different number of junctions in the arrays. In all cases  $\beta_C = 1$ ,  $\beta_L = M$  and  $i_b = 2.2$ . The arrows indicate the switching into different state at the boundary of stability in the case of sweeping the external magnetic field.

#### 4. Voltage - Flux Dependencies in the Case of $\sigma^{Ic} > 0$

Disorder influences the phase locking in Josephson junction arrays in a negative way. Therefore, to obtain a true picture of the dynamical properties of ACISL, it is necessary to take disorder into account. In our model, disorder is controlled by parameters  $\delta_{k,j}^{Ic}$ . It is necessary to define the distribution of these parameters. For simplicity we will suppose that the values of this parameters are distributed within

interval  $< -\sigma^{I_c}, \sigma^{I_c} >$  as  $\delta_{k,j}^{I_c} = (2(j-1)/(M-1)-1)\sigma^{I_c}$ . Applying the Floquet exponent method, it is possible to calculate the region of stability as it was done in the previous section. The stable parts of the voltage - flux dependencies for different  $\sigma^{I_c}$  are shown in Fig.5.

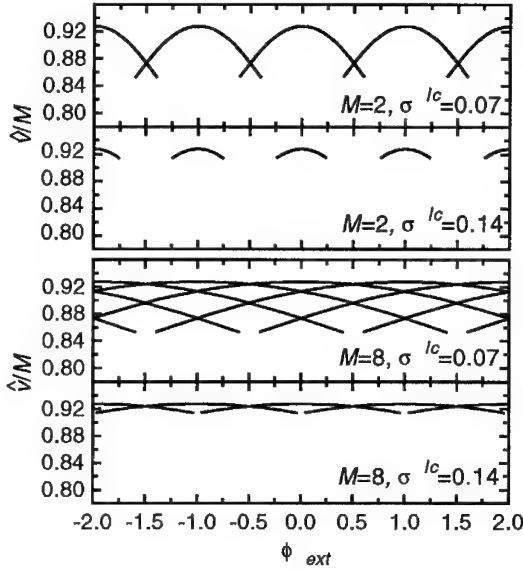


Fig. 5. The stable parts of voltage - flux dependencies of ACISL for different spreads in critical currents and number of junctions in array. In all cases  $\beta_C = 1$ ,  $\beta_L = M$  and  $i_b = 2.2$ .

As it is expected, the regions of stability decrease with increasing of disorder. This tendency also indicates that there is a limit in spread above which no phase locking exists. From Fig.5 we can estimate this limit to be  $\sigma^{I_c} \simeq 0.15$ . Comparing the results for  $M = 2$  and  $M = 8$ , we see that this limit does not depend on the number of junctions in the array. We note that the value of maximal allowed spread is about two times higher than the maximal spread in resistively shunted series array of Josephson junctions<sup>12</sup>. Therefore, an enhancement of stability of phase locking occurs in ACISL<sup>9</sup>. We also see that the highest stability at  $\phi_{ext} = 0$  has the state  $n = 1/2$  (or the state "closest" to  $n = 1/2$  in the case of even  $M$ ). It means that the most stable state is the state with maximal amplitude of oscillation between the array terminals (points A-B in Fig.1).

## 5. Conclusions

By calculating the voltage - flux dependencies the basic dynamical properties of circuit consisting of two arrays of Josephson junctions closed in a superconducting

loop (ACISL) have been analysed. It has been shown that in ACISL with  $M$  junctions in each array the voltage - flux dependence is a multivaluated function of external flux and consists of  $M$  different curves. The period of each curve is  $M$  and, for fixed inductance parameter  $\beta_L$ , the modulation depth scales with the number of junctions  $M$ . Using Floquet exponent method it has been shown that there are intervals of magnetic field where some phase locking states are unstable. The width of these intervals is determined by circuit parameters. In the case of sweeping the magnetic field the switching into a different state occurs at the boundary of stability. Disorder reduces the stability region. The maximal spread in critical currents allowing stable phase locking is  $\sigma^{I_c} \simeq 0.15$ . The maximal stability occurs in the state with maximal voltage  $\hat{v}$  and this is the state with maximal amplitude of oscillation between array terminals. The results listed above support the idea of application of ACISL as a source of coherent microwave radiation in the THz range. The enhanced stability against disorder also gives the possibility of successful fabrication of ACISL using high  $T_C$  superconductor technology<sup>10</sup>.

### Acknowledgements

We would like to thank A.I. Braginski, M. Siegel, S. Beuven, E. Sodtke and F. Busse for helpful discussions. The work was supported, in part, by German BMFT, contract No.13N6131, by Slovak Grant Agency (grant No. 2/999 185/92) and by Alexander von Humboldt Foundation. The author (M.D.) wishes also to thank the EU Human Capital and Mobility Program for Euroconference financial support.

### References

1. H.G. Meyer, T Roatsch, W. Krech, and M. Riedel, *Physica* **125B** (1984) 75
2. S. J. Lewandowski, *Phys. Rev. B* **43** (1991) 7776; **45** (1992) 2319
3. J.A. Blackburn, *J. Appl. Phys.* **56** (1984) 1477
4. T. Yamashita, Y. Ogawa and Y. Onodera, *J. Appl. Phys.* **50** (1979) 3547
5. T. Kobayashi, K. Hamsaki, N. Kondoh, T. Komata and T. Yamashita, *Appl. Phys. Lett.* **42** (1983) 475
6. D.G. McDonald, *Appl. Phys. Lett.* **45** (1984) 1243
7. K. Suzuki and Y. Okabe, *IEEE Trans. Appl. Supercond.* **3**, (1993) 1841
8. M. Darula, P. Seidel, F. Busse and S. Benacka, *J. Appl. Phys.* **74** (1993) 2674
9. M. Darula, P. Seidel, F. Busse and Š. Beňačka, *Supercond. Sci. Technol.* **7** (1994) 317
10. S. Beuven, M. Darula, J. Schubert, W. Zander, M. Siegel and P. Seidel, submitted to *IEEE Trans. Appl. Supercond.* (Proc. ASC'94) (1994)
11. M. Darula, S. Beuven, M. Siegel, A. Darulova and P. Seidel, submitted to *Phys. Rev. Lett.* (1994)
12. M. Darula, P. Seidel, B. Mišanik, F. Busse, E. Heinz and Š. Beňačka, *Physica B* **194-196** (1994) 1749
13. P. Hadley, M.R. Beasley, K. Wiesenfeld, *Phys. Rev. B* **38** (1988) 8172

## DOUBLE SQUID BEHAVIOR IN SUPERIMPOSED RF AND DC MAGNETIC FIELDS

BORIS CHESCA

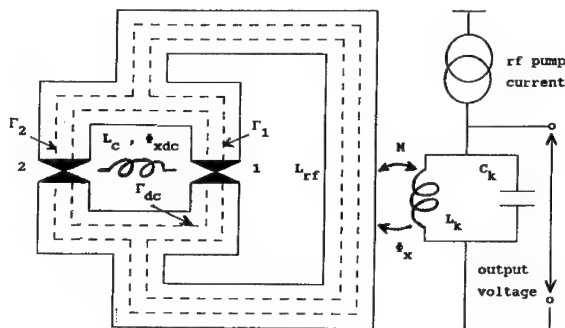
*Frank Laboratory of Neutron Physics  
Joint Institute for Nuclear Research  
141980 Dubna, Moscow Region, Russia*

### ABSTRACT

A calculation is presented which describes the behavior of a double SQUID, i.e., an rf-SQUID in which a dc-SQUID is used instead of the weak-link. Account is taken of possible differences between the individual critical currents of the two weak-links, and the asymmetrical current feed of the dc-SQUID. Depending on its parameter set values and the dc field, the system response to the rf perturbation qualitatively changes.

### 1. Theoretical model

Considering a traditional rf-SQUID and replacing the weak link with a dc-SQUID, what one has is a double SQUID (D-SQUID). Thus, as shown in fig.1, a D-SQUID consists of two quantization loops. The "dc-loop" contains two Josephson junctions, 1 and 2, and has an inductance  $L_1 + L_2$ . The "rf-loop" is connected in parallel to the junctions and has an inductance  $L_{rf}$ . Inductance  $L_{rf}$  is inductively coupled to the tank circuit  $L_k C_k$  via a mutual inductance  $M$ . An rf current generator supplies the tank circuit at its resonant frequency. Therefore, the resulting magnetic flux applied to the rf-loop is sine-shaped. Voltage picked up from the tank circuit provides the D-SQUID output signal. The input signal magnetic flux  $\Phi_{xdc}$  to be measured is applied via the signal coil to the dc-SQUID. Because the highest frequency of the signal flux spectrum is usually much less than the pumping frequency, this flux can be considered quasiconstant.



1. Schematic diagram of a D-SQUID

In <sup>1</sup> it was shown that the dynamics of a D-SQUID can be visualized as a motion in a two dimensional potential given by:

$$U(\phi_1, \phi_{dc}) = \frac{\Phi_0^2}{4\pi^2 L} \left\{ \frac{1}{2} [(\phi_{x1} - \phi_1) + \vartheta(\phi_{xdc} - \phi_{dc})]^2 + \frac{1}{2} \gamma (\phi_{xdc} - \phi_{dc})^2 - \frac{\beta}{2} [(1 + \alpha) \cos \phi_1 + (1 - \alpha) \cos(\phi_1 + \phi_{dc})] \right\}$$

$$\text{where } \alpha = \frac{I_{c1} - I_{c2}}{I_{c1} + I_{c2}}, \beta = 2\pi \frac{L(I_{c1} + I_{c2})}{\Phi_0}, \gamma = \frac{L}{L_1 + L_2}, \vartheta = \frac{L_1}{L_1 + L_2},$$

$$L = L_{rf} + \frac{L_1 L_2}{L_1 + L_2}, \phi(\cdot) = 2\pi \frac{\Phi(\cdot)}{\Phi_0}, \Phi_1(\Phi_{dc}) \text{ is the flux inside } \Gamma_1(\Gamma_{dc}),$$

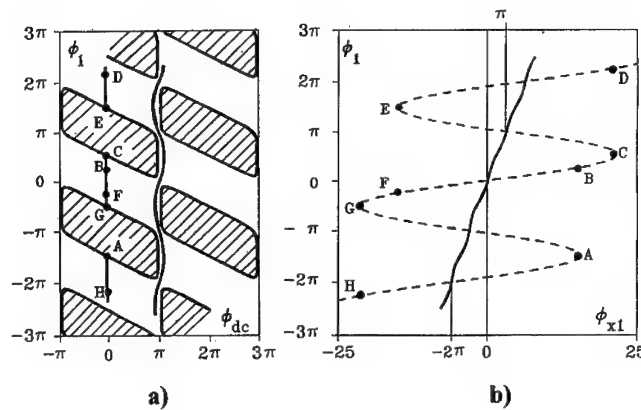
$\Phi_{x1}(\Phi_{xdc})$  is the flux applied to  $\Gamma_1(\Gamma_{dc})$ ,  $I_{c1}(I_{c2})$  is the critical current through the Josephson contact 1(2), and  $\Phi_0$  is the flux quantum. Here  $\alpha \in [0, 1]$ ,  $\beta > 1$ ,  $\gamma > 0$ ,  $\theta \in [0, 1]$  are the four D-SQUID parameters. In what follows, the D-SQUID will be characterized by its parameter set  $(\alpha; \beta; \gamma; \theta)$ .

In the steady states  $\partial U / \partial \phi_1 = 0$  and  $\partial U / \partial \phi_{dc} = 0$ . One obtains <sup>1</sup> thus, two coupled equations with respect to  $\phi_1$  and  $\phi_{dc}$ . There are no analytical solutions for this two equation set, so a computer simulation must be used. One finds that both  $\phi_1$  and  $\phi_{dc}$  are functions of  $\phi_{x1}$  and  $\phi_{xdc}$  having a  $2\pi$  periodicity in both variables. It should be pointed out that because  $\phi_{xdc}$  is quasiconstant, it must be taken as a parameter in what follows. Because of the  $2\pi$  periodicity, it is enough to consider only two cases:  $\phi_{xdc} = 2k\pi$ , where  $k$  is an integer (in this case the signal flux is an integer (1, 2, 3, ...) of quantum) and  $\phi_{xdc} = (2k+1)\pi$  (in this case the signal flux is half an integer (1/2, 3/2, 5/2, ...) of quantum). One should look for stable solutions which satisfy the requirement:  $\partial^2 U / \partial \phi_1^2 > 0$ ,  $\partial^2 U / \partial \phi_{dc}^2 > 0$  and  $\partial^2 U / \partial \phi_1 \partial \phi_{dc} > 0$ . By analyzing <sup>1</sup> the stable states domain  $D$  given by this set of three inequations one finds that there are three qualitatively different operating regimes. For each of them, one representative example will be discussed.

## 2. Results

In operating regime "a",  $D$  (unshaded areas in fig.2a) is a continuous domain with respect to both  $\phi_1$  and  $\phi_{dc}$ . The representative example is (0;20;200;0.5). The conditions which must be satisfied to have this situation are:  $\alpha\beta < 1$  and  $\gamma > \max(\gamma_1, \gamma_2)$ , where  $\gamma_1$  (lower signs) and  $\gamma_2$  (upper signs) are given by:

$$\gamma_{1(2)} = \frac{\beta}{4} \times \frac{\beta(1 - \alpha^2) \pm [2(1 - \alpha) - 4\beta(1 - \alpha + \alpha\beta)]}{1 \pm \alpha\beta}$$



2. Operating regime "a": a) stable steady states domain D (unshaded areas); a) and b) the operating point trajectories for different coordinates when the signal flux is an integer of flux quantum (capital letters, dashed line), and a half integer of flux quantum (solid line).

In fig. 2b, the flux inside  $\Gamma_1$  as a function of the flux applied to  $\Gamma_1$  is shown when the signal flux is an integer of flux quantum (dashed line) and a half integer of flux quantum (solid line). The variation of the signal flux by half the flux quantum implies that the system response to the rf perturbation changes from nonlinear (irreversible) to linear (reversible). This is a new aspect for rf pumped SQUIDs. As is well known for traditional rf-SQUIDs, this can be done only by changing the value of the  $\beta$  parameter from less than unity to greater than unity. This behavior can be well understood if one looks at the properties of the D domain (see fig. 2a). When the signal flux is an integer, the point operation must jump (see for example the jumps A-B, C-D and so on) over the unstable steady states, while when it is a half integer there is no need of jumps for the point operation to describe a continuous curve inside domain D.

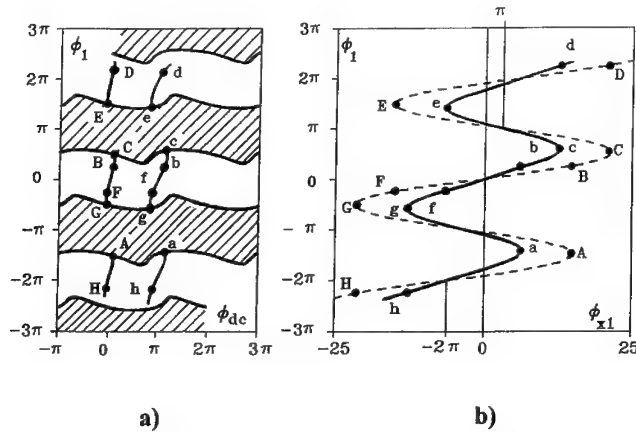
If the rf current amplitude is great enough, then a typical picture consists of flux transitions (like A-B C-D and so on) between different branches of the  $\phi_1(\phi_{x1})$  characteristic. What type of flux transitions are these? They are parallel to the  $\phi_1$  axis (see fig. 2a) which means that the flux inside dc-loop does not change. It changes only inside the rf-loop. Thus one can say that these transitions are one dimensional. It is as if we have only one quantization loop which participates in these transitions. From this point of view there is no qualitative difference between the flux transition occurring during the operation of a one quantization loop SQUID and the D-SQUID. These transitions will be referred to as "type A". The transition rule (the same as in the case of a traditional rf-

SQUID) is that for  $\beta$  values much greater than unity, the magnitude of the flux jumps inside the rf-loop is exactly one flux quantum.

In operating regime "b", D (unshaded areas in fig.3a) consists of a joining of bands. The representative example is (0.5;20;20;0.5). The conditions which must be satisfied to have this situation are:

$$\begin{cases} \alpha\beta < 1 \\ \gamma \in (\max(0, \gamma_2), \max(0, \gamma_1)) \end{cases} \quad \text{or} \quad \begin{cases} \alpha\beta > 1 \\ \gamma > \max(0, \gamma_2) \end{cases}$$

Compared with operating regime "a", the situation remains unchanged (see fig.3b) when the signal flux is an integer of flux quantum (dashed line) but it qualitatively changes when it is a half integer of flux quantum (solid line). In this later case, the system response is still

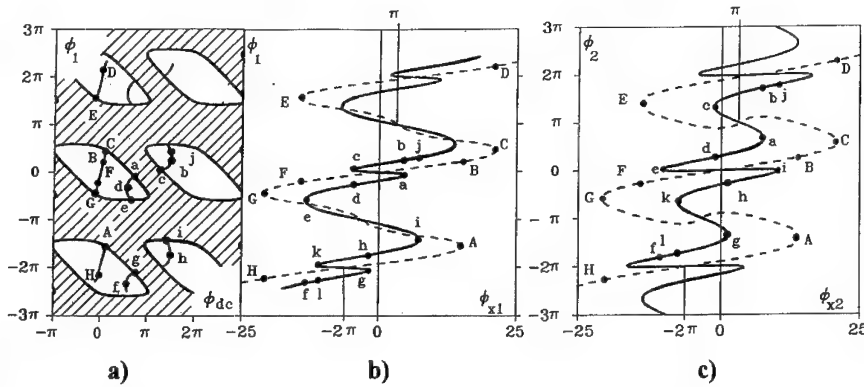


3. Operating regime "b": a) stable steady states domain D (unshaded areas); a) and b) the operating point trajectories for different coordinates when the signal flux is an integer of flux quantum (capital letters), and a half integer of flux quantum (small letters, solid line).

nonlinear but not as strongly as in the case when the signal flux was an integer. Again, one can look at the  $(\phi_1, \phi_{dc})$  plane (see fig.3a). Qualitatively there are no differences between how the stable states domain D looks around the lines, parallel to the  $\phi_1$  axis, that pass through  $\phi_{dc}=0$  and  $\phi_{dc}=\pi$ . All transitions (A-B C-D and so on, or a-b, c-d and so on) are parallel to the  $\phi_1$  axis, so they are also type A. Thus, in operating regime "b", independent of the dc field value, the system behaves nonlinearly (irreversible).

In operating regime "c", D (unshaded areas in fig.4a) consists of a joining of islands in two dimensional space. The representative example is (0.2;20;5;0.5). The conditions which must be satisfied to have this situation are:

$$\begin{cases} \alpha\beta < 1 \\ \gamma \in (0, \min(\gamma_1, \gamma_2)) \end{cases} \quad \text{or} \quad \begin{cases} \alpha\beta > 1 \\ \gamma \in (0, \max(0, \gamma_2)) \end{cases}$$



4. Operating regime "c": a) stable steady states domain D (unshaded areas); a), b) and c) the operating point trajectories for different coordinates when the signal flux is an integer of flux quantum (capital letters), and a half integer of flux quantum (small letters, solid line).

When the signal flux is an integer of flux quantum (dashed line in fig.4b) the system behaves the same as in the other two operating regimes. When the signal flux is a half integer of flux quantum a new qualitative factor appears (see fig.4a): besides type A flux transitions, like e-f or i-j, there is a new type, B, like a-b, c-d, g-h, whose directions are no longer parallel to the  $\phi_1$  axis, meaning that the flux changes inside both the dc and rf loops. Therefore, type B transitions are two dimensional. For this reason one must have a two dimensional representation. In fig.4c the dependence of the flux inside  $\Gamma_2$  is shown as a function of the flux applied to this path. In both figs.4b and 4c the case of the signal flux having values equal to half integers of flux quantum is represented by a solid line. For  $\beta$  values much greater than unity, the sum of the flux jumps occurring after a type B transition inside paths  $\Gamma_1$  and  $\Gamma_2$  is exactly one flux quantum (see, e.g., the a-b transition in figs.4b and 4c). With variation of the D-SQUID parameters, the magnitude of these separate jumps can take all possible spectrum values, but the sum will always be exactly one flux quantum. This is the rule for type B transitions.

A brief description of the influence of the D-SQUID parameters is as follows.  $\beta$  has the same influence as in the case of a traditional rf-SQUID, meaning that for higher  $\beta$  one has a larger hysteresis. The values of the other three parameters ( $\alpha$ ,  $\gamma$ ,  $\theta$ ) decide under what regime the D-SQUID will operate. For all possible values of the parameters the system's qualitative behavior will be one of the three described.

From the theoretical analysis developed here one can completely describe from the energetic point of view the operation of a D-SQUID. Therefore, one can separately obtain



the output characteristics (the average voltage as a function of current amplitude and signal flux) for each operating regime. Even more, the two rf pump modes (external and autodyne) can be optimized via the D-SQUID parameters <sup>1</sup>.

### 3. Physical interpretations

For  $\beta$  values much greater than unity, as in the case of a traditional rf-SQUID, one can give a physical interpretation for the flux transitions.

After one type A flux transition, the rf magnetic field line (MFL) corresponding to one vortex penetrates inside the rf-loop. Before and after this transition the MFL of this vortex does not cross the dc-loop. This may also be visualized as a magnetic flux simultaneously crossing both weak-links in packets having the size of one flux quantum. Because of the simultaneous switching of the two weak-links, one can say that the D-SQUID has the equivalent of a single flux gate with a one flux quantum periodicity.

After one type B transition two vortices are partially trapped inside the D-SQUID and the MFL of each vortex crosses both rf and dc loops. Consequently, weak-link 1 is penetrated by the fraction  $q_1$  from the first vortex and weak-link 2 is penetrated by the fraction  $q_2$  from the second vortex. Depending on the D-SQUID parameter set values,  $q_1$  and  $q_2$  can have different magnitudes from 0 to one flux quantum, but always the sum  $q_1 + q_2$  is equal to one flux quantum. This rule for a type B transition is not trivial and can be explained from energetic considerations. Simply stated: a system prefers a state where the potential has a minimum and this minimum is described by such a transition rule.

Unifying the physical pictures of the two types of flux transitions (A and B) one obtains the operational rule for the D-SQUID at the limit  $\beta$  being much greater than unity: the sum of the magnetic flux penetrating the two weak-links is two flux quanta for type A and one flux quantum for type B.

Let us try to explain the behavior of this two quantization loop SQUID in superimposed rf and dc fields by considering the flux quantification rule. It is well known that if one has a perfectly closed superconducting loop, meaning without weak-links, the flux must be quantified.

Now, if one applies a dc field equal to an integer quantum to the dc-loop, the "proposed" state for the flux inside the dc-loop satisfies the flux quantification rule. For this reason, the dc-loop needs no flux variations. But the external rf flux increases whether the dc-loop wants this or not. What happens is that the rf flux penetrates the D-SQUID in such a manner that only inside the rf-loop will the flux change by packets of one flux quantum. Therefore, the flux quantification rule tends to be satisfied inside the rf-loop, also. This is exactly the conclusion of our analysis for this case: for all three operating regimes, there will be no rf flux jumps inside the dc-loop but only inside the rf-loop, or in other words, during operation of a D-SQUID there will be type A transitions only.

Now, if one applies a dc field equal to a half integer quantum to the dc loop the "proposed" state for the flux inside the dc-loop does not satisfy the flux quantification rule, and one has three possibilities. In operating regime "a", the system is so "weak"

that the external condition applied to the dc-loop is "hard" enough to break the flux quantification rule inside both the dc and rf loops. For this reason with an increasing rf field there will be no rf flux jumps at all. In operating regime "b" the system is not as "weak", and the flux quantification is perturbed only inside the dc-loop. With an increase in the rf field, there will be flux jumps having the magnitude of one flux quantum inside the rf-loop only. In operating regime "c" the system is closest to a perfectly superconducting one. The dc-loop does not "accept" the state "proposed" by the applied dc field. It will jump between states that are closer to those predicted by the flux quantification rule, meaning states of an integer quantum. The jumps occurring inside both the dc- and rf-loops demonstrate that the flux quantification rule tends to be satisfied for both quantization loops.

#### 4. Magnetic flux amplitude modulator.

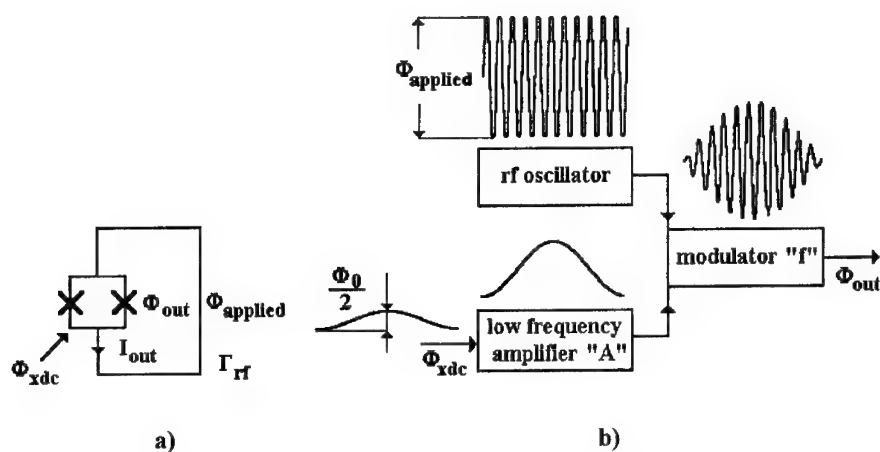
In the following, it is shown that a D-SQUID operating in regime "a" can be used as a magnetic flux amplitude modulation device.

Considering the case of the signal flux being equal to an integer of flux quantum, let us suppose that the amplitude  $\Phi_{\text{applied}}$  of the applied rf flux  $\Phi_{x1}$  is a little bit smaller than the  $(\Phi_{\text{applied}})^1$  needed for the system to describe the first hysteresis (ABCDEFGHA) in the  $(\Phi_1, \Phi_{x1})$  plane (see fig 2b). Therefore, during each oscillation of the rf flux applied to the rf-loop ( $\Gamma_1$ ), the flux  $\Phi_1$  inside the rf-loop oscillates with the same frequency, but with an amplitude equal to  $\Phi_0 / 4$ . In the case of the signal flux being equal to a half integer of flux quantum, the system response to the rf perturbation is linear so, the  $\Phi_1$  flux inside the rf-loop oscillates with the same amplitude as the flux applied to the loop. Therefore, the variation of the signal flux  $\Phi_{xdc}$  by only a half flux quantum implies that the oscillation amplitude  $\Phi_{\text{out}}$  of flux  $\Phi_1$  inside the rf-loop changes dramatically from  $\Phi_0 / 4$  to  $(\Phi_{\text{applied}})^1$ . It is not difficult to show that, as in the case of a traditional rf-SQUID, for a D-SQUID one has:

$$(\Phi_{\text{applied}})^1 2\pi/\Phi_0 = \sqrt{\beta^2 - 1} + \arccos(-1/\beta)$$

which for large  $\beta$  becomes  $(\Phi_{\text{applied}})^1 2\pi/\Phi_0 \cong \beta$ . The function carried out by a D-SQUID operating in regime "a" in the case of  $\Phi_{\text{applied}}$  being a little bit smaller than  $(\Phi_{\text{applied}})^1$  can be described by means of typical blocks used in standard electronics (figs. 5a and 5b). Thus, in order to modulate the output amplitude  $\Phi_{\text{out}}$  by a factor  $f$  one must amplify the signal  $\Phi_{xdc}$  by a factor  $A$  where:

$$f = \frac{\max(\Phi_{\text{out}}) - \min(\Phi_{\text{out}})}{\max(\Phi_{\text{out}}) + \min(\Phi_{\text{out}})} = \frac{2\beta - \pi}{2\beta + \pi}, \quad A = \frac{\max(\Phi_{\text{out}}) - \min(\Phi_{\text{out}})}{\max(\Phi_{xdc}) - \min(\Phi_{xdc})} = \frac{2\beta - \pi}{2\pi}$$



5. a) D-SQUID operating in regime "a", and b) its equivalent electronic circuit.

The fundamental physical variable is represented by the amplitude  $I_{\text{out}}$  of the rf screening current which is controlled by  $\Phi_{\text{xdc}}$ . Indeed, one has seen (section 3) that for the D-SQUID two loop system as a whole, in the sense of satisfying the flux quantification law and, therefore, implicitly in the sense of the magnitude of the screening current amplitude  $I_{\text{out}}$ , the superconducting properties are controlled by the value of the signal flux  $\Phi_{\text{xdc}}$  inside the dc-loop. This is the key point in explaining how a D-SQUID can operate as a flux amplitude modulator.

Finally, it should be pointed out that, to my knowledge, there are no references in the literature concerning the experimental fabrication of rf pumped D-SQUIDs operating in regime "a". Therefore it might be very interesting to build such a D-SQUID and to use the fundamentally new property of flux amplitude modulation discussed here in further applications.

## References

1. B.Chesca, to be published in *Physica C*.

# YBCO BICRYSTAL DC SQUIDS BY INVERTED CYLINDRICAL MAGNETRON

C. CAMERLINGO, H. HUANG<sup>+</sup>, B. RUGGIERO, M. RUSSO, E. SARNELLI,  
AND G. TESTA<sup>‡</sup>

*Istituto di Cibernetica del CNR, I-80072 Arco Felice (Napoli), Italy*

<sup>+</sup>*Tsinghua University, Dept. of Physics 100084, Beijing, China*

<sup>‡</sup>*and Istituto Nazionale di Fisica Nucleare, I-80127 Napoli, Italy*

## ABSTRACT

Preliminary results on  $\text{YBa}_2\text{Cu}_3\text{O}_{7.8}$  (YBCO) dc SQUIDS are presented. YBCO films have been deposited by inverted cylindrical magnetron sputtering technique on  $\text{SrTiO}_3$  bicrystal substrates. Grain boundary junctions, and both washer and hole-like SQUIDS have been fabricated. Good voltage modulation responses at temperatures as high as 87 K have been achieved. The obtained results show a very good agreement with data reported in the literature. Transport properties are discussed in the frame of a recent two-channel model.

Since the discovery of superconductive materials working at liquid nitrogen temperature<sup>1</sup> a rapid development of both theoretical analysis and experimental techniques has been followed. To date, in spite of the large effort of theoretical physicists, mechanisms of high temperature superconductivity are still matter of large debate. From the experimental standpoint, such uncertainties did not represent an obstacle for developing devices with high performances at 77 K. One of the simplest and highly developed high critical temperature ( $\text{HT}_c$ ) device which has been object of large investigations, is the dc SQUID magnetometer, constituted by a superconductive loop interrupted by two overdamped Josephson-like junctions. Very sensitive magnetometers (showing a magnetic field resolution  $S_H \approx 10 + 100 \text{ fT/Hz}^{1/2}$ ) in a wide range of frequencies have already been fabricated in many laboratories, even if their use in applications as biomagnetism or geomagnetism has remained, so far, at a demonstrative level. Other more complex circuits for applications in electronic devices as Rapid Single Flux Quantum logic<sup>2</sup>, infrared detectors<sup>3</sup>, or flux-flow based devices<sup>4</sup>, are obtained by combining many SQUIDS both in parallel and in series. Hence, in order to develop  $\text{HT}_c$  superconductive electronics, the basic requirement can be individuated in the capability of making high quality SQUIDS. Moreover, suitable geometries have to be obtained for developing high-speed devices. In fact serious limitations to the working velocity of a superconducting device can occur due to stray inductances of strip lines interconnecting the weak links constituting the device.

Due to intrinsic properties of  $\text{HT}_c$  superconductors, as their short coherence lengths, and stoichiometric complexity in comparison with most of low  $T_c$  materials, to date the best results in making Josephson-like weak links come from innovative technologies. Very high quality dc SQUIDS have been obtained by step-edge, biepitaxial and bicrystal techniques.<sup>5</sup> In this paper we report our activity on dc-SQUIDS obtained by growing highly oriented YBCO films on  $\text{SrTiO}_3$  bicrystal substrates. Recently we have obtained high quality dc SQUIDS working up to temperatures  $T = 87 \text{ K}$ . A relatively good control of transport

parameters has been achieved, allowing an a priori determination of electrical characteristics of Josephson junctions, as for instance critical current density and asymptotic resistance values.

## 1 Experimental Results

We have fabricated  $Y_1Ba_2Cu_3O_{7.8}$  grain boundary junctions (GBJs) and dc SQUIDs by evaporating thin superconducting films on  $SrTiO_3$  bicrystal substrates supplied by Wako Bussan (Japan). Typically, about 250-300 nm thick films have been deposited by inverted cylindrical magnetron dc sputtering.[6] Evaporation rate has been held at 2 nm / min, so that about two hours and half needed for each run. YBCO films have been evaporated at a nominal temperature  $T = 760^\circ\text{C}$ , with an accuracy of  $\pm 1^\circ\text{C}$ , in an  $Ar/O_2$  atmosphere (57%  $Ar$  : 43%  $O_2$ ). Thermal contacts to the heater were assured by silver paint. After YBCO deposition the temperature has been reduced down to  $450^\circ\text{C}$  to allow the formation of the orthorhombic phase. A 100 nm thick gold film has successively been deposited over the YBCO film to get contact pads. Contacts have been made wedge bonding 25  $\mu\text{m}$  diameter aluminum wires.

We have fabricated both single junctions and dc SQUIDs by a 2  $\mu\text{m}$  resolution photolithographic system. Samples have been patterned by wet etching superconductor films in a in-water saturated solution of ethylenediaminetetracetic (EDTA) acid.

We used  $SrTiO_3$  bicrystalline substrates with misorientation  $[001]$  tilt angles  $\theta$  ranging from  $10^\circ$  to  $45^\circ$ . GBJs were obtained by simple strip lines crossing the bicrystal line. In order to control quality and localization of GBJs, epitaxial films have to be fabricated. X-ray analysis by  $\Phi$ -scan technique of our films has been performed.<sup>6</sup> This allowed us to check both quality of deposited films and differences between real and nominal values of the misorientation angles.

We have fabricated two kinds of dc SQUIDs: washer and hole-like configurations, see Fig. 1. The first is the best geometry for making superconducting magnetometers since the possibility of coupling a multiturn input coil to the SQUID body leaving the two junctions outside the sensor area. From the other side, the hole-like configuration represents the right design for Josephson flux flow transistors and RSFQ applications. Even if such a configuration is not suitable for fabricating integrated superconducting magnetometers, strong voltage signals can be obtained due to the absence of a significative inductance coming from narrow strip-lines.<sup>7</sup> In fact the voltage modulation amplitude  $\Delta V \approx R_N \Phi_0 / 2L$  is inversely proportional to the loop inductance  $L$ ; here  $\Phi_0$  is the magnetic flux quantum, and  $R_N$  the junction ohmic resistance calculated at high voltages. Voltage modulation  $V(\Phi)$  of a washer-type dc-SQUID as a function of the applied magnetic flux is reported in Fig. 2a. Measurements refer to a  $10^\circ$  bicrystal SQUID at 77 K. Geometrical dimensions are:  $d = 10 \mu\text{m}$ ,  $w = 3 \mu\text{m}$ , and  $l = 75 \mu\text{m}$ , corresponding to a calculated inductance  $L \approx 1.25 \mu_0 d + \mu_0 l / 2 \approx 63 \text{ pH}$ . Normal resistance of the SQUID is  $R_N = 4 \Omega$ , leading to an expected voltage amplitude  $\Delta V \approx 0.71 I_c R_N [1 - 3.57 (k_B T L)^{1/2} / \Phi_0] / (1 + \beta_s) \approx 11 \mu\text{V}$ ;  $I_c$  is the single junction critical current,  $\beta_s = 2LI_c / \Phi_0$  the screening SQUID factor and  $k_B$  the Boltzman's constant . The experimental value is  $\Delta V \approx 2 \mu\text{V}$ , smaller than the expected one

by a factor of 5. A large reduction of  $\Delta V$  was also observed by Miklich et al.<sup>7</sup> From the  $V(\Phi)$  behavior a small value of the voltage to flux transfer parameter  $h = \partial V / \partial \Phi = 4 \mu V / \Phi_0$  is obtained. The flux focusing factor is  $f = \Phi_0 / (\Delta H A_g) = 3.4$  where  $\Delta H$  is the magnetic field for trapping one flux quantum in the SQUID loop and  $A_g$  the geometrical dimension of the SQUID hole.

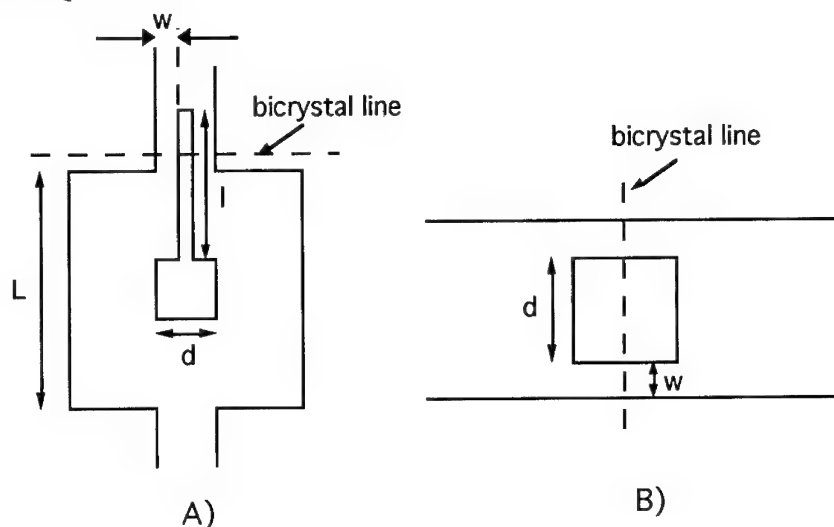


Fig. 1 Scheme of two possible dc-SQUID configurations: A) washer geometry; B) hole-like design.

Fig. 2b refers to the maximum voltage modulation ( $T = 77$  K) of a hole-like  $20^\circ$  bicrystal YBCO SQUID. The hole dimension is  $A_g = 64 \mu m^2$ , corresponding to an inductance  $L_h \approx 12.6$  pH. Each junction is  $3 \mu m$  wide and the additional inductance due to strip lines is  $L_w \approx 5$  pH. This time the ratio of the experimental value to the expected one is  $\Delta V_{exp} / \Delta V \approx 14.3 / 17.6 \approx 0.8$ . For this sample we have obtained larger values of both  $h = 43 \mu V / \Phi_0$  and  $f = 5.5$ . This SQUID worked with no appreciable decreasing of performances up to 82 K. Fig. 3 reports the voltage modulation for different bias currents at this temperature. At  $T$  close to  $T_c$  thermal noise<sup>8</sup> causes a rounding of current voltage characteristics ( $I$ - $V$ ) leading to a considerable reduction of the voltage modulation amplitude (about  $4 \mu V$  at  $T = 87$  K).

In Fig. 4 the  $I$ - $V$  characteristic of a  $20^\circ$  hole-like SQUID ( $w = 3 \mu m$ ) is reported. The behavior is well described in the frame of the resistively shunted junction (RSJ) model where thermal noise effects have been taken into account. Agreement between theory and experiment is excellent. At lower angles ( $\theta \approx 10^\circ$ ) a flux-flow like behavior is achieved. Sometimes, at such angles,  $I$ - $V$  characteristics are still RSJ-like, but an excess current is present. Actually the excess current is defined as the current value obtained by the intercept of the ohmic behavior (at  $V \gg I_c R_N$ ) extrapolated at zero voltage.

The characteristic voltages  $V_N = I_c R_N$  of a number of bicrystal SQUIDs as a function of the critical current density  $J_c$  are reported in Fig. 5 (dots) together with data available in the literature<sup>5,9</sup> (open triangles). At  $T = 4.2$  K,  $V_N$  values range between 0.1 and 0.8 mV.

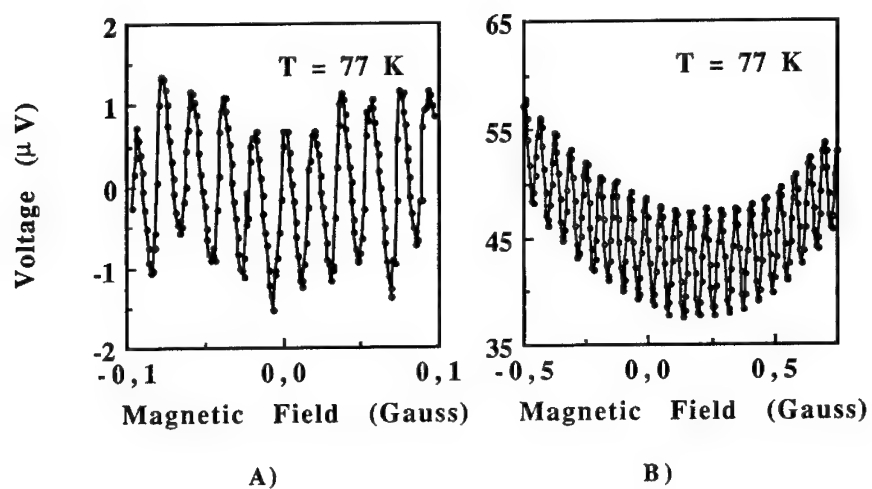


Fig. 2 Magnetic field dependence of the maximum voltage response: A) 10° bicrystal washer-type dc SQUID; B) 20° bicrystal hole-like dc SQUID.

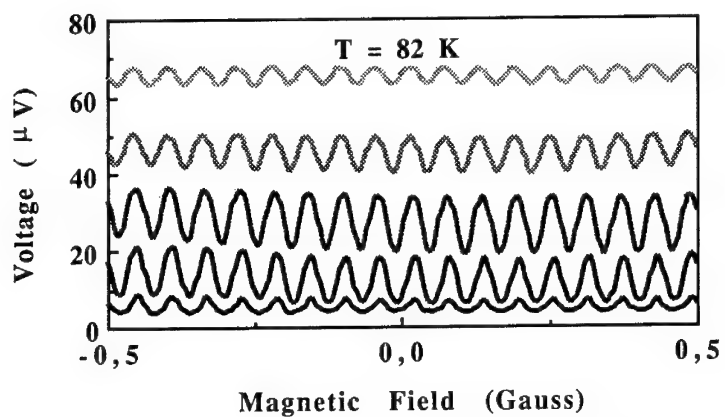


Fig. 3 Voltage modulation of a 20° bicrystal hole-like dc SQUID measured at different bias current.

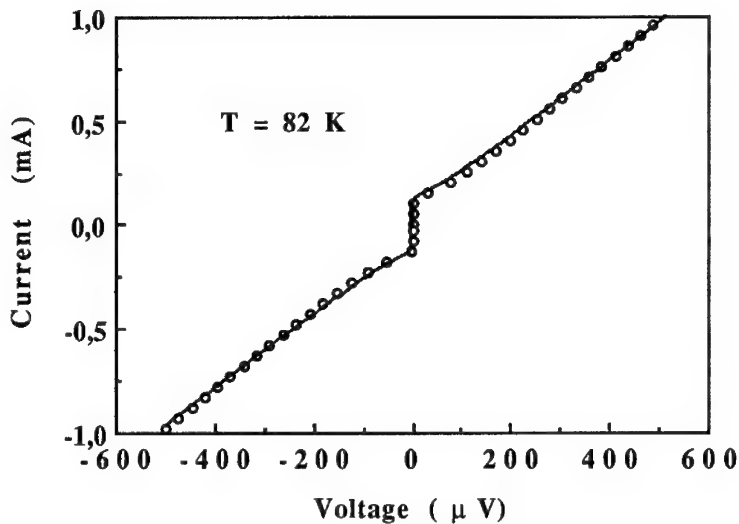


Fig. 4 Current-Voltage characteristic of a 20° bicrystal dc SQUID at  $T = 82$  K. Solid line is the experimental curve; dots represent the RSJ behavior.

A very good agreement of our data with other experimental results has been obtained. It is worth noting that, relatively to  $V_N$  vs.  $J_c$  dependence, bicrystal GBJs behave always in the same way, bringing to a sort of universal behavior, changing only for different substrates. For YBCO and TBCCO<sup>10</sup> on SrTiO<sub>3</sub> bicrystals  $I_c R_N \propto (J_c)^{0.6}$ , while for YBCO on MgO single crystals  $I_c R_N \propto (J_c)^{0.5,5,9}$

## 2 Discussion

As discussed in the first part of this work, the knowledge of microscopic properties of GBJs would allow computer simulations, useful to analyze complex circuits constituted by multi-junction systems. In particular, a deeper understanding of transport and noise properties is one of the constraints for a rational fabrication of devices.

Many models describing the microscopic configuration at the boundary have been developed; normal metal barriers<sup>11</sup> or insulating ones with direct or resonant tunneling<sup>5,9</sup> have been hypothesized. More recently<sup>12</sup> some of the authors developed a different model where a nonuniform barrier was considered. Actually, in the frame of such a model, superconductive properties are assumed to be locally depressed by oxygen deficiencies due to the presence of dislocations at the boundary which lead to the formation of non-superconducting regions. The macroscopic bicrystal grain boundary junction is then described as an array of microscopic filamentary junctions lying between non-superconducting regions. In this way two channels with different conducting properties



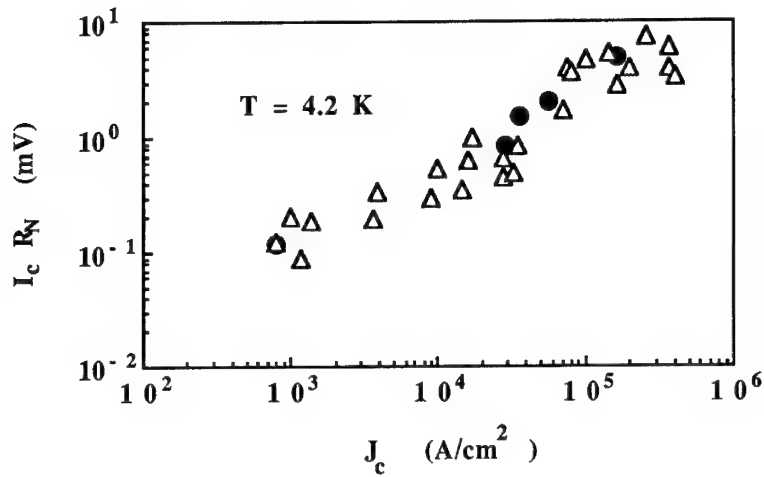


Fig. 5 Characteristic voltage  $I_c R_N$  plotted vs. critical current density  $J_c$  at  $T = 4.2$  K. Our data (dots) are plotted together with data (triangles) available in the literature.<sup>9</sup>

assure transport of current, superconductive filaments carrying both supercurrent and quasiparticle current, and non-superconducting regions carrying quasiparticle current only. Further details on the two-channel model are reported in Ref.12.

In the following we connect macroscopic and microscopic physical quantities in the analysis of transport properties and noise characteristics. Macroscopic parameters are those ones concerning the GB as a whole, like the critical current density  $J_c^{GB}$  and the specific resistance (resistivity times the junction length)  $\rho_{GB}$ . It is straightforward to get the following relations:

$$J_c^{GB} = \frac{J_c}{1 + \delta} \quad (1)$$

$$\rho_{GB} = \frac{\rho_s(1 + \delta)}{1 + \beta} \quad (2)$$

where:

$$\delta = \frac{w_I}{w_S} \quad (3)$$

$$\beta = \gamma\delta \quad (4)$$

$$\gamma = \frac{\rho_s}{\rho_I} \quad (5)$$

Here  $w_I$  ( $w_s$ ) and  $\rho_I$  ( $\rho_s$ ) are the width and specific resistivity of the non-superconducting region (filament) respectively. From Eqs. (1) and (2) the scaling behavior of transport parameters in GBJs is obtained:

$$J_c^{GB} \rho_{GB} = \frac{K}{\rho_{GB}} \left[ \frac{\rho_I}{(1 + \beta) + \frac{\rho_I}{\rho_{GB}}} \right] \quad (6)$$

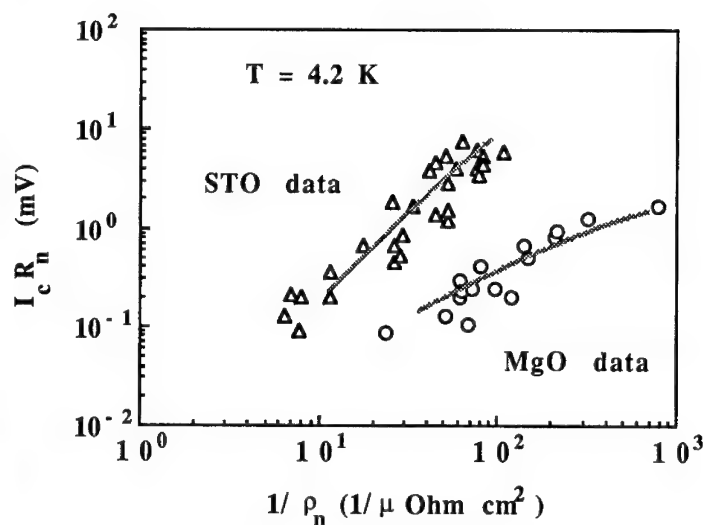


Fig. 6 Scaling behavior of the characteristic voltage  $I_c R_n$  with the conductance for unit area  $1/\rho_n$ . Triangles and circles are experimental data<sup>10</sup> for GBJs fabricated on STO bicrystal substrates and MgO single crystals respectively. Solid lines are theoretical curves calculated by Eq. 6.

$K = \rho_s J_c$  is assumed constant, meaning that transport mechanism of supercurrent through superconducting channel is similar to conventional Dayem bridges.<sup>13</sup> As the misorientation angle varies, the relative width  $w_s/w_I$  changes, so that  $J_c^{GB}$ ,  $\rho_{GB}$ , and  $\beta$  change too.  $\rho_I$  has to be assumed as a constant, since it depends on properties of the oxygen deficient region only. Using experimental values for  $\rho_{GB}$  and  $J_c^{GB}$ , and calculating  $\beta$  at each angle,  $\rho_I$  can be used as a fit-parameter. In this way we have obtained full lines in Fig. 6, which refer to data available in the literature<sup>9</sup> relative to GBJs on bicrystal  $\text{SrTiO}_3$  and single crystal MgO substrates. Reasonable fit values of  $\rho_I$  have been achieved:  $\rho_I = 0.06 \mu\Omega \text{ cm}^2$

for MgO and  $\rho_I = 0.09 \mu\Omega \text{ cm}^2$  for SrTiO<sub>3</sub>, respectively. It is worth noting that at large angles, when  $\beta \gg \rho_I / \rho_{GB}$ ,  $\rho_I$  is of the same order of  $\rho_{GB}$ .

An estimation of  $\beta$  at different angles can be made by considering that the critical current density is given by:

$$J_c^{GB} / J_c(\theta = 0) = \frac{1}{(1 + \beta)^2} \quad (7)$$

Finally, as shown by experimental results,<sup>14,15</sup> 1/f noise behavior in dc SQUIDs is well accounted for by considering contributions of both critical current and conductance fluctuations. In the two-channel model the ratio  $\alpha$  of these two components is connected to the parameter  $\beta$  by:

$$\alpha = \frac{(1 + \beta)^2}{2} \quad (8)$$

From calculated  $\beta$  a very good agreement between Eq. (8) and experimental values of  $\alpha$  has been obtained.

### 3 Conclusions

We have achieved a reliable and reproducible technique for the fabrication of YBCO bicrystal GBJs by using inverted cylindrical magnetron sputtering. High quality YBCO films with high critical current densities ( $J_c \approx 10^6 \div 10^7 \text{ A/cm}^2$  at  $T = 4.2 \text{ K}$ ) and critical temperatures ( $T_c = 89 \div 90 \text{ K}$ ) have been obtained. The characteristic parameters of our junctions have shown values in agreement with data reported in the literature. Two different geometrical configurations in fabricating dc SQUIDs have been employed. In particular SQUIDs with hole-type configurations show good performances up to 87 K. Transport parameters have been analysed in the frame of a two-channel model.<sup>13</sup>

### Acknowledgements

The work is partially supported by the CNR under the "Progetto Finalizzato Tecnologie Superconduttive e Criogeniche" and CNR under a cooperation agreement with Gruppo Nazionale di Struttura della Materia (GNSM). One of the authors (H. H.) thanks "ICTP Program for Training and Research in Italian Laboratories (Trieste, Italy) for financial support. Wako Bussan Company (Japan) is acknowledged for supplying very high quality SrTiO<sub>3</sub> bicrystal substrates.

### References

- 1 C. W. Chu, P. H. Hor, R. L. Meng, L. Gao, Z. J. Huang, and Y. U. Wuang, Phys. Rev. Lett. **58**, 405 (1987).

- 2 K. K. Likharev and V. K. Semenov, *IEEE Trans. on Appl. Superconductivity* **1**, 3 (1991); Z. G. Ivanov, V. K. Kaplunenko, E. A. Stepantsov, E. Wikborg, and T. Claeson, *Supercond. Sci. Technol.* **7**, 239 (1994); V. K. Kaplunenko, Z. G. Ivanov, A. Bogdanov, E. A. Stepantsov, T. Claeson, T. Holst, Z. J. Sun, R. Kromann, Y. Q. Shen, P. Vase, T. Freltoft, and E. Wikborg, *IEEE Trans. on Appl. Superconductivity*, 1994 (submitted); V. Kaplunenko (this volume); A. Davidson, M. J. Forrester, J. Talvacchio, J. Gavalier, and S. H. Talisa (this volume).
- 3 N. Bluzer and M. G. Forrester, *IEEE Trans. on Appl. Superconductivity*, 1994 (submitted).
- 4 J. M. Zhang, D. Winkler, P. Nilsson, and T. Claeson, *Appl. Phys. Lett.* **64**, 1153 (1994); L. Alff, B. Mayer, S. Shuster, O. Frolich, R. Gerdemann, A. Beck, and R. Gross, *J. Appl. Phys.* **75**, 3 (1994) 1843; P. Seidel (this volume).
- 5 R. Gross, in *Interfaces in Superconducting Systems*, S.L. Shinde and D. Rudman eds. (Springer, New York, 1992), Chap. 6; M. Kawasaki, P. Chaudhari, T. H. Newman, and A. Gupta, *Appl. Phys. Lett.* **58**, 2555 (1991); D. Grundler, B. David, R. Eckart, and O. Dössel, *Appl. Phys. Lett.* **63**, 2700 (1993);
- 6 A. Del Vecchio, C. Camerlingo, F. De Riccardis, H. Huang, B. Ruggiero, M. Russo, E. Sarnelli, M.A. Tagliente, L. Tapfer, G. Testa, *Il Nuovo Cimento* (to be published).
- 7 A.H. Miklich, D. Koelle, E. Dantsker, D.T. Nemeth, J.J. Kingston, R.F. Kromann and J. Clarke, *IEEE Trans. on Applied Superc.* **3**, 2434 (1993).
- 8 V. Ambegaokar, B. Halperin, *Phys. Rev. Lett.* **22**, 1364 (1969); R. Gross, P. Chaudhari, D. Dimos, A. Gupta, and G. Koren, *Phys. Rev. Lett.* **64**, 228 (1990).
- 9 R. Gross and B. Mayer, *Physica C* **180**, 235 (1991).
- 10 E. Sarnelli, P. Chaudhari, W.Y. Lee, E. Esposito, *Appl. Phys. Lett.* **65**, 362 (1994).
- 11 G. Deutscher and P. Chaudari, *phys. Rev. B* **44**, 235 (1991).
- 12 E. Sarnelli, *Interface Science* **1**, 287 (1993); E. Sarnelli, G. Testa and E. Esposito, *J. of Superconductivity* **7**, 387 (1994).
- 13 A. F. Volkov, *Sov. Phys. Solid State* **15**, 925 (1973).
- 14 M. Kawasaki, P. Chaudhari, and A. Gupta, *Phys. Rev. Lett.* **68**, 1065 (1992).
- 15 A.H. Miklich, J. Clarke, M.S. Colclough and K. Char, *Appl. Phys. Lett.* **60**, 1899 (1992).

# HIGH T<sub>c</sub> SQUID ARRAYS AS MICROWAVE GENERATORS

S. MATARAZZO and S. PAGANO

*Istituto di Cibernetica del CNR,  
I-80072 Arco Felice (NA), Italy*

G. FILATRELLA

*Dipartimento di Fisica, Università di Salerno,  
I-84081 Baronissi, Italy*

S. BARBANERA, F. MURTAS, C. ROMEO

*Istituto di Elettronica dello Stato Solido del CNR  
I-00156 Roma, Italy*

V. BOFFA, F. GATTA

*ENEA CRE Frascati  
I-00044 Frascati, Italy*

U. GAMBARDELLA

*INFN LNF Frascati  
I-00044 Frascati, Italy*

## ABSTRACT

We have investigated the dynamics of magnetic flux quanta in parallel arrays of Josephson junctions with the aim to implement flux-flow microwave generators employing high T<sub>c</sub> junctions. Systems of up to ten junctions have been numerically simulated. We have investigated the dependence of the emitted power on the system parameters (external magnetic field and bias current) and on the design characteristics (distribution of the external magnetic field and the SQUID screening parameter  $\beta$ ). The power available has been computed considering as a load either a resistor or a Josephson junction. The results show that the performance of such devices can be improved with appropriate design choices.

## 1. Introduction

In Josephson junctions the concept of propagating magnetic flux quanta (or fluxons) as solitonic wave has proved to be formidable tool both for theorists<sup>1</sup> and experimentalists<sup>2</sup>. The basic reason is perhaps that it allows the reduction of a system of an infinite number of degrees of freedom to the study of the motion of a particle-like object. More recently, with the discovery of High T<sub>c</sub> Superconductors (HTS) the interest has been focused on the discretized version of Long Josephson Junctions (LJJ). This was done essentially because Josephson junctions made of HTS materials are difficult to fabricate (due to the short coherence length and the anisotropy of the materials), and it seemed more realistic to try to realize short Josephson junctions with good reproducible parameters rather than LJJ. In chang-

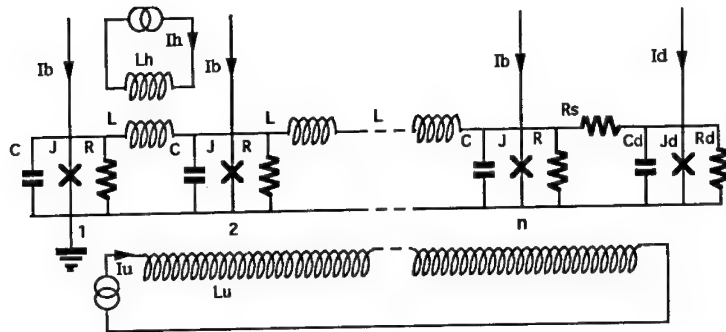


Fig. 1. Sketch of the circuit that models a one-dimensional array of Josephson junctions resistively coupled to another junction.

ing from LJJ to chains of inductively coupled Josephson junctions the concept of fluxon can still be a fruitful tool for a qualitative understanding, but a quantitative prediction of the behavior (based for instance on the perturbation method developed by McLaughlin and Scott<sup>1</sup>) is less reliable. For this reason numerical simulations are essential for an understanding of such systems, also considering that the simulation of arrays of short Josephson junctions, involving a small number of coupled differential equations is much faster than to simulate than that of LJJ involving the integration of a partial differential equation.

The purpose of this work is to investigate a simple device (a flux flow oscillator). We will show, with the help of numerical simulations, some key features of this device, like the mechanism of microwave generation and the effect on a junction employed as detector. In Section 3 preliminary experimental results on the fabrication of the device with HTS will be reported. Finally in Section 4 we will draw some conclusions.

## 2. Device Modeling

The device we are interested in is a parallel array of Josephson junctions, with common electrodes. In such systems each pair of junctions forms essentially a superconducting interferometer<sup>3</sup>, providing a coupling mechanism along the array.

Parallel arrays of Josephson junctions can sustain, under appropriate circumstances, fluxon propagation<sup>4</sup>. In our device a magnetic field, either spatially uniform or localized at one array edge, injects fluxons into the array. The fluxons are driven by the bias current and sent to a load which is represented by a resistively coupled Josephson junction. The equivalent circuit of the proposed device is shown in Fig. 1, where for the junctions we employ the *RSJ* model. The equations for the circuit in Fig. 1 can be derived in a simple form assuming that the magnetic field originated by the current flowing in each branch is confined in the two adjacent

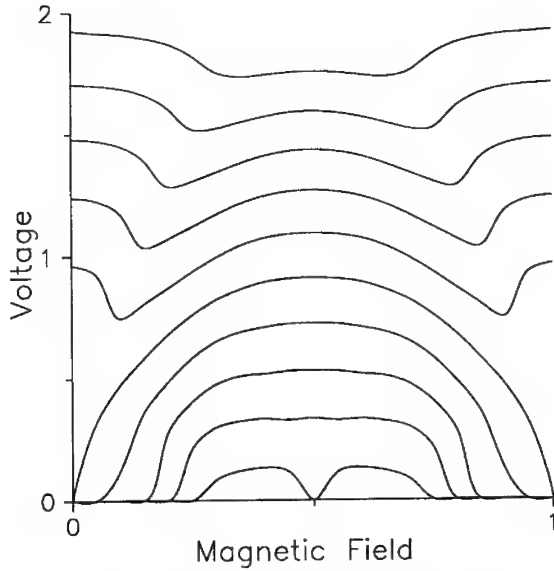


Fig. 2. Magnetic modulation of the array voltage. The current corresponds to bias values increasing from 0.2 (the lower) to 2 (the higher) in step of 0.2. Parameters of the simulations are:  $N = 10$ ,  $\beta = 1$ ,  $\alpha = 1$ ,  $\rho = 0$ .

cells (nearest neighbor approximation). In general one should take into account the contributions of the current flowing in each junction of the array, and write a mutual inductance matrix that couples each junction to each other. Under the simplifying hypothesis of nearest neighbours coupling, identical junctions and coupling inductances the equations can be cast in a simple adimensional form <sup>4</sup>:

$$\gamma + \gamma_c + \frac{2\pi}{\beta}(\eta_L^{(1)} + \eta_u) - \frac{1}{\beta}(\phi_1 - \phi_2) = \sin\phi_1 + \alpha\dot{\phi}_1 + \ddot{\phi}_1 \quad (1a)$$

$$\gamma + \frac{2\pi}{\beta}(\eta_L^{(n)} - \eta_L^{(n-1)}) - \frac{1}{\beta}(2\phi_n - \phi_{n-1} - \phi_{n+1}) = \sin\phi_n + \alpha\dot{\phi}_n + \ddot{\phi}_n \quad (1b)$$

$$\gamma - \frac{2\pi}{\beta}(\eta_L^{(N-1)} + \eta_u) - \frac{1}{\beta}(\phi_N - \phi_{N-1}) - \alpha\rho(\dot{\phi}_N - \dot{\phi}_D) = \sin\phi_N + \alpha\dot{\phi}_N + \ddot{\phi}_N \quad (1c)$$

$$\gamma_D + \alpha\rho(\dot{\phi}_N - \dot{\phi}_D) = \sin\phi_D + \alpha\dot{\phi}_D + \ddot{\phi}_D \quad (1d)$$

where the current is normalized to the junction critical current  $I_0$ , time is normalized to the inverse of the plasma frequency  $\omega_p$ ,  $\alpha = 1/\omega_p RC$ ,  $\beta = 2\pi LI_0/\Phi_0$  is the well known SQUID screening parameter,  $\rho = R/R_s$  represents the coupling between the array and the detector,  $\gamma_c$  is the normalized control current,  $\eta_u$  and  $\eta_L$  the normalized uniform and local magnetic flux, respectively.

Eq. (1) is the discretized version of the well known perturbed sine-Gordon equation which describes the dynamics of long Josephson junctions:

$$\phi_{xx} - \phi_{tt} - \sin\phi = -\alpha\phi_t + \gamma \quad (2)$$

where subscripts denote partial derivatives. In Eq. (2) the spatial operator is substituted by its discrete version  $\phi_{xx} \rightarrow (\phi_{i-1} - 2\phi_i + \phi_{i+1})/\Delta x^2$ . In this sense the parameter  $1/\beta$  corresponds to the spatial discretization, or, more exactly,  $\sqrt{\Delta x/\lambda_J} = 1/\beta$  ( $\lambda_J$  is the Josephson penetration depth). Thus in the limit  $\beta \rightarrow 0$ , this system tends to the continuum limit and in the condition  $L = \sqrt{\beta}N \gg 1$  all the dynamics of LJJ can be recovered.

Eq. (1) has been integrated using a fourth order Runge-Kutta method, first setting  $R_s = \infty$  to investigate the behavior of the system in the flux-flow regime without a load. A typical response of the array is summarized in Fig. 2 where the array voltage is shown as function of the external magnetic field. The behavior in Fig. 2 deviates from what is expected for a single loop SQUID, for the appearance of a double modulation within one flux quantum period (1 in the figure). For high bias values this effect is due to the presence of a flux flow state in the array, as can be seen in Fig. 3, where a contour plot of the magnetic field distribution in the array is shown. To further investigate this regime the magnetic field in the array is shown for different values of the  $\beta$  parameter (Fig. 3a-c).

The comparison of the three figures clearly demonstrates the effect of  $\beta$  on the fluxon motion. For small values of  $\beta$  ( $\beta < 1$ , Fig. 3a), there is no localization of the fluxons in correspondence to the underlying loop, giving rise to dynamical states equivalent to those of a single LJJ (with a length  $\simeq 3$ , in this case). By increasing  $\beta$  the fluxon, due to its motion, tends to be more and more localized in the loops (Fig. 3b) until a state is reached where it spends most of its time resting in the loop hole (Fig. 3c) and the overall motion becomes a hopping from one loop to the next.

In order to investigate the radiation emitted by the array when biased in the flux flow state we have simulated a load as a resistively coupled junction. In Fig. 4 the I-V characteristic of the "detector" junction is shown in the cases where the array is not biased (a) and biased (b) in the flux-flow state. In Fig. 4 the array is biased at a fixed value and the bias of the single junction is swept. A step structure is observed reminiscent of the Shapiro steps of a single junction when irradiated by a microwave field: the array is able to phase-lock the detector at the frequency generated by the flux flow. In this case, rather than pure microwave phase-locking, as occurs when an external radiation source is employed, it is more appropriate to describe the behavior shown in Fig. 4 as mutual phase-locking between the two subsystems: the array and the detector junction. Indeed the rf-induced step in the I-V characteristic of the junction is not vertical and the array voltage is pulled by the detector bias current.

In Fig. 5 is shown the open circuit power available as a function of the two tunable parameters: the bias current and the external magnetic field. The power is computed as follows: the output voltage of the junction at one end of the array (the end where fluxons are annihilated, see Fig. 3) is Fourier transformed, the amplitude of the component at the fundamental emitted frequency computed, and the corresponding power is determined. Fig. 5 shows that there is a maximum in the



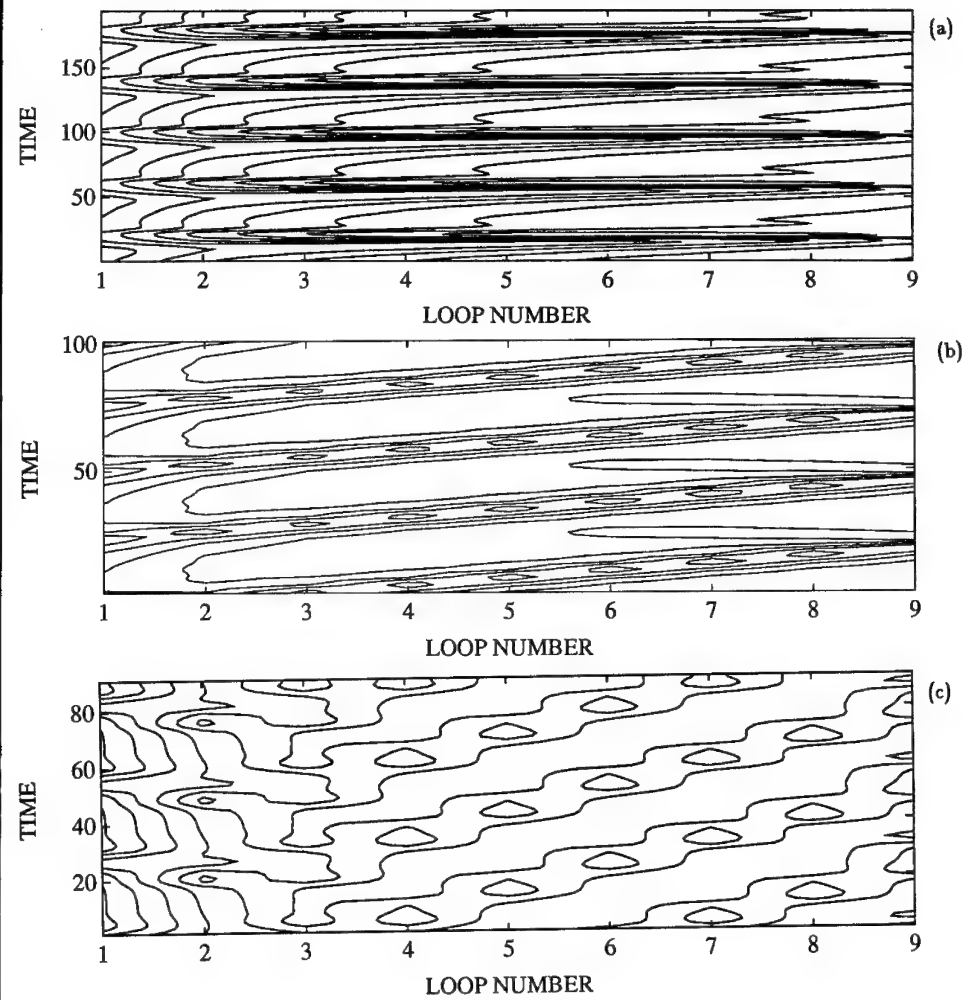


Fig. 3. Contour plot of the magnetic field distribution in the junction array. Parameters of the simulations are:  $N = 10$ ,  $\alpha = 1$ ,  $\rho = 0$ ,  $\eta_u = 0$ ,  $\gamma = 0.8$ , (a)  $\eta_l = 0.1$ ,  $\beta = 0.1$ , (b)  $\eta_l = 0.2$ ,  $\beta = 1$ , (c)  $\eta_l = 2$ ,  $\beta = 10$ .

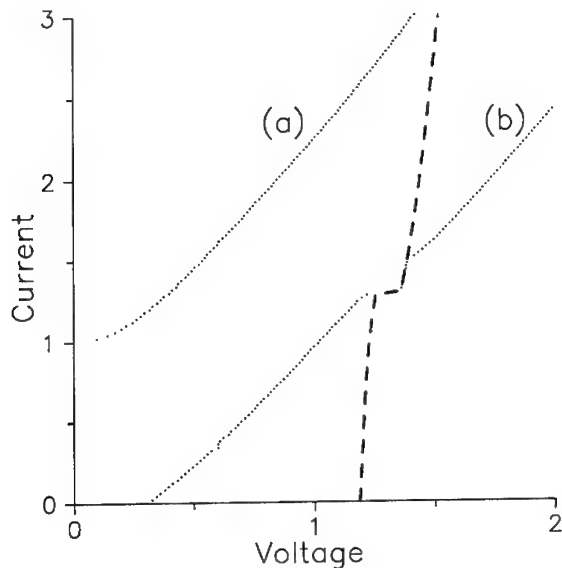


Fig. 4. Array (dashed curve) and detector (dotted curve) junction voltage as a function of the detector bias with use of unbiased (a) and biased (b) array. Parameters of the simulations are:  $N = 10$ ,  $\beta = 1$ ,  $\gamma = 1.5$ ,  $\alpha = 1$ ,  $\eta_l = 0.1$ ,  $\beta = 0.1$ .

emitted power corresponding to  $\gamma \simeq 1$  and  $\eta_L \simeq 0.5$ . That allows the determination of appropriate margins and performances for the flux flow oscillator

### 3. Experimental Results

We have taken the first steps toward the realization of a device exploiting the flux-flow dynamics just described (see Ref. <sup>7</sup> for details) employing HTS junctions. In Fig. 6 a microphotograph of a 10-junction array made using YBCO step edge junctions  $SrTiO_3$  substrate is shown. The step, determining the junction position is the white horizontal line. A control line, on the left, made by  $Au$  coated YBCO generates a local magnetic field, while a "detector" junction is placed to the right of the array. The detector is coupled to the array through a capacitor, not shown in the figure.

From preliminary experimental measurements on a number of arrays like that shown in Fig. 6 we can make the following considerations: The quality of the junctions made by the step-edge technique is relatively good, as suggested by the almost RSJ form of the I-V curve characteristic and the good magnetic field modulation of the critical current of a single junction <sup>7</sup>. Such behavior is not observed for the arrays. We believe that spreading of the junction parameters is the main responsible for the deviations from the expected behavior. This problem could be reduced by employing other junction fabrication techniques, like bicrystal-grain boundary junc-

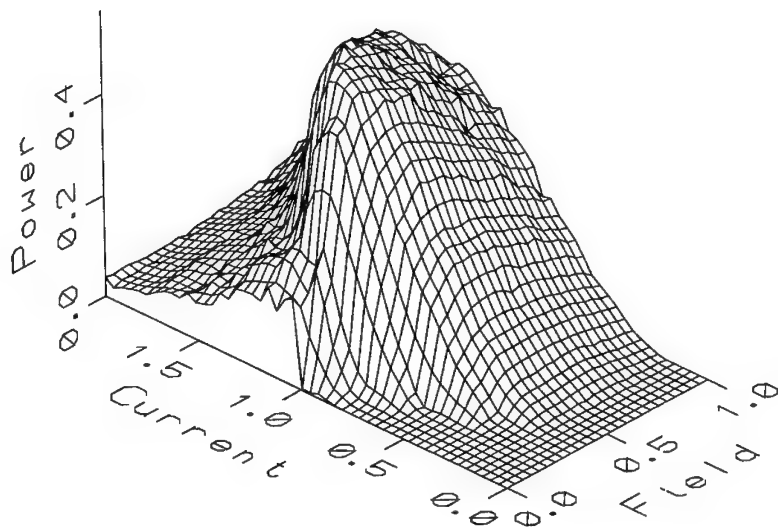


Fig. 5. 3D plot of the power vs bias current and magnetic field. Parameters of the simulations are:  $N = 10$ ,  $\beta = 1$ .

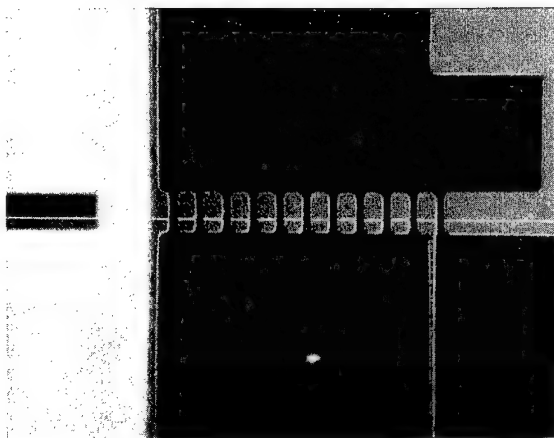


Fig. 6. Microphotograph of a YBCO 10 junctions array.

tions or epitaxially grown artificial junctions, which provide a better reproducibility of the junctions<sup>8</sup>.

#### 4. Conclusions

We have shown that the generation of microwave radiation in a simple system formed of a parallel of Josephson junctions is a realistic possibility. This system has been studied in detail to recover relevant information for an experimental realization employing HTS junctions. Numerical simulations can provide the range where the flux-flow regime is achieved, the effect of the SQUID parameter  $\beta$  on fluxons propagation, and the dependence of the emitted power on the tunable parameters. Preliminary measurements on step edge junction arrays hint that a relatively good degree of uniformity of the junction parameters along the array is necessary to achieve a correct operation of the device.

#### Acknowledgements

The work was supported by the MURST (Italy), the Progetto Finalizzato "Superconductive and Cryogenic Technologies" of the National Research Council of Italy, the EU Science Project no. *SCI\*-CT91-0760*. G.F. acknowledges the EU Human Capital and Mobility Program for Euroconference financial support.

#### References

1. D.W. McLaughlin and A.C. Scott, *Phys. Rev.* **A18**, 1652 (1981).
2. T. Nagatsuma, K. Enpuku, F. Irie, and K. Yoshida, *J. Appl. Phys.* **54**, 3302, (1983), *ibid* **56**, 3284 (1984).
3. A. Barone and G. Paternó, *Physics and Applications of the Josephson effect*, Wiley, New York, 1982.
4. G. Filatrella, S. Matarazzo, and S. Pagano, in *"Future directions of nonlinear dynamics in Physics and biological systems"*, Eds. P.L. Christiansen, J.C. Eilbeck, and R.D. Parmentier, p. 347 (Plenum Press, New York, 1993).
5. J.R. Phillips, H.S.J. van der Zant, J. White, and T.P. Orlando, *Phys. Rev.* **B47**, 5219 (1993).
6. D. Reinelt, W. Dietrich, T. Wolf, and A. Majhofer, *Phys. Rev.* **B49**, 9118 (1994).
7. C. Romeo, S. Barbanera, V. Boffa, G. Filatrella, U. Gambardella, F. Gatta, S. Matarazzo, F. Murtas, and S. Pagano, to appear in *IEEE Trans. Sup., Proceedings of Applied Superconductivity Conference*, (Boston 1994).
8. J.Z. Sun, L.S. Yu-Jahnes, V. Foglietti, R.H. Koch, and W.J. Gallagher, to appear in *IEEE Trans. Sup., Proceedings of Applied Superconductivity Conference*, Boston 1994. C.L. Pettiette-Hall, J.A. Luine, J. Murduck, J.F. Burch, J.R. Hu, M. Sergeant, and D. St. John, to appear in *IEEE Trans. Sup., Proceedings of Applied Superconductivity Conference*, (Boston 1994).

---

Chapter 6

## **Multilayer Structures**

# STACKED Nb-Al/AIO<sub>x</sub>-Nb JOSEPHSON TUNNEL JUNCTIONS

HERMANN KOHLSTEDT

*Institute of Thin Films and Ion Technology, Research Center Jülich (KFA)  
D-52425 Jülich, Germany*

## ABSTRACT

I review several new phenomena which occur in stacked Josephson tunnel Junctions. The interaction between Josephson vortices (fluxons) is investigated in stacked long Josephson tunnel junctions. Two phase-locked states characterized by different fluxon propagation velocities were found in strongly coupled two-fold stacks. The mode splitting can be described by dispersion relation for small amplitude waves in a system of two coupled sine-Gordon equations. Numerical simulations as well as experimental data showed that an out-of phase as well as in-phase propagation of vertically arranged fluxons is possible. In double barrier stacked long Josephson junctions with an access to the intermediate Nb layer, voltage-locking has been observed. Beside, the subject of stacked long Josephson junctions we experimentally investigated the range of locking to external rf-bias current for large 3D arrays. Up to 2000 series connected two-junctions stacks with in and 84 series connected stacks with four junctions in a stack were incorporated into a microstripline. Our measurement showed a drastical reduction of the phase locking range with increasing the number of stacked junctions. We investigated the dependence of the attenuation in the microstripline for different number of junctions in a stack. In addition, the attenuation of the rf current in the neighboring junctions in a stack was measured.

## 1. Introduction

Several research groups are presently pursuing the technological development of vertically oriented superconductor-insulator-superconductor-insulator-... (SISI...) Josephson tunnel junctions, so-called stacks, inspired by their immense potential for applications. Obvious of this three-dimensional (3D) approach is its advantage of higher packaging in comparison with a lateral, two-dimensional (2D), technology. Vertically arranged Josephson tunnel junctions are also opening new avenues for investigation of phase-locking to external rf-sources and mutual phase-locking between Josephson vortices (fluxons) moving in adjacent tunnel barriers. After the description of fabrication issues, the paper is separated into two main topics:

1. indications for a coherent motion of vertically coupled fluxons in double barrier stacks;
2. incorporation of stacked tunnel junctions in a Josephson voltage standard experiment.

These both examples are related to phase-locking effects, either due to the mutual

inductive interaction between the junctions or to an external rf-source. Since stacked devices only recently became a subject of detailed investigations, we expect more applications and the discovery of new physical effects in the near future, for example, in the field of x-ray detectors and non-equilibrium devices.

## 2. Fabrication issues

Regarding active superconducting devices, made of low and/or high- $T_c$  materials, the Nb-Al/ $\text{AlO}_x$ -Nb tunnel junction plays an outstanding role. After their first successful fabrication by Gurvitch et al.<sup>1</sup> in 1982, superconducting Nb-Al/ $\text{AlO}_x$ -Nb tunnel junctions are meanwhile well established in different fields of low temperature electronics. Examples include SQUIDs, millimeter wave receivers, cryogenic voltage standards, oscillators, and several Josephson computer related high speed circuits<sup>2</sup>. These all refractory tunnel junctions are stable at room temperature, are mechanically hard, and they have excellent thermal cycling stability, and, most important, desirable electrical properties, i.e. small leakage currents in the sub gap voltage region and a sharply defined gap voltage. In addition, no sophisticated deposition and dry-etching procedures are required to produce high quality textbook-like planar superconducting tunnel junctions. Consequently, most attempts with stacked tunnel junctions have been tried using this, so-called, all-niobium technology<sup>3,4</sup>. The cross-sectional view of a typical stacked device with three tunnel barriers is shown in Fig. 1. In order to

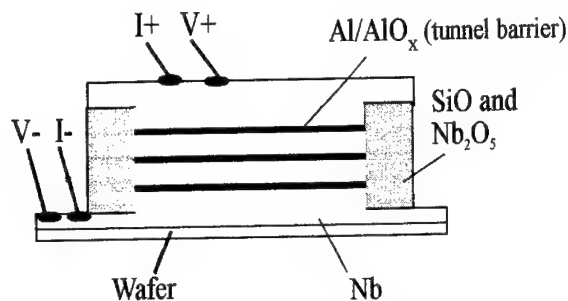


Fig. 1. Cross-sectional view of a stack with three tunnel barriers.

operate planar as well as 3D Josephson circuits, a small spread in the critical currents density  $J_c$  of the junctions typically, less than 10% is required. Since the critical current  $I_c$  of a tunnel junction is exponentially dependent on the barrier thickness, this is a task with many obstacles. In the case of planar arrays all tunnel barriers are formed during the same oxidation procedure and a small spread in  $I_c$ 's is achieved by adjusting carefully the oxidation and deposition parameters. The typical thickness  $t$  of the  $\text{AlO}_x$  tunnel barrier is 2 nm. In the fabrication of stacked Nb-(Al/ $\text{AlO}_x$ -Nb) $_n$  structures (here  $n$  is the number of junctions in the stack), compulsorily each tunnel junction is formed separately and small spread in  $I_c$ 's is much more difficult

to achieve. Deviations between the independent oxidation procedures could easily result in  $I_c$  spread larger than 50%. Additionally, surface roughness of niobium has a strong influence on the subsequent Al/ $\text{AlO}_x$  tunnel barrier formation. The surface roughness of niobium increases with its film thickness. We assume that on a rough surface the average number of thin tunnel barrier regions is larger than on a flat surface. Rougher surfaces result in lower normal resistance tunnel barriers because the tunnel current is dominated by thin barrier regions. Fujitsu group<sup>5</sup> showed that  $\text{AlO}_x$  act as a planarization layer. The growing process of the following Nb starts new on the former  $\text{AlO}_x$  tunnel barrier. The important consequence is that only each intermediate niobium layer thickness deposited on top of  $\text{AlO}_x$  is responsible for its roughness. Thus, the roughness in a stack does not increase with the total niobium layer thickness. For the  $\text{Nb}-(\text{Al}/\text{AlO}_x\text{-Nb})_n$  multilayer fabrication, we adjusted the oxidation conditions in dependence of the niobium thickness to get most uniform current density distribution within the stack. For example, in stacked devices with base Nb layer of 100 nm and the intermediate Nb layer thicknesses of 30 nm twice longer oxidation time for the formation of the tunnel barrier on the base electrode than for the oxidation of each following tunnel barrier. The oxidation temperature and the oxidation pressure were kept constant. By doing so, spreads of less than 3% were achieved in some samples. Nevertheless, spreads in  $I_c$  of 10% for tunnel junctions in a stack were usual. The run to run reproducibility for the critical currents was within 30%. The fabrication procedure for stacked  $\text{Nb}-(\text{Al}/\text{AlO}_x\text{-Nb})_n$  Josephson tunnel junctions with up to ten barriers is described in detail elsewhere<sup>6</sup>.

Most of previous investigations on vertically arranged Josephson tunnel junctions were carried out on double barrier Nb-Al/ $\text{AlO}_x$ -Nb-Al/ $\text{AlO}_x$ -Nb structures without an electrical contact to the intermediate Nb layer. For many important experiments, such as voltage-locking or fluxon pulling<sup>7</sup>, devices with access to common electrodes are necessary. Particularly, in the case of coupled flux-flow oscillators, the solution of this problem is of considerable importance in order to understand details of fluxons dynamics. Especially, to study fluxon coupling effects in stacked long junctions, two preconditions have to be fulfilled. First, the intermediate Nb layer thickness between two barriers has to be in the order of the London penetration depth, i. e. 90 nm for sputtered Nb films. Second, the area of the top and bottom tunnel junction should be equal to provide equal fluxons energies. By using a planarization process, we were able to avoid steep steps on the wafer and so to reduce the intermediate layer thickness to about 90 nm. We fabricated devices with the same area of the bottom and the top junction. The exact fabrication procedure is described elsewhere<sup>8</sup>.

### 3. Coherent motion of vertically coupled fluxons in stacked long tunnel junctions

Phase-locking of non-linear Josephson oscillators attracted much interest over the last two decades. Progress in this subject was paced by an intimated collaboration between mathematics, physics and thin film technology. Beside fundamental questions of phase-locking, arrays made of Josephson junctions are candidates for high



frequency oscillators in the mm and submm- wavelength range. Arrays are expected to overcome the limitation of single Josephson junctions, i.e. large line width and small output power. Mutual phase-locking between Josephson junctions in 1D and 2D arrays as well as the locking to resonators and external rf-bias sources were successfully proved<sup>9,10,11</sup>. With the advent of a reliable technology for the vertical arrangement of Nb-(Al/AlO<sub>x</sub>-Nb)<sub>n</sub> tunnel junctions experiments were extended to the third dimension. This technique allowed us to fabricate stacked long tunnel junctions in order to study the fluxon motion in closely spaced Josephson tunnel barriers<sup>12</sup>. Basis properties of long Josephson junctions have been reviewed by N. F. Pedersen and R. D. Parmentier<sup>13,14</sup>. A system of two vertically stacked Nb-Al/AlO<sub>x</sub>-Nb long Josephson junctions (LJJ's) is studied experimentally. In Fig. 2 the schematical view of such a device is shown without a potential contact to the intermediate Nb layer (a) and in Fig. 2(b) the device is shown with an access to the intermediate Nb layer. The

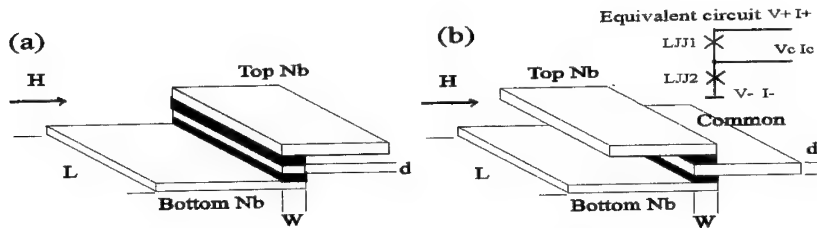


Fig. 2. Schematic view of (a) a double barrier stack and (b) a double barrier stack with a contact to the intermediate Nb layer. The external magnetic field is represented by  $H$ .

magnetic coupling between the two junctions in a stack is provided by their common electrode of the thickness  $d$  in the order of the London penetration depth  $\lambda_L$ . The critical current densities of approximately 250 A/cm<sup>2</sup> were adjusted to get so-called one-dimensional LJJ's. In this case the length  $L$  and width  $W$  have to be  $L/\lambda_J \gg 1$  and  $W/\lambda_J < 1$ . Here  $\lambda_J$  is the Josephson penetration depth. The external magnetic field  $H$  was applied parallel to the junction plane and perpendicular to the junction length  $L$  to create a unidirectional flow of Josephson vortices in either the top or the bottom junction or in both simultaneously. Each vortex carries one unit of flux quanta  $\Phi_0$ . We like to point out that many attempts were carried out to realize resonant (soliton) modes in which non or only small external magnetic field is applied, but usually these resonances do not appear stable in  $I - V$  characteristics.

### 3.1. Mode splitting in double barrier stacks

In this paragraph I explain the recent discovered mode splitting in the dispersion relation of strongly coupled stacked long Josephson tunnel junctions<sup>15</sup>. In Fig. 3 the current-voltage ( $I - V$ ) characteristic of a double barrier stacked LJJ is shown. The external magnetic field  $H$  was approximately 7 Oe. The examined device had no electric contact to the common Nb electrode. Thus, in the  $I - V$  characteristic

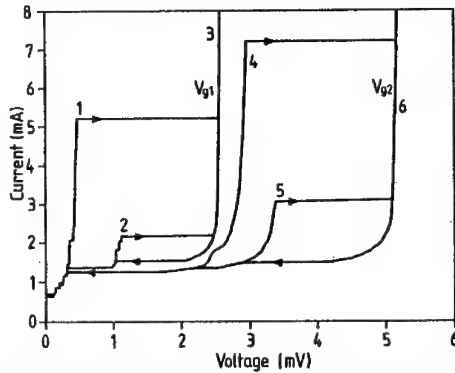


Fig. 3.  $I - V$  characteristic of a stack consisting of two junctions measured in the external magnetic field of  $H = 6.8$  Oe.

presented (Fig. 3) the stacked junctions were measured in series. The gap voltage  $V_g$  for a junction was found to be 2.6 mV and varied for the different junctions in one stack within 1 – 2%. The difference between the critical current densities in one stack was estimated from the maximum currents at the gap voltages and was found typically to be less than 15%. The intermediate Nb layer thickness was 30 nm. In the magnetic field applied in Fig. 3 one of the junctions with lower  $J_c$  contained fluxons, whereas the other junction (with larger  $J_c$ ) did not. In the  $I - V$  curve of Fig. 3 six singularities are shown and marked by numbers. Curve 3 is related to the gap  $V_{g1}$  of one junction of the stack. The gap  $V_{g2}$  of the second junction is marked by number 6 in Fig. 3. More important, two singularities below the first gap (number 1, 2) and also above the first gap (number 4, 5) are clearly seen. These singularities result from unidirectional flow of Josephson vortices in the barriers and denoted as flux-flow steps. In a single barrier long Josephson junction, for a given external magnetic field  $H$  only one flux-flow step is observed. The flux-flow step on the voltage scale is defined by  $V_{ff} = \bar{c}H\Lambda$ . Here,  $\bar{c}$  is the Swihart velocity and  $\Lambda = 2\lambda_L + t$  is the magnetic thickness of the barrier. The Swihart velocity is the maximum propagation velocity of an electromagnetic wave in a tunnel junction. Typical values are within 3 – 5% of the velocity of light in vacuum. The question is, why two flux-flow steps in double barrier stacks appear for an external magnetic field. This problem was considered theoretically by Ngai<sup>16</sup> who predicted the existence of two distinct phase velocities  $\bar{c}_+$  and  $\bar{c}_-$  for the linear electromagnetic waves in the double-junction stack linear model related to Giaever's experiment<sup>18</sup>. In a similar model, but where solitons were considered instead of linear waves, Sakai et al.<sup>17</sup> found two limiting fluxon velocities in the numerical simulations of a long double-barrier stack. According to the simplest theoretical model for two long junctions (A and B) coupled inductively through their common superconducting electrode of thickness  $d < 2\lambda_L$ , the phase difference  $\varphi(x, t)$  across each of them could be described by the equation

$$\varphi_{xx}^{A,B} - \varphi_{tt}^{A,B} = \sin \varphi^{A,B} + \alpha \varphi_t^{A,B} + \gamma - \delta \varphi_{xx}^{B,A}, \quad (1)$$

The spatial coordinate  $x$  is normalized to the single-junction Josephson penetration depth  $\lambda_J$ , the time  $t$  to the inverse plasma frequency  $\omega_0^{-1}$ ,  $\alpha$  is the dissipation coefficient, and  $\gamma$  is the bias current. Solving this equation for the small amplitude linear waves  $\varphi = \varphi_0 \exp[i(kx - \omega t)]$  with perturbative terms  $\alpha = \gamma = 0$  yields the dispersion relation  $\omega^2 = 1 + (1 \pm \delta) k^2$ , where  $\omega$  is normalized to  $\omega_0$ . Thus, for  $\delta \neq 0$  the plasma mode in each junction splits into two modes which are characterized by two different Swihart velocities

$$\bar{c}_{\pm} = \bar{c} \sqrt{1 \pm \delta}, \quad (2)$$

where  $\bar{c}$  is the Swihart velocity for the single-barrier junction. For a junction of length  $L$ , the Fiske step voltage spacing  $\Delta V_{FS} = \Phi_0 \bar{c} / (2L)$  ( $\Phi_0$  is the magnetic flux quantum) provides a direct experimental measure of the Swihart velocity, which allows an experimental estimate of the coupling parameter  $\delta$ . According to Eq. (2) the both Fiske step spacings  $\Delta V_{FS1}$  and  $\Delta V_{FS2}$  in the double stack can be calculated from the single-junction  $\Delta V_{FS}$  using the same value for  $\delta$ . The two flux-flow steps (for example 1 and 2) in Fig. 3 consisted of two different Fiske step spacing  $\Delta V_{FS1} = 18.5 \mu\text{V}$  and  $\Delta V_{FS2} = 45.8 \mu\text{V}$ . With this values we obtain a coupling parameter  $\delta \approx 0.7$ .

The observed splitting of phase velocities in coupled systems can be considered in a much more general sense. It is well known that the eigenfrequencies of two coupled oscillators split into two values if the coupling is strong enough. If the coupling parameter tends to zero, the previously different eigenfrequencies coincide and the system is in a degenerate state. From this qualitative analogy it appeared cogent to study the splitting of the dispersion relation as the function of coupling strength in stacked LJJ's. The coupling strength in two vertically arranged LJJ's is simply defined by the ratio  $d/\lambda_L$ . In Fig. 4 the splitting of the Swihart velocities in dependence of the thickness of the intermediate superconducting layer is shown. Clearly, the tendency of the two velocities to coincide with decreasing the coupling strength (increasing layer thickness) is visible<sup>20</sup>. For  $d \gg 2\lambda_L$ , one expects decoupled junctions.

### 3.2. The out-of phase locking in the lower mode

A further interesting question is whether a coherent motion of vertically arranged Josephson fluxons is possible<sup>21</sup>. In this case both tunnel junctions of the stack contain fluxons. Two possible configurations are schematically shown in Fig. 5(a) and 5(b). The first, (5 (a)) is called the out-of phase mode (there is a phase shift of  $\pi$  between fluxons in the junctions) and the second (5 (b)) the in-phase mode. The drawing below Fig. 5(a) shows two magnetic needles, one placed on top of the other. If the polarities of this two needles are the same, the needles repel each other. This simple model is transferable to vertically arranged Josephson fluxons. The magnetic field vector of Josephson vortices in a stacked LJJ's is parallel. So, naturally, one expects

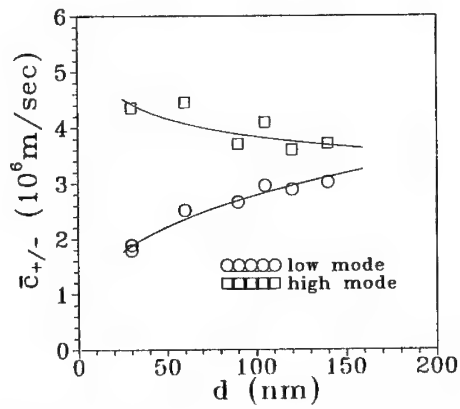


Fig. 4. Experimentally determined values for the higher mode velocities  $\bar{c}_+$  (open squares) and the lower mode velocities  $\bar{c}_-$  (open circles) in dependence of the intermediate Nb layer thickness  $d$ . The solid lines show power fits.

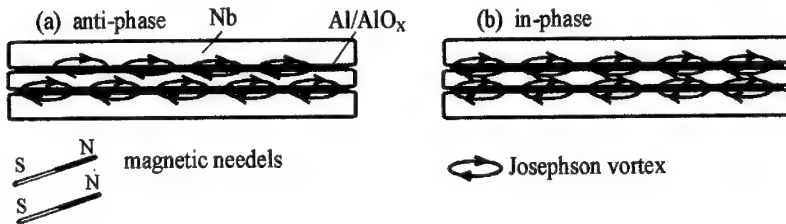


Fig. 5. Two possible arrangements of Josephson vortices: (a) the out-of phase mode and (b) the in-phase mode in vertically stacked LJJ's with two tunnel barriers.

a repulsion of the fluxons and, consequently, an out-of phase configuration (as shown in Fig. 5(a)) in the experiment.

Figure 6 exhibits the  $I-V$  curve of a stack with two tunnel barriers in zero external magnetic field. The intermediate Nb layer thickness was 100 nm. The difference between the critical current densities  $J_c$ 's for two junctions is found to be less than 5%. The ultimate switching of both junctions to the double gap voltage  $2V_g$  was found in a very broad magnetic field range. In the applied magnetic field  $H$ , a typical  $I-V$  curve is shown in Fig. 6(b). We observe two very pronounced resonances (steps) in  $I-V$  characteristics. The asymptotic voltages of both steps varied approximately linear with magnetic field, which indicates their flux flow origin. When the current  $I$  is increased from zero, the first flux-flow step (which is called "coherent mode", CM) is traced at  $V = V_{CM}$  below the first gap voltage  $0 < V_{CM} < V_g$ . From the top of this step the whole stack switches to  $V = 2V_g$ . With decrease of  $I$  another flux-flow step

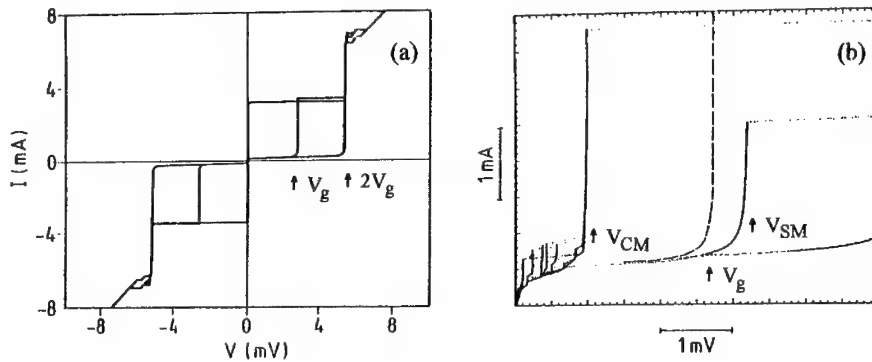


Fig. 6.  $I - V$  curve (a) of a two-fold stack at  $H = 0$ ; (b)  $I - V$  curve of a two-fold stack at  $H = 6.2$  Oe (solid line), dashed line shows to the single gap voltage branch at  $H = 0$ .

(called "single mode", SM) at  $V = V_{SM}$  is found, where  $V_g < V_{SM} < 2V_g$ . Clearly, SM accounts for one junction being at the gap voltage state  $V = V_g$  and another junction being at the flux flow state. The magnetic field tuning rate  $dV_{CM}/dH$  was measured to be by factor of 2 higher than  $dV_{SM}/dH$ . Figure 7 shows many traces of  $I - V$  curves (recorded using a digital storage oscilloscope) for this stack obtained at continuously varying the external magnetic field  $H$ . Each flux-flow step (CM and SM) consists of a series of cavity mode resonances (Fiske steps). As seen from a comparison of the horizontal scales in Fig. 7 (a) and 7(b), the CM branch displays twice larger Fiske step voltage spacing than the SM. This can be understood, as the CM regime accounts for the phase-locked state of two SM in two junctions. I note that the lowest observed CM Fiske step typically corresponds to the spacing between fluxons of about  $1.5 - 2\lambda_J$ , which indicates that the fluxon flow description might still be an appropriate model for this case. An interesting result is, that the CM could be tuned with the external magnetic field in a range from 150 GHz to 600 GHz which makes the device attractive for a sub-millimeter wave oscillator. Additional indications for the CM in the out-of phase configuration of fluxons were derived from Fiske step vs. external magnetic field dependence<sup>21</sup>, and spatially resolved measurements using low-temperature scanning electron microscopy (LTSEM)<sup>23</sup>. A strong hint for a mutually phase-locked state between two coupled Josephson junctions is the fact that the same voltages are simultaneously measured across each junction, while biasing in series. Such measurement requires a structure with an access to the intermediate Nb layer as shown in Fig. 2(b). Recently, so-called fluxon pulling effect<sup>7</sup> was observed in this kind of device, by using one LJJ's as a generator, while the other junction acted as a detector. Figure 8 shows the  $(I - V)$  characteristics of the bottom and the top junction of double barrier LJJ's with an access to the intermediate Nb layer. The junctions had the area of  $(10 \times 400 \mu m^2)$ . The junctions were biased in series and the

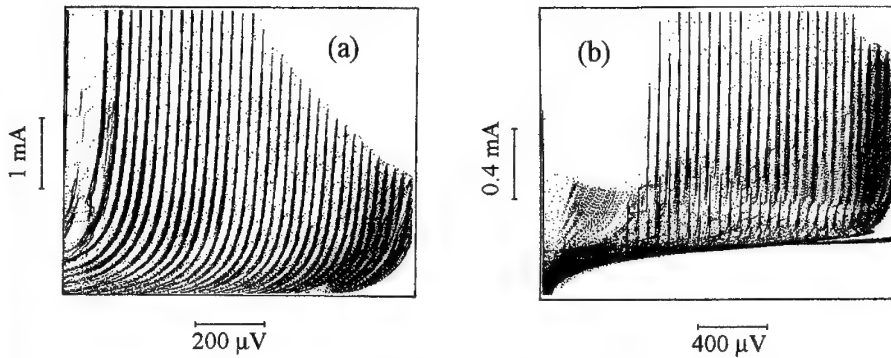


Fig. 7. Stored traces of  $I - V$  curves obtained in continuously varying external magnetic field  $H$ . The coherent mode (CM) in (b) displays twice larger Fiske step spacing than the single junction mode (SM) in (a).

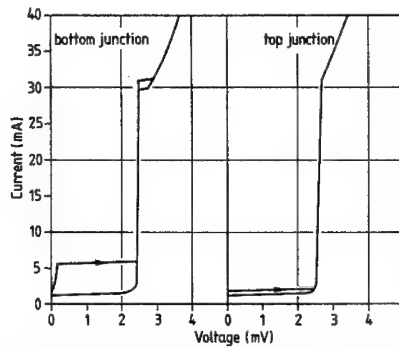


Fig. 8.  $I - V$  characteristics of the bottom and of the top junction of a stack biased in series.

voltage across each junction was measured separately. In Fig. 8, the large difference in the critical currents are due to the flux occasionally trapped in the junctions. At gap voltages of about 2.5 mV both junctions showed a strong quasi-particle current rise as expected for high quality junctions.

By applying a magnetic field parallel to the substrate plane and perpendicular to the junction length, Fiske steps were observed in the  $I - V$  characteristics. An example is shown in Fig. 9. Here, the voltage is measured across the whole stack. The voltage between Fiske steps spacing was determined to  $21\mu\text{V}$ , two times the value of a single junction. At  $H = 8\text{Oe}$  clear voltage locking of both junctions was observed, as shown in Fig. 9(b) and 9(c). The voltages on the top junction and on the bottom junction were equal within the accuracy of our voltage measurements of about  $0.5\mu\text{V}$ . The locking region is indicated in Fig. 9(b) and 9(c) by arrows. The voltage locking of two coupled Josephson junctions is a strong hint for phase-

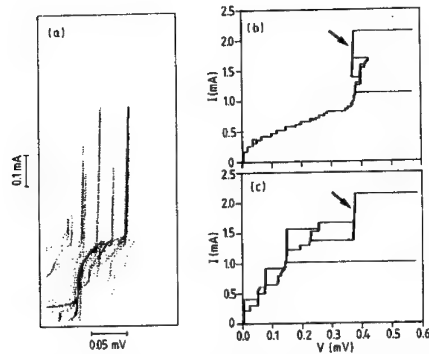


Fig. 9. Stored I-V data points (a) measured across the whole stack at continuously varying magnetic field  $H$  is shown. The I-V curves with voltages measured separately on the top and the bottom junctions are shown in (b) and (c), respectively.

locking phenomena between the junctions. For a direct proof, the measurement of microwave power and the line-width are required. Nevertheless, together with earlier reported experiments on double barrier stacks without an access to the intermediate Nb layer<sup>23,24</sup>, all obtained results make the picture of coherent fluxon states rather conceivable.

### 3.3. In-phase locking

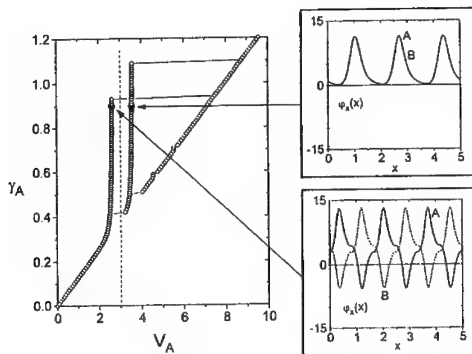


Fig. 10. Numerical calculated  $I - V$  curve for a two-fold stack with both junction (A and B) biased in series. The dashed line corresponds to the flux-flow step position in uncoupled single junction. The two insets show instantaneous profiles of magnetic fields  $\phi_A(x)$  and  $\phi_B(x)$  in two points of the I-V curve indicated by arrows.

As described earlier above with the simple model of two magnetic needles, the

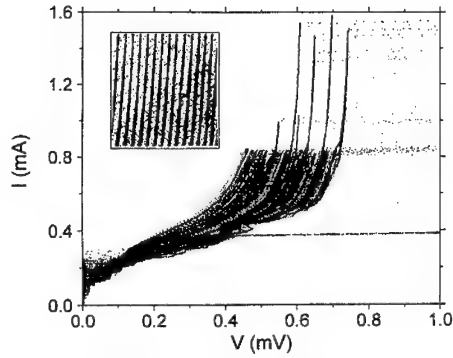


Fig. 11. Stored traces of  $I - V$  curves obtained in continuously varying external magnetic field  $H$ . The Fiske step spacing accounts for the phase-locked state with upper mode velocity  $\bar{c}_+$ . The inset shows Fiske steps of the single mode SM.

static interaction between Josephson vortices is repulsion. However, it has been shown numerically<sup>17</sup> as well as analytically<sup>19</sup> that the upper mode  $\bar{c}_+$  corresponds to the in-phase solution and accounts for the attraction between unipolar vortices. This configuration is schematically shown in Fig. 5(b). To illustrate this behavior, in Fig. 10 the numerically simulated  $I - V$  curve for a two-fold annular stack of the reduced length  $L/\lambda_J = 5$  is plotted<sup>22</sup>. In the lower branch  $\bar{c}_-$  the anti-phase locking is found, thus, individual fluxons repel each other, as expected. Surprisingly, the higher mode appeared to be the in-phase mode. More details are presented in recent work by Petraglia et al.<sup>22</sup>. Experimentally, for weakly-coupled stacks ( $d = 140$  nm) very stable phase-locked states with the upper mode  $\bar{c}_+$  were found. The voltage spacing between sharp resonances is equal to double of the highest Fiske step voltage spacing  $\Delta V_{FS2} = \Phi_0 \bar{c}_+ / (2L)$ . Comparison of these experimental observation with the numerical and analytical considerations brings us to the conclusion that Fig. 11 represents mutually in-phase locked resonances of two stacked junctions. This effect was only found if the fluxons move at high velocities. This mode is a nice example of a pure relativistic effect (with respect to the Swihart velocity, not to the speed of light in vacuum) which results in an attraction of unipolar vortices belonging to different junctions.



## 4. Incorporation of stacked tunnel junctions in a Josephson voltage standard experiment

### 4.1. Introduction

In the past, phase-locking in Josephson junctions with external rf-irradiation has been investigated for one- and two-dimensional junction arrays. An important application of Josephson junction arrays are cryogenic voltage standards<sup>25,26,27</sup>. Recent developments in this field focused on the decrease of the drive frequency from W-band (100 GHz) to the X-band region (10 GHz)<sup>28</sup>. In this case it will be possible to use semiconductor transistors for microwave oscillators (for example GaAs-MESFET's or HEMT's) at temperature of 4.2 K<sup>29</sup>. A drawback of this new approach is the necessarily large individual junction size of  $60 \times 260 \mu\text{m}^2$ . Since a modern voltage standard includes up to 20000 junctions, larger junction sizes lead to non-uniform microwave current distribution and undesirable chip sizes. Recently, we showed successfully that stacked tunnel junctions can be integrated into three-dimensional (3D) arrays and phase locking to an external rf-drive current was observed<sup>30,31</sup>. By the incorporation of stacked tunnel junctions in a voltage standard circuit, the package density can be increased. This yields a higher output voltage. In the following, the rf irradiation-induced phase-locking range in arrays with two and more junctions per stack is compared, with arrays which consisted of single barrier junctions. As the figure of merit of the phase locking range we defined the average voltage of maximal current step for one Josephson junction in an array. The locking range was measured with respect to the attenuation of the introduced microwave power along the stripline and within the stacks. Stacked Nb-(Al/AlO<sub>x</sub>-Nb)<sub>n</sub> tunnel junctions with up to ten barriers, and a critical current spread less than 15% have been fabricated<sup>6</sup>. We have combined this stacking technology with a fabrication process usually used to produce 2D arrays for a voltage standard<sup>32</sup>. A series of  $(X \times Y)$  tunnel junction arrays were fabricated.  $(X \times Y)$  means that each stack contains  $X$  tunnel barriers and  $Y$  of such stacks were connected in series to the dc power supply.

## 5. Results and discussion

### 5.1. Three-dimensional arrays

We investigated several arrays with different numbers of junctions. As two representative examples  $I - V$  curves of  $(2 \times 2000)$  and  $(4 \times 84)$  Josephson junction arrays are shown. Fig. 12(a) shows  $I - V$  curve of 2000 in series connected stacks. Each stack consisted of two tunnel junctions giving the 4000 junction in the array. Under rf-irradiation of 70 GHz, current steps were observed only up to maximal 510 mV. The average voltage per junction was 0.17 mV. This is approximately a factor 3 – 4 too low in comparison with the expected value<sup>26</sup>. Fig. 12(b) shows the  $I - V$  curve of a  $(4 \times 84)$  Josephson junction array. The spread of junction critical currents in

the array was between  $160\mu\text{A}$  and  $210\mu\text{A}$ . Upon applying rf-bias the critical current

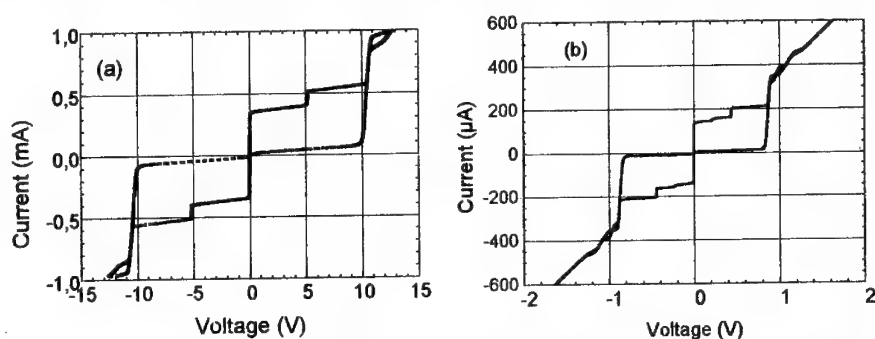


Fig. 12.  $I - V$  curve of an array with 2000 Nb-(Al/AlO<sub>x</sub>-Nb)<sub>2</sub> stacks (Fig. (a)) and  $I - V$  curve an array with 84 Nb-(Al/AlO<sub>x</sub>-Nb)<sub>4</sub> stacks (Fig. (b)).

spread increased. Moreover, critical currents splitted into four different values. In Fig. 13, the  $I - V$  curve of the first five stacks of this array is shown under 70 GHz irradiation. Clearly four critical currents of approximately  $0\mu\text{A}$ ,  $100\mu\text{A}$ ,  $130\mu\text{A}$  and  $180\mu\text{A}$  are visible. At this point it is clear that each critical current level corresponds to a certain tunnel barrier level. This could be due to a strong non-uniform rf-power distribution within a stack. Indeed, only for the first two stacks placed near to the input of the microstripline current steps with the maximal voltage  $V_n = 8\text{ mV}$  (average  $1\text{ mV}$  per junction) at external drive frequency of  $70 - 80\text{ GHz}$  are observed. The whole array with totally 336 junctions showed current steps only up to  $20\text{ mV}$ . That means an average voltage per junction of  $0.059\text{ mV}$ . Maximal and average  $V_n$  values

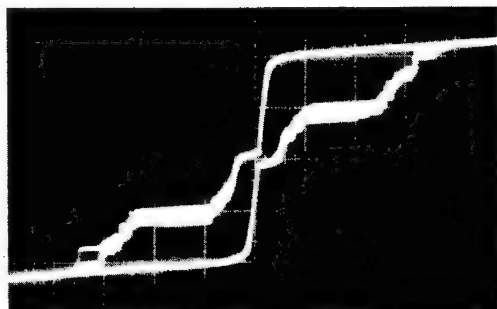


Fig. 13.  $I - V$  curve an array with  $(4 \times 5)$  junctions under  $70\text{ GHz}$  irradiation. Horizontal:  $50\text{ A/div.}$ ; Vertical:  $20\text{ mV/div.}$

for various arrays are summarized in Table 1. Data of Table 1 document a decrease of average voltage with increasing number of junctions in the array. Remarkable is the strong reduction of the average voltage with increasing number of tunnel barriers

in a stack. For example, the transition from the  $(2 \times 84)$  to the  $(4 \times 84)$  array caused average voltage to drop by an order of magnitude.

Number of JJ in a stack	Number of stacks in an array	Maximal voltage of the current steps, mV	Average voltage for one JJ in an array, mV
2	2	5	1.25
2	84	100	0.59
2	2000	510	0.17
4	2	8	1
4	84	20	0.059

Table 1. Parameters of the investigated samples.

To clarify this problem we concentrated on simpler arrays with small number of junctions. These array designs offered the possibility to measure the  $I - V$  curve of individual junctions or stacks located at different points of the microstripline.

### 5.2. Phase-locking in arrays of single barrier junctions

For the following investigations a circuit with a layout which is shown in Fig. 14 was used. The circuit consisted of following basic parts: a fin-line taper (A), the series array with 40 stacks or single barrier junctions (B), which acts as a stripline for the microwaves, a load (C), and a low-pass microstrip filter (D). Each junction has a length of  $l = 20 \mu\text{m}$  and a width of  $w = 40 \mu\text{m}$ . The junctions JJ1, JJ36, JJ40 were separately measured. Six chips with the layout of Fig. 14 were fabricated on a 2-inch wafer. A special fabrication procedure was performed in order to identify the tunnel

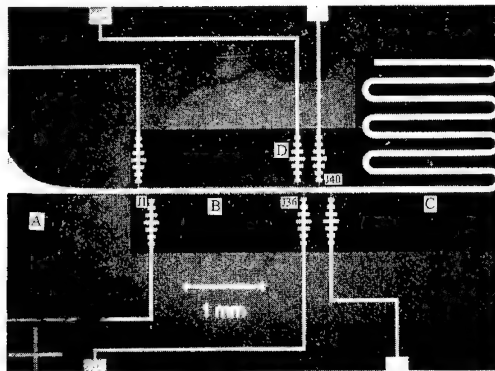


Fig. 14. Series-array microcircuit with 40 stacks or planar junctions.

barrier level with to a certain critical current. First, double barrier stacked arrays were deposited in niobium technology. The oxidation time of the bottom junctions

was 20 min and for the top junctions 80 min to differentiate the  $I_c$ 's. The temperature, as well as the oxidation pressure, were kept constant. Three chips of the wafer were then covered by photoresist. The top junctions on the other part of the wafer were removed by reactive ion etching. Afterwards both parts of the wafer were completed using identical procedures. From the  $I-V$  curves of the arrays with bottom junctions only, the critical currents  $I_c^{\text{top}}$  to be  $300 - 350 \mu\text{A}$  was determined. With this result it was possible to attribute the critical currents to the top and bottom junctions double barrier stacks. To determine the attenuation along the microstripline, the Shapiro step heights were measured as functions of rf-current at  $f_{\text{ext}} = 79 \text{ GHz}$  for the  $JJ_{36}$  and  $JJ_{40}$  junctions. The maximal Shapiro-step height is

$$\Delta I_n = I_c J_n \left( k \frac{I_{\text{rf}}}{I_c} \right) \quad (3)$$

where  $n = 0, 1, 2$  is the step number,  $J_n$  the Bessel function of the order  $n$  and  $I_{\text{rf}}$  the rf-current amplitude (in arbitrary units). The fit parameter  $k$  is inversely proportional to the rf-current dissipation along the microstripline. The experimental data were in good agreement with (3) for  $k_{36} = 1.05$  and  $k_{40} = 1.04$ , as shown in Fig. 15 and 5b. The attenuation coefficient

$$\alpha = 20 \log \left( \frac{k_{40}}{k_{36}} \right) \quad (4)$$

was determined to be  $0.017 \text{ dB/junction}$ . The theoretically expected value, using the

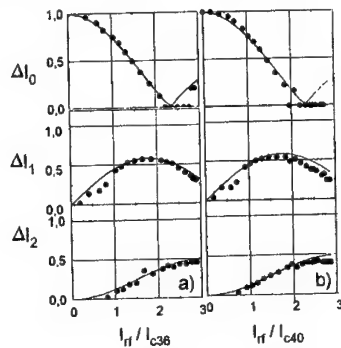


Fig. 15. Shapiro-steps height (with  $n = 0, 1, 2$ ) as a function rf current at  $f_{\text{ext}} = 79 \text{ GHz}$  for junctions  $JJ_{36}$  (a) and  $JJ_{40}$  (b). Continuous curves described by (1).

Stewart-McCumber model, is  $0.00033 \text{ dB/junction}$ <sup>33</sup>. In experiments, the attenuation coefficient is usually 10 to 50 times larger<sup>34</sup>. The reason behind is still unclear. One possible explanation for a high  $\alpha$  is a standing wave along the microstripline. Indeed, additional measurements between 78 GHz and 115 GHz showed standing waves in the microstripline. Nevertheless the distance between  $JJ_{36}$  and  $JJ_{40}$  is five times less than wavelength  $\lambda$  in the line. Therefore, standing waves were not responsible for

the high attenuation coefficient. Another mechanism, the surface resistance of the  $Nb - Al$  layer, could also lead to high attenuation but was not yet investigated.

### 5.3. Attenuation of the rf-current within a stack

In this paragraph first attempts to measure the attenuation of microwave power within vertically arranged tunnel junctions are reported. The  $I - V$  curve of a two-junction stack is shown in Fig. 16. The maximum current of  $350\mu A$  at the gap voltage  $V_g = 2.5$  mV corresponds to the critical current  $I_c^{bot}$  of the bottom junction, as mentioned above. The lower critical current  $I_c^{top} = 200\mu A$  at  $V = 0$  is related to the top junction. To determine the attenuation within the stack, the Shapiro step height

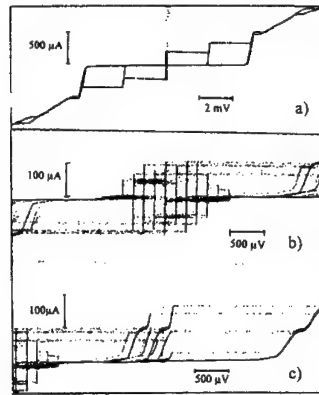


Fig. 16.  $I - V$  curve of the two junction stack (a). Shapiro steps at  $f_{ext} = 79$  GHz in the vicinity  $V = 0$  (b) and  $V = V_g$  (c).

as a function of rf-current at  $f_{ext} = 79$  GHz was measured separately for the top and bottom junctions around voltages  $V = 0$  ( Fig. 16(b)) and  $V = V_g$  ( Fig. 16(c)). In the vicinity of zero bias contribution of Shapiro steps from both junctions were found. However, at zero bias voltage only the step from the top junction was observed. In the vicinity of  $V_g$  all steps belonged to the junction with larger critical current, i.e. the bottom junction. In Fig. 17 experimental data with the fitting curves for the  $n = 0$  and  $n = 1$  Shapiro steps for the bottom junction are shown. The determined  $k_{bottom} = 1.4$ . The same procedure for the top junction (see Fig. 17b) was carried out and  $k_{top} = 0.9$  was obtained. Remarkable is the fact that at  $V = 0$  and  $V = V_g$  at higher rf-currents contribution of steps of order  $n = 1$  and  $n = -1$  are visible. The attenuation coefficient between junctions in a stack was determined from (4) to be  $\alpha = 3.8$  dB. This is a very high number. One possible explanation is that the tunnel capacitance of the stack represents a low-frequency block. The lower cut-off frequency is defined by equation  $f = (2\pi\sqrt{LC})^{-1}$ , where  $L$  is the inductance between the strip

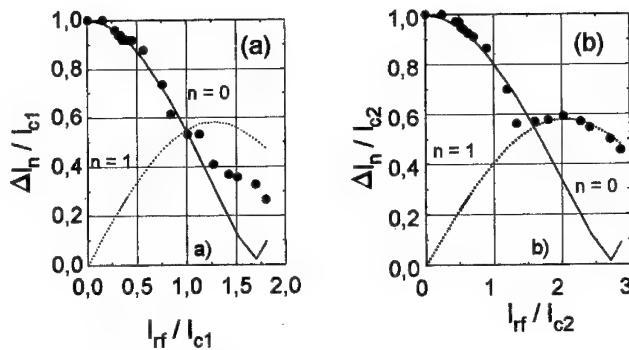


Fig. 17. Shapiro-step height vs rf-current at  $f_{ext} = 79$  GHz at  $V = V_g$  for the bottom junction (a) and at  $V = 0$  for the top junction of stack. The lines corresponds to simulation according (3) for  $n = 0$  (straight) and  $n = 1$  (dotted).

and the ground plane over the distance between junction centers and  $C$  is the junction capacitance<sup>33</sup>. For our single barrier Nb-(Al/AlO<sub>x</sub>-Nb)<sub>1</sub> junction the capacitance is  $C = 58$  pF. With an estimated  $L$  of 1.1 pH it follows  $f = 22$  GHz. With the assumption that two junctions in a stack act as two in series connected capacitors, the cut-off frequency is increased to 31 GHz. This value is more than two times lower than the applied external frequency and it should have a negligible influence on microwave losses. The present design of stacks in the microstripline allowed the microwave power to split into a few ways. If for example the upper junction in a double barrier stack is already in the resistive state, the rf-bias flows more along the microstripline, while in vertical direction high quasiparticle losses appear. New stack design approaches are needed. The aim of this work was to separate the influences of the attenuation of the introduced microwave power along the stripline and within the stacks. The attenuation per single barrier junction in the microstripline was not optimal. Nevertheless, the used parameter set was not imposing for the limitation of the phase-locking range. The reason for the reduced phase locking range in arrays is the high rf-loss in the vertical direction. Penetration of rf-bias current in the top junction may be depressed by its sub gap resistance. New approaches to the design of microstripline with stacked tunnel junctions are necessary.

## 6. Prospects

In this paper I described two examples for the applications of stacked Nb-(Al/AlO<sub>x</sub>-Nb)<sub>n</sub> tunnel junctions. Of course, the present research status do not allowed us to predict the usefulness of stacked devices in superconducting circuits. Nevertheless, the recently obtained results look promising. For the future voltage standard with low drive frequency and may be with an on-chip semiconductor oscillator stacked tunnel junctions are helpful. Coherent motion (either in-phase or out-of-phase) of Josephson vortices could offer large output power and narrow line width oscillators with  $\mu m$  di-

mensions in the submillimeter wavelength range. From the technology point of view, many developments are necessary. One need is the complete automatic deposition of the multilayers including the thermal oxidation. Figure 18 shows an  $I - V$  curve of a  $\text{Nb}-(\text{Al}/\text{AlO}_x\text{-Nb})_1$  tunnel junction for which the trilayer was deposited in an automatical run.

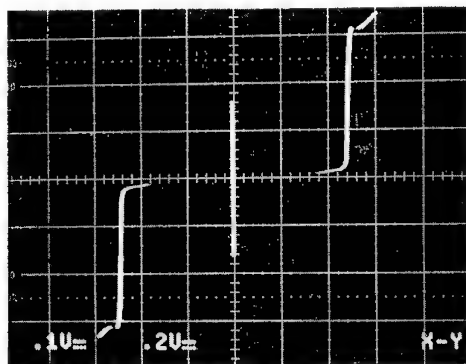


Fig. 18.  $I - V$  curve of a single barrier  $\text{Nb}-(\text{Al}/\text{AlO}_x\text{-Nb})_1$  tunnel junction. The trilayer was deposited in a full automatic cycle.

This technique has to be evaluated in the near future. For the etching of multilayer with more than ten junctions new dry etching procedures are may be required. In addition, technology is not restricted to  $\text{Nb} - \text{Al}$  layers. For example,  $\text{NbN}-(\text{MgO-NbN})_n$ ,  $\text{Nb}-(\text{AlN-Nb})_n$  or  $\text{NbN}-(\text{AlN-NbN})_n$  are surely candidates for stacks. The obvious advantage is the possibility to deposit the tunnel barrier, so long thermal oxidation times as in the case of  $\text{Nb}-(\text{Al}/\text{AlO}_x\text{-Nb})_n$   $\text{Nb}$  will be avoided. In addition the layered high temperature superconductors as  $\text{Bi}_2\text{Sr}_2\text{CaCu}_2\text{O}_{8+x}$  are stacked systems. Especially, since the recent discover of the intrinsic Josephson effect in single crystals  $\text{Bi}_2\text{Sr}_2\text{CaCu}_2\text{O}_{8+x}$  the question arises in which cases low- $T_c$  multilayers could play a model system for high- $T_c$  layered superconductors<sup>35</sup>. More details of this subject are in the contribution of P. Müller (this volume).

### Acknowledgements

The main part of the reported results on the stacked flux-flow oscillators was done together with A. V. Ustinov at the Institute for Thin Film and Ion Technology (ISI) in Jülich (Germany) and in cooperation with the Technical University of Denmark (N. F. Pedersen and A. Petraglia; Denmark), Electrotechnical Laboratory (S. Sakai; Japan), Walther-Meissner Institute (P. Müller, R. Kleiner; Germany), University of Tübingen (T. Doderer, S. G. Lachemann, D. Quenter; Germany). The voltage standard experiments were done together with A. M. Klushin\*also at ISI in cooperation with the Physikalisch-Technische Bundesanstalt in Braunschweig (J. Niemeyer, Ger-

\*On leave from the Institute of Electronic Measurements "KVARZ", 603009 Nizhny Novgorod, Russia

many). I would like to thank H. - G. Meyer from the IPHT in Jena for helpful discussions. G. Ockenfuss is gratefully acknowledged for his untiring support during the development of the automatical trilayer deposition procedure. C. Heiden and A. I. Braginski are gratefully acknowledged for discussions, comments and support from the early stage of this work.

## References

1. M. Gurvitch, M. A. Washington and H. A. Huggins, *Appl. Phys. Lett.* **42**, 472 (1983).
2. *Superconducting Electronics*, NATO ASI Series F, vol. 59, Springer-Verlag, 1989, ed. by H. Weinstock and M. Nisenoff.
3. M. G. Blamire, R. E. Somekh, G. W. Morris, and J. E. Evetts, *IEEE Trans. MAG. MAG.-25*, 1135 (1989).
4. I. P. Nevirkovets, H. Kohlstedt, G. Hallmanns, and C. Heiden, *Superc. Sci. and Techn.* **6**, 146 (1993).
5. T. Imamura and S. Hasuo, *Appl. Phys. Lett.* **58**, 645 (1991).
6. H. Kohlstedt, G. Hallmanns, I. P. Nevirkovets, D. Guggi, and C. Heiden, *IEEE Trans. Appl. Supercond.* **3**, 2197 (1993).
7. P. Barbara, A. V. Ustinov, G. Costabile, *Phys. Lett. A* **191**, 443 (1994).
8. H. Kohlstedt, A. V. Ustinov, and F. Peter, *IEEE Trans. on Supercond.* (in press)
9. S. Han, A. H. Worsham, and J. E. Lukens, *IEEE Trans. Appl. Supercond.* **3**, 2489 (1993).
10. S. P. Benz and C. J. Burroughs, *Appl. Phys. Lett.* **58**, 2162 (1991).
11. A. Davidson and N. F. Pedersen, *Appl. Phys. Lett.* **60**, 2017 (1992).
12. H. Kohlstedt, A. V. Ustinov, M. Cirillo, G. Hallmanns, and C. Heiden, *Physica B* **194-196**, 1711 (1994).
13. N. F. Pedersen, in *Solitons in Josephson Transmission Lines*, ed. by S. E. Trullinger, V. E. Zakharov and V. L. Pokrovsky (Elsevier Science Pub., North-Holland, 1986).
14. R. D. Parmentier, in *The New Superconducting Electronics*, ed. by H. Weinstock and R. E. Ralston (Kluwer Academic Pub., Netherlands, 1993).
15. A. V. Ustinov, H. Kohlstedt, M. Cirillo, N. F. Pedersen, G. Hallmanns, and C. Heiden, *Phys. Rev. B* **48**, 10614 (1993).
16. Ngai, *Phys. Rev.* **182**, 55 (1969).
17. S. Sakai, P. Bodin, and N. F. Pedersen, *J. Appl. Phys.* **73**, 2411 (1993).
18. I. Giaever, *Phys. Rev. Lett.* **14**, 904 (1965).
19. N. Groenbech-Jensen, D. Cai, and M. R. Samuelsen, *Phys. Rev. B* **50**, 16160 (1993).
20. S. Sakai, A. V. Ustinov, H. Kohlstedt, A. Petraglia, and N. F. Pedersen, *Phys. Rev. B* **50**, 12905 (1994).
21. A. V. Ustinov, H. Kohlstedt, and C. Heiden, *Appl. Phys. Lett.* **65**, 1457 (1994).



22. A. Petraglia, A. V. Ustinov, N. F. Pedersen, and S. Sakai, *it J. Appl. Phys.* (Feb.1, 1995) (in press).
23. A. V. Ustinov, T. Doderer, H. Kohlstedt, S. G. Lachemann, and D. Quenter", to be published.
24. A. V. Ustinov, H.- Kohlstedt, and C. Heiden, *Physica C* (in press.)
25. C. A. Hamilton, F. L. Lloyd, K. Ghich, and W. Goecke, *IEEE Trans. Instrum. Meas.* **38** 314, (1989).
26. R. Pöpel, J. Niemeyer, R. Fromknecht, W. Meier, L. Grimm, and F. W. Dünschede, *IEEE Trans. Instrum. Meas.* **40** 298, (1991).
27. Y. Sakamoto, H. Yoshida, T. Sakuraba, A. Odawara, Y. Murayama, and T. Endo, *IEEE Trans. Instrum. Meas.* **40** 312, (1991).
28. H.-G. Meyer, H.-J. Köhler, F. Müller, K. Blüthner, P. Weber, and A. Chwala, *IEEE Trans. Appl. Superc.* **3** 1870, (1993).
29. E. Vollmer, P. Gutmann, J. Niemeyer, *IEEE Trans. Appl. Superc.* **3** 2828, (1993).
30. A. M. Klush.in, H. Kohlstedt und G. Hallmanns, *4th International Superconductive Electronics Conference* (ISEC'93) Ext. Abstract 408-409, (1993).
31. A. M. Klushin, H. Kohlstedt und G. Hallmanns, *Applied Superconductivity* **2** 1261, (1993), DGM Informationsgesellschaft, ed. H.C.Freyhardt.
32. A. M. Klushin, H.Kohlstedt, *J. Appl. Phys.* 1995, (in press).
33. J. Niemeyer , J. H. Hinken, R. L. Kautz, *Appl. Phys. Lett.*, **45** 478, (1984).
34. Y. Sakamoto, *PTB-Mitteilung*, **104** 151, (1994).
35. R. Kleiner, P. Müller, H. Kohlstedt, N. F. Pedersen, S. Sakai, *Phys. Rev. B* **50** 3942, (1994).

# FLUXON DYNAMICS IN STACKED LONG JOSEPHSON JUNCTIONS: EXPERIMENTS AND NUMERICAL SIMULATIONS

P. BARBARA, J. MYGIND, N. F. PEDERSEN  
*Physics Department, The Technical University of Denmark,  
DK-2800 Lyngby, Denmark*

G. COSTABILE, A. D'ANNA, R. D. PARMENTIER  
*Department of Physics, University of Salerno,  
I-84081 Baronissi, Italy*

and

B. A. MALOMED  
*Department of Applied Mathematics, Tel Aviv University,  
Ramat Aviv 69978, Israel*

## ABSTRACT

Stacks of two junctions with access to the intermediate electrode have been successfully realized in a two-step double-trilayer deposition. Thus it was possible to experimentally investigate stacks with different bias conditions. The main results regard finite voltage states of the unbiased junction detected when the other is biased on a resonant flux-flow step. By using two inductively coupled JTL's to model the system, the main features observed in the physical system were obtained from numerical calculations.

## 1. Fabrication Process

The samples consist of stacks of two junctions which can be separately biased in the overlap configuration. We have used a fabrication technique which produces stacks of junctions with approximately the same area (within 10 %) and provides an electrical connection to the common electrode, while the bias current distribution is reasonably uniform. The process is based on the  $Nb/Al/AlO_x/Nb$  technology and the deposition of the layers has been made in two different steps. First, the trilayer corresponding to the bottom junction is deposited and patterned by lift-off with the geometry of the base electrode. The area of the bottom junction is then defined by a S(elective) N(iobium) A(nodization) P(rocess). As a second step, the samples come back to the vacuum chamber and the trilayer corresponding to the top junction is deposited. Let us stress that the thickness of the first Niobium layer in this deposition added to the thickness of the upper niobium film of the first trilayer would give a total thickness ranging from 50 to 120 nm. The London penetration depth for our Nb is estimated to be about 80 nm.

The middle electrode and the top junction area are, respectively, defined by lift-off

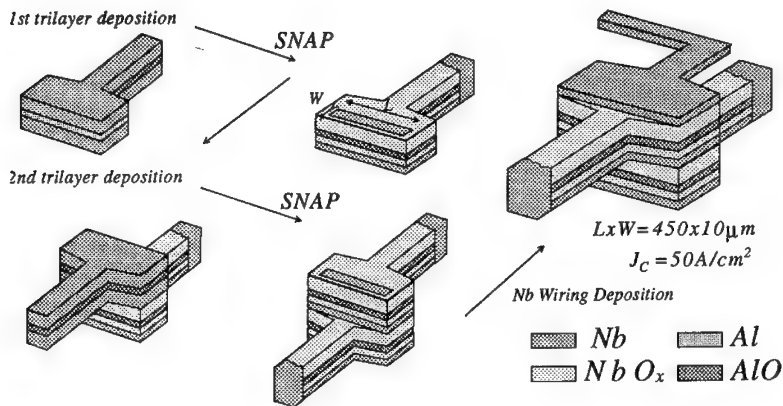


Fig. 1. Outline of the fabrication process.

and SNAP process as well. The Nb wiring is finally deposited and patterned by lift-off with the geometry of the top electrode. Whenever the samples were returned to the vacuum chamber, during the process, a light sputter-etching was made in order to clean the metallic surfaces previously deposited. The whole process and the geometry of our samples are summarized in Fig. 1.

## 2. Experiment

We have experimentally investigated a stack of two strongly coupled junctions under different bias configurations. The thickness of the common electrode was about 50 nm, the dimensions of the junctions  $L \times W = 450 \times 10 \mu m^2$  and the current density  $J_c \simeq 50 A/cm^2$ . It has been shown experimentally<sup>1</sup> that in two coupled stacked junctions a splitting of the Swihart velocity occurs, giving rise to the appearance of two families of flux flow steps in the presence of an external magnetic field. The two families are characterized by two different spacings of the Fiske resonances. The existence of the two modes was also verified to be independent of the bias configuration<sup>2</sup>, since the two Fiske step families were measured both biasing the junctions in series or separately.

In the experiments we biased the junction with higher (20 %) critical current (*generator*) on the resonant flux flow step corresponding to the lower Fiske step spacing and detected both the voltage of the generator and of the other junction (*detector*) in different bias conditions. An external magnetic field was applied in the plane of the substrate and in direction perpendicular to the long dimension of the junctions.

The different cases of bias current configurations and the related experimental

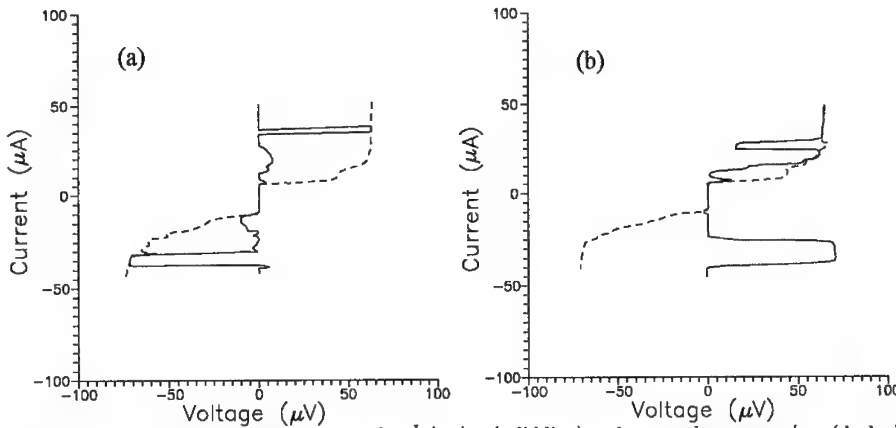


Fig. 2. Plots showing the voltages across the *detector* (solid line) and across the *generator* (dashed line) vs. the bias current in the *generator* when: (a) the *detector* is not biased; (b) the *detector* is biased by a constant current  $I = 12\mu A$ .

results are listed below. In the following, the current passing through the *detector* junction and the *generator* junction are respectively indicated as  $I_g$  and  $I_d$ .

1.  $I_g \neq 0$ ;  $I_d = 0$

In this configuration the generator junction is biased on a flux flow step of the first family and the detector junction is not biased. This case was already discussed in ref. 2, in which was described the appearance of a voltage across the unbiased junction within some ranges of the generator current bias and the occurrence of some small ranges of voltage locking in the case of stronger coupling.

In Fig. 2a a typical result corresponding to this bias configuration is shown. In general we can distinguish three kinds of response corresponding to different values of the current in the generator:

- at lower  $I_g$  we observe finite voltage,  $V_d$ , across the detector which does not change proportionally to the voltage across the generator,  $V_g$ ;
- also visible are small current ranges in which  $V_d$  shows an opposite polarity with respect to  $V_g$ ;
- at higher  $I_g$  the voltage across the detector is locked to the voltage of the generator (or to its integer fractions).

2.  $I_g$  variable;  $I_d = \text{const} > 0$

This case is shown in Fig. 2b. In this experiment the current passing through the generator junction is varied from positive to negative values while a constant

positive current is supplied through the detector. It is important to note that  $I_d$  is smaller than the critical current of the detector corresponding to the applied magnetic field,  $I_d < I_c^d(H_{ext})$ ; this means that by biasing the generator in a zero voltage state the detector would be in a zero voltage state too.

In this case we can distinguish two different situations:

a)  $I_d$  and  $I_g$  with the same polarity.

This configuration corresponds to the upper part of Fig. 2b. We observed that, due to the small current  $I_d$ , the voltage locking range is sensitively increased as compared to the case 1 (Fig. 2b shows the  $V_g, V_d$  vs.  $I_g$  curves when  $I_d$  is set to maximize the voltage locking range); in this case the dynamics of the system can be described as consisting of two fluxon chains, one in each junction, moving with the same mean velocity.

b)  $I_d$  and  $I_g$  with opposite polarity.

This configuration corresponds to the lower part of Fig. 2b. Here we observe that, in nearly the same current range, the generator and the detector are still voltage locked but now the voltages have different polarity, indicating that the fluxon chains in the two junctions are moving with the same mean velocity but in opposite directions.

3.  $I_g = I_d$

In this case the stack is biased in series. Ranges of voltage locking on the flux flow steps can be observed, as discussed in detail in ref. 1

4.  $I_g = \text{const}; I_d = \text{variable}$

If the generator is biased at certain values of bias current  $I_g$  on a flux flow step of the first family, corresponding to a voltage  $V_g$ , a step corresponding to the voltage  $V_g$  appears on the I-V curve of the detector and its critical current is suppressed.

5.  $I_g = -I_d$

When an external magnetic field is applied, wide current ranges in which the junctions show the same voltage, or integer voltage ratios, with opposite polarity, can be found on the first flux flow step.

As mentioned before, the role of the generator junction is played by the junction with higher critical current. If the roles are interchanged, no relevant voltage response can be measured across the detector junction. Moreover, in the experiments a response can be measured only when the generator junction is biased on a dynamical state corresponding the resonant flux flow step corresponding to the lower Fiske step spacing.

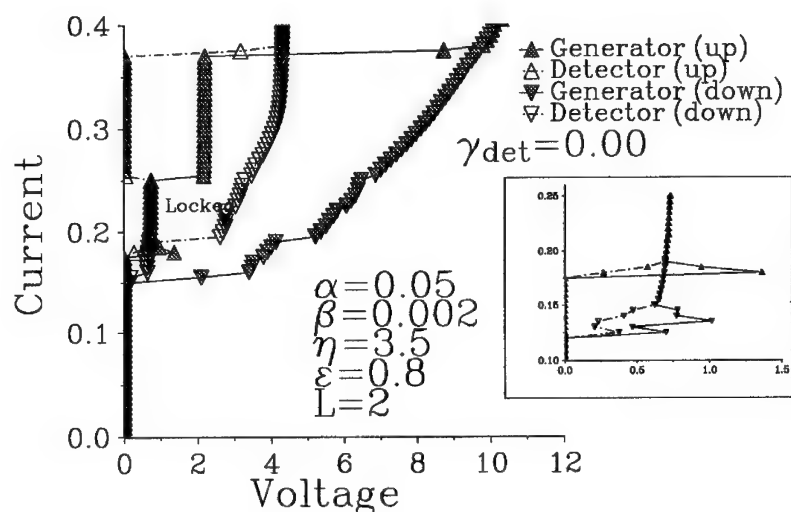


Fig. 4. Numerical simulations with the PDE's.

- finite voltage states of the unbiased junction;
- different steps whose asymptotic voltages agree fairly well with the ones that can be obtained by considering the splitting of the Swihart velocity;
- a large voltage locked region on the Fiske step with the lower Swihart velocity;
- the existence of a pulling region (see inset of Fig. 4), traced out when the junctions switch together to a finite voltage state, which evidences the dragging action exerted by the chain in the generator on the one in the detector at close relative velocities; this picture is also confirmed by the sudden switch forward of the generator voltage when the detector unlocks.

#### 4. A Dynamical Model

We have developed a simplified<sup>4</sup> description of the dynamical states of our system based on the collective coordinate representation. Starting from the coupled PSGE's and deriving from the Hamiltonian formalism (by inserting the solution corresponding to the unperturbed flux-flow state of a single junction) the forces acting on the fluxon chains due to the interaction with the external magnetic field, the dc drive and the mutual coupling, we obtain the equations of the motion for the collective coordinates. Introducing normalized quantities the pair of ODE's for the motions of each chain as a whole are:

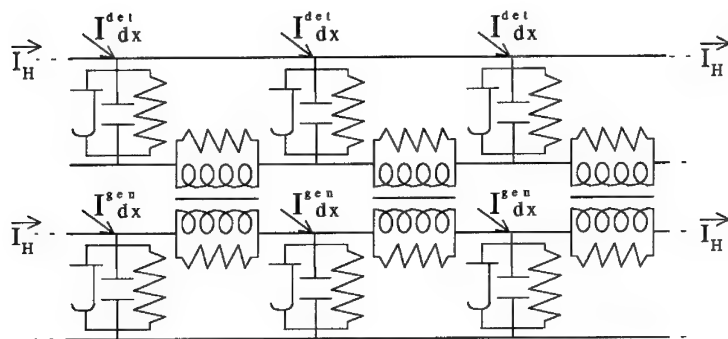


Fig. 3. Equivalent circuit for two inductively coupled Josephson junctions.

### 3. Numerical Simulations

In Fig. 3 is illustrated the circuit used to model two Josephson junctions inductively coupled through the intermediate electrode.

From this equivalent circuit a pair of normalized Perturbed Sine Gordon Equations with extra coupling terms can be obtained, ref. 3

$$\begin{cases} \Phi_{xx} - \Phi_{tt} - \sin \Phi = \alpha \Phi_t - \beta \Phi_{xxt} - \gamma_g - \epsilon \Psi_{xx} \\ \Psi_{xx} - \Psi_{tt} - \sin \Psi = \alpha \Psi_t - \beta \Psi_{xxt} - \gamma_d - \epsilon \Phi_{xx} \end{cases} \quad (1)$$

and the usual boundary conditions

$$\begin{cases} \Phi_x(0, t) + \beta \Phi_{xt}(0, t) = -\eta \\ \Psi_x(0, t) + \beta \Psi_{xt}(0, t) = -\eta \end{cases} \quad (2)$$

It should be noted that usually the influence of the  $\beta$  term on the dynamics of the PSGE is considered small and thus neglected during the calculations; we found, instead, in the preliminary results reported below, that as regards the dynamics of two *coupled* PSGE's, the  $\beta$  parameter plays an important role, inasmuch as some results depend on the value assumed for it. This point deserves further attention, for at least two reasons: (i) if the value of  $\beta$  is important, it should probably also be inserted into the coupling terms in Eqs. (1) <sup>5</sup>; (ii) one can also imagine a coupling between the junctions via the radiation emitted from their ends <sup>6</sup>, which would give rise to additional terms on the right-hand side of Eqs. (2).

We solved the system of Eqs. (1) by numerical integration using a finite difference scheme with standard integration routines. In Fig. 4 we show an example of the results obtained in the case of the unbiased detector,  $\gamma_d = 0$ . Fig. 4 shows the appearance of:

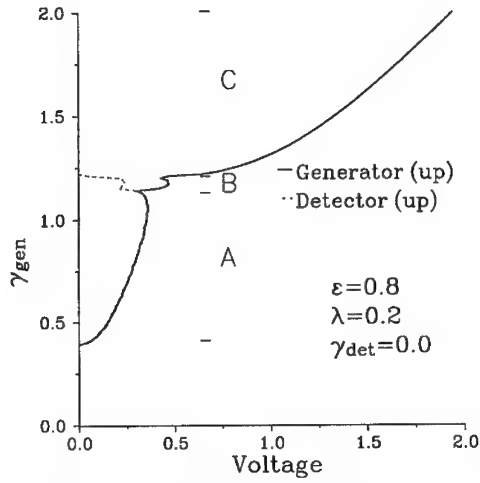


Fig. 5. Numerical simulations with the ODE's.

$$\left\{ \begin{array}{l} \ddot{\xi}_1 = \overbrace{-\alpha \xi_1}^{\text{dissipative term}} + \overbrace{\gamma_g}^{\text{bias term}} + \overbrace{\epsilon \sin(\xi_2 - \xi_1)}^{\text{mutual coupling}} + \overbrace{\lambda \sin \xi_1}^{\text{magnetic field}} \\ \text{the same equation with } \xi_1 \rightarrow \xi_2 \text{ and } \gamma_g \rightarrow \gamma_d \end{array} \right. \quad (3)$$

where  $\xi_1$  and  $\xi_2$  are, respectively, the collective coordinate of the fluxon chain in the generator and in the detector junction.

By integrating numerically these equations we obtained three different dynamical states (see Fig. 5). From the  $V_g, V_d$  vs.  $I_g$  curves we can identify states in which:

- the chains move with the same mean velocity (region A)
- the chains move with finite but different mean velocities (region B)
- for higher bias, the detector unlocks and drops into a zero mean velocity state, while the externally driven chain freely moves with a usual velocity-bias relation. (region C)

Moreover the plot shows a zero velocity state for both the junctions at bias less than a critical value depending on the applied magnetic field. Here the dc drive is not large enough to move the chains which remain *pinned* by the external magnetic field.



## 5. Conclusions

We have interpreted the experimental data concerning the behaviour of long stacked Josephson junctions in magnetic field in terms of the interaction between two inductively coupled fluxon chains since the thickness of the intermediate electrode is comparable to or less than  $\lambda_L$ .

The numerical simulations and the simplified dynamical model account essentially for all the phenomena observed, except for the case in which a small bias current is fed into the detector, opposite to the one flowing in the generator. In fact we never recorded in the simulations, except during transients, states voltage locked with opposite polarities. We believe that by extending the parameter space under investigation also this flux-flow configuration might be accounted for.

## References

1. A. V. Ustinov, H. Kohlstedt, M. Cirillo, N. F. Pedersen, G. Hallmanns and C. Heiden, *Phys. Rev. B* **48** (1993) 10614-17.
2. P. Barbara, A. Ustinov, G. Costabile, *Phys. Lett. A* **191** (1994) 443-448.
3. S. Sakai, P. Bodin and N. F. Pedersen, *J. Appl. Phys.* **73** (1993) 2411-18.
4. P. Barbara, G. Costabile, A. D'Anna, B. Malomed, and R. D. Parmentier, (unpublished).
5. M. R. Samuelsen, *private communication*.
6. A. Petraglia, *private communication*.

# DYNAMICS IN STACKED JOSEPHSON STRUCTURES

A. PETRAGLIA, N.F. PEDERSEN

*Physics Department, The Technical University of Denmark  
DK-2800 Lyngby, Denmark*

and

A.V. USTINOV

*Institute of Thin Film and Ion Technology, Research Centre (KFA)  
D-52425 Juelich, Germany*

## ABSTRACT

Layered superconductors consisting of two or more stacked long Josephson junctions have recently been studied experimentally by several groups as a possible technological improvement for most of the applications of Josephson junctions. Although such systems have mostly been realised as stacks of Nb-Al/AlO<sub>x</sub>-Nb tunnel junctions, there is also interest in such systems as a model of layered superconductors. Thus there have already been published experiments clearly demonstrating that BSCCO high  $T_c$  superconductors behave as a stack of Josephson junctions. One of the purposes of the present work is to study the variety of dynamical behaviours that can be expected in those systems. Our numerical investigations cover the parameter space for the two junction system, such as the coupling parameter, the boundary conditions (i.e. the external field) and the biasing conditions for the two junctions. Besides the dynamics, we are able to simulate the current-voltage characteristics of the stack so that we can compare with the data obtained experimentally. Highly interesting for possible applications are the locked states. The first result obtained for the two layer stack is the presence of in-phase and out-of-phase locking corresponding to two different characteristic velocities in the junctions. Besides the numerical approach, analytical methods have also been carried out in some cases. Analytical methods in the small signal (linear) approximation, applied to the case of  $N$  junctions have shown the splitting of the characteristic velocity in  $N$  branches. The phase shifts for various velocities are in agreement with numerical results. Explicit expressions for the  $N$  different limit velocities have also been calculated.

## 1. Introduction and Model

Recently many efforts have been spent in the experimental study and modeling of systems consisting of two or more stacked long Josephson junctions. Interest arises from the fact that stacked junctions are good candidates to solve some of the problems in application of Josephson junctions as high frequency oscillators, which are low power output, low output impedance, large emitted radiation linewidth. Moreover, such systems have been proposed as a model of very anisotropic high- $T_c$  superconductors.

In this work we present new results obtained in the framework of theory by Sakai,

Bodin and Pedersen (SBP)<sup>1</sup>.

The vertical stacks of Josephson junctions consist of alternating layers of superconductors and insulators. The complete derivation of the equations for an N-fold stack for an arbitrary magnetic field and different geometries may be found in Ref.<sup>1</sup>.

We consider a symmetric two-layer stack, which in the usual normalization<sup>2</sup> is described by:

$$\begin{pmatrix} \varphi_{xx} \\ \psi_{xx} \end{pmatrix} = \begin{pmatrix} 1 & S \\ S & 1 \end{pmatrix} \begin{pmatrix} \varphi_{tt} + \alpha\varphi_t + \sin\varphi - \gamma \\ \psi_{tt} + \alpha\psi_t + \sin\psi - \gamma \end{pmatrix}, \quad (1)$$

$\varphi$  and  $\psi$  are the superconducting phase differences for the two junctions. The coupling parameter between the junctions is defined as

$$S = -\frac{\lambda_L}{\sinh \frac{t}{\lambda_L} (d + \lambda_L \coth \frac{t}{\lambda_L} + \lambda_L \coth \frac{t_e}{\lambda_L})}. \quad (2)$$

Here the barrier thickness is  $d$ , the middle superconducting electrode thickness is  $t$  and the top and bottom electrodes have the thickness  $t_e$ ,  $\lambda_L$  is the London penetration depth. Note, the coupling parameter  $S$  depends only on geometry and physical parameters of the stack, indeed it is determined completely by the thickness of the insulating and superconducting layers in the structure. Typical experimental values<sup>3</sup> for  $S$  in a two junction stack are in the interval  $-0.2 - -0.7$ .

Eq.(1) gives a splitting of the characteristic (Swihart) velocity in two branches<sup>3,4</sup>. In the unperturbed case ( $\alpha$  and  $\gamma$  equal to zero) such velocities can be calculated from the dispersion relation of the plasma waves  $\varphi = A_1 e^{i(kx - \omega t)}$  and  $\psi = A_2 e^{i(kx - \omega t)}$  (in the hypothesis  $|A_1|, |A_2| \ll 1$ ). The two velocities are given by

$$c_{\pm} = \frac{1}{\sqrt{1 \pm S}}. \quad (3)$$

As has been shown by numerical<sup>5</sup> and perturbational<sup>6</sup> analysis these characteristic velocities are also limit velocities for solitonic solutions.

For an N-junction stack there exist N different velocities of the propagating waves, the explicit expressions for them are calculated as<sup>7,9</sup>

$$c_n = \frac{1}{\sqrt{1 + 2S \cos \frac{n\pi}{N+1}}}, n = 1, 2, \dots, N. \quad (4)$$

From the experimental point of view, the velocity splitting gives rise to the splitting of the so called flux-flow steps in the current-voltage (I-V) characteristic of the stack. In Fig. 1 we show an I-V curve for a 2 junction stack embedded in the normalized magnetic field  $\eta$  varied between 6.0 and 8.0 normalized units. The two different

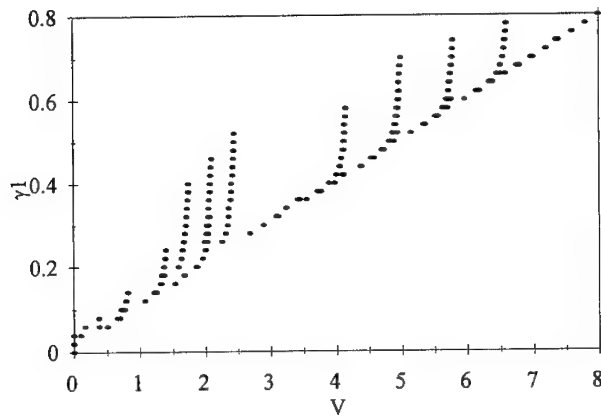


Fig. 1. I-V curve for a two junction stack embedded in magnetic field. Parameters:  $\alpha = 0.1$ ,  $l = 7.0$ ,  $S = -0.7$ , the normalized magnetic field varies from 6 to 8.

families of steps are characterized by different voltage spacings between them. The voltage spacing between neighboring steps is proportional to the characteristic velocity of the corresponding wave mode. Similar behavior has recently been observed experimentally<sup>3</sup>.

The linear analysis shows that different velocities correspond to different symmetry of the waves in the stack<sup>5,7</sup>. This is confirmed by numerical results. For example, in the case of equal biases for the  $c_-$  mode the fluxons in the two junctions repel each other, while for the  $c_+$  mode they attract each other forming a bunched mode<sup>1,6</sup>. This two state behavior continues to exist for more complex cavity modes, in Ref.<sup>5,8,9</sup>, for example, are shown the in- and out-of-phase motions corresponding to the two velocities. For N-fold stacks we have more complicated dynamics in which some layers are in-phase locked and others are out-of-phase locked<sup>9</sup>.

## 2. Different Biases

Recently Barbara *et al.*<sup>10</sup> have shown experimentally that for some parameter range there are locked states between the layers with different biases in the two junctions. Moreover, locked states have also been shown to exist even for just one junction biased.

For a simulation example we have chosen opposite biases ( $\gamma_2 = -\gamma_1$ ) and the magnetic field  $\eta$  different from zero. The basic attractive state for this bias orientation was fluxon-antifluxon while for the bias chosen in Ref.<sup>5,7</sup> it was the fluxon-fluxon state.

In Fig. 2(a),(b) the two types of locking of a fluxon train in one layer and an antifluxon train in the other layer are shown. We note the complicated shape in the

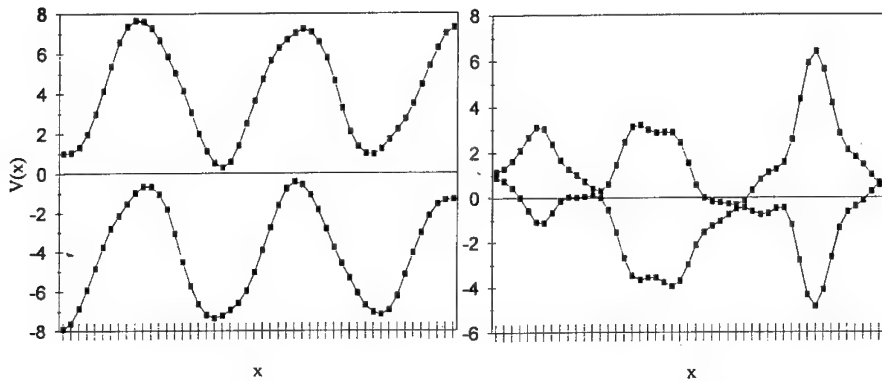


Fig. 2.  $V(=\phi_t)$  vs. the spatial coordinate  $x$  in a two junction stack. Parameters:  $\alpha = 0.1$ ,  $l = 5.0$ ,  $S = -0.7$ ,  $\eta = 6.0$ . (a)  $\gamma_1 = -\gamma_2 = 0.6$ , in-phase behavior; (b)  $\gamma_1 = -\gamma_2 = 0.3$ , out-of-phase behavior.

repulsive case.

The velocity of the bunched mode fluxon-antifluxon is  $c_-$  (see Ref.<sup>1</sup>). In Fig. 3 is shown the I-V characteristic for a Zero Field Step (ZFS): in Fig. 3(a) the two junctions have opposite bias currents and are in a bunched fluxon-antifluxon state. This state is stable over a wide range of the bias currents, and it continues to exist when the current in one of the layers is lowered to zero (see Fig. 3(b)).

### 3. Numerical Experiments on Junctions with Different Parameters

The results shown above assume that the layers have the same physical and geometrical properties. Now we will examine the more realistic case when the parameters are different. Also in this case it is possible to calculate the expressions for the N characteristic velocities in the small wave amplitude approximation. The procedure is similar to that described above with a more complex form of the determinant. Comparison of the data with experiments show a good quantitative agreement<sup>7</sup>.

For the numerical analysis we choose the case in which the junctions have different critical currents  $J_{c1}$  and  $J_{c2}$ , keeping all other parameters unchanged. Inspection of the dynamics shows some new states in which the phases in the two junctions move independently.

Fig. 4 shows one I-V characteristic for a two layers stack. There is the same bias in both junctions, the external magnetic field and the other parameters (the loss  $\alpha$  and length  $l$ ) have been chosen to have flux flow states with resonances. The two voltages across the layers are indicated by crosses and circles in Fig. 4. Besides the locked in- and out-of-phase states, there are other unlocked states indicating a more complex dynamic picture which arises due to the difference between the two junctions.

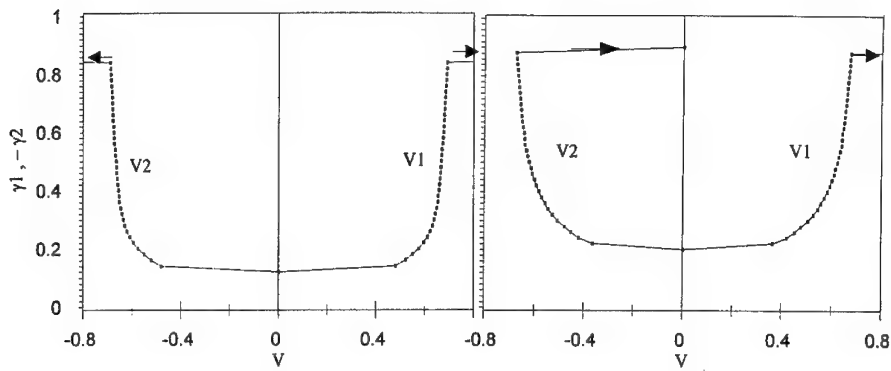


Fig. 3. I-V curves for a stacked junction in the ZFS state. Parameters:  $\alpha = 0.1, l = 7.0, S = 0.7$ .  $V_1 = \langle \varphi_t \rangle, V_2 = \langle \psi_t \rangle$ . (a)  $\gamma_1 = -\gamma_2$ ; (b)  $\gamma_2 = 0$ .

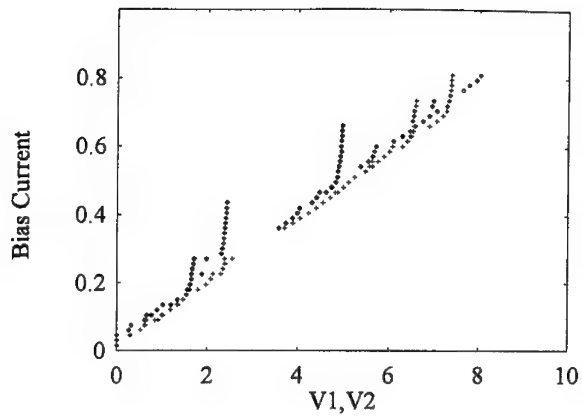


Fig. 4. I-V characteristic for a two junction stack with different critical current ( $J_{c1}/J_{c2} = 0.95$ ). The parameters are the same as in Fig. 3 but with  $\eta = 11.2$ .

#### 4. Conclusions

Structures consisting of  $N$  superconductor-interface layers vertically stacked have been analytically and numerically studied in the framework of the SBP theory. The explicit expressions for the  $N$  resulting characteristic velocities and for the spacing between the steps in the numerically calculated  $I$ - $V$  curves are in good agreement with the experiments. The analysis has shown different types of locking corresponding to different characteristic velocities; some of these complex regimes can explain strongly non-linear behaviors observed in experiments.

#### Acknowledgements

Two of us (A.P. and A.V.U.) gratefully acknowledge the EEC grant ERB-CHEC-CT93-0101 supporting their participation in the conference. N.F.P. acknowledges the support from ERO.

#### References

1. S. Sakai, P. Bodin, and N. F. Pedersen, *J. Appl. Phys.*, **73** (1993) 2411.
2. N. F. Pedersen, *Solitons* (Elsevier, Amsterdam, 1986), p. 469.
3. A. V. Ustinov, H. Kohlstedt, M. Cirillo, N. F. Pedersen, G. Hallmanns, and C. Heiden, *Phys. Rev. B* **48** (1993) 10614.
4. K. L. Ngai, *Phys. Rev.* **182** (1969) 555.
5. A. Petraglia, A. V. Ustinov, N. F. Pedersen, and S. Sakai, *J. Appl. Phys.* (January 15, 1995).
6. N. Grønbech-Jensen, D. Cai, and M. R. Samuelsen, *Phys. Rev. B* **48** (1993) 16160.
7. S. Sakai, A. V. Ustinov, H. Kohlstedt, A. Petraglia, and N. F. Pedersen, *Phys. Rev. B* **50** (1994) 12905.
8. R. Kleiner and P. Müller, *Phys. Rev. B* **49** (1994) 1327.
9. R. Kleiner, *Phys. Rev. B* **50** (1994) 6919.
10. P. Barbara, A. V. Ustinov, and G. Costabile, *Phys. Lett. A* **191** (1994) 443.

# MAGNETIC FIELD DIFFRACTION PATTERN IN MULTILAYERED JOSEPHSON JUNCTIONS

V.L.KONDRATIEV

*Moscow Institute for Steel and Alloys,  
Leninski pr.4, Moscow 117936, Russia*

R.VAGLIO

*Dipartimento dei Scienze Fisiche, Universita' di Napoli "Federico II"  
Napoli, Italy*

and

A.A.VARLAMOV

*Forum: Institute for Condensed Matter Theory of INFM  
Pisa - Florence, Italy  
L.E.Fermi, 2 Firenze 50125, Italy*

## ABSTRACT

The unusual behaviour of the loss of periodicity in the magnetic field diffraction pattern of Josephson current, which was observed in a multilayered Josephson structure experiment, is explained in terms of a simple model.

## 1. Introduction

The aim of the present paper is to present a simple theoretical model to account for a comparatively old experiment on multilayered Josephson structures<sup>1</sup> which, as far as we know, is being still unexplained.

Let us briefly summarize these results. The dependence of the critical current versus magnetic field was studied in complex junctions consisting of a multilayered Nb/Cu structure, a thin Nb film, a  $Nb_2O_5$  oxide barrier and a Pb counterelectrode ( $T_{c3} = 7.2K$ ) (see Fig. 1).

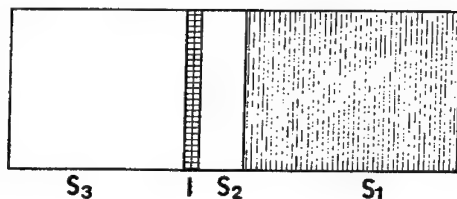


Fig. 1. Schematic view of the Josephson junction structure.  $S_1$ =Nb/Cu multilayer;  $S_2$ =Nb thin overlayer; I= insulating barrier,  $S_3$  = Pb counterelectrode.



The Nb/Cu multilayer period was in the range 0.4 - 30 nm with a total thickness of 300 nm with Nb as last layer. The quality of the superlattice was controlled by X-rays methods. It is important to stress that these films behaved as uniform superconductors with critical temperature  $T_{c1}$  depending on the lattice period. For the data reported it was always  $T_{c1} < T_{c3}$ . After the preparation of the superlattice, one additional layer of Nb 30nm thickness with  $T_{c2} = 9K$  was sputtered and then, after photolithography, its surface was back-sputtered and oxidized. As a result the thickness of this layer diminished of  $\sim 10nm$  and an insulating layer of  $Nb_2O_5$  with thickness 2 nm appeared on its surface. Finally, in order to create the tunnel junction a lead counterelectrode of thickness 500 nm was deposited.

The dimensions of the junctions  $L$  (ranging between  $50 \times 50 \mu m^2$  and  $1 \times 1 mm^2$ ) were small in comparison with the Josephson penetration depth, so the effects connected with the self magnetic field were not influent.

The current-voltage characteristics of this structure was measured at low temperatures and were found to be close to an ideal one. The critical currents versus magnetic field at different temperatures were also measured with the field applied along the junction surface. At temperatures below the critical temperature  $T_{c1}$  of the superlattice the dependence  $I_c(H)$  always exhibited the classical Fraunhofer-like diffraction pattern as expected. However for  $T_{c1} < T < T_{c3}$  the Fraunhofer pattern was replaced by a smooth curve of Gaussian type. At temperatures above  $T_{c3}$  the lead electrode was in the normal state and no supercurrent was detected.

As far as we know this type of loss of the Fraunhofer pattern in superconducting tunnel structures at  $T_{c1} < T < T_{c3}$  did not find any explanation until now. In the following we will report on a simple model to account for such an anomalous behaviour.

At temperatures above  $T_{c1}$  the superconductor  $S_1$  goes in the normal state and the magnetic field behaviour of the Josephson structure changes drastically. This cannot be simply connected to the bidimensional nature of the Nb layer  $S_2$ , whose thickness  $D_2 \simeq 20nm$  is less than the Nb coherence length ( $\xi \simeq 40nm$ ). By the fact this only means that the usual procedure of the carrying out of the  $I_c(H)$  dependence (see, for instance, <sup>2</sup>) is no more valid. However the influence of the electrode finite thickness on  $I_c(H)$  was studied in <sup>3</sup> and it was found that the only effect is indeed a renormalization of the magnetic field with the Fraunhofer pattern unchanged.

## 2. The model

We concentrated our attention on the fact, that the Nb film  $S_2$  is fairly thin and can possess a granular structure that may be difficult to defect by electron microscopy or other structural analysis. So we can assume, as a rough model, that this thin layer of Nb really is not homogeneous with normal grain boundaries between superconducting islands. If all the superconducting phases would be connected in one island nothing new would be expected for the properties of such structure. On the contrary, in the case where the islands of the superconducting phase are disconnected they compose a two-dimensional array of small Josephson junctions connected in parallel

through the barrier with the lead electrode. At temperatures  $T < T_{c1}$  they were connected by the superconducting Nb/Cu multilayer and the phase of the order parameter was unique. Above  $T_{c1}$  every "island" is independent and has its own phase. So in order to calculate the appropriate  $I_c(H)$  characteristics we have to accomplish the averaging of the total current over the random configuration of such "islands" and over their phases.

Let us suppose that we know the distribution function  $p(l)$  versus characteristic "island" size  $l$  (it is clear that  $p(l)dl$  is proportional to the square of the junction occupied by superconducting "islands" with sizes from  $l$  to  $l+dl$ ) and current density  $j(l, H)$  as the function of  $l$  and magnetic field  $H$ . So the total current flowing through the junction can be written as the integral

$$I(H) = \int_0^L j(l, H)p(l)dl \quad (1)$$

The distribution function  $p(l)$  has to satisfy the following requirements: 1) dimensions of islands have to be distributed in the vicinity of some most probable size  $a$  and the distribution function has to decrease rapidly as  $l$  goes away from this value, 2) negative values of  $l$  have to be excluded. A natural candidate is the lognormal distribution in which the  $\ln(l)$  is distributed normally

$$p(l) = \frac{1}{\sqrt{2\pi}\sigma l} \exp\left[-\frac{\ln^2(\frac{l}{a})}{2\sigma^2}\right] \quad (2)$$

where  $\sigma$  is the dispersion of the distribution.

### 3. 1D case

Let us begin from the analysis of the one-dimensional case, which is, of course an oversimplification in respect to the real experiment, but reflects the basics characteristic features of the problem. It may be treated, for instance, as the particular case of the junction with rectangular grains, oriented along the magnetic field. For a single junction we can write

$$j(l, H) = j_0 \left| \frac{\sin(\pi \frac{\phi}{\phi_0})}{\pi \frac{\phi}{\phi_0}} \right| \quad (3)$$

where  $\phi(l) = HlD$  ( $D \sim \lambda(T)$  for the lead electrode),  $\phi_0 = \frac{\pi \hbar c}{e}$  is magnetic flux quantum,  $j_0$  is a constant depending on the barrier transparency. Really, due to the variation of the barrier thickness, the value  $j_0$  can change from one grain to another. But it will enter in the formula for the total current in the combination  $j_0 p(l)$ , so we can adopt it as a constant and attribute its variation to the renormalization of the junctions over their sizes.

For the total current one can write

$$I(H) = \int_{\xi}^L j_0 \frac{\sin(\pi \frac{\phi(l)}{\phi_0})}{\pi \frac{\phi(l)}{\phi_0}} \frac{1}{\sqrt{2\pi\sigma l}} \exp[-\frac{\ln^2(\frac{l}{a})}{2\sigma^2}] dl \quad (4)$$

The limits of integration are chosen in accordance with the fact that the dimensions of small grain junctions cannot be less than  $\xi$  and larger than the junction size  $L$ . Below we shall adopt the approximation  $\xi \ll a$  and shall substitute the lower limit by 0.

The integral (4) cannot be calculated analytically. The results of numerical calculation of it for some values of parameters  $a$  and  $\sigma$  are presented in Fig.2.

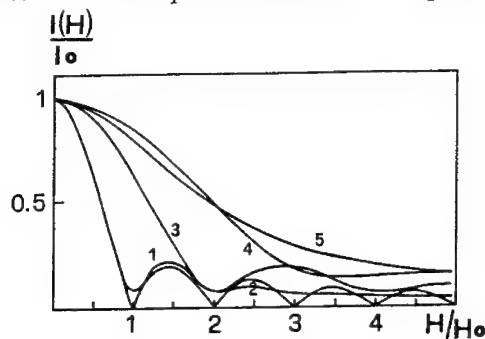


Fig. 2. Numerical results for the one-dimensional case:

1)  $a=L$ ,  $\sigma=0$ ; 2)  $a=L$ ,  $\sigma=0.1$ ; 3)  $a=0.5L$ ,  $\sigma=0.1$ ; 4)  $a=0.3L$ ,  $\sigma=0.2$ ; 5)  $a=0.3L$ ,  $\sigma=0.5$

At small values of the dispersion only weak smearing of the  $I_c(H)$  characteristics takes place, as dispersion increases the character of the dependence changes from the Fraunhofer pattern kind to a Gaussian-like form, as in the experiment.

#### 4. 2D case

Now we can pass to the discussion of the two-dimensional case. The average current density(per unit length along  $z$  direction) may be presented in the form

$$j = \frac{j_0}{L} \int_0^L a(z) \sin(\theta_0 + \pi \frac{\phi}{\phi_0} \frac{z}{L}) dz \quad (5)$$

where  $a(z)$  is the grain width in the field direction ( $y$ ),  $L$  is the junction width in  $z$ -direction,  $\theta_0$  is chosen in the way to obtain the maximum current. One can easily see that if  $a(z) = \text{const}$  formula (5) is reduced to the one-dimensional case which was discussed above.

Let us suppose now that the elementary junction has the form of a circle. In this case  $a(z)$  can be expressed in explicit form and after some trivial transformation one can find

$$j = \frac{1}{2} j_0 \sin(\theta_0 + \pi \frac{\phi}{2\phi_0}) \int_{-1}^1 \sqrt{1-x^2} \cos(\pi \frac{\phi}{\phi_0} \frac{x}{2}) dx = j_0 \frac{\phi}{\phi_0} J_1(\pi \frac{\phi}{2\phi_0}) \sin(\theta_0 + \pi \frac{\phi}{2\phi_0}) \quad (6)$$

where  $J_1(x)$  is the Bessel function. Evidently the current exceeds the maximal value when  $\sin(\theta_0 + \pi \frac{\phi}{2\phi_0}) = 1$ , so that

$$j_c(l) = j_0 \frac{\phi}{\phi_0} J_1(\pi \frac{\phi}{2\phi_0}) \quad (7)$$

and qualitatively the picture does not differ from the previous case.

Following the same procedure as in the one-dimensional case one can find, assuming that all "islands" are circular

$$I(H) = \int_0^L j_0 \frac{\phi_0}{\phi(l)} J_1(\pi \frac{\phi(l)}{2\phi_0}) \frac{1}{\sqrt{2\pi\sigma l}} \exp[-\frac{\ln^2(\frac{l}{a})}{2\sigma^2}] dl \quad (8)$$

This integral was calculated numerically and results for some typical values of grain dimensions and dispersions are presented at Fig.3.

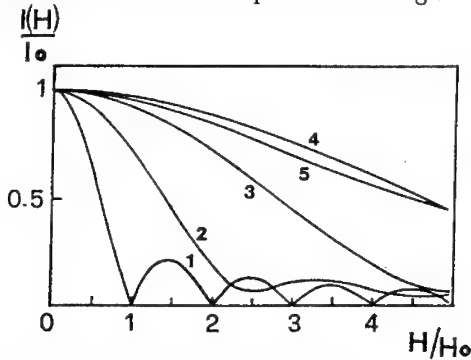


Fig. 3. Numerical results for the two-dimensional case:

1)  $a=L$ ,  $\sigma = 0$ ; 2)  $a=L$ ,  $\sigma = 0.1$ ; 3)  $a=0.5L$ ,  $\sigma = 0.1$ ; 4)  $a=0.3L$ ,  $\sigma = 0.2$ ; 5)  $a=0.3L$ ,  $\sigma = 0.5$

The general behaviour of these curves is as expected and in particular curve 3 reproduces well the experimental results<sup>1</sup>.

In conclusion it is worth to mention that in the last years a similar problem of smearing of the Fraunhofer diffraction pattern in arrays of granular superconductors has been discussed intensively in the literature (for instance, see<sup>4</sup>) in connection with the study of high  $T_c$  superconductivity.

#### Acknowledgements

We want to thank Prof. A.M.Cucolo for the valuable discussion. One of authors (A.V.) thanks the European Union Human Capital and Mobilities Conference Programme for financial support.

### References

1. R.Vaglio, A.M.Cucolo, C.M.Falco. *Phys. Lett.*, **A118** (1986) 89.
2. A.Barone, J.Paterno, *Josephson Effect: Physics and Applications* (J.Wiley & Sons, New York, 1982).
3. W.Weihnacht. *Phys. Stat. Solidi* **32** (1969) 169.
4. G.Paterno, C.Alvani, S.Casadio, U.Gambardella, and L.Maritato, *Appl. Phys. Lett.* **53** (1988) 609.

## INTRINSIC JOSEPHSON EFFECTS IN LAYERED SUPERCONDUCTORS

PAUL MÜLLER

*Walther-Meißner-Institut, Walther-Meißner-Str. 8  
D-85748 Garching, Germany*

## ABSTRACT

The large anisotropy and the extremely short coherence lengths of the high- $T_c$  superconductors suggest that the layered crystal structure is mapped onto a periodic modulation of the superconducting order parameter. Even an ideal single crystal should consist of a stacked series of superconducting and non-superconducting layers. Three-dimensional phase coherence is provided by Josephson currents between the layers. As the typical interlayer distance is approximately 15 Å, a single crystal of 3  $\mu\text{m}$  thickness should behave like a stack of 2000 Josephson junctions. This hypothesis is proved in every detail by measurements of the DC as well as the AC Josephson effects on single crystals of  $\text{Bi}_2\text{Sr}_2\text{CaCu}_2\text{O}_8$ ,  $(\text{Bi}_{1-y}\text{Pb}_y)_2\text{Sr}_2\text{CaCu}_2\text{O}_8$ ,  $\text{Tl}_2\text{Ba}_2\text{Ca}_2\text{Cu}_3\text{O}_{10}$  and  $\text{Pr}_{2-x}\text{Ce}_x\text{CuO}_4$ . Microwave emission experiments at frequencies between 3.5 and 95 GHz reveal explicitly the number of junctions in the samples. This number is given by the crystal thickness divided by 15 Å, i.e. every pair of  $\text{CuO}_2$  bilayers forms a Josephson junction. Similar results, including microwave emission, have been obtained recently on single crystals of the organic superconductor  $\kappa\text{-(BEDT-TTF)}_2\text{Cu(NCS)}_2$ . This observation supports the conclusion that in any layered superconductor with sufficiently high anisotropy the superconducting order parameter is spatially inhomogeneous a priori.

## 1. Spatial Homogeneity of the Superconducting Order Parameter

The essential universal property of the many-particle wave function of the superconducting state is the phase coherence over macroscopic distances. This phenomenon was discovered about 60 years ago by Walther Meißner und R. Ochsenfeld. Manifestations are the Ochsenfeld-Meißner effect<sup>1</sup>, the quantization of flux<sup>2</sup> and the Josephson effect<sup>3</sup>. The coherence length of a classical superconductor is extended over many lattice constants. Peculiarities of the crystallographic structure or lattice defects influence the superconducting state only marginally via the change of the Fermi surface. This property even prevents the occurrence of critical phenomena near the phase transition and leads to the conclusion that the superconducting state has a spatially constant order parameter a priori. In the high- $T_c$  superconductors, however, the Ginzburg-Landau coherence length parallel to the  $\text{CuO}_2$  planes is  $\xi_{ab} \approx 15\text{Å}$ . As calculated from  $H_{c2\parallel}(0) = \Phi_0/(2\pi\mu_0\xi_{ab}\xi_c)$ , the coherence length perpendicular to the planes,  $\xi_c$ , is less than 1 Å.<sup>4</sup> The basis for this evaluation, i.e. a homogeneous superconducting state, is no longer compatible with the atomic dimensions.

Therefore we draw a radical consequence: the layered crystal structure is mapped onto a periodic modulation of the order parameter along the direction perpendicular

to the planes, i.e. the crystallographic *c*-axis. The superconductor consists of a stack of superconducting layers, separated by non- or only weakly superconducting regions. Fig. 1 shows the crystal structures of different layered superconductors. The superconducting layers are represented by the fulvalene layers, and the  $\text{CuO}_2$  bi- or trilayers respectively. The observed Meißner effect of the whole volume of a crystal is provided by Josephson currents perpendicular to these planes. The experimental proof of this "intrinsic Josephson effect"<sup>5</sup> is the aim of this paper.

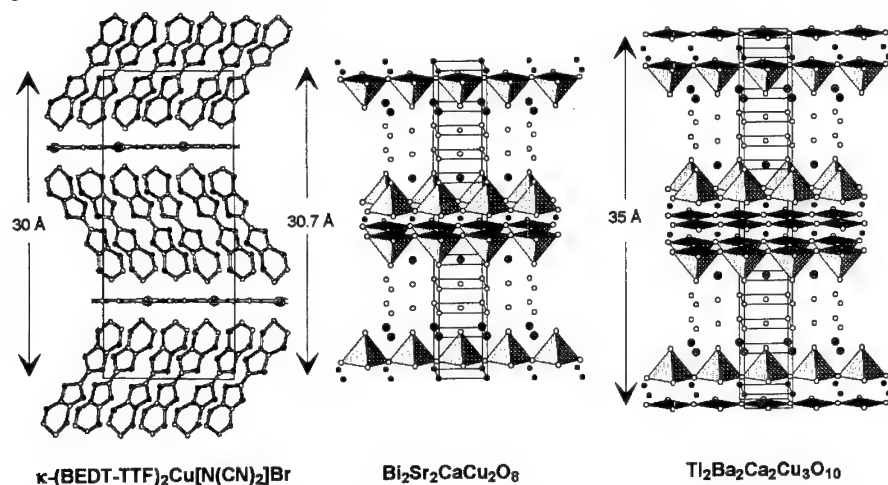


Fig. 1. Structural similarities of three different layered superconductors. The unit cells are marked by the lines. Left part: The organic superconductor  $\kappa\text{-(BEDT-TTF)}_2\text{Cu[N(CN)}_2\text{]Br}$  consists of layers of fulvalene molecule anions (double 5-fold rings), where 4 carbon atoms per fulvalene are substituted by sulphur. Each end of the fulvalene is bridged to ethylene groups by 2 S atoms (6-fold rings). Only the C or the (darkened) S atoms are shown. The BEDT-TTF layers are separated by layers of linear  $\text{Cu[N(CN)}_2\text{]Br}$  cations. Middle Part: The high- $T_c$  superconductor  $\text{Bi}_2\text{Sr}_2\text{CaCu}_2\text{O}_8$  is a stack of  $\text{CuO}_2$  bilayers intercalated with Ca. The bilayers are separated by a sequence of  $\text{SrO-BiO}_{1.5}\text{-SrO}$  layers. The Cu-O coordination is marked by the shaded half-pyramids. Right part: The triple-layer high- $T_c$  superconductor  $\text{Tl}_2\text{Ba}_2\text{Ca}_2\text{Cu}_3\text{O}_{10}$  evolves from the  $\text{Bi}_2\text{Sr}_2\text{CaCu}_2\text{O}_8$  structure by an additional intercalated planar  $\text{CuO}_2$  layer. Bi has to be substituted by Tl, and Sr by Ba.

## 2. Ginzburg-Landau Model of a Layered Superconductor

We propose, that even an ideal single crystal of a high- $T_c$  superconductor consists of a stack of superconducting layers, i.e. the copper oxide layers or bilayers. These layers are intercalated with non-superconducting or weakly superconducting material. In the case of  $\text{Bi}_2\text{Sr}_2\text{CaCu}_2\text{O}_8$ , the insulator is represented by the  $\text{Bi}_2\text{O}_3$  and  $\text{SrO}$  layers (fig. 2). Phase coherence is maintained by Cooper-pair tunneling. The transport currents perpendicular to the layers are described by the Josephson equations. Therefore the experimental proof consists of the measurement of all Josephson effects in *c*-axis transport experiments. Measurements of the angular dependence of

the critical current<sup>6</sup>, the upper critical field<sup>7</sup>, or the peculiarities of vortex motion under the influence of a temperature gradient<sup>8</sup> support this picture. It is well known, that  $\text{Bi}_2\text{Sr}_2\text{CaCu}_2\text{O}_8$  layers are superconducting, even if their thickness is only half of a unit cell<sup>9</sup>. We start with a simple layer model consisting of a periodic series of superconducting layers, separated by non-superconducting interlayers<sup>10,11</sup>.

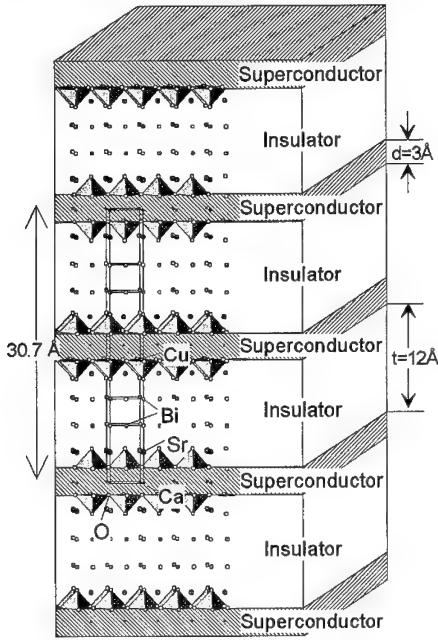


Fig. 2. Superposition of the lattice structure of  $\text{Bi}_2\text{Sr}_2\text{CaCu}_2\text{O}_8$  with the stacking sequence of the model.

The Ginzburg-Landau free energy functional is:

$$F = \int dV \left\{ \alpha(T)|\Psi|^2 + \frac{1}{2}\beta|\Psi|^4 + \frac{\hbar^2}{2m} \left| \left( \vec{\nabla} - \frac{2ie}{\hbar c} 2e\vec{A} \right) \Psi \right|^2 + \frac{B^2}{8\pi} \right\} \quad (1)$$

$\Psi$ : order parameter,  $\vec{A}$ : vector potential,  $B$ : magnetic induction. The superconducting layers are described by a negative condensation parameter  $\alpha$  and a small effective mass  $m$ , the non- or only weakly superconducting interlayers by  $\alpha \approx 0$  and a large effective mass.  $\alpha$  and the reciprocal mass  $1/m$  are modelled by functions which are periodic with the layer distance  $s$  (fig. 3a):

$$\begin{aligned} 2m_0 s^2 \alpha / \hbar^2 &= a(z) = a_0 + (a_0 - a_1)p(z) \\ m_0 / m(z) &= g(z) = g_{\min} + (g_{\min} - 1)p(z) \end{aligned} \quad (2)$$



$p(z)$  is a function with period  $s$  of the coordinate  $z$  perpendicular to the layers.  $m_0$  is the effective mass in the middle of the superconducting layers.  $\alpha_0$ ,  $\alpha_1$ , and  $g_{min}$  are constants. As a modulation of the (repulsive) Parameter  $\beta > 0$  influences the results only slightly, it is assumed to be constant.

Minimization of the free energy functional reveals a modified Ginzburg-Landau equation, There is a new term, which depends on the spatial derivatives along the  $z$ -direction.

$$\left(\vec{\nabla} - \frac{2ie}{\hbar c} 2e\vec{A}\right)^2 \Psi + \left(\frac{\partial}{\partial z} g\right) \left(\frac{\partial}{\partial z} - \frac{2ie}{c} A_z\right) \Psi = \alpha \Psi + \beta |\Psi|^2 \Psi \quad (3)$$

As expected, with geometry parameters of the  $Bi_2Sr_2CaCu_2O_8$  crystal structure, a numeric solution of this equation reveals a periodic modulation of the amplitude of the order parameter (fig. 3b, graph with  $\gamma_0 = 0$ ).

We evaluate the expression for the current (second Ginzburg-Landau equation):

$$\vec{j} = \frac{eg}{2i\hbar} (\Psi^* \vec{\nabla} \Psi - \Psi \vec{\nabla} \Psi^*) - \frac{e^2}{m} |\Psi|^2 \vec{A} \quad (4)$$

With  $\Psi = \Psi_0 e^{i\phi}$ , the current density perpendicular to the layers is:

$$j_z = \frac{eg}{\hbar} \Psi_0^2 \left( \frac{d\phi}{dz} - \frac{2\pi}{\Phi_0} \right) \quad (5)$$

We define a (continuous) gauge invariant phase difference  $\gamma$ :

$$\gamma = \phi(z) - \phi(0) - \frac{2\pi}{\Phi_0} \int_0^z A_z dz \quad (6)$$

Then, the current density becomes:

$$j_z = \frac{eg}{\hbar} \Psi_0^2 \frac{d\gamma}{dz} \quad (7)$$

This equation is to be compared with the first Josephson equation:  $j_z = j_c \sin(\gamma)$ . Inserting the definitions of  $\Psi$  and  $\gamma$  in the Ginzburg-Landau equation, estimating real and imaginary part, and using  $' := d/dz$ ,  $'' := d^2/dz^2$ :

$$g(\Psi_0'' - \gamma'^2 \Psi_0) + g' \Psi_0' - \alpha \Psi_0 - \beta \Psi_0^3 = 0 \quad (8)$$

$$g(\gamma'' \Psi_0 + 2\Psi_0' \gamma') + g' \gamma' \Psi_0 = 0 \quad (9)$$

The second equation is the current conservation law. With a free choice of the phase  $\gamma = 0$  in the middle of one electrode and a fixed phase difference to the next electrode,  $\gamma_0$  (arrow in fig. 3b), amplitude and phase of the order parameter in the whole space can be calculated (graphs with  $\gamma_0 \neq 0$  in figs. 3b and 3c).

Contrary to a homogeneous superconductor, where a constant current is caused by a constant phase gradient, in a layered superconductor a constant current across the

layers is accompanied by sudden jumps of the phase difference. For geometry parameters corresponding to the lattice structure of  $Bi_2Sr_2CaCu_2O_8$ , with the  $CuO_2$  bilayers as superconducting sheets and the SrO and  $Bi_2O_3$  layers as insulating interlayers, a sinusoidal current-phase relationship is obtained (fig. 3d). Weakening the modulation depth of the parameters results in a current-phase relation, which still is  $2\pi$ -periodic, but now contains higher order Fourier terms, in analogy to the proximity effect weak links. Compared to the Lawrence-Doniach model<sup>12</sup>, where Josephson coupling is as-

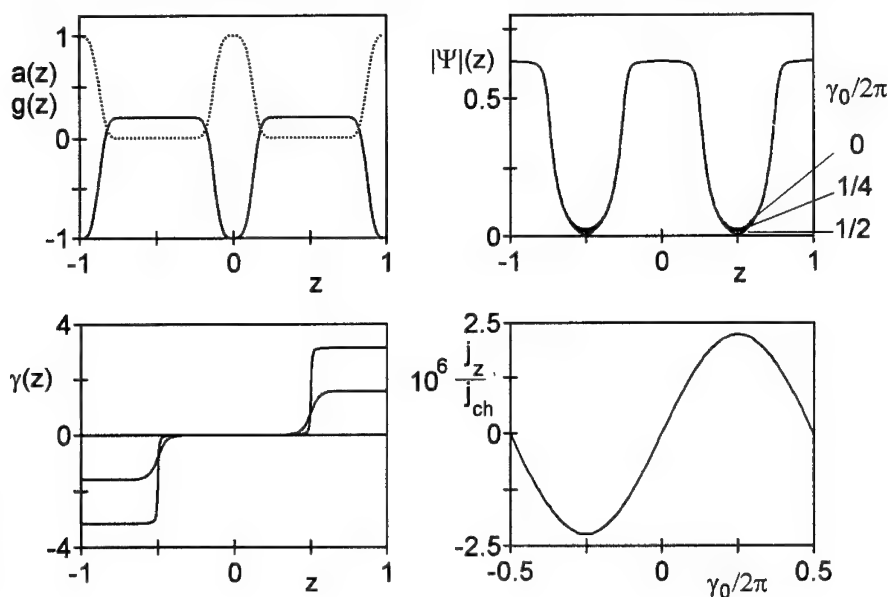


Fig. 3. Ginzburg-Landau model of a strongly modulated superconducting structure ( $a_0 = 0.2$ ,  $a_1 = -1$ ,  $g_{min} = 0.001$ ). The superconducting electrodes are located at  $z = 0$  and  $z = \pm 1$ . 3a: Condensation and effective mass parameters  $a(z)$  (dotted line) and  $g(z)$  (upper left). 3b: Order parameter at different phase differences between the layers (upper right). 3c: Continuous phase difference vs.  $z$  (lower left). 3d: Current-phase relation (lower right).  $j_z$  is normalized to the pairbreaking critical current density  $j_{ch}$ .

sumed a priori, the strength of this model is the possibility to check the conditions for Josephson coupling. It includes the limiting case of strong coupling between the layers, where the current-phase relationship is no longer  $2\pi$ -periodic. We note that no detail of the mechanism of superconductivity in the electrodes contributes to the Josephson effect.

The transport across a real Josephson junction at finite temperatures is the sum of a Cooper-pair and a quasiparticle transport channel. Including the finite capacitance, the simplest description is a parallel circuit of a resistor, a capacitor and the Cooper-pair channel made up of the idealized Josephson junction. The displacement current

of the capacitance controls the dynamics of the system. The simplest description is the Resistively Shunted Junction (RSJ) model. The time constant is described by the characteristic frequency  $f_c = I_c R / \Phi_0$ . As a measure for the quality factor  $Q$  the McCumber-Parameter  $\beta_c = 2\pi f_c R C = Q^2$  is used. The Josephson inductance is  $L_J = \Phi_0 / (2\pi I_c)$  and the plasma frequency  $f_{pl} = (4\pi^2 L_J C)^{1/2}$  is the resonant frequency of the linearized circuit.

### 3. Experiments

The  $\text{Bi}_2\text{Sr}_2\text{CaCu}_2\text{O}_8$  single crystals were prepared from a stoichiometric melt of the carbonates or oxides. The cooling rate from 980°C to 860°C was between 1 K/h and 3 K/h. Large single crystals were found to grow along the temperature gradient of the furnace. The shape of the crystals was mica-like. Samples for the measurements were cut and cleaved from these crystals. As freshly cleaved surfaces were insulating, electrical contacts had to be prepared by diffusion of an evaporated Au layer. The oxygen excess  $\delta$  in  $\text{Bi}_2\text{Sr}_2\text{CaCu}_2\text{O}_{8+\delta}$  and therefore the carrier concentration were controlled by annealing in flowing Ar or pure oxygen.  $\delta$  or the hole concentration per  $\text{CuO}_2$  layer was varied between 0.16 and 0.26. The critical temperature  $T_c$  varied between approximately 90 K and 70 K. The samples were characterized by DC and AC susceptibility, by Raman spectroscopy<sup>13</sup>, measurements of the plasmon dispersion<sup>14</sup>, and far-infrared spectroscopy<sup>15</sup>. The  $(\text{Bi}_{1-y}\text{Pb}_y)_2\text{Sr}_2\text{CaCu}_2\text{O}_8$  crystals were prepared at the CNET, Bagnex<sup>16</sup>, the  $\text{YBa}_2\text{Cu}_3\text{O}_7$  single crystals at the Walther-Meißner-Institute<sup>17</sup>, the  $\text{Tl}_2\text{Ba}_2\text{Ca}_2\text{Cu}_3\text{O}_{10}$  single crystals at the university of Göttingen<sup>18</sup>, the  $\text{Pr}_{2-x}\text{Ce}_x\text{CuO}_4$  single crystals at the university of Bochum<sup>19</sup> and the a-axis oriented  $\text{YBa}_2\text{Cu}_3\text{O}_7$  films at the TU München<sup>20</sup>. The  $\kappa-(\text{BEDT-TTF})_2\text{Cu}(\text{NCS})_2$  crystals were grown by electrocrystallization<sup>21</sup>. As the basic problem of detecting the Josephson effects is a homogeneous current distribution in the samples, sample sizes were as small as possible (typically  $30 \times 30 \times 1 \text{ } (\mu\text{m})^3$ ). The usual four-terminal contact procedure is no longer possible. Due to the giant anisotropy, Montgomery's method<sup>22</sup> allows no reliable results. The crystals were mounted between two contact rods, where the potential leads were fixed. Contact resistances were less than  $1 \text{ } \Omega$ , which is considerably smaller than typical sample resistivities of  $1 \text{ k}\Omega$  at  $T_c$ . In most of the figures the contact resistance is corrected. Further details were already published in refs.<sup>5,23</sup>.

As Shapiro-steps are clearly visible only if the AC current amplitude is of the order of the DC critical current, the critical currents of up to 100 mA and the small source impedance of few Ohms required special matching structures. Besides coaxial coupling we used a tunable cylindric resonator at frequencies up to 18 GHz. The maximum power of the sweep oscillator was 100 mW. Due to the relatively large dimensions of the standard sample holder, at higher frequencies the samples were mounted inside special impedance matching structures inside the waveguide. Frequencies between 26.5 GHz and 40 GHz were provided by an active frequency doubler with an output power of 50 mW. At  $94 \pm 1$  GHz a mechanically tunable Gunn diode was used. The output power was 50 mW.

Because Josephson junctions are nonlinear oscillators, which are able to lock to any resonance of the system, we avoided impedance matching devices in our microwave emission experiments. Fig. 4 shows the detection procedure. After emission into free space the radiation was detected by a horn antenna in front of a X band, K band or W band waveguide. In a low noise converter the signal was mixed down to intermediate frequencies up to 2 GHz. Further analysis was performed either in a spectrum analyzer or in a radiometric receiver with signal averaging. The bandwidths of the radiometer

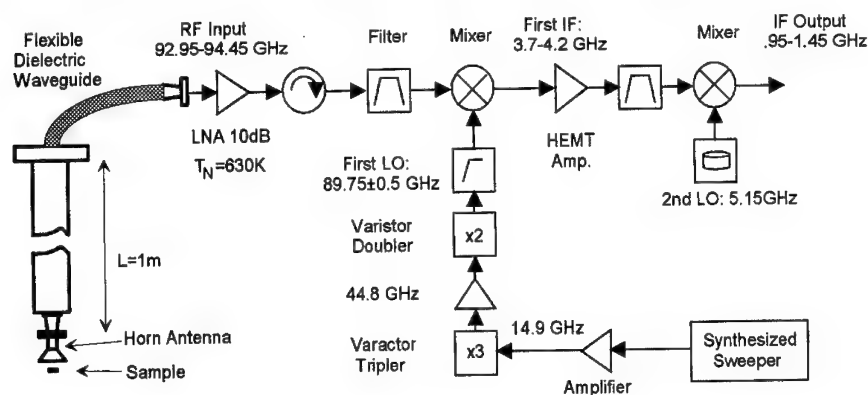


Fig. 4. Tunable W band radiometer (92.95-94.45 GHz). The radiation from the sample is collected by a horn antenna. Then the signal is fed to the input stage of the broadband preamplifier via a flexible dielectric waveguide. After mixing the signal is integrated over a bandwidth of 500 MHz.

branch were between 3 MHz and 500 MHz. Detected frequencies were 3.5 - 4.2 GHz, 10.9-12.3 GHz, 24.2 GHz and 93-95 GHz. System noise temperatures were 30 K - 60 K at the lower frequencies and 500 K - 630 K in the K and W band. With the background of the black-body radiation of the liquid He mirror of the cryostat, integration times of 1-3 s allowed detection sensitivities down to  $10^{-19}$  W in a bandwidth of 1 MHz.

#### 4. Results and Discussion

Special aspects of the c-axis transport measurements can be found in earlier publications<sup>5,23</sup>. Fig. 5 shows the temperature dependence of the resistivity of  $\text{Bi}_2\text{Sr}_2\text{CaCu}_2\text{O}_8$  samples with various hole concentrations. Besides the rounding due to fluctuations near  $T_c$ , the curves are very similar to  $\text{YBa}_2\text{Cu}_3\text{O}_7$ . The different carrier concentration shows up as a small  $T_c$  decrease at higher oxygen concentrations. Perpendicular to the planes, the resistivity is larger by four orders of magnitude. Due to the Ioffe-Regel criterion, resistivities of the order of 1  $\Omega\text{cm}$  are hardly consistent with a carrier concentration between 4 and 6  $10^{21} \text{ cm}^{-3}$ . The temperature coefficient of the Ar annealed samples (sample #GR in fig. 5) is strongly negative, but changes to positive with increasing oxygen excess. This temperature dependence is explainable by the assumption of a temperature dependent tunneling barrier, whose

height decreases with increasing carrier concentration. The observation of normal metal-insulator-normal metal tunneling supports this assumption: the upturn of  $\rho(T)$  coincides with the occurrence of a tunneling characteristic in the normal state<sup>5</sup>.

The anisotropy parameter of the London penetration depth,  $\gamma = \lambda_c/\lambda_{ab}$ , was determined by the measured angular dependence of the torque  $\tau(\theta)$  at constant external fields<sup>24</sup>. The  $\text{Bi}_2\text{Sr}_2\text{CaCu}_2\text{O}_8$  single crystals had  $\gamma$ -values between 150 ( $\text{O}_2$  annealing), and 900 (Ar annealing).  $\gamma$  of  $\text{Tl}_2\text{Ba}_2\text{Ca}_2\text{Cu}_3\text{O}_{10}$  was also very large ( $\gamma \approx 900$ ). For comparison, the anisotropy parameter of pure Nb is  $\gamma = 1.1$ , and  $\gamma = 3$  and  $\gamma = 5$  for  $\text{NbSe}_2$  and  $\text{YBa}_2\text{Cu}_3\text{O}_7$  respectively. Therefore the samples under consideration are characterized by an extremely high anisotropy.

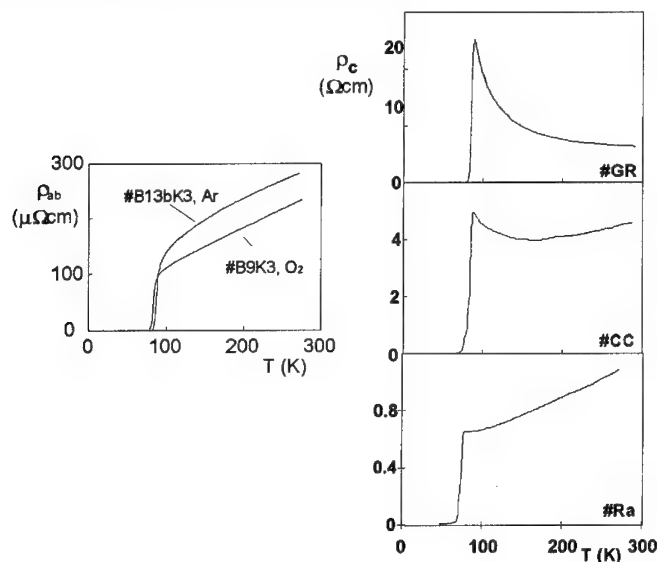


Fig. 5. Resistivity vs. temperature of  $\text{Bi}_2\text{Sr}_2\text{CaCu}_2\text{O}_8$  single crystals parallel (left part) and perpendicular (right part) to the  $\text{CuO}_2$  planes. Samples #GR and #CC correspond to the Ar and  $\text{O}_2$  annealed samples in the left part. 20 % of the Bi atoms of sample #Ra are substituted by Pb. Sample #Ra was annealed in oxygen.

In order to interpret the results from a series connection of hysteretic junctions, we start with the I-V characteristics of a  $\text{Nb}-\text{AlO}_x$  multilayer consisting of 7  $\text{Nb}/\text{Al}-\text{AlO}_x/\text{Nb}$  tunnel junctions<sup>25</sup>. The index of the branches in fig. 6 corresponds to the number of junctions in the resistive state, arranged according to the (different) size of their critical current. After each switching, the complete branch is obtained by decreasing the bias current by hand. The distances between different branches correspond to the energy gap. Above the highest critical current a (nonhysteretic) quasiparticle tunneling characteristic is seen. The increasing backbending of the

branches is due to energy gap decrease by quasiparticle injection, because the thickness of the electrodes is comparable to the diffusion length of quasiparticles.

Using the same reasoning, we are able to explain the huge variety of branches of a  $\text{Bi}_2\text{Sr}_2\text{CaCu}_2\text{O}_8$  single crystal, which contains approximately 660 intrinsic junctions per  $\mu\text{m}$  (fig. 6).<sup>23</sup> The curve consists of a series connection of hundreds of underdamped junctions. Note that the slope decreases by a constant amount from one branch to the next. This observation is the most important argument against the interpretation of those branches as zero-field steps of long Josephson junctions. The distance between the branches should be either the RSJ value of the critical voltage,  $V_c = \pi/2e \Delta$ , or the energy gap  $2\Delta/e$ . For Ar annealed samples with a critical current density  $j_c \approx 200 \text{ A/cm}^2$ , this distance is up to 16 mV, and therefore is consistent with  $\pi/2e \Delta$  and  $\Delta = 1.75k_B T_c$ . In analogy to the Nb model system, at large voltages

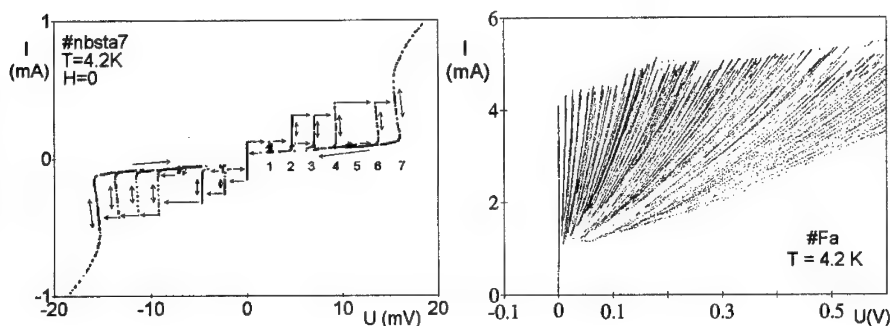


Fig. 6. Left part: I-V characteristic of a stack of 7 Nb/Al-AlO<sub>x</sub>/Nb tunnel junctions. The arrows mark the succession of data points produced by increasing or decreasing the bias current. The branch index corresponds to the number of junctions in the resistive state. Asymmetry and missing branches are caused by trapped flux. The backbending of the higher-order branches is due to quasiparticle injection.

Right part: I-V characteristic of an Ar annealed  $\text{Bi}_2\text{Sr}_2\text{CaCu}_2\text{O}_8$  single crystal (sample #Fa). Only the branches at positive current bias are shown. The single branches were obtained by a strategy similar to the one of the Nb stack.

the I-V curve exhibits a quasiparticle characteristic with a sum gap value of 3.4 V (fig. 7, left part). As the number of junctions in this crystal is approximately 1000, this corresponds to an average value of 3.4 mV per junction, far below the observed distance between the branches at low voltages. We suggest, that the gap value is considerably reduced by quasiparticle injection, when an increasing number of junctions is switching to the resistive state.

Increasing the oxygen excess leads to decreasing hystereses and narrower distances between the jumps. The reason for this decrease of the McCumber parameter  $\beta_c$  is still not clear. One possibility is metallic conduction in parts of the interlayer region. This interpretation is supported by photoemission data of oxygen annealed crystals, where some Bi bands were found to cross the Fermi energy<sup>26</sup>. Pb doped samples show

critical voltages below 1 mV. Then, especially at higher temperatures, all junctions can switch simultaneously to their resistive state. The upper right part of fig. 7 shows the I-V characteristic of sample # Ra from fig. 5, which corresponds to an ideal RSJ characteristic with  $\beta_c \approx 2.1$  and  $I_c R_N \approx 60$  mV. If the critical currents of single junctions are nearly equal, even stacks with large hystereses can switch simultaneously (fig. 7, lower right). The analysis of  $\beta_c$  reveals a RC time constant of approximately 1 ps. At higher temperatures, the critical currents are so small, that all junctions are overdamped, i.e. the I-V characteristic is no longer hysteretic (see fig. 14).

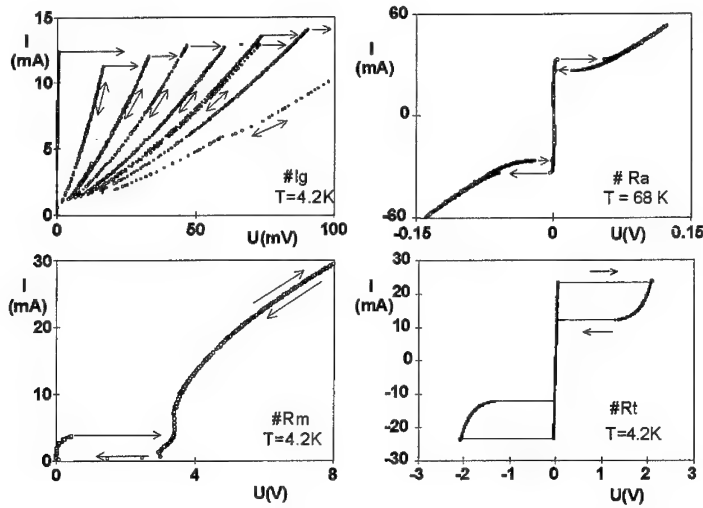


Fig. 7. Overview of different types of I-V characteristics. Left part: Ar annealed  $\text{Bi}_2\text{Sr}_2\text{CaCu}_2\text{O}_8$  single crystals on different voltage scales. The single branches of the upper part are not traced out in the lower part. Note the quasiparticle-like characteristic at high voltages. Right part: Ideal RSJ characteristic of a Pb doped sample (upper half). Abrupt switching of a strongly hysteretic I-V characteristic (lower half). The contact resistance is not corrected here.

In summary, for current flow perpendicular to the planes, all I-V characteristics are explainable by series connections of differently damped junctions in the framework of the RSJ model. The form of the resistive branches suggests an appreciable quasiparticle conduction below the energy gap.

In the BCS theory, the temperature dependence of the critical current  $I_c$  of superconductor-insulator-superconductor junctions is described by the Ambegaokar-Baratoff relation<sup>27</sup>. Here,  $I_c(T)$  is determined by the temperature dependence of the energy gap  $\Delta(T)$ :  $I_c R_N = \pi/2e \Delta \tanh(\Delta/2k_B T)$ .  $R_N$  is the asymptotic derivative of the I-V characteristic at large voltages. Other realizations of weak links like proximity junctions have concave curvatures near  $T_c$ . In order to avoid perturbations due to the interaction with already resistive junctions only the branches with the lowest critical

currents are discussed. Oxygen annealed samples show the Ambegaokar-Baratoff relation (fig. 8). However, the data of Ar annealed samples are considerably higher. If also here the temperature dependence of  $I_c$  is caused by the temperature dependence of the energy gap,  $\Delta(T)$  can be calculated from the data by numerical inversion of the equation above. The right part of fig. 8 shows the temperature dependence of the energy gap, normalized to its zero temperature value. These data correspond well to Raman data obtained from the temperature dependence of the quasiparticle intensity at small energy transfers<sup>13</sup>.

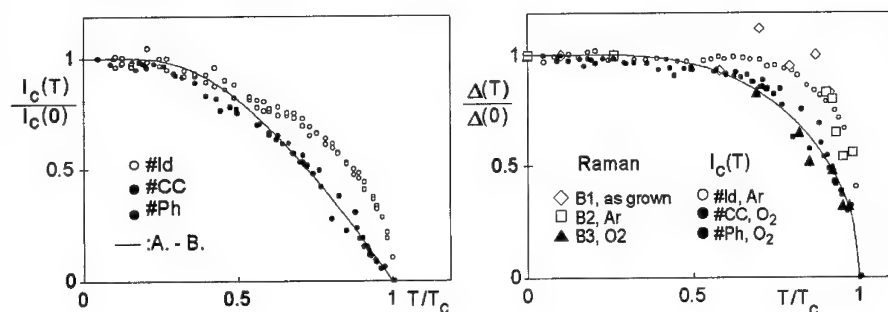


Fig. 8. Temperature dependence of the c-axis critical current for  $\text{Bi}_2\text{Sr}_2\text{CaCu}_2\text{O}_2$  samples with different oxygen excess (left part). The full line is the Ambegaokar-Baratoff relation. The right part shows the energy gap data, calculated by numerical inversion of this relation. The Raman data are marked by the large symbols. The full line is the BCS temperature dependence.

Therefore, the Ar annealed samples seem to have an energy gap which is nearly constant up to  $T_c$ . Both types of samples differ only by their critical current value in c direction, i.e. by their anisotropy parameter. Therefore the observed anomaly in  $\Delta(T)$  seems to be a pure anisotropy effect. All  $I_c(T)$  measurements performed to date are consistent with superconductor-insulator-superconductor junctions.

In a magnetic field perpendicular to the current direction (cf. fig. 10),  $I_c$  vs.  $H$  is given by a Fraunhofer function, if the junction dimensions are smaller than the field penetration depth. For a classic Josephson junction with infinitely extended electrodes, the zeroes  $nH_0$  of the Fraunhofer function are determined by the field penetration depth into the electrode material (fig. 10). With the ab penetration depth of  $\text{Bi}_2\text{Sr}_2\text{CaCu}_2\text{O}_8$ ,  $\lambda_{ab} \approx 1700 \text{ \AA}$ , one obtains:  $H_0 = \Phi_0/(\mu_0(2\lambda + t)b) \approx 2 \text{ Oe}$ . A stack of intrinsic junctions contains a new electrode every  $15 \text{ \AA}$ . As the thickness of these electrodes is only  $3 \text{ \AA}$ , which is considerably smaller than  $\lambda_{ab}$ , the flux penetrating such a junction is determined solely by the distance between the electrodes. Then,  $H_0 = \Phi_0/(\mu_0 tb) \approx 0.5 k\text{Oe}$ . In this case, the modulations of  $I_c$  in a magnetic field parallel to the planes reveal the geometry of the junctions. According to the proposed hypothesis, the penetration field  $H_0$ , plotted vs. the inverse width of the crystals,  $1/b$ , should reveal a straight line. The inverse slope of this line should be the distance between two  $\text{CuO}_2$  planes ( $15 \text{ \AA}$ ). Similar to the  $I_c(T)$  measurements



only the branches with the lowest critical currents were evaluated. As the field scale exceeds considerably the lower critical field, perfect alignment of the  $ab$ -planes with the external field had to be ensured, such as to avoid current inhomogeneities and flux creep due to Abrikosov vortices in the  $CuO_2$  planes. As expected, at temperatures above the irreversibility line, a weak modulation of  $I_c(H)$  (fig. 9, left part) was found. The insert in fig. 9 is the above-mentioned plot. The results are consistent with the distance between two  $CuO_2$  bilayers of 15 Å.

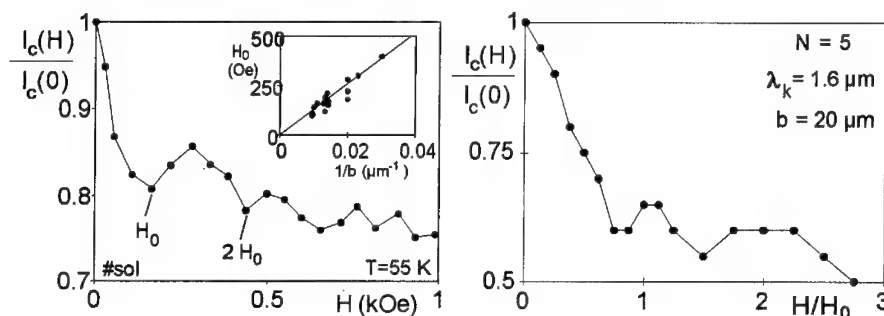


Fig. 9. Magnetic field dependence of the normalized critical current of sample #sol. The field orientation is parallel to the planes. The insert shows the first minimum of  $I_c(H)$  of several samples vs. the inverse width  $1/b$  of the crystals. The line was calculated by  $H_0 = \Phi_0/\mu_0 1/b$  (15 Å). Right part: Calculated  $I_c$  vs.  $H$  for a stack of 5 intrinsic junctions. The geometry parameters as well as the critical current density correspond to Ar annealed  $Bi_2Sr_2CaCu_2O_8$  crystals.

An interpretation of the large residual value of the critical current even at high fields deserves a more detailed analysis<sup>25</sup>. The electrodes of intrinsic junctions are considerably thinner than the London penetration depth for fields parallel to the  $CuO_2$  planes,  $\lambda_{ab} \approx 1700$  Å. Here, the field intersecting the crystal is only weakly screened. The large kinetic screening currents perpendicular to the direction of the transport current, lead to a coupling of adjacent junctions.

If the electrodes are thicker than the London penetration depth  $\lambda$ , the integration of the phase gradient parallel to an electrode can be performed along a path avoiding screening currents (fig. 10, left part). Combination with Maxwell's equation for  $H$  and the Josephson equation for  $j$  reveals the well-known sine-Gordon equation:

$$\gamma'' - \frac{1}{\bar{c}_m^2} \ddot{\gamma} - \frac{1}{\bar{c}_m^2 \tau} \dot{\gamma} = \frac{1}{\lambda_m^2} \sin \gamma \quad (10)$$

where  $\tau$  is the RC time constant. Time derivatives are marked by dots.

This is the equation of motion of a fluxon with phase velocity  $\bar{c}_m$ , the so-called Swihart velocity. In the static case and at small phase shifts, this equation is equivalent to the second London equation, i.e. the constant  $\lambda_m$  is the penetration depth of a magnetic field into the electrodes. If the width of the junction is smaller than  $\lambda_m$ , the above mentioned Fraunhofer relation holds.

The extremely thin electrodes of intrinsic Josephson junctions require an explicit calculation of the kinetic screening currents. As the bottom electrode of the  $n$ 'th junction coincides with the top electrode of the  $(n+1)$ 'th junction, a coupling of different junctions occurs (fig. 10, right part). Using the same procedure as above, the dynamics of a stack of  $N$  intrinsic junctions is described by a system of coupled sine-Gordon equations:

$$\ddot{\gamma}'' = \underline{M}(\beta_c \ddot{\gamma} + \dot{\gamma} + \vec{j}_S - \vec{j}_b) \quad (11)$$

The vectors are defined as:  $\vec{\gamma} = (\gamma_1 \dots \gamma_N)$ ,  $\vec{j}_S = (\sin \gamma_1 \dots \sin \gamma_N)$ , and  $\vec{j}_b = j_b(1 \dots 1)$ . The tridiagonal matrix  $\underline{M}$  couples adjacent junctions:  $M_{n-1,n} = M_{n+1,n} = (b/\lambda_k)^2$ ,  $M_{n,n} = b/\lambda_m^2 + 2b/\lambda_k^2$ .

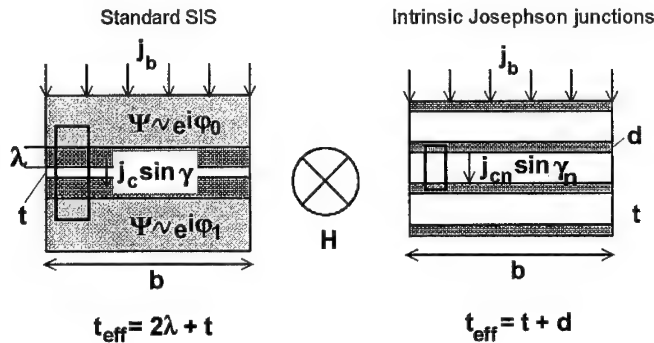


Fig. 10. Sketch of the calculation of junction dynamics in a magnetic field. Left: Standard junction with thick electrodes. Right: Stack of intrinsic junctions with electrodes, which are considerably thinner than the field penetration depth. The  $z$  direction is parallel to  $j_b$ , " $x$ " is perpendicular to both  $j_b$  and  $H$ , and " $y$ " is parallel to  $H$ .

In analogy to the "thick" single junction, the index " $m$ " marks the magnetic terms. Now " $k$ " marks the kinetic terms, which are caused by the screening currents flowing in  $x$  direction. The new length scale  $\lambda_k$  is the correlation length for inhomogeneities of a current front, whereas  $\lambda_m$  is still the screening length for an external magnetic field. Details of the theory can be found in refs. <sup>5,25</sup>. For the measured  $Bi_2Sr_2CaCu_2O_8$  single crystals,  $\lambda_k$  is between 0.1 and 1  $\mu m$ ,  $\lambda_m$  between 50 and 500  $\mu m$ . The typical crystal dimensions of 30  $\mu m$  are intermediate between those values. For small external fields, there is still a homogeneous current flow, whereas at higher fields current inhomogeneities in  $x$  direction are expected. A numeric solution of the above equation for a stack of 5 junctions with  $Bi_2Sr_2CaCu_2O_8$  parameters is shown in fig. 9 (right part). The weak modulation as well as the high socket value of approximately 50% are reproduced in the simulation. Due to computing time problems, the resolution for the current values is only 5%.

For a series connection of Josephson junctions, there is an additional degree of freedom, i.e. the phase of the AC currents in different junctions. Therefore mutual

phase lock either forced by an external field or by some internal interaction is to be considered.

A phase-locked loop, as it is described by the RSJ differential equation, can lock to an external excitation, if its free eigenfrequency is near an integer multiple  $n$  of the external frequency. The finite locking range shows up as constant voltage steps in the I-V characteristics (Shapiro effect). According to the second Josephson equation, the position of these steps is given by  $U_n = nh/2ef$ . For a series array of  $N$  junctions, the phases of the AC Josephson currents in all junctions have to lock to the external oscillation. Then:  $U_n = Nnh/2ef$ . This gives a straightforward method to determine

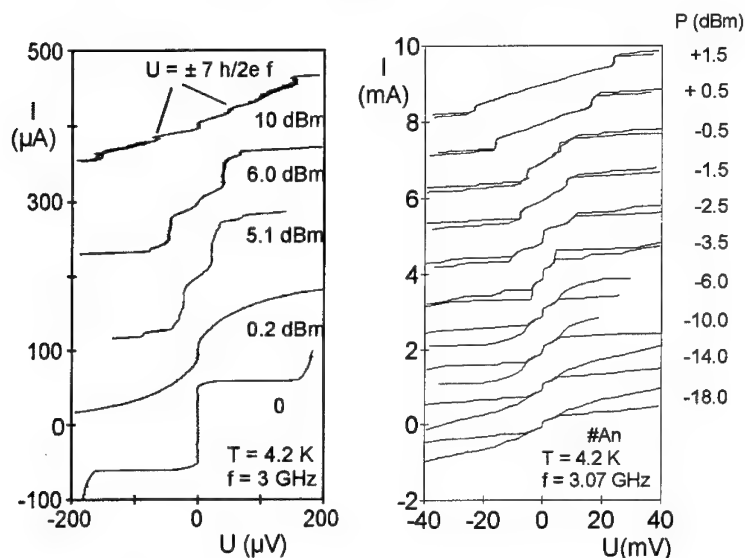


Fig. 11. I-V characteristic of Josephson stacks at increasing microwave power. Left part: I-V characteristic of a stack of 7 Nb/Al-AlO<sub>x</sub>/Nb tunnel junctions (cf. fig. 6). The I-V characteristics are shifted vertically by a current offset of 100  $\mu$ A. Note that the zero power curve is distorted due to trapped flux. Right part: Bi<sub>2</sub>Sr<sub>2</sub>CaCu<sub>2</sub>O<sub>8</sub> single crystal; the current offset here is 1 mA. With increasing microwave power, the steps of both samples shift to higher voltages. At the highest power, the I-V characteristics show the first Shapiro step for 7 junctions in series (Nb system, left part) and the third Shapiro step for a series array of 1200 junctions (single crystal, right part). Here, the first and second order steps are only weakly developed.

an unknown number of junctions in a series array. Indeed, at considerable excitation amplitudes, the phases of the AC Josephson currents can be synchronized. Shapiro steps, corresponding to the number of junctions in series are observed. Fig. 11 shows examples for the Nb/Al - AlO<sub>x</sub>/Nb model system and a Bi<sub>2</sub>Sr<sub>2</sub>CaCu<sub>2</sub>O<sub>8</sub> single crystal. Experimentally, however, for hysteretic junctions at frequencies far below the critical frequency, complete locking can be achieved only at very high excitation amplitudes.

By passive detection of the AC Josephson currents, synchronization problems can be avoided. According to the Josephson constant  $2e/h \approx (483.6 \text{ MHz}/\mu\text{V})$ , the expected frequencies are in the GHz region. At such frequencies, a considerable fraction of the AC amplitude is radiated. At a fixed detection frequency  $f$ , a maximum of the emitted power is expected, if the voltage across the junction is  $U = h/2e f$ . The maximum emitted power is of the order of nW. In practice, excitation of higher harmonics, impedance mismatch, and losses during emission and detection decrease this value to few femtowatts ( $10^{-15} \text{ W}$ ).

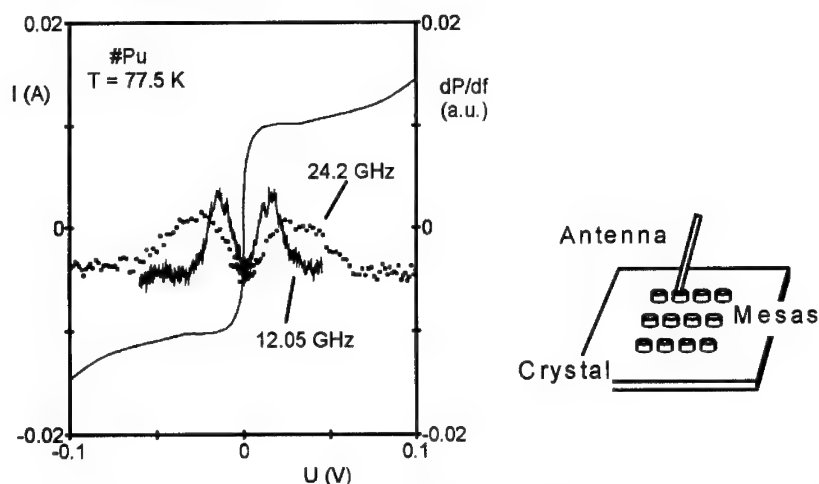


Fig. 12. I-V characteristic (left ordinate) and microwave power (right ordinate) of sample #Pu. The emission peaks correspond to a series array of  $N = 480$  junctions. The right part shows a sketch of the mesa array.

Independent of the phases, in a series array of  $N$  junctions at a fixed frequency  $f$ , a maximum of the emitted power should be observed at a voltage  $U = N h/2e f$ . Fig. 12 shows a radiometric measurement of a mesa etched out of a  $(\text{Bi}_{0.8}\text{Pb}_{0.2})_2\text{Sr}_2\text{CaCu}_2\text{O}_8$  single crystal surface<sup>28</sup>. Detection frequencies were 12.05 and 24.2 GHz. Aside from the high voltage of the peak, this characteristic is very similar to the one of a single junction<sup>29</sup>. However, the peak position corresponds to a series connection of approximately 500 junctions, doubles when the frequency is doubled, and conforms nicely with the mesa's height of approximately 7500 Å.

Characteristics of this kind were observed to date only with the oxygen annealed, Pb doped single crystals. For most of the oxygen annealed  $\text{Bi}_2\text{Sr}_2\text{CaCu}_2\text{O}_8$  single crystals, at low temperatures, characteristics like the one of fig. 13 are seen. Several sharp peaks are added to a broad background. This result can be interpreted by a superposition of the incoherent radiation of junctions, whose AC currents are out of phase, and the coherent radiation of groups of phase-synchronized junctions. This kind of characteristic was observed in all measured frequency bands. It is to be noted

that arbitrary voltages are impossible to achieve with such multiply valued, strongly hysteretic I-V characteristics.

Unfortunately, in most cases, we were not able to observe phase-lock of all junctions in a crystal. There is a considerably simpler possibility of counting the junctions. The decrease of the critical current at higher temperatures causes the intrinsic junctions to be overdamped in close vicinity to  $T_c$ .

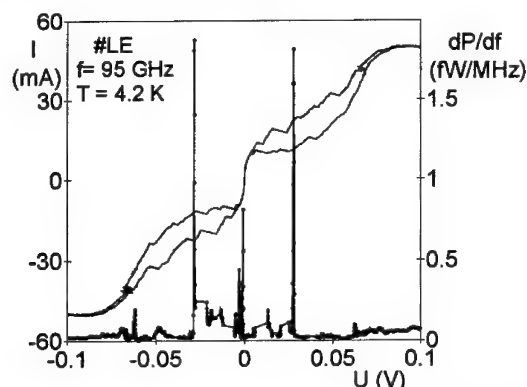


Fig. 13. I-V characteristic and microwave power at 95 GHz of a  $\text{Bi}_2\text{Sr}_2\text{CaCu}_2\text{O}_8$  single crystal. The single branches are not traced out in the figure.

This kind of nonhysteretic I-V characteristic makes it possible to adjust arbitrary voltages across the samples, such as to force emission in the available frequency band. In addition, at such high temperatures, self-synchronization can hardly be expected. As a single intrinsic junction can be only current biased, it has to be provided that the scatter of critical currents in a crystal is not too large. Then we expect intensity maxima, which correspond to an (incoherent) superposition of the emission of all junctions in a series array. This effect was observed in many oxygen annealed samples. Fig. 14 shows an example. The power peak at approximately 40 mV corresponds to a series connection of 1700 junctions. Supposing that the electrode distance of a single junction corresponds to the distance of two  $\text{CuO}_2$  bilayers, a total sample thickness of  $2.5 \mu\text{m}$  can be calculated. This is consistent with the thickness of the sample as measured in the scanning electron microscope. The shift of this power peak with frequency is shown in the inset. At positive as well as at negative voltages, the peaks coincide with the prediction of the Josephson frequency-voltage relation for a series array of 1700 junctions. The right part of fig. 14 shows this peak's position as a function of the measured crystal thickness. The results conform excellently with the assumption that every pair of  $\text{CuO}_2$ -bilayers in a crystal forms a Josephson junction. Apparently, the intrinsic Josephson effect is only marginally influenced by crystalline imperfections.

Our measurements on  $\text{YBa}_2\text{Cu}_3\text{O}_7$  single crystals and a-axis oriented films always revealed flux-flow I-V characteristics<sup>23</sup>. However, intrinsic Josephson effects in

$YBa_2Cu_3O_7$  cannot be definitely excluded. In order to prove that the intrinsic Josephson effect is not a peculiarity of high temperature superconductors with  $CuO_2$  bilayers we performed measurements on a triple layer compound, a single layer n doped material and an organic superconductor.

At first, similar to  $Bi_2Sr_2CaCu_2O_8$ , the  $Tl_2Ba_2Ca_2Cu_3O_{10}$  single crystals show multiple branching in the I-V characteristics<sup>23,29</sup>. Furthermore, the  $Pr_{1.85}Ce_{0.15}CuO_4$  single crystals showed the well-known picture<sup>5</sup>. We emphasize, that the crystal structure has only single  $CuO_2$  layers with a distance of 6 Å.

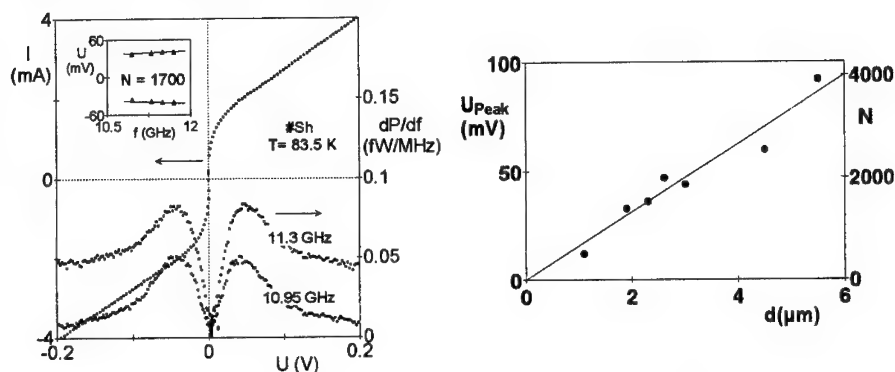


Fig. 14. Left part: I-V characteristic (left ordinate) and emission at 2 different frequencies (right ordinate) for the  $Bi_2Sr_2CaCu_2O_8$  single crystal sample #Sh. Note that the temperature was close to  $T_c$ . The inset shows the peak positions as a function of the detected frequency. The straight lines are the Josephson voltage-frequency relation for both polarities of the measured voltage. Right part: Position of the emission peak at a frequency of 10.95 GHz as a function of the measured thickness of the crystals. The straight line was calculated by  $U_{Peak} = h/2e f N$ . N was calculated by division of the crystal thickness by the distance of two  $CuO_2$  bilayers (15 Å).

We close with the organic superconductor  $\kappa-(BEDT-TTF)_2Cu(NCS)_2$ . The structure of this material is very similar to the one in fig. 1, but slightly distorted. Fig. 15 shows I-V characteristic and X band microwave emission. We note the nonhysteretic I-V characteristic and the relatively narrow linewidth. The position of the line corresponds to a series array of approximately 1100 junctions.

Due to the large energy gap of the high- $T_c$  superconductors, the characteristic frequencies and therefore the region of stable operation can extend up to the terahertz region. A series array of thousands of intrinsic Josephson junctions in a crystal could be a natural, tunable sub-millimeter source. If phase-lock can be achieved, the linewidth should not exceed 100 kHz. A second advantage is the high source impedance of series arrays, which allows matching with devices of conventional microwave engineering. There is an additional degree of freedom in the design of intrinsic junctions: the strength of Josephson coupling between the  $CuO_2$  planes can be varied "in situ" by oxygen annealing. At present, the conditions for self-synchronization are an active area of research. N coherently radiating junctions decrease the linewidth of a single

one by a factor of  $1/N$ .<sup>5,29</sup> Recently we were able to detect the radiation of more than 1000 junctions at a frequency of 93.7 GHz<sup>29</sup>. The extremely narrow bias interval of the line suggests coherent emission. In this case, the linewidth should be of the order of 100 kHz, far below our receiver bandwidth of 500 MHz.

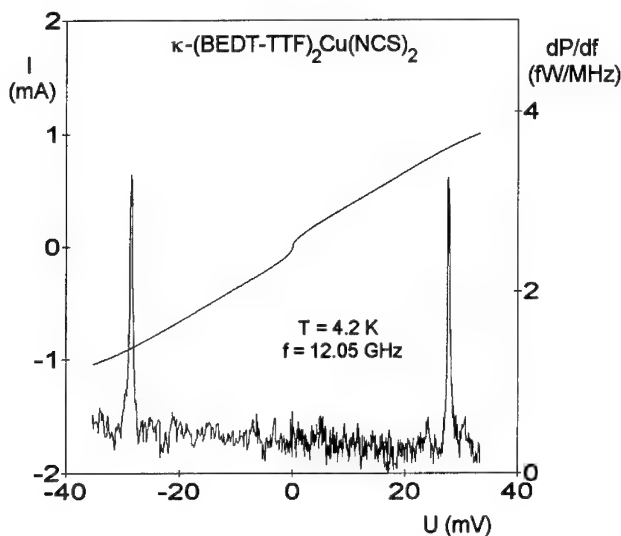


Fig. 15. I-V characteristics and microwave emission of a  $\kappa$ -(BEDT-TTF)<sub>2</sub>Cu(NCS)<sub>2</sub> single crystal. The detected frequency was 12.05 GHz. The peak corresponds to a series array of approximately 1100 junctions.

## 5. Conclusions

High- $T_c$  superconductors are Josephson junctions atomic layer by atomic layer. This hypothesis was confirmed in every detail by measurements on  $\text{Bi}_2\text{Sr}_2\text{CaCu}_2\text{O}_8$ ,  $(\text{Bi}_{1-y}\text{Pb}_y)_2\text{Sr}_2\text{CaCu}_2\text{O}_8$ ,  $\text{Tl}_2\text{Ba}_2\text{Ca}_2\text{Cu}_3\text{O}_{10}$  and  $\text{Pr}_{1.85}\text{Ce}_{0.15}\text{CuO}_4$ . From the I-V characteristics and from the temperature dependence of the critical current  $I_c$ , we conclude that the supercurrents perpendicular to the copper oxide planes flow across several thousands of superconductor-insulator-superconductor junctions. The absolute value of the c-axis critical current was 200-300 A/cm<sup>2</sup> for Ar annealed  $\text{Bi}_2\text{Sr}_2\text{CaCu}_2\text{O}_8$  single crystals. This corresponds to the maximum current density of Cooper-pair tunneling currents, as inferred from the energy gap. Therefore, these experiments are the first observation of nearly ideal tunnel junctions in high- $T_c$  superconductors. From the  $I_c$  modulations in parallel magnetic fields, the electrode distance of the junctions was deduced. The value of 15 Å agrees nicely with the distance between two  $\text{CuO}_2$  bilayers. At present, there is no observation of intrinsic Josephson effects in  $\text{YBa}_2\text{Cu}_3\text{O}_7$ .

The intrinsic Josephson effects showed up particularly clearly in the microwave absorption and emission experiments. At frequencies between 2 GHz und 95 GHz Shapiro steps were observed, which correspond to external synchronization of several hundreds of junctions. The AC Josephson currents were measured directly by their microwave emission. Even self-synchronization was observed, i.e. coherent emission with narrow linewidths and relatively high intensities. Near  $T_c$ , the incoherent emission allows the determination of the number of junctions in a crystal. At least in  $Bi_2Sr_2CaCu_2O_8$ , the intrinsic Josephson effect is not perturbed by crystal imperfections. Aside from measurement inaccuracies, every pair of  $CuO_2$  bilayers formed a Josephson junction. Similar results were obtained with the organic superconductors. This leads to the conclusion that this novel superconducting state of a periodically modulated order parameter is a genuine property of all layered superconductors with sufficiently high anisotropy. The same property of layered superconductors, which prevents high current density applications, provides a qualitatively novel application: the extremely short coherence lengths cause a modulation of superconductivity on an atomic scale.

#### Acknowledgements

The author wishes to thank K. Andres, B. Avenhaus, W. Biberacher, B. S. Chandrasekhar, R. Doll, R. Hackl, H. Hagn, G. Hechtfischer, R. Kleiner, C. Kreuzer, M. Kund, G. Kunkel, P. Pospischil, B. Schey, K. Schlenga, F. Steinmeyer, H. Veith, O. Waldmann, and W. Walkenhorst for valuable contributions to this work. Partial financial support by the Bayerische Forschungsförderung via the FORSUPRA consortium, by the Bundesministerium für Forschung und Technologie via the Josephson array consortium, and by the EU Human Capital and Mobility program is gratefully acknowledged.

#### References

1. W. Meissner, R. Ochsenfeld, *Naturwissenschaften* **21**, (1933), 787.
2. R. Doll, and M. Näbauer, *Phys. Rev. Lett.* **7**, (1961), 51.
3. B. D. Josephson, *Phys. Lett.* **1**, (1962), 251.
4. M. J. Naughton, R. C. Yu, P. K. Davies, J. E. Fisher, R. V. Chamberlin, Z. Z. Wang, T. W. Jing, N. P. Ong, P. M. Chaikin, *Phys. Rev.* **B38**, (1988), 9280.
5. P. Müller, *Advances in Solid State Physics* Vol. **34**, ed. by R. Helbig (Vieweg, Braunschweig, 1994), p. 1.
6. P. Schmitt, P. Kummeth, L. Schultz, G. Saemann-Ischenko, *Phys. Rev. Lett.* **67**, (1991), 267.
7. R. Marcon, E. Silva, R. Fastampa, M. Giura, *Phys. Rev.* **B46**, (1992), 3612.
8. A. V. Samoilov, A. A. Jurgens, N. V. Zavaritsky, *Phys. Rev.* **B46**, (1992), 6643.
9. I. Bozovic, J. N. Eckstein, M. E. Klausmeier - Brown, G. F. Virshup, *J. Superconductivity* **5**, (1992), 19.



10. R. Kleiner, *Phys. Rev.* **B50**, (1994), 6919.
11. N. Takezawa, T. Koyama, M. Tachiki, *Physica C* **207**, (1993), 231.
12. W. E. Lawrence, S. Doniach, in *Proceedings of the 12th International Conference on Low Temperature Physics*, E. Kanda ed., Academic Press, Kyoto (1971), p. 361.
13. T. Stauffer, R. Hackl, P. Müller, *Solid State Commun.* **75**, (1990), 975, and **79**, (1991), 409. T. Stauffer, R. Nemetschek, R. Hackl, P. Müller, and H. Veith, *Phys. Rev. Lett.* **68**, (1992), 1069.
14. N. Nücker, U. Eckern, J. Finck, P. Müller, *Phys. Rev.* **B44**, (1991), 7155.
15. A. Zibold, M. Dürler, A. Gaymann, H. P. Geserich, N. Nücker, V. M. Burlatov, P. Müller, *Physica C* **193**, (1992), 171.
16. F. X. Régi, J. Schneck, H. Savary, R. Mellet, P. Müller, R. Kleiner, *J. Phys. III (France)* **4**, (1994), 2249.
17. P. Müller, K. Andres, F. Groß, H. Veith, R. Hackl, *Physica C* **153-155**, (1989), 421.
18. K. Winzer, G. Kumm, P. Maaß, H. Thomas, E. Schwarzmann, A. Aghaie, F. Ladenberger *Ann. Physik (Leipzig)*, **1**, (1992), 479.
19. M. Brinkmann, H. Somnitz, H. Bach, K. Westerholt, *Physica C* **217**, (1993), 418.
20. F. Baudenbacher, K. Hirata, H. Kinder, TU München, 1991.
21. H. Müller, C.-P. Heidmann, D. Kellner, W. Biberacher, K. Andres, *Synthetic Metals* **39**, (1990), 261.
22. H. C. Montgomery, *J. Appl. Phys.* **42**, (1971), 2971.
23. R. Kleiner, F. Steinmeyer, G. Kunkel, and P. Müller, *Phys. Rev. Lett.* **68**, (1992), 2394. R. Kleiner and P. Müller, *Phys. Rev.* **B49**, (1994), 1327.
24. F. Steinmeyer, R. Kleiner, P. Müller, H. Müller, K. Winzer, *Europhys. Lett.* **25**, (1994), 459.
25. R. Kleiner, P. Müller, H. Kohlstedt, N. F. Pedersen, S. Sakai *Phys. Rev.* **B50** 1994, 3942. R. Kleiner, *Phys. Rev.* **B50**, (1994), 6919.
26. B. O. Wells, Z.-X. Shen, D. S. Dessau, W. E. Spicer, C. G. Olson, D. B. Mitzi, A. Kapitulnik, R. S. List, A. Arko, *Phys. Rev. Lett.* **65**, 3056 (1990)
27. V. Ambegaokar, A. Baratoff, *Phys. Rev. Lett.* **11**, 104 (1963).
28. F.-X. Régi, J. Schneck, J.-F. Palmier, P. Müller, and H. Savary, *to be published in Physica C*, proceedings of  $M^2S - HTSC$  IV, Grenoble (1994).
29. K. Schlenga, G. Hechtfisher, W. Walkenhorst, P. Müller, M. Veith, W. Brodtkorb, E. Steinbeiss, *these proceedings*.

# INTRINSIC JOSEPHSON JUNCTIONS IN LAYERED SUPERCONDUCTORS AS HIGH FREQUENCY SOURCES

K. SCHLENGA, G. HECHTFISCHER, W. WALKENHORST, P. MÜLLER  
*Walther-Meißner-Institut, Walther-Meißner-Str. 8  
D-85748 Garching, Germany*

and

M. VEITH, W. BRODKORB, E. STEINBEISS  
*IPHT Jena, Helmholtzweg 4, D-07702 Jena, Germany*

## ABSTRACT

We report on microwave emission experiments of  $Bi_2Sr_2CaCu_2O_{8+y}$ -single crystals at frequencies between 12 GHz and 95 GHz. Due to the intrinsic Josephson effect these samples form series connections of typically 2000 contacts. For the first time we observed phase-locking of more than 1000 junctions at 93.7 GHz in  $Bi_{1.8}Pb_{0.2}Sr_2CaCu_2O_{8+y}$  single crystals. Concerning the development of high frequency sources we report on first experiments on vertically structured thin films of  $Tl_2Ba_2Ca_2Cu_3O_{10}$ .

## 1. Introduction

The Josephson voltage-frequency relation  $f = 2eU/h$  provides the most natural tunable frequency sources. Bias voltages  $U$  from several microvolts to a few millivolts allow tuning of Josephson emission from the GHz to the THz region. In practice noise effects and source impedance mismatch decrease the emitted power considerably. Coherent emission of  $N$  junctions connected in series would increase the power by a factor of  $N$  and decrease the linewidth by  $1/N$ . Then the voltage-frequency relation is modified to

$$f = \frac{1}{N} \frac{2e}{h} U \quad (1)$$

where  $U$  is the bias voltage of the whole array.

Mutual phase lock can be achieved by especially designed networks of distributed junctions. However the geometrical size of those circuits soon exceeds the desired wavelength. Most design tricks at least reduce the tuning bandwidth of these oscillators<sup>1</sup>. This principal difficulty might be overcome by the extremely dense packed arrays of intrinsic Josephson junctions in high- $T_c$  materials. In a series of papers we were able to show the basic phenomena of this effect<sup>2-4</sup>. Due to periodic suppression of the superconducting order parameter between two  $CuO_2$  double layers every pair of  $CuO_2$  bilayers forms a Josephson junction. In case of  $Bi_2Sr_2CaCu_2O_{8+y}$  (BSCCO) and  $Tl_2Ba_2Ca_2Cu_3O_{10}$  (TBCCO) all dc- and ac- Josephson effects were found<sup>2,3</sup>. The

number of Josephson junctions in a single crystal is given by the crystal thickness divided by the interlayer distance.

Therefore a BSCCO single crystal of thickness  $1\mu\text{m}$  behaves like a series connection of 666 Josephson junctions. Junction properties can be varied by oxygen or lead substitution. Due to this ultimate packing density single crystals or thin films of BSCCO and TBCCO may find applications as high frequency sources. By appropriate structuring of single crystals or thin films these devices may be used in integrated circuits. First experiments on mesa patterned single crystals were reported recently<sup>5,6</sup>. Thin film technology provides the additional advantage of integrating coupling structures for better impedance matching. The most direct approach of analysing junction properties for high frequency sources is the radiometric investigation of ac- Josephson currents. Radiometer setups for frequencies between 10.9 GHz and 94.5 GHz give us the advantage of measuring microwave emission in a nonresonant system over one frequency decade.

## 2. Experimental

Single crystals of BSCCO and TBCCO were grown by standard methods described elsewhere<sup>3</sup>. Gold contacts were evaporated on both sides of the crystals followed by annealing in flowing Argon or Oxygen at  $550^\circ\text{C}$ . Typical crystal dimensions were  $30 \times 30\ \mu\text{m}^2$  in ab-direction and about  $3\ \mu\text{m}$  in c-direction. A two terminal technique was used for transport measurements with current flow perpendicular to the layers<sup>3</sup>. Thin films of  $\text{Ti}_2\text{Ba}_2\text{Ca}_2\text{Cu}_3\text{O}_{10}$  were deposited on (001)  $\text{LaAlO}_3$  substrates with ion etched step edges (fig. 1). These steps had slopes between  $60^\circ$  and  $75^\circ$  and heights between 400 nm and 500 nm. A precursor -  $\text{TlO}_x$  post anneal technique was used. The film thickness was between 250 nm and 450 nm. The height of the junction stack (step stack) is determined by the difference between step height and film thickness. Details of thin film preparation are reported in<sup>7</sup>.

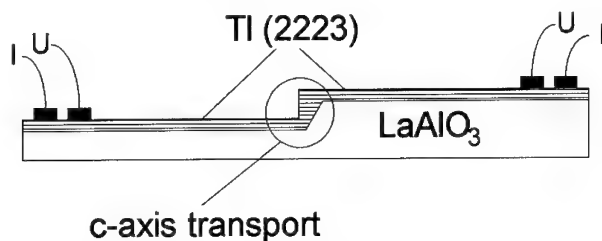


Fig. 1. Sketch of the vertically structured TBCCO thin films. In the marked region current flow is perpendicular to the layers.

At the steps microbridges were patterned by ion beam etching or laser patterning. The junction width varied between  $3\ \mu\text{m}$  and  $24\ \mu\text{m}$ . Current-voltage (I-V) characteristic was measured with a four lead technique. Electrical contacts were made by indium pressure contacts. For all measurements low pass filters in the bias leads were

used to shield external noise. The midpoint of the resistive transition was observed at  $T = 115$  K. Due to thermally activated phase slippage a broad foot structure was present. Zero resistance was reached at  $T = 93$  K. In order to prevent the nonlinear Josephson oscillators from locking to any resonances of impedance matching circuits we prefer emission into free space followed by broadband superheterodyne detection. Samples were mounted in front of a horn antenna. Three highly sensitive radiometers were used. Frequency bands were:

1. 10.9 – 12.3 GHz, noise temperature  $T_n = 60$  K
2. 24.15 – 24.25 GHz,  $T_n = 440$  K
3. 93.0 – 94.5 GHz,  $T_n = 630$  K.

The radiometer power was monitored as a function of bias voltage at fixed frequencies and various bandwidths. Measurement performance is shown in fig. 2. The sample is an  $YBa_2Cu_3O_{7-x}$  biepitaxial grain boundary junction<sup>8</sup>. Note that the decoupling of source and receiver had to be paid by a considerable loss of intensity.

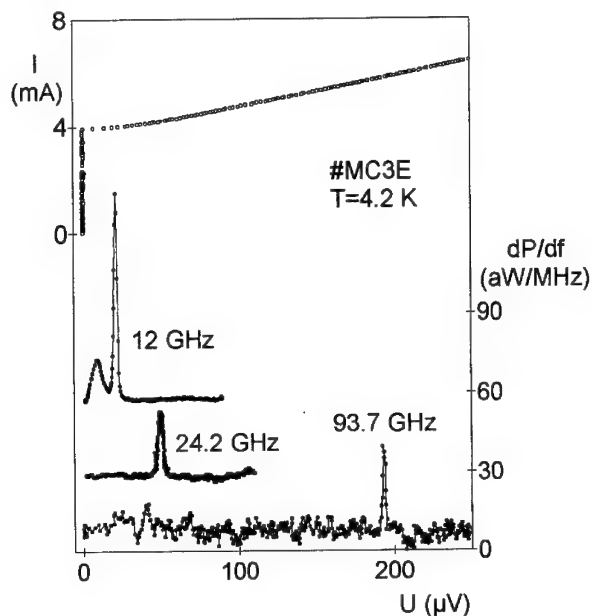


Fig. 2.  $I$ - $V$  characteristic of an  $YBa_2Cu_3O_{7-x}$  biepitaxial junction (left scale) and microwave power at three different detection frequencies (right scale). The zero of the three emission measurements is offset by 30 aW/MHz each. Note the second harmonic at the lowest frequency.

### 3. Results

A current-voltage curve is shown in fig. 3. The sample was an oxygen annealed  $Bi_{1.8}Pb_{0.2}Sr_2CaCu_2O_{8+y}$  single crystal. The I-V characteristic is strongly hysteretic. The large number of branches is omitted for clarity (cf. figs. 4 and 5). When a bias current of 7 mA is exceeded main part of the crystal switches to the resistive state. By further increasing current a second packet switches to the resistive state accompanied by a broad radiometer signal at a detection frequency of 24.2 GHz. The two sharp symmetric peaks are detected while decreasing bias current in the nearly vertical range of the I-V curve.

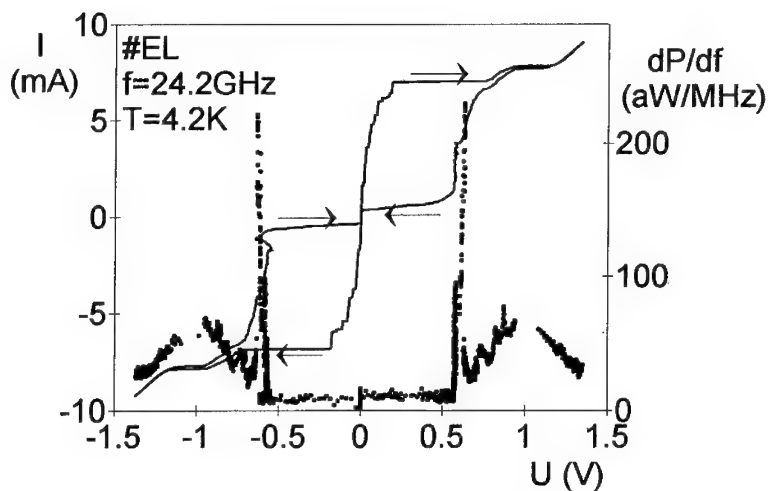


Fig. 3. Typical I-V characteristic of an oxygen annealed  $Bi_{1.8}Pb_{0.2}Sr_2CaCu_2O_{8+y}$  single crystal (left scale) and detected microwave power at  $f = 24.2$  GHz (right scale). The curves are corrected for contact resistance.

Fig. 4 shows the I-V characteristic of a  $Bi_{1.8}Pb_{0.2}Sr_2CaCu_2O_{8+y}$  single crystal. Some branches are traced out here. Radiometer detection frequency was  $f = 93.7$  GHz with a bandwidth of 500 MHz.

By decreasing the bias current, on the outermost branch where all junctions are in the resistive state, a very narrow signal can be detected. Here, the linewidth of the radiometer signal is determined only by the radiometer bandwidth. As can be seen in the spread of critical currents, linewidth of incoherent emission would be expected to be much larger. This strongly indicates phase locking of radiating junctions. Using voltage-frequency relation (1) we derive a number of  $N = 1200$  junctions. Such a large array should have a theoretical linewidth of approximately 100 kHz in the locked state<sup>1</sup>. The I-V curves of  $Tl_2Ba_2Ca_2Cu_3O_{10}$  thin film devices showed the characteristic of a Josephson junction stack as well known from c-axis

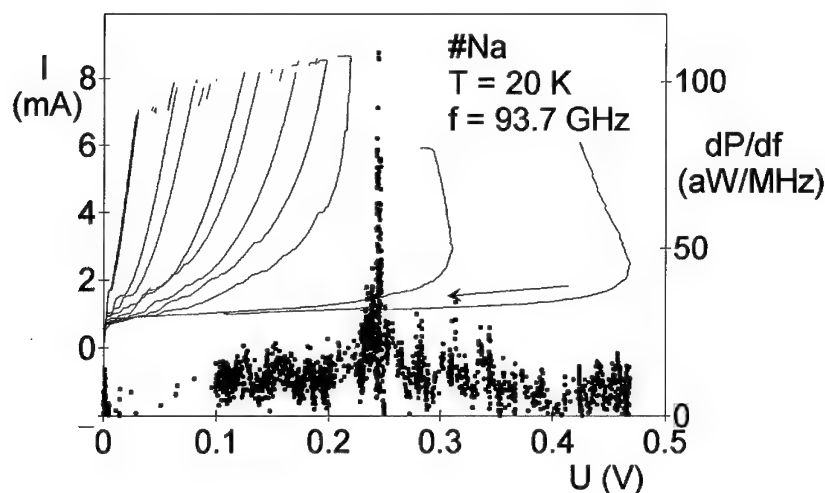


Fig. 4. I-V characteristic of an oxygen annealed  $Bi_{1.8}Pb_{0.2}Sr_2CaCu_2O_{8+y}$  single crystal (left scale). The contact resistance is subtracted. The narrow linewidth of detected microwave signal at  $f = 93.7$  GHz indicates phase locking (right scale).

transport in single crystals described before. The characteristic voltage  $V_c$  reaches values up to 26 mV. Using the Ambegaokar-Baratoff relation a gap value  $2\Delta(0)$  of 33.2 meV is derived in good agreement with the BCS value  $2\Delta(0) = 3.5 k_B T_c$ ,  $k_B$  is Boltzmann's constant. In case of sample #40a1 we recorded 130 branches in the I-V characteristic (fig. 5). The stack height was about 230 nm. By dividing this height by the interlayer distance of 17.8 Å we derive a number of 130 junctions. So we succeeded in observing all junctions in the stack. The junction area varies due to the slope at the step (cf. fig. 1). This fact is mirrored in the continuously increasing critical currents. With increasing number of junctions in the resistive state the characteristic voltage  $V_c$  decreases monotonously from 26 mV down to 5 mV. This is caused by gap suppression due to quasiparticle injection and maybe simple heating effect. The microwave emission of these thin films was observed up to  $T = 93$  K. A broad radiation peak at  $T = 90$  K is shown in fig. 6. The voltage at peak maximum indicates a number of 165 junctions. A comparison with the stack height of 300 nm shows that all intrinsic junctions in the stack radiate incoherently. This observation conforms with previous results in BSCCO single crystals.

Fig. 7 shows the I-V characteristic of a Tl (2223) thin film at  $T = 4.2$  K. Microwave emission was detected at 11.3 GHz and 24.2 GHz. Peaks at  $\pm 156 \mu V$  (11.3 GHz) and  $\pm 332 \mu V$  (24.2 GHz) result from simultaneous emission of 6 junctions.

This was confirmed at different detection frequencies in the range from 10.95 GHz to 11.62 GHz as shown in fig. 8.

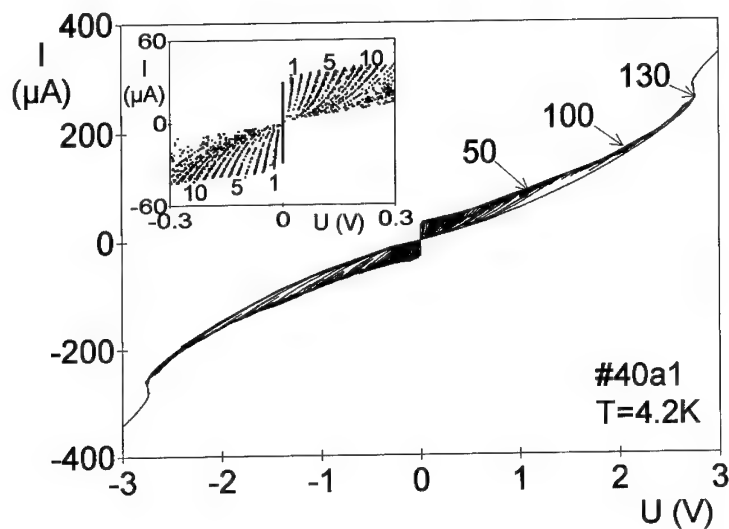


Fig. 5. I-V characteristic of a Tl (2223) step stack. The stack of 230 nm height contains 130 intrinsic Josephson junctions of thickness 17.8 Å each. The inset shows the first branches of the curve on a larger scale.

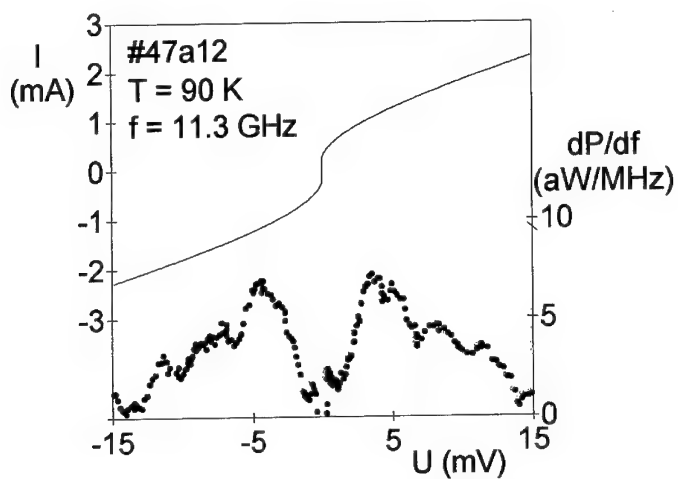


Fig. 6. Overdamped I-V characteristic of a Tl (2223) thin film at  $T = 90$  K (left scale) and detected microwave power at  $f = 11.3$  GHz (right scale). The voltage at peak maximum corresponds to incoherent emission of  $N = 165$  junctions.

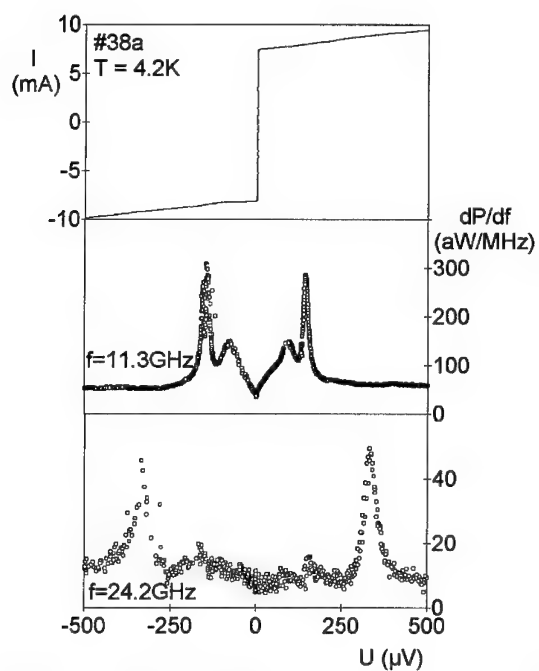


Fig. 7. I-V characteristic of a Tl (2223) thin film step stack at  $T = 4.2\text{ K}$  (upper panel), detected microwave power at  $f = 11.3\text{ GHz}$  (middle panel) and detected microwave power at  $f = 24.2\text{ GHz}$  (lower panel).

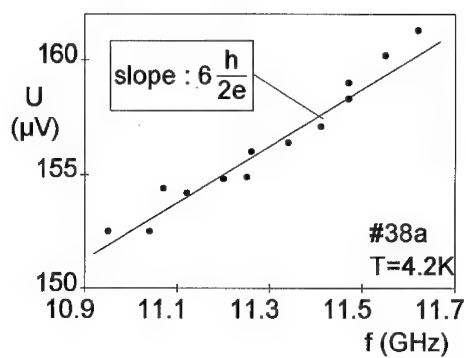


Fig. 8. Voltage at peak maximum vs. frequency. The solid line denotes the slope of the voltage shift for 6 junctions



With increasing detection frequency the peak position shifts towards higher voltages with a slope as determined from voltage frequency relation (1) with  $N = 6$ .

#### 4. Conclusions

By nonresonant detection up to 95 GHz we were able to observe microwave emission of intrinsic Josephson junctions over one whole frequency decade. The narrow emission linewidth of sample # Na (fig. 4) gives evidence for the observation of phase-locking at 93.7 GHz. For the first time, thin films of TBCCO could be structured with appropriate length scales to observe intrinsic Josephson effects with current transport perpendicular to the  $\text{CuO}_2$  layers. Thin film technology will provide the possibility to fabricate intrinsic Josephson stacks with a very small parameter spread. In these step stacks, we were able to detect microwave emission from 6 intrinsic Josephson junctions over more than one octave in frequency.

#### Acknowledgements

The authors would like to acknowledge financial support by the EU Human Capital and Mobility Program and the Bundesministerium für Forschung und Technologie.

#### References

1. A. K. Jain, K. K. Likharev, J. E. Lukens, and J. E. Sauvageau, *Mutual phase-locking in Josephson junction arrays*, *Phys. Rep.* **109**, (1984), 309.
2. R. Kleiner, F. Steinmeyer, G. Kunkel, and P. Müller, *Phys. Rev. Lett.* **68**, (1992), 2394.
3. R. Kleiner and P. Müller, *Phys. Rev.* **B 49**, (1994), 1327.
4. K. Schlenga et al., *to be published in Physica C*, Proc. of  $M^2S - HTSC$  IV, Grenoble (1994).
5. A. Yurgens, D. Winkler, Y. M. Zhang, N. Zavaritsky, and T. Claeson, *to be published in Physica C*, Proc. of  $M^2S - HTSC$  IV, Grenoble (1994).
6. F.-X. Régi, J. Schneck, J.-F. Palmier, P. Müller, and H. Savary, *to be published in Physica C*, Proc. of  $M^2S - HTSC$  IV, Grenoble (1994).
7. M. Veith et al., these proceedings.
8. M. Seitz et al., Proc. of EUCAS 93, 1359.

# INTRINSIC THIN FILM TI - Ba - Ca - Cu - O STEP STACK JOSEPHSON JUNCTIONS

M. VEITH, T. EICK, W. MORGENROTH, W. BRODKORB,  
T. KÖHLER, L. REDLICH, H.-G. SCHMIDT, E. STEINBEISS  
*Institut für Physikalische Hochtechnologie (IPHT) Jena*  
*D - 07743 Jena, Helmholtzweg 4, Germany*

and

H.-J. FUCHS

*Institut für Angewandte Physik, Friedrich-Schiller-University Jena, Max-Wien-Platz 1, D-07743 Jena*

and

K. SCHLENGA, P. MÜLLER

*Walther-Meißner-Institut, D-85748 Garching, Germany*

## ABSTRACT

For the first time we observed intrinsic Josephson effect for current flow perpendicular to the  $\text{CuO}_2$  - planes in HTC thin films. TI-Ba-Ca-Cu-O thin films have been deposited on step edge  $\text{LaAlO}_3$  substrates. Due to the special preparation process, microbridges across such steps act as stacks of intrinsic Josephson Junctions with current flow perpendicular to the  $\text{CuO}_2$  - planes (STEP STACK JUNCTION). Up to 130 individual junctions could be observed exhibiting high  $I_c R_N$  products up to 30 mV. Phase locked microwave emission peaks of substacks as well as broad emission of the whole stack could be detected for frequencies of 11 GHz and 24 GHz.

## 1. Introduction

High temperature superconductors of the Bi- and Tl- system exhibit a strong anisotropy of their superconducting parameters. Reason for this is the layered crystal structure of these substances. The superconducting  $\text{CuO}_2$  - planes are separated by relatively thick layers of the other metal compounds and therefore relatively weak coupled. Single crystal samples should therefore behave as a stack of intrinsic Josephson Junctions as could be observed by Kleiner and Müller<sup>1</sup>. Here the  $\text{CuO}_2$ -planes act as superconducting electrodes, the interlayers as tunnel barriers. Due to the technological fortune of applications of such Josephson contact types, a great progress would arise from transferring the basic single crystal experiments to thin film technology. Thin film samples would offer easier handling, standardizeable sample preparation and especially the possibility to integrate such junctions into cryoelectronic devices.

This motivated us to realize such intrinsic stacks in thin films approaching the pro-

blem by making use of the special growth behaviour of Tl-Ba-Ca-Cu-O thin films across step edge substrates.

## 2. Sample Preparation

Tl-Ba-Ca-Cu-O thin films were deposited on  $\text{LaAlO}_3$  substrates by a two step process established in our institute by Manzel and Bruchlos already described in detail elsewhere<sup>2</sup>. In a first stage, an amorphous precursor is deposited by high rate sputtering. The Ba : Ca : Cu - cation composition of the target is that of the later desired superconductor film phase, e.g. 2:2:3 for the Tl(2223) compound, hence at high rates and optimum  $\text{Ar}/\text{O}_2$  - pressure there is a 1:1 transfer from target to substrate. This precursor is then annealed at temperatures of  $860^\circ\text{C}$  to  $880^\circ\text{C}$  in a sealed furnace in  $\text{TlO}_x$  containing atmosphere, allowing the Thallium to incorporate and the film to build up the TBCCO - structure. Essential for pure phased films with low surface roughness, sharp  $\chi(T)$  - transition and high  $I_c$  is not only a short annealing time at the appropriate temperature for the desired phase but also a slow, controlled cool down with a rate of 1 K/min.

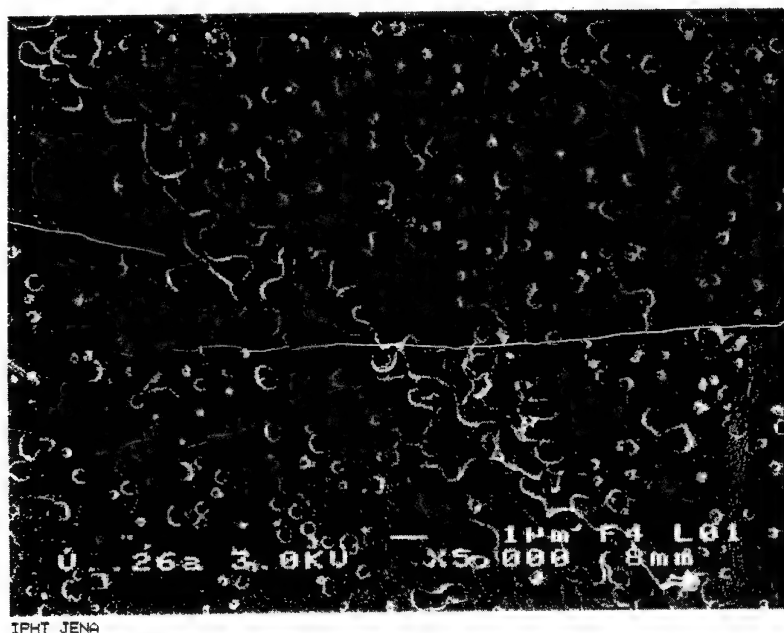


Fig. 1. SEM top view of a TBCCO thin film on a step edge  $\text{LaAlO}_3$  substrate ( step slope  $30^\circ$  )

In this work most samples were prepared as Tl(2212) phase, hence this offers a wider annealing temperature range and therefore greater chances for optimizing film quality. Furthermore, the annealing temperature is lower than that of the Tl(2223) phase, and therefore not as close to the melting point of the HTC-film – crucial especially for very thin films necessary for this work. Samples were successfully deposited on either MgO, SrTiO<sub>3</sub> and LaAlO<sub>3</sub> – substrates with equal quality. In SEM - surveys (fig. 1), one can see the films to consist of intergrown grains with diameters between 10  $\mu\text{m}$  and 100  $\mu\text{m}$ . XRD analysis reveals that the films are single phased Tl(2212). Pole figures even of samples deposited on substrates with a vicinal face of 5° show that almost all the grains are not only perfectly oriented in  $c$  – direction but also in the  $a$  – direction. Superconducting films could be prepared down to 200 nm film height. The  $T_c$  derived from  $\chi(T)$  - measurements is typically 100 K, with  $\Delta T_c = 1\text{K}$ . Nevertheless, there is a slight decrease of  $T_c$  for very thin films down to 95 K.

It could be observed that the double textured coarse grained structure of these TBC-CO films results in an overgrowth across substrate steps without changes in orientation. Obviously, to have any current flow across stacks at the step edge in  $c$  – direction, the substrate step has to be higher than or at least as high as the film thickness. As discussed above, the film height could not be reduced to less than 200 nm. Thin films of reproducible quality have heights of 250 nm to 300 nm. Therefore the substrate step has to be at least 400 nm high. To achieve the desired perpendicular stacks of TBCCO layers with current flow only parallel to the  $c$  – direction, the slope angle of the substrate step has to be as steep as possible. For small slope angles flux flow effects will wipe out any intrinsic Josephson effect. Our experiments show, that a slope angle of greater than 60° is required. For preparation of Josephson Junctions, step edges were patterned into (100)LaAlO<sub>3</sub> - substrates by ion beam etching with Cr- or Ti- metal masks. AFM and SEM surveys reveal that these steps had heights of 400 to 500 nm and slope angles between 60° and 75°.

After film deposition, microbridges were patterned into the samples across the step. As the boundary between two grains may be the source for some kind of misfit which ought to be avoided especially on the microbridge area, these have to be kept as small as possible. In our case the bridge length is only 24  $\mu\text{m}$ . Patterning was performed either by dry etching in Argon (bridge widths 3, 6, 12 and 24  $\mu\text{m}$ ) or by laser beam patterning (bridge width  $\geq 6 \mu\text{m}$ ). It furthermore turned out, that microbridges with effective widths larger than 12  $\mu\text{m}$  not only showed too high  $I_c$ , but also include possible low resistive grain boundary junction effects. Laser patterning was also used to narrow dry etched bridges which exhibited too high  $I_c$  and therefore did not act as Josephson Junctions.

### 3. Results

#### 3.1. Current – Voltage Characteristics

I-V-curves of these step stack junctions reveal very high  $I_c$  values up to 8 mA and also  $R_N$  values up to 1.5 k $\Omega$  (on different samples). The observed maximum  $I_c R_N$  was 27 mV. Principally, two types of I-V-curves could be distinguished. One class of samples exhibit a RSJ – like curve which is nonhysteretic, as shown in figure 5. Other samples displayed a strong hysteresis and furthermore also characteristic voltage jumps of some 10 millivolts in the resistive branch of the curve. By carefully tuning the current, we could resolve many branches as plotted in figure 2. In this sample (V40a1) 130 of these branches could be counted. These have regular, but nevertheless decreasing voltage distances ranging from 26 mV for the first jump down to 5 mV. The I-V-curve ends with a typical quasiparticle injection shape already observed at intrinsic single crystal junctions<sup>1</sup>.

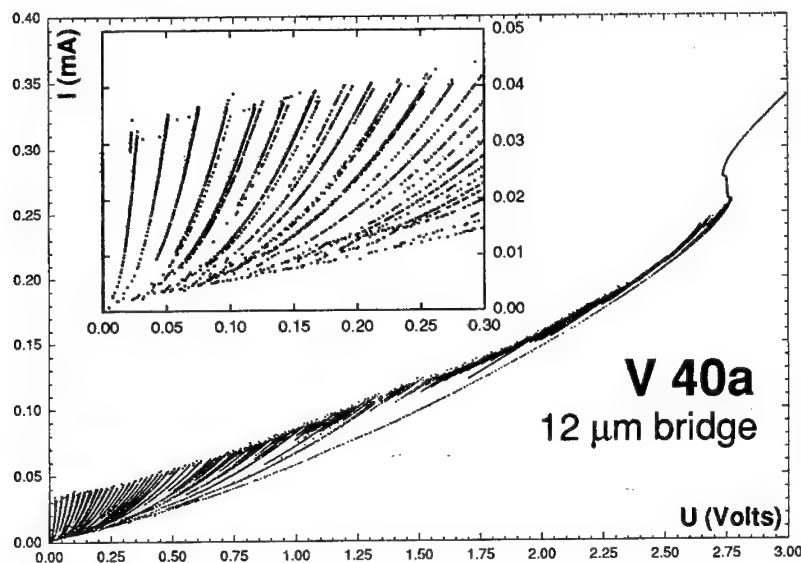


Fig. 2. I-V characteristic of a step stack junction with 130 uniform branches  
The insert is a zoom on the first 13 branches.

We associate each of these branches with the switching of a single intrinsic junction to the resistive state. As described above and sketched in figure 3, the height of the superconducting film is lower than that of the substrate step.

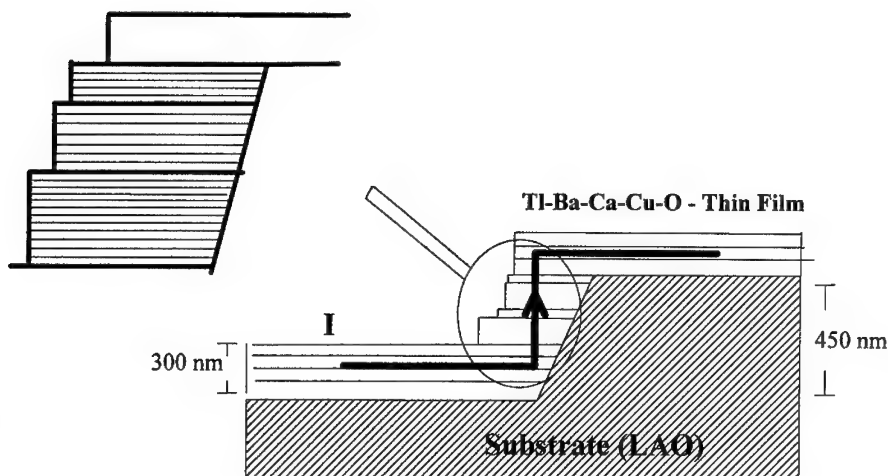


Fig. 3. Model of step stack film growth across a substrate step and current flow

As a consequence of the special two step formation process we expect that a perpendicular stack will build up along the substrate step. This could preferably be uniform in dimensions but might probably consist of some substacks of slightly different heights and cross sections. Such substeps could be observed in SEM topviews (fig. 4).

As the slope of the substrate step is less than  $90^\circ$  ( typically  $60^\circ$  ) but the open front of the stack appears almost perpendicular in SEM surveys, the area of the intrinsic layers will increase from the bottom of the stack to the top. We ascribe this as a reason for the relatively wide voltage spread of the branches.

As one confirmation for our model one can perform a simple comparison: For sample V40a1 the film height was 280 nm at a substrate step of 500 nm. From preparation parameters we expect a step stack height of 220 nm. On the other hand, multiplying the number of observed branches (130) with the spacing between the intrinsic  $\text{CuO}_2$  - planes of 1.78 nm for the TBCCO(2223), one ends up with 230 nm. We therefore believe to have observed *all* intrinsic junctions in this stack, one after the other switching to the resistive state.

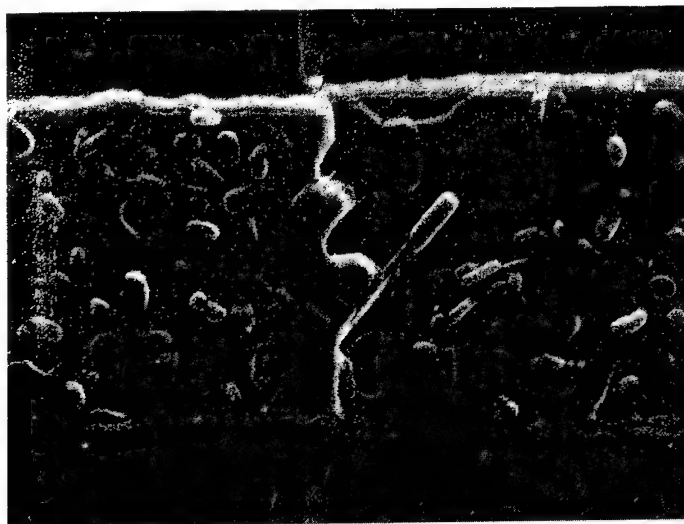


Fig. 4. SEM top view of a TBCCO step stack junction on a  $\text{LaAlO}_3$  substrate ( bridge width  $6\mu\text{m}$  )

### 3.2. Microwave Emission

The observed voltage jumps for a single junction of a stack are as in sample V40a1 between 5 and 25 mV. According to the Josephson frequency – voltage relation:

$$F = \frac{2e}{h}U \quad (1)$$

emitted microwave would be at frequencies in the THz range. For such samples, radiation at lower frequencies (GHz range) would only be expected at temperatures very close to  $T_c$ , where the energy gap is strongly suppressed or for intrinsically shunted arrays. The radiometers used detect the microwave power emitted into free space at frequencies of 11 GHz and 24 GHz. The sample is mounted in front of a horn antenna as described elsewhere in detail<sup>3</sup>.

Nevertheless, for a number of our samples microwave radiation could be detected in the 11 GHz range even at low temperatures. On one sample, we observed two wide peaks with maxima at 1.9 mV and 2.9 mV due to many contacts (60 or 100) emitting incoherently. At higher temperatures (90 K) the spectrum has a broad peak with a maximum corresponding to 160 emitting junctions (i.e. virtually all in this stack)<sup>3</sup>. More interesting is the sample shown in figure 5 (V38a).

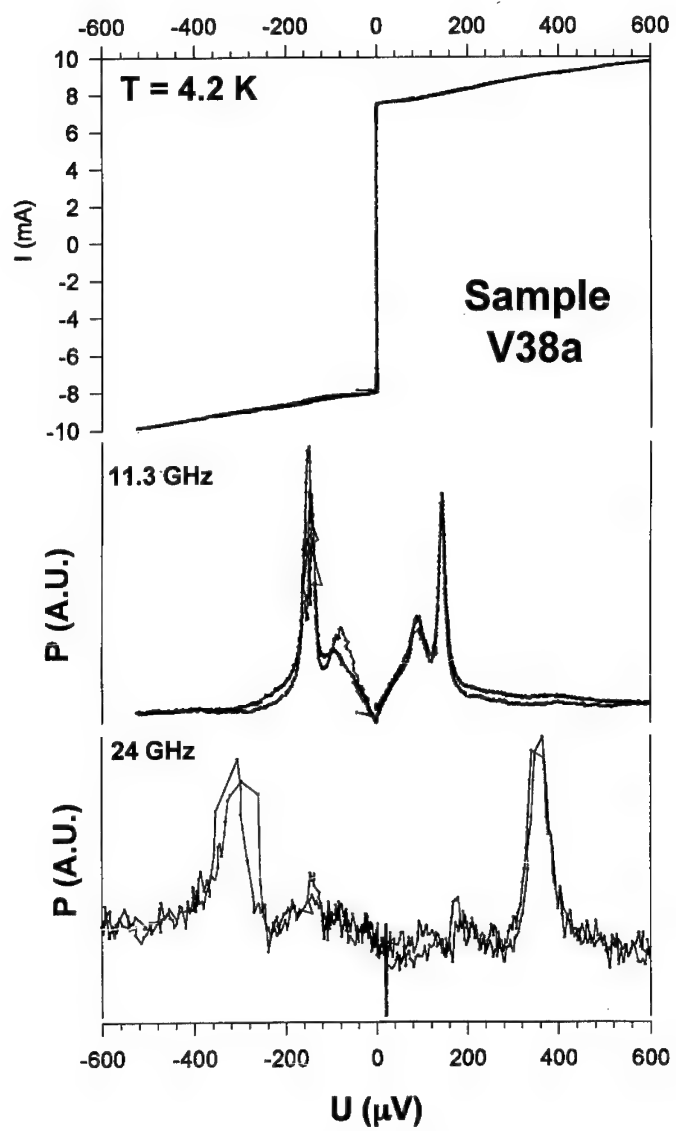


Fig. 5. I-V characteristics of sample V38a (top) , detected microwave power at  $F = 11.3 \text{ GHz}$  (middle) and  $F = 24.2 \text{ GHz}$  (bottom)



At 11.3 GHz detector frequency, we register two sharp peaks at  $100\mu\text{V}$  and  $155\mu\text{V}$ . The second peak could also be detected at 24.2 GHz at  $332\mu\text{V}$ . For  $N$  junctions in series (1) changes to:

$$U = NF \frac{h}{2e} \quad (2)$$

This therefore gives almost exactly 4 junctions for the lower peak and 6 junctions radiating synchronized for the second peak. As expected with increasing number of junctions, the peak width decreases. The number of emitting junctions was also determined by observing the shift of the voltage peak as a function of changing the detector frequency as discussed by Schlenga<sup>3</sup>.

Source of this radiation is to our opinion a relatively uniform substack. Additional intrinsic high Ohmic shunting could explain the low frequency.

#### 4. Conclusion

By making use of the special growth behaviour of a two step preparation process of TBCCO thin films deposited across a step edge substrate we succeeded in developing stacks of up to 130 intrinsic Josephson Junctions (step stack junctions). For some samples, we were able to detect synchronized microwave emission for 6 junctions at different frequencies.

#### Acknowledgements

This work was supported by the German BMFT under grant 13N6131

#### References

1. R. Kleiner and P. Müller, *Phys. Rev. B* 49 (1994) 1327
2. M. Manzel et al., *phys. stat. sol. (a)* 128 (1991) 175  
M. Manzel et al., *Physica C* 201 (1992) 337
3. K. Schlenga et al. *this conference*

---

Chapter 7

## **Junction Arrays**

## DYNAMICS OF CLASSICAL TWO-DIMENSIONAL JOSEPHSON ARRAYS

MIGUEL OCTAVIO

*Centro de Física, Instituto Venezolano de Investigaciones Científicas, Apartado 21827,  
Caracas 1020A, Venezuela.*

### ABSTRACT

We review the basic properties of two-dimensional arrays of classical Josephson junctions both in the absence and in the presence of an applied magnetic field. When no field is present, the properties of the system do not differ significantly from those of a single junction. For applied fields that are commensurate with the network such that the flux per plaquette is  $f = p/q$ , where  $p$  and  $q$  are integers, the ground state of the system is formed by a superlattice of  $q \times q$  cells which contain vortices. The presence of this vortex superlattice modifies both the dc and rf properties of the system. In the presence of an rf drive, Giant Shapiro steps are observed at  $Nh\nu/2e$ , where  $N$  is the number of junctions in the array in the direction of the dc current. More surprisingly, additional fractional-Giant Shapiro steps appear at voltages  $(N/q)h\nu/2e$  for each value of  $f = p/q$ . These fractional steps arise from the synchronization of the drive to the motion of the superlattice. For underdamped junctions, we find that the I-V characteristics are unusual. As  $\beta_c$  is increased the I-V characteristics have two very distinct regimes. At low voltages, the dynamics are dominated by the motion of the vortex superlattice, while at high voltages they are dominated by the oscillations of the junctions. To understand these regimes, we construct a mechanical analog. The mechanical analog of a massive particle moving in a two-dimensional potential allows for the understanding of the dynamics of the system and clearly shows how the novel dynamics arise from the additional degree of freedom.

### 1. Introduction

Two-dimensional Josephson junctions arrays are good model systems for the study of the thermodynamic properties of excitations in two-dimensional systems. The ability to tailor the properties of these arrays when they are microfabricated has allowed for the study of the Kosterlitz-Thouless vortex-unbinding transition and the effects of frustration and disorder on this transition<sup>1</sup>. In these studies, what is of interest is the near equilibrium properties or thermodynamic properties which take place with only a small current flowing through the system. A completely different regime occurs at large currents, when the current flowing through the array is comparable with the critical current of the Josephson array. In this regime, each of the junctions in the system behaves like a non-linear oscillator. If this nonlinear collection of oscillators is coupled through the application of a magnetic field, the arrays turn out to exhibit a rich variety of new nonlinear phenomena associated now with the motion of a vortex superlattice for fields commensurate with the basic structure of the lattice of

junctions. Furthermore, this collection of oscillators may under certain circumstances oscillate coherently which is of considerable interest for applications.

In this paper, we review what has been learned about the dynamical properties of two-dimensional Josephson arrays. First, we briefly introduce those basic thermodynamic properties which are important to understanding these dynamics. We then discuss how arrays can exhibit giant and fractional giant steps when they are irradiated with ac radiation and how this behavior originates in the motion of the vortex superlattice for commensurate magnetic fields. We also show how these ideas are confirmed experimentally by changing the direction of current injection into the arrays. We also study in detail the effects of capacitance on the dynamic properties of the arrays. In this case, the arrays can become chaotic and exhibit two different regimes depending on whether the vortex superlattice (flux-flow) or the junctions dominate the dynamics. Finally, we briefly discuss the possible use of arrays as radiation sources.

## 2. Basic Array Properties

A two-dimensional square array of Josephson junctions is shown in Fig. 1. The array has lattice constant  $a$  and junctions are located at each vertical and horizontal

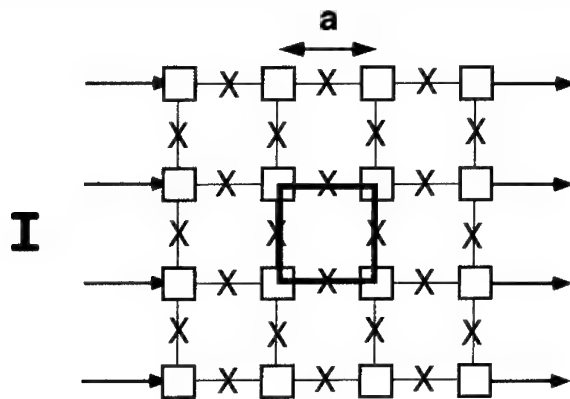


Fig. 1. Schematic diagram of a square array. The crosses indicate the junctions and  $a$  is the lattice size.

bond. The array is  $M \times N$  where  $M$  is the number of rows of junctions and  $N$  is the number of columns. Junctions are connected to superconducting islands at each node of the array. The array is biased by a current  $I = Mi$  as shown in the figure. The basic unit cell of the array going around the connected paths is called a plaquette.

In the absence of a magnetic field and at  $T = 0$ , assuming there are no inductive effects and the array is perfectly uniform (that is we neglect the disorder present in real arrays) any current fed into the array will flow uniformly from one side of the

array to the other, with no current flow occurring in the vertical junctions. Then, the total voltage drop across the array will simply be  $V = NV_i$ , where  $V_i$  is the voltage across each individual junction. However, this system of nonlinear elements may have more complicated solutions, since in the presence of a voltage each junction's phase will oscillate in time and the solutions will not necessarily be stable. While this problem of stability is interesting in its own right, what makes arrays so novel is the variety of new phenomena that may be observed whenever thermal effects or magnetic effects are present. As discussed below, in both of these cases vortices may occur in the system leading to novel dynamical properties.

While in the absence of a field and at  $T = 0$  the existence of a vortex will not be energetically favored, in the presence of a field the physics of the system changes completely. First of all, the system is a multiply connected superconductor so that fluxoid quantization imposes a constraint on the possible values that the gauge invariant phase  $\gamma$  can have around any loop in the array, so that

$$\sum_{\text{plaquette}} \gamma_i = \frac{2\pi}{\Phi_0} (\text{mod } 2\pi) = 2\pi f (\text{mod } 2\pi) = 2\pi(f - n). \quad (1)$$

where  $f = Ba^2/\Phi_0$  is called the frustration index,  $B$  is the applied magnetic field,  $n$  is an integer and  $a$  is the lattice constant. While the magnetic field imposes a constraint on the system, the value of  $n$  will be that which minimizes the free energy of the system. If we neglect capacitive effects as is the case for overdamped arrays, the Hamiltonian of the array is given by

$$\mathbf{H} = - \sum_{\langle ij \rangle} E_j \cos(\phi_j - \phi_i - \frac{2\pi}{\Phi_0} \int_i^j \mathbf{A} \cdot d\mathbf{r}) \quad (2)$$

where  $E_j$  is the Josephson coupling energy, the sum is over nearest neighbors only and  $i$  and  $j$  are the indices of two islands. Note that this Hamiltonian is just like that of the  $XY$  model for a system of spins in two dimensions.

Minimization of the Hamiltonian of Eq. 2, shows that in the absence of a field the energy is minimized by having all phases be equal to each other. In contrast, if a field is present minimization of the energy favors the presence of vortices in the system in which the phases change by  $2\pi$  as one goes around any closed loop of the system. These phase differences in the system will induce circulating currents forming a whirlpool of current. This vortex, in contrast to that found in superconductors, has no normal core in the center.

The phase diagram for an array as a function of temperature and phase can be quite complicated as shown in the schematic of Fig. 2. When  $f = 0$  and  $I = 0$ , the system exhibits a vortex binding phase-transition at  $T_{KT}$ . Above this temperature free vortices and anti-vortices are present in the system. Below  $T_{KT}$  these vortices bind together and form pairs. The introduction of a current in the system will unbind these pairs and in general will induce vortex flow. What is of interest from the point of view of dynamics is what happens for certain applied magnetic fields at  $T = 0$ , shown as solid lines in Fig. 2.

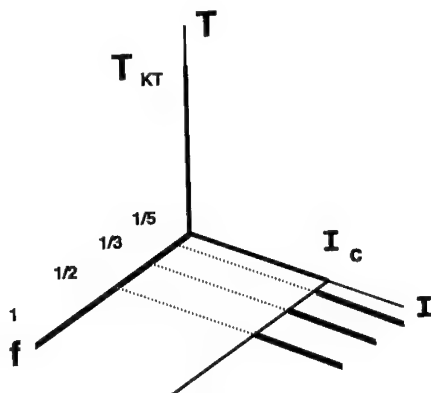


Fig. 2. Phase diagram in the temperature, current, and frustration space.

Whenever the applied field is such that the frustration index  $f = p/q$ , the ground state configuration of the system consists of a superlattice of vortices with a basic unit cell of size  $q \times q$  as shown in Fig. 3. This superlattice will move if a current is present and is quite rigid, that is the current flowing through the array has to be sufficiently large to move the whole superlattice.

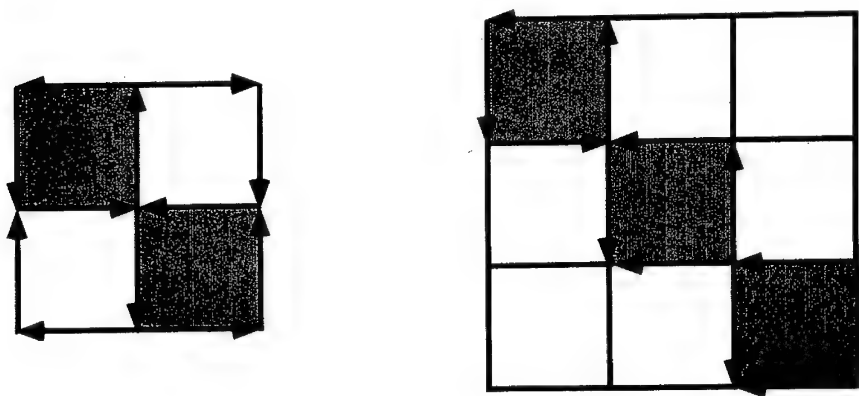


Fig. 3. Ground state configuration for  $f = 1/2$  (left) and  $f = 1/3$  (right).

### 3. rf Response of Arrays

#### 3.1. Giant Shapiro Steps

If an array in zero magnetic field is rf biased at  $T = 0$ , the system will respond just like a single junction with applied current  $I_{ext}/N$ . Since voltages in series add, the total voltage drop across the array will be  $N$  times the Josephson voltage of each junction. Then if the individual junctions synchronize to an external rf drive with frequency  $\nu$ , this will lead to so-called giant Shapiro steps at voltages

$$V = N \frac{n h \nu}{2e} \quad (3)$$

as shown in Fig. 4 taken from Sohn et al. <sup>2</sup>, where the dynamic resistance  $dV/dI$  as a function of the voltage is presented for various values of  $f$ . In the  $dV/dI$  plot the minima in the dynamic resistance correspond to each step. Giant Shapiro steps were first observed in SNS arrays of Pb-Cu-Pb junctions by Leeman et al <sup>3</sup>. Similar results have been observed in various types of arrays (Lee et al <sup>4</sup> and Hebboul and Garland <sup>5</sup>).

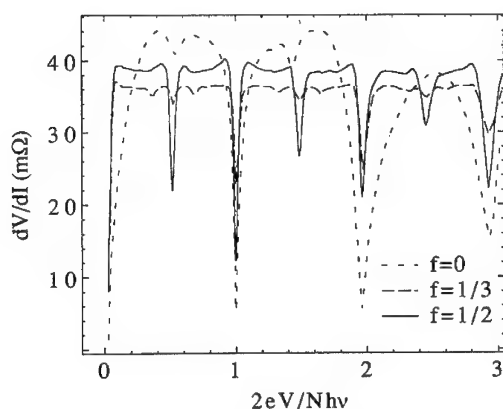


Fig. 4. Dynamic resistance as a function of the normalize voltage for various  $f$  values.

While giant Shapiro steps are expected from Eq. 3, one should not lose sight of the fact that this was obtained assuming that all junctions were identical and currents distributed themselves uniformly across the array. It is yet unclear whether their observation in real, disordered, microfabricated arrays implies that the coupling of the junctions in the planar array in some way stabilizes this solution or whether what is observed reflects the intrinsic disorder of the array.

If the description given by Eq. 3 were all that was required to understand these arrays in zero field, giant Shapiro step widths should be very much like those of single

junctions both in their frequency and power dependence. However, simulations<sup>6</sup> show this not to be the case as shown in Fig 5. In contrast to the behavior seen in single junctions, the power dependence of the rf induced steps does not decrease monotonically but may show anomalies such as the progressive reduction of the second lobe in the power dependence as the frequency is increased. These anomalies are a result of the higher degree of freedom of the system and may be understood in simple terms as shown later in the paper.

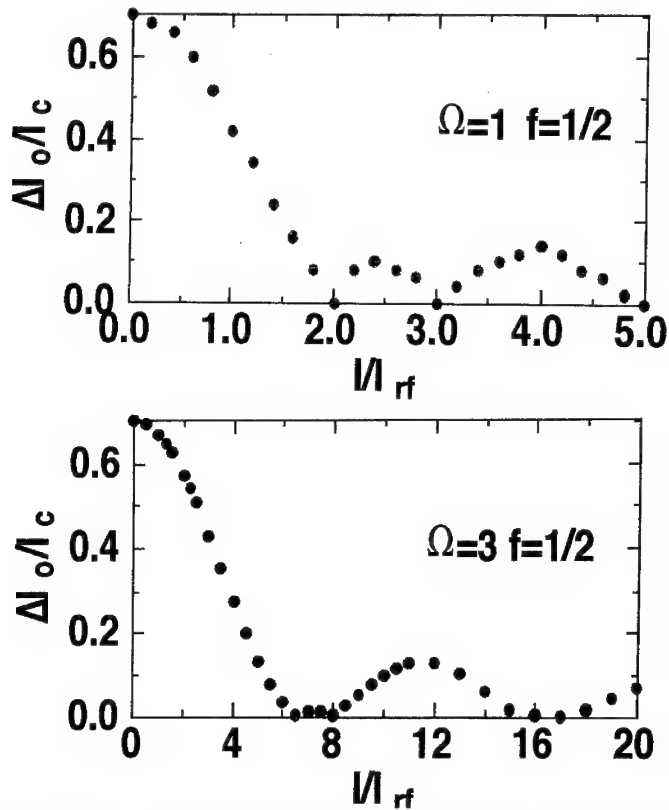


Fig. 5. Step widths for the critical current for  $f = 1/2$  and  $\Omega = 1$  (Top) and  $\Omega = 3$  (Bottom).

### 3.2. Fractional Giant Shapiro Steps

While the giant Shapiro steps in zero field described above were expected to occur if an array could be fabricated with sufficient uniformity, it was truly surprising that



additional "fractional giant Shapiro steps" were observed by Benz et al.<sup>7</sup> at voltages

$$V = \frac{1}{q} N \frac{n h \nu}{2e}, \quad n = 0, 1, 2, \dots \quad (4)$$

when the high-frequency response was measured in a magnetic field corresponding to  $f = p/q$  flux quanta per unit cell, where  $p$  and  $q$  are integers. This experimental observation is shown in Fig. 4 for  $f = 1/2$  and  $f = 1/3$  for the same temperature, rf amplitude and frequency. One can see both giant and the novel fractional steps.

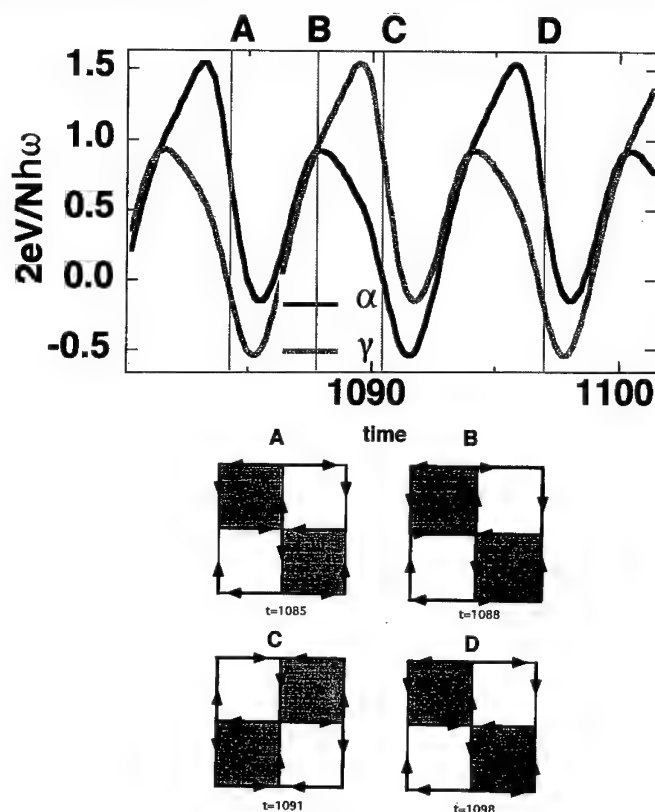


Fig. 6. Top: Voltages across two consecutive horizontal junctions as a function of time. Bottom: Ground state configurations at the point  $A, B, C$ , and  $D$  in the top figure.

Since for  $f = 0$  no subharmonic giant steps are observed when inductive effects are unimportant, as is expected for SNS junctions, the fractional giant steps must originate in the collective behavior of the junctions in the presence of the strongly commensurate field (Benz et al.<sup>7</sup>). Simulations, using as a model for the array

a network of Josephson junctions described by RSJ elements, show fractional giant steps in the I-V characteristic (Lee et al.<sup>8</sup> and Free et al.<sup>9</sup>) and show how the motion of the vortex superlattice is responsible for their existence. (Free et al.<sup>9</sup>).

To understand the origin of the fractional steps, consider first the case of the first giant step which occurs for  $f = 0$ . On this step, during one rf cycle of the external drive, each of the phase differences across the horizontal junctions in the array will advance by exactly  $2\pi$  in synchrony with the drive, thus leading to a step at  $N$  times that of a single junction since they are all in phase and synchrony. Since there is no magnetic field there will be no phase difference across the vertical junctions.

Consider now the case  $f = 1/2$ . The ground state corresponds to a  $2 \times 2$  cell, in which currents flow in the counter clockwise direction in all the diagonal plaquettes as in Fig. 3(a). These can be thought of as vortices that will move collectively in the direction perpendicular to the dc current, due to the Lorentz force. In Fig. 6 (Top), we show the voltages across two consecutive horizontal junctions of the  $2 \times 2$  unit cell labeled  $\alpha$  and  $\gamma$  when the system is on the fractional giant step  $n = 1$ ,  $q = 2$  in Eq. 4. Note first that the period of the oscillation of the two junctions is two times that of the rf drive. In addition, while the waveform of all the junctions is exactly the same, they are out of phase with each other by one period of the rf drive. This means that even though the junctions are out of phase, the average period for the  $2 \times 2$  cell is the same as the period of the rf drive. In terms of the phases of the individual junctions, Fig. 6 (Bottom) shows the evolution of the ground state as a function of time. Starting from the ground state, after one period the rf drive, the vortex superlattice has moved one unit cell, due to the Lorentz force, in the direction perpendicular to the dc current. Thus, it takes  $q$  periods of the rf drive to go back to the original configuration of the ground state as shown in Fig. 6 (Bottom). In terms of the gauge invariant phases across each junction, during each period of the rf drive, the phase only changes by  $\pi$  each rf cycle, taking two periods of the rf drive to change by  $2\pi$ . In terms of the Josephson voltage relationship, this means that the phases evolve by  $2\pi$  in two periods of the rf drive or  $w = 2\pi/(qT)$ , leading to the fractional steps. One may also think of this subharmonic response of the system to the rf drive as a spatial bifurcation, since the spatial distribution of the vortices is what induces the subharmonic response.

This picture can be extended to the full sequence of fractional giant steps for any value of  $f = p/q$ . It is known that the ground state of the system is spatially periodic with a  $q \times q$  unit cells. (Only the  $f = 1/2$  case provides some ambiguity, since in this case all plaquettes contain a circulating current, so that the system "contains" vortices of opposite polarity in alternating diagonals.). Then, the sequence of fractional giant steps with  $n = 1$  and  $q = 2, 3, 4, \dots$ , corresponds to the phase-locking of the rf drive to the motion of the vortex superlattice which has to move  $q$  times in order to synchronize with the rf drive, at this point all phases have changed by exactly  $2\pi$ . Higher order steps simply correspond to the synchronization of the rf drive to the  $2\pi n$  change in the phase differences across the junctions, in the case of the giant harmonic steps, and an average of  $n\pi$  for the fractional harmonic steps.

The correctness of this picture can be ascertained from experiments (Sohn et al.<sup>10</sup>)

in which the orientation of the current injection was varied. If the picture of a vortex superlattice moving in the direction perpendicular to the current motion is correct, then injection of the current in an array in which is oriented in the  $[11]$  direction should result in the disappearance of the fractional giant steps. since after each cycle the superlattice will be in the same configuration after one rf cycle. Sohn et al <sup>10</sup> found this to be the case as shown in Fig. 7 where we show the same plot as in Fig. 4. but for an array oriented in the  $[11]$  direction. In fact, Sohn et al <sup>10</sup> also performed experiments for an array in which the current was injected at a  $15^\circ$  angle and found that the fractional Giant steps were weaker than those of the current injection in the  $[10]$  direction. These experiments confirm the essential picture of the spatial origin of the steps.

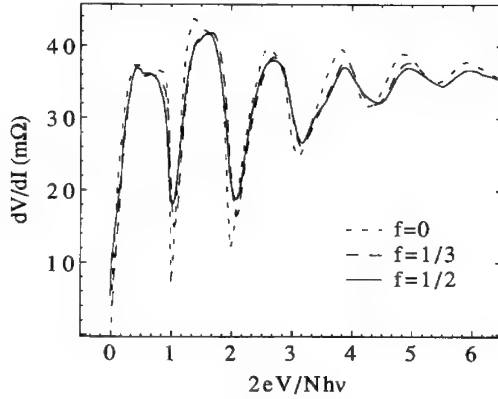


Fig. 7. Differential resistance as a function of the normalized voltage for three different frustrations in an array oriented in the  $[11]$  direction.

#### 4. Underdamped Josephson Arrays and the Potential Model

Up to this point, we have considered only arrays of overdamped Josephson-junctions in which the devices are junctions of the SNS type. The question arises as to what if any differences exist between an array of overdamped junctions and an array of underdamped junctions, since it is known that in single junctions underdamped junctions have rich dynamical behavior. Rather than simulating a full array, we will consider the case of  $f = 1/2$ . One can extend to underdamped arrays the reduced description of Rzchowski et al <sup>11</sup>, which allows for the fast exploration of parameter space. We find that underdamped arrays show interesting phenomena even in the absence of an rf field. As  $\beta_c$  is increased the I-V characteristics develop two distinct regimes at low and high voltages. Even more interesting is that this allows us to find an analog for the system which is quite useful for the understanding its dynamics.

To model the underdamped arrays <sup>12</sup>, we assume the ground state symmetry for  $f = 1/2$  shown in Fig. 3 for the gauge-invariant phase-differences. Each junction

is assumed to obey the RCSJ equation, to include the effect of capacitance. One can then write three equations for the gauge-invariant phases from fluxoid quantization, charge conservation at the central node and net current across the  $2 \times 2$  cell

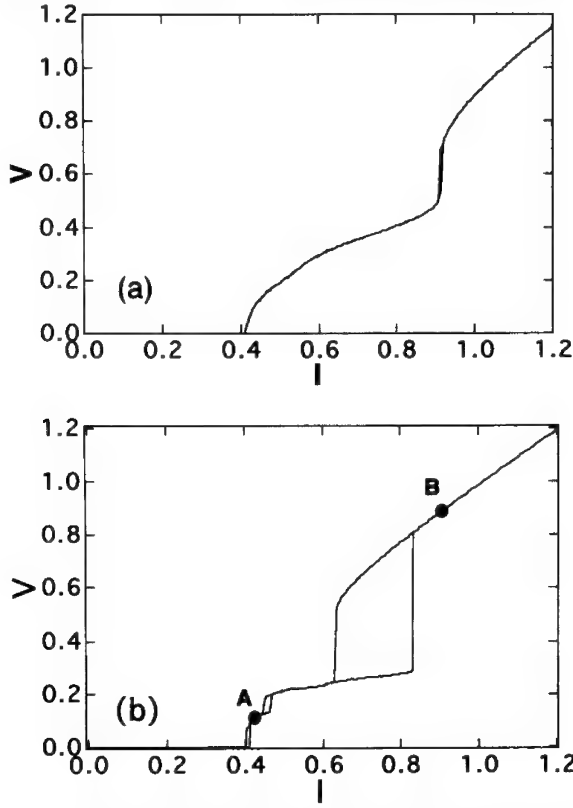


Fig. 8. I-V characteristics for a)  $\beta_c = 2$  and b)  $\beta_c = 5$ .

$$\alpha + \gamma + 2\beta = \pi, \quad (\text{mod } 2\pi) \quad (5)$$

$$-2\beta_c \frac{d^2\beta}{dt^2} - 2\frac{d\beta}{dt} - 2\sin\beta + \beta_c \frac{d^2\gamma}{dt^2} + \frac{d\gamma}{dt} + \sin\gamma + \beta_c \frac{d^2\alpha}{dt^2} + \frac{d\alpha}{dt} + \sin\alpha = 0 \quad (6)$$

$$I/I_c = \beta_c \frac{d^2\gamma}{dt^2} + \frac{d\gamma}{dt} + \sin\gamma - \beta_c \frac{d^2\alpha}{dt^2} - \frac{d\alpha}{dt} - \sin\alpha \quad (7)$$

where  $I$  is the total applied current normalized to the array critical current  $I_c = 2i_c$  where  $i_c$  is the single junction critical current. It is convenient to use the variables

$\eta = (\alpha + \gamma)/\sqrt{2}$  and  $\xi = (\alpha - \gamma)/2$  for whose motion one finds from (5)-(7):

$$\beta_c \frac{d^2 \xi}{d\tau^2} = -\frac{\partial U(\xi, \eta)}{\partial \xi} - \frac{d\xi}{d\tau} \quad (8)$$

$$\beta_c \frac{d^2 \eta}{d\tau^2} = -\frac{\partial U(\xi, \eta)}{\partial \eta} - \frac{d\eta}{d\tau} \quad (9)$$

where  $U(\xi, \eta)$  describes a particle of mass  $\beta_c$  sliding down the gradient of the potential in the presence of friction and is given by:

$$U(\xi, \eta) = -\cos \frac{\xi}{\sqrt{2}} \cos \eta - \sin \frac{\xi}{\sqrt{2}} + \frac{I}{2I_c} \eta \quad (10)$$

Fig. 8 shows the I-V curve for  $\beta_c = 2$  and  $\beta_c = 5$  for comparison. For  $\beta_c = 2$  there is a dramatic change. The I-V curve is divided into two distinct regions, separated by a jump at  $I/I_c \sim 0.915$ . In the low voltage region, the differential resistance depends on  $I$  and  $\beta_c$ . Above the jump, the I-V curve approaches the Ohmic asymptote much faster than for  $\beta_c = 0$ ; the differential resistance is essentially constant. At higher values of  $\beta_c$  we have found that the I-V characteristics still contain two different regions. As  $\beta_c$  is increased, the low voltage region contains additional structure with hysteresis being present. At the same time, the hysteresis between the low and high voltage regions, which was barely discernible for  $\beta_c = 2$ , become quite large for larger  $\beta_c$  values.

Detailed examination of the voltage waveforms reveal<sup>12</sup> that in the low voltage regime, the dynamics are dominated by the vortex motion. i.e. the voltage waveform contains large pulses every time a vortex moves across. At high voltages the waveforms are like those of single junctions.

Further physical insight can be obtained by the equivalence of Eqs. (8)-(10) to the equation of motion of a particle. In Figs. 9 (a) and (b) we plot the potential in the  $-\eta$  direction together with two trajectories. The tilt of the potential in the  $-\eta$  direction is proportional to  $I$ , while the velocity of the particle is proportional to the voltage across the array. For low  $\beta_c$ , the frictional force dominates and the particle follows the gradient of the potential. For  $I/I_c < \sqrt{2} - 1$ ,  $U(\xi, \eta)$  has local minima, in which the particle can be trapped. With increasing  $\beta_c$ , the influence of inertia grows, and the path of the particle now also contains parts moving uphill. The trajectories are quite complex; they become unstable at certain current values, a jump occurs in the I-V curve and chaotic-like solutions may be present.

The large hysteretic jump between the low voltage and high voltage regimes is the analog of the row switching observed by Van der Zant et al<sup>13</sup>. This jump can be understood as follows: For low voltages, the particle follows the side valleys of the potential. With increasing  $I$  and  $\beta_c$ , the trajectory moves closer to the crest of the hill separating two side valleys. At the jump, the particle is fast enough to overcome the hill and no longer has to follow the side valleys. This allows the speed to increase in the  $-\eta$  direction and the voltage increases.

Half-integer Shapiro steps can also be understood in terms of the mechanical analog. Along trajectories of the type shown in Fig. 9 (a), the period of  $d\eta/dt$  is half that of the individual phases. In this sense, a half-integer step of the  $f = 1/2$  array corresponds to an integer step of a single junction. The presence of the extra degree of freedom  $\xi$ , allows for trajectories which have no counterpart in single junctions. This is the origin of the anomalies of the power dependence of Shapiro steps, as well as the fact that half-integer steps decrease faster with frequency than the integer steps.

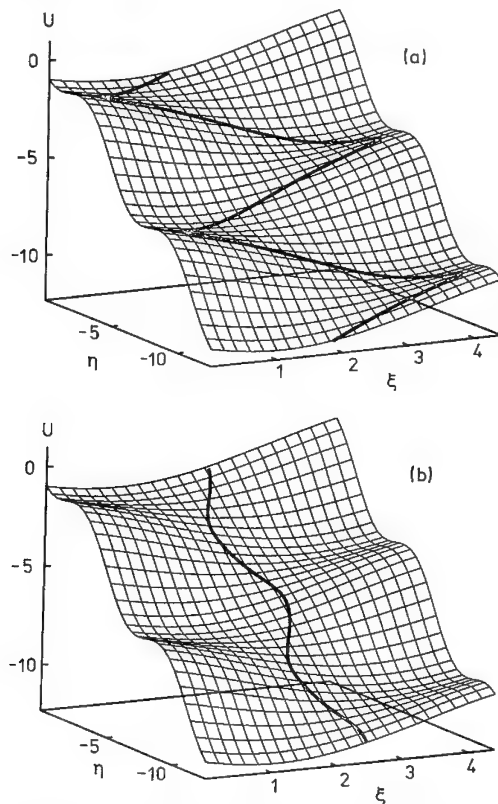


Fig. 9. Motion of the particle in the potential for two points in the I-V curve below and above the jump.

The anomalies shown in Fig. 4, can be understood as follows. In a single junction, the lobes in the power dependence of the Shapiro steps correspond to the number of wells of the washboard potential visited in a single rf cycle. In the case of the array for  $f = 1/2$ , there is an extra degree of freedom. As the frequency is increased, locking onto the half-integer step motion becomes more difficult (that is the range of stability is reduced) thus reducing the lobe amplitude and thus the anomaly. At

high frequencies the motion follows only the  $-\eta$  direction and thus is just like a single junction leading to the classical dependence of step widths on power.

## 5. Conclusions

In conclusion, we have shown that two-dimensional arrays can exhibit rich dynamics that are interesting and novel. We have ignored important effects such as the fact that in most arrays one can't usually neglect inductance as their size is smaller than the Josephson penetration depth. As shown by Lee et al<sup>4</sup>, self-fields can induce fractional giant Shapiro steps even in zero magnetic field if the sample is smaller than the penetration depth. By including a ground plane in their experiment they were able to show the correctness of this picture as the rf induced steps disappeared with the ground plane. Domínguez and José<sup>14</sup> also showed that giant Shapiro steps may exist if there is disorder in the sample. Finally, Phillips et al<sup>15</sup> have done extensive studies using simulations in which the effect of all inductances was included and how this affects the giant Shapiro steps. Even more complicated effects may be observed in arrays of underdamped junctions where the inductance of the individual junctions is important. However, these additional effects do not change the essential picture of the origin of the fractional giant steps in two-dimensional Josephson arrays.

## Acknowledgments

The author would like to thank C.J. Lobb, U. Geigenmüller, R. Newrock, C.B. Whan, and L.L. Sohn for numerous conversations and their collaboration in part of the material presented here; as well as A. Octavio for typesetting the paper.

## References

1. For a general view of this field, see Proc. of the NATO Workshop on Phase Coherence in Superconductor Networks, J.E. Mooij and G. Schön, editors, *Physica*. **B 152** (1988).
2. L.L. Sohn, Ph.D. Thesis, Harvard University, 1991
3. Ch. Leeman, Ph. Lerch, and P. Martinoli, *Physica*. **126B** (1984) 475.
4. H.C. Lee, R.S. Newrock, D.B. Mast, S.E. Hebboul, J.C. Garland, and C.J. Lobb, *Phys. Rev.* **B44** (1991) 921.
5. S. E. Hebboul and J. C. Garland, *Phys. Rev.* **B47** (1993) 5190.
6. M. Octavio, J.U. Free, S.P. Benz, R.S. Newrock, D.B. Mast and C.J. Lobb, *Phys. Rev.* **B44** (1991) 4601.
7. S.P. Benz, M. Rzchowski, M. Tinkham and C.J. Lobb, *Phys. Rev. Lett.* **64** (1990) 693.
8. K.H. Lee, D. Stroud, and J.S. Chung, *Phys. Rev. Lett.* **64** (1990) 962.
9. J.U. Free, S.P. Benz, M.S. Rzchowski, M. Tinkham C.J. Lobb and M. Octavio, *Phys. Rev.* **B41** (1990) 7267.
10. L.L. Sohn, M.S. Rzchowski, J.U. Free, S.P. Benz, M. Tinkham and C.J. Lobb,

- 
- Phys. Rev.* **B44** (1991) 925.
11. M.S. Rzchowski, L.L. Sohn, and M. Tinkham, *Phys. Rev.* **B43** (1991) 8682.
  12. M. Octavio, C.B. Whan, U. Geigenmüller, and C.J. Lobb, *Phys. Rev.* **B47** (1993) 1141.
  13. H.S.J. van der Zant, F.C. Fritschy, T.P. Orlando, and J.E. Mooij, *Phys. Rev. Lett.* **66** (1991) 2531.
  14. D. Domínguez, J.V. José, A. Karma, and C. Wiecko, *Phys. Rev. Lett.* **67** (1991) 2367.
  15. J.R. Phillips, H.S.J. van der Zant, J. White, and T.P. Orlando, *Phys. Rev.* **B47** (1993) 5219.



## TWO-DIMENSIONAL JOSEPHSON JUNCTION ARRAYS IN THE PRESENCE OF A MAGNETIC FIELD

G. FILATRELLA

*Dipartimento di Fisica, Università di Salerno,  
I-84081 Baronissi, Italy*

and

K. WIESENFELD

*School of Physics, Georgia Institute of Technology,  
Atlanta, GA 30332, USA*

### ABSTRACT

We have decomposed a 2D array of  $N \times M$  short overdamped Josephson junctions into  $N$  rows of  $M$  elements coupled to each other. For the single row we develop an approximate analytic solution for relatively high bias and low magnetic field that captures most of the features of the system when compared with numerical simulations. By coupling two rows we show that the magnetic field is responsible for phase locking, i.e., in the zero magnetic field limit there is an arbitrary phase shift between the solutions of the two rows, whereas this arbitrariness is removed by the presence of a magnetic field. This suggests that the neutral stability of bare 2D arrays, which is a drawback for the practical applications of such arrays as local oscillators in the millimeter and submillimeter region, might be avoided by the application of a weak magnetic field. The effect of a spread of the critical currents is also considered.

### 1. Introduction

Two-dimensional Josephson Junctions Arrays (JJA) have been proposed as an alternative to one-dimensional series arrays for microwave generation<sup>1,2</sup>. One reason for considering two-dimensional arrays is that one-dimensional arrays suffer a fundamental problem, if either there is no external load – what we call a bare array – or if the load is purely resistive and the junctions have negligible capacitance. Namely, the in-phase state is neutrally stable, i.e. the phase relation between the oscillators can be arbitrary so that any perturbation leads to a different configuration<sup>3</sup>. On the other hand it was proven<sup>4,5</sup> that also the in-phase solution of two-dimensional arrays is neutrally stable, thus suggesting that something should be modified to achieve a stable solution.

To remove the neutral stability, we suggest (and describe in detail elsewhere<sup>6</sup>) the following idea. By applying a magnetic field, the boundary conditions are modified, which prevents the in-phase state from setting in. Numerical simulations show that the new state is dynamically stable. Here, we will give an analytical argument (but not a rigorous proof) that this is plausible. This same approach can

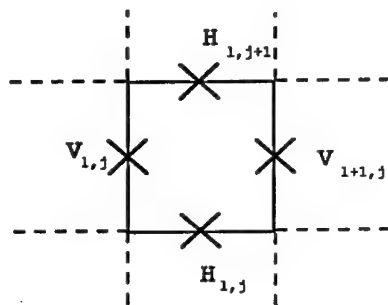


Fig. 1. An elementary cell of the array. Each cross denotes a Josephson junction.

furnish an approximate solution for the dynamics of a two-dimensional JJA in the presence of a magnetic field. Finally, the case of arrays formed by junctions of non uniform critical current will be discussed.

## 2. The Analytical Approach

One of the questions that we want to address in this work is the effect of non identical junctions. As will be shown later, two-dimensional JJA are characterized by three parameters:  $I_0$ ,  $R$  (the critical current and the normal resistance of the junctions, respectively), and  $L$  (the self inductance of the superconducting loops). The first quantity can be considered the most important because the resistance and the inductance of the loops can be fabricated with a smaller range of tolerance. We therefore assume that the critical currents of the junctions are not identical:

$$^V I_0^{l,j} = I_0(1 + \delta_{l,j}^V) \quad (1)$$

$$^H I_0^{l,j} = I_0(1 + \delta_{l,j}^H) \quad (2)$$

(here  $V$  and  $H$  refer to vertical and horizontal junctions, respectively; the index  $l, j$  specifies a node, see Fig. 1). An appropriate model for two-dimensional square JJA in the presence of a magnetic field is the following set of differential equations for the junctions in the interior of the array<sup>7</sup> ( $V_{l,j}$  and  $H_{l,j}$  denote the Josephson phase difference, and overdots indicate time derivative):

$$\begin{aligned} \dot{V}_{l,j} &= -(1 + \delta_{l,j}^V) \sin V_{l,j} + \gamma + \\ &\quad \frac{1}{\beta_l} [V_{l+1,j} - 2V_{l,j} + V_{l-1,j} + H_{l,j} - H_{l,j+1} + H_{l-1,j+1} - H_{l-1,j}] \\ \dot{H}_{l,j} &= -(1 + \delta_{l,j}^H) \sin H_{l,j} + \end{aligned} \quad (3)$$

$$\frac{1}{\beta_l} [H_{l,j+1} - 2H_{l,j} + H_{l,j-1} + V_{l,j} - V_{l+1,j} + V_{l+1,j-1} - V_{l,j-1}] \quad (4)$$

The boundary conditions are ( $N$  denotes the total number of vertical junctions and  $M$  the total number of horizontal junctions):

$$\begin{aligned} \dot{V}_{1,j} &= -(1 + \delta_{1,j}^V) \sin V_{1,1} + \gamma - \eta + \\ &\quad \frac{1}{\beta_l} [V_{2,j} - V_{1,j} + H_{1,j} - H_{1,j+1}] \quad j = 1, \dots, M-1 \end{aligned} \quad (5)$$

$$\begin{aligned} \dot{V}_{N,j} &= -(1 + \delta_{N,j}^V) \sin V_{N,j} + \gamma + \eta + \\ &\quad \frac{1}{\beta_l} [V_{N-1,j} - V_{N,j} - H_{N-1,j+1} + H_{N-1,j}] \quad j = 1, \dots, M-1 \end{aligned} \quad (6)$$

$$\begin{aligned} \dot{H}_{l,1} &= -(1 + \delta_{l,1}^H) \sin H_{1,j} + \eta + \\ &\quad \frac{1}{\beta_l} [H_{l,2} - H_{l,1} + V_{l,1} - V_{l+1,1}] \quad l = 1, \dots, N-1 \end{aligned} \quad (7)$$

$$\begin{aligned} \dot{H}_{l,M} &= -(1 + \delta_{l,M}^H) \sin H_{l,M} - \eta + \\ &\quad \frac{1}{\beta_l} [H_{l,M-1} - H_{l,M} - V_{l,M-1} + V_{l+1,M-1}] \quad l = 1, \dots, N-1 \end{aligned} \quad (8)$$

Here,  $\gamma = I_B/I_0$  is the normalized bias current,  $\beta_l = 2\pi LI_0/\Phi_0$  is the usual SQUID parameter,  $\eta = \Phi^e/LI_0$  is the normalized external flux per elementary cell ( $\Phi^e$ ), and the unit of time is  $\hbar/2eRI_0$ .

The main assumption necessary to derive this model is that the magnetic field generated by the current flowing in each junction is supposed to be confined in the two adjacent cells (nearest neighbor approximation) instead of considering the whole inductance matrix<sup>8,9</sup>.

In this section we will assume the array is uniform ( $\delta_{l,j}^{V,H} = 0$ ). The method used to tackle this set of equations is to decompose the array into rows (i.e., we consider an  $N \times 2$  array). The dynamics of each row is, to first approximation, further simplified by assuming that the horizontal junctions are inactive. In the limit of high bias current it is possible to use a harmonic balance method to derive the equation of motion for the vertical junctions. More precisely, we assume that the solution of Eq. (3) is of the form

$$V_{l,1}(t) = \theta_{l,0} + vt + A_v \sin(\theta_{l,0} + vt) + B_v \cos(\theta_{l,0} + vt) \quad (9)$$

This expression contains four parameters, but in order to satisfy the boundary conditions we must have  $\theta_{l,0} = l\eta\beta_l$ . The other three quantities  $v$ ,  $A_v$ , and  $B_v$  may be found by substitution of Eq.(9) into Eq.(3) and enforcing the balance of the constants and of the first harmonic. In the limit of  $\gamma \gg 1$  we find

$$v \simeq \gamma, \quad A_v \simeq 0 \quad B_v \simeq \frac{1}{\gamma}. \quad (10)$$

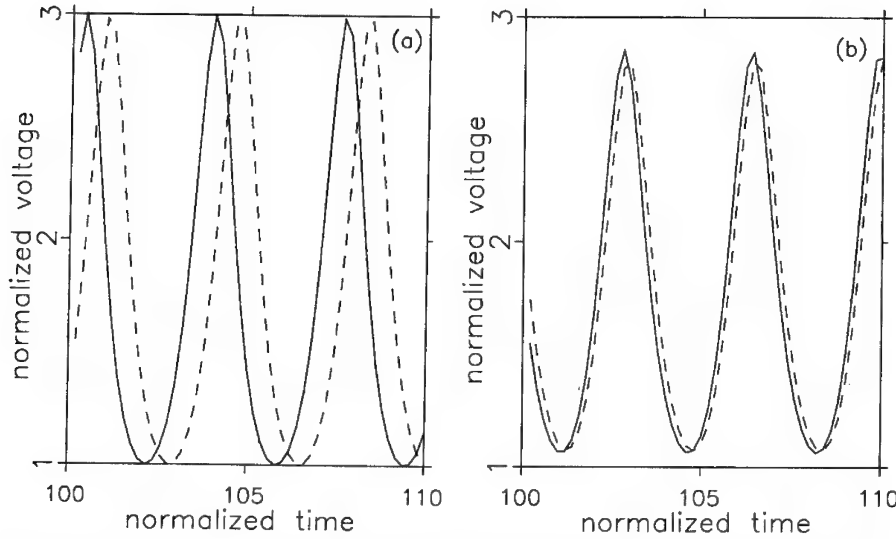


Fig. 2. Time evolution of the instantaneous voltage across two vertical junctions in the same column for a)  $\eta = 0$  and b)  $\eta = \pi/4$ . Parameters of the simulations are:  $M = 3$ ,  $N = 10$ ,  $l = 5$ ,  $\beta_l = 1$ ,  $\gamma = 2.0$ .

In the next step of the calculation, we substitute this result for the behavior of the vertical junctions into Eq.(4) in order to solve for the behavior of the horizontal junctions. It is easy to show that  $H_{i,2} = -H_{i,1}$ ; using this and assuming a solution of the form:

$$H_{i,1}(t) = H_0 + A_H \sin(\theta_{i,0} + vt) + B_H \cos(\theta_{i,0} + vt) \quad (11)$$

we determine the coefficients  $H_0$ ,  $A_H$  and  $B_H$  again using harmonic balance. The constant balance yields:

$$\sin H_0 = \frac{-2H_0}{\beta_l}. \quad (12)$$

The physical meaning of this constant is analogous to the classical SQUID phase shift induced by a magnetic field trapped in the loop<sup>10</sup>; the factor 2 takes into account the fact that in this case there are 4 rather than 2 junctions for each elementary loop. In the limit of high bias current ( $\gamma \gg 1$ ) and no trapped magnetic field ( $H_0 = 0$ ) one gets:

$$A_H = \frac{1}{\gamma^2(\beta_l + 2)^2} \left[ \frac{-\sin \eta \beta_l}{\beta_l + 2} + \frac{1}{\beta_l} (1 - \cos \eta \beta_l) \right] - \frac{\eta \beta_l}{\gamma(\beta_l + 2)} \quad (13)$$

$$B_H = \frac{1}{\beta_l \gamma^3(\beta_l + 2)} \left[ \frac{-\sin \eta \beta_l}{\beta_l + 2} + \frac{1}{\beta_l} (1 - \cos \eta \beta_l) \right] \quad (14)$$

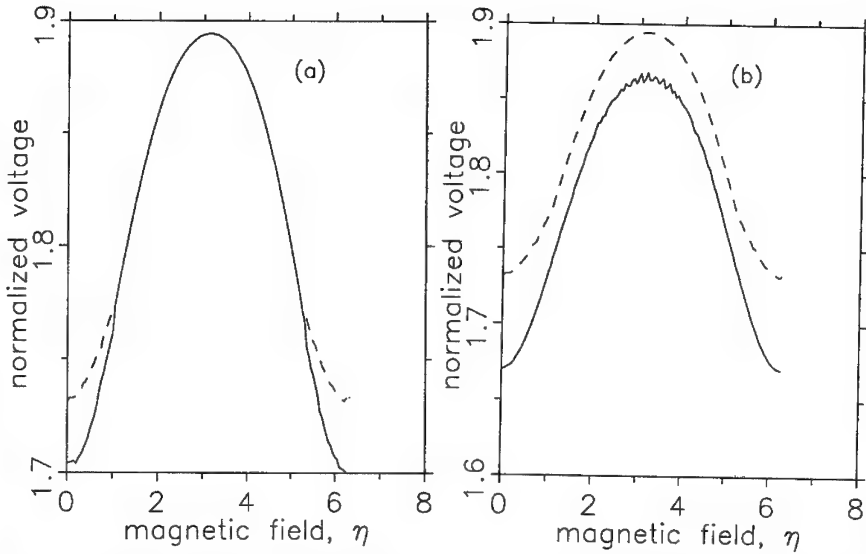


Fig. 3. Average voltage across the upper (solid line) and lower (dotted line) rows of the array for a)  $\delta_1^V = 0.05$  and b)  $\delta_1^V = 0.1$ . Parameters of the simulations are:  $M = 3$ ,  $N = 10$ ,  $\beta_l = 1$ ,  $\gamma = 2$ .

When the applied magnetic field vanishes ( $\eta = 0$ ) the horizontal junctions are inactive. Even when the magnetic field is present the amplitudes of the oscillations for the horizontal junctions are much smaller than those of the vertical junctions. Finally, the horizontal junctions do not overturn, but just oscillate around the equilibrium point  $H_0$ .

The same scheme is repeated for the system of two rows (an  $N \times 3$  array), where now the solution of the first row is supposed to drive the junctions in the second row, i.e.,  $V_{i,1}$ ,  $H_{i,1}$ , and  $H_{i,2}$  are given by Eqs (9-14) and the horizontal junction  $H_{i,3}$  is supposed to be inactive. Under these assumptions it is possible to estimate the behavior of the junctions in the second row. As usual the solution is assumed to be of the type

$$V_{i,2}(t) = \theta_{i,0} + \delta + vt + \bar{A}_v \sin(\theta_{i,0} + \delta + vt) + \bar{B}_v \cos(\theta_{i,0} + \delta + vt). \quad (15)$$

By means of harmonic balance we can determine the three parameters  $\delta$ ,  $\bar{A}_v$ , and  $\bar{B}_v$ . In particular it is possible to prove that the phase shift  $\delta$  between the two rows is arbitrary when the magnetic field is set to zero, and is fixed when the magnetic field is not zero. This is the main result of the approach: it suggests that the magnetic field might prove to be effective in removing the arbitrary shift between the two rows that is the signature of the neutral stability. In fact numerical simulations (see Fig. 2) show that the phase of the upper and lower rows are essentially uncorrelated if the magnetic field is zero, and are phase-locked if the magnetic field is turned on.

### 3. The Non-uniform Case

To investigate the non-uniform case we make the further simplifying assumptions that: 1) The array consists of only two rows; 2) Defects are present only in vertical junctions; and 3) Defects are the same along a row (i.e.,  $\delta_{1,j}^V = \delta_{2,j}^V = \dots = \delta_{N,j}^V = \delta_j^V$ ). Figure 3a shows the behavior of the average voltage across each row  $\bar{V}_j = 1/N \sum_{i=1}^N \bar{V}_{i,j}$  as a function of the external magnetic field, for a certain spread of the parameters ( $\delta_1^V = 0.05$ ,  $\delta_2^V = 0$ ). We see that for a certain range of the parameters the magnetic field is able to lock together the voltages of the two rows. In contrast, the average voltage across the rows are different when the magnetic field is 0.

Figure 3b shows a similar behavior for a larger spread of the criticals currents ( $\delta_1^V = 0.1$ ,  $\delta_2^V = 0$ ). In this case it is evident that the two rows somehow interact but are never locked together.

To further investigate the mechanism of the locking between the rows, Fig. 4 shows the oscillations of the voltage in two adjacent vertical junctions belonging to the same column. In Fig. 4a there is no spread between the two critical currents, and the phase difference between the two junctions (in the asymptotic regime) is 0. In Fig 4b a spread of  $\delta_1^V = 0.05$  has been introduced, and the phase shift between the rows becomes apparent. Finally, Fig. 4c shows a case of intermediate spread ( $\delta_1^V = 0.03$ ), and it is clear that the phase shift is decreased, as expected. Finally, we note that our results seem to indicate that a spread of parameters is not able to lock together the rows in the absence of magnetic field. In other words, we have checked that changing the critical current of one row alone is insufficient to break the symmetry that is responsible for the neutral stability of two-dimensional JJA. A systematic search for the types of non-uniformities – if any – that could lead to a stabilization of the array dynamics is worthwhile and potentially important. Unfortunately, at this point our simulations suggest that a spread between two rows seems to be ineffective.

### 4. Conclusions

The problem of a two-dimensional array of Josephson junctions can be conveniently separated into the problem of rows of Josephson junctions coupled each other. This separation has proved to be useful in allowing us to obtain an approximate solution for the dynamics of the array and to furnish a first hint of the conditions that break the symmetry that causes the neutral stability of bare two-dimensional arrays. For the more complicated case of non-uniform arrays we have not produced any analytical results, but even so the separation into rows is conceptually useful. However, numerical simulations show an interesting behavior: for certain values of the magnetic field and of the spread of critical currents it is possible to achieve a phase locked state, even if the natural oscillation frequencies of the two rows are different.

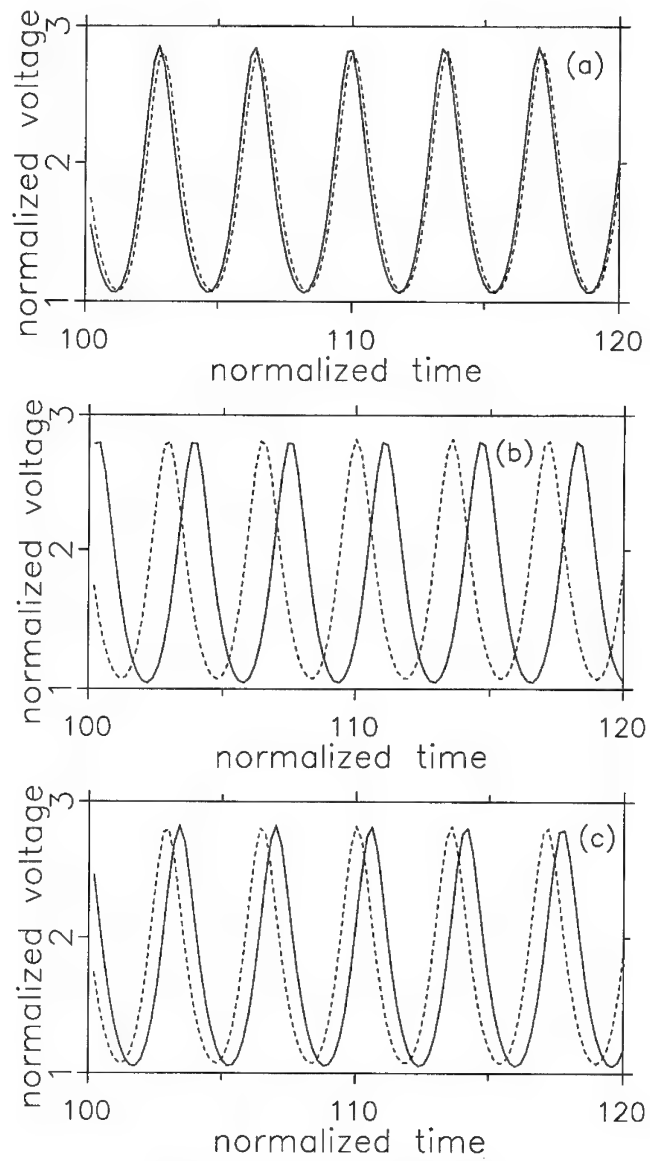


Fig. 4. Time evolution of the instantaneous voltage for the upper (solid line) and lower (dotted line) vertical junctions in the same column for a)  $\delta_1^V = 0$ , b)  $\delta_1^V = 0.05$  and c)  $\delta_1^V = 0.03$ . Parameters of the simulations are:  $M = 3$ ,  $N = 10$ ,  $l = 5$ ,  $\beta_l = 1$ ,  $\eta = \pi/4$ ,  $\gamma = 2$ .

### Acknowledgements

We wish to thank Y. Braimann, T. Doderer, R.P. Huebener, S.G. Lachenmann, and B. Larsen and especially S. Benz and R.L. Kautz for useful comments and discussions. This work was partially supported by a grant from the U.S. Office of Naval Research under contract number N00014-J-91-1257. GF wishes to thank Georgia Tech for their hospitality during the preparation of this work and the EU for financial support through the Human Capital and Mobility program (Contract No *ERBCHRXCT*920068 and Euroconference financial support), the MURST (Italy), and the Progetto Finalizzato "Superconductive and Cryogenic Technologies" of the National Research Council of Italy.

### References

1. S.P. Benz and C.J. Burroughs, Appl. Phys. Lett. **58**, 2162 (1991).
2. P.A.A. Booij and S.P. Benz, Appl. Phys. Lett. **64**, 2163 (1994).
3. S. Watanabe and S.H. Strogatz, Physica D **74**, 197 (1994); A.K. Jain, K.K. Likharev, J.E. Lukens, and J.E. Savageau, Phys. Rep. **109**, 310 (1984).
4. K. Wiesenfeld, S.P. Benz, and P.A.A. Booij, J. Appl. Phys. **76**, 3835 (1994).
5. P. Hadley, *Dynamics of Josephson Junction Arrays*, Ph.D. dissertation, Stanford University, 1989 (unpublished).
6. G. Filatrella and K. Wiesenfeld, unpublished.
7. K. Nakajima and Y. Sawada, J. Appl. Phys. **52**, 5732 (1981).
8. J.R. Phillips, H.S.J. van der Zant, J. White, and T.P. Orlando, Phys. Rev. B **47**, 5219 (1993).
9. D. Reinel, W. Dietrich, T. Wolf, and A. Majhofer, Phys. Rev. B **49**, 9118 (1994).
10. A. Barone and G. Paternó, *Physics and Applications of the Josephson Effect*, Wiley, New York, 1982.



**DYNAMICS IN COMPLEX RSJ SUPERCONDUCTING SYSTEMS:  
FROM DISCRETIZED LARGE JUNCTIONS TO 2-D ARRAYS.  
A MICROSCOPIC VIEW.**

J. C. CIRIA

*Dipartimento di Fisica, Università di Roma "Tor Vergata",  
Via della Ricerca Scientifica 1, I-00133 Roma, Italy.*

and

C. GIOVANNELLA

*Dip. di Fisica, Sez. INFN and Sez. INFN dell'Università di Roma "Tor Vergata",  
Via della Ricerca Scientifica 1, I-00133 Roma, Italy.*

**ABSTRACT**

Subharmonic Shapiro Steps (SSS) are commonly observed in current biased arrays of superconducting junctions when their single junction-like behavior is perturbed by the introduction of disorder, frustration or current inhomogeneities. A microscopic insight is compulsory in order to obtain a full description of the dynamics of these arrays. In particular we show that the determination of the average voltage of a Shapiro Step does not define univocally the state of the system that, on the other hand, may depend on the initial configuration of the phases and on the experimental protocol that has been followed. Dynamical states having different vortex configurations and showing domain walls are possible. In order to have a better insight into the physical conditions needed to generate these states we have focused ourselves on the effect of the geometry of the array investigating the dynamical behavior of very simple systems like the superconducting junction ladders. They turn out to be systems where the properties of larger square arrays can be found and studied.

**1. Introduction**

Shapiro Steps, observed in current biased arrays of superconducting junctions<sup>1,2,3</sup>, are an example of locking between an external periodic force (the ac-injected current) and the intrinsic frequency of the system<sup>4</sup>.

Giant Shapiro Steps (GSS), appearing at voltage  $\langle V \rangle = n \frac{N_y h \nu}{2e}$  (where  $\nu$  is the frequency of the ac external current,  $N_y$  the number of junctions along the direction of this bias current and  $n$  any integer number) are the trivial generalization of the Shapiro Steps found in a single junction. If by any means the symmetry along the direction perpendicular to that of the incoming current breaks, locking on non-trivial dynamical states is observed and evidenced by the appearance of half-integer or Subharmonic Shapiro Steps (SSS)<sup>2,5</sup>. Under these conditions the array cannot be reduced to an effective 1-dimensional system, and a 2D-cooperative behaviour comes into play.

In general, the SSS are interpreted as caused by a coherent displacement of super-

arrays of vortices commensurate to the array dimension <sup>6,7</sup>. However, this interpretation is somewhat contradicted by the numerical simulations of the dynamical behaviour of a single plaquette <sup>8</sup>, a ladder <sup>9</sup> and of small square arrays <sup>10</sup>, which show locked states at fractional values of the normalized voltage corresponding to commensurate vortex arrays larger than the one considered for the simulation.

In this paper we will first comment on some of the conditions under which SSS appear (application of an external magnetic field, introduction of disorder, non-uniformity in the injected current). Then we will also show that a microscopical study is of a fundamental importance in order to have a deeper insight into the dynamical states of the superconducting junction arrays. Such a local view may be relevant to the interpretation of experiments that monitor the vortex dynamics on a microscopical scale. Finally we will present a study on the influence of the lattice size and geometry (single plaquettes, ladders perpendicular or parallel to the direction of the current, square lattices) in the presence of an external magnetic field.

## 2. The Model

We have simulated an array of overdamped Josephson junctions, the dynamics of which is described by the set of coupled equations <sup>11</sup>

$$\sum_j \frac{V_{ij}}{R_{ij}} + I_c \sin(\Phi_i - \Phi_j + A_{ij}) = I_i(\text{external}), \quad (1)$$

where  $i, j$  stand for nearest-neighbour points,  $V_{ij}$  is the voltage across the junction, shunted by a resistance  $R_{ij}$ , and  $I_c$  is the critical current.  $A_{ij}$  is the circulation of the vector potential between  $i$  and  $j$ . The frustration is defined in terms of the external magnetic field  $B$  as  $f = BS/\Phi_0$ , where  $S$  is the plaquette surface, and  $\Phi_0$  the fundamental quantum flux.  $V_{ij}$  is given by the Josephson relation

$$\frac{d}{dt}(\Phi_i - \Phi_j) = \frac{2e}{\hbar} V_{ij}. \quad (2)$$

The array is biased by an external current  $i_{ext} = i_{dc} + i_{ac} \sin(2\pi\nu t)$ , with  $i_{ac} = 1$ . We take it parallel to the  $y$  axis. Time is measured in units of the adimensional quantity  $t/\tau$ , with  $\tau = \hbar/(2eI_c R)$ .

We have fixed  $\nu = 0.1$ . The physical quantities have been recorded at the steady state, after a transient time of  $1000 - 2000\tau$ . Every magnitude is averaged after  $1000 - 5000\tau$ , depending on the array size.

## 3. Conditions for the Appearance of SSS

As stated above, the necessary and sufficient physical condition required to observe SSS is the existence of a mechanism that breaks the homogeneous laminar flux of the injected current. In fact, SSS have been found in systems with inhomogeneous current disorder and frustration; in this last case, a devil staircase structure, with a fractal dimension  $D = 0.88$  <sup>10</sup> has been observed.

We now consider a different mechanism. Fig. 1 shows the I-V curves obtained by introducing non uniform external current. As expected, SSS appear. It is worthwhile to remark that 2D arrays are convenient systems also to study the effect of inhomogeneities on a single extended junction, thing that may turn out to be very useful also for the investigations of the step junction based on the high  $T_c$  superconducting thin films. We stress that in the ordered homogeneous case no fractional Shapiro steps are seen.

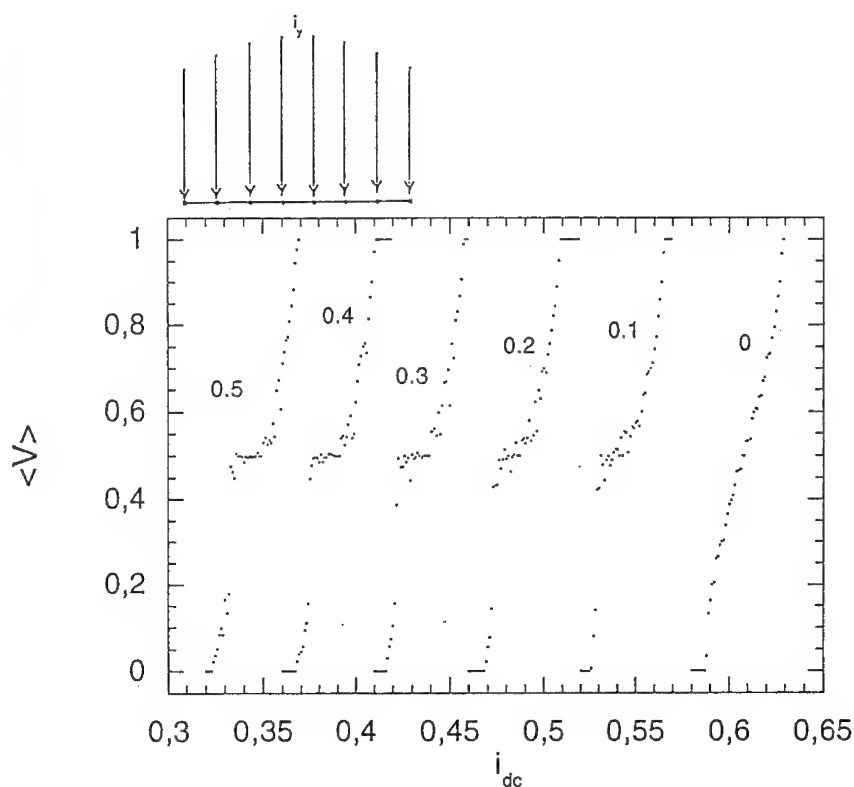


Fig. 1. I-V plot for a 7x7 array with non uniform injected current. This has the form  $i_{ext}(x) = g(x)[i_{dc} + i_{ac} \sin(2\pi\nu t)]$ , where  $g(x) = 1 + \Delta i * \sin(\pi x/Np_x)$  ( $Np_x$  is the number of plaquettes along the  $x$  axis, in this case equal to 6).  $\Delta i$  varies from  $0 \rightarrow 0.5$ .

#### 4. Univocality of the Microscopic States

The most pronounced SSS are those for which, during the dynamical evolution, the vortices arrange themselves in configurations that are commensurate to the network geometry. Usually, it is assumed that the width of the Shapiro Steps is related to the extension of the attraction basin of a certain dynamical state. We will show that within a given plateau the microscopic state of the system is not univocally determined, but different states with different values of the energy are allowed.

We will restrict ourselves to the dynamical states accessible to a system with frustration  $f = 1/2$  at the  $\langle V \rangle = 1/2$  Shapiro Step. We consider a square array with periodic boundary conditions.

Following the current model<sup>6</sup> one would expect this locked state to be described by a checkerboard vortex superlattice, the elementary cell of which consists on  $2 \times 2$  plaquettes, moving transversally respect to the direction of the external current. Moreover, when the external current is zero, internal currents and gauge-invariant phases should exhibit a staircase symmetry (i.e. along any staircase definable on the array, see the inset of fig. 2, these microscopical quantities remain constant). Indeed, this results to be one of the states accessible to the system: the ground state. For this specific state, if we neglect the currents along links close to the injection and extraction edges, all the evolution curves of the currents flowing along a staircase links group into two families, depending on the vertical or horizontal direction of the link (see fig. 2). One can see that the dynamical configuration of this state is strictly connected to that expected in the case with null external current: in fact, if we substrate to the  $y$ -currents the term  $i_{\text{external}}$  we obtain an almost perfect superposition between the curves belonging to both families.

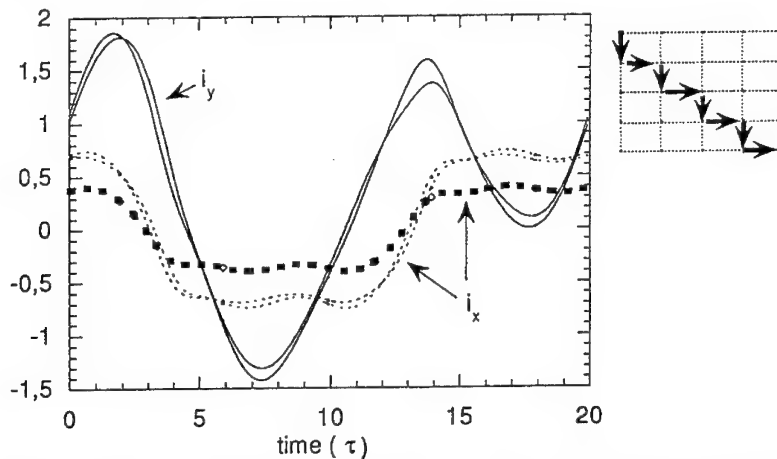


Fig. 2.  $4 \times 4$  cell array with periodic boundary conditions,  $f = 1/2$ . Currents along the links belonging to the largest staircase of the array, drawn on the small top picture. As reported in the text they group quite nicely in two families, if one neglects the last horizontal current (thick points).

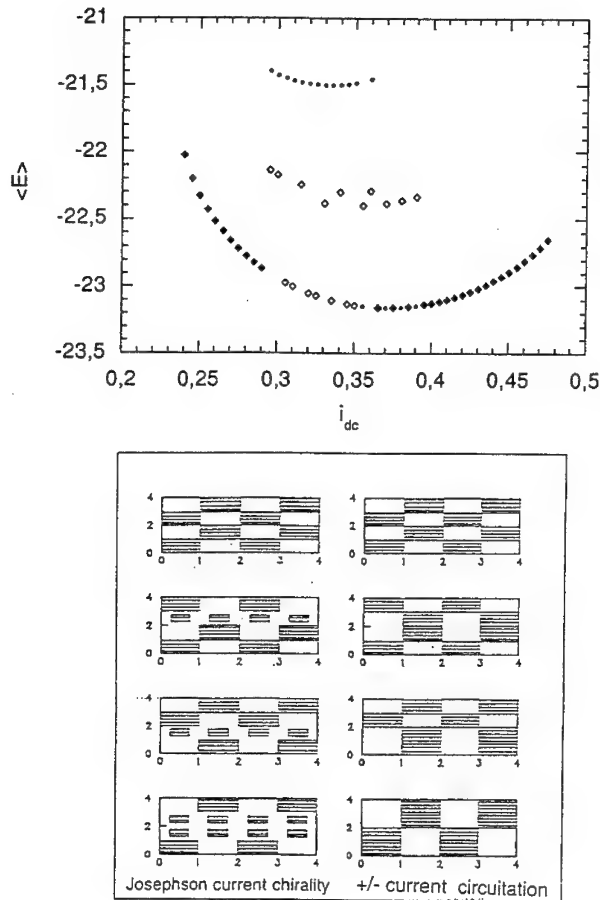


Fig. 3.  $4 \times 4$  cell array with periodic boundary conditions,  $f = 1/2$ . a) Energy of the array averaged over one period-time for different values of the biased current with the system locked on the first half-integer Shapiro Step ( $\langle E_{Josephson} \rangle = -J \sum_{ij} \cos(\Phi_i - \Phi_j + A_{ij})$ ). b) Example of the microscopic configurations corresponding to the four parabola appearing in fig. 2a). On the left: plaquettes with clockwise Josephson current chirality are represented with large dashed squares, counterclockwise Josephson chirality by large white squares, no defined Josephson chirality by small dashed squares; on the right, positive current circulations are represented by large dashed squares.

The superconducting array, however, does not always set univocally in the above described state. We have simulated different kinds of experimental situations. In one of these, after have raised the value of  $i_{dc}$  we let the system evolve starting from the

phase configuration reached with the previous value of the bias current; for the first  $i_{dc}$  the gauge-invariant phases were forced either in the zero-current  $f = 1/2$  ground-state configuration<sup>12</sup> or randomly chosen. According to another possible procedure one can initialize the phases, in any one of the above described configuration, for every value of  $i_{dc}$ . The result is that several states may be reached, with energies lying on different parabolas. In our  $4 \times 4$  cell system we have observed four different parabolas, corresponding respectively (in order of increasing energy) to a checkerboard-like vortex configurations with no domains, with one domain wall placed at the centre of the array, with one domain wall displaced at the top or at the bottom of the array and with two domain walls.

These observations may be relevant for the interpretation of the experiments that aim to investigate the array dynamics on a microscopic scale<sup>13</sup>. Indeed as for the static case<sup>14</sup> it seems to us very improbable that a fully developed ground state could be observable all over the sample. This could be a consequence of localized defects, of the free boundary condition the particular protocol followed in cooling down the sample.

We also stress that although temperature fluctuations may help, in general, in erasing some of the dynamical attractors<sup>15</sup>, in the cases considered here they seem not to be very effective, at least up to values of the temperature  $KT/J = 10^{-2}$ <sup>16</sup>.

## 5. From Discretized Large Junctions to Large Arrays

We now turn to the following question: to which extent can we scale down the system and still observe the properties found in large  $2D$  systems? Which is the influence of the size and the geometry of the lattice on the appearance of the dynamical features we have detected in square arrays?

In order to answer these questions we decided to perform a microscopic study of the dynamics of an array of small size subjected to an external field with a frustration  $f$ . We want to investigate the relationship between the commensurability of  $f$  with the dimensions of the array and the generation of domains showing coherent dynamical behaviour (SS).

First we consider horizontal ladders of plaquettes (arrays with  $N \times 2$  sites). For a frustration  $f = 1/q$  the minimum array commensurable with  $f$  is composed by  $q$  plaquettes. Now let us impose periodic boundary conditions to this commensurate array, in order to simulate an infinite ladder. Under these conditions the expected features are exactly reproduced: Only Shapiro steps with  $\langle V \rangle = \frac{n}{q}$  are observed and a microscopic analysis shows configurations with one vortex every  $q$  plaquettes moving at constant velocity. In fact all the physical quantities (currents, gauge invariant phases and so on) show a periodic behaviour with a period equal to  $qT$ , where  $T = \frac{1}{\nu}$  is the period of the external current. If we take a *stroboscopic* look at these microscopic quantities every  $T\tau$ , we observe that the single plaquette behavior repeats itself exactly on the next one after after the same  $T\tau$  time period.

Let us consider ladders with free boundary conditions, still commensurable with  $f$ . The  $p/r$  ( $r \neq q$ ) steps coexist with  $p/q$  ones. As  $N \rightarrow \infty$  the behaviour of the

system tends to that of the infinite ladder array, and the non commensurable steps become smaller and smaller. On ladders with a number of plaquettes different from  $nq$ , we observe both kinds of SSS, and non-commensurable ones survive even for very large arrays.

These perpendicular ladders, thus, show many of the characteristic features of the square arrays and constitute an adequate laboratory where the behaviour of a large square array can be studied, at least qualitatively, with the advantages of spending a much smaller amount of CPU time. As an example in fig. 4 we show the effect of injecting a non uniform current.

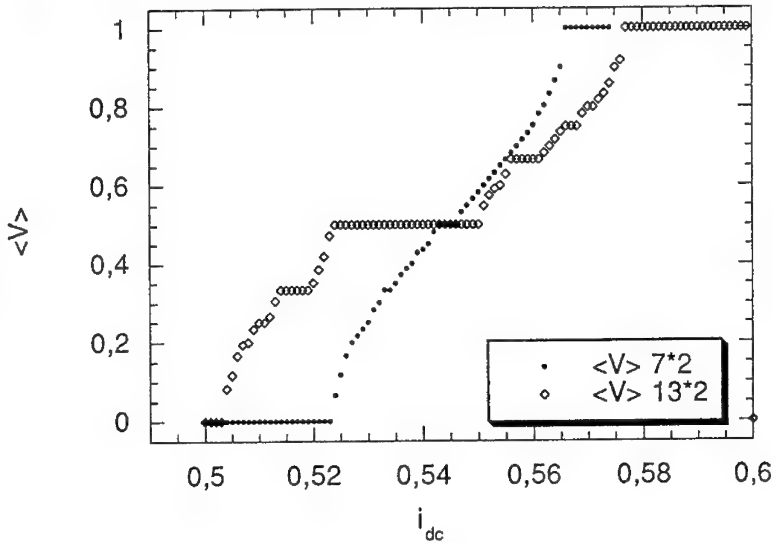


Fig. 4. The effect of non-uniform injected current, such as described in figure 1, in horizontal ladders (free boundary conditions). We note that in the larger array (with 12 plaquettes, thus allowing super-lattices with 2, 3 and 4 cells) plateaus appear at  $\langle V \rangle = n/4$  and  $\langle V \rangle = n/3$  and the plateau at  $\langle V \rangle = 1/2$  is amplified.

We now turn to ladders parallel to the direction of the bias current (e.g. vertical ones). When plotting  $\langle E_{\text{Josephson}} \rangle$  versus  $i_{dc}$  the existence of SS is indicated by the observation of energetic states that may lie on more than one parabola. Thus, even for very small systems (ladders with 3 or 4 plaquettes) we find that, along the same Shapiro Step, several states are possible. This is the same scenario observed for the 2D arrays, and points out again for a non-univocal determination of the state of the system from its  $\langle V \rangle$ <sup>16</sup>.

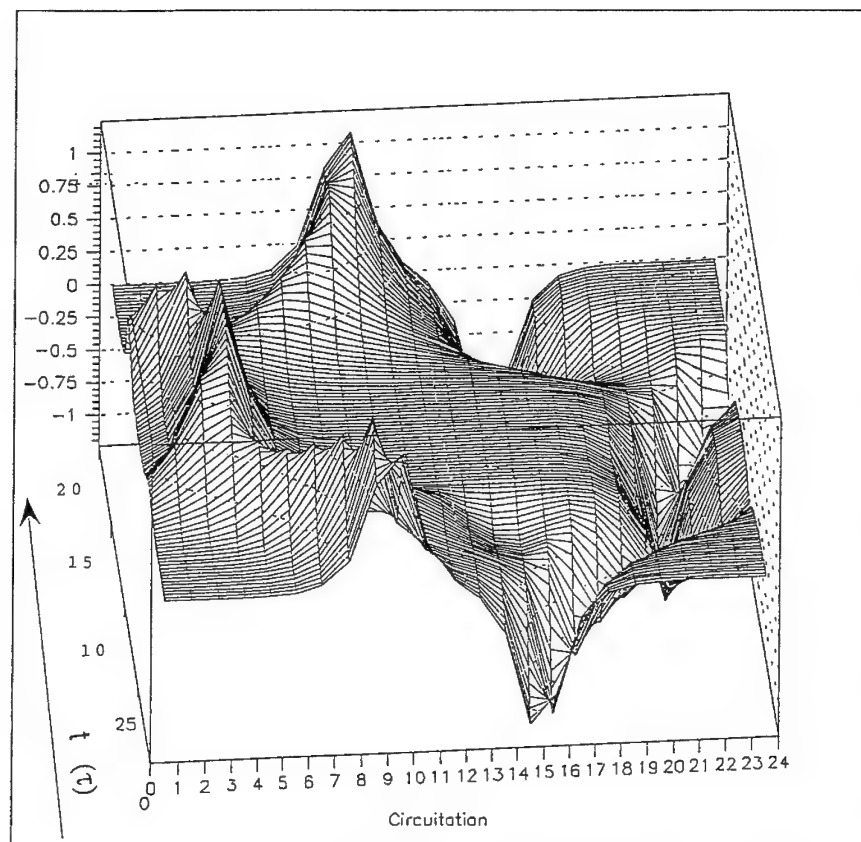


Fig. 5. Horizontal ladder with  $25 \times 2$  sites (24 plaquettes). We show the temporal evolution of the current circulations with a non-uniform injected current as that defined in figure 1 ( $\Delta i = 0.1$ ), on the  $\langle V \rangle = 1/2$  Shapiro Step. A pair vortex-antivortex appears in the centre of the ladder, and they move towards opposite directions till reaching the edges of the array, where they disappear. After that (the behaviour is perfectly periodic) a new pair appears again. Axis  $x$  represents the position of the plaquettes; axis  $y$ , the time; axis  $z$ , the circulation.

## 6. Conclusions

We have shown that, on square arrays, a very rich "zoology" is found when they are studied microscopically. In particular the dynamical basins (known as Shapiro Steps) where the system is found for certain values of the bias current are not univocally defined by giving the value of  $\langle V \rangle$ .

We have also studied very simple systems (ladders of plaquettes) in order to verify the relevance of parameters like the frustration, the dimension and geometry of the



array on their dynamical behaviour with the aim of clarify that of square arrays.

In parallel ladders we were able to reproduce the amplification of the SS width of some locked states, (those with  $\langle V \rangle = \frac{n}{q}$ ) for which there exists a commensurability between the value of  $f$  and the length of the ladder. In particular in the case of infinite ladders, the dynamical behavior results controlled by the uniform motion of vortex superlattices with a lattice period of  $q$  plaquettes. Non commensurability or border effects lead to the formation of domain walls with the consequent development of vortex superlattices with a non commensurable lattice period. As a general remark we would like to stress that the effect of increasing the dimension of the ladder is to enforce the SS corresponding to vortex configurations commensurate to the length of the array.

On the other hand, in perpendicular ladders we observed the existence of different microscopic states for the same value of  $\langle V \rangle$ , states that turned out to be characterized by the presence of a variable number of domain-walls.

#### Acknowledgements

We acknowledge financial support provided by the EEC under contract CHRX-CT92-0068.

#### References

1. T.D. Clark, Phys. Rev. B; Ch. Leemann, Ph. Lerch and P. Martinoli, *Physica* **126B** (1984), 475.
2. S.P. Benz, M. S. Rzchowski, M. Tinkham and C. J. Lobb, *Phys. Rev. Lett.* **64**, 693 (1990).
3. C.H. Lee, R.S. Newrock, D.B. Mast, S.E. Hebboul, J.C. Garland and C.J. Lobb, *Phys. Rev. B* **44**, (1991), 921; S.E. Hebboul and J.C. Garland *Phys. Rev. B* **43** (1991), 13703 and **47** (1993), 5190; M. Octavio, J. U. Free, S. P. Benz, R. S. Newrock, D. B. Mart, and C. J. Lobb, *Phys. Rev B* **44** 4601 (1991).
4. T. Bohr, P. Bak and M. H. Jensen, *Phys. Rev. A* **4**, 1970 (1984).
5. D. Domínguez, J.V. José, A. Karma and C. Wiecko, *Phys. Rev. Lett.* **67**, 2367 (1991).
6. J. U. Free, S. P. Benz, R. S. Newrock, D. B. Mart, C. J. Lobb and M. Octavio, *Phys. Rev B* **41** 7267 (1990);
7. K. H. Lee, D. Stroud and J. S. Chung, *Phys. Rev. Lett.* **64**, 692 (1990); K. H. Lee and D. Stroud, *Phys. Rev. Lett.* **43**, 5280 (1991).
8. J. Kim and H.C. Lee, *Phys. Rev. B* **47**, 582 (1993).
9. H.C. Lee, R.S. Newrock, D.B. Mast, S.E. Hebboul, J.C. Garland and C.J.Lobb, *Phys. Rev. B* **44**, 921 (1991). W. Yu, E.B. Harris, S.E. Hebboul, J.C. Garland and D. Stroud, *Phys. Rev. B* **45**, 12624 (1992).

- 
10. A. Giannelli, F. Ritort and C. Giovannella, submitted to Europhys. Lett.
  11. K.K. Mon and S. Teitel, Phys. Rev. Lett. **62**, 673 (1989). J.S. Chung, K.H. Lee and D. Stroud, Phys. Rev. B **40**, 6570 (1989).
  12. S. Teitel and C. Jayaprakash, Phys. Rev. **B27** (1983) 598.
  13. S.G. Lanchenmann, T. Doderer, D. Hoffmann, R.P. Huebner, P.A. Booii and S.P. Benz, to be published.
  14. K. Runge and B. Pannetier, Europhys. Lett. **24** (1993) 737 and references therein.
  15. H. Eikmans and J.E. Van Himbergen, Phys. Rev. **B44** (1991) 6937.
  16. J.C. Ciria, C. Giovannella, to be published.

**FULL MATRIX INDUCTANCE AND "EXPERIMENTAL"  
PROTOCOLS: TWO KEY ASPECTS IN THE  
DETERMINATION OF THE STATIC MAGNETIC  
PROPERTIES OF THE 2D ARRAYS OF  
SUPERCONDUCTING RSJ**

A. NUVOLI<sup>°</sup>, A. GIANNELLI<sup>°\*\*</sup>, J.C. CIRIA<sup>°</sup>, C. GIOVANNELLA<sup>°\*\*</sup>  
<sup>°</sup>Dip. di Fisica e <sup>\*</sup>Sez. INFN e <sup>+</sup>Sez. INFN dell'Universita' di Roma Tor Vergata  
 Via della Ricerca Scientifica 1, 00133 Roma, Italia

ABSTRACT

2D arrays of superconducting junctions are interesting model systems for many physical phenomena. The description of their physical properties achievable through the numerical simulations may depend: a) on the a priori approximations enclosed in the theoretical model used for the simulations and b) on the particular "experimental" protocol followed. We show here that in order to describe properly the magnetic status of the arrays one has to use the full inductance matrix and to specify clearly the approach and the protocol followed to perform the computer simulations.

## 1. Introduction

2D arrays of superconducting junctions are already on their own very interesting systems both on the fundamental and on the technological points of view<sup>1</sup>. In addition, in the recent past, they have been chosen also as model systems to study the physical properties of the granular superconductors<sup>2</sup>, including the High  $T_C$  materials<sup>3</sup> that, as well known now, may present even nested networks of junctions<sup>4</sup>. Since few years a continuously increasing number of papers has been devoted to the study of the magnetic properties of 2D arrays of superconducting junctions. Following the pioneer works by Ebner and Stroud<sup>2</sup>, and Morgesten, Müller and Bednorz<sup>3</sup> we have first studied in details the equilibrium magnetic hysteresis loops of these model systems<sup>5</sup>. Our simplified description however: a) did not take into account the correction to the local field due to the screening currents, and thus were restricted essentially to the narrow temperature range below the critical temperature for which the array penetration depth,  $\lambda_L$ , can be considered infinite and the screening extremely weak; b) was focused basically on what we may call the "geometrical" magnetism of the array (i.e. on that part of the magnetic properties that depends only on the geometry of the system)<sup>6</sup> and did not look after the effects of the temperature (thermal fluctuations and variation of the junction coupling energy), effects that we will also neglect in this paper.

In the following we will also avoid to discuss the dependence of the coupling junction energy on the intensity of the magnetic field so that we will focus our attention basically on the consequences of the approximation (a).

When the temperature is decreased somewhat below the critical one, such an approximation is not any longer valid and the introduction of a corrective term for the screening currents is compulsory. In the recent past there have been many works realized on the basis of the above consideration; almost everywhere the magnetic properties of the superconducting junction arrays<sup>7-12</sup> have been worked out by making use of a dynamical approach basically derived in ref.13. The main draw back of this approach is that since the "static" properties, like the magnetic hysteresis loop, are calculated at an arbitrary time they can only represent, at the best, the steady state limit of the dynamical evolution and, thus, might not coincide with those calculated at the equilibrium. In some of these papers the effect of the screening currents has been taken into account by introducing an average cell self-inductance<sup>7-9</sup>, but the texts of these papers do not allow us to understand if the internal field has been allowed to relax to the "equilibrium" at each time step. After the observation of José and Dominguez<sup>10</sup> about the need of considering at least also the near-neighbors mutual inductances, many groups have included in their model the contribution to the internal field derived from a more or less full mutual inductance matrix<sup>11,12,14</sup> but still in the framework of a dynamical model. Only recently the full inductance matrix has been introduced into the framework of a static approach to calculate the magnetic properties of the arrays, in order to investigate either the one-vortex magnetic properties<sup>15</sup> or more collective quantities like the magnetization loops<sup>16</sup>. In this paper we want to address three questions: how relevant is the use of the full inductance matrix to calculate the magnetic properties of the array (as an example we will consider the effect on the value of the lower critical field of the array)? How similar are the magnetic states of the array (i.e. the vortex configurations) obtained following the dynamical approach with those obtained following the static one? And finally how relevant can be the "experimental" conditions? In the following we will answer these questions using only simulations done at  $T = 0$ , but the indications we have allow us to state that the basic conclusions drawn here maintain their validity still at somewhat higher temperatures.

## 2. Model

As usual, in the static approach we consider a square array and assign a single phase,  $\phi_i$ , at each knot (we consider here point junctions, but it would be very easy to generalize this model to extended junctions; indeed the array itself can be considered as an extended junction). Each knot interacts directly only with its first four nearest-neighbors and the resulting XY Hamiltonian is the following<sup>17</sup>:

$$H = -J \sum_{ij} \cos(\phi_i - \phi_j + A_{ij})$$

where  $A_{ij}$  is the vector potential term.

The main difference with our previous simulations<sup>5,6</sup> is that now the  $A_{ij}$  contribution is composed by two distinct terms (the second one allows for the long range interaction between the currents):

$$A_{ij} = \frac{2\pi}{\Phi_0} \oint_{\mathbf{r}_i}^{\mathbf{r}_j} [A_{\text{ext}}(\mathbf{r}) + A_{\text{int}}(\mathbf{r})] d\mathbf{r} = A_{ij;\text{ext}} + A_{ij;\text{int}}$$

where

$$A_{ij;ext} = f = (S \cdot B / \Phi_0)$$

$$A_{ij,int} = \mu_0 a / 2\Phi_0 (\sum_{mn} I_{mn} f_{mn;ij} + \text{self});$$

of course

$$B_{ext} = \mu H = \nabla \times A_{ext}$$

$$B_{int} = B - B_{ext} = \nabla \times A_{int}$$

the external field is applied in the z direction and the gauge is such that:

$$A_{ij;ext} = (\pi B / \Phi_0)(x_i y_j - x_j y_i)$$

$f$  is the frustration,  $S$  the surface of the plaquette,  $B$  the total magnetic field and  $\Phi_0$  the

Fig. 1a

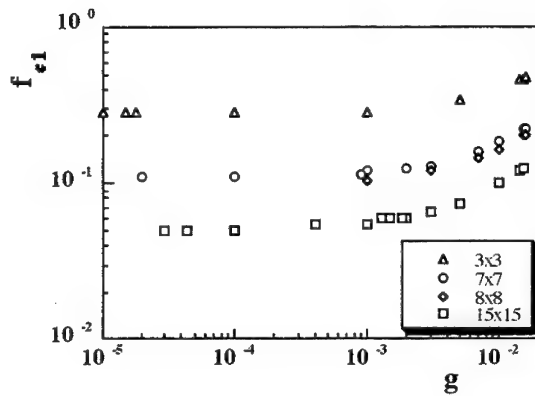


Fig. 1b

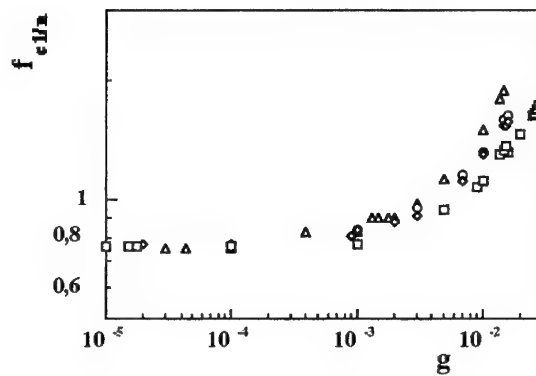


Fig. 1c

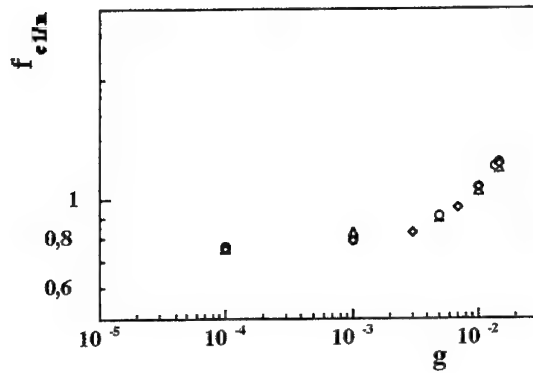


Fig. 1d

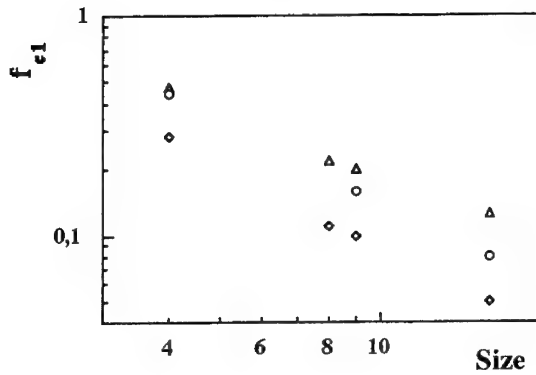


Fig. 1 - a) Lower critical fields,  $f_{c1}$ s, obtained by making use of the full inductance matrix as function of the  $g$  factor for superconducting junction arrays of different sizes (in plaquettes): 3x3 (triangles), 7x7 (circles), 8x8 (rhombi) and 15x15 (squares). b) As for fig. 2a but normalized to the size of the array in cells. c)  $f_{c1}$ s obtained making use only of the self inductance normalized to the size of the array; symbols like for the previous figures. d)  $f_{c1}$  as function of the size of the array:  $g = 0$  (rhombi),  $g = 0.015$  only self inductance (circles),  $g = 0.015$  full inductance matrix (triangles).

elemental flux quanta,  $ff$  is the factor form that depends only on the distance between the sites, and  $I_{mn}$  is the current that flows in the  $m$ th- $n$ th link and it is normalized to  $I_c = E_j * 2\pi / \Phi_0$ , with  $E_j$  the coupling energy.

As a consequence one can define a quantity  $g$  such that :

$$g = \mu_0 E_j a / 2\Phi_0^2 = 1 / 8\pi^2 \lambda_{\perp}$$

where  $\lambda_{\perp}$  can be considered as a sort of penetration depth of the array; for  $g = 0$  one recovers the limit  $\lambda_{\perp} = \infty$ .

The simulations we performed following the dynamical approach are based on a standard model<sup>18</sup> modified to include the correction to the internal field due to the full inductance matrix; in our runs we let the magnetic field relax at each time step, until the relative change of the total field becomes less than one part on  $10^{-5}$ .

### 3. Results and discussion

Let us start with the first question raised in the introduction: how relevant is the use of the full inductance matrix to calculate the magnetic properties of the array? Although it may not be important for the determination of some of the array properties<sup>15,19</sup> it is certainly relevant to the determination of the lower critical field,  $f_{c1}$ . In fig. 1 we show the influence that the  $A_{ij,int}$  term has on  $f_{c1}$ . From the row data of fig. 1a one immediately sees that  $f_{c1}$  undergoes substantial changes with increasing  $g$ . In particular, for very low values of  $g$  we

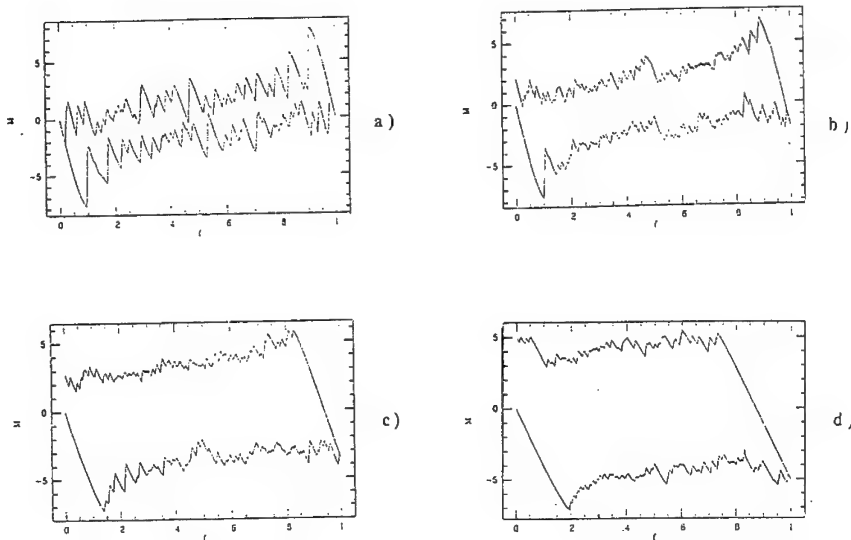


Fig. 2 - 8x8 cell-array; examples of magnetic hysteresis loops for different  $g$  values (full inductance matrix): a)  $g = 0$ , b)  $g = 0.001$ , c)  $g = 0.007$ , d)  $g = 0.015$

observe a plateau that correspond to the limit  $\lambda_{\perp} = \infty$ . It is worth noting that the  $f_{c1}$  attains the plateau value when  $\lambda_{\perp}$  becomes of the order of the array size (that is equivalent to have  $\lambda_{\perp} = \infty$ ), so that this value is reached before, as expected, in the case of the smaller arrays. Figures 1b and 1c put in evidence the relevance of making use of the full inductance matrix. After normalization to the size of the array (in cells) the data of fig. 1a nicely overlap (with the exception of the 3x3 cell-array, that has been slightly shifted) up to the limit where  $\lambda_{\perp}$  can be still considered infinite; than the curves spread away, fig. 1b. This spreading is not observed in fig. 1c, where the lower critical fields have been obtained taking into account only the self-inductance. Another way to work out the relevance of the full-inductance matrix is to plot  $f_{c1}$  vs the size of the array, fig. 1d. Looking at this figure one can conclude that both the data obtained either without corrective terms or using only the self inductance decrease inversely with the size of the array (that is equivalent to say that there exist a critical size of the array for which  $f_{c1}$  is equal to zero); on the other hand the slope of the data obtained employing the full-inductance matrix tends to slow down with the size of the array, suggesting the existence of an asymptotic value for  $f_{c1}$ . This conjecture has to be checked on arrays of larger size.

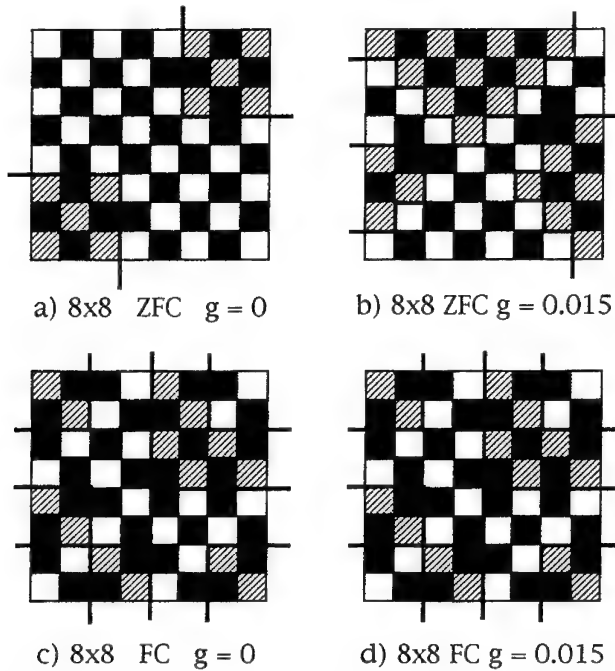


Fig.3 - Vortices configurations at  $f = 0.5$  obtained, as described in text, for: a) ZFC static procedure and  $g = 0$ ; b) ZFC static procedure and  $g = 0.015$  (full inductance matrix); c) FC static procedure and  $g = 0$ ; d) FC static procedure and  $g = 0.015$  (full inductance matrix);



Examples of magnetic hysteresis loops for different  $g$  values are reported in fig. 2. These are loops obtained at the equilibrium by means of the static approach and following a procedure experimentally called zero field cooling, ZFC, that is: first the sample is cooled down in zero magnetic field, then the magnetic field is switched on and increased step by step paying attention to achieve the state of equilibrium for each new value of the field. The influence that the use of the full inductance matrix can have on the vortices configuration at  $f = 0.5$  is put in evidence by the couple of figures 3a-3b. Surprisingly no differences are detected in the case of the field cooling, FC, procedure, figures 3c-3d. In this procedure first the magnetic field is switched on and then the sample is cooled down. Fig. 3 answers to the third question of paragraph 1: how relevant can be the experimental conditions?

It remains still to answer the second question raised in the introduction: how similar are the vortices configuration obtained following a dynamical approach with those obtained

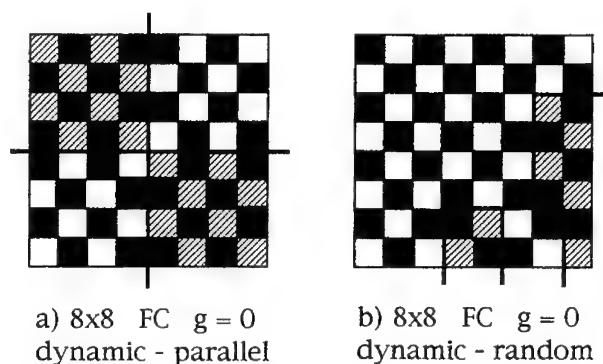


Fig. 4 - Vortices configurations at  $f = 0.5$  obtained following a) FC dynamic procedure with  $g = 0$  and phases initially aligned; b) FC dynamic approach with  $g = 0$  and phases initially random distributed; these two configurations settled on firmly respectively after  $200 \tau$  and  $300 \tau$  with  $\tau = h/2eRl_c$

following the static one? Fig. 4 tell us that at  $T = 0$  they are very dissimilar notwithstanding with the stringent requirement we imposed to the relaxation of the internal magnetic field. Moreover fig. 4 shows that the vortices configuration attained may be different even if we simply start the simulation from two different initial phase configurations. We stress that in our simulations, at  $T = 0$ , we observed always the formation of domains. A more quantitative analysis of our findings will appear in a paper to come.

#### Acknowledgements

We acknowledge financial support provided by EEC under contract CHRX-CT92-0068

## References

1. see for example "Coherence in Superconducting Networks" ed. by J.E. Mooij and G.B.J. Schön, *Physica B* **152** (1988)
2. C. Ebner, D. Stroud **31** (1985) 165
3. I. Morgensten, K.A. Müller, J.G. Bednorz, *Z. Phys. B* **69** (1987) 33
4. C. Giovannella, C. Chappert, P. Beauvillain, *Europhys. Lett.* **5** (1987) 535
5. A. Giannelli, C. Giovannella, *J. of Les Common Metals* **164-165**, 1488 (1990)
6. A. Giannelli, C. Giovannella, M. Bernaschi, *Europhys. Lett.* **22** (1993) 29, A. Giannelli, C. Giovannella, M. Bernaschi, *Physica B* **194-196** (1994) 1695 and references therein
7. A. Majhofer, T. Wolf, W. Dieterich, *Phys. Rev. B* **44** (1991) 9634
8. T. Wolf, A. Majhofer, *Phys. Rev. B* **47** (1993) 5383
9. R. Vaccarone, *J. of Super.* **6** (1993) 161 and references therein
10. D. Dominguez, Jorge V. José, *Phys. Rev. B* **48** (1993) 13717 and references therein
11. C. Auletta, R. De Luca, S. Pace, G. Raiconi, *Phys. Rev. B* **47** (1993) 14326 and references therein
12. J.H. Miller jr, G. H. Gunaratne, Z. Zou, M.F. Davis, H.R. rampersad, J.C. Wolfe, *Phys. Rev. B* **49** (1994) 15317
13. K. Nakajima and Y Sawada, *J. Appl. Phys.* **52** (1981) 5732 and references therein
14. F. Busse, P. Seidel, M. Darula, in "Weak Superconductivity" edited by S. Benacka, P. Seidel, V. Strbik, IEEASAS, 1994
15. J.R. Phillips, H.S.J. van der Zant, J. White, T.P. Orlando, *Phys. Rev. B* **47** (1993) 5219
16. A. Giannelli, C. Giovannella, A. Nuvoli, in "Weak Superconductivity" edited by S. Benacka, P. Seidel, V. Strbik, IEEASAS, 1994, p. 196
17. K.K. Mon and S. Teitel, *Phys. Rev. Lett.* **62** (1989) 673  
J.S. Chung, K.H. Lee, D. Stroud, *Phys. Rev. B* **40** (1989) 6570
18. J.C. Ciria, C. Giovannella, in this volume and references therein.
19. P. Pacetti, J. C. Ciria, C. Giovannella, to be published

## POSITIVE FIELD COOLED D.C. SUSCEPTIBILITY IN JOSEPHSON JUNCTION NETWORKS

P. CAPUTO, G. COSTABILE, R. DE LUCA, S. PACE, A. SAGGESE

*Department of Physics, University of Salerno, Via S.Allende  
I-84081 Baronissi (Salerno), Italy*

### ABSTRACT

We show that the recent finding of a paramagnetic Meissner effect on polycrystalline samples of High- $T_c$  cuprates can be interpreted on the basis of a traditional analysis of a superconducting ring interrupted by Josephson junctions. In fact, this system is the simplest junction array model for granular superconductors. By the analysis of the potential energy of this simple network, we show that the field cooled magnetization exhibits paramagnetic responses, depending on the strength of the applied field.

### 1. Introduction

Recently, several groups<sup>1,2</sup> have observed a positive field cooled susceptibility at very low values of the applied magnetic fields in high temperature superconducting BiSrCaCuO ceramic systems. This behavior is referred to as *paramagnetic Meissner effect* in the literature, to stress its anomaly when compared to the usual diamagnetic response of traditional superconductors. The appearance of spontaneous magnetic moments might evoke exotic properties of the superconducting state, like the assumption of *d*-wave pairing in High- $T_c$  superconductors. In the latter hypothesis, the  $\pi$ -contacts present in granular superconductors are responsible for spontaneous currents and magnetic moments<sup>3,4</sup>.

We propose a classical explanation for the appearance of spontaneous paramagnetic moments, on the basis of a simple representation of polycrystalline ceramic systems in terms of superconducting islands coupled by Josephson junctions. In fact, granular superconductors can be modeled by means of a network of weak links, represented by Josephson junctions. We study the simplest of such systems; namely, a superconducting ring interrupted by *N* junctions. For this system we analyze the stationary states in presence of magnetic field, and calculate the temperature dependence of the d.c. susceptibility.

### 2. The model

The Gibbs potential energy for a superconducting loop containing *N* Josephson

junctions in series is given by<sup>5,6</sup>:

$$G = \sum_{k=1}^N \frac{I_k^0 \Phi_0}{2\pi} (1 - \cos \phi_k) + \frac{(\Phi^L - \Phi_{ext}^L)^2}{2L}, \quad (1)$$

where  $I_k^0$  is the maximum Josephson current of the  $k$ -junctions,  $\phi_k$  the gauge invariant superconducting phase difference and  $\Phi_0$  the magnetic flux quantum. The external magnetic field  $H$  is applied along the normal to the loop, with area  $S_L$ , and produces a geometrical flux  $\Phi_{ext}^L = \mu_0 H S_L$ .  $L$  is the inductance associated to the loop.

When the external field is applied, the flux  $\Phi^L$  linked to the loop is given by:

$$\Phi^L = \Phi_{ext}^L + LI, \quad (2)$$

where  $I$  is the induced screening current.

The phase difference across the junction is related to the effective flux in the loop by the fluxoid quantization condition:

$$\sum_{k=1}^N \phi_k + \frac{2\pi \Phi^L}{\Phi_0} = 2\pi n_f, \quad (3)$$

where  $n_f$  is an integer which is linked to the number of magnetic flux quanta trapped in the loop, when cooling down the system from  $T > T_c$  to  $T < T_c$ .

We study the stationary magnetic states of this system after field cooling by finding the absolute minimum of the energy  $G$  with respect to the flux  $\Phi^L$ , for each fixed value of  $\Phi_{ext}^L$ .

Taking into account a non negligible thickness of the superconducting ring, the total flux  $\Phi$  is the sum of the flux into the material (intragranular flux  $\Phi^S$ ) and the flux into the hole (intergranular flux  $\Phi^N$ ),

$$\Phi = \Phi^S + \Phi^N. \quad (4)$$

The flux  $\Phi^S$  is due to the penetration of the external field in a thickness proportional to the magnetic depth<sup>7</sup>. Then the total magnetization has two contributions: the diamagnetic effect of the superconducting material and the magnetic effect of the hole. The d.c. magnetic susceptibility of the system can be easily defined as:

$$4\pi\chi_L = \frac{\Phi - \Phi_{ext}}{\Phi_{ext}}, \quad (5)$$

where  $\Phi_{ext}$  is the flux generated on the total area  $S = S^L + S^S$ .

From eq.(4) and eq.(5) we calculate the temperature dependence of the total d.c. susceptibility as follows<sup>8</sup>:

$$4\pi\chi(T) = (4\pi\chi_L + 1)\alpha(T) - 1, \quad (6)$$

where  $\alpha(T) = S^L(T)/S$  is the normal fraction of the sample, being  $S^L(T)$  the effective area of the normal region ( area of the loop plus the field penetrated area of the

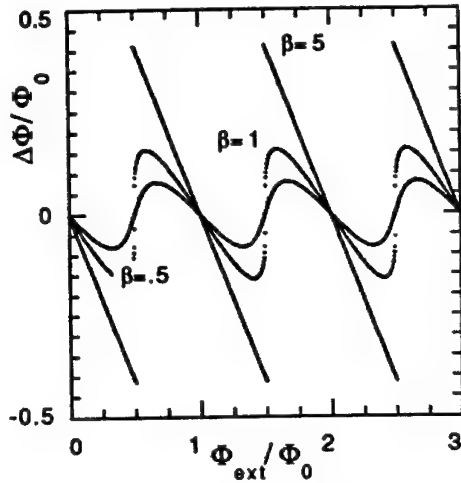


Fig. 1.  $\Delta\Phi$  vs.  $\Phi_{ext}$  curves calculated for different values of the SQUID parameter  $\beta = 2\pi LI^0/\Phi_0$  and  $N = 1$ . When  $\Phi_{ext}$  is in the range  $n\Phi_0 > \Phi_{ext} > (n - 1/2)\Phi_0$  the internal flux is larger than the applied flux. This effect is larger for increasing  $\beta(T)$ .

superconducting material). We fix the values of the normal fraction  $\alpha(T)$  at  $T = 0$  K and  $T = T_c$ , and, for intermediate temperatures, we assume  $\alpha(T)$  to have an empiric behavior, tied to the penetration of the magnetic field in the superconducting region.

### 3. Results

The analysis of the stationary magnetic states of the network is carried out for different values of the SQUID parameter  $\beta = 2\pi LI_k^0/\Phi_0$ . In order to specify the temperature dependence of the maximum critical current, we use the Ambegaokar-Baratoff equation:

$$I_k^0 = \frac{\pi\Delta(T)}{2R_N} \tanh\left(\frac{\Delta}{2K_B T}\right), \quad (7)$$

being  $R_N$  the normal resistance of the junction. The temperature dependence of the gap energy  $\Delta(T)$  is given in ref.(9). In the calculations, all the junctions are supposed to be identical, so that no inhomogeneity of the maximum critical current is considered. We start by considering only one junction in the ring.

Fig.1 shows the dependence of the flux  $\Delta\Phi$ , defined as

$$\Delta\Phi = \Phi_{min} - \Phi_{ext}, \quad (8)$$

$\Phi_{min}$  being the flux at the absolute minimum point of  $G$ , as a function of the external flux  $\Phi_{ext}$ . Both  $\Delta\Phi$  and  $\Phi_{ext}$  are normalized to the magnetic flux quantum. If  $\Phi_{ext}$

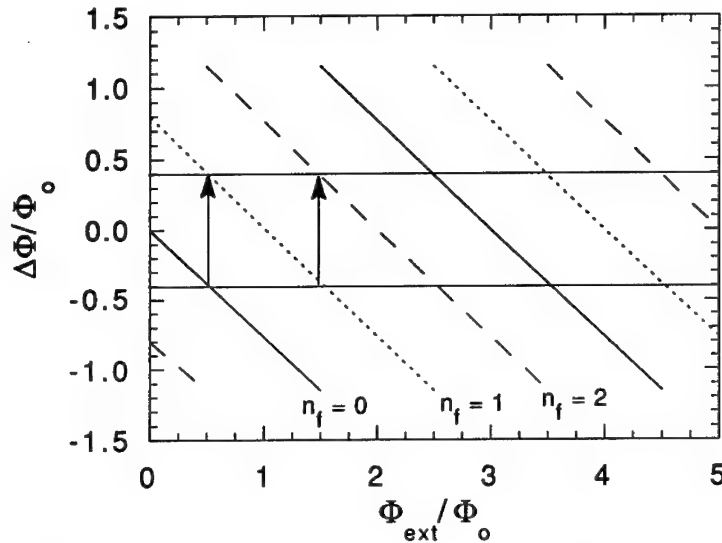


Fig. 2.  $\Delta\Phi$  vs.  $\Phi_{ext}$  curves calculated for  $\beta = 10$  and  $N = 3$ , referred to the three possible values of the number  $n_f$  of the trapped flux quanta. The arrows show the path corresponding to the flux at the absolute minimum point of  $G$ : depending to  $\Phi_{ext}$ , it switches through the 3 curves characterized by a different parameter  $n_f$ .

lies in the ranges  $n\Phi_0 > \Phi_{ext} > (n - 1/2)\Phi_0$ , with  $n$  integer, the system shows a paramagnetic behavior, evaluated from eq.(5). This effect is larger for increasing  $\beta(T)$ . In the higher inductance limit, a situation in which the applied flux is  $(\frac{\Phi_0}{2} + \epsilon)$  corresponds to a magnetic flux of  $\Phi_0$  through the ring.

If  $N$  junctions are in the ring, there are  $N$  different  $G(\Phi)$  curves for a fixed value of  $\Phi_{ext}$ , each one characterized by a different  $n_f$ . By plotting all these curves, it is easy to see that the absolute minimum of  $G$  corresponds to a different  $n_f$  for different ranges of the external field.

In fig.2 the dependence  $\Delta\Phi$  vs.  $\Phi_{ext}$  for the three possible values of  $n_f$  when  $N = 3$  is given. The path followed by the absolute minimum of  $G$  is shown by the arrows. This absolute minimum point moves through the  $n_f$ -different curves, so that, during each field cooling, the system traps the number of magnetic flux quanta that minimizes its energy at that fixed field. We notice that the same magnetic response of the single junction loop is reproduced.

In order to calculate the total field cooled d.c. susceptibility  $\chi$  (eq.7), we take into account the two contributions (one from the intragranular flux  $\Phi_S$  and the other one from intergranular  $\Phi_N$ ), and we use the eq.(7).

In fig.3 is reported the behavior of  $\chi$  for a ring with one junction as a function of the temperature  $T$ , for different values of the normalized external magnetic flux  $\Phi_{ext}/\Phi_0$ . Here  $\alpha_0$ , the normal fraction at zero temperature, is 0.8 and the SQUID parameter

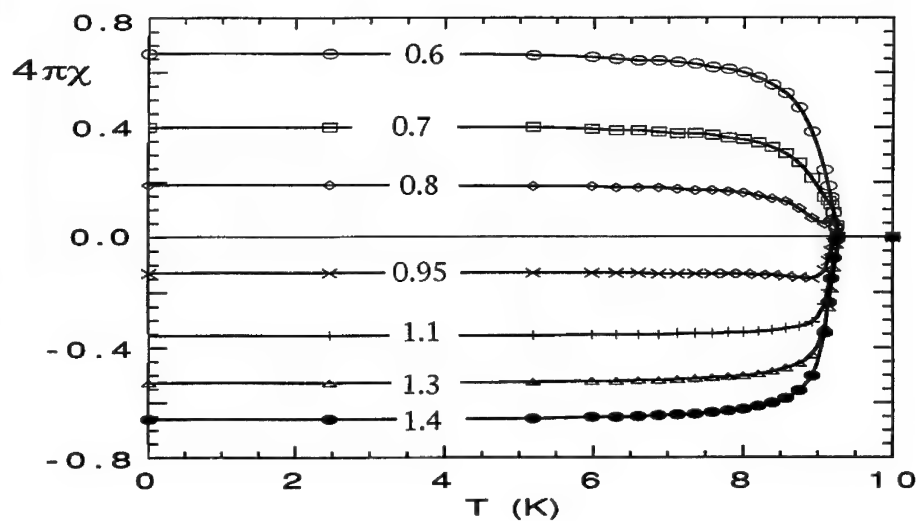


Fig. 3. Total field cooled susceptibility versus  $T$ , calculated for different values of the normalized external magnetic flux  $\Phi_{ext}/\Phi_0$ . Here  $\alpha_0 = 0.8$  and  $\beta = 10$ . Each curve reports the corresponding normalized flux value.

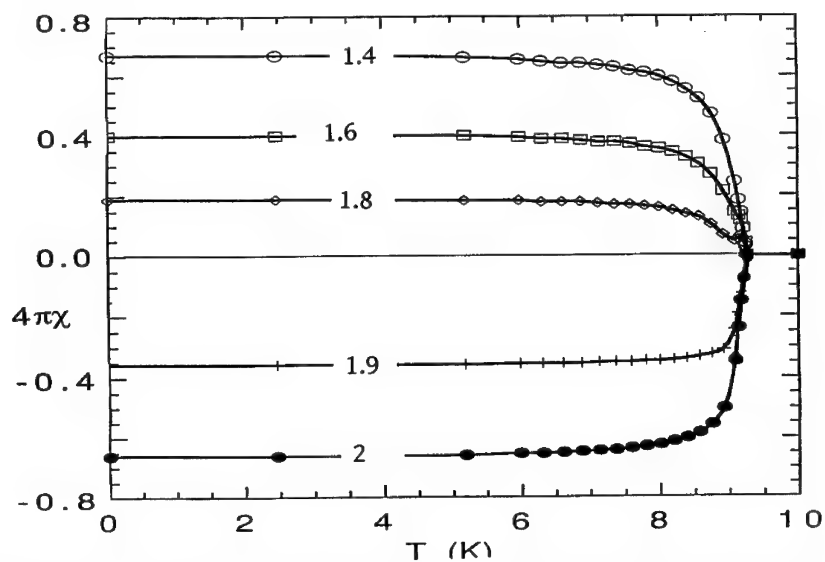


Fig. 4. Total field cooled susceptibility when the ring is interrupted by 3 junctions. The same values for  $\alpha_0$  and  $\beta$  are chosen.

$\beta$  is 10. We notice that, for high value of the external flux, the diamagnetic behavior is always dominant. In addition, we notice that for  $\Phi_{ext}$  going to zero the system always shows a diamagnetic behavior independently of  $\beta$ . Therefore, for extremely low values of the applied field, we expect a diamagnetic experimental response.

The same analysis, carried out when three junctions are in the ring (fig.4), shows that the same properties survive even if the ring is interrupted by more than one junction.

In conclusion, we show that the analysis of the magnetic response of a simple model consisting of a superconducting loop with Josephson junctions can reproduce, at least qualitatively, the same positive field-cooling d.c. susceptibility detected in High- $T_c$  ceramic superconductors for low field ranges. In order to describe real system, however, more complex models must be analyzed. A work on a two-dimensional array consisting of an ensemble of loops with a given distribution of inductances is in progress.

#### 4. Acknowledgement

We would like to thank Dr. Alberto M. Testa and Dr. Umberto Gambardella for valuable discussions about magnetic properties of High- $T_c$  superconductors. One of the authors (P.C.) gratefully acknowledges financial support from INFM.

#### References

1. W. Braunisch, N. Knauf, G. Bauer, A. Kock, A. Becker, B. Freitag, A. Grütz, V. Kataev, S. Neuhausen, B. Roden, D. Khomskii, D. Wohlleben, J. Bock and E. Preisler, *Paramagnetic Meissner effect in high-temperature superconductors*, *Physical Review B*, **48**, 4030-4042 (1993).
2. B. Schliepe, M. Stindtmann, I. Nikolic, and K. Baberschke, *Positive field-cooled susceptibility in high- $T_c$  superconductors*, *Physical Review B* **47**, 8331-8334 (1993).
3. L.N. Bulaevskii, V.V. Kuzii, and A.A. Sobyanin, *Superconducting system with weak coupling to the current in the ground state*, *JEPT Lett.* **25**, 290-294 (1977).
4. L.N. Bulaevskii, V.V. Kuzii, and A.A. Sobyanin, *On the possibility of the spontaneous magnetic flux in a Josephson junction containing magnetic impurities*, *Solid State Communication* **25**, 1053-1057 (1978).
5. K.K. Likharev, *Dynamics of Josephson junctions and circuits*, Gordon and Breach Science Publ. (1986).
6. A. Barone and G. Paterno, *Physics and application of the Josephson effect*, (John Wiley and sons, New York 1982).



7. L.Solymar, *Superconductivity of metals and alloys*, Benjamin- New York- Amsterdam (1966).
8. C.Auletta, P.Caputo, G.Costabile, R.De Luca, S.Pace, A.Saggese, *Paramagnetic field cooled susceptibility in superconductor loops with Josephson junctions*, to be published on *Physica C*, M<sup>2</sup>S-HTSC IV, in press.
9. T.P.Shlahen, *Phys.Rev.* **149**, 368 (1966).

---

## Chapter 8

# **Diagnostic Techniques**

## NOVEL VORTEX DYNAMICS IN TWO-DIMENSIONAL JOSEPHSON ARRAYS\*

SUSANNE G. LACHENMANN, T. DODERER, and R.P. HUEBENER

*Lehrstuhl für Experimentalphysik II, Universität Tübingen, Auf der Morgenstelle 14  
D-72076 Tübingen, Germany*

and

P.A.A. BOOI and S.P. BENZ

*National Institute of Standards and Technology, 325 Broadway, Boulder, CO 80303, U.S.A*

### ABSTRACT

We present spatially resolved studies of vortex dynamics in two-dimensional Josephson-junction arrays. For bias currents smaller than the array critical current, a small local thermal perturbation at the array boundaries lowers the vortex entry barrier and the array switches to the resistive state. For bias currents slightly above the array critical current, vortices and antivortices are nucleated at opposite edges of the array. An alternating crossing vortex motion is observed experimentally.

## 1. Introduction

In two-dimensional (2D) Josephson-junction arrays, vortices play a central role for the static and dynamic properties.<sup>1</sup> In the static case, several vortex configurations, depending on a perpendicular applied magnetic field are discussed in the literature. For a direct observation of these configurations, spatially resolved measurements are necessary. Runge and Pannetier<sup>2</sup> used magnetic decoration, where small particles of a magnetic material are deposited on the sample, yielding an image of the local magnetic field variation. Hallen et al.<sup>3</sup> used scanning Hall probes and Vu et al.<sup>4</sup> used scanning SQUID microscopy. Both methods directly measure the local magnetic fields of the vortices. Depending on the applied magnetic field, regions of periodically arranged vortices separated by domain walls are observed.<sup>2,3,4</sup> In Refs. <sup>5,6</sup>, we have reported on imaging results of the vortex dynamics in 2D arrays. We have discussed the vortex dynamics in 2D arrays in close analogy to the dynamics of Abrikosov vortices in the current-induced resistive state of thin-film type-II superconductors.<sup>7,8</sup>

## 2. Experimental Procedures

### 2.1. Samples

Figure 1 shows a typical array geometry. The arrays consist of square networks

of superconducting wires (Nb and PbInAu) with Josephson junctions placed between the line crossings. The Nb/AlO<sub>x</sub>/Nb junctions (area  $\approx 5 \mu\text{m} \times 5 \mu\text{m}$ ) have critical currents on the order of  $i_c = 150 \mu\text{A}$ . Typically, the  $1\sigma$ -spread in  $i_c$  is less than 3%.<sup>9,10</sup> Each of the junctions is externally shunted with an InAu resistor  $R_s$  of about  $1.5 \Omega$ , so the McCumber parameter is  $\beta_{c,j} = 2\pi i_c R_s^2 C / \Phi_0 < 0.7$ ;<sup>9</sup>  $\Phi_0 = h/2e$  is the flux quantum. The Josephson coupling energy  $E_J = \hbar i_c / 2e$  is about  $E_J \approx 10^{-20} \text{J}$  and is 5 to 6 orders of magnitude larger than the charging energy  $E_C = e^2 / (2C)$  ( $C$  is the junction capacitance). Hence, we deal with the classical limit, where charging effects can be neglected.<sup>11</sup> The bias current is fed to each of the array columns through InAu feeding resistors (not shown in Fig. 1) of about  $0.5 \Omega$  each. In 2D superconducting

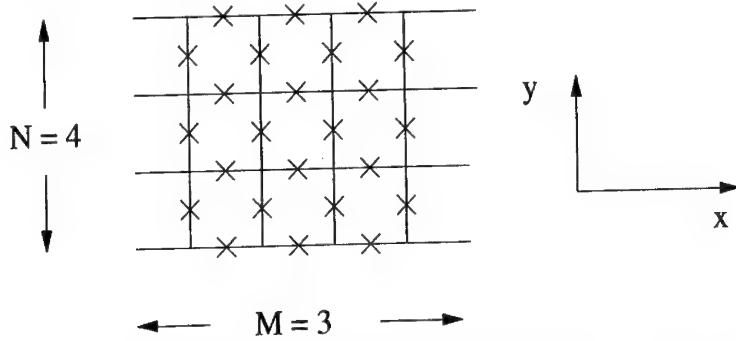


Fig. 1. Sketch of a typical array geometry with  $N$  columns of  $M$  junctions. The arrays consist of square networks of superconducting wires with Josephson junctions placed between the line crossings. Each junction is symbolized by a cross. The notation of the  $x$  and  $y$  direction is shown. The dc-bias current flows along the  $x$ -axis. The array voltage drop along the whole array is measured in the same direction.

arrays, flux quantization has to be taken into account so that the total sum of the junction phase differences  $\phi$  around a loop is related to the flux  $\Phi$  passing through the loop by

$$\sum_{\text{loop}} \phi = -2\pi \frac{\Phi}{\Phi_0} + 2\pi n, \quad (1)$$

where  $n$  is an integer. There are two contributions to  $\Phi$ :  $\Phi = \Phi^{\text{ext}} + \Phi_{i,j}^{\text{ind}}$ , where  $\Phi^{\text{ext}}$  is due to an external magnetic field perpendicular to the array, and  $\Phi_{i,j}^{\text{ind}}$  is the self-induced flux through the cell  $(i, j)$  due to the currents in the array.<sup>12</sup> The frustration  $f = Ba^2/\Phi_0$  is defined as the normalized applied flux per unit cell.  $B$  is the externally applied magnetic field. The size of the square array unit cell is  $a \approx 16.7 \mu\text{m}$ . The electromagnetic radius of the vortex is given by the magnetic penetration depth

$$\lambda_1 = \Phi_0 / (2\pi\mu_0 i_c), \quad (2)$$

where  $\mu_0$  is the permeability of the free space.<sup>13</sup> For our arrays,  $\lambda_{\perp} < a$ .

## 2.2. Electron beam imaging

Low temperature scanning electron microscopy (LTSEM) enables the spatially resolved investigation of superconducting devices and circuits during their operation at liquid helium temperatures. The basic principles are described in Ref.<sup>14</sup>. The essential points are the following: the sample film (on top of the substrate) is directly irradiated with an electron beam. The bottom side of the substrate is in contact with a liquid helium bath, thereby ensuring effective sample cooling. The temperature  $T$  of the sample is about 5 K. The electron beam focused at the coordinates  $(x_0, y_0)$  on the sample surface acts as a local heat source. The lateral dimension of the thermally perturbed area near  $(x_0, y_0)$  determines the spatial resolution of our images. This resolution is estimated to be about 3  $\mu\text{m}$  for the samples used in the present studies. Typical values for the beam voltage and current are 25 kV and 100 pA, respectively, yielding a local temperature increment of about 1 K.

The difference of the time scales of the array dynamics and of the scanning procedure is important. The junction oscillation period is on the order of 10 ps, whereas the decay time of the beam-induced thermal perturbation is about 100 ns.<sup>14</sup> During scanning, the electron beam typically stays 3 ms at each position. Hence, the measured sample response to the beam irradiation represents time-averaged information on the time scale of the Josephson dynamics.

The sample is shielded from dc and ac magnetic fields by means of  $\mu$ -metal screens at both room and liquid-helium temperature. Measuring the critical current as a function of the externally applied magnetic field  $B$ , we estimated the residual magnetic field to be smaller than 700 nT. This value corresponds to a frustration  $f < 1/10$ . During our measurements, the electron beam is scanned across the current-biased array. The beam is chopped at a frequency of 20 kHz, and the change in array voltage  $\Delta V(x_0, y_0)$  induced by the beam is phase-sensitively recorded using a lock-in technique. Near the beam focus, the junction is heated from about 5 K to 6 K, which reduces the junction critical current  $i_c$  by about 20%. In these experiments, the local heating induces an array voltage signal  $\Delta V(x_0, y_0) < 10\mu\text{V}$ .

## 3. Experimental Results and Discussion

In this section we present results of our spatially resolved investigations on two-dimensional Josephson-junction arrays.

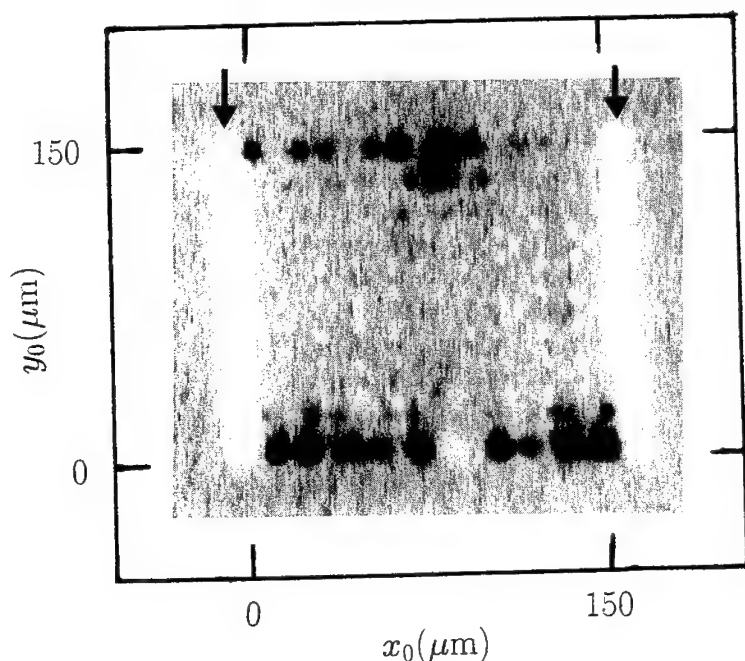


Fig. 2. Gray value representation of the voltage image  $\Delta V(x_0, y_0)$  of a  $10 \times 10$  array without groundplane at  $T \approx 5K$ . The array is biased at  $I_b \approx 0.9 I_c$ . The dc bias current flows horizontally through the array. The array boundaries lie between  $0 \mu m$  and  $150 \mu m$  in both directions. A positive (negative) electron beam induced voltage signal  $\Delta V(x_0, y_0)$  is indicated by the dark (bright) areas, whereas  $\Delta V(x_0, y_0) \approx 0$  is shown by the area surrounding the array. The signal level  $|\Delta V|$  is about  $100 \text{ nV}$ . The rows of the feeding resistors are marked by arrows.

### 3.1. The Subcritical Region: $I_b < I_c$

First, we report on measurements where the bias current  $I_b$  was chosen smaller than the critical current  $I_c$  of the array.

Figure 2 shows the voltage image  $\Delta V(x_0, y_0)$  for a  $10 \times 10$  array. The array is biased at  $I_b \approx 0.9 \text{ mA}$ . The array critical current is  $I_c \approx 1 \text{ mA}$ . Since  $I_b < I_c$ , the sample is in the zero-voltage state without e-beam irradiation. In Fig. 2, a positive (negative) signal  $\Delta V(x_0, y_0)$  is indicated by the dark (bright) areas, whereas the zero signal is shown by the gray level in the area surrounding the array.

Figure 2 is explained by edge nucleation of vortices induced by the self-field of the array's dc-bias current. The array's self-field is strongly peaked at the edges of the array (parallel to the bias current) and is antisymmetric with respect to the array center axis. Since for these studies  $\lambda_L < a$ , each magnetic flux quantum is confined

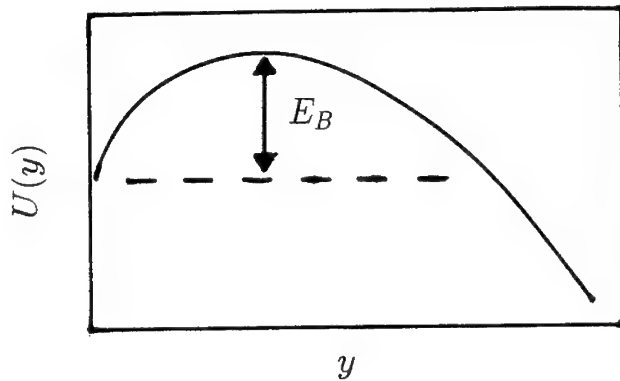


Fig. 3. Sketch of the energy  $U(y)$  of a single vortex versus the  $y$ -coordinate for a bias current smaller than the array critical current.

to one unit cell. When the array is biased below  $I_c$ , the current-induced vortices are pinned at the array edges. One edge of the array supports vortices, the opposite side antivortices. The entrance barrier  $E_B$ , which prevents the vortices from entering the array, can be calculated from the Gibbs energy of a single vortex in the array.<sup>5,15</sup>

Figure 3 shows a sketch of the Gibbs energy  $U(y)$  and  $E_B$  for bias currents smaller than the critical current.  $E_B$  is decreasing with increasing temperature  $T$ .

When the electron beam heats a junction at the edge of the array,  $E_B$  may be decreased below 0, and the vortices enter into the array. The vortices move perpendicular to the bias current and produce a voltage across the array. This process gives rise to voltage signals  $+\Delta V(x_0, y_0)$  at each junction where vortices have formed and are depinned by the local heating due to the electron beam. From the spatial dependence of  $\Delta V(y_0)$  we conclude that  $\lambda_L < a$ .

In Fig. 2, voltage signals  $\Delta V < 0$  of about -5 nV are observed at the positions of the feeding resistors (marked by arrows). The resistance change  $\Delta R = \Delta V/I_b$  is about  $-5 \mu\Omega$ . The origin of these signals is unclear.

Summarizing, for  $I_b < I_c$ , we observed electron-beam-induced vortex motion.

### 3.2. The Alternating Crossing Vortex Motion (ACVM)

Second, we report on measurements, where the bias current  $I_b$  was chosen slightly above the critical current.

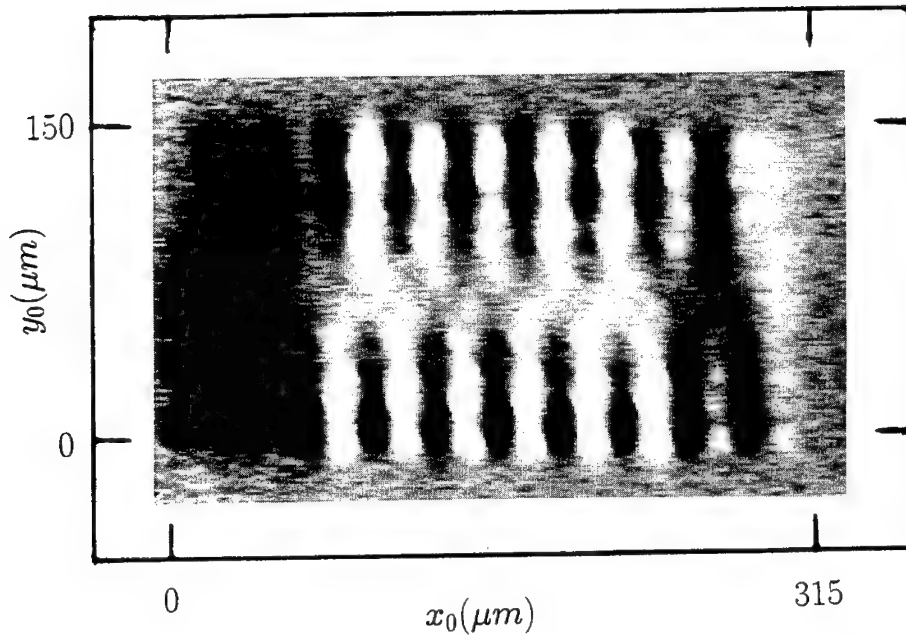


Fig. 4. Gray value representation of the voltage image  $\Delta V(x_0, y_0)$  of a  $20 \times 10$  array with a superconducting groundplane at  $T \approx 5$  K. The array is biased at  $I_b \approx 1.25$  mA and a corresponding voltage of 3 mV. The array critical current is  $I_c \approx 750 \mu A$ . The dc bias current flows horizontally through the array. The array boundaries lie between  $0 \mu m$  and  $150 \mu m$  in y-direction and between  $0 \mu m$  and  $315 \mu m$  in the x-direction. A positive (negative) electron beam induced signal  $\Delta V(x_0, y_0)$  is indicated by the dark (bright) areas, whereas  $\Delta V(x_0, y_0) \approx 0$  is shown by the gray value of the areas surrounding the array. The signal level  $|\Delta V|$  is about  $5 \mu V$ .

During their nucleation at the edges of the array, the vortices experience a Lorentz force perpendicular to the external current.

Figure 4 shows an imaging result for a  $20 \times 10$  array. In simple terms, this can be explained as follows: when a vortex moves across a junction, this junction phase slips and the resulting voltage drop causes dissipation. When the electron beam is focussed at a junction where vortices are moving across, the vortex motion is changed due to the junction critical current reduction caused by the e-beam. No voltage signal is observed when the e-beam is focussed at a junction at which no vortices are crossing. The imaging thus resolves the vortex tracks. From a more detailed quantitative analysis of our imaging,<sup>5</sup> we calculate that the junctions where vortices enter the array give a positive voltage signal  $\Delta V(x_0, y_0)$  (dark areas in Fig. 4). A negative



voltage change  $\Delta V(x_0, y_0)$  (bright areas in Fig. 4) is measured at the positions where the vortices leave the array.

Inspection of Fig. 4 shows that for the bulk of the array, vortices are nucleated at the upper edge and anti-vortices at the lower edge of the array. They subsequently move through the array, perpendicular to the bias current, until they reach the opposite boundary, where they leave the array. Along the current direction there is a strong tendency to alternate between the direction of the vortex/antivortex motion. We call this behavior alternating crossing vortex motion (ACVM). Such alternation is favored due to the repulsion between vortices of the same vorticity and attraction between vortices of opposite vorticity.

For bias currents very close to, but larger than  $I_c$ , we did not observe the ACVM but an uncorrelated vortex motion. With increasing  $I_b$  the ACVM area grows, starting from the inner part of the array. Increasing  $I_b$  beyond the region where the ACVM is observed, the vortex density is increased and we observe a more complicated vortex motion.<sup>6</sup>

Recent numerical simulations based on the actual array parameters<sup>16</sup> have reproduced the ACVM.

### Acknowledgments

We thank T. Hagenaaers and F. Hilbert for fruitful discussions, and D. Hoffmann for his help during the early stage of this work. S.G.L. was supported by the Studienstiftung Gerhard Rösch and by the EU through its "Human Capital and Mobility" Euroconference program. P.A.A.B. and S.P.B. are partially funded by the BMDO Office of Innovative Science and Technology with technical program management from Rome Laboratory, and partially supported by the Office of Naval Research. We gratefully acknowledge financial support from the EU under the program "Human Capital and Mobility" (Contract No. CHRX-CT92-0068) and from the BMFT under Grant No. 13N6436.

### References

- [\*] U.S. Government work not protected by U.S. copyright.
- 1. Conference volume *Coherence in Superconducting Networks, Proceedings of the NATO Advanced Research Workshop, Delft, The Netherlands, 1987*, [Physica B **152** (1987)]
- 2. K. Runge and B. Pannetier, Europhys. Lett. **24**, 737 (1993)
- 3. H.D. Hallen, R. Seshadri, A.M. Chang, R.E. Miller, L.N. Pfeiffer, K.W. West, C.A. Murray, and H.F. Hess, Phys. Rev. Lett. **71**, 3007 (1993)

4. L.N. Vu, M.S. Wistrom, D.J. Van Harlingen, Appl. Phys. Lett. **63**, 1693 (1993)
5. S. G. Lachenmann, T. Doderer, D. Hoffmann, R.P. Huebener, P.A.A. Booij, S.P. Benz, Phys. Rev. B **50**, 3158 (1994)
6. T. Doderer, S.G. Lachenmann, R.P. Huebener, P.A.A. Booij, S.P. Benz, to be published in IEEE Trans. Appl. Supercond.
7. R.P. Huebener, *Magnetic Flux Structures in Superconductors*, Springer-Verlag, Berlin, Heidelberg, New York (1979)
8. L.G. Aslamazov and A.I. Larkin, Sov.Phys.-JETP **41**, 381 (1975)
9. S. P. Benz and C. J. Burroughs, Appl. Phys. Lett. **58**, 2162 (1991)
10. S. P. Benz and C. J. Burroughs, Supercond. Sci. Technol. **4**, 561 (1991)
11. H.S.J. van der Zant, F.C. Fritschy, T.P. Orlando, and J.E. Mooij, Phys. Rev. B **47**, 295 (1993)
12. J.R. Phillips, H.S.J. van der Zant, J. White, and T.P. Orlando, Phys. Rev. B **47**, 5219 (1993)
13. K.K. Likharev, *Dynamics of Josephson junctions and circuits*, Gordon and Breach Science Publishers, New York (1986)
14. R.P. Huebener in: *Advances in Electronics and Electron Physics*, P.W. Hawkes, ed., Academic Press, New York, Vol. **70**, (1988), p. 1
15. H.S.J. van der Zant, H.A. Rijken, and J.E. Mooij, J. Low Temp. Phys. **79**, 289 (1990)
16. Th. Hagenaars, University of Utrecht, private communication (1994)

**IN-SITU SPATIALLY RESOLVED INVESTIGATIONS  
OF JOSEPHSON STRUCTURES WITH  
A SCANNING LASER MICROSCOPE**

J. HOLM AND J. MYGIND

*Physics Department, Technical University of Denmark  
DK-2800 Lyngby, Denmark*

**ABSTRACT**

Most of the experimental studies of the static and dynamical states in Josephson junctions are limited to measuring the current-voltage characteristic under various experimental conditions, which, however, only provides a spatially averaged information on the processes inside the junction. We have therefore constructed a simple and reliable Cryogenic Scanning Laser Microscope for *in-situ* spatially resolved investigations of Josephson junctions. Usually the dynamical processes are very sensitive to external noise, making it essential for a microscope of this kind to have a very low noise level. This is met in combination with the demands for a high spatial resolution using a laser beam emitted from a  $3.5\ \mu\text{m}$  diameter optical fiber mounted on a piezoelectric scanner. Recent measurements on static and dynamical states of Josephson junctions are presented and discussed.

## 1. Introduction

Due to recent improvements in the fabrication of integrated superconducting circuits based on Josephson tunnel junctions it has become important to understand in detail the very complex dynamics on which their operation is based. For many years the only way to characterize the junctions has been to investigate their dc properties under various experimental conditions, like measuring the current-voltage ( $IV$ ) characteristic and the critical current as function of magnetic field ( $I_c(H)$ ). Such integral experiments do not provide direct spatially resolved information on the dynamics of this highly nonlinear device.

Several attempts have been made to overcome this. Already in 1983 Scheuermann et al.<sup>1</sup> designed the first scanning laser microscope consisting of two parts: (i) A room temperature optical setup with a helium-neon laser and focusing optics, and (ii) a standard optical cryostat with windows providing access for the laser beam to the sample which is positioned on a cold finger in the vacuum space. Josephson junctions with various geometries were investigated in the static state by measuring the reduction of the critical current caused by heating the junction with a  $15\text{-}20\ \mu\text{m}$  diameter laser spot<sup>2</sup>.

Doderer et al.<sup>3</sup> utilized a conventional scanning electron microscope (SEM) in which the standard sample holder was replaced by a small liquid helium cryostat. The electron beam can be focused within a hundred nanometers so used as heating

source the resolution is limited only by the relevant thermal heating length which usually is 1-3  $\mu\text{m}$  for Nb/AlOx/Nb Josephson tunnel junctions on silicon substrates. The sample is mounted on a sapphire disk separating the SEM vacuum space from the liquid helium in the cryostat. The scanning is performed by moving the electron beam with magnetical mirrors.

We have constructed a Cryogenic Scanning Laser Microscope (CSLM) relying on the detection of the electrical response of the circuit to a very localized heating induced by irradiation with 675 nm wavelength light from a AlGaInP semiconductor laser mounted with an optical fiber. The scanning is performed by moving the fiber tip (kept a few micrometers above the chip) with a novel piezoelectric scanner, specially designed to meet the requirements for a large scanning range area. A scanning range well above 500  $\mu\text{m}$  has been demonstrated at 4.2 K.

Sec. 2 introduces the relevant physical models for CSLM experiments on a long Josephson tunnel junction, i.e. with a length  $L \gg \lambda_J$ , the Josephson penetration length. In Sec. 3 we give an overview of the microscope design and the experimental setup. In Sec. 4 we present and discuss the results. Sec. 5 concludes the paper.

## 2. A model for localized laser heating on superconductors

When light with an energy  $hf$  much larger than the energy gap  $\Delta$  is irradiated on a superconductor the photons will split the Cooper pairs and excite the hereby generated quasiparticles to high-lying states. Within a few picoseconds, the quasiparticles relax to the bottom of the conduction band in a phonon avalanche where they eventually undergo a recombination process to form Cooper pairs accompanied by an additional phonon emission. The phonons may break other pairs before they leave the film and spread into the substrate. For materials like Nb and Pb the phonon lifetime is shorter than the quasiparticle lifetime<sup>4</sup>. Furthermore, in the limit of high phonon trapping, it can be shown that the nonequilibrium structure generated by the laser beam can be adequately described by an effective temperature structure. Here we will for simplicity assume that the only effect of the beam irradiation is a local rise in the temperature at the laser-spot.

Let us consider a two-dimensional film of thickness  $d$  deposited on a substrate which has the bath temperature  $T_b$ . By assuming that the local temperature  $T$  of the film depends only on the distance  $r$  from the point of irradiation, we get the following heat diffusion equation in the stationary case:

$$\kappa \left( r^2 \frac{\partial^2 T}{\partial r^2} + r \frac{\partial T}{\partial r} \right) + \frac{\alpha}{d} r^2 (T - T_b) = \frac{S_A}{d} r^2 \quad (1)$$

where  $\kappa$  is the heat conductivity per volume of the film and  $\alpha$  the heat transfer coefficient per area between the substrate and the superconducting film.  $S_A = S_A(r)$  is the power per unit surface area of the Gaussian beam, i.e.

$$S_A(r) = \frac{2}{\pi w_0^2} P_0 e^{-2r^2/w_0^2} \quad (2)$$

where  $w_0$  is the Gaussian beam radius and  $P_0$  the optical power. The final resolution of the microscope measured as the full width half maximum of the temperature distribution then depends on a combination of  $w_0$  and the thermal healing length

$$\eta_0 = \left( \frac{\kappa d}{\alpha} \right)^{1/2} \quad (3)$$

Typically  $\eta_0 = 1\text{--}3\text{ }\mu\text{m}$  for Nb/AlOx/Nb-junctions on silicon substrates<sup>5</sup> and  $w_0 = 2\text{--}2.5\text{ }\mu\text{m}$  for laser beams from flat cleaved fiber ends just outside the near-field region<sup>6</sup>. This gives a resolution of  $4\text{--}5\text{ }\mu\text{m}$  in agreement with experiments. It should be noted that  $w_0$  may be significantly improved in a very simple way by fabricating small lenses directly at the end of the fiber or by shaping the end of the fiber itself,  $w_0 < 1.0\text{ }\mu\text{m}$  has been reported<sup>7</sup>.

We assumed before that the silicon substrate itself works as a thermal reservoir. This assumption has been tested by locally heating a  $12 \times 6 \times 0.625\text{ mm}$  large substrate with the laser beam from the single mode fiber and measure the reduction of the overall gap voltage of a Nb/AlOx/Nb long Josephson junction as function of power and the distance between the fiber and the junction. The reduction of the gap voltage was found to depend linearly on the optical power. By applying  $650\text{ }\mu\text{W}$  optical power, the largest available power for our system and more than 10 times the power usually needed in our experiments, we saw a reduction of the gap voltage of the order of  $1\text{ }\mu\text{V}$ , corresponding to an increase in temperature in the low mK range. This reduction was independent of the distance between laser beam and junction. From this we may conclude that the silicon chip works as a excellent thermal reservoir.

### 3. The microscope

The CSLM is mounted with a damped spring system to the bottom flange of a standard cryogenic test probe in order to reduce interference from extraneous mechanical vibrations. The probe with built-in electronics may be used in helium cryostats or directly immersed in an ordinary liquid helium transport vessel. In this way we can mount and thermally cycle samples several times per day, still keeping the operational costs low. Cooling from  $273\text{ K}$  to  $4\text{ K}$  takes 1 hour with the use of  $1.5\text{ l}$  liquid helium. The evaporation rate caused by the microscope during experimental runs is only  $30\text{--}40\text{ ml/hour}$ .

A schematic diagram of the experimental setup is shown in Fig. 1. A personal computer with a standard A/D interface is used interactively to perform the scanning process. The signal from the computer is led to a pair of high-voltage amplifiers able to deliver a voltage swing of  $\pm 200\text{ V}$  to the piezo-scanner from two mutually inverted outputs. The heating source is a commercially available laser diode mounted to a single mode optical fiber with a core diameter of  $3.5\text{ }\mu\text{m}$ . The optical output of the laser is usually modulated in the frequency range  $4\text{--}8\text{ kHz}$  by the signal from the reference oscillator in the lock-in amplifier which is also used for detection of the response signal from the sample under investigation.

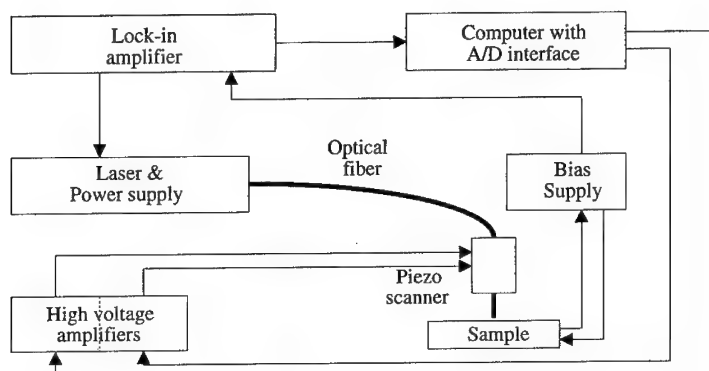


Fig. 1. Experimental setup for the CSLM. The semiconductor laser output power is modulated by the reference oscillator in the lock-in-amplifier.

A maximum scan rate of 40 lines per second is given by the software and not by the high-frequency cut-off of the piezo-scanner. Normally we use a scan rate of a few lines per second in order to utilize the low-pass filtering of the output signal from the lock-in amplifier.

In order to achieve this relatively large scanning range we have implemented a novel piezoelectric scanner consisting of two series-connected cantilevered bimorph actuators mounted perpendicular to each other. The design is shown in Fig. 2. By applying a voltage  $V$  to one outer electrode of the bimorph and  $-V$  to the other and keeping the center electrode voltage constant, the bimorph will bend and move the fiber tip horizontally with respect to the sample. The displacement of the fiber tip  $\Delta x_s(V)$  (or  $\Delta y_s(V)$ ) is

$$\Delta x_s(V) = \left(\frac{l_x}{t_x}\right)^2 \frac{d_{31}}{2} V \left(1 + \frac{2r_x}{l_x}\right) \quad (4)$$

where  $l$  and  $t$  is the length and the thickness of the single piezo-electric plate, respectively, and  $d_{31}$  is the piezoelectric constant. The total scanning range is then  $2\Delta x_s(V)$  and  $2\Delta y_s(V)$  respectively, since the voltage of each electrode in our setup can be reversed utilizing the dual output of the high voltage amplifiers. The piezoelectric constant  $d_{31}$  depends on the operating temperature and it is therefore necessary to calibrate the bending of the bimorph at the actual temperature. By utilizing the optical resonance effect between the flat fiber tip and the sample surface when the scanner is dilatated by employing the same voltage to both center electrodes, we observe a weak modulation of the response signal from the junction corresponding to a periodicity of half an optical wavelength when it is biased in the thermal tunneling regime. For the piezoelectric constant we find  $d_{31} = 47 \cdot 10^{-12}$  m/V at 4.2 K, which is in excellent agreement with other experiments<sup>8</sup>.

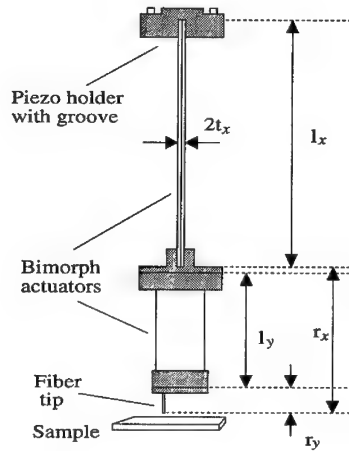


Fig. 2. The piezo-scanner consisting of two cantilever mounted bimorph actuators oriented perpendicular to each other. Typical dimensions in millimeters are:  $(l_x, t_x) = (42, 0.35)$  and  $(l_y, t_y) = (20, 0.4)$ .

Fine alignment of the fiber tip relative to the sample is performed by moving the entire piezoscanner with a mechanical alignment system that during experiments is operated from the top of the cryoprobe. The vertical alignment (perpendicular to the sample surface) of the fiber relative to the sample surface is performed by a differential screw moving the piezoscanner  $50 \mu\text{m}$  per turn. The horizontal fine-positioning (parallel to the sample surface) is performed by two spindle driven wedges made so that one turn of the spindle corresponds to  $80 \mu\text{m}$ . The total horizontal operating range is  $3.5 \text{ mm} \times 3.5 \text{ mm}$ .

The beam emanating from the fiber end can within a distance of  $20\text{--}30 \mu\text{m}$  from here be considered collimated, so as long as the sample is in this region, vertical aligning is not critical. If we increase the distance between the sample surface and the fiber end to  $50 \mu\text{m}$ , the half power width of the beam is only  $6 \mu\text{m}$ , which still is usable for many practical applications.

#### 4. Measurements

##### 4.1. Quasiparticle tunneling distribution

Assume that a long Josephson junction is current biased in the subgap region, and that it is operated in the weak perturbation limit. It can then be shown that the change in measured voltage  $\delta V$  as function of beam position  $(x, y)$  can be written as<sup>9</sup>

$$\delta V_{qp}(x, y) \simeq \frac{\partial V}{\partial I} \Big|_{I=I_b} \frac{\sigma_n(x, y)}{e} K_0 \quad (5)$$

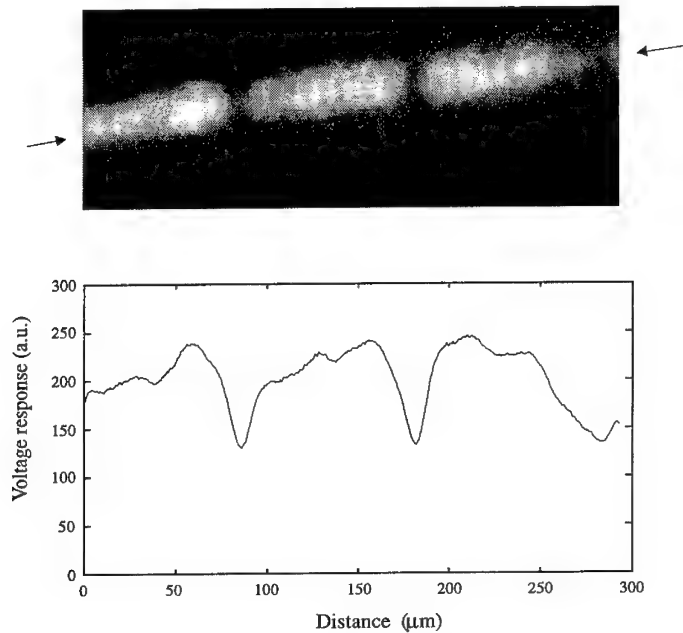


Fig. 3. Quasiparticle tunneling distribution of a  $5\text{ }\mu\text{m}$  wide inhomogeneous long Josephson tunnel junction. The picture, not drawn to scale, showing a sample area of  $300 \times 35\text{ }\mu\text{m}^2$ , was recorded in 7 min. with a scan rate of 1.2 lines per second in an 8 bit resolution. Besides demonstrating a high resolution, it also proves the long term stability of the CSLM. The arrows mark the position and the direction of the line-scan shown below the image.

where  $\sigma_n$  is the normal state conductance and  $\mathcal{K}_0$  a constant. As long as the perturbed area is kept small compared to the entire junction area,  $\partial V/\partial I$  is the differential resistance of the unperturbed junction at the bias point,  $I_b$ . Fig. 3 shows an image of a part of a  $5\text{ }\mu\text{m}$  wide and  $500\text{ }\mu\text{m}$  long Josephson junction fabricated with  $5\text{ }\mu\text{m}$  wide inhomogeneities placed with a mutual distance of  $100\text{ }\mu\text{m}$ . The voltage response reflects the variation of the quasiparticle tunneling conductance caused by the inhomogeneities as expected from Eq. (5). Dark regions correspond to minimum response signal, white to maximum. The arrows mark the direction and position of the linescan shown below.

If the junction is biased at the gap, its local variation can no longer be neglected and it can be shown that the change in the quasiparticle tunneling current,  $\delta I_{qp}$  reflects the local gap voltage. Therefore when scanning a long Josephson junction having a spatially inhomogeneous gap, only those regions where  $V_{bias} = 2\Delta(x, y)/e$  yield a large signal. Hence, the spatial distribution of the gap state inside the junction can be measured by recording a series of scans at different bias points. It can be shown



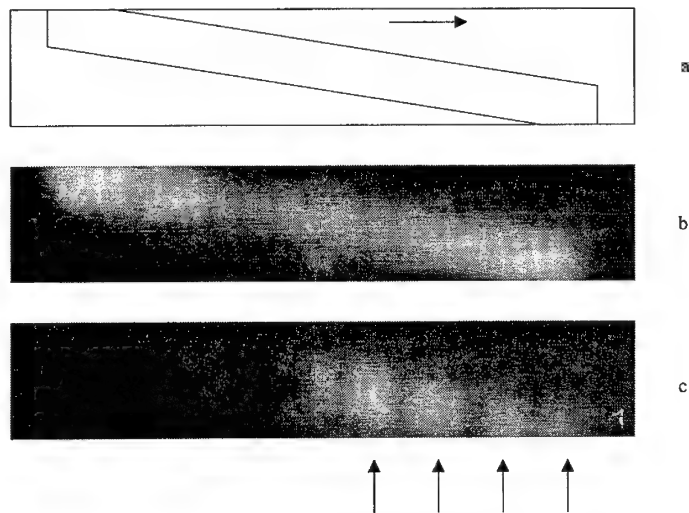


Fig. 4. a)-Sketch of the junction in the scanning window. The horizontal arrow indicates the scan direction in b) and c). b)-Voltage response from the junction when biased in the subgap regime at  $V = 2.4$  mV below the gap voltage but above the flux flow region. c)-Voltage response with the junction biased at 0.7 mV with an applied magnetic field.

that positions where we observe a larger quasiparticle tunneling conductance, e.g. a microshort, correspond to a lowering of the gap voltage<sup>9,10</sup>.

#### 4.2. Flux flow oscillators

The unidirectional viscous flow of magnetic flux quanta in long Josephson junctions with high damping has recently been successfully used for the development of local oscillators for fully superconducting integrated sub-mm wave receivers<sup>11,12,13</sup>. The CSLM has been used to investigate samples containing these so-called flux flow oscillators (FFO). Fig. 4a shows a sketch of the  $500 \times 5 \mu\text{m}^2$  large FFO placed in the scanned area. Fig. 4b shows the voltage response recorded with the FFO biased near the gap voltage at 2.4 mV above the flux flow region. The voltage response shown in Fig. 4c is obtained with a bias point at  $V = 0.7$  mV below the flux flow region in the presence of a magnetic field. It is noteworthy that the distance between the peaks (marked with vertical arrows) is around  $60 \mu\text{m}$ . This example demonstrates that we without any special precautions are able to *in-situ* trace out a dynamical state of the flux flow oscillator. This work is in progress. Experiments on one- and two-dimensional arrays, stacked junctions as well as on high- $T_c$  flux flow devices are in preparation.

## 5. Concluding Remarks

We have constructed a novel cryogenic scanning laser microscope where in contrast to earlier designs, the entire microscope including sample stage, piezoelectric scanner and mechanical alignment system is maintained at low temperatures in a compact design. Due to the small interference from electromagnetic noise and mechanical vibrations, the microscope is well suited for spatially resolved *in situ* experiments on operating Josephson junction circuits. The sample can be directly cooled by the cryogenic liquid (He or N<sub>2</sub>). External magnetic fields may be applied without influencing neither the movement of the fiber tip nor the spatial resolution. Experiments performed on various geometries of long Josephson junctions have demonstrated that the CSLM may work as an important diagnostic tool in the development of fully integrated superconducting receiver systems.

## Acknowledgements

We thank T. Doderer, S. G. Lachenmann, V. Koshelets, A. Petraglia and A. V. Shchukin for valuable discussions. The Human Capital and Mobility programme are acknowledged for financial support.

## References

1. M. Scheuermann, J. R. Lhota, P. K. Kuo and J. T. Chen, *Phys. Rev. Lett.* **50** (1983) 74.
2. J. R. Lhota, M. Scheuermann, P. K. Kuo and J. T. Chen, *Appl. Phys. Lett.* **44** (1984) 255.
3. T. Doderer, H.-G. Wener, R. Moeck, C. Becker and R. P. Huebener, *J. Low Temp. Phys.* **56** (1984) 237.
4. R. Gross and m. Koyanagi, *J. Low Temp. Phys.* **60** (1985) 277.
5. S. G. Lachenmann, T. Doderer, R. P. Huebener, D. Quenter, J. Niemeyer and R. Pöpel, *Phys. Rev.* **B48** (1993) 3295.
6. D. J. Butler, K. A. Nugent and A. Robert, *J. Appl. Phys.* **75** (1994) 2753.
7. P. D. Bear, *Appl. Opt.* **19** (1980) 2906.
8. K. G. Vandervoort, R. K. Zasadzinski, G. G. Galicia and C. W. Crabtree, *Rev. Sci. Instrum.* **64** (1993) 896.
9. R. Gross and D. Koelle, *Rep. Prog. Phys.* **57** (1994) 651.
10. J. Holm, Ph.D. Thesis, Technical University of Denmark (1994).
11. A. V. Ustinov, T. Doderer, R. P. Huebener, J. Mygind, V. A. Oboznov and N. F. Pedersen, *IEEE Trans. on Appl. Supercond.* **3** (1993) 2287.
12. V. P. Koshelets, A. V. Shchukin, S. V. Shitov and L. V. Filippenko *IEEE Trans. on Appl. Supercond.* **3** (1993) 2524.
13. Y. M. Zhang, D. Winkler and T. Claeson, *Appl. Phys. Lett.* **62** (1993) 3195.

---

Chapter 9

**Electronic Applications**

## INTEGRATED FLUX FLOW OSCILLATORS FOR SUB-MM WAVE RECEIVERS\*

V.P. KOSHELETS, S.V. SHITOV, A.V. SHCHUKIN,  
L.V. FILIPPENKO, I.L. LAPITSKAYA

*Institute of Radio Engineering and Electronics, Russian Academy of Sciences,  
Mokhovaya St. 11, Moscow 103907, Russia,*

and

J. MYGIND

*Physics Department, Technical University of Denmark, B309, DK-2800 Lyngby, Denmark*

### ABSTRACT

The concept of a fully integrated superconducting receiver looks very attractive especially for sub-mm astronomy and space research where low weight and volume are required. In order to realize a fully superconducting receiver one should integrate on a few chips the different planar components: a SIS mixer detector with quasioptical antenna, a superconducting local oscillator (LO), an intermediate frequency amplifier and the circuits for digitizing of down-converted signals and their real time processing. The SIS mixer itself is undoubtedly the best choice as low noise front-end detector at frequencies from 100 to 1000 GHz; its noise temperature is limited only by the fundamental quantum value  $\sim hf/k$ . All other components for proposed integrated receiver are still under investigations. One of the best LO candidates is the Flux-Flow Oscillator (FFO) based on unidirectional and viscous flow of magnetic vortices in a long Josephson tunnel junction with high damping. The frequency of the Flux-Flow Oscillator (FFO) can be tuned in a wide range and is limited only by the superconducting gap frequency; moreover the FFO provides sufficient output power to pump SIS array mixers. In combination this is why the simple and reliable FFO looks so promising as local oscillator for integrated submillimeter wave receivers.

Superconducting FFO, integrated on the same chip with the microwave detector, have been investigated in the frequency range 100 - 850 GHz. The possibility of adjusting the FFO frequency and power by changing the magnetic field and /or the bias current has been demonstrated and an available microwave power as high as 5  $\mu$ W has been detected at 440 GHz. A front-end noise temperature of 85 K has been measured at 140 GHz for a waveguide integrated receiver with a FFO.

A first implementation of a real integrated quasioptical receiver for frequencies up to 500 GHz is described. The one-chip receiver comprises a double dipole antenna, SIS mixer and Josephson FFO with matching circuits. The results of extensive investigations of the integrated receiver are presented.

\* Research was supported in part by the International Science Foundation (Contract MCH000), the Russian Program of Fundamental Research (G 92-02-3484), NATO (LG 921040), and the Danish Research Academy.

## 1. Introduction

There is an urgent need for fully integrated receiver in the field of sub-mm space astronomy where low weight, power consumption and volume are required. The integrated receiver should comprise different planar components: a SIS mixer detector with quasioptical antenna, a superconducting local oscillator (LO), an intermediate frequency amplifier and the circuits for digitization of down-converted signals and their real time processing. The SIS mixer itself is undoubtedly the best choice for a low noise front-end detector at frequencies from 100 to 1000 GHz. In the past few years SIS heterodyne receivers have been successfully used in radio astronomy for observation of spectra showing the lowest possible noise temperature in the mm and sub-mm wave range. The noise temperature of a SIS mixer is ultimately limited by the fundamental quantum value  $\sim hf/k$ <sup>1</sup>. All other components for proposed integrated receiver are still under investigations.

At high frequencies (above 100 GHz) the lack of compact and easily tuneable local oscillators is a serious problem that motivates the direct on-chip integration of the superconducting local oscillator with the SIS mixer. The two major types of circuits which have been successfully used for the mm and sub-mm superconducting LO: synchronous arrays of the lumped Josephson junctions<sup>2-4</sup> and long Josephson junctions where fluxon motion takes place<sup>5-8</sup>. For the synchronous arrays large output power (up to 40  $\mu$ W) has been obtained at frequencies about 400 GHz in a matched load<sup>4</sup>; but no linewidth narrower than 10 MHz has been measured for Josephson 10-junctions array<sup>3</sup>. Two different modes of oscillations in long tunnel junctions can be used as microwave source: i) resonant soliton motion (at weak applied magnetic field in a junction with low damping), conventionally this device is called the soliton oscillator; ii) unidirectional and viscous magnetic flux-flow (at relatively large magnetic field applied) in a junction with high damping. The soliton oscillator has very narrow linewidth<sup>5</sup>, but its frequency is strictly determined by the junction length. Only a relatively small power can be delivered to the load in this case. The frequency of the Flux-Flow Oscillator (FFO)<sup>6-8</sup> can be tuned in a wide frequency range and is limited only by the superconducting gap frequency. Moreover the FFO provides nearly sinusoidal output with low content of higher harmonics and sufficient power to pump SIS array mixers. In combination this is why the FFO in our opinion looks so promising as local oscillator for integrated submillimeter wave receivers.

Superconducting FFO, integrated on the same chip with the microwave detector, have been investigated over the frequency range 100 - 450 GHz<sup>8-10</sup>. The possibility of adjusting the FFO frequency and rf power has been demonstrated and an available microwave power as high as 0.3  $\mu$ W has been detected at 375 GHz. The spectral linewidth of the FFO was about 1 MHz, as has been inferred from different mixing experiments<sup>8-10</sup>. A front-end noise temperature (DSB) of 85 K of a waveguide receiver with FFO has been achieved at 140 GHz<sup>8</sup>.

Superconducting intermediate frequency amplifiers ( $f_{IF} \sim 100$  MHz) have been realized on the base of dc SQUIDs with noise temperatures about 1 K<sup>11, 12</sup>. Important advantages of the IF SQUID Amplifier (SQA) are: i) its extremely low power dissipation ( $< 1$  nW); ii) its small size ( $\sim 1$  mm<sup>2</sup>); iii) full electrical and temperature compatibility with the superconducting sensitive devices such as Josephson and SIS mixers. The signal frequency of the SQA can be considerably raised by increasing the frequency of "parametric pump" (e.g. Josephson frequency) as well as by using a multi-loop SQA with integrated input circuits. In order to increase the SQA bandwidth one can use a parallel combination of single amplifiers with slightly different frequencies.

A superconducting digital correlator might be used as a back-end device for a fully integrated receiver. The proposed concept<sup>13</sup> is based on the employing the ultrafast RSFQ elements<sup>14, 15</sup> in the digital sign correlator architecture that is well developed for semiconductor circuitry. One of the most important features of the new approach is a possibility of cascading of relatively simple "building blocks" (each with about 1000 Josephson junctions) which will be connected only by low frequency (about 1 GHz) lines.

The integration of SIS mixer, planar antenna and FFO together with the circuits for analog to digital conversion and real time data processing provides an excellent opportunity for the realization of a modular satellite cryogenic receiver. This receiver will have according to our estimations unique parameters: low noise temperature (only 10 times above the quantum limit) at frequencies possibly as high as 700 GHz, good spectral resolution (better than 1 MHz over a 1 GHz bandwidth), and low power dissipation (about 1 W), and high reliability.

In this report the results of a comprehensive study of the dc and high frequency properties of the FFO are described. The first encouraging result of the integration of a SIS mixer with planar quasioptical antenna and a FFO for frequency around 500 GHz is also presented.

## 2. Fabrication of the Integrated Circuits

The technological procedure for fabrication of high quality Nb-AlO<sub>x</sub>-Nb junctions and integrated circuits<sup>16, 17</sup> is based on well known Selective Niobium Etching and Anodization Process (SNEAP)<sup>18,19</sup>. Nb-AlO<sub>x</sub>-Nb trilayer is deposited in oil free vacuum system equipped with DC and RF magnetrons and a liquid nitrogen Meisner trap. The background pressure in this configuration typically is better than  $5 \cdot 10^{-7}$  mbar. All layers were deposited on substrates thermally attached to a water-cooled copper substrate holder. Nb base and counter electrodes (thickness  $d = 200$  nm and  $100$  nm, respectively) were deposited by DC magnetron sputtering (rate  $v = 3$  nm/s), Al - by RF magnetron sputtering ( $v = 0.2$  nm/s).

The junction area was defined by Reactive Ion Etching (RIE) in a mixture of CF<sub>4</sub> + 15% O<sub>2</sub>. In order to decrease the stray capacitance SiO (or SiO<sub>2</sub>) layer ( $d = 250$  nm)

was used; RIE photoresist pattern was employed as a mask for the SiO ( $\text{SiO}_2$ ) layer lift-off process (self alignment contact). After RIE but before insulator deposition a "light" anodization up to 10 - 20 V was carried out to avoid microshorts at the lateral sides of the Nb electrodes that could be insufficiently covered by insulator layer. The final step of junction fabrication is the Nb wiring electrode deposition ( $d = 400 \text{ nm}$ ) which was performed after RF sputter cleaning. The geometry of the wiring layer was defined by lift-off process.

The reproducible fabrication of very small area junctions (about  $1 \mu\text{m}^2$ ) by optical photo-lithography is problematic because of light diffraction during photoresist exposure at so small dimensions. To overcome this problem the small area junctions are prepared in a two-step procedure. Firstly a comparatively long (length about  $10 \mu\text{m}$ ) and narrow (width about  $1.3 \mu\text{m}$ ) junction is defined. After second line orthogonal to the long junction is patterned; and the square junction was realized on the crossing of the lines. In our RIE set-up it is possible to provide controllable underetching about 0.1 - 0.3  $\mu\text{m}$  per one side of the photoresist stencil. So it is possible to decrease the linear dimensions of the junctions from  $1.3 \mu\text{m}$  (which can be obtained by regular optical lithography) to approximately 0.8 -  $1 \mu\text{m}$ . In consequence the high quality submicron Nb- $\text{AlO}_x$ -Nb junctions (areas as low as  $0.7 \mu\text{m}^2$ ) have been successfully fabricated and used as the elements of superconducting integrated circuits.

The intrinsic stress in the junction electrodes deteriorates a junction quality. The relaxation of the stress during Nb patterning leads to the breakdown of a tunnel barrier and creates the microshorts which shunt the SIS junctions. The value of the stress depends on the dc voltage in the discharge during Nb sputtering. The conditions for preparation of the stress-free films have been determined in special experiments<sup>16</sup>. The optimal conditions for sputtering of zero-stress Nb films in our case are realized at 300 W power and  $10^{-2}$  mbar argon pressure resulting in 220 V dc voltage. The typical IV curves for junctions fabricated at optimal conditions are shown in the Fig. 1. The IVC of the series/parallel array<sup>20</sup> is presented in Fig. 1b; the area of each junction in the array is  $1 \mu\text{m}^2$  and all four junctions in the array are connected in parallel for dc current. One can see that the junctions prepared at optimal conditions demonstrate high quality characteristics with an subgap to normal state resistance ratio  $R_j/R_n$  up to 50 and the gap smearing of about 200  $\mu\text{V}$  even for junction areas as small as  $1 \mu\text{m}^2$ .

For Large Scale Integration (LSI) circuits based on Nb- $\text{AlO}_x$ -Nb junctions we have developed a technological process for multilayer circuits fabrication and successfully employed it for the preparation of the RSFQ and microwave microcircuits<sup>15,17,20</sup>. The quality of the insulation layers between superconducting electrodes is serious problem for LSI circuits. We use the combination of the double layer SiO ( $\text{SiO}_2$ ) film and "light" anodization up to 10 - 20 V to obtain good insulation between Nb electrodes. Special experiments have shown perfect insulating properties even for a few  $\text{mm}^2$  overlap area of the Nb electrodes.

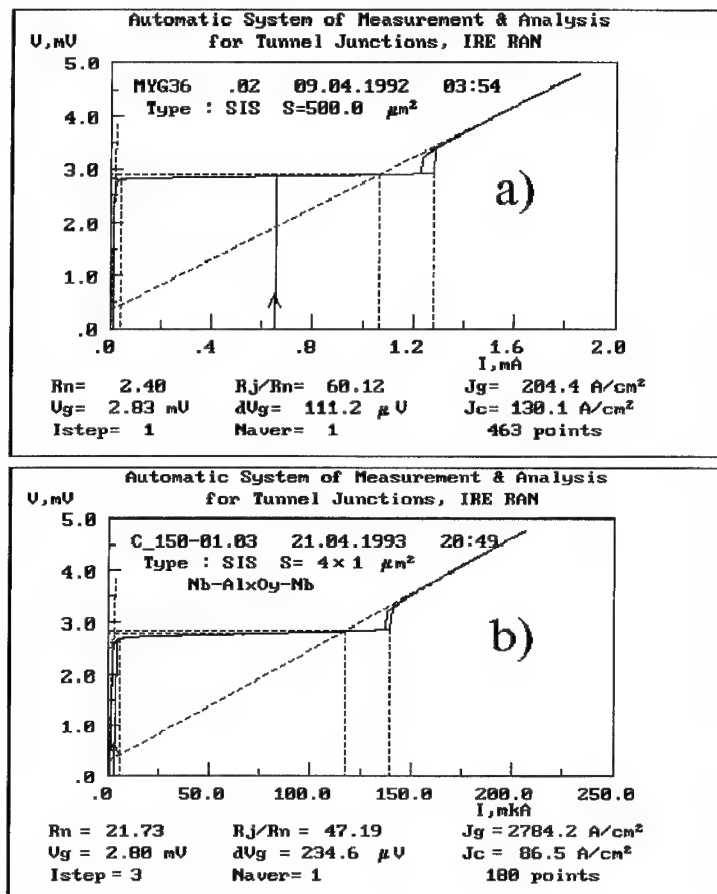


Fig. 1 IVCs of high quality Nb-AlO<sub>x</sub>-Nb junctions fabricated at optimal conditions, and measured by data acquisition system:

a) IVC of large area junction. Note that even for area 500  $\mu\text{m}^2$  the tunnel oxide is uniform and of excellent quality.

b) IVC of series/parallel SIS mixer array. The array comprises four 1  $\mu\text{m}^2$  area junctions which are connected in parallel for dc current. It should be noted that for junction area as low as 1  $\mu\text{m}^2$  the R<sub>j</sub>/R<sub>n</sub> ratio about 50 can be obtained in a complicated microwave circuit with tuning elements.



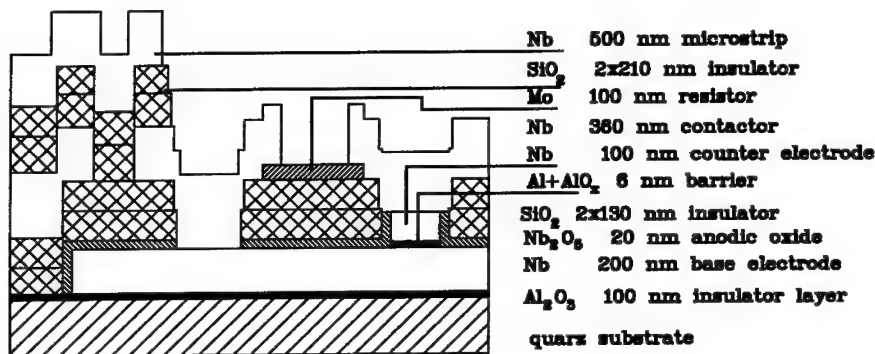


Fig. 2 Schematic cross-section of the FFO multilayer integrated circuit.

The schematic cross section of FFO multilayer structure is shown in the Fig. 2. One can see three superconducting layers: two Nb electrodes of the tunnel junction and the Nb film of the superconducting microstrip (upper left Nb layer); the Mo (or Ti) resistor is placed on the SiO<sub>2</sub> insulator layer in the upper part of the circuit; the Al oxide layer has been used for protection of a silicon or quartz substrate during RIE. The total number of different layers in these circuits may be as high as 11.

### 3. Experimental system

For a comprehensive study of the FFO properties different integrated circuits comprising long Josephson junctions and microwave SIS detectors have been designed. Fig. 3 shows: a) a cross-section; b) a layout; and c) a simplified equivalent diagram of one of the tested on-chip integrated circuit. The circuit comprises two identical FFOs (FFO1 - "10" and FFO2 - "11"; junction length,  $L = 200 \mu\text{m}$ , width,  $W = 1.5 \mu\text{m}$ ), a SIS mixer array detector with a capacitance-tune-out circuit ("14", area,  $S = 1.3 \times 1.3 \mu\text{m}^2$ ), three impedance matching transformers ("9", "12" and "13"), and a fin-line antenna ("8"). The tuning-out inductance for the two SIS junction (parallel dc biased<sup>20</sup>) array ("14") and the transformers ("12", "13") were designed for optimum performance at 450 GHz. All microcircuits had three superconducting Nb layers and two double insulating SiO layers. The integrated circuits have been fabricated with a technique developed for producing SIS mixer elements and Rapid Single Flux Quantum, RSFQ, digital devices<sup>17</sup>. Details of the circuit design and experimental set-up will be described elsewhere<sup>21</sup>. The high quality Nb-AlO<sub>x</sub>-Nb tunnel junctions have a critical current density,  $j_c = 8 \text{ kA/cm}^2$ , and a Josephson penetration depth,  $\lambda_j = 4 \mu\text{m}$ . The product of the normal state resistance and the junction area,  $R_n S$ , is  $25 \Omega \mu\text{m}^2$ .

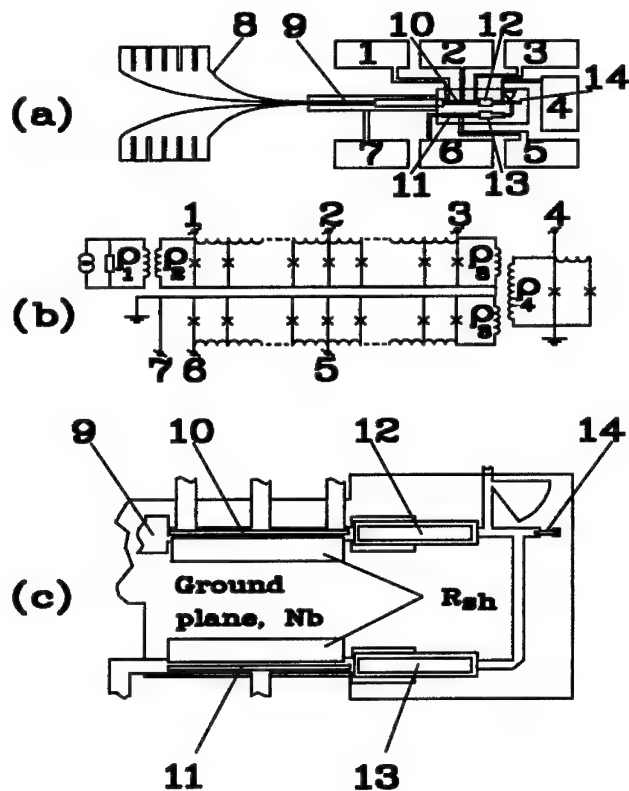


Fig. 3 Schematic drawing (a), simplified equivalent diagram (b) and central part (c) of the experimental on-chip integrated circuit. "1" - "7" - contact pads; "8" - fin-line antenna; "9", "12", "13" - Chebyshev impedance matching transformers; "10" - FFO1; "11" - FFO2; "14" - two junction SIS array with tuning-out circuit.

For investigation of the properties of the autonomous FFO we used a simplified version of the described above integrated circuit. The test circuit consists of two independent parts; each comprises identical FFO (length,  $L = 500 \mu\text{m}$ , width,  $W = 4.5 \mu\text{m}$ ), a SIS mixer array detector (area,  $S = 1.1 \times 1.1 \mu\text{m}^2$ ) with capacitance tune-out elements and impedance matching transformer. The tuning-out inductance for the two SIS junctions array (connected in parallel for both dc and rf currents) and two step impedance transformers were differently designed: one for wide-band operation around the 400 GHz central frequency (circuit WB); and other one for 600 GHz frequency range (HF).

#### 4. Properties of the autonomous FFOs

Typical FFO I-V characteristics (IVC) measured for the test circuits WB and HF at different values of the magnetic field, produced by a current,  $I_{c,l}$ , through a control line are shown in Fig 4; the dependence of the FFO critical current  $I_c$  on control line current  $I_{c,l}$  is presented in Fig. 5. The control line was integrated in the base electrode of the FFO. We used a small value resistor ( $R \leq 1$  Ohm) incorporated in the base electrode in order to disconnect superconducting film. Both the usual "overlap" geometry and geometry with special "finger" layout for uniform bias current distribution<sup>8</sup> result in very similar IVCs and  $I_c(I_{c,l})$  dependencies. It should be noted that for WB and HF circuits the FFO had extended overlap (length about  $50 \mu\text{m}$ )<sup>6, 8</sup> where bias current was not supplied. These unbiased "tails" considerably decrease the self-field effects and results in very steep flux-flow steps in the IVCs.

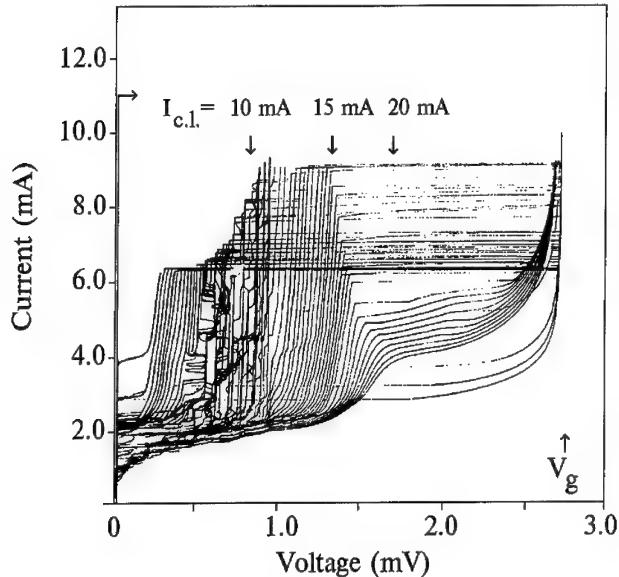


Fig. 4: IV-characteristics of the FFO at different magnetic fields produced by the integrated control line.

The peculiarities of the IVCs at voltages below  $900 \mu\text{V}$  are typical for our FFOs. They are fully reproducible and might be explained by some remain of external or internal resonances. The damping parameter  $\alpha$  is very low for our junctions (typically  $\alpha \sim 0.01$ ) and even at a reduced length of  $l = L/\lambda_J \sim 100$  we have non-pure flux-flow regime for  $V < 900 \mu\text{V}$ . At higher voltages the surface losses of the films,  $\beta$ , start to play a more significant role, because of strong frequency dependence of the quality factor  $Q_j$ :

$$Q_j = \{ \alpha + \beta * (f / f_p)^2 \}^{-1}, \quad (1)$$

where  $f_p$  is the maximum plasma frequency. The peculiarities at low voltages can not be attributed to resonances in the external microwave system, because very similar behaviour is observed also for "naked" FFOs (not integrated with transformers and detectors).

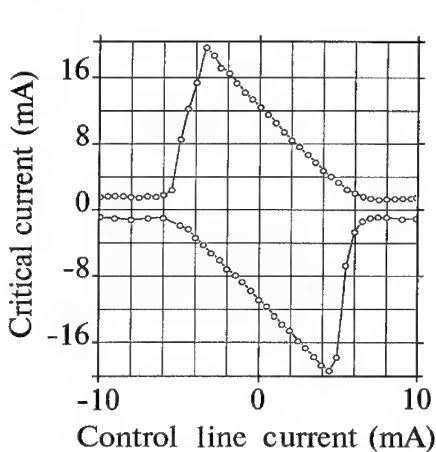


Fig. 5 Dependence of the FFO critical current on control line current,  $I_{c,1}$ .

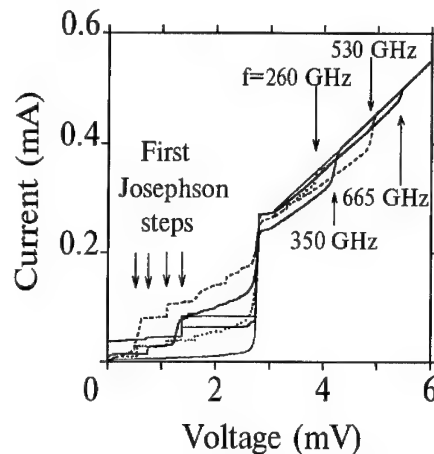


Fig. 6 IVCs of the SIS detector (wide band design) pumped by FFO at different frequencies.

Numerous experiments where microwave power was detected from similar FFOs by different SIS elements and transformers have demonstrated that the FFO itself can oscillate in a very wide frequency range. The IVCs of the SIS detector (test circuit WB) pumped by the FFO at different frequencies are shown in Fig. 6. One can see that there is enough power to pump the SIS mixer in a wide frequency range from 250 up to 650 GHz, especially taking into account that microwave detector in this case comprises two parallel connected SIS junctions. The highest detectable frequency was as high as 850 GHz significantly above the gap frequency,  $f_g = 2eV_g/h$ . The dependence of the first Josephson step on the FFO frequency is shown in Fig. 7 for HF integrated test circuit. The SIS detector in this case was shunted by 10 Ohm resistor what simplify the Josephson steps detection. Note the well-defined Riedel peak at frequency 635 GHz that corresponds to the gap voltage of the junction,  $V_g = 2.63$  mV.

The possibility of FFO microwave power adjustment at constant frequency is demonstrated in Fig. 8. It was possible to tune the microwave power by changing of the FFO dc bias current at approximately constant FFO voltage (moving mainly along the so-called flux-flow steps (FFS) or velocity matched steps (VMS) see Fig. 4). The microwave power received by the detector was measured by recording of the critical current and Josephson step power-dependent amplitude. At the 440 GHz it was possible to suppress the critical current of the shunted junction ( $I_c = 1.3$  mA,  $R_n = 2.2$  Ohm) to zero and realize the maximum amplitude of the first Josephson step  $\Delta I_1 = 0.55$  mA. It corresponds to an amplitude of the microwave current in the detector  $I_0 \approx 1.8$  mA and a delivered power of about  $5 \mu\text{W}$ .

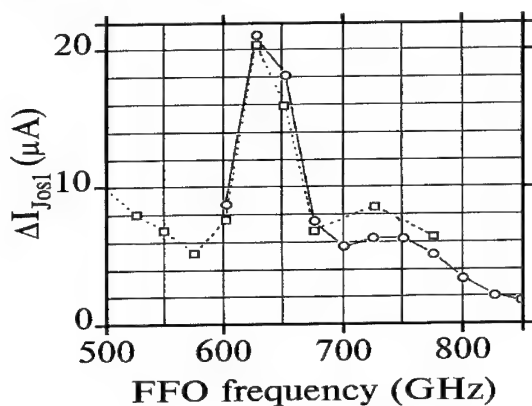


Fig. 7 Amplitude of the first Josephson step for HF SIS detector as a function of the FFO frequency.

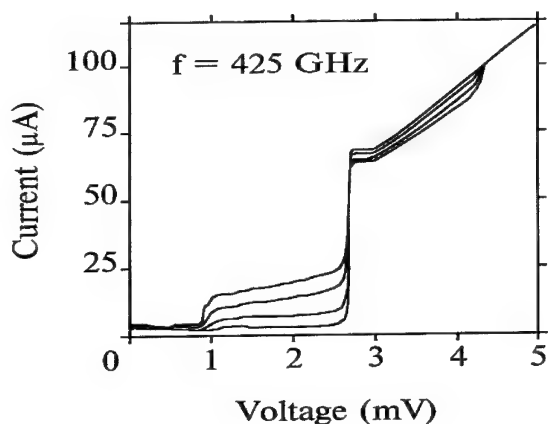


Fig. 8 SIS IVCs measured for different values of the FFO dc bias current at constant FFO frequency  $f = 425$  GHz.

### 5. Integrated Receiver Chip: Design and Main Parameters

For the design of an integrated receiver chip several (sometimes contradictory) requirements should be taken into account. First of all it is necessary to pump a SIS mixer element close to its optimal operational point ( $\alpha = eV/hf \approx 1$  at signal frequency). But at the same time one should avoid too large leakage of the signal power to the LO port so that the major part of the received by antenna signal can be delivered to the detector. It means that the coupling of the FFO to the SIS element should be not too strong to provide a reasonable isolation between the signal input and the LO circuit. In addition a separate control line for suppression of the supercurrent and thus the Josephson noise in the SIS mixer should be placed close to the SIS junction and in such a way that it does not deteriorate the antenna performance.

With extensive numerical calculations a suitable circuit was chosen and its main parameters were optimized. We use a single SIS junction as a mixer element situated in the centre of a double dipole antenna. The antenna and the SIS tuning elements are designed for a central frequency of 450 GHz. The symmetry of the antenna allows to introduce additional leads positioned opposite to the IF output utilizing the same "choke filter" design. These leads are used for connecting the SIS control line as well as the ground plane for the microstrip line through which the FFO power is supplied. The layout of the central part of the receiver chip of one of our designs (a) as well as an enlarged view of the antenna and mixer with tuning circuits (b) are shown in Fig. 9. The integrated receiver chips are fabricated on 4 mm by 4 mm and 0.15 - 0.2 mm thick glass or crystalline quartz substrates. Only a few chips have been fabricated at this moment. The chip is placed on the flat back side of a hyper-hemispherical quartz lens. Ten spring loaded contacts are used for connecting the bias and the control lines of the FFO and SIS mixer.

The integrated circuits are fabricated with a technique developed for producing high quality Nb-AlO<sub>x</sub>-Nb SIS mixers and RSFQ digital devices<sup>17</sup>. Actually only two superconducting Nb layers are needed in the new design<sup>22</sup> of a dc block between FFO and SIS mixer. Both SIS and FFO junctions were fabricated in one process run; the critical current density is in the range of 5 - 8 kA/cm<sup>2</sup> which corresponds to a specific resistivity  $R_n \cdot S = 40 - 25 \text{ Ohm} \cdot \mu\text{m}^2$ . Different designs for biasing of the FFO are used<sup>10</sup>; the long Josephson junctions have the dimensions: length,  $L = 450 \mu\text{m}$ ; width,  $W = 3 \mu\text{m}$ . A control line in the base electrode is employed to adjust the magnetic field.

An attenuation of 7 dB (about 20 % coupling) between FFO and SIS is realised by using an impedance mismatch and additional coupling resistors. Injection of the LO power into the mixer is realized in two different ways: either i) to the antenna via a resistor placed between the first sections of the choke filter; or ii) directly to the SIS junction in the centre of the antenna. Both these designs result in less than 30 % leakage of the incoming signal. The details of the chip design and calculations will be described elsewhere<sup>22</sup>.

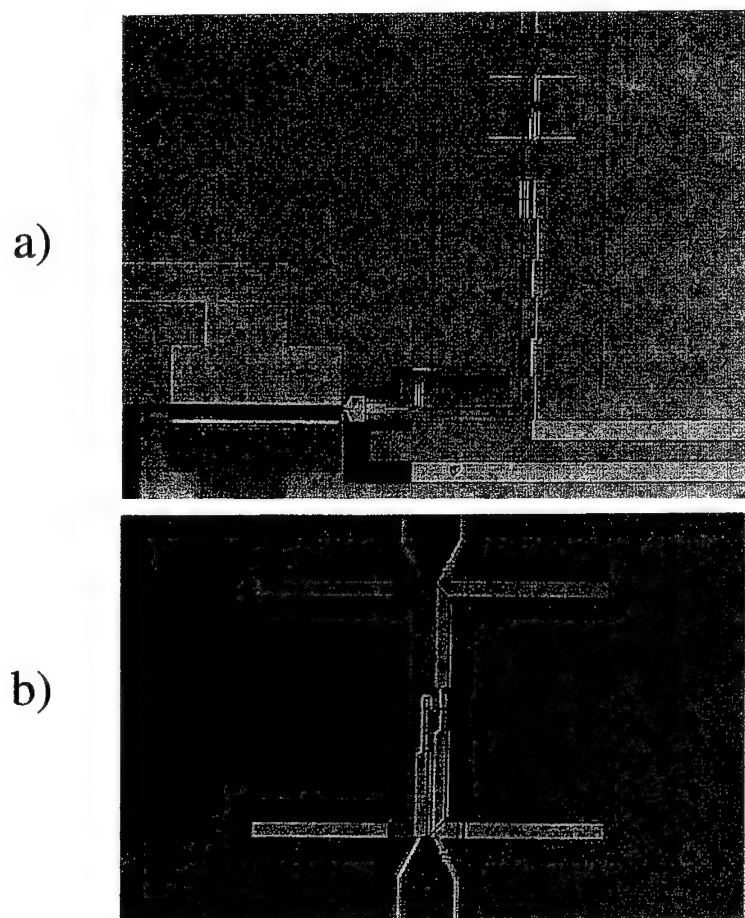


Fig. 9. A photograph of the chip: a) shows from bottom left to upper right: FFO, 3 stage Chebyshev transformer, dc block, interconnecting microstrip line lying on a top of the choke filter, double dipole antenna; b) detail of the antenna and mixer with tuning circuit.

## 6. Test of the Integrated Receiver

The interconnecting circuits provide a reasonable coupling between the LO and the SIS mixer over a wide frequency range. Fig. 10 shows the family of the FFO IVCs at

different currents through the control line. The ranges where the FFO pumping leads to more than 20 % suppression of the SIS gap current (pump parameter  $\alpha > 1$ ) are marked by horizontal bars at different bias currents. One can see that a frequency tuning range as large as 21 % has been obtained. This value is limited by the SIS mixer tuning and the FFO interface circuits. A much wider operating range (up to 800 GHz) has been observed<sup>10</sup> for the same FFO followed by specially designed matching circuit and a wideband detector. The range of the FFO voltage (i.e. frequency) tuning by the control line current is shown in the inset of Fig. 10. One can see that there is a continuous tuning range from 350 up to 700 GHz. The I-V curves of the SIS mixer pumped by FFO at different frequencies within the mixer tuning range are shown in Fig. 11. A pumping level as high as  $\alpha \geq 2$  has been obtained at a frequency of 435 GHz.

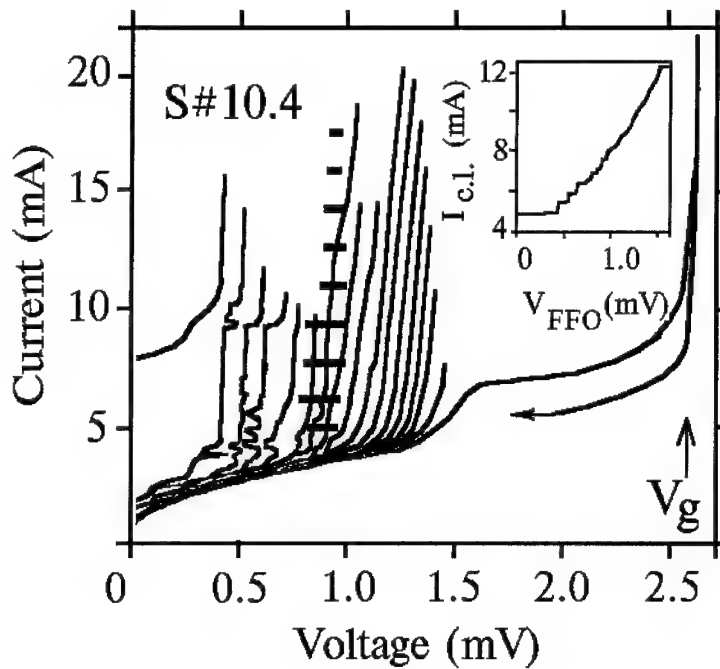


Fig. 10. I-V curves of the FFO at different control line currents in the range 5 - 15 mA. Horizontal bars show the regions where pumping of the SIS junction in the mixer with  $\alpha > 1$  has been obtained. The dependence of the FFO dc voltage on the control line current at a bias current of 9 mA is shown in the inset.



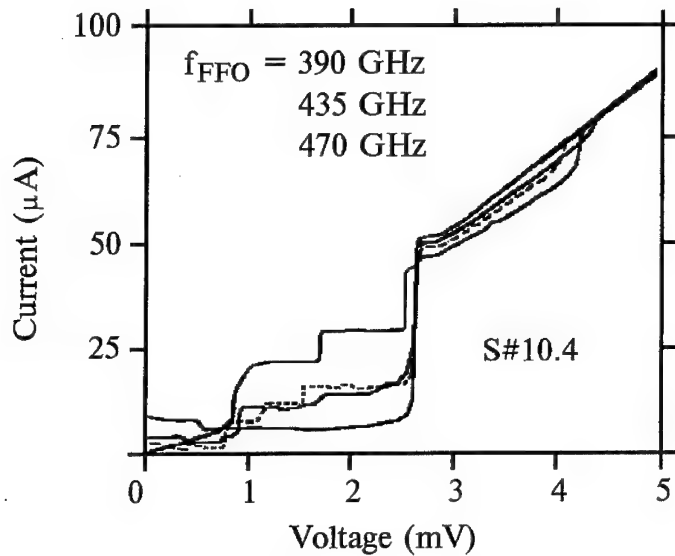


Fig. 11. I-V characteristics of the SIS mixer without pumping and pumped by the FFO at 3 different frequencies (FFO bias current was 9 mA, see Fig. 10).

The output power of the FFO can be adjusted by changing the bias current while keeping the frequency constant by fine tuning the magnetic field. Fig. 12 shows the variation of the critical current and first Josephson step of the SIS junction (at FFO frequency  $f_{\text{FFO}} = 450$  GHz) as a function of the square root of the dc power applied to the FFO (which is proportional to the high frequency current  $I_{\omega}$  detected by the SIS). This value is calculated from the expression  $P_{\text{dc}} = V_{\text{FFO}} * (I_b - I_{\text{qp}})$ , where  $I_b$  is FFO bias current and  $I_{\text{qp}} = 5.5$  mA is the quasiparticle current which value is subtracted from  $I_b$ . From Fig. 12 one can see that the critical current of the SIS junction is suppressed to zero when  $P_{\text{dc}}$  is about  $7 \mu\text{W}$  (it corresponds to  $I_b = 13$  mA). The critical current of the SIS junction is  $57 \mu\text{A}$ ; the junction was shunted by a 16 Ohm resistor. It gives  $V_c = I_c * R_n \approx 910 \mu\text{V}$ , and a normalized pump frequency  $\Omega = hf_{\text{FFO}}/eV_c \approx 1$ . In the Resistively Shunted Junction Model (RSJM) the first zero of the  $I_c(I_{\omega})$  dependence takes place at  $I_{\omega}/I_c = 2.5$  (at  $\Omega = 1$ ) see, e.g.<sup>23</sup>. It means that  $I_{\omega} = 180 \mu\text{A}$  and the rf power delivered to the SIS junction is  $P_{\omega} = 0.26 \mu\text{W}$ . It should be emphasized that these values are measured directly in the SIS mixer integrated with planar antenna. These results have been obtained for a receiver chip design with direct injection of the FFO power to the SIS junction.

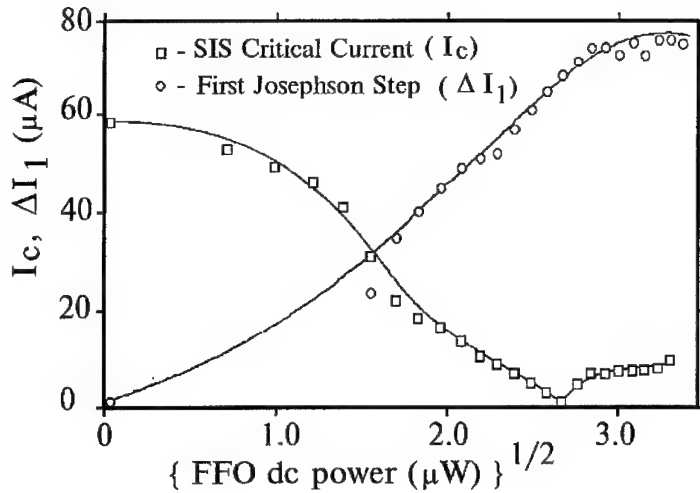


Fig. 12. Critical current of the SIS mixer and amplitude of its first Josephson step as a function of FFO dc power (see text).

The suppression of the Josephson effect by the integrated SIS control line<sup>22</sup> is demonstrated in Fig. 13 where two SIS IVCs are shown for zero magnetic field and for the second minimum of the critical current. The inset presents the dependence of the SIS critical current on the control line current,  $I_{\text{SIS c.l.}}$ . A narrow Nb control line (width  $\approx 4 \mu\text{m}$ ) can carry a current of about 50 mA without switching to the normal state. This current is sufficient to reach the first minimum of  $I_c(I_{\text{SIS c.l.}})$  even for the smallest tested junctions ( $S \approx 1 \mu\text{m}^2$ ).

All these measurements were performed at 4.2 K in a liquid He cryostat with a specially designed cryoprobe. It should be noted that an additional resistor was introduced in the bottom Nb electrode to allow the magnetic tuning by the control line. The value of this resistor for a batch that was fabricated on the crystalline quartz substrates was too high. It gave rise to a considerable overheating and made most integrated receiver experiments in a vacuum cryostat impossible for these samples.

Several chips have been tested with a Fourier Transform Spectrometer (FTS) to check the performance of the antenna and mixer combination (see Fig. 14). The values obtained for the central frequency and the bandwidth (400 and 100 GHz respectively) correspond well to both the resonance on the dc I-V curve and region of the effective pumping in the case of the FFO operation. The mixer and antenna of similar design have been measured in a vacuum cryostat with external local oscillator. An uncorrected receiver noise temperature (DSB) as low as 300 K has been obtained at 430 GHz<sup>22</sup>.

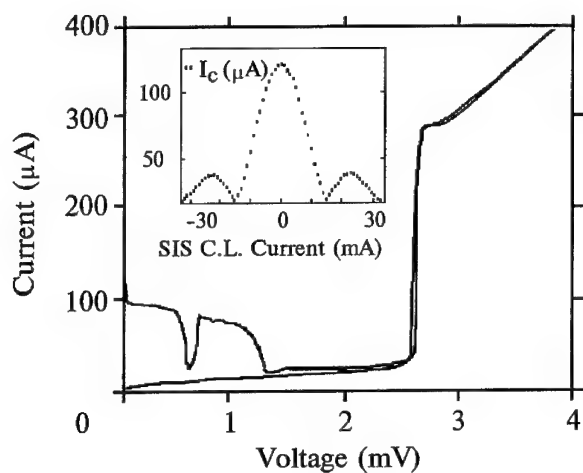


Fig. 13. I-V curves of the SIS mixer at zero magnetic field and at a magnetic field corresponding to the second minimum of the SIS critical current. The magnetic field is generated by a current through the SIS integrated control line. The dependence of the SIS critical current on the control line current is shown in the inset.

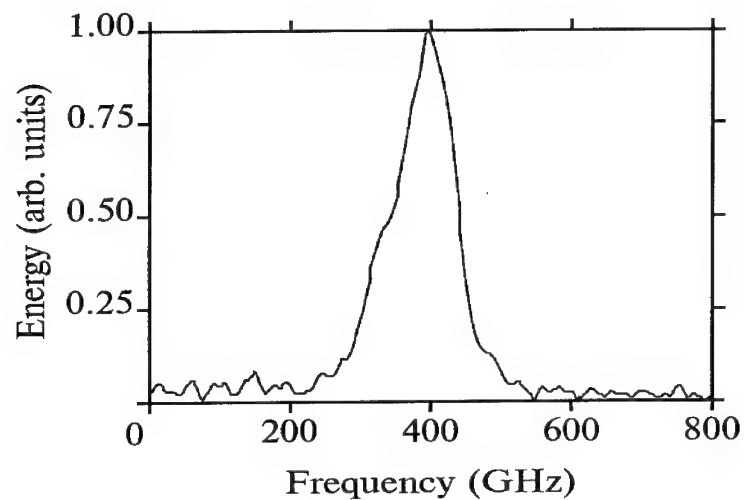


Fig. 14. Spectral sensitivity of the integrated receiver as measured by Fourier Transform Spectrometer. Autonomous SIS I-V curve with self resonance is shown in the Fig. 13.

## 7. Conclusion

We have presented the first experimental observation of the Flux-Flow Oscillations near and above the gap frequency with a power level sufficient for the pumping of the SIS mixer. The possibility of fine tuning the FFO frequency and power in a wide range (especially for  $f \geq 500$  GHz) has been experimentally demonstrated. Taking into account the moderate linewidth of the autonomous FFOs it makes these devices one of the main candidates for integration with a SIS quasioptical mixer in planar submillimeter wave receivers for space application. The ability of the FFO to be phase locked to external narrow band source makes these oscillators very promising also for ground based submillimeter radioastronomy.

We conclude that well operating integrated 500 GHz receiver chips have been designed, fabricated and investigated. We have shown that the FFO delivers sufficient power to pump an integrated SIS mixer placed in a planar antenna without considerable leakage of the incoming signal. We also have demonstrated that the FFO frequency and power can be precisely tuned over a wide range. The integrated control line has been successfully used for suppression of the Josephson noise in the SIS mixer.

## Acknowledgements

The authors thank A.M. Baryshev, G.M. Fischer, H. Golstein, Th. de Graauw, B. H. Larsen, W. Luinge, H. Schaeffer, H. van de Stadt, and A.V. Ustinov for help and fruitful discussions.

## References

1. J.R. Tucker, M.J. Feldman, "Quantum detection at millimeter wavelengths," *Rev. of Mod. Phys.* **4** (1985) 1055.
2. A.K. Jain, K.K. Likharev, J.E. Lukens and J.E. Sauvageau "Mutual phase-locking in Josephson junction arrays", *Physics Reports* **109** (1984) 309.
3. B. Bi, S. Han, and J.E. Lukens "Distributed Josephson junction arrays as local oscillators", *IEEE Trans. on Appl. Superconduct.* **3** (1993) 2303.
4. S. Han, B. Bi, W. Zhang, A.H. Worsham, and J.E. Lukens "High power submillimeter wave source using series biased linear Josephson effect array", *Proceedings of the Fourth International Symposium on Space Terahertz Technology*, UCLA, Los-Angeles, USA (1993) 474.

5. E. Joergensen, V.P. Koshelets, R. Monaco, J. Mygind and M.R. Samuelsen, "Thermal fluctuations in resonant motion of fluxons on a Josephson transmission line, theory and experiment", *Phys. Rev. Lett.* **49** (1982) 1093.
6. T. Nagatsuma, K. Enpuku, F. Irie, and K. Yoshida, "Flux-Flow type Josephson oscillator for millimeter and submillimeter wave region", *J. Appl. Phys.* **54** (1983) 3302; see also Pt. II: *J. Appl. Phys.* **56** (1984) 3284; Pt. III: *J. Appl. Phys.* **58** (1985) 441; Pt. IV: *J. Appl. Phys.* **63** (1988) 1130.
7. A.V. Ustinov, T. Doderer, R.P. Huebener, J. Mygind, V.A. Oboznov, and N.F. Pedersen, "Multi-fluxon effects in long Josephson junctions", *IEEE Trans. on Appl. Supercond.* **3** (1993) 2287.
8. Y.M. Zhang, D. Winkler, and T. Claeson, "Linewidth measurements of Josephson flux-flow oscillators in the band 280-330 GHz," *Appl. Phys. Lett.* **62** (1993) 3195, see also *Proceedings of the Fourth International Symposium on Space Terahertz Technology*, UCLA, Los-Angeles, USA (1993) 485.
9. V.P. Koshelets, A.V. Shchukin, S.V. Shitov, and L.V. Filippenko, "Superconducting millimeter wave oscillators and SIS mixers integrated on a chip," *IEEE Trans. on Appl. Supercond.* **3** (1993) 2524.
10. J. Mygind, V.P. Koshelets, A.V. Shchukin, S.V. Shitov, and I.L. Lapytskaya, "Properties of the autonomous and injection locked Flux-Flow Oscillators" was presented on ASC-94, Boston, USA, report EQA-4 (1994)
11. C. Hilbert, and J. Clarke, "DC SQUID as a radio frequency amplifier", *J. Low Temp Phys* **61** (1985) 263.
12. M.A. Tarasov, V.Yu. Belitsky, G.V. Prokopenko, L.V. Filippenko, V.P. Koshelets "DC SQUID RF amplifier with external mm-wave pumping and its testing by SIS junction noise", *Super. Sci. Technology* **4** (1991) 644.
13. E.B. Goldobin, V.M. Golomidov, P.G. Litskevitch, and V.P. Koshelets, "Superconducting digital correlator for integrated receivers," *to be published*
14. K.K. Likharev and V.K. Semenov. "RSFQ logic/memory family: a new Josephson junction technology for sub teraHertz clock frequency digital systems" *IEEE Trans. on Appl. Supercond.* **1** (1991) 3.
15. V.P. Koshelets "Single Flux Quantum digital devices", *Supercond. Sci. Technol.* **4** (1991) 555.
16. An.B. Ermakov, V.P. Koshelets, S.A. Kovtonyuk, I.L. Serpuchenko, S.V. Shitov, A.N. Vystavkin "Investigation of the Nb-AlOx-Nb junctions and mm wave mixers", *Proceedings ISEC-89*, Tokyo, Japan (1989) 294.

17. V.P.Koshelets, S.A.Kovtonyuk, I.L.Serpuchenko, L.V.Filippenko, and A.V.Shchukin "High quality Nb-AlO<sub>x</sub>-Nb tunnel junctions for microwave and SFQ logic devices", *IEEE Trans.on Magn.* **MAG-27** (1991) 3141.
18. M. Gurvich, M.A. Washington, and H.A. Huggins "High quality refractory Josephson tunnel junctions utilizing thin Al layers", *Appl.Phys.Lett.* **42** (1983) 472.
19. T. Imamura, T. Shiota, and S. Hasuo "Fabrication of high quality Nb/AlO<sub>x</sub>-Al/Nb Josephson junctions: PtI - Sputtered Nb films for junctions electrodes", *IEEE Trans. Appl. Supercond.* **2** (1992) 1.
20. An.B. Ermakov, V.P. Koshelets, S.A. Kovtonjuk, S.V. Shitov, "Parallel biased SIS arrays for mm wave mixers: Main ideas and experimental verification," *IEEE Trans. on Magn.* **MAG-27** (1991) 2642.
21. V.P. Koshelets, A.V. Shchukin, S.V. Shitov, I.L. Lapitskaya, and J. Mygind, "Integrated flux flow Oscillators for Sub-mm Wave Receivers", *to be submitted to IEEE Trans. on Appl. Supercond.* (1995).
22. S.V. Shitov, V.P. Koshelets, A.M. Baryshev, A.V. Shchukin, L.V. Filippenko, and I.L. Lapytskaya, "Superconducting integrated receiver for 500 GHz range," *to be published*
23. K.K. Likharev, "*Dynamics of Josephson Junctions and Circuits*", Gordon and Breach Science Publishers, New York (1986).

## SUBMILLIMETER WAVE RADIATION EMISSION FROM FLUX FLOW OSCILLATORS

A. V. SHCHUKIN and V. P. KOSHELETS  
*Institute of Radio Engineering and Electronics, RAS  
Moscow 103907, Russia*

and

J. MYGIND  
*Physics Department, Technical University of Denmark  
DK-2800 Lyngby, Denmark*

### ABSTRACT

Long Josephson tunnel junction Flux Flow Oscillators (FFO) integrated on the same chip with an array SIS junction mixer detector have been experimentally investigated in the frequency range up to 500 GHz. Both the emitted power and the frequency of the FFO can be varied by adjusting the dc bias current and the applied dc magnetic field. The spectral width of the free-running FFO is about 1 MHz but may be reduced considerably by frequency- and phase-locking. Here we report on measurements of the integral linewidth when mixing two free-running FFOs, as well as the single FFO linewidth obtained when beating one autonomous FFO with an other FFO injection-locked to the 6th harmonic of an external 70 GHz reference oscillator. The dependence of the linewidth on the dynamic resistance indicates that different types of noise are dominant.

### 1. Introduction

Recently the uni-directional and viscous flow of magnetic flux quanta in a long (length,  $L \gg \lambda_J$ , the Josephson penetration depth) Josephson tunnel junction with high damping<sup>1</sup> has attracted much attention in the development of local oscillators (LO) for fully integrated superconducting submillimeter wave SIS receivers<sup>2,3,4,5</sup>. The frequency of this so called Flux Flow Oscillator (FFO) can be tuned over a wide frequency range, limited only by the superconductor gap frequency. Moreover, the FFO provides sufficient output power to pump a SIS array mixer detector. Preliminary FFO spectral linewidth measurements<sup>2,4,5</sup> have demonstrated encouraging values (130 kHz at 70 GHz<sup>2</sup>, about 1 MHz at 140 GHz<sup>4</sup> and 2.1 MHz at 320 GHz<sup>5</sup>). We report on measurements of the FFO linewidth as function of applied dc bias current and magnetic field, both with two autonomous FFOs as well as with one of the FFOs locked by injection to harmonics of a narrow-band external microwave source. An more extensive discussion of the noise mechanisms as well as harmonic phase-locking will be given elsewhere<sup>6</sup>. Recently, we have investigated FFOs at frequencies up to 850 GHz and observed an emitted power as large as 5  $\mu$ W at 440 GHz<sup>7,8</sup>.

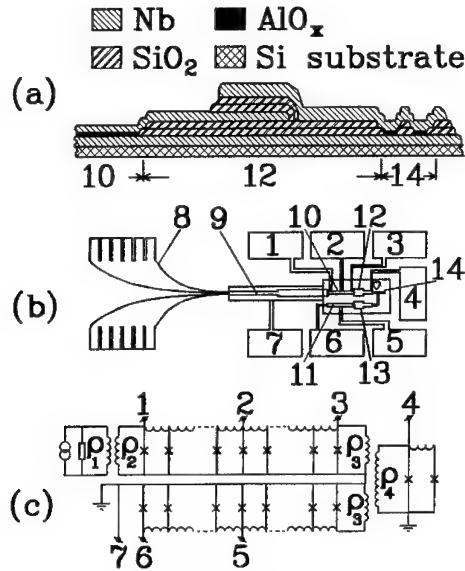


Figure 1: Cross-section (a), schematic drawing (b) and simplified equivalent diagram (c) of the experimental on-chip integrated circuit. “1” - “7” - contact pads; “8” - fin-line antenna; “9”, “12”, “13” - Chebyshev impedance matching transformers; “10” - FFO1; “11” - FFO2; “14” - two-junction SIS array with tuning-out circuit.

## 2. Experimental Circuit

The layout and a simple equivalent diagram of the on-chip integrated circuit is shown in Fig. 1. The circuit comprises two identical FFOs (FFO1 - “10” and FFO2 - “11”; length,  $L = 200 \mu\text{m}$ , width,  $W = 1.5 \mu\text{m}$ ), a SIS mixer array detector with a capacitance-tune-out circuit (“14”, area,  $S = 1.3 \times 1.3 \mu\text{m}^2$ ), three impedance matching transformers (“9”, “12” and “13”), and a fin-line antenna (“8”). The tuning-out inductances for the two SIS junction (parallel dc biased) array (“14”) and the transformers (“12”, “13”) were designed for optimum performance at 450 GHz. The integrated circuits have been fabricated in a system developed for producing SIS mixer elements and Rapid Single Flux Quantum, RSFQ, digital devices. Details of the circuit design and experimental set-up will be described elsewhere<sup>6,7</sup>. The high quality Nb- $\text{AlO}_x$ -Nb tunnel junctions have a critical current density,  $j_c = 8 \text{ kA/cm}^2$  and a Josephson penetration depth,  $\lambda_j = 4 \mu\text{m}$ . The product of the normal state resistance and the junction area,  $R_n \times S$ , is  $25 \Omega \mu\text{m}^2$ .

## 3. Two Autonomous FFOs, Integral Linewidth

Signals from two free-running autonomous FFOs were mixed in the small SIS



array detector in the first experiments. The frequency and power of each FFO may be individually tuned by adjusting the dc bias current and the applied dc magnetic field. The dc bias currents could be injected either to the ends of the long junctions or evenly distributed along the sides as shown in Fig. 1. Usually a homogeneous magnetic field from an external coil was applied and first used to optimize the operation of FFO2, and subsequently an additional field from a control line positioned near FFO1 was used to fine tune the frequency of FFO1 so that their difference frequency was within the band of the intermediate frequency (IF) amplifier connected to the SIS mixer array. The room temperature IF amplifier (center frequency,  $f_{IF} = 1.5$  GHz, bandwidth,  $\Delta B_{IF} = 600$  MHz) had an effective noise temperature of 100 K referred to the SIS junction array.

Using this set-up we have observed mixing of the signals up to a FFO frequency of 450 GHz. The measured total (integral, 3dB; half power, full width) linewidth of the two FFOs was as low as 750 kHz at 280 GHz<sup>6</sup>. In order to minimize the influence from external disturbances (fluctuations in temperature and dc current bias conditions) the measurements were made at  $T = 2.0$  K (below the  $\lambda$ -point of liquid helium) on one of the sharp (low dynamic resistance) resonant steps present in the  $IV$ -curves of the FFOs.

The results confirm the rather similar experiments done by Y. M. Zhang et al.<sup>5</sup>. The inherent problem with this integral linewidth measurement, however, is that one may find an unrealistic (too small) linewidth because most external disturbances are common mode to the FFOs placed on the same chip. If the FFOs were identical only signals from uncorrelated internal noise sources can contribute to the integral linewidth observed as the average of the fluctuations around the difference frequency,  $f_{IF}$ . Mutual interaction between the FFOs (over a frequency band larger than  $f_{IF}$ ) may also lead to a reduced integral linewidth.

#### 4. One FFO used as Harmonic Multiplier

An alternative high frequency scheme was used to overcome the above-mentioned problems. This method allows us to measure the correct linewidth of a *single* FFO at different frequencies produced e. g. by varying the bias point along the flux flow step (FFS or velocity-matched step<sup>1</sup>) in the  $IV$ -curve. A signal from an external narrow-band frequency-locked Gunn oscillator (frequency,  $f_G = 56 - 74$  GHz and linewidth,  $\Delta f_G \leq 80$  kHz) was applied to FFO1 via the fin-line antenna ("8" in Fig. 1) and the three-step Chebyshev stripline transformer ("9" in Fig. 1) both designed for 70 GHz center frequency. As a result rf-induced steps with voltage spacing,  $\Delta V = hf/(2e)$ , could be generated in the  $IV$ -curve of FFO1.

With low applied power (virtually no suppression of the FFO1 critical current), since the applied frequency is much lower than the maximum plasma frequency of FFO1,  $f_{p0} > 200$  GHz, the fundamental microwave signal cannot propagate inside the FFO1 tunnel junction. Nevertheless, from the rf-induced steps in the  $IV$ -curve of the SIS array at voltages corresponding to *higher harmonics* of the applied signal it is evident that higher harmonic signals (generated by the non-linearity of the FFO1)

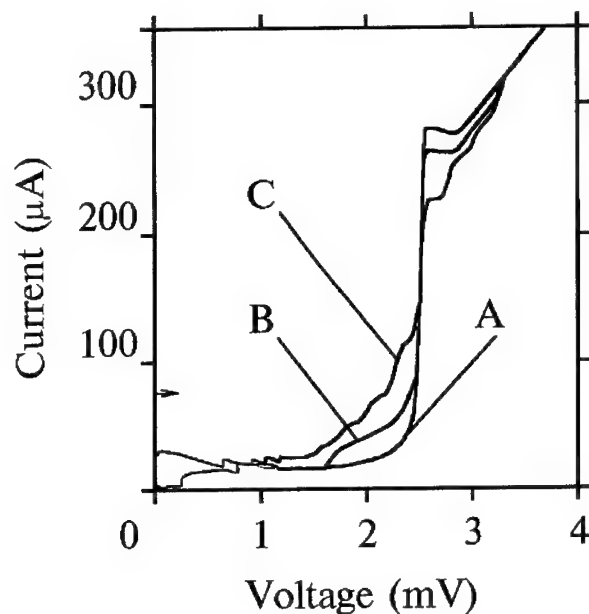


Figure 2: *IV*-characteristics of the SIS detector for different levels of the external microwave signal  $f_G = 65.4$  GHz applied via the fin-line antenna to FFO1 (see text); attenuation (A)  $> 70$  dB (autonomous *IV*-curve), (B) 28 dB, and (C) 14 dB.

actually reached the SIS detector. Curve "A" in Fig. 2 shows the unperturbed dc *IV*-curve of the SIS mixer array. For small levels of applied power the third harmonic signal (frequency  $3 \times f_G \approx 220$  GHz, which roughly coincides with half the design frequency for the transformer ("12" in Fig. 1) and the SIS mixer tuning-out inductance) dominantly affects the detector (see curve "B" in Fig. 2). At higher power levels (where the critical current of the FFO1 and thus the plasma frequency is suppressed) also a signal at the fundamental frequency of the Gunn oscillator reaches the detector (curve "C" in Fig. 2). In both cases no dc current was applied to the FFO1. Usually it remained in the zero voltage state but often - due to self-detection - zero-crossing constant-voltage steps were seen.

On the spectrum analyzer we observed a strong signal at the IF frequency,  $f_{IF}$ , resulting from the mixing of the  $n$ 'th harmonic of the Gunn oscillator with the FFO2 signal (frequency  $f_{FFO2}$ ) obeying

$$f_{FFO2} = n \times f_G \pm f_{IF} \quad (1)$$

so it is concluded that the FFO1 has successfully been used as a harmonic multiplier<sup>2</sup>. We saw harmonic mixing at  $n = 4, 5, 6$  and  $7$  and could measure both lower and upper sidebands ( $\pm f_{IF}$  in Eqn. (1) by changing slightly the FFO2 bias. Due to the

inserted series of filters and isolators in the waveguide leading to the cryostat we are confident that no higher harmonic signals from the Gunn oscillator can circumvent FFO1 and reach the SIS array. Also no detectable influence of the Gunn signal or its harmonics on FFO2 was observed.

### 5. Single FFO Linewidth and Discussion

Fig. 3 shows the observed dependence of the linewidth of the mixed signal,  $\Delta f$ , on the differential resistance,  $R_d$ , of FFO2. The corresponding  $IV$ -curve of FFO2 is depicted in the inset of Fig. 3. The frequency of the FFO2 was changed by more than 15 GHz around 350 GHz; the 6th harmonic of the Gunn was used in this case. The contribution from the Gunn oscillator linewidth,  $\Delta f_G < 80$  kHz, to the measured linewidth can be neglected in this context since  $80 \text{ kHz} \times 6 \approx 0.5 \text{ MHz}$ . The  $R_d$  values used in Fig. 3 were derived from the slope of the dc  $IV$ -curve in the bias point.

From Fig. 3 it is clear that the FFO2 linewidth is proportional to  $R_d^2$  above 5 MHz while below this value,  $\Delta f$  approaches a linear dependence (slope = 1).

Presently, no theory exists for the linewidth of the radiation emitted from a FFO. The related theoretical models for the single Josephson junction<sup>9</sup> and the low-damping soliton oscillator<sup>10</sup> both give the same dependence of the linewidth on the differential resistance:  $\Delta f \propto R_d^2$  assuming a *wideband* ( $0 < f_{\text{noise}} \leq \Delta f$ ) Nyquist noise spectrum. The linewidth of the high frequency oscillations in a short Josephson tunnel junction in the limit of small junction current fluctuations is given by<sup>9</sup>

$$\Delta f_{\text{WB}} = 2\pi \frac{R_d^2}{\Phi_0^2} e I_{dc} \coth\left(\frac{e V_{dc}}{2 k_B T_{\text{eff}}}\right) \quad (2)$$

where the subindex on  $\Delta f_{\text{WB}}$  refers to the wideband noise spectrum with effective temperature  $T_{\text{eff}}$ .  $V_{dc}$  and  $I_{dc}$  is the dc voltage and current in the bias point.  $\Phi_0$  is the flux quantum.

A best fit (solid line in Fig. 3) to Eqn. (2) using the experimental values for  $R_d$ ,  $V_{dc}$  and  $I_{dc}$  is obtained for  $T_{\text{eff}} = 32 \text{ K}$ , which is approx. eight times the physical temperature,  $T = 4.2 \text{ K}$  (dot-and-dash line in Fig. 3). It should be noted that in experiments with the same sample (repeated on other days with apparently the same experimental conditions) the  $\Delta f \propto R_d^2$  dependence is still observed but a  $T_{\text{eff}}$  as large as 90 K was needed to obtain the best fit. The results of this run are also shown (open  $\diamond$ 's) in Fig. 3. In retrospect, the original experiments with the linewidth of the low-damped soliton oscillator<sup>10</sup> gave  $T_{\text{eff}} \approx 3 \times T$ ; this excess noise discrepancy has never been resolved.

The calculated excess noise temperature for the FFO may have several origins. The wideband noise (with roll-off frequency higher than 1.5 MHz, corresponding to the width of the unperturbed spectral line) will act as thermal noise for the Josephson junction increasing the effective noise temperature. Since any high frequency signal (e. g. from TV transmitters) may contribute additional noise, the measurements were performed in a shielded room and all wires connecting to the sample were carefully hf shielded and filtered.

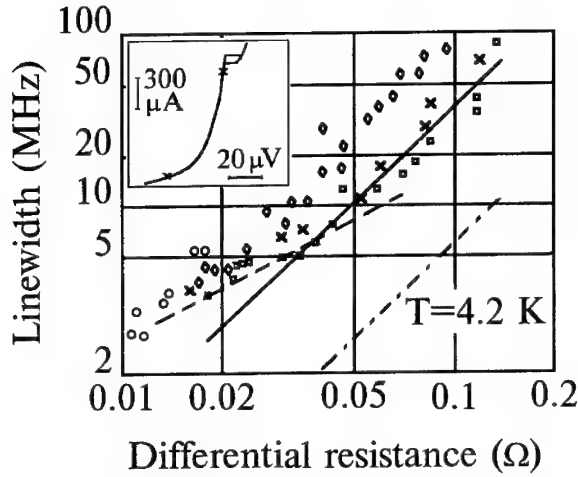


Figure 3: Linewidth of FFO2 versus dynamic resistance. The four runs were recorded with the same sample on different days (see text).  $T = 4.2$  K. Solid line and dot-and-dash line - Eqn. (2) with effective temperature,  $T_{\text{eff}} = 32$  K and 4.2 K, respectively; dashed line - Eqn. (3) with the amplitude of the low frequency noise current,  $I_f = 0.17 \mu\text{A}$ .

An other likely reason for the large FFO linewidth may be fluctuations in the fluxon velocity when moving along Josephson junction due to i) inhomogeneities in the barrier and/or ii) perturbations imposed by trapped flux in the superconducting films near the junction region. The configuration of the trapped flux and thus the noise level might be different from one experiment to another resulting in the observed changes in the effective noise temperature.

Low frequency noise with cut-off frequency much smaller than the width of the spectral line ( $0 \approx f_{\text{noise}} \ll \Delta f$ ) e. g. from external disturbances (bias supplies, temperature fluctuations, hum,  $1/f$  noise, etc. ) may be directly converted and give rise to excess noise. A low frequency current noise with amplitude  $I_f$  will increase the linewidth proportional to  $R_d$

$$\Delta f_{\text{LF}} = \frac{2}{\Phi_0} I_f R_d \quad (3)$$

This is shown in Fig. 3 by the dashed line which for  $I_f = 0.17 \mu\text{A}$  fits well to the experimental results for  $\Delta f < 5$  MHz. For the above-mentioned data with  $T_{\text{eff}} = 90$  K  $I_f = 0.35 \mu\text{A}$  gives the best fit. Subjected to the validity of Eqns. (2) and (3) for the FFO, the fits in Fig. 3 support the assumption that additional noise sources (both high and low frequency) were present in the experiments.

Based on numerical simulations using the perturbed sine-Gordon equation with boundary conditions it has recently been suggested<sup>11</sup> that the dynamics of the fluxon

chain moving along the tunnel junction is chaotic in certain regions of the parameter space. Fundamental problems are to model the boundary conditions, the losses, and whether the small signal sinusoidal "ansatz" used by Nagatsuma et al.<sup>1</sup> to solve the perturbed sine-Gordon equation is applicable in this very nonlinear system. As pointed out early<sup>1</sup> the magnitude of the junction dissipation, as amply described by the quality factor,  $Q_j$ , is of major importance.

$$Q_j = \frac{1}{(\frac{f_j}{f_{j0}})^2 \beta + \alpha} \quad (4)$$

where  $f_j = V_{dc}/\Phi_0$  is the Josephson frequency in the bias point,  $\beta$  is the surface loss, and  $\alpha$  is the shunt loss (in high- $Q_j$  junctions usually the quasiparticle loss). The effect of resistive loading of the FFO has been simulated by Y. M. Zhang<sup>5</sup> also using the perturbed sine-Gordon equation.

In our case the FFO junctions are externally damped by deposition of an overlaying resistive film shunting the top and bottom Nb electrodes. A normalized damping,  $\alpha L/\lambda_j > 2$ , is the condition<sup>1,5</sup> for supporting unidirectional flux flow. In our experiments the effective  $Q_j$  value even with our relatively high current density is still so large (of order 5-10) that we clearly see the Fiske steps and Fiske resonances superimposed on the FFS at low bias voltages. Also locking to resonant structures in the embedding network appeared in the  $IV$ -curve. The numerical simulations<sup>11</sup> showing chaotic dynamics used  $\alpha = 0.1$  close to the experimental value for the shunted FFO. Since the external shunting is ineffective due to the self-induction of the resistive film above 200 GHz  $\alpha = 0.02$  seems more appropriate in the linewidth measurements. At frequencies above 450 GHz the surface loss term in Eqn. (4) will dominate due to its strong frequency dependence.

In order to serve as a feasible LO in modern radio-astronomy receivers for spectral measurements the linewidth of the FFO must be significantly below 1 MHz. This seems rather difficult especially for higher frequencies near the superconducting gap. At  $f_{\text{FFO}} > 500$  GHz the surface losses increase considerably and even for "optimal" biasing without self-field effects the differential resistance on the FFS increases<sup>1,5</sup> leads to an unacceptable broadening of the linewidth. The FFO in our opinion has superior properties with respect to tuneability, large output power, sinusoidal output with low harmonic content, etc. and we propose to overcome the linewidth problem by phase-locking it (e. g. by harmonic injection<sup>6</sup>) to external oscillators or to high-Q superconducting on-chip resonators.

### Acknowledgements

The authors thank G. M. Fischer, Britt H. Larsen, S. V. Shitov and A. V. Ustinov for fruitful discussions. The work was supported by NATO (LP # 921040), the International Science Foundation (# MCH000), the Russian Program of Fundamental Research (# 92-02-3484), and the Danish Research Academy.

## References

1. T. Nagatsuma, K. Enpuku, F. Irie, and K. Yoshida, J. Appl. Phys. **54** 3302 (1983); see also Part II-IV in: J. Appl. Phys. **56** 3284 (1984); J. Appl. Phys. **58** 441 (1985); J. Appl. Phys. **63** 1130 (1988).
2. A. V. Ustinov, J. Mygind, and V. A. Oboznov, J. Appl. Phys. **72** 1203 (1992).
3. A. V. Ustinov, T. Doderer, R. P. Huebener, J. Mygind, V. A. Oboznov, and N. F. Pedersen, IEEE Trans. on Appl. Supercond. **3** 2287 (1993).
4. V. P. Koshelets, A. V. Shchukin, S. V. Shitov, L. V. Filippenko, G. M. Fisher, and J. Mygind, Physica B **194-196** (1994).
5. Y. M. Zhang, D. Winkler, and T. Claeson, Appl. Phys. Lett. **62** 3195 (1993), see also Proc. Fourth Int. Symp. on Space Terahertz Techn. LA, USA pp. 485-499 (1993).
6. V. P. Koshelets, A. V. Shchukin, I. L. Lapytskaya, and J. Mygind, "Spectral linewidth of autonomous and injection locked flux flow oscillators", submitted to Phys. Rev. B1 (1994).
7. V. P. Koshelets, S. V. Shitov, A. V. Shchukin, L. V. Filippenko, I. L. Lapytskaya, and J. Mygind, "Integrated flux flow oscillators for submillimeter wave receivers", *ibid.* (1995).
8. J. Mygind, V. P. Koshelets, A. V. Shchukin, S. V. Shitov, and I. L. Lapytskaya, "Properties of autonomous and injection locked flux flow oscillators", submitted to IEEE Trans. on Appl. Supercond. (1995).
9. K. K. Likharev, *Dynamics of Josephson Junctions and Circuits*, Gordon and Breach Science Publishers, New York (1986).
10. E. Joergensen, V. P. Koshelets, R. Monaco, J. Mygind, M. R. Samuelsen, and M. Salerno, Phys. Rev. Lett. **49** 1093 (1982).
11. M. R. Samuelsen and M. Salerno, private communication (1994)

## NONLINEAR PHENOMENA IN RSFQ LOGIC DEVICES

VSEVOLOD KAPLUNENKO

*Chalmers University of Technology, S-41296, Gothenburg, Sweden*

JESPER MYGIND, NIELS FALSIG PEDERSEN

*Physics Department, Technical University of Denmark, DK-2800 Lyngby, Denmark*

VALERY KOSHELETS

*Institute of Radio Engineering and Electronics, Russia Academy of Sciences, Mokhovaya street 11, Moscow, 103907 Russia*

THOMAS DODERER

*Physikalisches Institut, Lehrstuhl Experimentalphysik II, Universität Tübingen, D-72076 Tübingen Germany*

### ABSTRACT

Rapid Single Flux Quantum (RSFQ) Logic is a promising basis for fast digital signal processors. This logic consists of small (in comparison with the Josephson penetration depth) shunted junctions that are connected with superconducting inductances. This provides propagation and storing of a Single Flux Quantum (SFQ) as a carrier of digital information. RSFQ logic is expected to be valid up to frequencies about 100GHz and this limitation is imposed by the dynamics of fluxons within the discrete Josephson structure.

Another application of RSFQ elements is as analog devices, for instance, high frequency generators, voltage amplifiers and dividers. One of the new phenomena observed in such circuits is a self-induced magnetic field effect caused by edge current in a parallel array of junctions. This problem has been investigated experimentally and numerically for parallel arrays of identical junctions. Steps with extremely low differential resistance are found to be due to the self-induced magnetic field produced by the edge current. The underlying mechanism is that the non-uniform field divides the array into domains consisting of several (unit) cells, each containing the same number of flux quanta. The first experimental results obtained by Low Temperature Scanning Electron Microscopy (LSTEM) on a transmission line are reported. The spatially resolved measurements enable us to observe the above mentioned domains; the number of observed domains corresponds to the step position.

### 1. Introduction.

Recently much progress has been achieved in developing Rapid Single Flux Quantum (RSFQ) Logic<sup>1-13</sup> (another definition<sup>1</sup> is "Phase-Mode logic"). This logic consists of small (in comparison with the Josephson penetration depth) overdamped junctions that are connected with the superconducting inductances. This provides propagation and storage of a Single Flux Quantum (SFQ) (another definition is "fluxon") as a carrier of digital information. From the other side, starting from investigations of long

Josephson junctions with inhomogeneities<sup>14-18</sup>, a new class of effects had been discovered in discrete Josephson arrays<sup>19-24</sup>. Figure 1 illustrates those two sides mentioned above. The two important parameters shown in Figure 1 define the array properties. One of them is well known McCumber parameter  $\beta_c$ <sup>25</sup>:

$$\beta_c = 2\pi I_c R_N^2 C / \phi_0, \quad (1)$$

where  $I_c$  is critical current,  $R_N$  is normal resistance and  $C$  is capacitance of a single junction,  $\phi_0 = h/2e = 2.07 \cdot 10^{-7} \text{ G}\cdot\text{cm}^2$  is the flux quantum. In Figure 1 the vertical dashed line and hatched area split a plane in two areas: the one with  $\beta_c < 1$  corresponds to overdamped (shunted, nonhysteretic) junctions; and the one with  $\beta_c > 1$  corresponds to the underdamped (unshunted, hysteretic) junctions. The other parameter in the figure is a discreteness parameter and its definition varies in papers of different authors. The physical meaning of this parameter is the ratio between the Josephson inductance  $L_j$ :

$$L_j = \phi_0 / 2\pi I_c \quad (2)$$

and the total inductance  $L$  of the loop that forms the primitive cell of the array. For a 2D net of Josephson junctions the primitive cell can comprise up to four junctions, but for a parallel 1D array, it is a two junction SQUID. The well established SQUID parameter  $\beta_L$ :

$$\beta_L = L/L_j = 2\pi I_c L / \phi_0 \quad (3)$$

that can be a discreteness parameter also, but in practice authors most often use the square root of this parameter:

$$a = (\beta_L)^{1/2} \quad (\text{see Ref. 19-24}) \quad (4)$$

$$\Lambda_j = (\beta_L)^{-1/2} \quad (\text{see Ref. 21}) \quad (5)$$

This is because that if we define the size of a primitive a cell as  $x$ , the value  $D = \Lambda_j x = x/a$  has the same meaning for the discrete array as the Josephson penetration depth  $\lambda_j$  for the long Josephson junction. When  $\Lambda_j > 1$  (or  $a < 1$ )  $D$  corresponds to the fluxon size but for opposite case  $\Lambda_j < 1$ , seems there is no physical meaning for it. The latter is typical for the RSFQ circuits (see Figure 1), that is why another parameter  $\eta$  is used:

$$\eta = I_c L / \phi_0 = \beta_L / 2\pi \quad (6)$$

The magnitude of  $\eta$  directly shows how many fluxons the primitive cell of the array can keep in the absence of any bias currents and magnetic fields. The horizontal dashed line at  $\eta = 1$  in Figure 1 marks the frontier between multi fluxon states and single fluxon states of the primitive cell. The application of magnetic fields and bias currents are broadening the frontier as the horizontal hatched field shows.



The area "1" in Figure 1 is an area where the main features of continuum long Josephson junctions, like zero-field step, Fiske steps, and flux-flow steps exist. At higher discreteness parameter  $\eta$  in the area "2", new resonances appear due to the discreteness of an unshunted array<sup>19-24</sup>. These resonances can be described in the same way as it is done for quasiparticle motion in a periodic potential<sup>19</sup>, and for these resonances both optical and acoustic dispersion relations has been found experimentally<sup>21</sup>. These two areas in Figure 1 are not discussed in this report.

To fabricate RSFQ circuits (area 3 in Figure 1) one sometimes uses a complicated connection of two kinds of interferometers. The first group of them with parameter  $0.5 < \eta < 1$  is used mainly for transferring fluxons and the other one with  $1 < \eta < 2$  for the storing of a single fluxon (see for example Ref.4). RSFQ logic is expected to be valid up to the frequencies about 100GHz; this limitation is imposed by the dynamics of fluxons within the discrete Josephson structure. This limitation and another application of RSFQ elements as analog devices, for instance, high frequency generators<sup>26</sup>, voltage amplifiers<sup>27-31</sup> and dividers<sup>5,6</sup> will be discussed in Section 4 and 5 respectively. One of the new phenomena observed in such circuits is a self-induced magnetic field effect caused by edge current in a parallel array of junctions<sup>32</sup>. It will be discussed in Section 2 and the first experimental results obtained for this array by Low Temperature Scanning Electron Microscopy (LTSEM)<sup>33</sup> will be presented in Section 3. Unfortunately space limitation does not allow us to discuss the RSFQ based voltage standard<sup>34</sup> that also can be considered a quasidigital circuit.

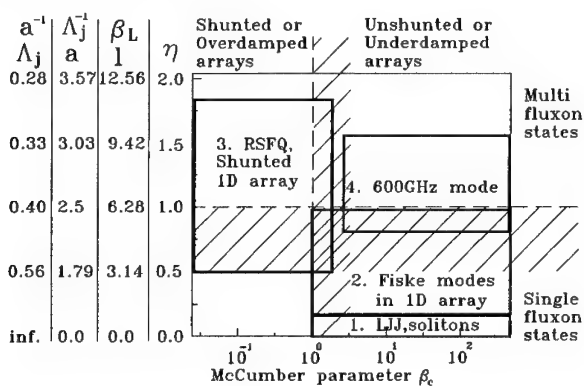


Figure 1. Areas of existence of phenomena vs. McCumber and discreteness parameters.

The high frequency properties of the one-dimensional transmission line are vital in RSFQ logic. This is because there may be unanticipated effects caused by the high frequency properties of the interconnecting circuit elements such as, for example, the microstrip lines connecting the junctions. To elucidate the influence of the inherent resonance frequencies it is important to test an RSFQ circuit in the low damping limit,

with all shunting resistances removed. In this limit (see area "4" in Figure 1) a resonant step has been observed at a voltage corresponding to 600GHz in the dc *IV*-curve of a parallel array of 20 small Nb-AlO<sub>x</sub>-Nb junctions interconnected by short superconducting microstrip line sections<sup>35</sup>. Since this kind of circuit is not strictly an RSFQ element we do not discuss it here and refer to Ref. <sup>35</sup>.

## 2. Self-induced Magnetic Field Effect Caused by Edge Current in Parallel Array of Josephson Junctions

One of the base elements of RSFQ logic is the transmission line consisting of a parallel connection of shunted Josephson junctions. This line may be employed to transfer the SFQ pulses between active elements, to amplify the magnetic field energy connected with the flux quantum (see for example Ref.4) and to provide a time delay of fluxon propagation<sup>5,6,7,36,37</sup>. The high frequency properties of RSFQ devices can be tested by rather simple dc measurements<sup>5</sup> relying on the Josephson relation:

$$f = (2e/h)V_{dc} \quad (7)$$

which relates the frequency, *f*, of the internal Josephson oscillation to the average voltage, *V*<sub>dc</sub>, across the junction. In these tests the parallel junction array is used as a SFQ generator. When an additional bias current is applied to the edge junction, it generates flux quanta, which propagate down the transmission line. In such experiment a number of characteristic steps appear in the *IV*-curve of the fluxon generator junction. These steps have practically zero differential resistance and render the analysis of RSFQ circuits more difficulty. In the discussion of our experiments we show that neither internal junction (geometric) resonances nor cavity resonances (in the loop formed by the junction capacitance and the inductances of the superconducting strips connecting the junctions) are responsible for these steps. The extremely low differential resistance of the steps cannot be explained by the usual two junction interferometer model. In this chapter we discuss the nature of these nonlinear phenomena.

### 2.1 Equivalent circuit

Figure 2 shows the equivalent diagram of the circuit under investigation. The one-dimensional array consists of twenty parallel connected Josephson junctions *J*<sub>1</sub> - *J*<sub>20</sub> each of which are externally resistively shunted to provide a McCumber parameter, β<sub>c</sub> ≈ 1. The unit cell is a two-junction interferometer sharing its junctions with the neighboring cells. There are three bias currents supplied to the array. *I*<sub>b</sub>, is a uniformly distributed current applied to the individual junctions through the resistances *R*<sub>1</sub> - *R*<sub>20</sub>. These resistances are ten times larger than the junction shunt resistances. *I*<sub>e1</sub> is fed directly to the edge junction *J*<sub>1</sub>. *I*<sub>e2</sub> is fed directly to *J*<sub>20</sub> and is used only when applying a magnetic field, which is

controlled by adding a dc current,  $I_h$ , to  $I_{e1}$  and having  $I_{e2} = -I_h$  at  $J_{20}$ . The array voltage,  $V$ , is measured across one of the edge junctions.

## 2.2 Fabrication technique

Standard trilayer Nb-AlO<sub>x</sub>-Nb technique was employed to fabricate the 20-junction arrays with a critical current density of about 1 kA/cm<sup>2</sup>. The junctions were identical with the following characteristics: Critical current  $I_c = 265 \mu\text{A}$ , junction resistance (including the external shunt resistance)  $R = 1.75 \Omega$ . The junction capacitance is estimated to be  $C = 0.8 \text{ pF}^{38}$ , giving a McCumber parameter  $\beta_c = 2$ . We have estimated the capacitance connected with the overlap geometry to be negligible. This is confirmed by measurements using different geometries. The inductances,  $L_1 - L_{20}$ , as measured with a two-junction interferometer located on the substrate close to the array had the self-inductance  $L = 9.4 \text{ pH}$ . The junctions were circular with a diameter of  $5 \mu\text{m}$ .

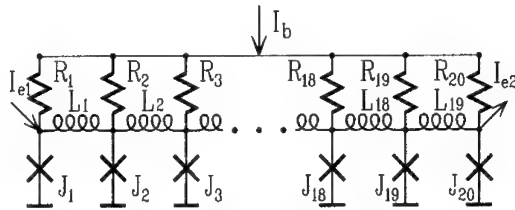


Figure 2. Equivalent circuit of one-dimensional array of over-damped Josephson tunnel junctions (crosses). The resistances  $R_1 - R_{20}$  provide a uniform bias current. A magnetic field may be introduced by adding a current,  $I_h$ , to one of the edge currents, say  $I_{e1}$  and subtracting it from the other,  $I_{e2}$ . The array voltage,  $V$ , is measured across one of the edge junctions.

## 2.3 Experimental results

The measured  $V(I_h)$ -curve with fixed  $I_{e1}$  appears as a smooth curve that accurately fits to the predictions of the Resistively Shunted Junction (RSJ) model for a single junction:

$$V = R_t (I_b^2 - I_{cb}^2)^{1/2} \quad (8)$$

here  $R_t$  is the total shunt resistance of the junctions in the array and  $I_{cb}$  is a critical value of  $I_b$ . An external magnetic field introduced by  $I_h$  does not change the shape of the  $IV$ -characteristic. It means that the bias current  $I_b$  is uniform and does not influence the magnetic field distribution in the array. On the contrary, an applied edge current  $I_{e1}$

significantly changes this distribution. The experimental  $V(I_{e1})$ -curves obtained with zero magnetic field ( $I_h = 0$ ) for ten different fixed values of  $I_b$  are presented in Figure 3.

The bias current,  $I_b$ , defines the velocity of fluxons moving through the array and influences the voltage positions of the (nearly) horizontal steps. From the experimental curves we have found that the current width,  $\Delta I_{e1}$ , of the steps is given by  $\Delta I_{e1} = \phi_0 / L$ , where  $L$  is the inductance connecting the junctions. The numerical simulations confirmed this picture. Accordingly, a new step appears when an additional fluxon penetrates into the array. This effect is similar to the one observed for a non-symmetrically biased two-junction interferometer, where the bias current induces a magnetic field in the interferometer loop, resulting in the well-known modulation of the  $IV$ -curve. The extremely small differential resistance of the steps in the junction array may be interpreted as being due to some kind of nonlinear resonant interaction as will be shown in the next chapter. It is definitely not a geometrical resonance since the step voltage varies with the common bias current  $I_b$  (as given above), and also because the  $V(I_b)$ -characteristic is smooth. Furthermore the damping of the circuit is much too large for the observation of geometrical resonances.

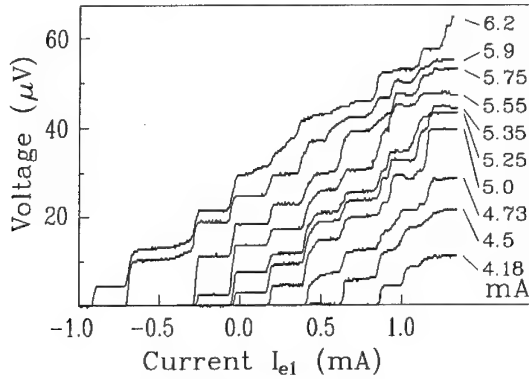


Figure 3. Array voltage,  $V$ , versus edge current,  $I_{e1}$ , measured for different values of the common bias current,  $I_b$  (values given in the right column) for zero external magnetic field ( $I_h = 0$ ,  $I_{e2} = 0$ ).

Figure 4a-d shows a family of  $V(I_{e1})$ -curves for different values of the uniformly applied magnetic field (fixed  $I_b$ ). It is obvious that decreasing the magnetic field shifts the steps towards larger  $I_{e1}$  values. Actually, experiments show that a new step appears whenever the magnetic field is incremented by  $\Delta I_h = \phi_0 / L$ , corresponding to one more fluxon threading the array (see Figure 4a-b). In the range  $\Delta I_h$  the magnetic field is unable to change the number of fluxons in the array.

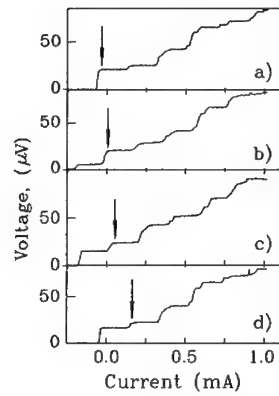


Figure 4. Experimental  $V(I_{e1})$ -curves at different values of the magnetic field and fixed common bias current,  $I_b = 5.2$  mA; a)  $I_b = 0.4$  mA, b)  $I_b = 0.31$  mA, c)  $I_b = 0.22$  mA, and d)  $I_b = 0.07$  mA. The arrow indicates the shift of the same step.

Figure 5 shows the array voltage as function of magnetic field at the fixed edge current,  $I_{e1}$ , where the steps appeared in Figure 4c. One can see that each new step reduces the critical current and results in an increase of the voltage. Each time after the step has moved on to the right in Figure 4 the critical current becomes large again.

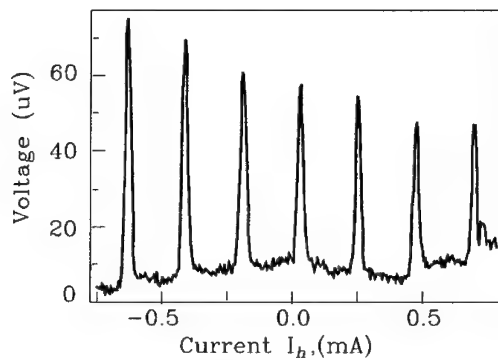


Figure 5. Array voltage as function of magnetic field for fixed  $I_b = 5.2$  mA and  $I_{e1} = -0.22$  mA

#### 2.4 Computer simulation

The 20-junction array has been simulated within the framework of the simple RSJ model as justified by the small shunt resistance. The junction parameters used in the

simulations were close to the experimental values: critical current  $265 \mu\text{A}$ , resistance  $1 \Omega$ , capacitance  $0.8 \text{ pF}$ , and inductance  $9.4 \text{ pH}$ . The sample design was made in such a way that we avoided the influence of the microstrip lines used in the circuit. That was done by a careful use of filters, damping parameters and geometrical dimensions. If these precautions were not taken resonances due to such effects were easily observed in the experiment. Hence in our simulations we do not include such effects.

Figure 6 shows the calculated  $V(I_{e1})$ -curves at different values of the common bias current,  $I_b$ . There is good general agreement between the simulations and the experimental curves in Figure 3. We note that the size of the steps and their voltage position agree between simulation and experiment. The same simulation made with zero junctions capacitance gave the same IV-curve, indicating that the steps are not caused by any LC resonance. We will show later that the discrepancy between Fig. 3 and 6 for  $I_{e1} > 0$  is caused by an additional parasitic magnetic field in the experiment.

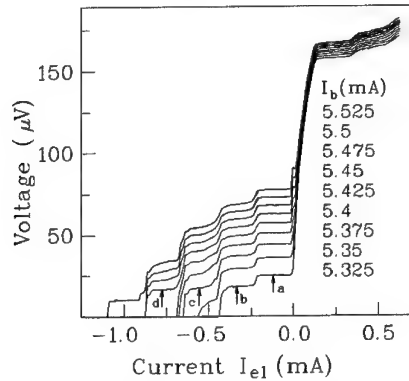


Figure 6. Computer simulation using the experimental parameter values of the circuit elements (see text). Calculated  $V(I_{e1})$ -curve for different values of the total uniform bias current,  $I_b$ . The step voltages are strictly proportional to  $(I_b^2 - I_{c0}^2)^{1/2}$ .

In order to understand the processes causing the step structure, two kinds of curves with bias points indicated **a** - **d** in Figure 6 were calculated. The first is shown in Figure 7a-d presenting the quantity  $N = (\phi_{i+1} - \phi_i) / 2\pi$  as a function of cell number,  $i$ , and time,  $t$ , where  $\phi_i$  is the quantummechanical phase of junction  $i$ .  $N$  thus becomes the number of fluxons in the cell defined by junctions  $i$  and  $i+1$ , i.e.  $N = \phi / \phi_0$ , where  $\phi$  is a magnetic flux within the cell and  $\phi_0$  is flux quantum. By its definition  $N$  may take noninteger values during the transient flux propagation as can be seen in Figure 7. Figure 8a-d shows the instantaneous voltage across the individual junctions as function of the same arguments. The voltage pulses observed appear when a fluxon is transferred from one cell to the next. From Figure 7 and Figure 8 we see that the edge current causes a

splitting of the array into sections (domains) each having predominantly the same number of fluxons per unit cell.

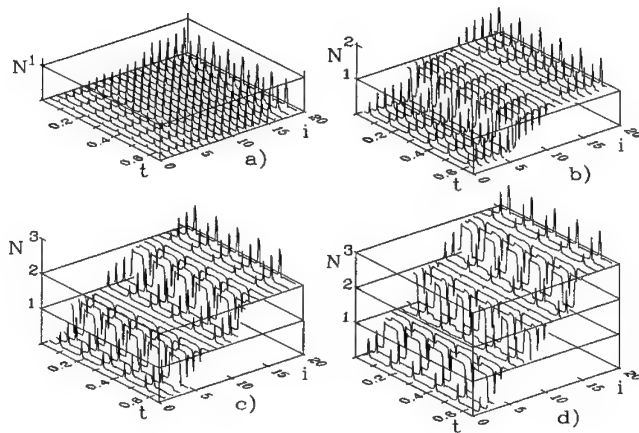


Figure 7. Number of fluxons ( $N$ , see text) located in a unit cell as function of cell number,  $i$ , and time,  $t$ . The time unit is 1 ns. The corresponding bias points are marked a - d in Figure 6. The edge current was introduced to the 20th junction.

One can see that the non-uniform magnetic field caused by the edge current penetrates into the array over a distance significantly larger than the Josephson penetration depth observed in long tunnel junctions. This is somewhat unexpected since the ratio of the Josephson inductance to the geometric inductance is only about 0.12. The first step (Figure 7a and Figure 8a) seems to be due only to the edge current which is constant and dictates the repetition rate of the fluxon excitation. The step voltage depends on this repetition rate and on the average velocity of the fluxon. This also explains the increase of the step voltage with increasing total bias current depicted in Figure 3 and Figure 6.

A more complex picture appears for higher order steps. In Figure 7b-d and Figure 8b-d one can see that we have two types of domains; the one near the left edge looks like the one discussed above. The domains not reaching the edges are spatially symmetric; the junction in the middle of the domain (in the following called the leading junction) switches first, producing a fluxon and an antifluxon which in turn propagate in opposite directions. That means that the total fluxon number within a symmetrical domain is conserved at all times. This intrinsic feature characterizes all the symmetrical domains in Figure 7b-d. The simulation shows that the number of domains changes as we go from one step to another, and that a variation of the edge current within the same voltage step only changes the

spatial position of the leading junction in the edge domains. It looks as if there is a mutual phase-locking between the leading junctions belonging to different domains. The junctions are connected by a superconductor and must be synchronized, leaving only the spatial location of the leading junction as the free parameter. The LTSEM experiment is described in the next section confirms that claim.

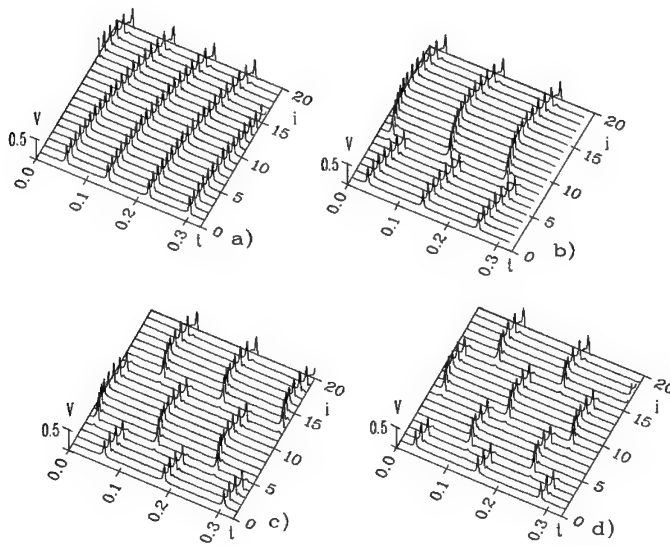


Figure 8. Voltage (in mV) across individual junctions as function of its number,  $i$ , and time,  $t$ . The time unit is 1 ns. The edge current is introduced to the 20th junction.

### 3. Imaging of the dynamic magnetic structure in a parallel Array of shunted Josephson junctions

In the previous chapter we have considered the new effect that was verified from computer simulations to be due to the self-induced magnetic field produced by the edge current. This is a dynamic state in a highly nonlinear system and the influence of differences in junction and array parameters on the domain stability is still unknown. The main aim of this section is to experimentally confirm and visualize the domains by using Low Temperature Scanning Electron Microscopy (LTSEM) and thus to determine which junctions are responsible for the different steps observed in the IV curve.



### 3.1 Sample and experimental technique

The LTSEM technique offers the possibility of a spatially resolved *in situ* investigation of superconducting tunnel junctions and integrated circuits<sup>39-43</sup>. In that technique the top surface of the sample is scanned with an electron beam, while the bottom of the substrate carrying the junction is in intimate thermal contact with a bath of liquid helium. The main effect at the focus point ( $x, y$ ) of the electron beam is a local heating (0.1 - 10 K depending on the beam parameters) of the sample. The spatial resolution of about 1 - 3  $\mu\text{m}$  is determined by the thermal healing length of the sample configuration. The beam power - typically 2.5  $\mu\text{W}$  - can be adjusted over a wide range to ensure that the electron beam acts only as a passive probe on the sample. Scanning over the sample, the beam induced signal, say the change in the voltage across the array, is simultaneously recorded with a digital imaging system.

In this experiment we have tested circuits for which the equivalent circuit is the same as in Figure 2. The only difference is that the transmission line consists of a one-dimensional array of twenty Josephson junctions  $J_2 - J_{21}$  connected in parallel (like in Figure 2) and an additional generator junction  $J_1$  with higher critical current. This is a typical connection for RSFQ logic (for example ref. 5,6). The parameters of the circuit are the following: for junctions  $J_2 - J_{21}$  the critical current is 0.115 mA, shunt resistance 1.2  $\Omega$ , capacitance 0.5 pF, while for junction  $J_1$  we have a critical current of 0.23 mA, shunt resistance 0.6  $\Omega$ , and capacitance 1.0 pF. Each of the junctions are resistively shunted (externally) to provide a McCumber parameter,  $\beta_c \approx 1$ . The unit cell is a two-junction interferometer sharing its junctions with the neighboring cells. The inductances were  $L_1 - L_{20} = 5$  pH.

The same technology as described in sec 2.2 was used for junction fabrication. The junctions were circular with a diameter of 4  $\mu\text{m}$ . The total size of the array was 2.5 mm. The edge currents  $I_{e1}$  and  $I_{e2}$  are fed directly to junction  $J_1$  and  $J_{21}$ , respectively. The array dc voltage  $V$  and the electron beam induced voltage signal  $\Delta V(x, y)$  are measured across one of the edge junctions.  $\Delta V(x, y)$  is detected by standard lock-in technique with the chopping frequency (20 kHz) of the electron beam as reference. The output from the lock-in detector is fed into a digital imaging system. The underlying mechanism of  $\Delta V(x, y)$ , giving rise to the image of the above-mentioned domains, is a sequential heating of the individual Josephson junctions resulting in a reduction of their critical currents.

### 3.2 Experimental results

The experimental  $V(I_{e1})$  curves obtained with  $I_{e2} = 0$  for four different fixed values of  $I_b$  are presented in Figure 9. Qualitatively this result is similar to what we observed with a similar array without generator junction (see Figure 3). From comparisons with the homogeneous array results we infer that the main effect of the generator junction is that it produces the small additional substeps barely visible on the  $IV$  curves shown in Figure 9.

In both cases the bias current  $I_b$  defines the velocity of fluxons moving through the array and defines the voltages of the (nearly) horizontal steps.

The main experimental results are shown in Figure 10. Let us assume the array under investigation to be along the  $x$ -axis. In the experiment one usually has a slight misorientation between the scan line and the line connecting the centers of the junctions. This is the reason to present in Figure 10 a series of line scans recorded with successive small off-sets to new  $y$ -axis positions of the beam in order to completely cover all the junctions in the array. The images 0 through 5 in Figure 10 correspond to the points with the same numbering in Figure 9. The images in Figure 10 are off-set vertically for clarity. Image 6 in Figure 10 is obtained from a usual Scanning Electron Microscope (SEM) picture, and the maximum signals in these curves correspond to the shunting resistances. The positions of the midpoints of the shunting resistances coincide geometrically with the junctions centers. This allows a conclusion that the junction positions correspond to the maxima on images 0 - 5 thus confirming that the signals really come from the junctions. We also notice that the signals extend beyond the circumference of the junctions due to the heating of the area outside the junctions. The smooth envelope spanning several junction sites indicates that different junctions in the array play different roles in setting up the particular step voltages and that for different steps there are different groups of junctions producing the LTSEM response. Below this is discussed in more detail. It should be pointed out that the images were sensitive to parasitic magnetic flux trapped in the superconducting films. One procedure used to remove such trapped flux was to slowly scan the sample with high beam power. After this procedure the measured IV curves in Figure 9 fit better to the simulated ones even with positive edge current.

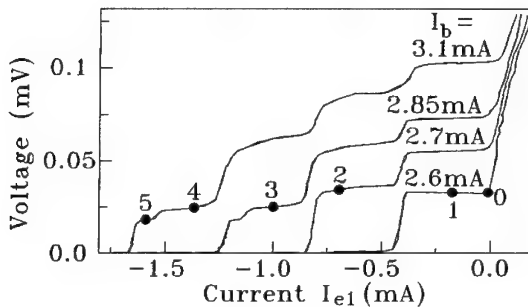


Figure 9. Array voltage  $V$  versus edge current  $I_{e1}$ , measured for different values of  $I_b$ . The other second edge current  $I_{e2} = 0$ . Marked points correspond to  $I_{e1} = -0.008$  mA (0);  $-0.173$  mA (1);  $-0.695$  mA (2);  $-1.0$  mA (3);  $-1.367$  mA (4);  $-1.589$  mA (5).

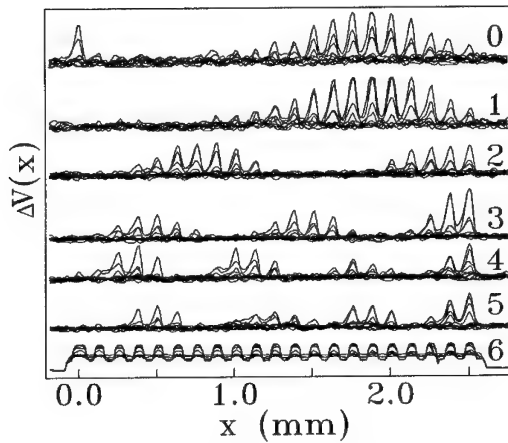


Figure 10. LTSEM response  $\Delta V(x)$  as a function of the beam position along the array. Images 0 - 5 are the signals proportional to the voltage increment of the steps at the marked points in Figure 9. Each image consists of several lines scans around the junction position (see text). Image 6 shows a usual SEM image of the sample. The images are vertically off-set for clarity.

### 3.3 Computer simulations and discussion.

In order to understand the nature of the recorded images a number of computer simulations were made. An important parameter for the calculations is the critical current reduction of a single junction produced by the electron beam. This parameter was determined experimentally by focusing the beam on the 11th junction and then measure the reduction,  $\Delta I_{bc}$ , of the total critical current of the array. To our first surprise we found  $\Delta I_{bc} = 0.120$  mA, which is a little bit larger than the critical current  $I_c = 0.115$  mA of a single junction. A numerical simulation, however,  $\Delta I_{bc}$  as function of  $I_c$  of the 11th junction gave the result shown in Figure 11. Here we notice that  $\Delta I_{bc}$  is about three times larger than the change in  $I_c$  of a single junction. Considering this simulation result, we can estimate the suppression of the critical current of a single junction to be 0.035 mA, that is about 30%. This effect is due to internal rearranging of currents and magnetic flux in the array, and may be related to the operation of the HTS flux flow transistor<sup>44</sup>. Alternatively it may be utilized as a new kind of amplifier.

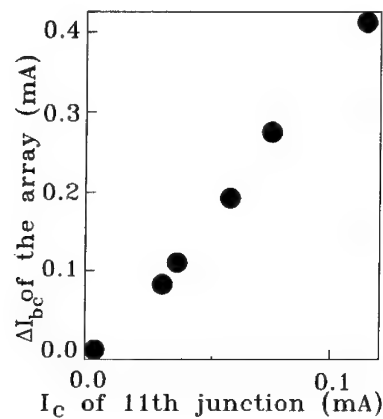


Figure 11. Computer simulated dependence of the reduction in the critical current of the array (critical value of  $I_b$ ) as a function of the critical current of the 11th junction in the array.

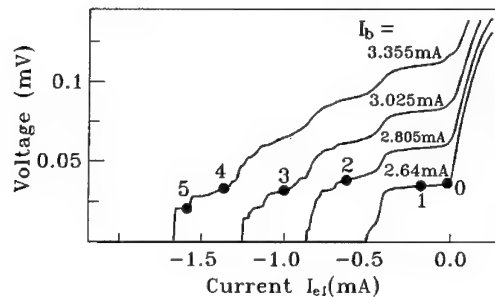


Figure 12. Simulated array voltage  $V$  vs. edge current  $I_{e1}$  for different values of the uniform bias current  $I_b$ . The other edge current is set to  $I_{e2} = -0.0625$  mA (see text). Marked points correspond to  $I_{e1} = -0.0125$  mA (0);  $-0.175$  mA (1);  $-0.625$  mA (2);  $-1.000$  mA (3);  $-1.3625$  mA (4);  $-1.5875$  mA (5).

Figure 12 shows the simulated IV curves obtained for the transmission line with parameters close to the experimental ones. Notice that without any fitting parameters most of the features of the experimental curves in Figure 9 are reproduced. We further simulated the change in the array voltage  $\Delta V$  at the enumerated points in Figure 12 as function of the junction number for which the critical current was suppressed by 30%. The results of these simulations are presented in Figure 13. When these curves are compared with the experimental images in Figure 10 there is a convincing overall resemblance.

Experimentally we found that the images were sensitive to the presence of trapped magnetic flux. This effect was also investigated numerically. In order to obtain the best fit

to Figure 10 we had to introduce an additional edge current  $I_{e2} = -0.0625$  mA. Further simulation showed that this small current had no visible effects on the simulated IV curve, and did not change the size of the domains with respect to the number of active junctions (see Figure 13). Only minor details within the domains were modified.

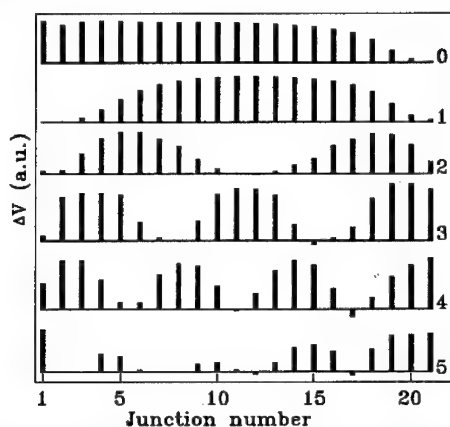


Figure 13. Simulated LTSEM response  $\Delta V$  (arbitrary units) as a function of the junction number. Images enumerated 0 - 5 show the voltage increment at the marked points in Figure 12

With the good agreement between experiment and simulations we now look into the dynamics of the transmission line. Figure 14a-f shows the instantaneous voltage across the individual junctions as function of the junction number and time calculated with parameters corresponding to Figure 13. The voltage pulses appear whenever a fluxon is transferred from one cell to the next. As was described in detail in a previous chapter (Ref.32) the edge current causes a splitting of the array into domains each having predominantly the same number of fluxons per unit cell. It means that the magnetic field produced by the edge current does not penetrate into the array smoothly as in a long Josephson junction.

There are two kinds of domains in Figure 14a-f: (i) The domains not reaching the edges are spatially symmetric; the junction in the middle of the domain (leading junction) switches first, producing a fluxon and an antifluxon that in turn propagate in opposite directions. This means that the total fluxon number within a symmetrical domain is conserved at all times; (ii) The other kind of domains touch the edges; for those domains the position of the leading junction can be shifted from the center of the domain depending on the applied edge currents. Comparing the simulated images in Figure 13 with the domain structures in Figure 14 one may conclude that the experimental LTSEM images reproduce the position of the leading junctions. This is corroborated by the fact that the number of junctions within a given domain is approximately the same as seen in Figure 14. Actually in the experiment the number of junctions in each domain may appear lower if the sensitivity of the LTSEM is reduced by e.g. too low e-beam intensity.

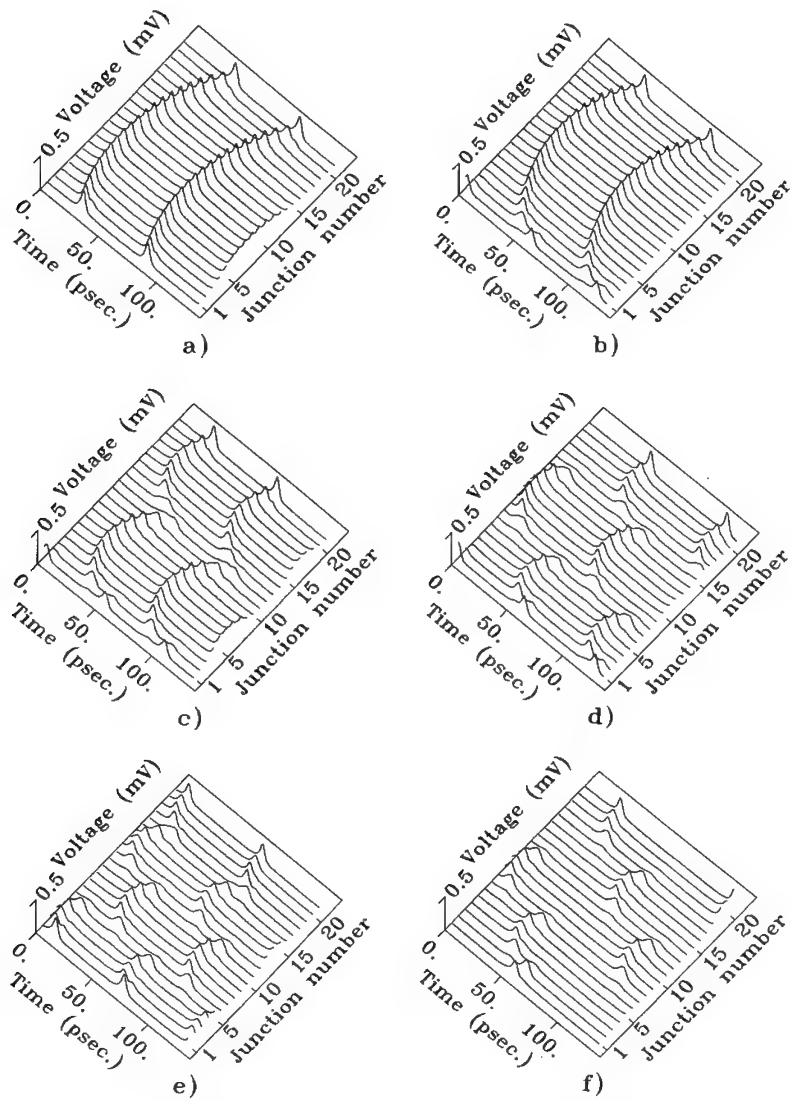


Figure 14. Simulated instantaneous voltage across the individual junctions as function of the junction number and time. The edge current  $I_{e1}$  is injected to the first junction. Figs. a - f correspond to the points marked 0 - 5 in Figure 12

The simulations depicted in Figure 14 reveals one more feature. As was pointed out above, a generator junction with two times higher critical current creates substeps. Each step is associated with a definite number of domains and the substeps seem to originate in a redistribution of junctions among the domains (compare Figure 14e and Figure 14f). The experiment seems to confirm this result when one compares the LTSEM image 4 with 5 in Figure 10.

#### 4. How the dynamics of 1D shunted array impose the high frequency limit for RSFQ circuits.

Despite the separate elements of RSFQ logic demonstrate frequency of operation up to the Josephson frequency  $f_{\max} = \phi_0^{-1} I_c R_n = \phi_0^{-1} V_c$ , there is a new limitation that appears when one connects these elements together. Typically the transmission line or a parallel connection of shunted Josephson junctions is used to interconnect these elements. The computer simulation shows that fluxon repulsion appears when the time interval between them is comparable with the  $1/f_{\max}$ .

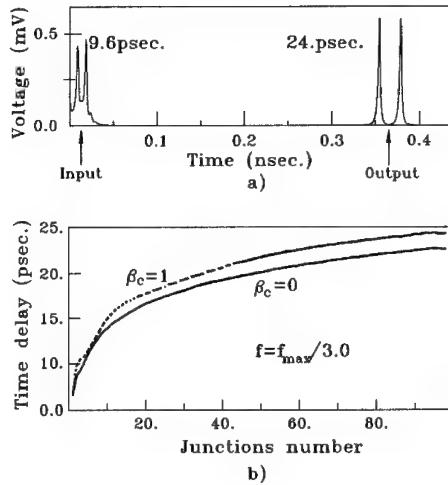


Figure 15. Propagation of two fluxons in an array of 100 shunted junctions. a) Instantaneous voltage on the first junctions (input) where fluxons were introduced and the same voltage on the 100th junction (output); b) Time distance between the fluxons as function of the junction number at two McCumber parameters  $\beta_c$ . The transmission line parameters were: critical current of single junction - 0.125mA, resistance -  $2\Omega$ , bias current for each junction - 0.1mA, interconnecting inductances - 7.8pH.

Figure 15a shows the instantaneous voltage on the input of the 100 junction array (transmission line) when two fluxons are introduced to the input with a time delay of

9.6psec. This delay corresponds to the  $1/f_{\max}$  value. During the propagation within the line, the time delay grows up and is reaching 24psec at the output of the line. Figure 15b presents the delay as function of junction number. One can see from this figure that the time delay is saturated at a value corresponding approximately to  $0.3f_{\max}$ . The fluxons present a digital code in RSFQ circuits. Their interaction may change a consequence of the bits during the propagation on a JTL and result in may produce loosing of digital information. That is why the absolute limitation of an RSFQ circuit is about  $0.3f_{\max}^{-1}$ .

To minimize the repulsion, Josephson junctions with higher  $I_c R_n$  products are demanded. Typical  $Nb/AlO_x/Nb$  junctions have critical current densities is about  $1\text{kA}/\text{cm}^2$  and  $I_c R_n = 0.25\text{--}0.3\text{mV}$ . It means that the highest frequency of operation of RSFQ devices based on them is about 30-50GHz. This is already comparable to the best semiconductor circuits. There are two ways to improve the performance of RSFQ circuits. The first one is to increase the critical current density of niobium junctions<sup>45</sup>, and the second is to use novel high  $T_c$  based Josephson junctions with inherently higher  $I_c R_n$  values. Both ways imply more complicated technologies but it seems that this is the only way to make superconducting digital circuits competitive with existing semiconductor devices.

## 5. Quasidigital devices as examples for nonlinear phenomena in RSFQ circuits.

RSFQ circuits can be considered as a net of Josephson junctions with defects in a regular lattice. The present technology (e.g. ref. 38) enables us to fabricate rather complicated systems that can be used both as a digital device and as so called quasidigital circuits. Quasidigital effects appear in RSFQ logic due to their digital properties and at the same time there is a specific dynamic state within them. This state can exist at voltages even higher than the characteristic voltage of the used junctions. For examples the RSFQ flip-flop cell passes only every second fluxon from the input to its output. If one applies a permanent voltage to the input of this cell, a stream of fluxons is coming to the input with the corresponding voltage given by Eq. 7. This produces a frequency on the flip-flop output, and a voltage, that are two times smaller than the input ones<sup>3,6</sup>. So from a quasidigital point of view, this cell is a precise voltage divider. In this chapter we discuss another circuit: a phase-locked serial dc SQUID array<sup>26</sup> and a voltage doubler<sup>29,30,31</sup> that shows more quasidigital properties than digital ones. We expect that the dynamics in these devices may have similar features at different discreteness and shunting parameters (see Figure 1).

### 5.1 Radiation detection from phase-locked serial dc SQUID arrays.

Figure 16a shows the equivalent circuit that involves three SQUID loops formed by pairs of junctions  $J_1\text{--}J_2$ ,  $J_3\text{--}J_4$ , and  $J_5\text{--}J_6$ , respectively (the fabrication technique is described in section 2.2 or in<sup>38</sup>). All these SQUIDs have common inductances  $L_2$  and  $L_3$  which provide a strong coupling between them. All the circuits are biased with the total



currents  $I_1$ ,  $I_2$ . The fluxon interaction in this circuit may be understood from an energy point of view. When the three junctions **J1**, **J3**, and **J5** in the left arm are switched simultaneously and three fluxons are sitting in the corresponding interferometers, the total currents through the inductances  $L_2$  and  $L_3$  are minimized, giving rise to a configuration having the lowest energy for passing a bunch of flux quanta. The height of the energy barrier is proportional to the mutual inductance, however, the inductance should be small enough to prevent trapping of fluxons ( $\eta < 1$  in Figure 1). A numerical simulation confirms this suggested mechanism of SQUID interaction<sup>26</sup>.

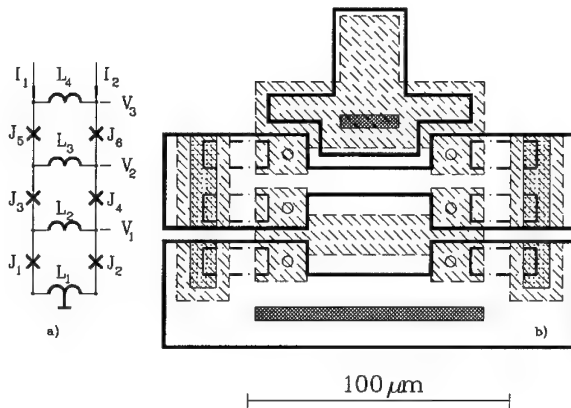


Figure 16. Three series connected SQUIDs. (a) Equivalent circuit;  $L_1=L_2=L_3=L_4=7.8\text{pH}$ . Identical shunted junctions with  $I_c=82\mu\text{A}$ ,  $R=1.9\Omega$ , and  $C=0.7\text{pF}$  were used. (b) Actual layout; thick line- base electrode, dashed area - wiring, circles - Josephson junctions, dash point area - resistances, area with crosses - full connection between base and wire electrodes, cross-hatched area - contacts of base electrode with the ground plane.

The total dc resistance  $R_s$  of the three-SQUID array was  $2.8\Omega$  and the differential resistance  $R_d$  measured as the slope of the dc IV curve of the array was the order  $1\text{-}10\Omega$ . The full width at half-power  $\Delta f$  of the emitted radiation may be estimated from:

$$\Delta f = 4\pi k_B T R_d^2 / \phi_0^2 R_s \quad (9)$$

where  $T$  is the Kelvin temperature and  $k_B$  is Boltzmann's constant. Eq. (9) refers to the well-known RSJ model with Nyquist type thermal noise. With the parameters stated the expected linewidth is as large as  $2\text{GHz}$  at  $4.2\text{K}$ . For the detection of signals with such a large linewidth a standard mm-wave spectrum analyzer with its harmonic mixer was not feasible. Instead a low-noise direct mm-wave mixer powered at  $f_{LO}$  from a frequency locked Gunn diode local oscillator was used. The output from the mixer was (if-) amplified and fed to a dc-  $1.8\text{GHz}$  spectrum analyzer. The receiver therefore had two

windows (side-bands) placed symmetrically with respect to  $f_{LO}$ . Typically 1 MHz wide sidebands at  $f_{LO} \pm 20$  MHz were used. The substrate with finline antenna was inserted in a slit cut symmetrically in the broad walls of the 60-90 GHz waveguide. The external magnetic field was generated by a 2-mm-diameter ring shaped wire which was positioned under the sample at a distance of about 1 mm.

Figure 17 shows the detected power vs. voltage for a three-SQUID array in the presence of an applied magnetic field. One can see a mutual phase locking of SQUIDs at zero magnetic field as it should be. Moderate magnetic fields only reduce the amplitude of the emitted radiation correspondingly to the simulation and strong magnetic field destroys the coherent state completely giving in Figure 17 three peaks separately produced by the SQUIDs. In the synchronous state the linewidth of emitted radiation corresponds to Eq. (9) if the resistance of a single SQUID was taken. This means that the linewidth is independent of the number of SQUIDs  $N$  giving rise a power of  $N^2$  times the power of a single SQUID. The important fact is that this type of series connection of  $N$  phase-locked SQUIDs leaves the linewidth of the emitted radiation generation unchanged while the output resistance increases linearly with  $N$ .

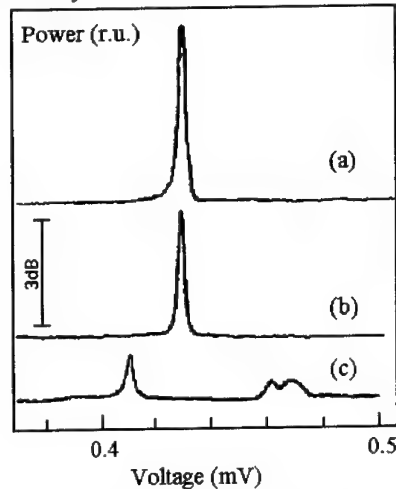


Figure 17. Detected power vs. voltage for a three-SQUID array in the presence of an applied magnetic field  $B$ . (a)  $B=0.0$ , (b)  $B=3.0$ , and (c)  $B=21.0$  in relative units.  $f_{LO}=69.5$  GHz,  $T=4.2$  K.

The above result has also been verified for ten coherently radiating SQUIDs placed on an eleven-cell array substrate. The number of coherently working stages was inferred from the measured dc voltage and the frequency of the radiation peak using  $V_N = N f \Phi_0$ . The computer simulations of an eleven-SQUID array have shown that the coherent state depends on the initial conditions. If a flux quantum is placed near the center of such an array, the array splits into two coherent sections with a mutual phase difference between them.

### 5.2 Single flux quantum voltage amplifiers.

In the previous section we have observed the synchronous interaction of fluxons in the neighboring SQUID loops. There is another quasidigital circuit, the voltage doubler, that is based on the so-called asynchronous coupling between SQUID loops where a fluxon and an antifluxon are passing simultaneously through the interferometers.

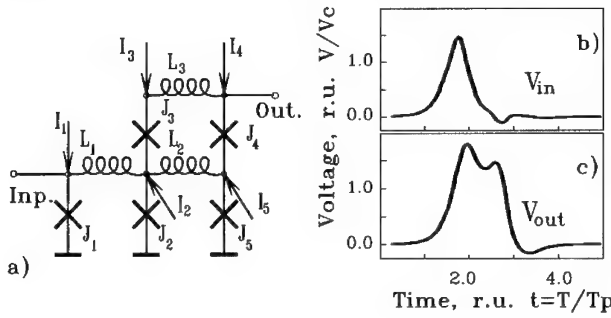


Figure 18. (a) Equivalent circuit of quasi-digital voltage amplifier. Calculated input (b) and output instantaneous voltages (c).  $J_{c1}=J_{c3}=J_{c5}=0.3\text{mA}$ ,  $J_{c2}=J_{c4}=0.15\text{mA}$ ,  $L_1=L_2/2=10L_3=1.3\text{pH}$ ,  $I_1=0.24\text{mA}$ ,  $I_2=0.21\text{mA}$ ,  $I_3=I_4=0.12\text{mA}$ ,  $I_5=0.03\text{mA}$ ,  $I_c R_n=0.3\text{mV}$  for all junctions.

Figure 18a shows the equivalent circuit of a voltage doubler. The elements marked by the crosses are overdamped Josephson junctions with a McCumber parameter  $\beta_c \approx 1$ . The main part of the circuit consists of two interferometers  $J_2L_2J_5$  and  $J_3L_3J_4L_2$  strongly coupled via the inductance  $L_2$ . When a fluxon arrives at the input, the junction  $J_1$  switches (see Figure 18b) and a flux quantum enters the interferometer  $J_1L_1J_2$ . The inductance  $L_1$  is small enough to prevent the catching of this quantum by the interferometer  $J_1L_1J_2$  ( $J_2L_1 < \Phi_0$ ) and the fluxon passes to the bottom interferometer  $J_2L_2J_5$ . As a result a phase difference appears on the inductance  $L_2$ , inducing a clockwise current in the loop  $J_3L_3J_4L_2$ . This reduces the bias current through  $J_3$  and increases it through junction  $J_4$ . The inductances were chosen small to produce a circular current sufficient for switching  $J_4$ . As result of the switching, an antifluxon penetrates into the top interferometer  $J_3L_3J_4L_2$ . When the fluxon and antifluxon are in corresponding interferometers they produce bias currents which exceed the critical values for junctions  $J_4$  and  $J_5$ . The last ones are switching and the circuit is returning to its initial state. Summing up, two voltage pulses appear on the output of the multiplier when only one pulse is introduced to the input. This is a result of the fluxon passing through the bottom and antifluxon through the top interferometers as Figure 18c shows. If one applies a dc voltage  $V_{in}$  to the input of the doubler, a stream of fluxons occurs with frequency  $\Phi_0^{-1}V_{in}$ , producing on the output a frequency  $2\Phi_0^{-1}V_{in}$  giving  $V_{out}=2V_{in}$ . The result of such a measurement is presented in Figure 19. The Nb/AlO<sub>x</sub>/Nb junctions used for the experiment were fabricated as

described in section 2.2. They have a characteristic voltage  $V_c=0.3\text{mV}$  and the experiment clearly shows the voltage doubling described above.

There are two ways to connect 'n' doublers. In the case of series connection, the output of one doubler is connected to the input of another and a voltage multiplication by  $2^n$  is realized. In this case the output voltage will be limited by the characteristic voltage as it is for a single doubler<sup>31</sup>.

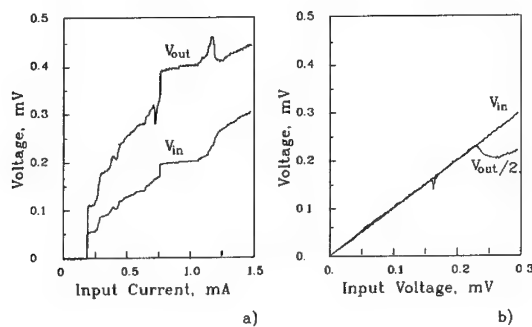


Figure 19. Experimental results for the voltage doubler. (a) Input  $V_{in}$  and output  $V_{out}$  voltages in dependence of the input current that biased the generator junction in the input transmission line; (b) Input and divided on two output voltages as a function of the input voltage  $V_{in}$ ,  $T=4.2\text{K}$ .

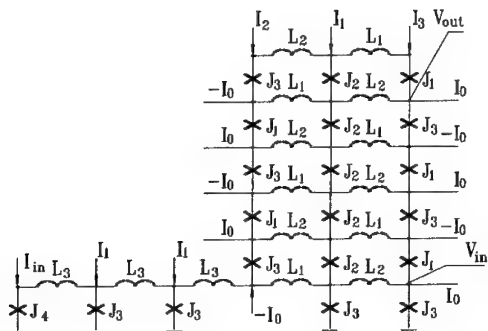


Figure 20. Equivalent circuit of six stage parallel amplifier.  $J_1=0.11\text{mA}$ ,  $J_2=0.165\text{mA}$ ,  $J_3=0.22\text{mA}$ ,  $J_4=0.33\text{mA}$ ,  $L_1=0.26\text{pH}$ ,  $L_2=4.2\text{pH}$ ,  $L_3=4.7\text{pH}$ ,  $I_0=0.05\text{mA}$ ,  $I_1=0.13\text{mA}$ ,  $I_2=0.165\text{mA}$ ,  $I_3=0.01\text{mA}$ . All junctions have  $\beta_c=1$ .

For the parallel connection an amplification of  $(n+1)$  times can be obtained and the output voltage will be limited by the number of stages. Compared to the simplicity of the series connection of doublers, the parallel one looks more complicated. Figure 20 shows the equivalent circuits of a six stage parallel amplifier and Figure 21 presents an experimental result that shows that only five stages work properly. There are two basic ideas of building the parallel amplifier. The first idea is the voltage doubling that is the same as was discussed above. The relatively large mutual inductances  $L_2$  (see Figure 20) provide this process. The other idea is increasing of flux energy  $LI^2/2$  before the doubling. A transmission line is used for this purpose. This is a reason that for the parallel amplifier we have more than one SQUID in one level and the circuit looks like a **2D** array. The problem was how to prevent an interaction between the transmission lines in different levels. The solution was coming from a special design within the standard Nb/AlO<sub>x</sub>/Nb technology that allows to make the relatively large inductance  $L_2$  and simultaneously small inductance  $L_1$ . The circuits is operating in the following way. The input fluxon switches junction  $J_1$  and produces an antifluxon in the second level because of the doubling effect. The energy of this antifluxon is amplified by junction  $J_2$  and it becomes ready for doubling and switches the next junction  $J_1$  in the following level.

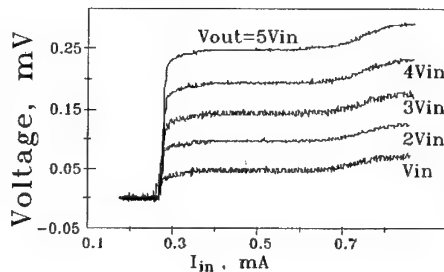


Figure 21. Experimentally obtained voltages on each stage of parallel QDVA vs. bias current of the input junction.

## 6. Conclusion

In this report we have observed nonlinear phenomena in RSFQ circuits. The main points were the following.

We have demonstrated that the new effects appear in an overlapping region between RSFQ logic and Long Josephson junctions.

The RSFQ design tricks enable us to build many interesting quasidigital circuits that in particular case are **1D** and **2D** arrays of Josephson junctions.

The dynamics of RSFQ imposes rigid limitations for high frequency performance of RSFQ logic, giving the necessity to use Nb based junctions with higher critical current

density or novel HTS based junctions. This is extremely important for HTS technology, because shunted junctions were used to fabricate RSFQ circuits.

We have computer simulated and experimentally investigated the new effect of non-uniform magnetic field penetration into a one-dimensional array of over-damped Josephson junctions. Many of the experimental features have been found in the simulations but obviously a more reliable theory is required in order to analyze complex RSFQ circuits. Self-induced magnetic field effects can be also observed in non-uniform arrays and in magnetically extended Josephson structures such as the novel HTS junctions. The inhomogeneity of these junctions produces a complicated magnetic field distribution which in turn may result in the peculiarities seen in their IV-characteristics. We also expect this effect to exist in 2D arrays of shunted junction, that can be considered as a possible model for HTS granular films. The understanding of the effects described here also seems to offer an explanation of the deficiencies in the high frequency operation<sup>36,37</sup> of the Josephson sampler. The presence of domains on the transmission line causes an altered dependence of the time delay on the input voltage.

LTSEM is a powerful tool for a spatially resolved investigation of the dynamics of circuits based on shunted Josephson junctions. It enables us to recognize and visualize directly the dynamics of a one-dimensional parallel connected array of junctions. We envision many applications for this technique within areas such as RSFQ logic and HTS based Josephson junction circuits.

## References

- 1 . K. Nakajima, H. Sugahara, A. Fujimaki, Y. Sawada, *J. Appl. Phys.* **66** (1989) 949.
- 2 . A. Fujimaki, K. Nakajima and Y. Sawada, *Phys. Rev. Lett.* **59**, (1987), 2895.
- 3 . K. Nakajima, H. Mizusawa, Y. Sawada, H. Akoh, S. Takada, *Phys. Rev. Lett.* **65**, (1990), 1667.
- 4 . K. K. Likharev, V. K. Semenov, *IEEE Superconductivity* (1991) **1** 13
- 5 . V. K. Kaplunenko, M. I. Khabipov, V. P. Koshelets, K. K. Likharev, O. A. Mukhanov, I. L. Serpuchenko, A. N. Vystavkin, *IEEE Trans on Magn.* (1989) **25** 861
- 6 . V. K. Kaplunenko, M. I. Khabipov, V. P. Koshelets, I. L. Serpuchenko, A. N. Vystavkin, *ISEC'89, Tokyo* (1989) 411
- 7 . V. K. Kaplunenko, L. V. Filipenko, M. I. Khabipov, V. P. Koshelets, K. K. Likharev, S. V. Rylov, V. K. Semenov, A. N. Vystavkin, *ASC-90, IEEE Trans on Magn.* (1991) **27** 2464
- 8 . O. A. Mukhanov, *IEEE Trans. on Applied Superconductivity* (1993) **3** 2578.
- 9 . S. P. Benz, C. J. Burroughs, and C. A. Hamilton, *IEEE Trans. on Appl. Supercond.*, (1993) **3** 2582
- 10 . Y. K. Kwong, V. Nandakumar, *IEEE Trans. on Appl. Supercond.* (1993) **3** 2666
- 11 . J. Fleischman, T. Van Duzer, *IEEE Trans. on Appl. Supercond.* (1993) **3** 2716

- 12 . S. V. Polonsky, V. K. Semenov, P. I. Bunyk, A. F. Kirichenko, A. Yu. Kidiyarova-Shevchenko, O. A. Mukhanov, P. N. Schevchenko, D. Yu. Zinoviev, K. K. Likharev, *IEEE Trans. on Applied Superconductivity* (1993) **3** 2566
- 13 . Z. G. Ivanov, V. K. Kaplunenko, E. A. Stepantsov, E. Wikborg and T. Claeson, *Supercond. Sci. Technol.* (1994) **7** 239
- 14 . A. V. Ustinov, in: *Nonlinear Superconductive Electronics and Josephson Devices*, eds. G. Costabile et. al. (Plenum Press, New York) (1991) 315.
- 15 . I. L. Serpuchenko and A. V. Ustinov, *Solid State Commun.* (1988) **68** 693.
- 16 . B. A. Malomed, A. V. Ustinov, *J. Appl. Phys.* (1990) **67** 3791.
- 17 . R. Fehrenbacher, V. B. Geshkenbein, and G. Blatter, *Phys. Rev. B* (1992) **45** 5450.
- 18 . B. H. Larsen, J. Mygind, A. V. Ustinov, *Physica B194-196* (1994) 1729
- 19 . M. Cirillo, *J. Appl. Phys.* (1985) **58** 3217
- 20 . A. V. Ustinov, M. Cirillo, and B. A. Malomed, *Phys. Rev. B* (1993) **47** 8357
- 21 . H. S. J. van der Zant, D. Berman, T. P. Orlando, and K. A. Delin, *Phys. Rev. B* (1994) **49** 12945
- 22 . M. Cirillo, B. H. Larsen, A. V. Ustinov, V. Merlo, V. A. Oboznov, R. Leoni, *Phys. Lett. A*, (1993) **183** 383
- 23 . A. V. Ustinov, M. Cirillo, B. A. Malomed, and Yu. S. Kivshar, *Physica B* (1994) **194-196** 1765
- 24 . A. V. Ustinov, M. Cirillo, B. H. Larsen, V. A. Oboznov, P. Carelli, G. Rotoli, *Submitted to Phys. Rev. B: July 16*, (1994)
- 25 . K. K. Likharev, *Dynamics of Josephson Junction and Circuits*, Gordon and Breach, Philadelphia (1991). p.34, p.47
- 26 . V. K. Kaplunenko, J. Mygind, N. F. Pedersen, A. V. Ustinov, *J. Appl. Phys.* (1993) **73** 2019
- 27 . V. K. Semenov, M. A. Voronova, *IEEE Trans. on Mag.* (1989) **25** 1432
- 28 . V. K. Semenov, *Ext. Abstracts ISEC'87* (1987), 138
- 29 . V. K. Kaplunenko, *Superconductivity: physics, chemistry, engineering (Soviet journ.)* (1991) **4** 629
- 30 . V. K. Kaplunenko, V. P. Koshelets, M. I. Khabipov, V. M. Golomidov, S. A. Kovtonyuk, *Extended abstract of ISEC Glasgow, UK*, (1991) 175
- 31 . V. M. Golomidov, V. K. Kaplunenko, M. I. Khabipov, V. P. Koshelets, O. V. Kaplunenko, *ICEC 14 Proceedings, Cryogenics* (1992), **32** 509
- 32 . V. K. Kaplunenko, E. B. Goldobin, M. I. Khabipov, B. H. Larsen, J. Mygind, N. F. Pedersen, *J. Appl. Phys.*, (1993) **74** 5854
- 33 . T. Doderer, V. K. Kaplunenko, J. Mygind, N. F. Pedersen, *Phys. Rev. B Rap. Comm.* (1994) **50** 7211
- 34 . C. A. Hamilton *IEEE Tr. on Applied Superc.* (1992) **2** 139
- 35 . V. K. Kaplunenko, H. B. Larsen, J. Mygind, N. F. Pedersen, *J. Appl. Phys.* (1994) **76** 3172.
- 36 . V. K. Kaplunenko, M. I. Khabipov, E. B. Goldobin, *Supercond. Sci. Technol.* (1991) **4** 674

- 37 . E. B. Goldobin, V. K. Kaplunenko, M. I. Khabipov, L. V. Filipenko, *Cryogenics ICEC Supplement* (1992) **32** 549
- 38 . V. P. Koshelets, S. A. Kovtonyuk, I. L. Serpuchenko, L. V. Filippenko, and A. V. Shchukin, *IEEE Trans. on Magn.* (1990) **27** 3141
- 39 . R. P. Huebener, in: *Advances in Electronics and Electron Physics*, Ed. P.W. Hawkes (Academic Press, New York) (1988) **70** 1
- 40 . T. Doderer et al. in: *Nonlinear Superconductive Electronics and Josephson Devices*. Eds. G. Costabile, S. Pagano, N. F. Pedersen, and M. Russo (Plenum, New York), (1991) 353
- 41 . T. Doderer, D. Hoffmann, R. P. Huebener, N. Kirchmann, C. A. Krülle, Susanne G. Lachenmann, D. Quenter, J. Schmidt, S. Stehle, J. Niemeyer, R. Pöpel, S. P. Benz, and P. A. A. Booi, *IEEE Trans. App. Supercond.* (1993) **3**, 2724
- 42 . D. Quenter, S. Stehle, T. Doderer, C. A. Krülle, R. P. Huebener, F. Müller, J. Niemeyer, R. Pöpel, T. Weimann, R. Ruby, and A. T. Barfknecht, *Appl. Phys. Lett.* (1993) **63** 2135.
- 43 . Susanne G. Lachenmann, T. Doderer, D. Hoffmann, R.P. Huebener, P.A. A. Booi, and Benz S.P., *Phys.Rev. B* (1994) **50** 31581.
- 44 . J. S. Martens, V.M. Hietala, T.A. Plut, D.S. Ginley, G.A. Vawter, C.P. Tigges, M.P. Siegal, Julia M. Phillips, and S.Y. Hou, *IEEE Trans. on Appl. Supercond.*, (1993) **3**, 2295.
- 45 . P.L. Bunyk, A. Oliva, V.K. Semenov, M. Bhusan, K.K. Likharev, J.E. Lukens, *EH-4 in Appl. Supercond. Conf., Boston* (1994)



## A LONG JOSEPHSON JUNCTION-BASED DEVICE FOR PARTICLE DETECTION

S. PAGANO, C. NAPPI, R. CRISTIANO, E. ESPOSITO\*, L. FRUNZIO

*Istituto di Cibernetica del Consiglio Nazionale delle Ricerche*

*Arco Felice, Naples, Italy,*

*Istituto Nazionale di Fisica Nucleare INFN, Napoli, Italy*

*\* also Dept. of Physics, Particle & Nuclear Physics, University of Oxford, Oxford, UK*

and

L. PARLATO, G. PELUSO, G. PEPE, U. SCOTTI DI UCCIO

*Dipartimento Scienze Fisiche, Università di Naples "Federico II", Napoli, Italy*

*Istituto Nazionale di Fisica Nucleare INFN, Napoli, Italy*

### ABSTRACT

A new type of particle detector, based on fluxon propagation in long Josephson junctions, is discussed. The proposed device is based on the fluxon injection in long junctions induced by radiation, and provides a very fast ( $\leq 1$  ns) response, together with the possibility of energy resolution. The output of the detector is intrinsically in digital form and could be directly coupled to fast superconducting digital circuits, e.g., Rapid Single Flux Quantum counting logic. Details on the dynamic operation of the proposed detector are discussed. Preliminary experimental results without radiation obtained from some prototypes made of high quality Nb-based junctions are also reported.

### 1. Introduction

Thanks to the very low value of the energy gap of the superconducting materials, Superconducting Tunnel Junctions (STJs) offer the attractive possibility of very high energy resolution (down to few eV) when used as nuclear radiation detectors. Since the first proposal of STJs as nuclear radiation spectrometers<sup>1,2</sup> important achievements have been obtained in this direction, and investigations are still actively in progress.

Another important property of STJs, which makes them a very competitive candidate for nuclear detection applications, is their ultra fast switching time capability: only few picoseconds are needed in order that a STJ switches from the zero voltage to finite voltage state. Such a switching can be triggered by incoming nuclear radiation and, based on this property, fast nuclear radiation detectors have also been proposed<sup>3</sup>.

The device presented in this article is new in that it uses the incoming radiation to induce a flux-flow state in a *Long* Josephson Junction. (LJJ)<sup>4</sup>. The obtained switching is temporary and, once the effects of the passage of the radiation are damped out, the equilibrium is restored and the junction settles back to the zero voltage state. In order to achieve this result, the shape of the junction must be specially tailored. Hereafter, together with the working principle of the device and the preliminary experimental characterization of produced prototypes, we analyze in some details the dynamics of the fluxon propagation in specially shaped LJJ, remarking those aspects which are relevant for the proposed application. On the other hand, the important issue of the interaction

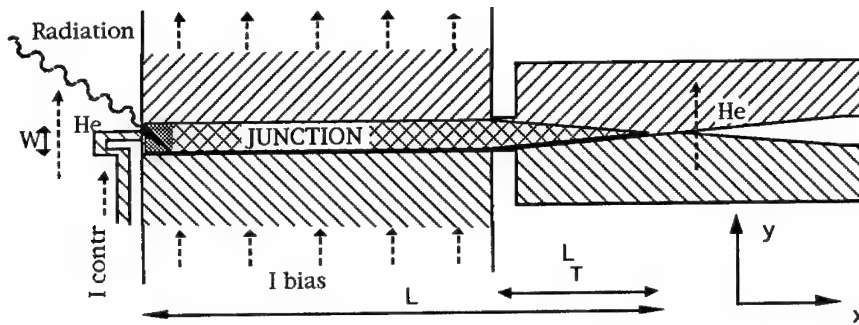


Fig.1 Sketch of the geometry of the proposed detector

between the junction and nuclear radiation will not be present in this paper.

## 2. Working Principle

The design of the proposed device is based on the idea that the interaction of radiation with one of the extremes of a long junction can produce a temporary fluxon injection. The injected fluxons, or magnetic flux quanta ( $\Phi_0 = 2.07 \cdot 10^{-15} \text{ Wb} \approx 2 \text{ mV ps}$ ), are driven by the bias current towards the opposite side of the LJJ. Here, by a suitable choice of the junction shape, they are transmitted to an attached Superconducting Transmission Line (STL). The proposed geometry is sketched in Fig.1. A long junction, ending with a narrowing unbiased "tail", is biased on the zero voltage state. The left edge of the junction (and the whole zone nearby) acts as "sensitive area" while the right point shaped edge gradually matches the STL. This guarantees that the fluxons undergo no reflection, as we discuss in some detail hereafter.

Fluxons are forced, in fact, to propagate on the connected STL, as a train of very fast (few ps wide) voltage pulses. A suitable electronic circuitry is then necessary to process them. A possibility is offered by the recently developed Rapid Single Flux Quantum (RSFQ) counting logic circuits<sup>5</sup>. The control line, at the left edge, produces the necessary local magnetic field, with a value chosen just below the threshold for the entrance of fluxons.

The mechanism which triggers the fluxon injection is a lowering of the local critical current density,  $j_c$ . When an ionizing particle hits the left side of the junction it generates a non-equilibrium process which ultimately leads to the breaking of a large number of Cooper pairs. The external magnetic field screening capability of the junction is locally reduced and one or more fluxons, can enter the junction. It is important to note that the ultimate speed of the device depends, among other things, on the time related to the process leading from the nuclear radiation impact to a significant decrease of the  $j_c$ .

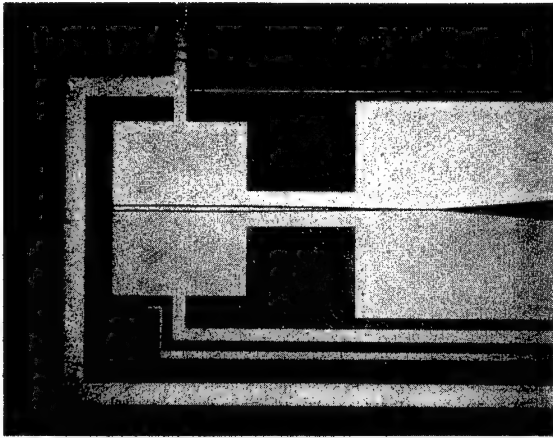


Fig. 2 Microphotograph of a LJJ detector

This process, which involves a non equilibrium treatment of the Josephson effect, is not yet completely clarified and is still object of investigation.

The detector described above has the advantage to be self-resetting. In fact, after a very short time, depending on the junction materials, temperature and geometrical configuration, the non equilibrium quasiparticles recombine, so that the original  $j_c$  is restored. By a suitable choice of the working conditions, it is possible to decrease this dead time to very short values ( $<1\text{ns}$ ) and then pile-up effects can be avoided.

### 3. Design and Characterization

An important point to be realized is that the fluxons must not be reflected in passing from the LJJ to the STL. A LJJ acts as a transmission line for small amplitude waves with a characteristic impedance given by

$$Z_j = \frac{Z_0}{W} \sqrt{\frac{(2\lambda_L + d)d}{\epsilon_r}} \quad (1)$$

where  $Z_0 \approx 120\pi$  Ohm is the impedance of the free space,  $\lambda_L$  is the London penetration depth,  $d$  and  $\epsilon_r$  are the thickness and the relative dielectric constant of the junction barrier respectively, and  $W$  is the junction width. For a microstripline the characteristic impedance  $Z_T$  is given by ( $W \gg d_T$ )<sup>6</sup>:

$$Z_T = \frac{Z_0}{\sqrt{\epsilon_r}} \frac{d_T}{W} \quad (2)$$

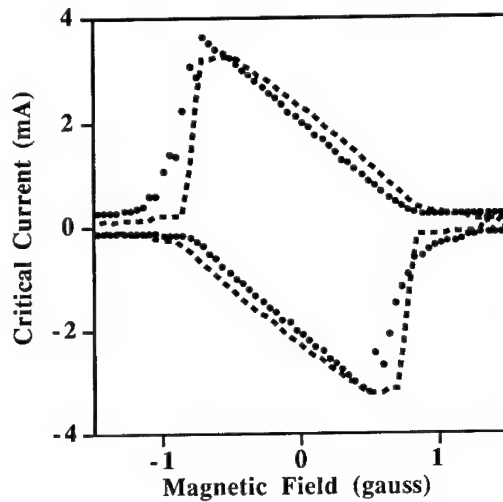


Fig.3 Magnetic field dependence of the critical current for the device proposed. The dots are experimental results of a  $1000+300\text{ }\mu\text{m}$  long junction, and the dashed curve is the result of the numerical simulation (see text for details).

where  $d_T$  and  $\epsilon_r$  are the insulation thickness and relative dielectric constant, and  $W$  the is strip width. In order to optimize the matching it is necessary that  $Z_T=Z_j$ . Now using typical experimental values it is easy to verify that for a LJJ with  $W=10\text{ }\mu\text{m}$ ,  $Z_j \approx 0.2\text{ }\Omega$ . For a microstrip transmission line with the same width is  $Z_s \approx 3\text{ }\Omega$ . To avoid this mismatch and the related fluxon reflection, we have gradually reduced the junction width till the matching of the  $Z_T$  value is obtained. Moreover, the variable width region of the junction is not biased. This latter circumstance contributes to avoid possibility of fluxon reflections, as we shall explain in sections 5 and 6. Finally this configuration affects the fluxon dynamics helping their transfer to the transmission line.

Summarizing, the proposed configuration has the following advantages: it realizes an optimum impedance matching, it avoids fluxon reflection, and it generates an extra force, which pushes the fluxons toward the attached transmission line.

An important point to stress is that the condition of impedance matching alone does not guarantees the fluxon transmission. This happens because a LJJ is a nonlinear transmission line for which a characteristic impedance can be defined only for small amplitude waves. When fluxons are involved, the nonlinear effects are strong and there will be always some energy released during the transition from LJJ to the transmission line.

We have realized a number of test devices based on Nb/AlOx/Nb junctions fabricated using the trilayer technique<sup>7</sup>. Each test chip contains, among other things, three long Josephson junction detectors (LJJD), having the geometry sketched in fig. 1 but different sizes. Moreover samples with different current densities (from 50 to 5000 A/cm<sup>2</sup>) have been produced. In Fig. 2 a photograph of one of the LJJ ( $L=1\text{ }\mu\text{m} + 300\mu\text{m}$ ,  $W=10\text{ }\mu\text{m}$ ) is reproduced. For this preliminary realization of the LJJ detector

we have used a variable size slot-line instead of a microstrip transmission line. This choice, while providing a better geometrical matching to the LJJ, introduces a somewhat larger impedance mismatch.

We have performed preliminary tests of the LJJD in absence of radiation to characterize its performances in terms of magnetic field threshold and flux flow dynamics. In Fig. 3 it is shown the magnetic field dependence of the critical current at  $T=4.2\text{K}$  of the sample in the photograph. The magnetic field is applied uniformly by an external coil along the direction perpendicular to the long junction side. The pattern shows a characteristic asymmetry due to the non uniformity of the current bias<sup>8</sup>. Moreover, the absence of secondary lobes indicates that it is not possible to statically trap fluxons in this junction. This is also due to the particular geometrical shape, because if a fluxon enters the junction it is immediately pushed forward and absorbed at the pointed edge. On the contrary, in the presence of a larger magnetic field generated either by the control line or by the coil surrounding the device, the junction exhibits a flux flow state as indicated by the presence of a characteristic step in the I-V curve. The flux flow step is observable up to about 1.2 mV, corresponding to the generation of microwave signals up to 600 GHz.

#### 4. Modelling of a Non Uniform Width Josephson Junction

In order to investigate the dynamics of the proposed detector, we have developed a model of the device based on a perturbed (1+1)D sine-Gordon equation. Since we are dealing with a two dimensional junction with irregular shape, it is necessary to resort to the basic equations describing the Josephson junction electrodynamics. Starting point are Maxwell's equations:

$$\nabla \times \mathbf{E} = - \frac{\partial \mathbf{B}}{\partial t} \quad (3)$$

$$\nabla \times \mathbf{H} = \frac{\partial \mathbf{D}}{\partial t} + \mathbf{J} \quad (4)$$

together with the Josephson relation, and the expression for the tunneling current flowing through the junction:

$$V = \left( \frac{\Phi_0}{2\pi} \right) \frac{\partial \phi}{\partial t} \quad (5)$$

$$j_T = j_c \sin \phi + \frac{\hbar}{2e\rho_n} \frac{\partial \phi}{\partial t} \quad (6)$$

where  $\rho_n$  is the normal state resistivity. We note that Eq. (6) is valid only if the frequency is much lower than that corresponding to the energy gap of the superconducting electrodes. If this is not the case, then one has to resort to the complete microscopic derivation and expressions more complicated than Eq. (6) are obtained.

As a first step the effects of electrode surface impedance have to be included<sup>9</sup>. This is done by considering the frequency domain and introducing the total impedance of the junction  $Z = j\omega L_0 + 2Z_s$ . Here  $L_0 = \mu_0 d$  is the inductance of the barrier and  $Z_s$  the electrode surface impedance. According to BCS theory,  $Z_s$  can be expressed as<sup>10</sup>

$$Z_s = k\omega^2 + j\omega\mu_0\lambda_L \quad (7)$$

where  $k$  is a constant depending solely on the electrode material and temperature but not on the frequency, and we are assuming the electrode thickness much larger than  $\lambda_L$ . The relation between  $H$  and  $\phi$  is<sup>9</sup> (see Fig.4, where the geometry is sketched):

$$H = - \left( \frac{\Phi_0}{2\pi} \right) \left( \frac{1}{Z} \right) j\omega (\nabla\phi) \times \hat{z} \quad (8)$$

where  $\nabla$  is a two-dimensional nabla operator. Moreover, in the case of low frequency or low electrode dissipation (i. e.  $k\omega^2 \ll \omega\mu_0\lambda_L$ ) we can express the total impedance  $Z$  as a parallel combination of an inductance  $L$  and a resistance  $R$ , i.e.

$$\frac{1}{Z} = \frac{1}{j\omega L} + \frac{1}{R} \quad (9)$$

where  $L = \mu_0(2\lambda_L + d)$  and  $R = (\mu_0(\lambda_L + d))^2 / 2k$  do not depend on frequency.  $2\lambda_L + d$  is the "magnetic" thickness of the barrier. Eq.(8) can be written in the time domain as

$$H = - \left( \frac{\Phi_0}{2\pi L} \right) \left( 1 + \frac{L}{R} \frac{\partial}{\partial t} \right) (\nabla\phi) \times \hat{z} \quad (10)$$

By inserting Eq.(10) in the  $z$  - component of Eq.(4):

$$\frac{\partial H_y}{\partial x} - \frac{\partial H_x}{\partial y} = j_T + \frac{\partial}{\partial t} \epsilon E_z \quad (11)$$

The following equation for  $\phi$  is obtained

$$\left( 1 + \frac{L}{R} \frac{\partial}{\partial t} \right) \left( \frac{\partial^2 \phi}{\partial x^2} + \frac{\partial^2 \phi}{\partial y^2} \right) - \frac{1}{c^2} \frac{\partial^2 \phi}{\partial t^2} = \frac{1}{\lambda_J^2} \sin \phi + \frac{L}{\rho_n} \frac{\partial \phi}{\partial t} \quad (12)$$

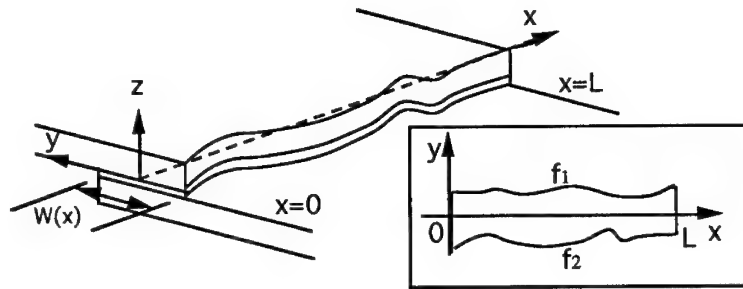


Fig. 4. A schematic view of a long junction with variable width and its boundary C

where  $\epsilon$  is the dielectric constant of the barrier,  $\lambda_J = (\Phi_0/2\pi L j_C)^{1/2}$  and  $\bar{c} = (d/L\epsilon)^{1/2}$ , are the Josephson penetration depth and the Swihart velocity, respectively. Eq.(12) can be further recast in dimensionless units if the space coordinate  $x$  is normalized to  $\lambda_J$ , the time  $t$  is normalized to the inverse of the plasma frequency  $\omega_J = \bar{c}/\lambda_J$ , and the dimensionless loss parameters  $\alpha = \lambda_J L \bar{c} / \rho_n$  and  $\beta = \omega_J L/R$  are introduced:

$$\left(1 + \beta \frac{\partial}{\partial t}\right) \left( \frac{\partial^2}{\partial x^2} + \frac{\partial^2}{\partial y^2} \right) \phi - \frac{\partial^2}{\partial t^2} \phi - \alpha \frac{\partial}{\partial t} \phi = \sin \phi \quad (13)$$

So far no direct reference to the geometry of the junction has been necessary. Geometric considerations enter, of course, through the boundary conditions.

Let us consider an irregular overlap type long junction as shown in Fig.4. We will consider the case in which the junction boundary can be described by means of two smooth functions  $f_1(x) > 0$  and  $f_2(x) < 0$ . Thus the junction width can be expressed as  $W(x) = f_1(x) - f_2(x)$ . We assume that  $f_1$  and  $f_2$  vanish at the junction edges,  $x=0$  and  $x=L$ , with infinite derivatives (Note that from this point the symbol  $L$  indicates the junction length instead of the inductance). Boundary conditions now requires that the normal component of  $\nabla\phi$  is given at the junction boundary C:  $\nabla\phi \cdot \hat{n}|_C$ . From Eq.(10) we obtain

$$\begin{aligned} -\frac{df_1}{dx} \left(1 + \beta \frac{\partial}{\partial t}\right) \frac{\partial\phi}{\partial x} \Big|_{y=f_1(x)} + \left(1 + \beta \frac{\partial}{\partial t}\right) \frac{\partial\phi}{\partial y} \Big|_{y=f_1(x)} = \\ \left( -\eta_y \Big|_{y=f_1(x)} \right) \frac{df_1}{dx} - \eta_x \Big|_{y=f_1(x)} \end{aligned} \quad (14a)$$

$$-\frac{df_2}{dx} \left(1 + \beta \frac{\partial}{\partial t}\right) \frac{\partial \phi}{\partial x} \Big|_{y=f_2(x)} - \left(1 + \beta \frac{\partial}{\partial t}\right) \frac{\partial \phi}{\partial y} \Big|_{y=f_2(x)} =$$

$$\left( \eta_y \Big|_{y=f_2(x)} \right) \frac{df_2}{dx} + \eta_x \Big|_{y=f_2(x)} \quad (14b)$$

where  $\eta = \mathbf{H}/j_c \lambda_j$  is the dimensionless magnetic field and the  $x$  and  $y$  magnetic field components at the junction boundary have been explicitly introduced. If the junction width is much smaller than  $\lambda_j$ , i.e.  $W(x) = f_1(x) - f_2(x) \ll 1$ , we expect  $\phi$  to depend very weakly on  $y$ . To the first order in  $W$ , integrating Eq.(13) along  $y$ , between  $f_2(x)$  and  $f_1(x)$  and using Eqs. (14), we have

$$(1 + \beta \partial_t) \phi_{xx} + \frac{W'(x)}{W(x)} (1 + \beta \partial_t) \phi_x - \eta_y \frac{W'(x)}{W(x)} + \gamma(x) =$$

$$= \sin \phi + \alpha \phi_t + \phi_{tt} \quad (15a)$$

where

$$\gamma(x) = \frac{\eta_x \Big|_{f_2} - \eta_x \Big|_{f_1}}{W(x)} \quad (15b)$$

and primes indicate derivatives with respect to the argument. Eq.(15a) is a 1+1 dimensional pde, where the original 2+1-D problem for the non uniform-width junction is recalled by the terms in  $W'(x)/W(x)$  and  $\gamma(x)$ . A similar type of perturbed sine Gordon equation (PSGE) has been investigated by Sakay et al.<sup>11</sup> in the context of non-uniform inductance long junctions.

We assume that  $\eta$  is made by two contributions: an external magnetic field  $\eta^e$  in the  $y$  direction, and a  $x$ -component,  $\eta_x$ , resulting from the bias current density  $j(x)$  which flows in the  $y$  direction:  $\eta \equiv (\eta_x, \eta^e)$ . We note that the bias current generates a magnetic field having opposite values at the junction boundaries: it is negative at  $y=f_1(x)$  and positive at  $y=f_2(x)$ . With these conditions we have:

$$\gamma(x) = \frac{2j(x)\lambda_L}{j_c \lambda_J W(x)} \quad (15c)$$

The appropriate boundary conditions for Eq.(15a) are obtained from Eqs.(14) in the limit  $x \rightarrow 0$ ,  $x \rightarrow L$ , (which implies  $W' \rightarrow \infty$ ) as

$$\left(1 + \beta \frac{\partial}{\partial t}\right) \phi_x \Big|_{x=0} = \eta^e \quad (16a)$$



$$\left(1 + \beta \frac{\partial}{\partial t}\right) \phi_x \Big|_{x=L} = \eta^e \quad (16b)$$

In the case of the geometry shown in Fig.1  $W(x)$  is

$$W(x) = \begin{cases} w_0 & 0 < x < L - L_T \\ w_1 + \left(\frac{w_1 - w_0}{L_T}\right)(x - L) & L - L_T < x < L \end{cases} \quad (17)$$

where  $L_T$  is the length of the pointed junction tail,  $L$  the length of the uniform junction part,  $w_1$  and  $w_0$  the minimum and maximum width, respectively. The bias  $\gamma$  term is given in this case by

$$\gamma(x) = \begin{cases} \gamma_0 & 0 < x < L \\ 0 & L < x < L + L_T \end{cases} \quad (18)$$

With this model it is possible to describe the complete dynamics of fluxon propagation in specially shaped junctions and to account for the experimental observed features.

## 5. Numerical Simulations

We have numerically solved Eq. (15a) with the conditions Eqs. (16) and (17) by using a standard implicit finite-difference method based on a stabilized leapfrog scheme. This method is fast and easy to implement providing that there are no third order terms in the equation ( $\beta=0$ ).

The value of the parameters for the simulation are chosen close to the experimental ones so that a direct comparison can be made. As an example we show in Fig. 3 the computed magnetic field pattern dependence from the junction critical current. This pattern has been obtained considering a spatial distribution of the bias current peaked at the electrode edges<sup>12</sup>. A comparison with the experimental result shows that the derived PSGE is able to closely reproduce the experimentally observed features of the LJJ detector.

In Fig. 5 we show the effect of the variable width on the fluxon motion for two particular situations. In the first one (Fig.5, left)) the junction has a constant width so that there is a mismatch ( $Z_j/Z_T=0.1$ ) with the attached STL. In the second case (Fig.5, right) the junction has a narrowing width ( $w_1/w_0=0.1$ ) and a good matching is obtained ( $Z_j/Z_T=1$ ). In the first case the fluxon travels to the unbiased region, is reflected at the boundary as antfluxon, and reaches again the biased region, where it gains energy and is reflected as a fluxon at the left edge. The whole process repeats, generating a periodic motion of the fluxon in the junction. In the second case the fluxon, when enters the unbiased region, is accelerated rightwards by the extra force due to the shrinking

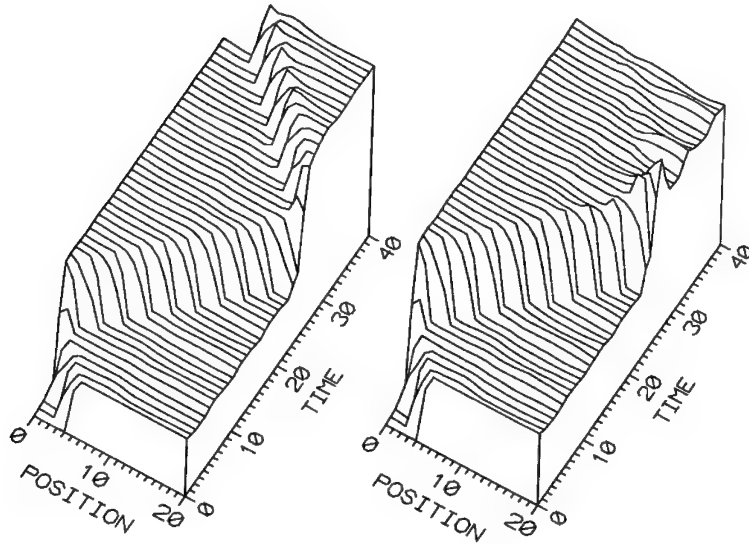


Fig.5 Numerical simulations of the phase evolution for a constant width (left), and a narrowing width (right) junction. The values of the parameters are:  $\alpha=0.02$ ,  $\beta=0$ ,  $\gamma=0.3$ ,  $u(0)=-0.9964$ ,  $L=20$ ,  $L_T=10$ .  $w_1/w_0=1$ ,  $Z_j/Z_T=0.1$  (left) and  $w_1/w_0=0.1$ ,  $Z_j/Z_T=1$  (right).

width. When it reaches the right edge, it is almost fully transmitted, thanks to the good impedance matching. In any case the energy left at the boundary is not enough to create an antfluxon capable to climb up against the extra force due to the shrinking width. The simple case shown in the figure illustrates the advantage of the chosen geometrical configuration in providing a unidirectional fluxon motion in the junction.

## 6. One Parameter Perturbation Analysis

To better illustrate the dynamics of the fluxons in such type of junction we have performed a simple perturbation analysis, along the traditional line introduced by McLaughlin and Scott<sup>13</sup> and Kaup and Newell<sup>14</sup> for the PSGE. A more complete analysis will be presented elsewhere<sup>15</sup>.

It is well known that in the case of the unperturbed sine-Gordon equation (sGE) it is possible to define the energy as

$$H = \int \left[ \frac{1}{2} \phi_x^2 + \frac{1}{2} \phi_t^2 + (1 - \cos \phi) \right] dx \quad (19)$$

such that, if  $\phi$  is any localized solution of sGE, it is an integral of motion:

$$\frac{dH(\phi)}{dt} = 0 \quad (20)$$

Let us focus our attention on the kink solution of the sGE representing a fluxon:

$$\phi(x,t) = 4 \tan^{-1} \left\{ \exp \left[ \frac{x - ut - x_0}{\sqrt{1-u^2}} \right] \right\} \quad (21)$$

This solution is characterized by two free parameters: the initial phase  $x_0$  and the velocity  $u$ . When perturbations are present, as in Eq. (15), Eq. (21) is no longer a solution. One can then adopt the following point of view: assume as a solution the same form Eq. (13), and allow at the same time a slow modulation of the parameters  $x_0$  and  $u$ . In this case  $x_0$  and  $u$  represent unknown functions of the time to be determined from the requirement that the solutions ansatz satisfies some criteria. One can further assume (and we do that here) that the main effect of the perturbations is to slowly modulate in time only one of the parameter of the kink, say the velocity  $u$ . Our ansatz for the solution of Eq.(15) may be written as:

$$\phi(x,t) = 4 \tan^{-1} \left\{ \exp \left[ \frac{x - X(t)}{(1 - u^2(t))^{1/2}} \right] \right\} \quad (22)$$

where

$$X(t) = \int_0^t u(t') dt' + x_0 \quad (23)$$

represents the soliton center position. Inserting the ansatz Eq.(22) into Eq.(19) it is easy to show that

$$H = \frac{8}{\Gamma(t)} \quad (24)$$

where

$$\Gamma(t) = \sqrt{1 - u(t)^2} \quad (25)$$

The time derivative of Eq.(24) can be calculated and, for the case considered, the result reads:

$$\frac{dH}{dt} = \int \left[ \gamma^* \phi_t - \alpha^* \phi_t^2 - \beta \phi_{xt}^2 + \frac{W'}{W} \phi_x \phi_t \right] dx \quad (26)$$

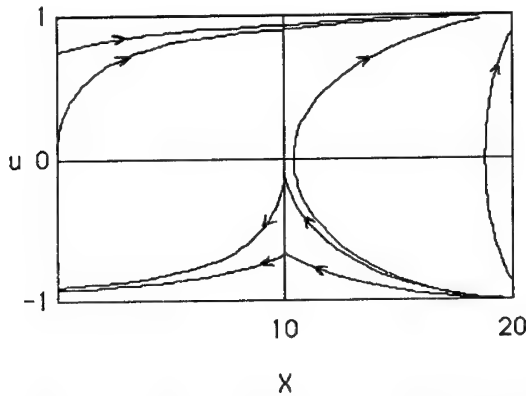


Fig.7 Phase-space associated to Eq.(30). The parameters are  $\alpha=0.02$ ,  $\beta=0$ ,  $\gamma=0.2$ ,  $L=20$ ,  $L_T=10$ ,  $W_1/W_0=0.1$

$$\gamma^* = \gamma - \eta_y \frac{e W'}{W} \quad (27a)$$

$$\alpha^* = \alpha + \beta \frac{W'' W - W'^2}{W^2} \quad (27b)$$

The various terms in the integral Eq.(26) are significantly different from zero only within an interval centered around  $X(t)$  and of size  $\leq 1$ . For smooth non uniformity ( $W' = dW/dx \ll 1$ ) it is possible to explicitly compute them and the following equation is obtained:

$$\dot{u} = \pm \frac{\pi}{4} \gamma^*(X(t)) (1 - u^2)^{3/2} - \alpha^*(X(t)) u (1 - u^2) - \frac{\beta}{3} u - \frac{W'(X(t))}{W(X(t))} (1 - u^2) \quad (28)$$

where the minus sign refers to fluxons and plus to antifluxons, and terms in  $\dot{\Gamma}^2$  have been neglected (slow modulation hypothesis).

Eq.(28) with Eq.(23) describe the dynamics of the kink position as a particle subject to external forces and dissipation. In the case  $W'=0$  this equation reduces to the results previously obtained for a junction with uniform width<sup>16</sup>. In general, Eq.(28) is a nonlinear second order differential equation for  $X(t)$ . It is useful, however, to analyze the case in which losses and bias are not included ( $\alpha=\beta=\gamma=0$ ) and the only perturbation is due to the geometry

$$\dot{u} = - \frac{W'(X)}{W(X)} (1 - u^2) = - \frac{d \ln W(X)}{dX} (1 - u^2) \quad (29)$$

This shows that, in presence of a narrowing width, the fluxon (as well as the antifluxon) sees a net positive driving force. The fluxon is pushed, in this case, towards the edge of

the junction or, in other words, it is attracted by the pointed edge. In particular, it is easily recognized that Eq.(29) does not introduce dissipation. This can be seen directly noting that it admits the integral of motion

$$E = \frac{8W(X)}{\sqrt{1-u^2}} \quad (30)$$

from which one can easily deduce that the fluxon speed increases when the junction width shrinks.

In Fig. 7 it is shown the phase space of Eq. (29), in a case corresponding to the detector geometry ( $L=20$ ,  $L_T=10$ ,  $\alpha=0.02$ ,  $\beta=0$ ,  $\gamma=0.2$ ,  $W_1/W_0=0.1$ ). This diagram shows that fluxons starting at  $t=0$  with a positive speed will reach the pointed edge at  $x=20$  with a speed very close to the limit velocity,  $u=1$ . At this point the reflection process converts the fluxon into an antfluxon having a speed of opposite sign and a somewhat smaller magnitude, due to the reflection losses. An antfluxon generated at  $x=20$  with negative speed can follow two routes: either it can reach the biased region and be pushed towards the left side or it may not be able to reach such region and be attracted again towards the pointed edge. In the latter case the energy losses during this trajectory confine the fluxon closer and closer to the pointed edge, until it finally gets absorbed.

## 7. Conclusions

The analysis of the fluxon dynamics in a point shaped long Josephson junction has demonstrated an attracting effect of the point on fluxons. This behavior has been verified using numerical simulations and perturbation analysis. The choice of a point shape junction geometry provides also a better coupling to a transmission line eventually attached. As far as the fluxon dynamics is concerned, all the obtained results confirm that the chosen configuration can be usefully adopted in designing a new type of particle detector. It is worth noting that the derived equations are valid for any arbitrary smooth variable-width long junction.

## Acknowledgements

The authors thank Dr. G. Filatrella for useful suggestions in reading the manuscript. The financial contributions from Progetto Finalizzato "Superconductive and Cryogenic Technologies" of National Research Council, Italy, the EU Science Project no. SC1\*-CT91-0760 "Coupled Josephson junctions", and the EU-Human Capital and Mobility Program "Cryogenic Detectors" contract no. ERBCHRXCT930341, are gratefully acknowledged.

## References

1. G.H. Wood, and B. White, *Appl. Phys. Lett.* **15** (1969) 237
2. G.H. Wood, and B. White, *Can. J. Phys.* **51** (1973) 2032
3. A. Barone, and S. De Stefano, *Nucl. Instr. and Meth.* **202** (1982) 513

4. R. Cristiano, E. Esposito, L. Frunzio, C. Nappi, S. Pagano in *Superconductivity and Particle Detection* (World Scientific, Singapore, to be published in 1995)
5. K.K. Likharev, and V.K. Semenov, *IEEE Trans Appl. Superc.* **1** (1991) 3.  
K.K. Likharev in *The New Superconducting Electronics* ed. H. Weinstock and R. W. Ralston (Kluwer Academic Publisher, Dordrecht 1993) p.423.
6. T. C. Edwards, *Foundations for Microstrip Circuit Design*, (John Wiley & Sons, Chichester, 1981)
7. R. Cristiano, E. Esposito, L. Frunzio, S. Pagano, A. Barone, G. Peluso, G. Pepe, H. Akoh, H. Nakagawa, and S. Takada, *J. Appl. Phys.* **75**, (1994) 5210.
8. A. Barone and G. Paternò *Physics and Applications of the Josephson Effect* (John Wiley & Sons, New York, 1982).
9. F. Irie, K. Yoshida; in *SQUID '85, Superconducting Quantum interference Devices and their applications* (W. de Gruyter & Co., Berlin, 1985), p. 431.
10. R. S. Withers, in *The New Superconducting Electronics* ed. H. Weinstock and R. W. Ralston (Kluwer Academic Publisher, Dordrecht Dordrecht, 1993), p.277.
11. S. Sakai, M.R. Samuelsen, O.H. Olsen, *Phys. Rev.* **B36** (1987), 217.
12. G.W. Swan, *J. Math. Phys.* **9** (1968) 1308.
13. D.W. McLaughlin, and A.C. Scott, *Phys. Rev.* **A18** (1978) 1652.
14. D.J. Kaup, A.C. Newell, *Proc. R. Soc. London* **A361** (1978) 413.
15. C. Nappi, S. Pagano, manuscript in preparation.(1994).
16. R.D. Parmentier. in *The New Superconducting Electronics* ,ed. H. Weinstock and R.W. Ralston (Kluwer Academic Publisher, Dordrecht ,1993) p.221.

## NbN/Nb BILAYERS FOR STJ PARTICLE DETECTORS

L. PARLATO, G. PELUSO, G.P. PEPE, U. SCOTTI DI UCCIO

*Dipartimento di Scienze Fisiche, Università di Napoli Federico II, Italy  
Istituto Nazionale di Fisica Nucleare, Sezione di Napoli, Napoli, Italy*

R. CRISTIANO, E. ESPOSITO\*, L. FRUNZIO, S. PAGANO

*Istituto di Cibernetica del C.N.R., Arco Felice, Napoli, Italy  
Istituto Nazionale di Fisica Nucleare, Sezione di Napoli, Napoli, Italy*

*\* also Dept. of Physics, Particle and Nuclear Physics, University of Oxford, Oxford, UK*

H. AKOH, H. NAKAGAWA, S. TAKADA

*Electrotechnical Laboratory, Tsukuba, Ibaraki, Japan*

### ABSTRACT

Interest in Josephson Tunnel Junctions as X-ray detectors arises mainly from the very good predicted intrinsic energy resolution. The detection principle is based on the collection of the quasi-particles created by X-ray absorption through their tunneling across the barrier. Junctions with trapping layers have been proposed in order to improve the detection performances in term of energy resolution and collected charge. In this paper we present a preliminary experimental investigation of Nb/AlO<sub>x</sub>/Nb junctions with a NbN backlayer. The results show an induced, weak proximity effect in the relatively thick Nb top electrode. Experiments under X-Ray radiation exhibit effects due to enhanced tunneling rate because of trapping effect.

### 1. Introduction

The absorption of a X-Ray photon in a superconductor produces a large number of Cooper-pair breaking which result in a population of quasi-particles and phonons with non-equilibrium distributions. These excitations are produced at the end of an energy cascade, characterized by different relaxation processes, such as electron-electron scattering, electron-phonon scattering, anharmonic decay of phonons, Cooper pair-

breaking by phonons, escape of phonons outside the detector environment, etc.. The number of created quasi-particles, is directly related to the deposited energy of the incident radiation and can be determined by measuring the tunneling current produced in a Superconducting Tunnel Junction (STJ) connected to the absorber.

The intrinsic energy resolution of such a type of a detector is in principle limited only by fluctuations in the number of produced excitations, i.e.  $\Delta E = 2.35 (F\epsilon E)^{1/2}$ , where  $\epsilon$  is the mean energy required to create two quasi-particles,  $F$  is the Fano factor and  $E$  is the released energy. In the case of Nb,  $F=0.2$  and  $\epsilon=1.7 \Delta$  ( $\Delta$  is the superconducting energy gap) and the energy resolution is  $\Delta E=5$  eV<sup>1,2</sup>. However, the best experimental energy resolution so far achieved is still far from the intrinsic value. Several loss mechanisms and the electronic noise in the signal amplification chain often represent serious limitations to the energy resolution.

In order to improve the energy resolution and increase the collected charge for a given X-ray event, different detector configurations have been proposed. Most of them are based on the idea of quasi-particle trapping, firstly proposed by Booth<sup>3</sup>. It consists in depositing on a large volume superconducting absorber with an high energy gap a STJ made by a smaller volume superconductor with a lower energy gap. Quasi-particles from the absorber can diffuse in the low energy gap region, where they rapidly relax to energies lower than the absorber energy gap. In this way they became trapped in the low energy gap region, where their tunneling rate is faster because of the smaller volume.

Recently, detector configurations using this effect have exhibited very encouraging results, improving both the energy resolution and the collected charge<sup>4</sup>. These results have been obtained by junctions essentially based on the Al/AlOx/Al trilayer which then operates at millikelvin temperatures. However, it is still interesting to explore the possibility of using a detector configuration based on a Nb/AlOx/Nb trilayer, which has the advantage of a possible working temperature in the Kelvin region. Since in this case the Nb should act as trapping layer, the absorber must be realized with an higher energy gap superconductor, such as NbN.

In this paper we present a preliminary tunneling characterization of STJs based on a Nb/AlOx/Nb trilayer, with either a Nb or a NbN backlayers. In the latter case the NbN acts as absorbing layer and the Nb top electrode is the trap. Tunneling and Josephson effect measurements without radiation of both the two type of junctions are presented and features related to the NbN presence are discussed. Preliminary experimental results concerning with X-ray response are also presented.

## 2. Quasi-particle Trapping

The basic principle of the quasi-particle trapping is illustrated in Fig. 1a. A superconductor  $S_1$  with a gap parameter  $\Delta_1$  encloses another superconductor  $S_2$ , the trap, with a smaller gap parameter  $\Delta_2$ .



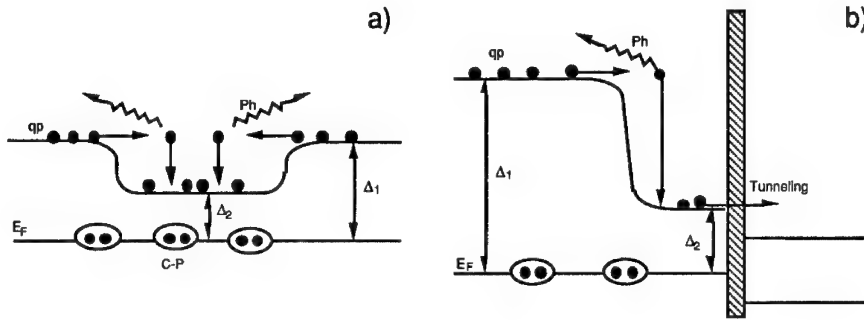


Fig. 1 Energy diagram for the trapping mechanism: a) a depressed energy gap region inside a superconductor; b) two superconducting layers with different gaps  $\Delta_1$  and  $\Delta_2$  with the trap near the tunneling barrier.

Quasi-particles in  $S_1$  with energy  $E = \Delta_1$  can diffuse into  $S_2$  and can lose energy by electron-phonon scattering, relaxing to an energy  $\Delta_2 < E < \Delta_1$ . Once quasi-particles have relaxed to near  $\Delta_2$ , they are unable to return to  $S_1$ , and therefore remain trapped in  $S_2$ . This trapping effect can be a disadvantage for STJ based detectors. In fact when regions of reduced energy gap are created by impurities, trapped magnetic fields or heat in regions inside the absorbing layer, quasi-particles remain trapped until they ultimately recombine in Cooper pairs and therefore cannot be detected.

On the contrary, one can take advantage of the trapping effect, if the reduced gap region is near the tunneling barrier as shown in Fig. 1b. In this case, working at sufficiently low temperature so that the recombination rate is negligible, the quasi-particles are trapped in a smaller volume, characterized by an increased tunneling rate.

The trapping rate depends on the fraction of time spent by the quasi-particles in  $S_2$  and on the scattering time  $\tau_s(E/\Delta_2)$  in  $S_2$ <sup>5,6</sup>. Assuming that the probability of finding a quasi-particle in  $S_2$  is equal to the volume fraction between the total and the trapping volume, the effective trapping rate is<sup>3,6</sup>:

$$\frac{1}{\tau_{tr}} = \left( \frac{v}{V+v} \right) \frac{1}{\tau_s} \quad (1)$$

where  $V$  and  $v$  are the volumes of the absorber and trapping layer respectively.

The scattering time is strongly dependent on the quasi-particle energy  $E$  and on a material characteristic time  $\tau_0$ <sup>7</sup>. Assuming that the initial energy is  $E = \Delta_1$  we have:

$$\tau_s = \tau_0 \left( \frac{\Delta_1}{\Delta_2} \right)^{-3} \quad (2)$$

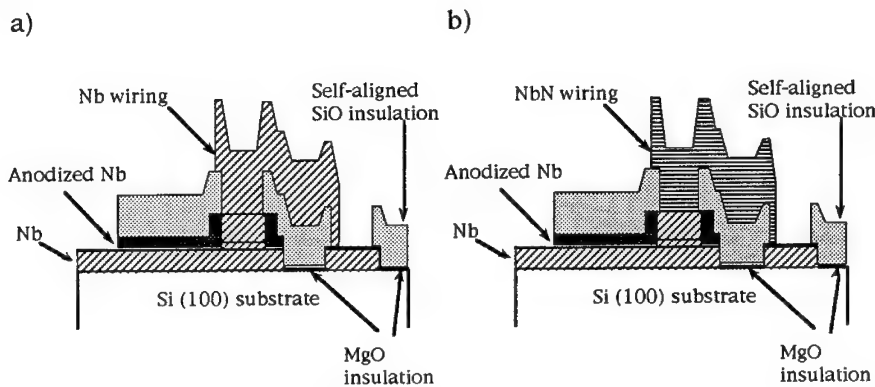


Fig. 2 Cross sectional view of the junctions: a) Nb-wiring type; b) NbN-wiring type.

In Tab.I values of  $\tau_0$  for some commonly used superconductors for STJ detectors are reported. In Tab.II the scattering time  $\tau_s$  are reported for some interesting bilayer, which could be used in detectors configurations. From these values it is clear that Nb can be a good trapping material, because  $\tau_0$  is quite short. Moreover, the NbN/Nb bilayer is also interesting, since it has the best scattering rate, which enhances the trapping process. Due to the short value of the scattering time in this case the trapping process can be very effective also for high values of the  $V/v$  volume ratios. This is of course a simplified picture which does not take into account the effect of proximity, as recently investigated in Ref. 6.

Indicating with  $N(E)$  the number of quasiparticles with energy  $E$ , it is possible to show that at low temperatures and when the equilibrium is established between the trapping rate and the rate of excitation out of the trap for phonons absorption,  $N_2(\Delta_2)/N_1(\Delta_1) > 1$ . This ratio is proportional to trapping rate, thus increasing the number of quasi-particles in the trapping layer with respect to the one initially generated in the absorber.

Table I. Energy gap  $\Delta$  and characteristic time  $\tau_0$ , superconductors.

Material	$\tau_0$ [ns]	$\Delta$ [meV]
Nb	0.15	1.5
Al	100	0.3
Ta	1.8	1.3
Sn	2.3	0.5
NbN	0.002	2.6

Table II. Scattering time for some bilayers

Bilayers	$\tau_s$ [ns]
Nb/Al	0.80
Ta/Al	1.56
Nb/Ta	1.04
NbN/Nb	0.03

### 3. Device Fabrication

The two types of structures investigated in this paper are based on the Nb/AlO<sub>x</sub>/Nb trilayer technology. They were fabricated at the ElectroTechnical Laboratory, Japan, using a modified process. The details of the fabrication procedure can be found elsewhere <sup>8</sup>. A cross sectional view of the two devices either with the Nb or the NbN wiring is shown in Fig.3a and 3b respectively. Here we remark that the polycrystalline base electrode was made by directly depositing on a Si substrate a Nb underlayer (150 nm) followed by a thin Nb (50 nm) layer. The top Nb film was typically 200 nm thick.

The deposition conditions for the Nb wiring were the same as for the junction trilayer, whereas for NbN wiring they are reported in Tab.III. In both Nb and NbN cases, the wiring thickness was 400 nm and it covered all the junction area strongly affecting to the detection process of the top electrode.

Although the realized chips contain several devices, the junctions investigated in this work had an island type geometry, in order to optimize the detection performances. A more complete description of the chip and of the devices contained therein, can be found in Ref. 9.

Tab.III. NbN Sputtering conditions

Sputtering Mode	RF
Process Gas	Ar, N <sub>2</sub> , CH <sub>4</sub>
Gas Pressure [mTorr]	8.5 (total) 0.45 N <sub>2</sub> (partial) 0.12 CH <sub>4</sub> (partial)
Power Density [W/cm <sup>2</sup> ]	2.2
Deposition Rate [nm/min]	36

### 4. Experimental Results

The samples were characterized by measuring the current-voltage (I-V) curves at various temperatures and the Josephson critical current versus temperature (I<sub>c</sub>-T). I-V curves were recorded by using a computer based acquisition data system. The samples were mounted on an insert equipped with low noise preamplifiers, directly assembled on the top of the insert and with low pass filters near the junctions. The cryostat was in a shielded environment, with a shielding factor of about 80 dB. Temperatures above 4.2 K were obtained by changing the position in the helium vapours, whereas lower temperatures

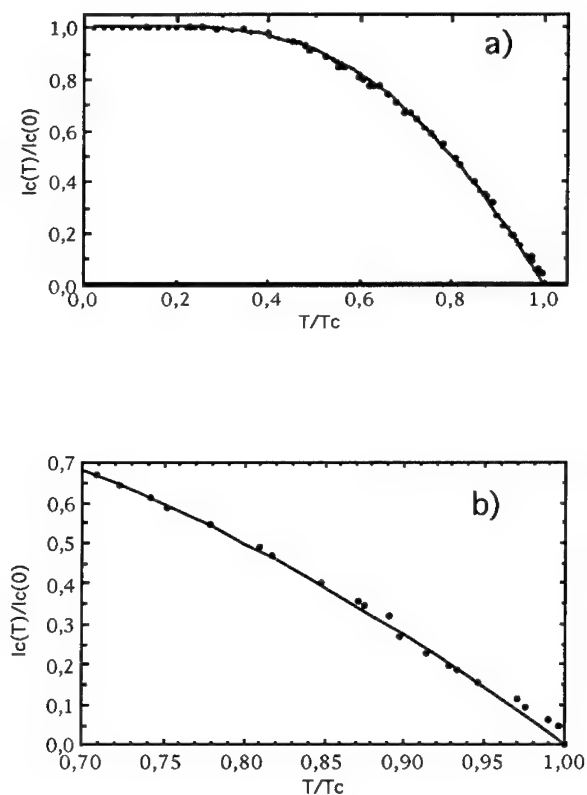


Fig. 3 Normalized Josephson critical current versus the normalized temperature: a) full temperature range; b) near  $T_c$ .

down to 1.2 K were controlled by directly pumping on the helium bath and were stabilized by a manostat, with a millikelvin accuracy.

The magnetic field, necessary to suppress the Josephson current, was supplied by a Cu solenoid around the sample. The junctions had island configurations with a wiring consisting of a narrow lead ( $5\mu\text{m}$ ) and a contact area covering all the top electrode. This means that in our case the counterelectrode is the sum of the Nb top layer and either a Nb or a NbN wiring. Assuming that a clean contact exists at the interface between the top and

the wiring layers, in the Nb junctions we have a thick Nb electrode, in the NbN junctions we have a Nb/NbN bilayer structure. A critical temperature  $T_C = 16.4$  K for the NbN was measured. The appearance of the Josephson current occurred at  $T = 8.9$  K for junctions with a NbN wiring, whereas typically occurred at  $T = 8.6$  K for junctions with a whole Nb counterelectrode. Moreover, on junctions with the NbN wiring it was observed on I-V characteristic a small structure at very low voltage, that is typically attributed to the existence of two different gaps of the two Nb electrodes across the junctions. It can be concluded that the presence of the thick NbN backlayer affects the superconducting properties of the Nb top electrode, in particular increasing both the gap and the critical temperature values. This can be explained in terms of a weak proximity effect, as expected from the relative thickness of the two bilayer parts. This circumstance is confirmed by the behaviour of the I<sub>c</sub>-T curve, as shown in Fig. 3. As it can be seen in Fig. 3a the experimental points are almost well described by an Ambegaokar and Baratoff theoretical prediction<sup>10</sup>, where the strong coupling effect has been taken into account simply assuming for Nb a modified, experimentally determined, ratio between the gap and the critical temperature. However, a careful inspection of the region near  $T_C$ , shows small deviations, typically observed in proximized structures. This is shown in Fig. 3b in more details. As a further indication also an increased value of the voltage position of the sum of gaps structure was observed at low temperature. At the lowest temperature, this increase was of about 0.1 mV.

Since an important figure of merit of a junction as a detector is the subgap current, a careful investigation of I-V curves at low temperatures and low bias voltages was performed. In order to observe the quasiparticle branch of the I-V characteristics, a suitable magnetic field in the junction plane was applied. In these very high quality junctions<sup>8</sup>, a relatively strong magnetic field value was necessary to reduce the Josephson critical current and the related resonances below the very small thermal current. The current-voltage I-V characteristics of our Nb-based junctions exhibit very low leakage currents, high dynamical resistances and interesting subgap structures, characterized by current onsets at  $V_g/2$  and sometimes at  $V_g/3$ ,  $V_g$  being the voltage position of the sharp current onset typically referred as the sum of the energy gaps. In Fig. 4 we show the low voltage region of the I-V curve at  $T = 1.2$  K. Curves a and b respectively show the I-V characteristics corresponding to junctions with the Nb or NbN wiring. As it can be seen, the presence of the NbN layer significantly reduces the quasiparticle tunneling current, thereby improving the junction quality. An increase of the dynamical resistance is also observed. These aspects are of a quite important relevance in improving the detection performances. A further beneficial effect is the absence of the large unstable region in the I-V characteristics, as observed in the curve b. Finally, the I-V curve corresponding to the Nb wiring junctions exhibits a pronounced current onset at the gap voltage, typically attributed either to MultiParticle tunneling or to Josephson self-coupling<sup>11,12</sup>. This structure is still observed in NbN wiring junctions, although it is highly depressed and smeared. This behaviour could also be considered as a further evidence of the proximity effect. In conclusions, since the tunnel barrier parameters, the insulation steps and Nb thicknesses

are exactly the same in the two types of junctions, such a different behaviour is to be related to the presence of the NbN layer that slightly modify the superconducting properties of the top Nb electrode.

The junctions were tested under X-Ray from an  $^{55}\text{Fe}$  X-rays source (20 mCi, Mn  $K\alpha$  5.895 KeV, Mn  $K\beta$  6.401 KeV). The source was located 3 mm away from the chip. An externally controllable mechanical shutter provided a shielding of the junction from the nuclear radiation. No masks or collimators were used in the measurements thus allowing nuclear radiation to hit the whole area of the chip. A complete description of the experimental apparatus has been reported elsewhere <sup>9</sup>. The junctions under test were biased with a current source and the bias voltage was kept constant against slow drift by using an electronic feedback circuit. The extra current generated by the absorption of X-ray was amplified, integrated and filtered by a charge amplifier, Amptek A250. The resulting voltage pulse signal is then digitized by a Tektronix 2430 oscilloscope and stored in a personal computer. A suitable software provides an amplitude and risetime estimation for each waveform: the amplitude is proportional to the total amount of generated charges, while the risetime is to be related with the complete timing of the signal directly generated across the junction. A suitable electronic line provides a calibration of the charge amplifier. Spectra obtained with both the two kind of structure were recorded.

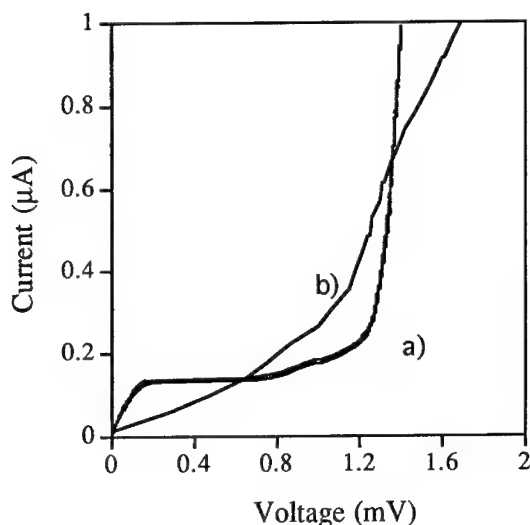


Fig. 4 I-V characteristics at  $T=1.2$  K. Curve a) refers to a Nb-wiring junction, curve b) refers to a NbN-wiring junction.

Tab. IV. Comparison between NbN/Nb and Nb based STJs

Type	Area [ $\mu\text{m}^2$ ]	$R_{\text{NN}}$ [ $\Omega$ ]	$R_{\text{D}}$ [K $\Omega$ ]	$Q_{\text{c}}^{\text{max}}$ [Me]	$\Delta E$ [eV]
Nb wiring	50x50	1.3	3.1	0.15	600
NbN wiring	50x50	2.2	4.4	0.60	320

The collected charge per event was always higher when NbN-wiring junctions are used. Although the background due to the substrate is still present, the larger collected charge allow to better distinguish the two  $K_{\alpha}$  and  $K_{\beta}$  emission lines for events directly occurred in junction volume. The energy resolution, while being still poor (about 350 eV) probably due to the high working temperature ( $T=1.4$  K) and to electronics noise, was also improved with respect to Nb-wiring structures (600 eV) <sup>13</sup>.

## 5. Conclusions

Superconducting Tunnel Junctions with a bilayer NbN/Nb as a top electrode have been characterized and tested under irradiation with <sup>55</sup>Fe X-rays. The presence of NbN layer produces some effects on the subgap and Josephson tunnel current. These effects can be qualitatively explained in terms of a weak proximity effect. Nevertheless, the NbN/Nb bilayer is effective as trapping structure, since the collected charge is increased by more than a factor three with respect to the Nb-wiring case. This is in agreement with the hypothesis that the created quasi-particles are confined in the Nb trapping layer, whose thickness is also three times thinner than the total NbN/Nb bilayer thickness.

A more careful analysis based on the proximity model of the tapping effect proposed in Ref. 6 in our case shows that the tunneling rate is negligibly modified with respect to values obtained from our simplified hypothesis. This is expected because the Nb layer is relatively thick and the proximity effects are weak. In order to improve the efficiency of the trapping layer, fabrication of samples with thinner Nb layers is in progress. Measurements in such devices will provide new insights in the theoretical model, which include the proximity effect, as well as can test the efficiency of to the NbN/Nb bilayer with respect to the trapping effect, in order to improve the performances of these junctions as detectors.

## Acknowledgements

This work has been partially supported by The Progetto Finalizzato "Superconductive and Cryogenic Technologies" of the National Research Council (CNR) of Italy, and by the EEC-Human Capital and Mobility Program "Cryogenics Detectors", Contract n. ERBCHRXCT930341.

## References

1. M. Kurakado, Nucl. Instrum. and Methods **196**, 275 (1982)
2. N. Rando, et al., Nucl. Instrum. and Methods **A313**, 173 (1992)
3. N.E. Booth, Appl. Phys. Lett. **50**, 293 (1987)
4. C.A. Mears, et al., J. Low Temp. Phys. **93**, 561 (1993)
5. H. Kraus, et al., to be published in Superconductivity and Particle Detection, Proc. of a Conference held in Toledo, Spain in April 1994 by World Scientific
6. A.A. Golubov et al., Phys. Rev. **B49**, 12953 (1994)
7. S.B. Kaplan et al., Phys. Rev. **B14**, 4854 (1976)  
NbN data are taken from M. Gurvitch et al., Proc Applied Superc. Conf. 1987
8. H. Nakagawa et al. Jpn.J. Appl. Phys. **32**, 4535 (1993)
9. R. Cristiano et al., J. Appl. Phys **75** 5210, (1994)
10. V. Ambegaokar and A. Baratoff, Phys. Rev. Lett. **10**, 486 (1963)
11. C. L. Foden, et al., Phys. Rev. **B47** (1993) 3316.
12. R. Cristiano et al. Phys. Rev. **B49**, 429 (1994)
13. R. Cristiano et al., to be published in Superconductivity and Particle Detection, Proc. of a Conference held in Toledo, Spain in April 1994 by World Scientific



## DEVELOPMENT OF A HYBRID INTEGRATED JOSEPHSON VOLTAGE STANDARD

F. X. HEBRANK, E. VOLLMER, P. GUTMANN, F. MÜLLER, J. NIEMEYER  
*Physikalisch-Technische Bundesanstalt, Bundesallee 100  
D-38116 Braunschweig, Germany*

### ABSTRACT

We have designed and fabricated a new type of Josephson device to be hybrid integrated with microstripline oscillators. For optimum matching of the Josephson series array to the oscillator the samples make use of a new stripline design. The first circuits were fabricated in a simplified Nb/AlOx/Nb technology and exhibit excellent dc characteristics and good microwave coupling to the junctions of the array. At 70 GHz constant voltage steps up to 350 mV could be observed. By hybrid integrating different samples with a new 10-GHz oscillator, constant voltage steps were created. For this experiment the Josephson current density had to be low enough to reduce the plasma frequency of the junctions to well below the driving frequency.

### 1. Introduction

Superconducting microwave monolithic integrated circuits (SMMICs) based on series arrays of Josephson junctions are used to establish a dc voltage of extreme precision<sup>1,2,3</sup>. The SMMICs are operated at frequencies of several tens of GHz and at a temperature of 4.2 K. At present the microwave is applied with oscillators such as a klystron or a Gunn-diode at room temperature and supplied to the SMMICs by rectangular hollow waveguides.

The hybrid integration of a planar microwave oscillator with the SMMIC results in an experimental setup which is easy to operate, which has a small size, and which reduces the cost of the microwave system. In previous work we have shown that stripline oscillators based on GaAs-MESFETs can be integrated with SMMICs, working well at a temperature of 4.2 K<sup>4,5,6</sup>.

To establish good coupling between the SMMIC and the stripline of the oscillator the impedance of the Josephson series array should be matched to 50  $\Omega$ . This implies that the silicon substrate is used as the dielectric of the stripline with the groundplane placed on the back of the substrate<sup>7</sup>. This improves the preparation process because the Nb/Al<sub>2</sub>O<sub>3</sub>/Nb-sandwich can now be deposited directly onto the silicon substrate surface<sup>8</sup>. In addition, the groundplane may be omitted if an electrically conducting sample holder can be used as the groundplane. Furthermore, the SMMICs can be designed in such a way that the whole Josephson series array acts like *one* microstripline.

In this paper we present the first experiments performed with samples of a com-

pletely new design, satisfying the need for hybrid integration with a stripline oscillator.

## 2. X-Band Microstrip-line Oscillator

Microstrip-line oscillators based upon a GaAs-MESFET as the active element can not only be used at room temperature, but also at a temperature of 4.2 K. We have recently investigated the properties of such an oscillator working at 11.3 GHz<sup>4,9</sup>. Based upon these results we have designed a new oscillator for a microwave frequency of 10 GHz. The GaAs-MESFET is a CFY 19 (Siemens). Tuning the gate-source voltage of the FET, the frequency of the oscillator can be varied at 4.2 K within 300 MHz. The stability of the frequency was better than  $2.5 \cdot 10^{-5}$  within 5 minutes without using a dielectric resonator or a phase lock loop to improve the frequency stability. For the use in a primary dc voltage standard the frequency stability of the planar oscillator has to be improved by more than two orders of magnitude. The output power of the microwave was 20 mW maximum and could be adjusted by changing the drain-source voltage of the FET. This resulted in a variation of the microwave power of 20 dB.

## 3. Concept of the Josephson Series Arrays

### 3.1. New Design of the Josephson Circuits

Completely new Josephson circuits have been designed to match the needs of a hybrid integrated voltage standard. The main idea is to use the whole SMMIC as one oversized stripline with an impedance of  $\approx 50 \Omega$ . Then the microwave can couple directly between the striplines of the oscillator and the SMMIC. No antipodal finline taper is needed and the microwave load resistors may be realised on a separate chip connected on the stripline output of the Josephson sample.

All samples of the new design have the same dimensions of  $3 \text{ mm} \times 25 \text{ mm}$ , allowing different Josephson chips with diverse properties to be used in the hybrid integrated circuits by simple exchange. The samples are designed for various microwave frequencies, concentrating on 10 and 70 GHz, so that they can be used with a 10 GHz stripline oscillator or within the 70 GHz experimental setup of the voltage standard established at PTB.

A series array of the new type designed to define 1.0 V at a frequency of 70 GHz is shown in Fig. 1. The circuit consists of 10 identical blocks with 198 tunnel junctions each (cf. Fig. 1(a)), i.e. the whole SMMIC includes 1980 Josephson junctions connected in series. The area of a single junction is  $25 \mu\text{m} \times 60 \mu\text{m}$ . The microwave enters the stripline structure on one side and leaves it on the other side. The splitting of the series array into smaller parts, with only a portion of the tunnel junctions has several advantages. First, each block can be connected with electrical bond pads for the dc-current, allowing the SMMIC to be used as a voltage standard or as a potentiometer. Secondly, the circuit may be used to examine the microwave attenuation of the stripline and the circuit using the different blocks as microwave detectors. More-

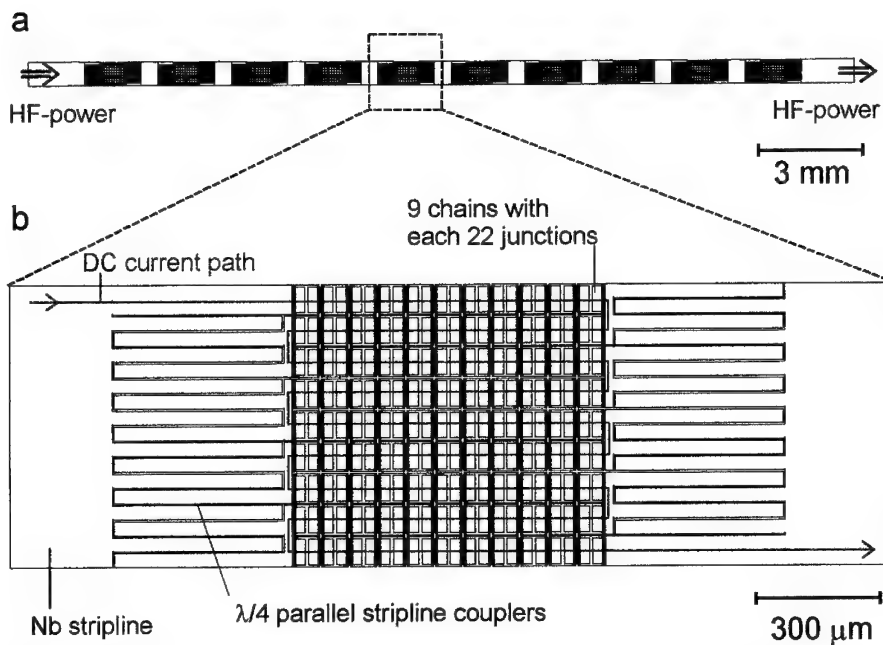


Fig. 1. Layout of a Josephson series array with 1980 tunnel junctions designed for a microwave frequency of 70 GHz. (a) The sample has a length of 25 mm and behaves as one stripline for the incoming microwave. It consists of 10 identical blocks with 198 tunnel junctions each. An enlarged view of one block is shown in (b). The block consists of 9 chains with Josephson junctions which are connected in series (indicated by the DC-current path). The microwave power is coupled to the different chains via  $\lambda/4$  parallel stripline couplers.

over, even if single arrays fail due to problems during the preparation process, the remaining part of the circuit works with a reduced number of Josephson junctions. On the other hand, if a maximum number of junctions is desired for integration on one chip (e.g. for the realisation of 10 V), just one array which is not split into different blocks can be used.

Fig. 1(b) shows an enlarged view of a single block. The 198 Josephson junctions are arranged in 9 parallel chains, each with 22 junctions. As regards the DC bias current, the 9 chains are connected in series (cf. DC current path drawn in Fig. 1(b)), whereas with respect to microwave coupling the junction chains are connected in parallel. The microwave is guided to the Josephson series array by the oversized niobium stripline. The microwave  $\lambda/4$  parallel stripline couplers connected in parallel to the main stripline distribute the incoming microwave to the different chains of junctions. In the same way the outgoing microwave is coupled back to the stripline which connects the array to the next one.

### 3.2. Fabrication Process and DC-characteristics

All samples were prepared with a simplified Nb/Al<sub>2</sub>O<sub>3</sub>/Nb-fabrication technology using silicon wafers as the substrate. The Nb groundplane is deposited onto the back side of the substrate, improving the quality of the tunnel sandwich which can now be deposited directly on the blank silicon frontside. The microwave load resistors are no longer integrated on the SMMIC, so the steps for evaporating and patterning of the normal metal layer are omitted. Furthermore, the junction definition process was simplified by using a modified variant of the basic SAWW (self-aligning whole wafer) process proposed in <sup>10</sup>. This process does not require an isolating layer, but uses an anodisation process to passivate the edges of the base electrode. After the deposition of the Nb/Al<sub>2</sub>O<sub>3</sub>/Nb-sandwich, the base electrodes are patterned using reactive ion etching (RIE). The same photoresist mask can be used for the anodisation process. The last steps are the deposition of the Nb wiring and the subsequent etching of this layer, defining not only the wiring lines but also the tunnel junctions. The modified SAWW process is described in more detail elsewhere <sup>8</sup>.

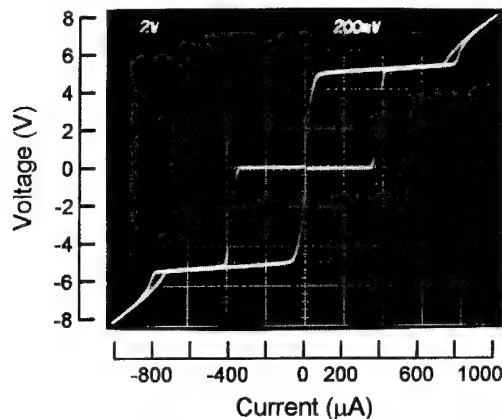


Fig. 2. Current-voltage characteristic of a Josephson series array with 1980 tunnel junctions. The design of the sample is shown in Fig. 1. The tunneling area of each junction is  $25\text{ }\mu\text{m} \times 60\text{ }\mu\text{m}$ .

All Josephson circuits showed excellent DC current voltage characteristics (IVC). Fig. 2 shows the IVC of a sample of the type described in Fig. 1. Although this Josephson circuit was designed to include 1980 tunnel junctions with an area of  $25\text{ }\mu\text{m} \times 60\text{ }\mu\text{m}$ , in this sample only 1848 junctions were active because of shorts between adjacent  $\lambda/4$  parallel stripline couplers in two blocks. This was the reason for the bypassing of 6 chains with altogether 132 junctions. The Josephson current density of this series array is  $j_C = 28\text{ A/cm}^2$ . For different samples  $j_C$  was varied between  $6\text{ A/cm}^2$  and  $71\text{ A/cm}^2$ . When realising low current densities the gap voltage was

reduced and the subgap current was increased due to the thicker Al-Al<sub>2</sub>O<sub>3</sub> barrier and the higher oxidation temperature<sup>8</sup>.

#### 4. Experimental Results

##### 4.1. Microwave Properties of the Circuits (70 GHz)

A sample with a Josephson series array of the type shown in Fig. 1 (10 blocks with 198 tunnel junctions each) was investigated using the normal experimental setup for microwave measurements at 70 GHz. The IVC of this circuit is shown in Fig. 2. Although the SMMIC was mounted in the E-plane of a rectangular waveguide with the stripline parallel to the propagation direction of the microwave, the microwave power coupled into the circuit was sufficient.

Comparing the power detected at the first and last (10th) block, a microwave attenuation of about 9 dB could be determined. In another experiment the attenuation of the  $\lambda/4$  parallel stripline couplers was examined. We found that each transition from the stripline to the chains of tunnel junctions reduces the power by 0.25 dB. Taking this value into account, the attenuation of the Josephson series array was only 4.5 dB for 1584 junctions, or 8.5 dB for 3000 tunnel junctions, which is rather low compared to other designs<sup>8,11</sup>.

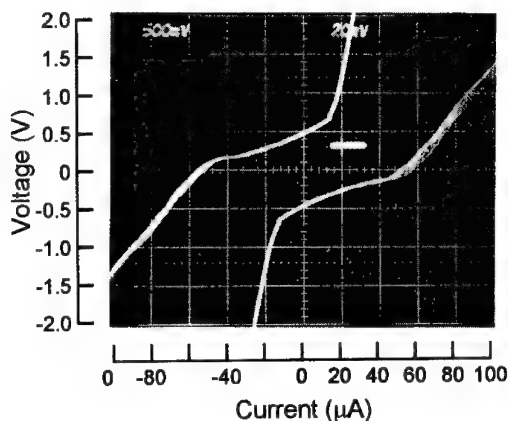


Fig. 3. Hysteretic current voltage characteristic of a Josephson series array with 1848 tunnel junctions induced by a microwave of 70 GHz. The constant voltage step at 350 mV was recorded with a much higher voltage resolution of 100  $\mu$ V/div.

The hysteretic IVC of the whole series array (1848 tunnel junctions) under the influence of a 70 GHz microwave is shown in Fig. 3. Note that the constant voltage step included in the curve was taken with a voltage resolution of the oscilloscope of 100  $\mu$ V/div. The maximum voltage which could be reached with stable steps was

350 mV. The step amplitudes were up to 20  $\mu\text{A}$ . Looking at the different blocks of the circuit, we found that the first block reached constant voltage steps up to 50 mV, whereas with the last block of junctions — due to the attenuation of the microwave — voltage steps up to 35 mV could be obtained. Averaging over all blocks, and taking into account that 132 junctions were missing, gives the 350 mV which could be observed for the whole circuit.

The voltage steps realised were lower than expected (100 mV per block). We suppose that this is due to an inhomogeneous distribution of the microwave within one block. Further experiments will be carried out at 70 GHz to examine and eliminate this problem.

#### 4.2. Measurements with the X-Band Oscillator (10 GHz)

A sample with two Josephson tunnel junctions designed for a microwave frequency of 10 GHz was hybrid integrated with the stripline oscillator. The tunneling area of the junctions is  $80\text{ }\mu\text{m} \times 200\text{ }\mu\text{m}$ ,  $j_C = 6.7\text{ A/cm}^2$ .

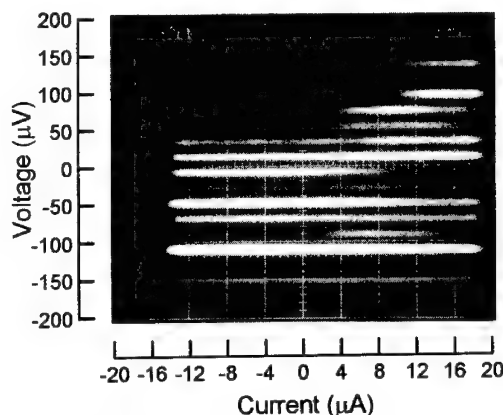


Fig. 4. Set of microwave-induced voltage steps at  $f_{HF} = 9.82\text{ GHz}$  for a sample with two Josephson junctions.

Fig. 4 shows a set of microwave-induced voltage steps of the SMMIC operated at  $f_{HF} = 9.82\text{ GHz}$  and with a HF-power of 1.7 mW. The difference between adjacent steps is 20  $\mu\text{V}$ , but the sample could only be driven near the chaotic regime. This is due to the fact that the plasma frequency  $f_P = 9.27\text{ GHz}$  of that sample was not sufficiently below the driving frequency. According to the work of Meyer et al.<sup>12</sup>,  $f_P$  should have been smaller than 6.6 GHz to achieve stable steps with 0.5 mV per junction. To reach this value with Nb/Al<sub>2</sub>O<sub>3</sub>/Nb-tunnel junctions the Josephson current density has to be reduced by a factor of 2 to  $\approx 3.4\text{ A/cm}^2$ .

In another experiment, we used a Josephson circuit with 12 tunnel junctions which was designed for 10 GHz at IPHT in Jena, Germany. The fabrication of this sample had been effected in Nb/Nb<sub>x</sub>O<sub>y</sub>/PbInAu-technology at the University of Jena. The Josephson current density of this sample was also  $j_C = 6.7 \text{ A/cm}^2$  but, due to the higher specific capacitance of Nb/Nb<sub>x</sub>O<sub>y</sub>/PbInAu-junctions, the resulting plasma frequency  $f_P = 7.18 \text{ GHz}$  was well below the microwave frequency of the oscillator (9.82 GHz).

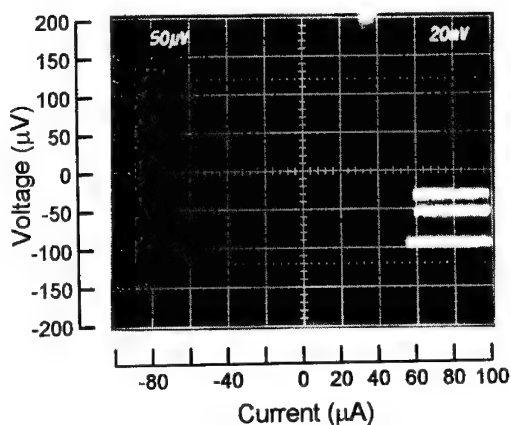


Fig. 5. Microwave-induced constant voltage steps at 9.82 GHz for a sample with 12 Josephson junctions. The absolute voltage of the steps was near 6 mV.

The sample showed stable constant voltage steps up to 7.4 mV, i.e. 0.62 mV per junction. The amplitude of the voltage steps reached 100  $\mu\text{A}$ . Fig. 5 shows 3 constant voltage steps which were taken at an absolute voltage of  $\approx 6 \text{ mV}$ .

#### Acknowledgements

This work was supported by the German Bundesministerium für Forschung und Technologie under Grant No. 13N6142. We thank H.-G. Meyer and H.-J. Köhler of the IPHT in Jena and K. Blüthner of the Friedrich-Schiller-Universität in Jena for delivering a sample. The help of J. Kohlmann, Th. Weimann and H. Wolf is gratefully acknowledged.

#### References

1. C. A. Hamilton, R. L. Kautz, M. Stieg, K. Chiek, W. F. Avrin, M. B. Simmonds, "A 24-GHz Josephson Array Voltage Standard", *IEEE-IM* 40 (1991) 301-304

2. Y. Sakamoto, H. Yoshida, T. Sakuraba, A. Odawara, Y. Murayama, T. Endo, "Josephson Junction Array Voltage Standard at the ETL", *IEEE-IM* **40** (1991) 312-316
3. R. Pöpel, J. Niemeyer, R. Fromknecht, W. Meier, L. Grimm, F. W. Dünschede, "Nb/Al<sub>2</sub>O<sub>3</sub>/Nb Josephson Voltage Standards at 1 V and 10 V", *IEEE-IM* **40**, (1991) 298-300
4. E. Vollmer, P. Gutmann, J. Niemeyer, "Characterisation of a GaAs MESFET Oscillator at 4.2 K", *IEEE Appl. Supercond.* **3** (1993) 2828-2831
5. E. Vollmer, P.G. Gutmann, J. Niemeyer, "Hybrid Integration of a Microwave Oscillator with a Josephson Series Array", *IEEE-IM* **42** (1993) 600-602
6. P. Gutmann, E. Vollmer, J. Kohlmann, D. Quenter, J. Niemeyer, "Hybrid integration of a microwave MESFET oscillator and a Josephson tunnel junction", *Cryogenics* **33** (1993) 1005-1007
7. P. Gutmann, E. Vollmer, J. Kohlmann, F. Müller, T. Weimann, J. Niemeyer, "Implementation of Josephson Tunnel Junction Series Array Stripline with high characteristic Impedance for Quantum Voltage Standards", *Electron. Lett.* **28** (1992) 1422-1423
8. F. Müller, F. X. Hebrank, J. Niemeyer, J. Kohlmann, H. Wolf, T. Weimann, "Performance of Josephson Array Systems Related to Fabrication Techniques and Design", submitted to *IEEE Appl. Supercond.*
9. E. Vollmer, P. Gutmann, "X-Band GaAs MESFET Oscillator for cryogenic Application at 4.2 K", *Electron. Lett.* **27** (1991) 2210-2211
10. M. G. Blamire, J. E. Evetts, D. G. Hasko, "A new Self-Aligning Process for Whole Wafer Tunnel Junction Fabrication", *IEEE Trans. Magn.* **25** (1989) 1123-1126
11. Y. Sakamoto, "Experimental study on millimeter wave attenuation in Josephson junction striplines for voltage standards", *PTB Mitteilungen* **104** (1994) 151-157
12. H.-G. Meyer, H.-J. Köhler, F. Müller, K. Blüthner, P. Weber, A. Chwala, "Josephson Voltage Standard at low Drive Frequencies", *IEEE Appl. Supercond.* **3** (1993) 1870-1873



# DISCRETE VORTEX FLOW TRANSISTORS USING ELECTRON-BEAM SCRIBED JOSEPHSON JUNCTIONS IN YBCO

BRUCE A. DAVIDSON, R. D. REDWING, T. NGUYEN, J. E. NORDMAN

*Department of Electrical and Computer Engineering*

*University of Wisconsin - Madison*

*Madison, WI 53706, USA*

## ABSTRACT

Discrete versions of the well-known Vortex Flow Transistor (VFT) have recently attracted much attention, as implemented both in low-temperature superconductors (LTS)<sup>1</sup> and high-temperature superconductors (HTS)<sup>2,3</sup>. In general, individual grain boundary Josephson junctions in HTS have shown non-uniform critical current distributions and lack reproducibility in fabrication<sup>4</sup>. Furthermore, from a device perspective, the most desirable of these ( $\sim 12$ – $18^\circ$  bicrystal junctions) are difficult to fabricate in arbitrary array geometries. To resolve these shortcomings and to allow prototyping of devices using uniform and reproducible junctions, we have investigated the properties of junctions produced by scribing  $Y_1Ba_2Cu_3O_7$  (YBCO) with a focussed electron beam<sup>5,6</sup>. Resistively Shunted Junction (RSJ)-like behavior is observed within a certain temperature window below  $T_{c0}$  ( $\sim 10$  K) for a certain range of electron dose ( $\sim 1$ – $4 \times 10^{12}$  electrons/ $\mu\text{m}$ ), even for a critical current density as high as  $2 \times 10^5$  A/cm<sup>2</sup>. The operating temperature can be chosen anywhere between 4.2 K to above 77 K by means of an appropriate low-temperature anneal following the scribing. We discuss the nature of individual junctions formed by this technique, as well as the potential for such junctions placed in parallel arrays and configured as a discrete VFT (DVFT), evaluating device parameters such as transresistance, current gain, maximum output voltage and output resistance. Comparison is made to previously published results on DVFTs, indicating the usefulness of this technique for the study of this device in HTS.

## 1. INTRODUCTION

Practical devices at liquid nitrogen temperatures that can interface between superconducting and semiconducting electronics are required in certain foreseeable applications, for example between RSFQ and CMOS circuitries. At 77 K, HTS thin film junctions reported to date have small damping parameters and thus exhibit non-hysteretic current versus voltage (I-V) characteristics. Thus, devices analogous to the LTS Superconducting Current-Injection Transistor (SCIT)<sup>7</sup>, which utilize a long junction that is artificially shunted to be non-hysteretic, are the first to receive attention<sup>2,3</sup>. Typically, VFTs based on single long Josephson junctions in HTS materials (whether grain boundary, edge-type, or electron beam scribed) do not offer sufficient voltage swing or impedance levels to match to CMOS devices, and one solution may be the use of arrays of junctions. In turn, the experimental study of two

dimensional arrays of Josephson junctions in YBCO thin films requires a controllable and reproducible junction technology.

High-angle grain boundary techniques (such as step-edge and biepitaxial<sup>4</sup>) yield low critical current density ( $J_c$ ) junctions, not desirable from a device point of view, compounded by problems of reproducibility. Bicrystal grain boundary junctions appear to be more uniform and reproducible<sup>4,8</sup>, showing an increasing  $J_c$  with decreasing bicrystal angle, but this technique seriously constrains the 2D array geometries which can be studied. A desirable technique would combine uniform junctions operating at liquid nitrogen temperatures with the ability to place junctions in arbitrary 2D array geometries. Even better would be the realization of junctions whose critical current-normal resistance ( $I_c R_n$ ) product approaches the gap voltage of some 20 mV. While there are reports in the literature of an  $I_c R_n$  product of 10 mV at 4.2 K in SNS junctions using Au as the normal metal<sup>9,10</sup>, this goal remains elusive for all other techniques. Setting aside this latter question, one technique which appears to satisfy these basic device requirements is the creation of Josephson junctions by scribing with a focussed electron beam.

## 2. E-BEAM JUNCTION CHARACTERISTICS

### 2.1. Experimental Technique

The films used in this study were 200-500 Å YBCO films grown on Lanthanum Aluminate (LAO) by Pulsed Laser Deposition (PLD) in our lab. They were patterned into 4 to 10 links each 2-10  $\mu\text{m}$  wide by conventional photolithography and Ar-ion milling, as described earlier<sup>11</sup>. Before scribing, the films had a  $T_c$  of 89-90 K, a  $J_c$  of  $5 \times 10^6$  A/cm<sup>2</sup> at 77 K and a room temperature resistivity  $\rho_n$  of 250  $\mu\Omega\text{-cm}$ . A 20 Å layer of Ag or Au was deposited to avoid charging during scribing, which was removed by a brief Ar ion milling prior to testing. Control links (not scribed but immediately adjacent to the scribed links) were monitored to assure that the processing before, during and after the microscope didn't alter the film properties. These links had the typical flux-flow shaped I-V curves and the usual low sensitivity to small magnetic field as seen previously<sup>11</sup>.

The links were irradiated in a JOEL 200CX Scanning/Transmission Electron Microscope (STEM) in high resolution mode equipped with a  $\text{LaB}_6$  filament. Prior to scribing, care was taken to align and focus the beam to reach its specified beam diameter of about 20 Å. Beam current as measured by a Faraday cup fixture was typically 0.4 nA. A variety of energies were used between 120 and 200 keV. At the beginning of this study the beam was scanned repeatedly across the links for the duration of exposure (5 to 90 minutes), and later the scan coils were interfaced to a digital-to-analog converter (DAC) board in a PC to allow a single programmed scan across the links (see below). A carbon residue was always observed following the scanning procedure, identifying the junction location.

The links were tested in a variable temperature test station which allowed four-

point measurement of transport properties down to 4.2 K in a uniform magnetic field up to  $\sim 100$  G, or under microwave irradiation. A mu-metal shield surrounding the sample reduced the residual DC magnetic field to about 10 mG. A lockin amplifier setup was used to provide voltage sensitivity of order nanovolts in a dynamic resistivity measurement, and was used to measure both resistance versus temperature (R-T) and dynamic resistivity versus bias current. The latter was integrated directly to obtain the I-V characteristics shown below. Data were acquired by LabView software on a Macintosh IIfx (outside the screen room) connected on a GPIB bus to the measurements electronics. Temperature was controlled to within 50 mK by a Lakeshore Model 330 temperature controller using a Si diode sensor.

## 2.2. Junction Characteristics

Early tests using irradiation by multiple scans of the electron beam (linescan mode) showed no evidence of Josephson coupling across the scribed region, although a creation of a "foot" of a few Ohms in the R-T curve could be controllably produced. The resistance of the foot, as well as the  $T_{c0}$ , could be correlated to the electron fluence. The lack of coupling and the presence of the foot were attributed to a damaged region that was wide enough with respect to the coherence length in the a-b plane  $\xi_{ab}$  to preclude Josephson coupling. It was observed that, even when the STEM electronics and scan coils were allowed to thermally stabilize for several hours, there was a noticeable drift of the beam position in the direction perpendicular to the scan. This drift could easily be 100 to 500 Å over the duration of irradiation, which would distribute the damage over a larger volume than desired.

To eliminate the problem of drift, a single scan was performed by stopping the beam at an number of equally spaced points across the link for a certain dwell time. In this manner, drift is not expected to affect the irradiated region unless the drift during a dwell time prevents two adjacent points from overlapping sufficiently. Since the dwell time is typically 1 second, the center-to-center spacing between points is typically 30 Å, and the extent of the damaged region is  $\sim 200$  Å<sup>5,6</sup>, a single scan will likely eliminate the problem of drift. Some "waviness" of the line of the junction is possible through drift, but this not expected to alter the behavior of the junction if the "waviness" is on a scale much less than the Josephson penetration depth  $\lambda_J$ . All the results discussed here involve links irradiated with a single scan.

Following scribing with the electron beam, for a dose larger than  $\sim 10^{11}/\mu\text{m}$  a "foot" appears in the R-T curve whose resistance times area (RA) product scales linearly with dose. Typically a dose of  $1 \times 10^{12}/\mu\text{m}$  creates an RA product of  $2 \times 10^{-9}$  Ω-cm and a  $T_{c0} \sim 65$  K, as shown in Figure 1. This RA product is similar to the lowest values given in the literature for grain boundary junctions and epitaxial SNS edge junctions<sup>4</sup>. A brief anneal at 100° C for 30 minutes in  $O_2$  can recover  $T_{c0}$ , for example increasing a  $T_{c0}$  from 44 K to 74 K.

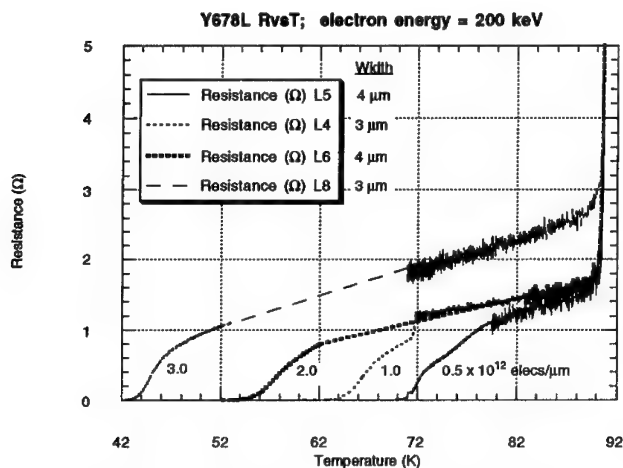


Figure 1. R-T following electron beam scribing.

The I-V curves of irradiated links can show a variety of behaviors. If the beam width is too large (the damaged region is too wide), the original flux-flow-shaped I-V curve can become quite linear, and show somewhat more sensitivity to small magnetic fields than the original link. Similar behavior is observed in links that are irradiated with a sufficiently tight beam, but below the threshold dose for junction formation. This threshold (linear) dose (at 200 keV) is about  $1 \times 10^{12}$  electrons/ $\mu\text{m}$  in our microscope with our beam conditions, which corresponds to an irradiation time of  $\sim 10$  minutes for a  $2 \mu\text{m}$  link. At present it is not clear what mechanism is responsible for such a linear I-V curve below threshold, nor which oxygen displacement above threshold is responsible for the observed Josephson coupling<sup>5,6</sup>.

In the range of doses  $1\text{--}4 \times 10^{12}/\mu\text{m}$ , there is a temperature window of less than 10 K where RSJ-like behavior is observed, persisting to critical current densities in excess of  $2 \times 10^5 \text{ A/cm}^2$ . Shown in Figure 2 is the I-V curve of an annealed link at a temperature  $\sim 2.5 \text{ K}$  below  $T_{c0}$ . The critical current in magnetic field shows a saturated  $I_c$  at fields larger than a few Gauss, consistent with long junction behavior, as expected since the Josephson penetration depth  $\lambda_J$  is less than  $1 \mu\text{m}$  at this  $J_c$ . At lower temperatures the I-V curve assumes a flux-flow-like curvature and sensitivity to small magnetic fields decreases significantly. A more detailed study of critical current as a function of magnetic field in this RSJ window, as well as the characteristics of this RSJ- to flux-flow transition, will be published separately.

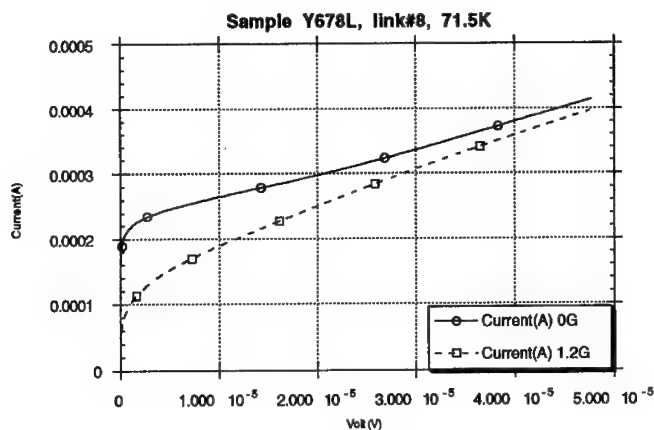


Figure 2. I-V curve of 3  $\mu\text{m}$  wide junction in field.

### 3. DISCRETE VORTEX FLOW TRANSISTOR

#### 3.1. Analysis

The discrete Vortex Flow Transistor (DVFT) can be considered an N-junction interferometer configured with a control (or "gate") current line, shown schematically in Figure 3. It can be recognized that the N-junction interferometer is the circuit equivalent to a long Josephson transmission line when the (dimensionless) Josephson penetration depth  $\Lambda_J = \sqrt{L_j/L_s}$  is much greater than 1. Here the penetration depth is scaled to the cell size,  $L_s$  is the loop inductance and  $L_j = \Phi_0/2\pi I_c$ . When this characteristic length approaches 1, the discreteness of the equivalent circuit becomes important and the fluxon dynamics change. Two conceivable geometries for the gate line are the "parallel" gate, which couples to the length of the array, and the "loop" gate which couples only to one end. In the "parallel" gate the magnetic coupling between the gate line and the array is uniform, whereas in the "loop" geometry the flux is coupled primarily to the first few cells of the array. Berman et al<sup>1</sup> have applied a simple model that predicts well the basic behavior (current gain, transresistance, etc.) of the devices they have fabricated in Nb, as well as published HTS grain boundary-based DVFTs of Satchell and Humphreys et al<sup>2</sup> and Alff et al<sup>3</sup>. Using this model one can predict the behavior of devices built using different HTS Josephson junction technologies, for example, electron beam scribed junctions or the high  $I_c R_n$  junctions reported by Rosenthal et al<sup>9</sup>. As discussed below, the higher  $I_c$ s achievable with SNS Josephson junctions or electron beam scribed junctions offer certain advantages over

their grain boundary counterparts. Note the following discussion assumes Berman's convention where individual junction properties are denoted by capital letters and array properties by small letters.

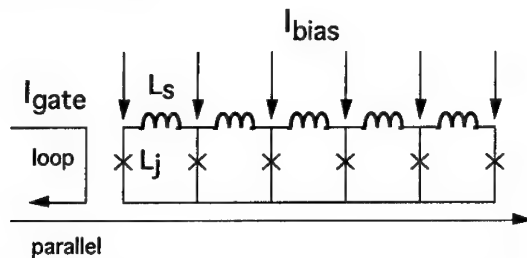


Figure 3. Schematic of DVFT with control line geometries.

The Berman model is straightforward. Each junction in the array is assumed identical and described by (known) non-hysteretic RSJ characteristics (i.e., Stewart-McCumber damping parameter  $\beta_c \sim 1$  or less). Since the coupled equations for the phases of each junction linearize<sup>12</sup>, the resulting I-V characteristic of the array is likewise RSJ, described by the equation  $v = r_{eq} \sqrt{i^2 - i_c^2}$ , where  $i_c$  represents the array critical current and  $r_{eq}$  is the equivalent resistance of  $N$  individual junctions in parallel (including any added shunt resistance). A priori, the suppression of the array critical current in an applied magnetic field for arbitrary  $\Lambda_J$  is not known, and so must be estimated or measured experimentally. Once this is known, all relevant (low-frequency) characteristics of the device can be predicted. The maximum voltage swing  $v_{max}$  occurs when the array is biased near  $i_{co}$  (the array critical current in zero applied field) and when the critical current is suppressed much below  $i_{co}$ . It is then  $v_{max} \simeq r_{eq} i_{co} = R_n I_{co}$ , i.e., it is equal to the critical voltage of an individual junction. The output resistance  $r_o = \partial v / \partial i \simeq r_{eq}$  from the above RSJ equation. The current gain is defined as  $G = -\partial i / \partial i_g$  ( $i_g$  is the gate current), and thus the transresistance  $r_m = \partial v / \partial i_g \simeq r_{eq} G i_c / \sqrt{i_{co}^2 - i_c^2}$  when biased near  $i_{co}$ . For both  $G$  and  $r_m$ , the behavior of the array critical current as a function of the gate current must be known.

Berman approximates the suppression of the array critical current due to a gate current from experimental data in uniform field. First, the gate-line generated magnetic flux which threads the array is calculated and then divided by the number of cells to give the average flux per cell. Then, the suppression of the array critical current is estimated from measurements of the array critical current in a uniform applied magnetic field. The uniform data is characterized by the "frustration" of each cell, that is, the fraction of a half flux quantum each cell contains. They show that the suppression of  $i_c$  is a (linear) function of  $\Lambda_J$ , thus allowing a prediction of the gain and transresistance as the inductance ratio is varied. This approximation is expected to be reasonable in the "parallel" gate line configuration because the generated flux is the same for all cells, but not in the "loop" geometry where most of the flux is

contained in the first one or two cells. McGinnis<sup>13</sup> and Yoshida<sup>14</sup> have shown that, in a SCIT configuration, it is necessary to couple the flux only to the first few  $\lambda_J$  of the long junction to produce the same measured gain and transresistance, which cannot be accounted for without a modification to the model. We also note that this correlation between suppression of array critical current and  $\Lambda_J$  is measured only for the case of uniform bias current; a non-uniform bias current distribution would be expected to behave quite differently<sup>12</sup>, amongst other effects showing an increase in the small-signal current gain.

The important conclusions of this (low frequency) analysis are first, the DVFT has an optimum  $\Lambda_J$  of  $\leq 1$  cell. Second, like its continuous long junction counterpart, the DVFT has a (large signal) current gain which increases linearly with the array length (i.e., number of cells), and an output resistance which decreases linearly in length. Thus, from this analysis, a current gain larger than one is readily achievable with  $N \geq 5$ . Small signal current gain, under non-uniform bias conditions, could be much larger. They cite the potential advantage of using high- $J_c$  Nb junctions (such as required for RSFQ circuitry), which are intrinsically non-hysteretic, which may significantly improve the current gain and output voltage, the latter because the full gap voltage of 1.75 mV can be reached.

### 3.2. Comparison with Experimental Results

This model does reasonably well predicting the measured current gain of their LTS devices, as well as some parallel-gate DVFTs based on grain boundary Josephson junctions in HTS from the literature, as shown in Table 1. In the first column are the parameters of the Nb DVFT, taken from the original Berman work. In the second column are their estimates of analogous parameters for the Nb SCIT<sup>7</sup>. In the third column are the measured parameters of the YBCO Flux Flow Transistor<sup>8</sup> using a continuous long bicrystal grain boundary junction on YSZ. In the fourth column are the parameters of the YBCO DVFT of Satchell et al using grain boundary junctions on MgO<sup>2</sup>. In the fifth column are the parameters of the YBCO DVFT of Alff et al using bicrystal grain boundary junctions on STO<sup>3</sup>. In the last three columns are the projected device characteristics of DVFTs based on 1) high- $J_c$  Nb junctions<sup>1</sup>; 2) electron beam scribed junctions<sup>5</sup>; and 3) high- $I_c R_n$  SNS step-edge junctions<sup>9</sup>. These might represent the limiting low-frequency behavior of DVFTs based on technologies existing at the time of this writing.

To minimize the transit time, small values of the loop inductance are desirable since the phase velocity on the transmission line is inversely proportional to its inductance per unit length. In turn, small values of junction inductance (large junction critical currents) are required to keep  $\Lambda_J$  less than one.

Thus, a larger gain can be achieved by adding more cells, though at the expense of a longer transit time for vortices. Also we note that the phase velocity on a discretely constructed long junction transmission line will be slower than on a continuous long junction (made of identical junction parameters) because the inductance per unit length will always be larger in the discrete case. Thus, although one sacrifices gain

and bandwidth in comparison to the SuperCIT, one can achieve a larger output resistance, which is of considerable practical importance. For example, taking the gain  $G$  of a SuperCIT as  $(a/2\lambda_J) - 1^7$ , the gain-bandwidth product (fabricated from high  $J_c$  Nb junction technology, and ignoring Fiske and Shapiro resonances) has an upper bound around 100 GHz. The gain-bandwidth product for an analogous DVFT would be lower by a factor of  $\sim 5$ , due to the lower phase velocity (longer transit time) and lower gain per unit length. But a realistic output resistance of a few  $\Omega$  is reasonable, larger than the continuous device by an order of magnitude or more. As such, the circuit designer would have more flexibility to choose the appropriate device for a given application.

parameter	Nb DVFT	Nb SCIT	YBCO FFT	YBCO DVFT	YBCO DVFT	DVFT high $J_c$	ebeam	SNS high $I_c R_n$
reference	[1]	[1]	[8]	[2]	[3]	[1]	[5]	[9]
$J_c(A/cm^2)$	450	1000	20000	2700	80000	45000	100000	70000
$A_j(\mu m^2)$	9	[75]		0.3	0.3	0.22	0.2	0.4
$I_c(mA)$	0.04	[0.75]		0.008	0.24	0.1	0.2	0.28
$R_n(\Omega m)$	43	[2.7]		8.5	5.4	17.5	2	36
$R_s(\Omega m)$	5	[0.8]						
$I_c R_n(mV)$	0.2			0.07	1.3	1.75	0.4	10
$C(fF)$	405	[640]		0.1	0.1	10	0.1	0.1
$L_j(pH)$	8	[0.44]			1.3	3.3	1.6	1
$L_s(pH)$	14	[0.44]		40	10	14	6	6
$\lambda_{mda}/p$	0.77	[1]		6	0.4	0.5	0.5	0.4
$N$	9	[30]		5	11	9	7	7
$i_c(mA)$	0.37	22.5	1.2	0.04	2.64	0.9	1.4	1.96
$r_{eq}(\Omega m)$	0.55		0.7	1.7	0.5	1.94	0.3	5
$i_{crn}(mV)$	0.2		0.8	0.07	1.3	1.75	0.4	10
$p(\mu m)$	10	[25]		4	3.5	10	6	6
$l(\mu m)$	80	750	30	16	35	80	35	35
Temp(K)	4	4	30	77	30	4	77	4
$r_m(\Omega m)$	0.43	0.2	1.2	0.23	0.5	2.7	0.5	5
$G_{par, meas}$	1.2	10	1.8	0.14	1-1.3*			
$G_{par, calc}$	1.66	15		0.14	1.4	2.8	1.7	3
$G^* \lambda_{mda}$	0.15*N			0.07*N	0.05*N		0.17*N	0.17*N
Gloop	0.35					0.52		
$V_{max}(mV)$	0.15	0.2	0.8	0.015	1.3	1.75	0.4	10
$r_o(\Omega m)$	0.55	0.025	1	1.7	0.5-1	2	0.3	5
$\tau(ps)$	50	100				5	10	10

Table 1. Comparison of parameters of various published or proposed VFTs.

\*indicates gain measured from large features of the I-B curve; the fine features show a gain of 5 over a small dynamic range.



#### 4. CONCLUSIONS

Development of device technology in HTS requires a reproducible and flexible technique to produce Josephson junctions. We have fabricated Josephson junctions in YBCO by scribing with a focussed electron beam which exhibit characteristics that are RSJ-like and tunable over a large temperature range. These junctions offer flexibility in prototyping potential devices, such as the DVFT. An analysis based on the model of Berman et al works adequately to predict the measured behavior of certain published DVFT devices. This analysis is then extended to proposed DVFTs, based on electron beam scribed and high- $I_c R_n$  SNS junctions each of which show certain advantages over their grain-boundary counterparts. We note that existing low frequency measurements show promising behavior for these devices, but at the current time there are no experimental measurements at high frequencies. Though such measurements are by no means trivial, they are necessary in evaluating their real potential, and are the subject of future work.

#### Acknowledgements

We gratefully acknowledge useful discussions with G. K. G. Hohenwarter, J. B. Beyer, and J-U. Lee, and technical assistance from G. A. Daniels. BAD acknowledges the helpful support of A. Ruosi throughout this process. This work is supported in part by the Air Force Office of Scientific Research (AFOSR) under grant number AFOSR-91-0396.

1. D. Berman, H. S. J. van der Zant, T. P. Orlando, and K. A. Delin, *IEEE Transactions on Applied Superconductivity* **4** (3) (1994) p. 161.
2. J. S. Satchell, R. G. Humphreys, J. A. Edwards, and N. G. Chew, *IEEE Transactions on Applied Superconductivity* **3** (1993) p. 2273.
3. L. Alff, B. Mayer, S. Schuster, O. Frohlich, R. Gerdemann, A. Beck, and R. Gross, *Journal of Applied Physics* **75** (1994) p. 1843.
4. R. Gross, in *Interfaces in Superconducting Systems*, eds. S. L. Shinde and D. A. Rudman, (Springer-Verlag, New York, 1992), Ch. 6.
5. S. K. Tolpygo, S. Shokhor, B. Nadgorny, J.-Y. Lin, and M. Gurvitch, *Applied Physics Letters* **63** (12) (1993) pp. 1696-8.
6. A. J. Pauza, A. M. Campbell, D F. Moore, R. E. Somekh and A. N. Broers, in the proceedings of the *XXth International Conference on Low Temperature Physics*, Eugene, Oregon, USA, 4-11 Aug 1993.
7. B. J. van Zeghbroeck, *Applied Physics Letters* **39** (1983) pp. 736-8.
8. Y. M. Shang, D. Winkler, P. A. Nilsson, and T. Claeson, *Applied Physics*

- Letters* **64** (9) (1994) pp. 1153-5.
9. P. A. Rosenthal, E. N. Grossman, R. N. Ono, and L. R. Vale, *Applied Physics Letters* **63** (14) (1993) pp. 1984-6.
  10. M. G. Forrester, J. Talvecchio, and J. R. Gaines, *IEEE Transactions on Magnetism* **27** (1991) pp. 3098-3101.
  11. B. A. Davidson, R. D. Redwing, T. N. Nguyen, J. O'Callaghan, F. Raissi, J. U. Lee, J. P. Burke, G. K. G. Hohenwarter, J. E. Nordman, J. B. Beyer, S. H. Liou, J. Eckstein, M. P. Seigal, S. Y. Hou, and J. M. Phillips, *IEEE Transactions on Applied Superconductivity* **4** (1994) pp. 228-35.
  12. K.K. Likharev, *Dynamics of Josephson Junctions and Circuits* (Gordon and Breach Scientific Publishers, New York, 1986), Ch. 8.
  13. D. McGinnis, Ph. D. thesis, University of Wisconsin - Madison, 1988.
  14. K. Yoshida, T. Nagatsuma, K. Sueoka, K. Enpuku, and F. Irie, *IEEE Transactions on Magnetism* **21** (2) (1985).